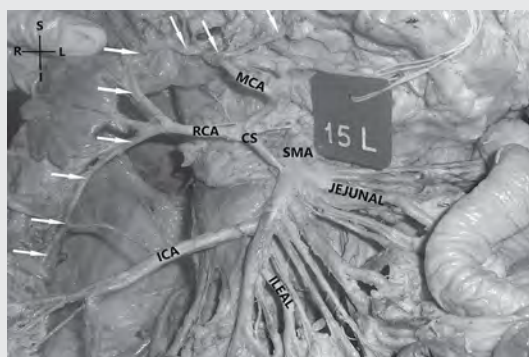


*ISSN 0015-5659*  
*eISSN 1644-3284*  
*Impact Factor: 1.183*

*POLISH ANATOMICAL SOCIETY*

# **FOLIA** **MORPHOLOGICA**



*Vol. 81      2022      No. 2*

  
VIA MEDICA

[https://journals.viamedica.pl/fovia\\_morphologica](https://journals.viamedica.pl/fovia_morphologica)

# FOLIA MORPHOLOGICA

An international multidisciplinary journal devoted to fundamental research in the morphological sciences

Official Journal of the Polish Anatomical Society

(a Constituent Member of European Federation for Experimental Morphology — EFEM)

EDITOR-IN-CHIEF

Janusz Moryś

Department of Normal Anatomy,

Pomeranian Medical University, Szczecin, Poland

**[https://journals.viamedica.pl/folia\\_morphologica](https://journals.viamedica.pl/folia_morphologica)**

*See our website for information on manuscript status, aims and scope,  
instructions for authors as well as editorial board.*

## Folia Morphologica

Publishing, Subscription and Advertising Office:

VM Media sp. z o.o. VM Group sp.k., Grupa Via Medica

ul. Świętokrzyska 73, 80–180 Gdańsk, Poland

tel. (+48 58) 320 94 94, fax (+48 58) 320 94 60

Managing editor

Joanna Niezgoda

e-mail: [joanna.niezgoda@viamedica.pl](mailto:joanna.niezgoda@viamedica.pl)

Cover designer

Sylvia Scisłowska

The journal is published at: [www.fm.viamedica.pl](http://www.fm.viamedica.pl) in one volume per year consisting of four numbers. **Subscription rates:** Paper subscription, 4 issues incl. package and postage institutional — 140 euro. The above prices are inclusive of regular postage costs. Payment should be made to: VM Media sp. z o.o. VM Group sp.k., Grupa Via Medica, Bank BGŻ Paribas SA account number: 15 1600 1303 0004 1007 1035 9021; SWIFT: PPABPLPK. Single issues, subscriptions orders and requests for sample copies should be send to e-mail: [prenumerata@viamedica.pl](mailto:prenumerata@viamedica.pl). Electronic orders option available at: [https://journals.viamedica.pl/folia\\_morphologica](https://journals.viamedica.pl/folia_morphologica). The publisher must be notified of a cancellation of access to electronic version not later than two months before the end of a calendar year. After that date electronic access will be automatically prolonged for another year.

**Advertising.** For details on media opportunities within this electronic version of journal please contact the advertising sales department, ul. Świętokrzyska 73, 80–180 Gdańsk, Poland, tel: (+48 58) 320 94 94, e-mail: [viamedica@viamedica.pl](mailto:viamedica@viamedica.pl)

The editors accept no responsibility for advertisement contents.

**Folia Morphologica** is the official journal of the Polish Anatomical Society. For information about the Society, please contact: Prof. Marek Grzybiak, Department of Clinical Anatomy, Medical University of Gdansk, ul. Dębinki 1, 80–211 Gdańsk, Poland, tel: +48 58 349 14 22, e-mail: [grzybiak@gumed.edu.pl](mailto:grzybiak@gumed.edu.pl)

All rights reserved, including translation into foreign languages. No part of this periodical, either text or illustration, may be used in any form whatsoever. It is particularly forbidden for any part of this material to be copied or translated into a mechanical or electronic language and also to be recorded in whatever form, stored in any kind of retrieval system or transmitted, whether in an electronic or mechanical form or with the aid of photocopying, microfilm, recording, scanning or in any other form, without the prior written permission of the publisher. The rights of the publisher are protected by national copyright laws and by international conventions, and their violation will be punishable by penal sanctions.

Editorial policies and author guidelines are published on journal website: [https://journals.viamedica.pl/folia\\_morphologica](https://journals.viamedica.pl/folia_morphologica)

Legal note: [https://journals.viamedica.pl/folia\\_morphologica/about/legalNote](https://journals.viamedica.pl/folia_morphologica/about/legalNote)

**Folia Morphologica** is indexed by: BIOSIS Previews, CAS, CINAHL, CrossRef, Dental Abstracts, EBSCO, Elsevier BIOBASE, EMBIOLOGY, FMJ, Google Scholar, Index Copernicus (160.66), Index Medicus/MEDLINE, Index Scholar, Ministry of Science and Higher Education (70), NCBI/National Center for Biotechnology Information, Polish Medical Bibliography, Scopus, SJR, Thomson Reuters, Thomson Scientific Products — Biological Abstracts, Ulrich's Periodicals Directory, Veterinary Bulletin, WorldCat and Zoological Record. Position in Index Copernicus ranking systems is available at: [www.indexcopernicus.com](http://www.indexcopernicus.com). Current Impact Factor of Folia Morphologica (2020) is 1.183.



# FOLIA MORPHOLOGICA

Editor-in-Chief  
**JANUSZ MORYŚ**

Department of Normal Anatomy, Pomeranian Medical University  
Al. Powstańców Wielkopolskich 72, 70-110 Szczecin, Poland  
tel. (+48 91) 466 15 43, e-mail: jmorys@pum.edu.pl

## EDITORIAL ADVISORY BOARD

**Rafael BOSCOLO-BERTO**, Department of Neuroscience,  
University of Padova, Italy

**Franciszek BURDAN**, Experimental Teratology Unit  
of the Human Anatomy Department, Medical University  
of Lublin, Poland

**Małgorzata BRUSKA**, Department of Anatomy,  
University Medical School, Poznań, Poland

**Mafalda CACCIOTTOLO**, USC Leonard Davis School  
of Gerontology, University of Southern California,  
Los Angeles, United States

**Stephen W. CARMICHAEL**, Department of Anatomy,  
Mayo Clinic, Rochester, United States

**Bogdan CISZEK**, Department of Human Anatomy,  
Medical University of Warsaw, Poland

**Om Prakash CHOUDHARY**, Department of Veterinary Anatomy  
and Histology, Central Agricultural University, Aizawl, India

**Carla D'AGOSTINO**, Neuromuscular Center, University  
of Southern California, Los Angeles, CA, United States

**Halina DOBRZYNSKI**, Cardiovascular Sciences, Faculty of Biology,  
Medicine and Health, University of Manchester, United Kingdom

**Zygmund Antoni DOMAGAŁA**, Department of Anatomy,  
Medical University of Wrocław, Poland

**Rastislav DRUGA**, Department of Functional Anatomy,  
2<sup>nd</sup> Medical Faculty Charles University, Prague, Czech Republic

**Sergio Domenico GADAU**, Department of Veterinary Medicine,  
University of Sassari, Italy

**Marek GRZYBIAK**, Elbląg University of Humanities and  
Economics, Elbląg, Poland

**Hans Jorgen GUNDERSEN**, Stereological Research  
Laboratory, University of Aarhus, Denmark

**Kazimierz JĘDRZEJEWSKI**, Department of Anatomy,  
Medical University of Łódź, Poland

**Leszek KACZMAREK**, Department of Molecular Cell  
Neurobiology, Nencki Institute, Warsaw, Poland

**Zbigniew KMIEĆ**, Department of Histology,  
Medical University of Gdańsk, Poland

**Henryk KOBRYŃ**, Department of Morphological Sciences,  
Warsaw, Agricultural University, Poland

**Przemysław KOWIAŃSKI**, Department of Human Anatomy  
and Physiology, Pomeranian University in Słupsk, Poland

**Dariusz KOZŁOWSKI**, 2<sup>nd</sup> Department of Cardiology,  
Medical University of Gdańsk, Poland

**Marios LOUKAS**, Department of Anatomical Sciences, School  
of Medicine, St. George's University, Grenada, West Indies

**Andrzej ŁUKASZYK**, Department of Histology and Embryology,  
University Medical School, Poznań, Poland

**Alexander J. McDONALD**, Department of Cell Biology  
and Neuroscience, USC School of Medicine,  
Columbia, United States

**Stanisław MOSKALEWSKI**, Department of Histology  
and Embryology, Medical University of Warsaw, Poland

**Łukasz OLEWNIK**, Department of Normal and Clinical Anatomy,  
Medical University of Łódź, Poland

**Orlando PACIELLO**, Dipartimento di Patologia e Sanità animale,  
Univesita degli Studi di Napoli Federico II, Napoli, Italy

**Asla PITKÄNEN**, Department of Neurobiology,  
A.I. Virtanen Institute, University of Kuopio, Finland

**Michał POLGUJ**, Department of Angiology,  
Medical University of Łódź, Poland

**Michał K. STACHOWIAK**, Department of Molecular and  
Structural Neurobiology and Gene Therapy, State University  
of New York, Buffalo, United States

**Paweł SYSA**, Department of Histology and Embryology,  
Warsaw University of Life Sciences, Poland

**Michał SZPINDA**, Department of Anatomy, Nicolaus  
Copernicus University in Toruń, Collegium Medicum  
in Bydgoszcz, Poland

**Edyta SZUROWSKA**, 2<sup>nd</sup> Department of Radiology,  
Medical University, Gdańsk, Poland

**Jean-Pierre TIMMERMANS**, Laboratory of Cell Biology and  
Histology/Central Core Facility for Microscopic Imaging,  
Department of Veterinary Sciences,  
University of Antwerp, Belgium

**Mirosław TOPOL**, Department of Angiology,  
Medical University of Łódź, Poland

**Mehmet Cudi TUNCER**, Department of Anatomy,  
University of Dicle, Medical School, Diyarbakir, Turkey

**Krzysztof TURLEJSKI**, Department of Biochemistry  
and Cell Biology, Cardinal Stefan Wyszyński University,  
Warsaw, Poland

**Jiro USUKURA**, Structural Biology Research Center,  
Nagoya, Japan

**Jerzy WALOCHA**, Department of Anatomy, Jagiellonian  
University, Collegium Medicum, Kraków, Poland

**Mark J. WEST**, Department of Neurobiology,  
Institute of Anatomy, Århus University, Denmark

**Sławomir WÓJCİK**, Department of Anatomy and Neurobiology,  
Medical University of Gdańsk, Poland

**Maciej ZABEL**, Collegium Medicum University of  
Zielona Góra, Poland

**Marco ZEDDA**, Department of Veterinary Medicine,  
University of Sassari, Italy



# Identification of hepatosensitive region and their neural connections in the hippocampus of rats

Z. Cheng<sup>1, 2\*</sup>, R. Wei<sup>3\*</sup>, N. Cao<sup>1</sup>, Z. Li<sup>1</sup>, M. Li<sup>1</sup>, M. Liu<sup>4</sup>, L. Zhu<sup>4</sup>, C. Xia<sup>1</sup>

<sup>1</sup>Department of Human Anatomy, Basic Medical College of Guilin Medical University, China

<sup>2</sup>Department of Anatomy, Basic Medical Department of Henan Vocational College of Nursing, China

<sup>3</sup>College of Biotechnology, Guilin Medical University, China

<sup>4</sup>Affiliated Hospital of Guilin Medical University, China

[Received: 24 December 2020; Accepted: 1 February 2021; Early publication date: 23 February 2021]

**Background:** Visceral function localisation of the brain is very complex. For many years, people have been actively exploring the neural mechanism regulating visceral and substance metabolism, clarifying the complex relationship between the brain and peripheral nervous system related to the regulation of visceral activity, and analysing its complex neural pathways. The brain is the advanced centre of visceral function regulation. As an advanced centre for substance metabolism and visceral regulation, the hippocampus is crucial for regulating visceral function. The liver is the core organ of material metabolism, and its afferent signals are mainly projected to the nucleus of the solitary tract (NTS) through vagus nerve, and then they are projected to the hypothalamus and limbic system.

**Materials and methods:** We placed a stereotaxic instrument on the head of each rat and performed craniotomy to open a window above the left hippocampus. We used gold-plated tungsten electrodes to monitor hippocampal neuronal discharges. Grounding was achieved using screws and silver wire. We electrically stimulated the liver branch of the vagus nerve and observed changes in hippocampal neuron discharges using a biological method; in this way, we identified hepatosensitive hippocampal region. We injected FluoroGold into this region and related brain areas. After 3 days, the rats were sacrificed and perfused; the hippocampi were fixed, dehydrated, frozen, sectioned, and subjected to fluorescence microscopy.

**Results:** Nerve discharge frequency and amplitude significantly increased in the hippocampal CA3 region (AP: –4.9, ML: –5.1, DV: –5.0 mm). After FluoroGold was injected into the left hepatosensitive region in the hippocampus, labelled cells were found in the contralateral hippocampus, ipsilateral piriform cortex (PC), locus coeruleus (LC) and bilateral lateral hypothalamus (LHA); fluorescence in the ipsilateral hypothalamus was stronger than that of the contralateral hypothalamus. FluoroGold was injected into the LHA, PC, and LC; no labelled cells were found in the hippocampal CA3 region or in the control group.

**Conclusions:** The hippocampal CA3 area of rats may contain a hepatosensitive region that plays important roles in the regulation of liver and other organ function. This region may receive input from the LHA, PC, and LC. (Folia Morphol 2022; 81, 2: 261–270)

**Key words:** neural regulation of liver function, hepatic branch of the vagus nerve, hippocampus, neural pathways

Address for correspondence: Dr. C. Xia, Department of Human Anatomy, Basic Medical College of Guilin Medical University, China, e-mail: xiachunbo910@163.com

\*Co-first author

This article is available in open access under Creative Common Attribution-Non-Commercial-No Derivatives 4.0 International (CC BY-NC-ND 4.0) license, allowing to download articles and share them with others as long as they credit the authors and the publisher, but without permission to change them in any way or use them commercially.

## INTRODUCTION

The hippocampus plays a crucial role in visceral regulation. Recent works on limbic system connections in the human brain have revealed a close relationship between that system and visceral information [5]. The hippocampus affects visceral function by regulating the excitability of the hypothalamic, autonomic nerve centre. The liver is the core metabolic organ; afferent signals project principally to the nucleus of the solitary tract (NTS) of the visceral centre, via the vagus nerve, and then from the nucleus to the hypothalamus and limbic system [10]. Neuroanatomical studies [8] have revealed that visceral sensory feedback signals reach the hypothalamus and the limbic brain, which controls food intake. Anatomically, direct neural projections from the hippocampus to the lateral hypothalamus and bisynaptic connections from the hippocampus to other known hypothalamic sites involved in feeding control have been identified [6, 7]. The hippocampus is key in terms of integrating peripheral signals with other sensory information. Vagus nerve stimulation triggers the typical hippocampal evoked potentials. Electrophysiologically, various afferent nerves of hepatic branch of the vagus nerve respond to slight changes in glucose concentration, osmotic pressure, and portal circulation temperature. These afferent systems may thus contribute to blood sugar, extracellular osmotic pressure, and body temperature homeostasis. Normal liver function involves the central nervous system; the marked dependence of the liver on the brain, and the neuromodulatory complexity of liver function, may be underestimated. Sensory signals from the liver travel to many areas of the central nervous system, including the hippocampus and hypothalamus, which regulate autonomic and endocrine homeostasis. However, little is known about the mechanisms involved. The hippocampal-hepatic neural pathway has not been studied. As a first step, we identified a hepatosensitive region in the hippocampus and explored the hippocampal-liver neural pathway via nerve tracing. Hence, our results set the experimental foundation for in-depth research on how the nervous system regulates liver function.

## MATERIALS AND METHODS

### Experimental animals

Male Sprague-Dawley rats aged 6–8 weeks were purchased from the laboratory animal centre of Guilin Medical College (certificate #SCXK GUI 2007-0001).

Ethical Approval number is GLMC201703022. Fluoro-Gold (FG) was from KeyGen Biotech (Jiangsu, China, cat. no. kgmp023/kgmp023–1). We used 190 rats divided into two groups that underwent electrical stimulation of the hepatic branch of the vagus nerve (30 rats), or neural tracing (160 rats). FG was injected into the hepatosensitive area of the left hippocampus, the ipsilateral piriform cortex (PC), the locus coeruleus (LC), and the bilateral lateral hypothalamus (LHA) (0.1, 0.3, and 0.5  $\mu$ L, respectively) and the rats were divided into three subgroups of 10 rats. Each control subgroup (10 rats) was injected with normal saline. During preliminary electrical stimulation of the hepatic branch of the vagus nerve, we recorded hippocampal neuron discharges using gilded tungsten wire (KEDOUBC, Suzhou, China) as the recording electrode. We delivered stimuli of 3, 6, and 9 V to fasted rats (water was allowed). Animals were allowed to acclimate for at least 1 week before experimentation. Animal suffering and death were minimised, in line with the regulations of the People's Republic of China that address the use of experimental animals.

### Experimental methods

#### *Electrical stimulation of the hepatic branch of the vagus nerve*

After intraperitoneal injection of 1% (w/v) pentobarbital sodium in saline (40 mg/kg), rats under anaesthesia were positioned on a stereotaxic instrument and the scalp was incised along the median sagittal line using the fontanelle as the origin. With reference to a brain stereotaxic atlas, the hippocampal skull projection area was marked. Brain tissue was exposed by drilling a hole about 0.8 mm in diameter, followed by placement of a grounding screw of depth about 0.7 mm, 12 mm from the recording electrode. A gold-plated tungsten electrode (The exposed tip is 5–10 microns in diameter, impedance 1–2 M $\Omega$ ) was fixed to the instrument holder and adjusted to the required coordinates. We confirmed that all electrodes were well-insulated; only the tips conducted electricity. The belly was disinfected and laparotomy was performed to expose the liver and oesophagus. A saline swab was used to move the left lobe to the right of the oesophagus, thus completely exposing the oesophagus; then the vagus nerve of the oesophagus and the hepatic vagus nerve of the porta hepatis were visible. We placed the electrodes of an in-house vagus nerve stimulator (a peripherally insulated bare silver wire that touched only the liver branch of the

nerve) about 1 cm apart, close to and distant from the centre of the liver branch of the vagus nerve; both electrodes were wound around the nerve (1.5 loops), the negative pole was placed at the proximal end of the nerve and the positive pole was placed at the distal end. We were careful to minimise tension to prevent nerve damage. The stimulatory electrodes were fixed to the abdominal wall and the front abdominal wall muscle to prevent slippage. The stimulatory electrode and recording electrodes were connected to the signal acquisition system (gain: 5 mV, time constant: 0.1 s, filtering: 10000 Hz) and the grounding wire was wound tightly around a screw and slowly passed into the hippocampal region. When the signal-to-noise ratio became greater than 3:1, we recorded neuronal discharges. We implanted the recording electrodes into different hippocampal areas and structures, and then restimulated the hepatic branch of the vagus nerve; the threshold intensity is the minimum output voltage that can increase or decrease the discharge amplitude and frequency of hippocampal neurons by 20%. Amplitude and frequency changes > 20% were considered to be indicative of hepatosensitive region. As a control, saline solution containing tetrodotoxin (TTX: 2.5 ng/0.1  $\mu$ L) was injected into the liver sensitive region in the hippocampus, and then vagus nerve was stimulated to observe the changes of neuron discharge in the liver sensitive area of hippocampus. Procedures for local microinjections have been described in detail elsewhere [24]. The signals were 1 ms in duration after 100 ms of delay, and 3, 6, or 9 V in intensity. Intermittent stimulation featured single coarse-voltage stimuli. Only stable discharges with signal-to-noise ratio > 3 were recorded.

#### **FluoroGold nerve tracer**

The rats' skulls were drilled as described above and 3% (w/v) FG (0.1, 0.3, or 0.5  $\mu$ L) was subdurally injected into hepatosensitive region (AP: -4.9, ML: -5.1, DV: -5.0 mm), the left HLA (AP: -4.8, ML: -1.0, DV: -8.1 mm), the PC (AP: -4.8, ML: -7.5, DV: -8.5 mm), and the LC (AP: -9.16, ML: -1.0, DV: -6.5 mm). Control rats received the same amounts of normal saline. The needle remained in place for 10 min after injection and the rats were held for 72 h. After sacrifice via re-anaesthesia, the chest cavity was opened and the heart was exposed. An in-house blunt needle was used to enter the ascending aorta from the apex of the heart, and fixed with a needle holder to

prevent slipping. The right auricle was removed and successively perfused with phosphate buffered saline (PBS) followed by 4% (v/v) paraformaldehyde, first rapidly and then slowly. The brains were collected, fixed in 4% (v/v) paraformaldehyde at 4°C for at least 24 h; and successively placed in 10%, 15%, and 30% sucrose solutions at 4°C until the tissue sank to the bottom. The samples were dehydrated, frozen, and sectioned (15–20  $\mu$ m), and then the sections were placed on adhesive slides, which were sealed after washing with PBS. Finally, the samples were observed under a fluorescence microscope. FG was excited using ultraviolet light (irradiation 418 nm, excitation 331 nm). All operations proceeded in the dark. Labelled cells were counted. Sections of the neuronal cell body and axon served as retrograde markers when counting cells. For each case, five typical sections were selected and labelled cells were counted at 40 $\times$  and 200 $\times$ .

#### **Statistical analysis**

Discharge frequencies and amplitudes and FG-labelled cell counts using SPSS ver. 25.0 software. Data are given as arithmetic means with standard deviations. The paired t-test was used to compare discharges before and after stimulation. Comparison of groups with different electrical stimulation intensity and different FG injection doses were evaluated via one-way ANOVA. The independent samples t-test was used to compare differences in the bilateral LHA; a p-value < 0.05 was taken to indicate statistical significance.

## **RESULTS**

### **Identification of hepatosensitive region in the hippocampus**

The hepatic branches of the vagus nerve of 30 rats were electrically stimulated and hippocampal discharge frequencies and amplitudes were recorded. Most rats (26/30) exhibited increased (> 20%) discharge frequencies and amplitudes from the hippocampal CA3 region (AP: -4.9, ML: -5.1, DV: -5.0 mm). The basic discharge frequency was  $124.31 \pm 16.31$  Hz and the amplitude was  $90.77 \pm 14.23$   $\mu$ V; stimulation with 3, 6, and 9 V yielded values of  $157.81 \pm 16.94$  Hz and  $180.81 \pm 10.50$   $\mu$ V,  $187.77 \pm 10.66$  Hz and  $264.88 \pm 10.94$   $\mu$ V, and  $193.31 \pm 13.08$  Hz and  $265.23 \pm 12.91$   $\mu$ V, respectively (all p < 0.05, ANOVA). Thus, both the frequency and amplitude of discharge increased as the stimulation increased (Fig. 1E, F), and

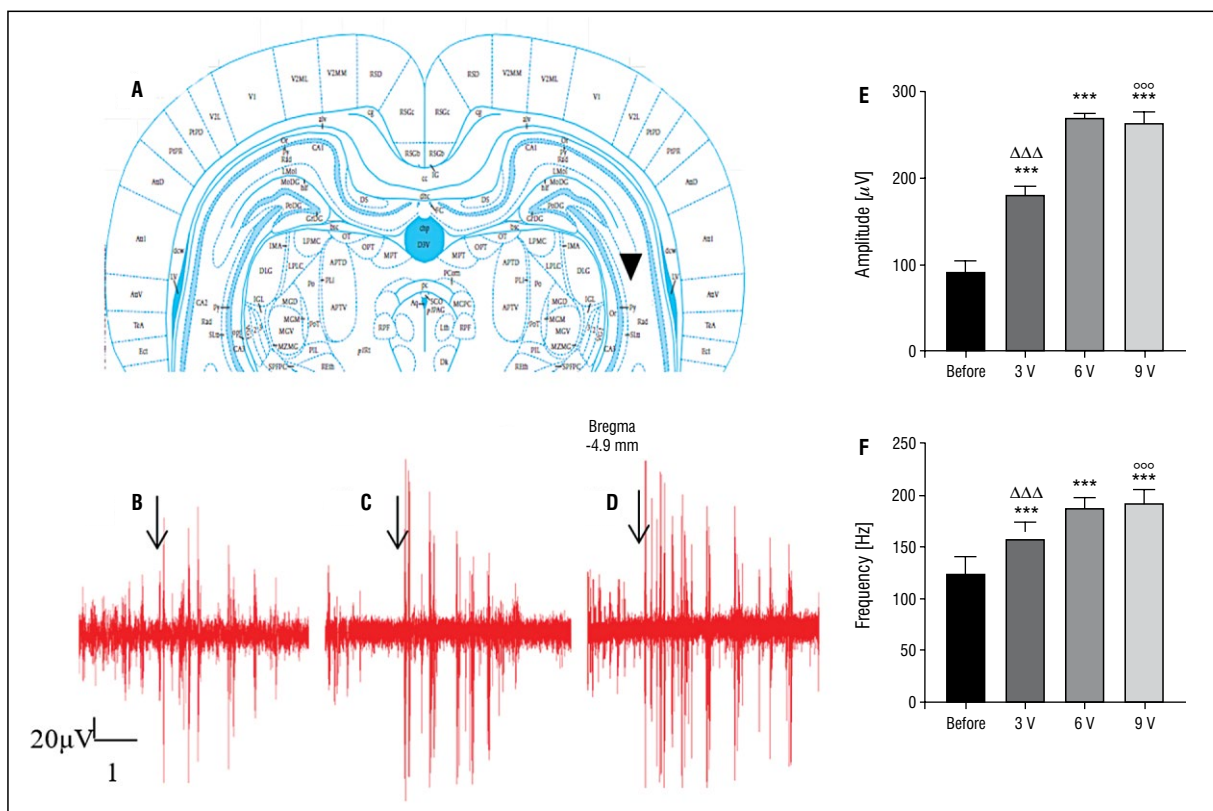


**Figure 1.** A. Schematic diagram of the location of recorded and microinjection in the hippocampus. Record and injections sites are indicated by inverted triangles ( $\blacktriangledown$ ); B–D. Variations of neuron discharge in rat hippocampal CA3 region of vagus nerve with different electrical stimulation ( $n = 26$ ); B. 3 V; C. 6 V; D. 9 V;  $\downarrow$ : electrical stimulation; E, F. Rats hippocampal neuronal discharge frequency and amplitude ( $n = 26$ ) with different intensity of liver branch of the vagus nerve stimulation; E. The firing frequency of hippocampal region before stimulation and after stimulation of vagus nerve with different intensities; F. The discharge amplitude of hippocampal region after basal discharge before stimulation and hepatic branch of vagus nerve after electrical stimulation with different intensity. Data are processed with paired t test and single factor variance analysis. \*\*\* $p < 0.001$  — comparison before and after stimulus with different intensity;  $\Delta\Delta\Delta p < 0.001$  — comparison of results stimulated with 3 V and 6 V;  $\circ\circ\circ p < 0.001$  — comparison of results stimulated with 3 V and 9 V.

basically reached the saturation stimulation intensity at 6 V, while the discharge changes of 6 V and 9 V in the liver sensitive areas of hippocampus showed no significant change. After stimulation ceased, the frequency and amplitude gradually returned to the basic level. As stimulus intensity increased, the recovery time was prolonged (Fig. 1B–D), After TTX injection, the local hippocampal action potential was blocked, eliminating the response to the stimulation of the hepatic branch of the vagus nerve.

Figure 1A shows the location of the injection and record site in hippocampus. Though there were variations in the placements among animals, the histology indicated that electrode implantation and TTX were injected into the hepatic sensitive regions of the hippocampus of the rats used in the study. Rats with inaccurate localisation were excluded.

### Conduction pathways of hepatosensitive region in the hippocampus

FluoroGold was injected into hepatosensitive region in the left hippocampus to explore the nerve conduction pathways. Haematoxylin and eosin staining and fluorescence microscopy of defined areas of the left hippocampus (excluding instances of injection inaccuracy or FG overflow) revealed various numbers of labelled cells. Different amounts of FG were injected into hepatosensitive areas of the left hippocampus, in the right hippocampus containing the FG labelled neurons, including both LHAs and the left sides of the PC and LC were seen with fluorescence labelling cells (Figs. 2–5). Labelled cell numbers significantly increased as the FG dose increased ( $p < 0.05$ ; Table 1). The left lateral hypothalamus exhibited more labelled cells than the right side ( $p < 0.05$ ; Fig. 3M). After

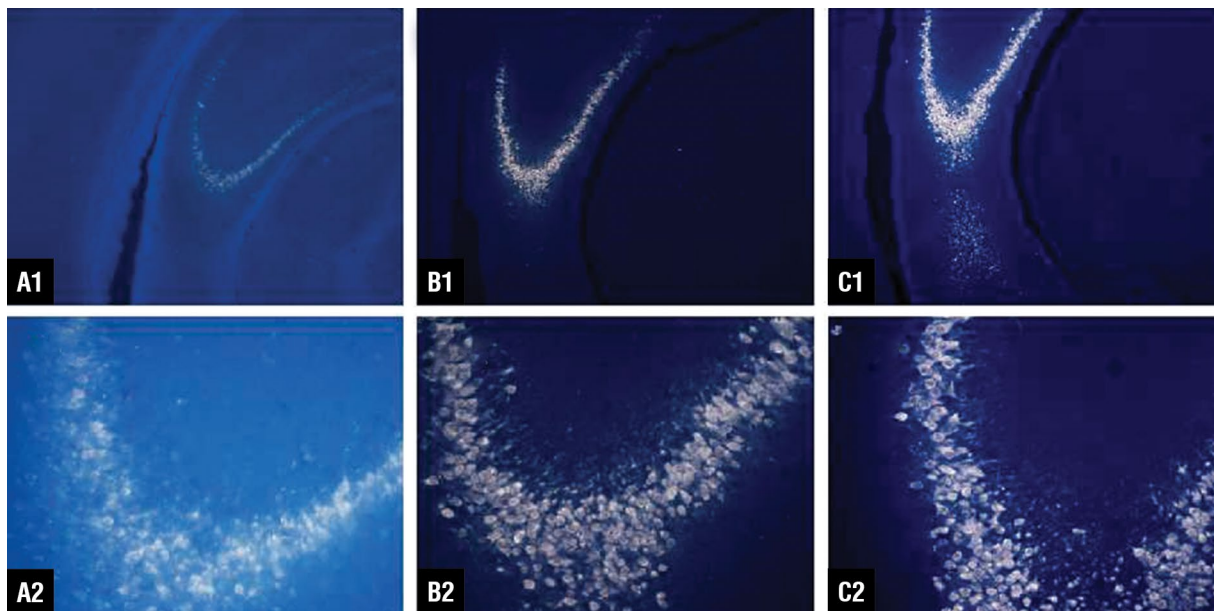


**Figure 2.** Fluorescence tracer results of right hippocampus after different doses of FluoroGold (FG) were injected into left hippocampal liver sensitive region of rats (0.1  $\mu\text{L}$ ,  $n = 10$ ; 0.3  $\mu\text{L}$ ,  $n = 10$ ; 0.5  $\mu\text{L}$ ,  $n = 10$ ; **A1.** FG 0.1  $\mu\text{L}$ , 40 $\times$ , **A2.** FG 0.1  $\mu\text{L}$ , 200 $\times$ ; **B1.** FG 0.3  $\mu\text{L}$ , 40 $\times$ ; **B2.** FG 0.3  $\mu\text{L}$ , 200 $\times$ ; **C1.** FG 0.5  $\mu\text{L}$ , 40 $\times$ ; **C2.** FG 0.5  $\mu\text{L}$ , 200 $\times$ ). The bright white neurons are FG labelled cells.

saline injection, no labelled cells were found in the right hippocampus, the bilateral LHAs, the PC, or LC. After FG was injected into the LHA, PC, and LC, no labelled cells were found in the hippocampus (Fig. 6).

## DISCUSSION

The hippocampus plays an important role in visceral regulation [2]; research on this topic is of both theoretical and clinical significance. The liver sends signals to the central nervous system through the vagus nerve [31]. We electrically stimulated the liver branch of the vagus nerve and found hepatosensitive region in the hippocampus. The method used was developed in 1986 by Kobashi and Adachi [15], who studied the projections of related nuclei. Other studies featuring electrical stimulation of the liver branch of the vagus nerve have revealed a functional relationship between the liver and the nucleus tractus solitarius (NTS). We found that, in the hippocampal CA3 region (AP:  $-4.9$ , ML:  $-5.1$ , DV:  $-5.0$  mm), the discharge frequencies and amplitudes increased by  $> 20\%$ , and then gradually reverted to the basic rates, consistent with the findings of previous studies [17]. We speculate that the increased discharges in specific hippocampal areas caused by stimulation of the hepatic branch of the vagus nerve may reflect projections of the hippocampal liver region [32]. In a previous study, stimulation of the hepatic branch

of the vagus nerve reduced weight gain in rats fed a high-fat diet [20]. Such stimulation also triggers loss of weight and appetite in other animals; the vagus nerve transmits signals to both the hippocampus and other brain regions [23]. In young mice, metabolic data on the liver are transmitted to the brain via the hepatic vagus nerve [3, 28–30]. These works, combined with our present data, suggest that hepatic afferent signals may be projected to specific hippocampal areas by the hepatic branch of the vagus nerve. We found that the hippocampus (AP:  $-4.9$ , ML:  $-5.1$ , DV:  $-5.0$  mm) may be sensitive to signals from the liver vagus nerve, playing an important role in the regulation of liver and other organ function. Different neurons exhibit different action potential thresholds. For example, intermediate hippocampal neurons (inhibitory neurons) have lower thresholds than pyramidal cells (primary neurons). That cone cell discharges might be inhibited by local intermediate neurons activated by certain stimuli delivered to their afferent fibres. Although computational modelling supports this hypothesis [21], *in vivo* data are lacking. In 1 study [9], neuronal stimulation had both inhibitory and excitatory effects. In addition, the stimulation frequency may affect neuronal discharge [25]. We used 3, 6, and 9 V to stimulate the hepatic branch of the vagus nerve. The neuronal discharge gradually increased as stimulation intensity increased, perhaps

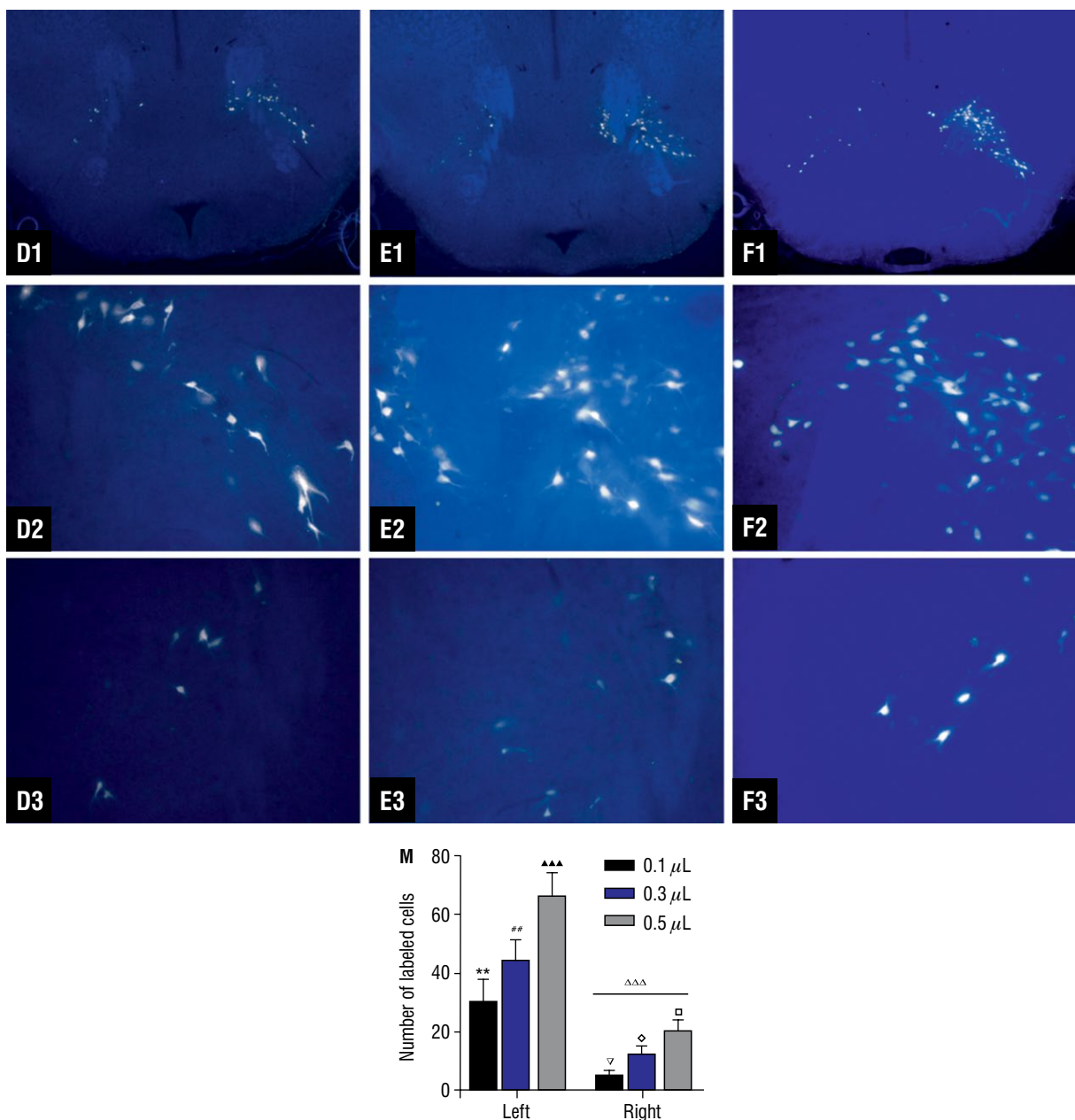


**Figure 3.** D–F. Fluorescence tracer results of bilateral lateral hypothalamus after different doses of FluoroGold (FG) were injected into left hippocampal liver sensitive region of rats (0.1 μL, n = 10; 0.3 μL, n = 10; 0.5 μL, n = 10; **D1.** FG 0.1 μL, 40×; **D2.** FG 0.1 μL, left side 200×; **D3.** FG 0.1 μL, right side 200×; **E1.** FG 0.3 μL, 40×; **E2.** FG 0.3 μL, left side 200×; **E3.** FG 0.3 μL, right side 200×; **F1.** FG 0.5 μL, 40×; **F2.** FG 0.5 μL, left side 200×; **F3.** FG 0.5 μL, right side 200×). The bright white neurons are FG labelled cells; **M.** Number of fluorescence-labelled cells in the left and right lateral hypothalamus of the hippocampal hepatosensitive region injected with different doses of FG (0.1 μL, n = 10; 0.3 μL, n = 10; 0.5 μL, n = 10). One-way ANOVA and independent sample t test are used;  $\Delta\Delta\Delta p < 0.001$  — compare lateral hypothalamus (LHA) of left and right at the same dose;  $**p < 0.01$  — left LHA: 0.1 μL vs. 0.3 μL;  $###p < 0.01$  — 0.3 μL vs. 0.5 μL;  $\Delta\Delta\Delta p < 0.001$  — 0.1 μL vs. 0.5 μL; Right LHA:  $\nabla p < 0.05$  — 0.1 μL vs. 0.3 μL;  $\diamond p < 0.05$  — 0.3 μL vs. 0.5 μL;  $\square p < 0.05$  — 0.1 μL vs. 0.5 μL.

attributable to the stimulation of pyramidal cells. The neuronal discharge frequency and amplitude gradually increased with stimulation intensity, perhaps reflecting increasing pyramidal cell excitation. Changes in hippocampal neuronal discharge developed within

0.1 s after electrical stimulation of the vagus nerve; the neuroregulatory effects were rapid, accurate, and transient. Compared to injection of glucose or lipids into the hepatic portal vein, nerve stimulation detects sensitive brain areas more rapidly and ac-

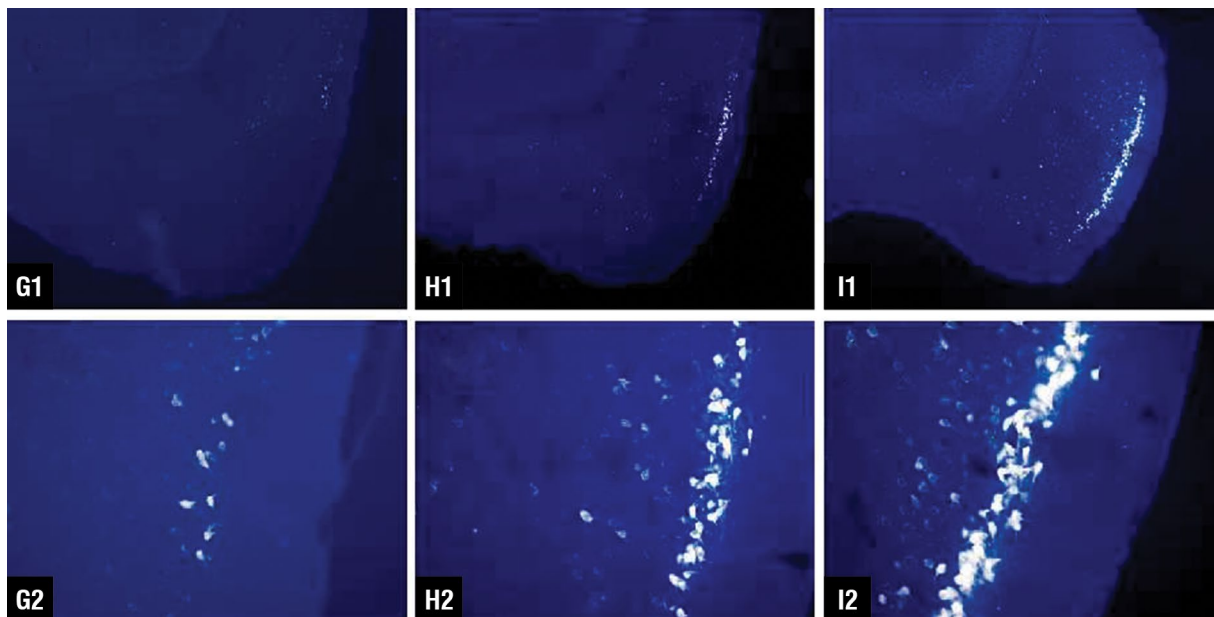


**Figure 4.** Fluorescence tracing results of ipsilateral pyriform cortex after different doses of FluoroGold (FG) were injected into left hippocampal liver sensitive region of rats (0.1  $\mu\text{L}$ , n = 10; 0.3  $\mu\text{L}$ , n = 10; 0.5  $\mu\text{L}$ , n = 10; **G1.** FG 0.1  $\mu\text{L}$ , 40 $\times$ ; **G2.** FG 0.1  $\mu\text{L}$ , 200 $\times$ ; **H1.** FG 0.3  $\mu\text{L}$ , 40 $\times$ ; **H2.** FG 0.3  $\mu\text{L}$ , 200 $\times$ ; **I1.** FG 0.5  $\mu\text{L}$ , 40 $\times$ ; **I2.** FG 0.5  $\mu\text{L}$ , 200 $\times$ ). The bright white neurons are FG labelled cells.

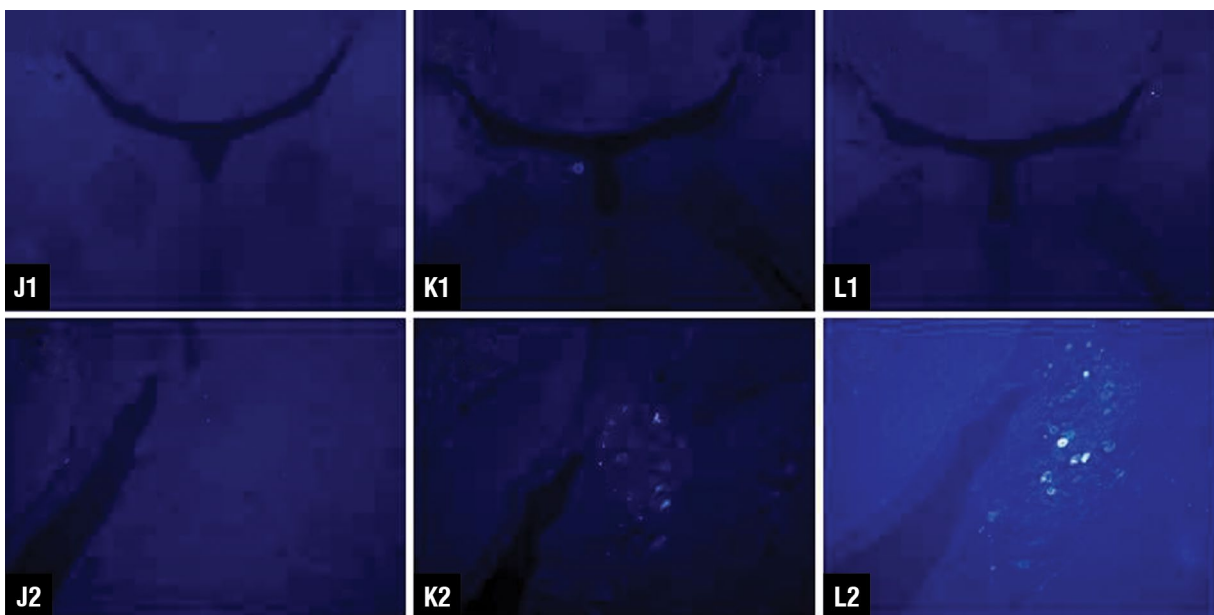


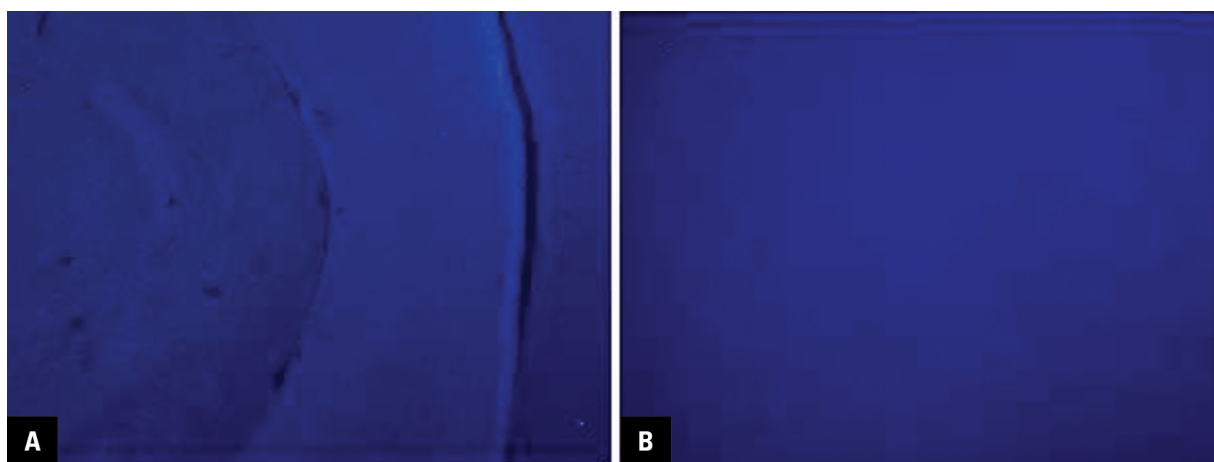
**Figure 5.** Fluorescence tracing results of ipsilateral locus coeruleus after different doses of FluoroGold (FG) were injected into left hippocampal liver sensitive region of rats (0.1  $\mu\text{L}$ , n = 10; 0.3  $\mu\text{L}$ , n = 10; 0.5  $\mu\text{L}$ , n = 10; **J1.** FG 0.1  $\mu\text{L}$ , 40 $\times$ ; **J2.** FG 0.1  $\mu\text{L}$ , 200 $\times$ ; **K1.** FG 0.3  $\mu\text{L}$ , 40 $\times$ ; **K2.** FG 0.3  $\mu\text{L}$ , 200 $\times$ ; **L1.** FG 0.5  $\mu\text{L}$ , 40 $\times$ ; **L2.** FG 0.5  $\mu\text{L}$ , 200 $\times$ ). The bright white neurons are FG labelled cells.

curately. It is possible that the observed changes in nerve discharges reflect only signals transmitted via the hepatic branch of the vagus nerve. It is also possible that stimulation of this branch affects not only the liver but also the gastrointestinal tract [1]. Given

the unique features of the nerve, the affected brain regions become apparent upon neuronal stimulation. However, associations among vagus nerve-sensitive regions remain poorly understood. The nerve exhibits many and varied functions that may overlap; roles

**Table 1.** Numbers of fluorescently labelled cells in the right hippocampus, bilateral lateral hypothalamus (LHA), left piriform cortex (PC), and locus coeruleus (LC) after hepatosensitive region in the left hippocampus were injected with different doses of FluoroGold

Group	Samples	Right hippocampus	Left LHA	Right LHA	Left PC	Left LC
0.1 $\mu$ L	10	50.63 $\pm$ 5.04	30.50 $\pm$ 7.39	5.25 $\pm$ 1.67	21.38 $\pm$ 5.71	10.25 $\pm$ 3.24
0.3 $\mu$ L	10	136.00 $\pm$ 9.64	44.43 $\pm$ 7.00	12.71 $\pm$ 2.63	56.43 $\pm$ 9.88	19.14 $\pm$ 2.41
0.5 $\mu$ L	10	267.67 $\pm$ 16.92	66.44 $\pm$ 7.99	20.67 $\pm$ 3.39	115.33 $\pm$ 8.34	25.11 $\pm$ 5.06
F-value		707.33	49.59	69.28	294.85	31.53
P-value		< 0.05	< 0.05	< 0.05	< 0.05	< 0.05

**Figure 6.** Fluorescence labelled results of FluoroGold injection in the left lateral hypothalamus, piriform cortex and locus coeruleus in rats (n = 10). There are not fluorescent labelled cells in the left hippocampal liver sensitive area; **A.** 0.5  $\mu$ L, 40 $\times$ ; **B.** 0.5  $\mu$ L, 200 $\times$ .

may be exchanged. Thus, it remains to be confirmed that stimulation of the vagus nerve of the liver triggers the hippocampal discharges. Despite the several neuroanatomical possibilities, we have confirmed a connection between the hippocampus (the visceral regulatory centre) and the liver. The BL-420E experimental instrument used in this experiment may have some limitations, and the specific mechanism of the hippocampal hepatic sensitive nerve area and its related neural pathways still needs to be further studied.

We used FG (a retrograde nerve tracer) to explore the morphological and anatomical connections of conduction pathways in hepatosensitive areas of the hippocampus. FG reveals fibres that run from the brain to target organs, and is the gold standard tracer for rodents. We injected it into hepatosensitive areas in the left hippocampus; labelled cells were apparent in the right hippocampus, bilateral LHA, left PC and LC, and ipsilateral LHA, at levels much higher than in the contralateral regions. Recent studies have shown that the LHA is involved in the regulation of gastrointestinal movement and feeding behaviour

via the brainstem NTS and the dorsal vagus motor nucleus. Thus, the hypothalamus is involved in visceral regulation. Previous studies have found that PC fibres project into the hypothalamus and amygdala and regulate appetite. The LC-norepinephrine (NE) system mediates many visceral responses and is associated with hippocampal fibres. We have shown that fibrous connections may exist between the left and right hippocampi. Both LHAs, and the ipsilateral PC and LC, project fibres to the hepatosensitive area of the hippocampus; the ipsilateral LHA projection is stronger than the contralateral projection. One side of the hepatosensitive area of the hippocampus accepts fibres projecting from the bilateral hypothalamus; this tissue centrally regulates energy and metabolic balance [27] including liver lipid and lipoprotein metabolism. Hypothalamic fibres project to the hippocampus. Orexin is found in both the hippocampus and LC; both tissues regulate feeding behaviour and energy balance. Our results are consistent with those of recent studies on the anatomy of the association between the hippocampus, hypothalamus, and LC

[11, 14]. We speculate that liver function regulation by hepatosensitive region in the hippocampal CA3 region may involve the LHA, PC, and LC. When FG was injected into these regions, no labelled cells were found in the hepatosensitive areas, suggesting that the fibre connections between the hepatosensitive region and the LHA, PC, and LC may be one-way [19]. Some recent studies [4, 12, 22] found that the hippocampus was directly or indirectly linked to the hypothalamus, PC, and LC. The hippocampal control hierarchy [16] is: hippocampus to the hypothalamus, to the brain stem, to the vagus nerve. Functional fibres linking the hippocampus and hypothalamus have been found in previous studies [26]. The responses in the hippocampus to vagal stimulation are likely to result from stimulation of vagal afferents and reach the hippocampus via NTS and the data do not test whether there is a vagal efferent pathway involved. A recent study found that the PC and hippocampus were involved in the sense of smell [13]. Furthermore, the hippocampus and LC affect cognitive function [18]. However, few studies have explored whether the PC and LC regulate internal organs. The hepatosensitive hippocampal CA3 region may be connected to the lateral hypothalamus, PC, and LC. The roles played by the latter two regions will be explored in future experiments.

## CONCLUSIONS

There may be liver sensitive region in the CA3 area of rat hippocampus, and the area receives nerve fibre projections from lateral hypothalamic area, piriform cortex and blue spots, and is unidirectional fibre projection. The CA3 area received nerve fibre projection from bilateral lateral hypothalamus area, and the ipsilateral projection was stronger than the contralateral side.

## Funding

National Natural Science Foundation of China (81760159, 81960163); Guangxi Natural Science Foundation (2017GXNSFAA198307, 2018GXNSFBA138029); Open Project of Guangxi Key laboratory of Brain and Cognitive Neuroscience (gklbcn-20180105-05).

**Conflict of interest:** None declared

## REFERENCES

- Agster KL, Burwell RD. Hippocampal and subicular efferents and afferents of the perirhinal, postrhinal, and entorhinal cortices of the rat. *Behav Brain Res.* 2013; 254: 50–64, doi: [10.1016/j.bbr.2013.07.005](https://doi.org/10.1016/j.bbr.2013.07.005), indexed in Pubmed: [23872326](https://pubmed.ncbi.nlm.nih.gov/23872326/).
- Arrigo A, Mormina E, Calamuneri A, et al. Amygdalar and hippocampal connections with brainstem and spinal cord: a diffusion MRI study in human brain. *Neuroscience.* 2017; 343: 346–354, doi: [10.1016/j.neuroscience.2016.12.016](https://doi.org/10.1016/j.neuroscience.2016.12.016), indexed in Pubmed: [28003162](https://pubmed.ncbi.nlm.nih.gov/28003162/).
- Bernal-Mizrachi C, Xiaozhong L, Yin Li, et al. An afferent vagal nerve pathway links hepatic PPARalpha activation to glucocorticoid-induced insulin resistance and hypertension. *Cell Metab.* 2007; 5(2): 91–102, doi: [10.1016/j.cmet.2006.12.010](https://doi.org/10.1016/j.cmet.2006.12.010), indexed in Pubmed: [17276352](https://pubmed.ncbi.nlm.nih.gov/17276352/).
- Blessing EM, Beissner F, Schumann A, et al. A data-driven approach to mapping cortical and subcortical intrinsic functional connectivity along the longitudinal hippocampal axis. *Hum Brain Mapp.* 2016; 37(2): 462–476, doi: [10.1002/hbm.23042](https://doi.org/10.1002/hbm.23042), indexed in Pubmed: [26538342](https://pubmed.ncbi.nlm.nih.gov/26538342/).
- Catani M, Dell'acqua F, Thiebaut de Schotten M. A revised limbic system model for memory, emotion and behaviour. *Neurosci Biobehav Rev.* 2013; 37(8): 1724–1737, doi: [10.1016/j.neubiorev.2013.07.001](https://doi.org/10.1016/j.neubiorev.2013.07.001), indexed in Pubmed: [23850593](https://pubmed.ncbi.nlm.nih.gov/23850593/).
- Cenquizca LA, Swanson LW. Analysis of direct hippocampal cortical field CA1 axonal projections to diencephalon in the rat. *J Comp Neurol.* 2006; 497(1): 101–114, doi: [10.1002/cne.20985](https://doi.org/10.1002/cne.20985), indexed in Pubmed: [16680763](https://pubmed.ncbi.nlm.nih.gov/16680763/).
- Cenquizca LA, Swanson LW. Spatial organization of direct hippocampal field CA1 axonal projections to the rest of the cerebral cortex. *Brain Res Rev.* 2007; 56(1): 1–26, doi: [10.1016/j.brainresrev.2007.05.002](https://doi.org/10.1016/j.brainresrev.2007.05.002), indexed in Pubmed: [17559940](https://pubmed.ncbi.nlm.nih.gov/17559940/).
- Davidson TL, Chan K, Jarrard LE, et al. Contributions of the hippocampus and medial prefrontal cortex to energy and body weight regulation. *Hippocampus.* 2009; 19(3): 235–252, doi: [10.1002/hipo.20499](https://doi.org/10.1002/hipo.20499), indexed in Pubmed: [18831000](https://pubmed.ncbi.nlm.nih.gov/18831000/).
- Feng Z, Wang Z, Guo Z, et al. High frequency stimulation of afferent fibers generates asynchronous firing in the downstream neurons in hippocampus through partial block of axonal conduction. *Brain Res.* 2017; 1661: 67–78, doi: [10.1016/j.brainres.2017.02.008](https://doi.org/10.1016/j.brainres.2017.02.008), indexed in Pubmed: [28213155](https://pubmed.ncbi.nlm.nih.gov/28213155/).
- Hannapel RC, Henderson YH, Nalloor R, et al. Ventral hippocampal neurons inhibit postprandial energy intake. *Hippocampus.* 2017; 27(3): 274–284, doi: [10.1002/hipo.22692](https://doi.org/10.1002/hipo.22692), indexed in Pubmed: [28121049](https://pubmed.ncbi.nlm.nih.gov/28121049/).
- Jennings JH, Rizzi G, Stamatakis AM, et al. The inhibitory circuit architecture of the lateral hypothalamus orchestrates feeding. *Science.* 2013; 341(6153): 1517–1521, doi: [10.1126/science.1241812](https://doi.org/10.1126/science.1241812), indexed in Pubmed: [24072922](https://pubmed.ncbi.nlm.nih.gov/24072922/).
- Jeon SG, Kim YJ, Kim KA, et al. Visualization of altered hippocampal connectivity in an animal model of Alzheimer's disease. *Mol Neurobiol.* 2018; 55(10): 7886–7899, doi: [10.1007/s12035-018-0918-y](https://doi.org/10.1007/s12035-018-0918-y), indexed in Pubmed: [29488134](https://pubmed.ncbi.nlm.nih.gov/29488134/).
- Jiang H, Schuele S, Rosenow J, et al. Theta oscillations rapidly convey odor-specific content in human piriform cortex. *Neuron.* 2017; 94(1): 207–219.e4, doi: [10.1016/j.neuron.2017.03.021](https://doi.org/10.1016/j.neuron.2017.03.021), indexed in Pubmed: [28384472](https://pubmed.ncbi.nlm.nih.gov/28384472/).
- Kempadoo KA, Mosharov EV, Choi SeJ, et al. Dopamine release from the locus coeruleus to the dorsal hippocam-

- pus promotes spatial learning and memory. *Proc Natl Acad Sci USA*. 2016; 113(51): 14835–14840, doi: [10.1073/pnas.1616515114](https://doi.org/10.1073/pnas.1616515114), indexed in Pubmed: [27930324](https://pubmed.ncbi.nlm.nih.gov/27930324/).
15. Kobashi M, Adachi A. Projection of nucleus tractus solitarius units influenced by hepatoportal afferent signal to parabrachial nucleus. *J Auton Nerv Syst*. 1986; 16(2): 153–158, doi: [10.1016/0165-1838\(86\)90006-8](https://doi.org/10.1016/0165-1838(86)90006-8), indexed in Pubmed: [3722718](https://pubmed.ncbi.nlm.nih.gov/3722718/).
  16. Kobrzycka A, Napora P, Pearson BL, et al. Peripheral and central compensatory mechanisms for impaired vagus nerve function during peripheral immune activation. *J Neuroinflammation*. 2019; 16(1): 150, doi: [10.1186/s12974-019-1544-y](https://doi.org/10.1186/s12974-019-1544-y), indexed in Pubmed: [31324250](https://pubmed.ncbi.nlm.nih.gov/31324250/).
  17. Larsen LE, Wadman WJ, Marinazzo D, et al. Vagus nerve stimulation applied with a rapid cycle has more profound influence on hippocampal electrophysiology than a standard cycle. *Neurotherapeutics*. 2016; 13(3): 592–602, doi: [10.1007/s13311-016-0432-8](https://doi.org/10.1007/s13311-016-0432-8), indexed in Pubmed: [27102987](https://pubmed.ncbi.nlm.nih.gov/27102987/).
  18. Lashgari R, Khakpour-Taleghani B, Motamedi F, et al. Effects of reversible inactivation of locus coeruleus on long-term potentiation in perforant path-DG synapses in rats. *Neurobiol Learn Mem*. 2008; 90(2): 309–316, doi: [10.1016/j.nlm.2008.05.012](https://doi.org/10.1016/j.nlm.2008.05.012), indexed in Pubmed: [18577458](https://pubmed.ncbi.nlm.nih.gov/18577458/).
  19. Letzner S, Simon A, Güntürkün O. Connectivity and neurochemistry of the commissura anterior of the pigeon (*Columba livia*). *J Comp Neurol*. 2016; 524(2): 343–361, doi: [10.1002/cne.23858](https://doi.org/10.1002/cne.23858), indexed in Pubmed: [26179777](https://pubmed.ncbi.nlm.nih.gov/26179777/).
  20. López-Soldado I, Fuentes-Romero R, Duran J, et al. Effects of hepatic glycogen on food intake and glucose homeostasis are mediated by the vagus nerve in mice. *Diabetologia*. 2017; 60(6): 1076–1083, doi: [10.1007/s00125-017-4240-4](https://doi.org/10.1007/s00125-017-4240-4), indexed in Pubmed: [28299379](https://pubmed.ncbi.nlm.nih.gov/28299379/).
  21. Mahmud M, Vassanelli S. Differential modulation of excitatory and inhibitory neurons during periodic stimulation. *Front Neurosci*. 2016; 10: 62, doi: [10.3389/fnins.2016.00062](https://doi.org/10.3389/fnins.2016.00062), indexed in Pubmed: [26941602](https://pubmed.ncbi.nlm.nih.gov/26941602/).
  22. Manchanda S, Kaur G. *Withania somnifera* leaf alleviates cognitive dysfunction by enhancing hippocampal plasticity in high fat diet induced obesity model. *BMC Complement Altern Med*. 2017; 17(1): 136, doi: [10.1186/s12906-017-1652-0](https://doi.org/10.1186/s12906-017-1652-0), indexed in Pubmed: [28253924](https://pubmed.ncbi.nlm.nih.gov/28253924/).
  23. O'Leary OF, Ogbonnaya ES, Felice D, et al. The vagus nerve modulates BDNF expression and neurogenesis in the hippocampus. *Eur Neuropsychopharmacol*. 2018; 28(2): 307–316, doi: [10.1016/j.euroneuro.2017.12.004](https://doi.org/10.1016/j.euroneuro.2017.12.004), indexed in Pubmed: [29426666](https://pubmed.ncbi.nlm.nih.gov/29426666/).
  24. Pereira de Vasconcelos A, Klur S, Muller C, et al. Reversible inactivation of the dorsal hippocampus by tetrodotoxin or lidocaine: a comparative study on cerebral functional activity and motor coordination in the rat. *Neuroscience*. 2006; 141(4): 1649–1663, doi: [10.1016/j.neuroscience.2006.05.023](https://doi.org/10.1016/j.neuroscience.2006.05.023), indexed in Pubmed: [16797129](https://pubmed.ncbi.nlm.nih.gov/16797129/).
  25. Qiu C, Feng Z, Zheng L, et al. Selective modulation of neuronal firing by pulse stimulations with different frequencies in rat hippocampus. *Biomed Eng Online*. 2019; 18(1): 79, doi: [10.1186/s12938-019-0700-z](https://doi.org/10.1186/s12938-019-0700-z), indexed in Pubmed: [31337402](https://pubmed.ncbi.nlm.nih.gov/31337402/).
  26. Reppucci CJ, Petrovich GD. Organization of connections between the amygdala, medial prefrontal cortex, and lateral hypothalamus: a single and double retrograde tracing study in rats. *Brain Struct Funct*. 2016; 221(6): 2937–2962, doi: [10.1007/s00429-015-1081-0](https://doi.org/10.1007/s00429-015-1081-0), indexed in Pubmed: [26169110](https://pubmed.ncbi.nlm.nih.gov/26169110/).
  27. Taher J, Farr S, Adeli K. Central nervous system regulation of hepatic lipid and lipoprotein metabolism. *Curr Opin Lipidol*. 2017; 28(1): 32–38, doi: [10.1097/MOL.0000000000000373](https://doi.org/10.1097/MOL.0000000000000373), indexed in Pubmed: [27906714](https://pubmed.ncbi.nlm.nih.gov/27906714/).
  28. Tsukita S, Yamada T, Uno K, et al. Hepatic glucokinase modulates obesity predisposition by regulating BAT thermogenesis via neural signals. *Cell Metab*. 2012; 16(6): 825–832, doi: [10.1016/j.cmet.2012.11.006](https://doi.org/10.1016/j.cmet.2012.11.006), indexed in Pubmed: [23217261](https://pubmed.ncbi.nlm.nih.gov/23217261/).
  29. Uno K, Katagiri H, Yamada T, et al. Neuronal pathway from the liver modulates energy expenditure and systemic insulin sensitivity. *Science*. 2006; 312(5780): 1656–1659, doi: [10.1126/science.1126010](https://doi.org/10.1126/science.1126010), indexed in Pubmed: [16778057](https://pubmed.ncbi.nlm.nih.gov/16778057/).
  30. Uno K, Yamada T, Ishigaki Y, et al. A hepatic amino acid/mTOR/S6K-dependent signalling pathway modulates systemic lipid metabolism via neuronal signals. *Nat Commun*. 2015; 6: 7940, doi: [10.1038/ncomms8940](https://doi.org/10.1038/ncomms8940), indexed in Pubmed: [26268630](https://pubmed.ncbi.nlm.nih.gov/26268630/).
  31. Yahagi N. Hepatic control of energy metabolism via the autonomic nervous system. *J Atheroscler Thromb*. 2017; 24(1): 14–18, doi: [10.5551/jat.RV16002](https://doi.org/10.5551/jat.RV16002), indexed in Pubmed: [27592630](https://pubmed.ncbi.nlm.nih.gov/27592630/).
  32. Zanos TP, Silverman HA, Levy T, et al. Identification of cytokine-specific sensory neural signals by decoding murine vagus nerve activity. *Proc Natl Acad Sci USA*. 2018; 115(21): E4843–E4852, doi: [10.1073/pnas.1719083115](https://doi.org/10.1073/pnas.1719083115), indexed in Pubmed: [29735654](https://pubmed.ncbi.nlm.nih.gov/29735654/).

# The influence of functional pinealectomy and exogenous melatonin application on healing of a burr hole in adult rat calvaria: a histological and immunohistochemical study

H.K. Basaloglu<sup>1</sup>, M. Turgut<sup>2,3</sup>, C. Şirin<sup>4</sup>, Y. Uyanıkgil<sup>4,5,6</sup>, B. Demirci<sup>7</sup>, E.O. Cetin<sup>8</sup>

<sup>1</sup>Department of Histology and Embryology, Adnan Menderes University, Faculty of Medicine, Aydın, Turkey

<sup>2</sup>Department of Neurosurgery, Adnan Menderes University, Faculty of Medicine, Aydın, Turkey

<sup>3</sup>Department of Histology and Embryology, Adnan Menderes University, Health Sciences Institute, Aydın, Turkey

<sup>4</sup>Department of Histology and Embryology, Ege University, Faculty of Medicine, Izmir, Turkey

<sup>5</sup>Department of Stem Cell, Ege University, Health Science Institute, Izmir, Turkey

<sup>6</sup>Cord Blood, Cell and Tissue Research and Application Centre, Ege University, Izmir, Turkey

<sup>7</sup>Department of Pharmacology, Adnan Menderes University, Faculty of Medicine, Aydın, Turkey

<sup>8</sup>Department of Pharmaceutical Technology, Department of Biopharmaceutics and Pharmacokinetics, Ege University Faculty of Pharmacy, Izmir, Turkey

[Received: 20 March 2021; Accepted: 19 April 2021; Early publication date: 6 May 2021]

**Background:** Even today, repair of the cranial defects still represents a significant challenge in neurosurgery and various options have been used for their reconstruction to date. However, there are very few studies investigating the effects of exogenous administration of melatonin (MEL) as an agent that promotes bone regeneration. The goal of this study was to investigate the effects of functional pinealectomy (Px) and exogenous MEL administration on the bone repair properties and surrounding connective tissue alterations in a rat calvaria model.

**Materials and methods:** The total of 30 adult female Wistar-Albino rats was randomly divided into three groups ( $n = 10$ ): control group (CO; 12 h light/12 h dark exposure), functional Px group (24 h light exposure, light-induced functional Px), and Px+MEL group (light-induced Px + MEL, 20 mg/kg/day for 12 weeks). Critical-sized burr-hole defects (diameter: 3.0 mm) were surgically created by a single operator in the calvarium of all rats, using an electric drill. Animals in Px+MEL group received MEL 20 mg/kg/day for 12 weeks. At the end of the study, bone healing and connective tissue alterations surrounding drilled defect area in the rat calvaria were determined in haematoxylin-eosin-stained and Mallory Azan slices applied in anti-bone sialoprotein. Image Pro Express 4.5 programme was used for histomorphometric calculation of areas of new bone and fibrotic tissue. Normality control was performed by Shapiro-Wilk test. Variance homogeneities were examined by Shapiro-Wilk and Levene tests; Tukey HSD test was used as a post hoc method since there was no homogeneity problem. All hypothesis tests were performed at the 0.05 significance level.

**Results:** Histological analysis showed that the bone repair process in the Px+MEL group was similar to that of the CO group, whereas the functional Px group showed a delay. Histomorphometrically, it was found that the Px group had the largest hole diameter and the most fibrotic scar area, although no binary statistical significance was found between the CO and Px+MEL groups ( $p = 0.910$ ).

Address for correspondence: E.O. Cetin, PhD, Ege University Faculty of Pharmacy, Department of Pharmaceutical Technology, Department of Biopharmaceutics and Pharmacokinetics, 35100 Bornova, Izmir, Turkey, tel: +90 232 3905908, fax: +90 2323422142, e-mail: emel.oyku.cetin@ege.edu.tr

This article is available in open access under Creative Common Attribution-Non-Commercial-No Derivatives 4.0 International (CC BY-NC-ND 4.0) license, allowing to download articles and share them with others as long as they credit the authors and the publisher, but without permission to change them in any way or use them commercially.

*In terms of vascularisation, it was observed that the most vascular structure was found in the Px+MEL group among the scar tissue and ossification areas, while the vascularisation was the least in the Px group ( $p < 0.001$ ).*

*Conclusions: Our findings revealed that bone repair process was impaired in functional Px group, but exogenous MEL replacement was able to restore this response. Thus, it is concluded that utilisation of MEL may improve the bone repair in calvarial defects. (Folia Morphol 2022; 81, 2: 271–279)*

**Key words: bone regeneration, calvaria, melatonin, pinealectomy, rat**

## INTRODUCTION

Bone healing, also called bone turnover or restoration of the bone microarchitecture, after various acquired defects or congenital deformities of the cranium, such as traumatic injuries, congenital deformities, decompressive craniectomies, or bone flap loss due to infections still represents a significant challenge in neurosurgery. Although numerous studies have been conducted to develop biomaterials displaying osteoconductive and/or osteoinductive properties to date, utilisation of autogenous bone for repair of the cranial defects seems to be the most appropriate option, possibly due to its biosafety and cost advantage [29]. However, risks of additional morbidity to the patient related to obtaining the graft and resorption of the autogenous bone grafts limit their utilisation in the repair of the cranial defects. As a result, there is still no consensus on which agent to be used in cranioplasty is better in reconstruction of the cranial defects in humans. To improve the bone regeneration and quality of the bone, therefore, use of various agents such as topical or systemic application of growth factors, cytokines and melatonin (MEL) has attracted the attention of scientists [3–5, 7–9, 14, 16, 21, 22, 25, 26, 30, 33–37].

In normal remodelling cycle of the bone, which is balanced between bone-forming osteoblasts and bone resorbing osteoclasts, the resorption phase is followed by bone formation phase, including osteoid formation and then mineralisation [1, 2, 10]. In recent years, it has been reported that MEL can have a pivotal role in this process when age-related osteoporosis is manifested, possibly due to an imbalance in bone turnover related to decreased level of the circulating MEL hormone; thus, MEL could act as an autacoid or a local growth factor for the bone cells [4, 6, 7, 30, 36]. Importantly, it has also been reported that the proliferation of osteoblasts and the expression of type I collagen and biochemical markers of bone turnover,

including bone sialoprotein (BSP) are also promoted by MEL [7, 9, 17, 25, 26, 35]. Despite promising results, however, very few studies have been conducted to investigate the effects of exogenous administration of MEL as an agent that promotes bone regeneration to date and there is still no consensus on which agent to be used in cranioplasty is better in reconstruction of the cranial defects in humans.

In this experimental study, our main purpose was to investigate the effects of exogenous MEL administration on bone healing and connective tissue alterations surrounding the bone defect histopathologically after production of a burr hole in the calvarium of the rats exposed to functional pinealectomy (Px).

## MATERIALS AND METHODS

In this study, 30 adult 200 g female Wistar-Albino rats were used. The experimental protocol was approved by the Ethical Committee of Aydın Adnan Menderes University (HADYEK 64583101/2014/063). Animals were housed in rat cages in standard conditions ( $24 \pm 2^\circ\text{C}$  and  $50 \pm 5\%$  humidity), exposed to 12:12-h light/dark cycle, fed with standardised rodent chow and tap water *ad libitum*.

The rats were divided into three groups, with 10 animals per group. The first group of animals formed the control group (CO), which was exposed to 12:12-h light/dark cycle. The second and third groups were exposed to 24-h continuous light for 12 weeks in order to produce light-induced functional Px, as described in a previous study [23]. Next, all rats underwent ketamine/xylazine (50 and 5 mg/kg, respectively) anaesthesia, and a burr hole (diameter: 3.0 mm) was produced using an electric drill (CLASS Mini Grinder sets, PRC) on the right side of the calvarium. Then the wound was closed (Fig. 1). The animals in the second and third groups were moved back to the continuous light-burning room; meanwhile exogenous MEL treatment (Px+MEL) was applied to only the third group.

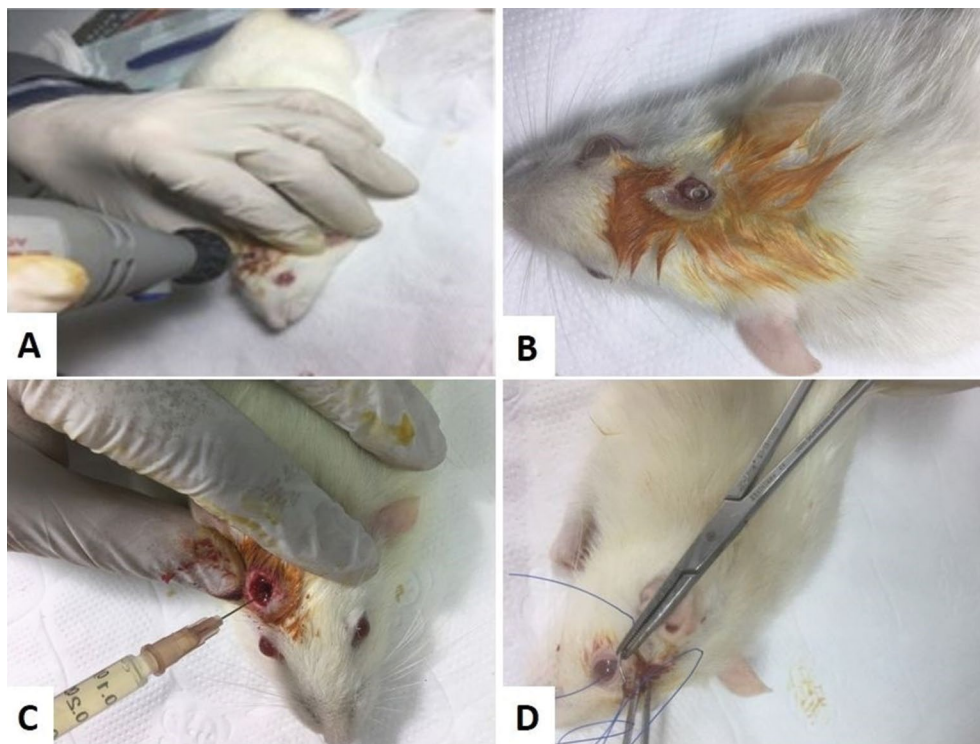


**Figure 1.** The process of establishing the animal model of bone defect as burr hole on the right side of the rat calvarium using a drill with 3 mm in diameter.

Melatonin (N-acetyl-5-methoxytryptamine, cat. no: M-5250, Sigma Chemical Co., St. Louis, MO, USA) was first dissolved in pure ethanol and kept in  $-20^{\circ}\text{C}$ . The second dilution of this stock was freshly prepared in saline to have 5% ethanol concentration [13]. In the third group, 20 mg/kg/day of MEL was given intraperitoneally as a single injection for 12 weeks.

At the end of 12 weeks, all the rats were decapitated under the ketamine/xylazine (50 and 5 mg/kg, respectively) anaesthesia. The calvarial area which underwent the burr hole operation was removed for further histological study.

#### Histological examination of calvaria

Following sacrifice, calvaria were collected into 10% formalin solution for at least 24 h before placement in decalcification solution containing 10% formaldehyde and 20% formic acid for 2 months, softening of the tissue was controlled by punching irregularly. Tissues were embedded to block in blue-beaded paraffin solution after processing in alcohol and xylol series.  $5\ \mu\text{m}$  sections were obtained by Leica RM 2145 microtome, transferred to water bath at  $45^{\circ}\text{C}$  and microwaved to ensure adhesion and to remove any paraffin remaining. Haematoxylin

and eosin (H&E), Mallory Azan staining and anti-BSP (bs-4729R, Bioss, 1:100) were applied to the related calvarial area and the surgical specimens were evaluated at  $10\text{--}20\times$  magnification using an Olympus C5050 camera attached to Olympus BX51 light microscope.

#### Histomorphometry

For histomorphometric analysis, counting and measurements were made for hole diameter, fibrotic scar areas, ossification areas and number of vessels in the sections taken from calvaria samples from each subject in the experimental groups [15, 18, 42]. Measurement for new ossification areas and fibrotic scar areas was calculated in square micrometres ( $\mu\text{m}^2$ ) using Image Pro Express 4.5 (Media Cybernetics, Inc., Rockville, MD, USA) programme.

#### Statistical analysis

Data analysis was carried out in IBM SPSS (Statistical Package for Social Sciences) Statistics for Windows, Version 25.0 (IBM Corp. Released 2017, Armonk, NY) package programme. Group comparisons were performed using one-way analysis of variance method. Normality control was performed by Shapiro-Wilk test

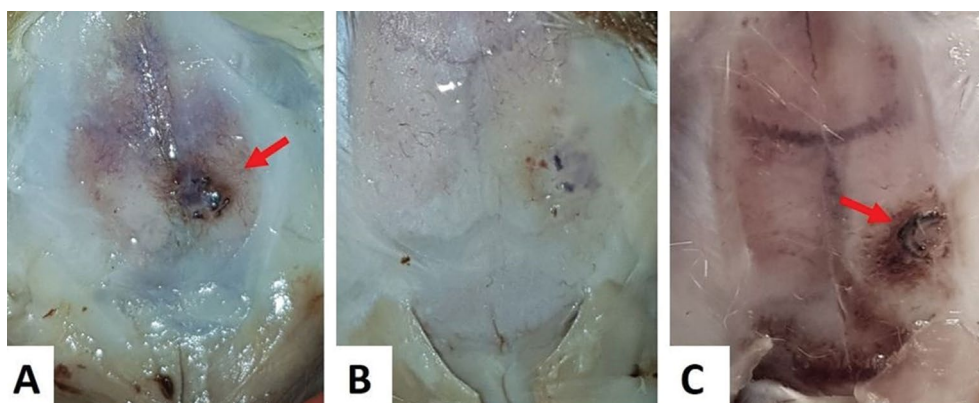


**Figure 2.** Demonstration of the experimentally produced bone lesions in all rat groups; **A.** Control (CO) group; **B.** Pinelectomy (Px) group; **C.** Pinelectomy plus melatonin (Px+MEL) group.

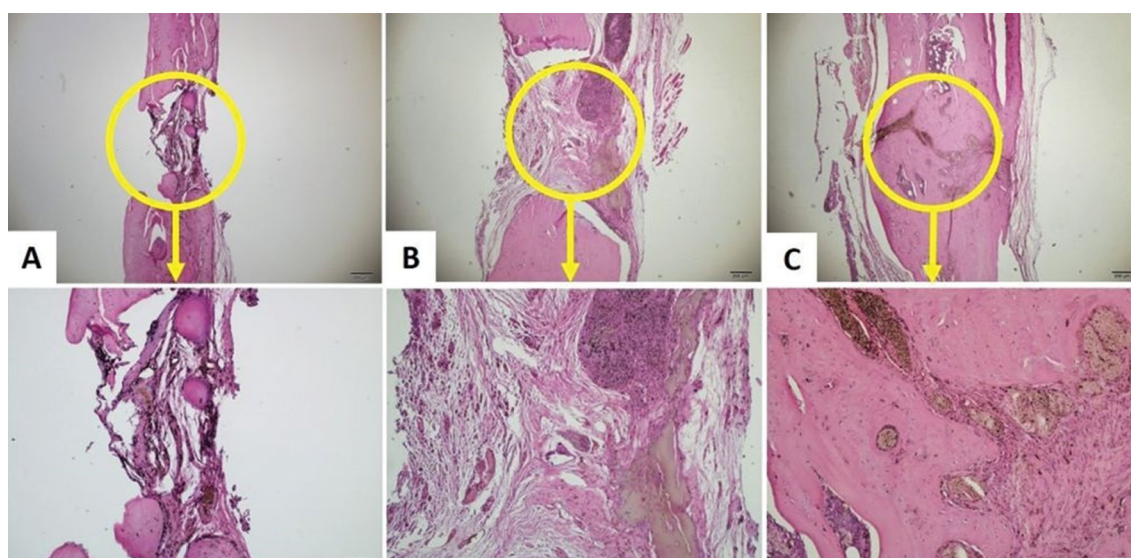


**Figure 3.** Microscopic evaluation of all groups; **A.** Control (CO) group; **B.** Pinelectomy (Px) group; **C.** Pinelectomy plus melatonin (Px+MEL) group.

that obtained from estimated error. Since there was no problem of adaptation to normal distribution, the study continued with one-way analysis of variance. Variance homogeneities were examined by Levene test; Tukey HSD test was used as a post hoc method, since there was no homogeneity problem. All hypothesis tests were performed at the 0.05 significance level, thus  $p < 0.05$  was considered significant.

## RESULTS

### Macroscopic examination

When the skin on the calvarium was dissected, drilled holes were detected on the bone and these closed holes were observed macroscopically (Fig. 1). It

was found that the scar tissue in the Px+MEL samples were closer to normal when compared with the other two groups (Fig. 2).

### Microscopic examination

In the microscopic sections, the orientation of the hole in the bone was adjusted and serial sections were taken. These sections were stained in H&E and Mallory Azan in order to show the general structure and were applied in anti-BSP immunohistochemistry. Histologically, the holes were found in the sections. Importantly, it was found that these hole structures were filled with irregular dense connective tissue called fibrotic in both control group and Px group (Fig. 3).

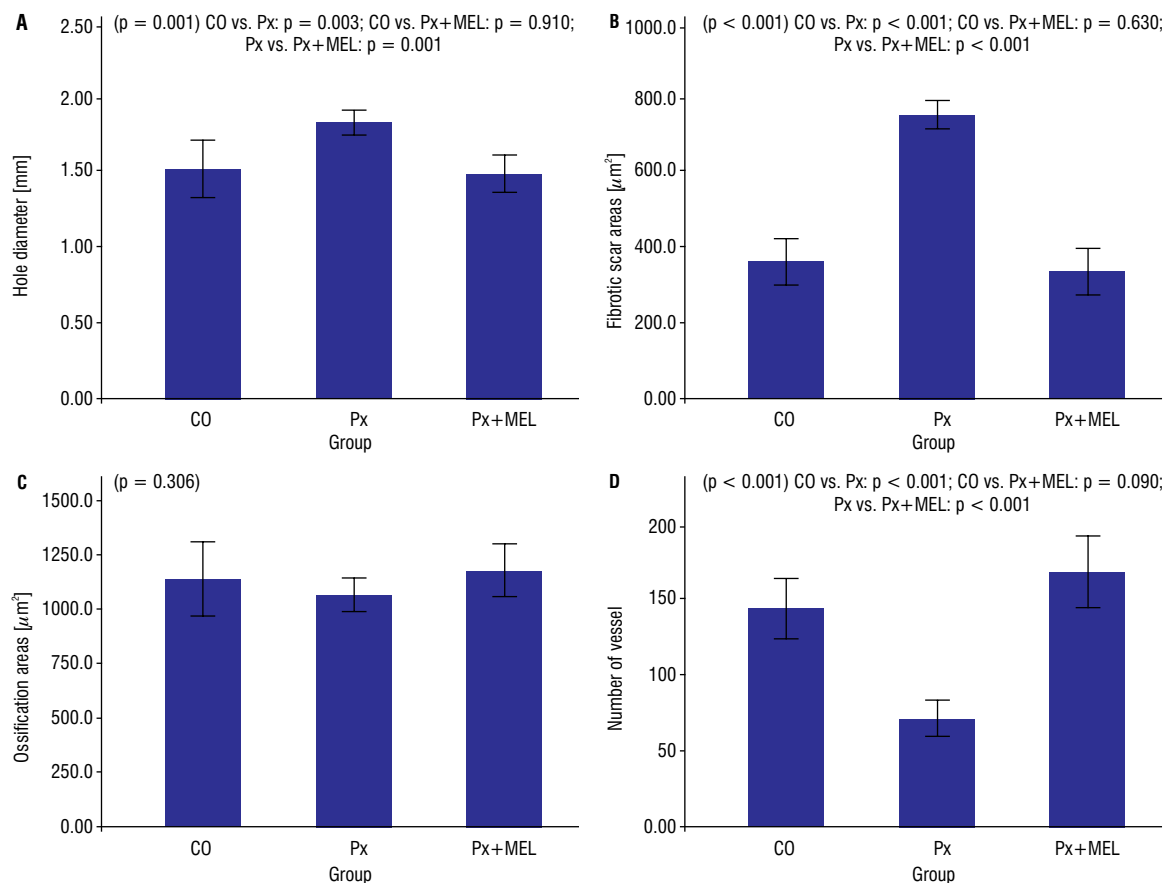


**Figure 4.** Statistical evaluation graph of histomorphometric analysis. Graphical representation of hole diameter (A), fibrotic scar area (B), ossification area (C) and number of vessels (D) in all groups; CO — control group; Px — pinealectomy; MEL — melatonin.

When the hole diameters were evaluated statistically, it was seen that the Px group had the largest hole diameter. No statistical significance was found in the comparison of the groups with each other (Fig. 4A). When evaluated in terms of fibrotic scar area, it was calculated that the most scar area was in the Px group, although no binary statistical significance was found between the CO and Px+MEL groups. Importantly, a statistical significance was found when comparing these two groups with the Px group ( $p < 0.001$ ) (Fig. 4B). When evaluated in terms of ossification areas, it was observed that the most ossification was in the Px+MEL group, while the highest ossification was found in the Px group. However, there was no statistical significance between the groups ( $p = 0.306$ ) (Fig. 4C). In terms of vascularisation, it was observed that the most vascular structure was found in the Px+MEL group among the scar areas and ossification areas, while the vascularisation was the least in the Px group. When the CO and Px groups were compared, a statistically significant reduction was observed ( $p < 0.001$ ).

There was also a statistical significance difference between Px and Px+MEL groups ( $p < 0.001$ ) (Fig. 4D).

When this connective tissue structure was examined at larger magnification, it was found that it contains fibroblast-like cells and type I collagen bundles. In Px group, however, new bone splices were found that they were localised to different sites located within the connective tissue, possibly formed by intramembranous ossification. More importantly, in Px+MEL group, it was noted that this connective tissue area was small and ossification developed in most of the structure. With this appearance, it was the experimental group, which was closest to the normal histological structure of the other groups. Mallory Azan staining showed that the type I collagen bundles were stained blue while the newly formed bone areas were red (Fig. 5).

## DISCUSSION

This experimental study evidenced that MEL replacement is related to the improvement of bone healing,

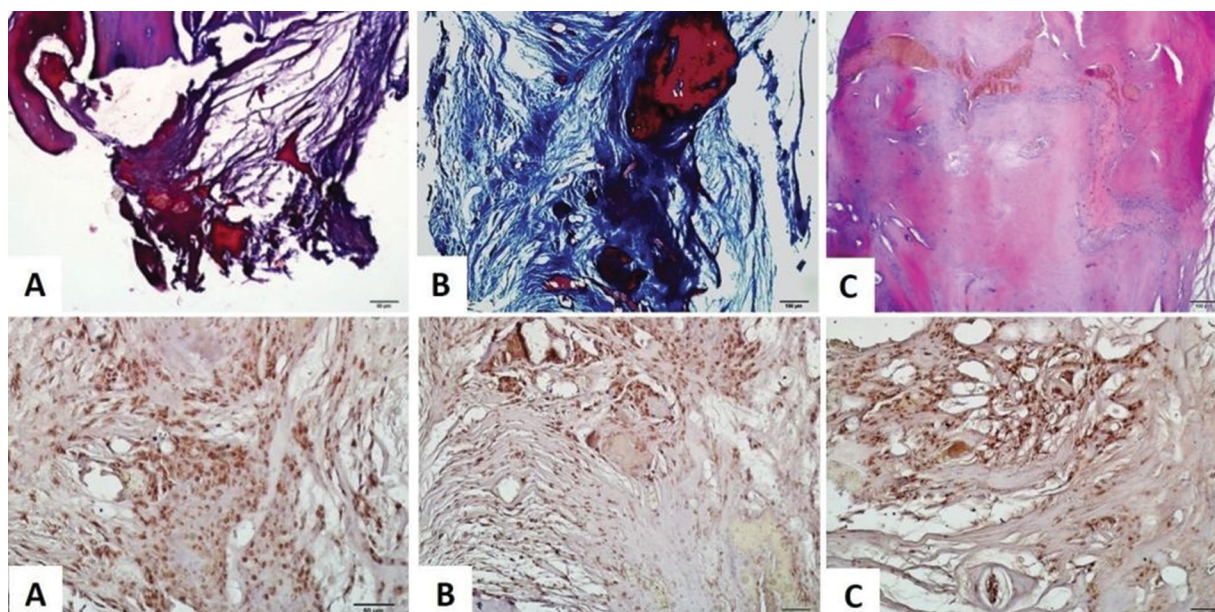


**Figure 5.** Microscopic evaluation of all groups; **A.** Control (CO) group; **B.** Pinealectomy (Px) group; **C.** Pinealectomy plus melatonin (Px+MEL) group.

in contrast to functional Px group, possibly due to increased osteoblastic activity and modulation of connective tissue alterations surrounding the bone defect driven by exogenous MEL administration in adult rats.

Previous studies reported that matrix cellular proteins, such as BSP, also called SPARC or BM40, osteopontin, tenascin C, and thrombospondin-1 and -2, were the critical regulators of bone healing process [1, 10]. BSP is composed of mineralised tissues such as bone, dentin, cementum and calcified cartilage. It binds to hydroxyapatite crystals and an integral part of the mineral matrix in bone tissue. Now, it is known to be an important component of the extracellular matrix of bone and forms all non-collagen proteins found in bone and cementum. In our study, the cell characterisation of the osteoblast lineage was via immunostaining for BSP. The CO and Px+MEL groups are similar in terms of BSP, both groups have a high level of immune reaction. A lower degree of immunoreaction was detected in the Px group.

Several studies documented that MEL had been linked to osteoblastic differentiation and bone metabolism [4, 6, 30, 36]. In a previous study, Witt-Enderby et al. (2006) [41] demonstrated that MEL influences bone cell precursors in rat bone marrow which has high concentrations of MEL. Koyama, et al. (2002) [14] showed that the administration of pharmacological doses of MEL during the growth of young rats increased the bone mass through the inhibition of bone resorption.

To date, however, the role of MEL replacement has not yet been widely evaluated in adult animals with lower production of endogenous MEL, as did in our functional Px group. In this study, we intended for investigation its role on bone healing; therefore we applied a functional Px rat model to evaluate the effect of exogenous MEL administration histopathologically [23].

Experimental studies revealed that action of exogenous and endogenous MEL upon bone tissue is due to an increased osteoblastic activity, a decreased osteoclastic activity, and an increased osteoclastogenesis inhibitory factor, also known as osteoprotegerin, thus increasing its mass [14, 19, 20, 33, 40]. In addition to its stimulating effect on bone metabolism and production of type I collagen, inhibitory effect on proteasomes has also been suggested [14, 19, 20, 33, 40]. Thus, promotion of bone healing by MEL could be related to one or more of the following possible mechanisms: the promotion of the osteoblast differentiation and/or activity, an increased expression of the osteoprotegerin by osteoblasts, resulting with a decreased differentiation of osteoclasts, and increased scavenging of free radicals which were generated by osteoclasts [31]. Further, and more specifically, it has been speculated that MEL interferes with bone healing in several ways: through modulation of oxidative stress [27, 28, 32], collagen fibril formation [19], differentiation of osteoblasts via PDGF/AKT signalling pathway [9, 25,

26, 35, 43], or activity of osteoblasts and osteoclasts via MEL-MT2 receptor pathway [9, 34, 41] or RANK/NF- $\kappa$ B signalling pathway [14, 26] or Wnt/ $\beta$ -catenin signalling pathway [16, 25, 40]. Moreover, MEL has also been found to stimulate gene expression of BSP and other bone marker proteins including alkaline phosphate, secreted protein, osteocalcin and osteopontin [30].

Despite accumulating evidence about the effects of MEL upon regeneration of the bone tissue during the last decades, its use for cranial defects has received little attention and to date, healing of the bone after application of MEL has been evaluated in few experimental animal studies using model of calvaria [9, 25, 26, 35]. In addition to stimulatory action of MEL related to bone formation, however, possible effects of MEL upon the connective tissue surrounding the cranial defect have been also investigated for the first time in this study. Based on our findings, it is evident that the ossification process is accelerated by the effect of exogenous MEL, while the absence of endogenous MEL also negatively affects ossification.

On the other hand, it has been reported that a lower production of MEL, by some genetic modifications (pineal MEL deficient mice, C57BL/6 and Swiss strains) [12, 34], or various Px techniques (surgical or functional) [21, 22, 24, 37–39] results in alterations in structure, density and mechanical strength of the bone in animals including mice, rat, rabbit, chicken, sheep, and fish [9, 34]. To the best of our knowledge, however, no study was performed to evaluate the healing in endogenous MEL deficiency and exogenous MEL administration, when added to biomaterials or implants [3–6, 36]. Thus, the process of how the absence of endogenous MEL interferes with the bone healing is unclear. Considering this, the purpose of this study was to evaluate the cellular changes that occur in the bone of rats undergoing Px that received or did not receive daily exogenous MEL replacement as a possible therapy for conditions characterised by a decrease in the secretion of this hormone by the pineal gland.

In a previous *in vitro* study, it has been suggested that exogenous MEL administration has positive effects on both angiogenesis and wound healing [19]. In a recently published paper, Filipowska et al. (2017) [11] also suggested the role of production of vascular endothelial growth factor (VEGF) by either hypertrophic chondrocytes or differentiating mesenchymal cells in bone development and regeneration. In fact, our findings confirm that beneficial effects of MEL on blood vessel invasion for initiation of bone

tissue formation, possibly as a result of increased VEGF production by MEL.

Taken together our findings provide an evidence that the absence of MEL delays repair and exogenous MEL replacement regulates this alteration, which would emphasize the role of this neurohormone in bone remodelling, especially in conditions in which a decrease occurs in the circadian release capacity of this hormone by the pineal gland, as did in various clinical disease conditions. Undoubtedly, further understanding of pathological changes in the bone tissue and their reversion is critical for the success of MEL replacement treatment. Two limitations of our study that created an *in vivo* rat calvaria model are as follows: absence of any analysis for inorganic material content of bone tissue and difference of drilled defects from those in humans in terms of bone remodelling. Also, lack of any imaging study illustrating bone healing and angiogenesis is another limitation of the study. Future studies including imaging are needed for better understanding of modulation of osteoblast and osteoclast function and mineralization with MEL in cases of bone defect that simulates the situation in human.

## CONCLUSIONS

Based on the results of this study, we may notice an interaction in cellular responses and protein activity in the absence of MEL, suggesting that when there is a delay in the production of proteins that stimulate bone formation, ossification because of hormone administration increases vascularisation and may result in less scar tissue formation. The MEL replacement, in most parameters evaluated in this study, showed behaviour very close to that of the CO group. Therefore, the absence of the pineal gland impairs the bone repair process during osseointegration; however, the daily exogenous MEL replacement was able to partially restore this response. However, the authors believe that further studies should confirm this information in future.

## Acknowledgements

The authors thank to Research Foundation of Aydin Adnan Menderes University (ADU-TPF-15019) for funding of this research. We also thank the anonymous reviewers of the journal "Folia Morphologica" for their constructive comments and help with the manuscript.

**Conflict of interest:** None declared

## REFERENCES

- Alford AI, Hankenson KD. Matricellular proteins: Extracellular modulators of bone development, remodeling, and regeneration. *Bone*. 2006; 38(6): 749–757, doi: [10.1016/j.bone.2005.11.017](https://doi.org/10.1016/j.bone.2005.11.017), indexed in Pubmed: [16412713](https://pubmed.ncbi.nlm.nih.gov/16412713/).
- Bilezikian JP, Raisz LG, Rodan GA. Principles of bone biology. 2nd. Academic Press, San Diego 1696.
- Calvo-Guirado JL, Gómez-Moreno G, Barone A, et al. Melatonin plus porcine bone on discrete calcium deposit implant surface stimulates osteointegration in dental implants. *J Pineal Res*. 2009; 47(2): 164–172, doi: [10.1111/j.1600-079X.2009.00696.x](https://doi.org/10.1111/j.1600-079X.2009.00696.x), indexed in Pubmed: [19570131](https://pubmed.ncbi.nlm.nih.gov/19570131/).
- Calvo-Guirado JL, Gómez-Moreno G, López-Marí L, et al. Actions of melatonin mixed with collagenized porcine bone versus porcine bone only on osteointegration of dental implants. *J Pineal Res*. 2010; 48(3): 194–203, doi: [10.1111/j.1600-079X.2009.00743.x](https://doi.org/10.1111/j.1600-079X.2009.00743.x), indexed in Pubmed: [20443224](https://pubmed.ncbi.nlm.nih.gov/20443224/).
- Calvo-Guirado JL, Gómez-Moreno G, Maté-Sánchez JE, et al. New bone formation in bone defects after melatonin and porcine bone grafts: experimental study in rabbits. *Clin Oral Implants Res*. 2015; 26(4): 399–406, doi: [10.1111/clr.12364](https://doi.org/10.1111/clr.12364), indexed in Pubmed: [24602080](https://pubmed.ncbi.nlm.nih.gov/24602080/).
- Calvo-Guirado JL, Ramírez-Fernández MP, Gómez-Moreno G, et al. Melatonin stimulates the growth of new bone around implants in the tibia of rabbits. *J Pineal Res*. 2010; 49(4): 356–363, doi: [10.1111/j.1600-079X.2010.00801.x](https://doi.org/10.1111/j.1600-079X.2010.00801.x), indexed in Pubmed: [20666975](https://pubmed.ncbi.nlm.nih.gov/20666975/).
- Cardinali DP, Ladizesky MG, Boggio V, et al. Melatonin effects on bone: experimental facts and clinical perspectives. *J Pineal Res*. 2003; 34(2): 81–87, doi: [10.1034/j.1600-079x.2003.00028.x](https://doi.org/10.1034/j.1600-079x.2003.00028.x), indexed in Pubmed: [12562498](https://pubmed.ncbi.nlm.nih.gov/12562498/).
- Chaves LH, Giovanini AF, Zielak JC, et al. Growth hormone effects on healing efficacy, bone resorption and renal morphology of rats: histological and histometric study in rat calvaria. *Heliyon*. 2020; 6(10): e05226, doi: [10.1016/j.heliyon.2020.e05226](https://doi.org/10.1016/j.heliyon.2020.e05226), indexed in Pubmed: [33102851](https://pubmed.ncbi.nlm.nih.gov/33102851/).
- Clafshenkel WP, Rutkowski JL, Palchesko RN, et al. A novel calcium aluminate-melatonin scaffold enhances bone regeneration within a calvarial defect. *J Pineal Res*. 2012; 53(2): 206–218, doi: [10.1111/j.1600-079X.2012.00989.x](https://doi.org/10.1111/j.1600-079X.2012.00989.x), indexed in Pubmed: [22462771](https://pubmed.ncbi.nlm.nih.gov/22462771/).
- Delany AM, Hankenson KD. Thrombospondin-2 and SPARC/osteonectin are critical regulators of bone remodeling. *J Cell Commun Signal*. 2009; 3(3-4): 227–238, doi: [10.1007/s12079-009-0076-0](https://doi.org/10.1007/s12079-009-0076-0), indexed in Pubmed: [19862642](https://pubmed.ncbi.nlm.nih.gov/19862642/).
- Filipowska J, Tomaszewski KA, Niedźwiedzki Ł, et al. The role of vasculature in bone development, regeneration and proper systemic functioning. *Angiogenesis*. 2017; 20(3): 291–302, doi: [10.1007/s10456-017-9541-1](https://doi.org/10.1007/s10456-017-9541-1), indexed in Pubmed: [28194536](https://pubmed.ncbi.nlm.nih.gov/28194536/).
- Gómez-Corvera A, Cerrillo I, Molinero P, et al. Evidence of immune system melatonin production by two pineal melatonin deficient mice, C57BL/6 and Swiss strains. *J Pineal Res*. 2009; 47(1): 15–22, doi: [10.1111/j.1600-079X.2009.00683.x](https://doi.org/10.1111/j.1600-079X.2009.00683.x), indexed in Pubmed: [19522737](https://pubmed.ncbi.nlm.nih.gov/19522737/).
- Kerem H, Akdemir O, Ates U, et al. The effect of melatonin on a dorsal skin flap model. *J Invest Surg*. 2014; 27(2): 57–64, doi: [10.3109/08941939.2013.835892](https://doi.org/10.3109/08941939.2013.835892), indexed in Pubmed: [24063690](https://pubmed.ncbi.nlm.nih.gov/24063690/).
- Koyama H, Nakade O, Takada Y, et al. Melatonin at pharmacologic doses increases bone mass by suppressing resorption through down-regulation of the RANKL-mediated osteoclast formation and activation. *J Bone Miner Res*. 2002; 17(7): 1219–1229, doi: [10.1359/jbmr.2002.17.7.1219](https://doi.org/10.1359/jbmr.2002.17.7.1219), indexed in Pubmed: [12096835](https://pubmed.ncbi.nlm.nih.gov/12096835/).
- Li J, Jin L, Wang M, et al. Repair of rat cranial bone defect by using bone morphogenetic protein-2-related peptide combined with microspheres composed of polylactic acid/polyglycolic acid copolymer and chitosan. *Biomed Mater*. 2015; 10(4): 045004, doi: [10.1088/1748-6041/10/4/045004](https://doi.org/10.1088/1748-6041/10/4/045004), indexed in Pubmed: [26154695](https://pubmed.ncbi.nlm.nih.gov/26154695/).
- Li X, Li Z, Wang J, et al. Wnt4 signaling mediates protective effects of melatonin on new bone formation in an inflammatory environment. *FASEB J*. 2019; 33(9): 10126–10139, doi: [10.1096/fj.201900093RR](https://doi.org/10.1096/fj.201900093RR), indexed in Pubmed: [31216173](https://pubmed.ncbi.nlm.nih.gov/31216173/).
- Liu J, Huang F, He HW. Melatonin effects on hard tissues: bone and tooth. *Int J Mol Sci*. 2013; 14(5): 10063–10074, doi: [10.3390/ijms140510063](https://doi.org/10.3390/ijms140510063), indexed in Pubmed: [23665905](https://pubmed.ncbi.nlm.nih.gov/23665905/).
- Liu W, Kang N, Seriwatanachai D, et al. Chronic kidney disease impairs bone defect healing in rats. *Sci Rep*. 2016; 6(1): 23041, doi: [10.1038/srep23041](https://doi.org/10.1038/srep23041), indexed in Pubmed: [26955758](https://pubmed.ncbi.nlm.nih.gov/26955758/).
- Nakade O, Koyama H, Arijii H, et al. Melatonin stimulates proliferation and type I collagen synthesis in human bone cells in vitro. *J Pineal Res*. 1999; 27(2): 106–110, doi: [10.1111/j.1600-079x.1999.tb00603.x](https://doi.org/10.1111/j.1600-079x.1999.tb00603.x), indexed in Pubmed: [10496146](https://pubmed.ncbi.nlm.nih.gov/10496146/).
- Ohlsson C, Bengtsson BA, Isaksson OG, et al. Growth hormone and bone. *Endocr Rev*. 1998; 19(1): 55–79, doi: [10.1210/edrv.19.1.0324](https://doi.org/10.1210/edrv.19.1.0324), indexed in Pubmed: [9494780](https://pubmed.ncbi.nlm.nih.gov/9494780/).
- Ostrowska Z, Kos-Kudła B, Marek B, et al. The influence of pinealectomy and melatonin administration on the dynamic pattern of biochemical markers of bone metabolism in experimental osteoporosis in the rat. *Neuro Endocrinol Lett*. 2002; 23 Suppl 1: 104–109, indexed in Pubmed: [12019362](https://pubmed.ncbi.nlm.nih.gov/12019362/).
- Ostrowska Z, Kos-Kudła B, Nowak M, et al. The relationship between the daily profile of chosen biochemical markers of bone metabolism and melatonin and other hormone secretion in rats under physiological conditions. *Neuro Endocrinol Lett*. 2002; 23(5-6): 417–425, indexed in Pubmed: [12500163](https://pubmed.ncbi.nlm.nih.gov/12500163/).
- Özkaya M, Gündoğdu A, Seyran M, et al. Effect of exogenous melatonin administration on pain threshold in exercise trained rats under light-induced functional pinealectomy. *Biol Rhythm Res*. 2014; 45(6): 849–859, doi: [10.1080/09291016.2014.923619](https://doi.org/10.1080/09291016.2014.923619).
- Pawlicki B, Henry BM, Tomaszewski KA, et al. Neonatal pinealectomy in rats: a simple micro-suction technique. *Folia Med Cracov*. 2017; 57(1): 39–46, indexed in Pubmed: [28608861](https://pubmed.ncbi.nlm.nih.gov/28608861/).
- Ping Z, Hu X, Wang L, et al. Melatonin attenuates titanium particle-induced osteolysis via activation of Wnt/ $\beta$ -catenin signaling pathway. *Acta Biomater*. 2017; 51: 513–525, doi: [10.1016/j.actbio.2017.01.034](https://doi.org/10.1016/j.actbio.2017.01.034), indexed in Pubmed: [28088671](https://pubmed.ncbi.nlm.nih.gov/28088671/).
- Ping Z, Wang Z, Shi J, et al. Inhibitory effects of melatonin on titanium particle-induced inflammatory bone resorption and osteoclastogenesis via suppression of NF- $\kappa$ B sig-

- naling. *Acta Biomater.* 2017; 62: 362–371, doi: [10.1016/j.actbio.2017.08.046](https://doi.org/10.1016/j.actbio.2017.08.046), indexed in Pubmed: [28867647](https://pubmed.ncbi.nlm.nih.gov/28867647/).
27. Ramírez-Fernández MP, Calvo-Guirado JL, de-Val JEM, et al. Melatonin promotes angiogenesis during repair of bone defects: a radiological and histomorphometric study in rabbit tibiae. *Clin Oral Investig.* 2013; 17(1): 147–158, doi: [10.1007/s00784-012-0684-6](https://doi.org/10.1007/s00784-012-0684-6), indexed in Pubmed: [22323056](https://pubmed.ncbi.nlm.nih.gov/22323056/).
  28. Reiter RJ, Calvo JR, Karbownik M, et al. Melatonin and its relation to the immune system and inflammation. *Ann N Y Acad Sci.* 2000; 917: 376–386, doi: [10.1111/j.1749-6632.2000.tb05402.x](https://doi.org/10.1111/j.1749-6632.2000.tb05402.x), indexed in Pubmed: [11268363](https://pubmed.ncbi.nlm.nih.gov/11268363/).
  29. Rogers GF, Greene AK. Autogenous bone graft: basic science and clinical implications. *J Craniofac Surg.* 2012; 23(1): 323–327, doi: [10.1097/SCS.0b013e318241dcba](https://doi.org/10.1097/SCS.0b013e318241dcba), indexed in Pubmed: [22337435](https://pubmed.ncbi.nlm.nih.gov/22337435/).
  30. Roth JA, Kim BG, Lin WL, et al. Melatonin promotes osteoblast differentiation and bone formation. *J Biol Chem.* 1999; 274(31): 22041–22047, doi: [10.1074/jbc.274.31.22041](https://doi.org/10.1074/jbc.274.31.22041), indexed in Pubmed: [10419530](https://pubmed.ncbi.nlm.nih.gov/10419530/).
  31. Sánchez-Barceló EJ, Mediavilla MD, Tan DX, et al. Scientific basis for the potential use of melatonin in bone diseases: osteoporosis and adolescent idiopathic scoliosis. *J Osteoporos.* 2010; 2010: 830231, doi: [10.4061/2010/830231](https://doi.org/10.4061/2010/830231), indexed in Pubmed: [20981336](https://pubmed.ncbi.nlm.nih.gov/20981336/).
  32. Seema R, Chandana H. Melatonin ameliorates oxidative stress and induces cellular proliferation of lymphoid tissues of a tropical rodent, *Funambulus pennanti*, during reproductively active phase. *Protoplasma.* 2013; 250(1): 21–32, doi: [10.1007/s00709-011-0367-1](https://doi.org/10.1007/s00709-011-0367-1), indexed in Pubmed: [22205185](https://pubmed.ncbi.nlm.nih.gov/22205185/).
  33. Sethi S, Radio NM, Kotlarczyk MP, et al. Determination of the minimal melatonin exposure required to induce osteoblast differentiation from human mesenchymal stem cells and these effects on downstream signaling pathways. *J Pineal Res.* 2010; 49(3): 222–238, doi: [10.1111/j.1600-079X.2010.00784.x](https://doi.org/10.1111/j.1600-079X.2010.00784.x), indexed in Pubmed: [20626586](https://pubmed.ncbi.nlm.nih.gov/20626586/).
  34. Sharan K, Lewis K, Furukawa T, et al. Regulation of bone mass through pineal-derived melatonin-MT2 receptor pathway. *J Pineal Res.* 2017; 63(2): e12423, doi: [10.1111/jpi.12423](https://doi.org/10.1111/jpi.12423), indexed in Pubmed: [28512916](https://pubmed.ncbi.nlm.nih.gov/28512916/).
  35. Shino H, Hasuike A, Arai Y, et al. Melatonin enhances vertical bone augmentation in rat calvaria secluded spaces. *Med Oral Patol Oral Cir Bucal.* 2016; 21(1): e122–e126, doi: [10.4317/medoral.20904](https://doi.org/10.4317/medoral.20904), indexed in Pubmed: [26595835](https://pubmed.ncbi.nlm.nih.gov/26595835/).
  36. Tresguerres IF, Tamimi F, Eimar H, et al. Melatonin dietary supplement as an anti-aging therapy for age-related bone loss. *Rejuvenation Res.* 2014; 17(4): 341–346, doi: [10.1089/rej.2013.1542](https://doi.org/10.1089/rej.2013.1542), indexed in Pubmed: [24617902](https://pubmed.ncbi.nlm.nih.gov/24617902/).
  37. Turgut M, Kaplan S, Turgut AT, et al. Morphological, stereological and radiological changes in pinealectomized chicken cervical vertebrae. *J Pineal Res.* 2005; 39(4): 392–399, doi: [10.1111/j.1600-079X.2005.00263.x](https://doi.org/10.1111/j.1600-079X.2005.00263.x), indexed in Pubmed: [16207295](https://pubmed.ncbi.nlm.nih.gov/16207295/).
  38. Turgut M, Yenisey C, Bozkurt M, et al. Analysis of zinc and magnesium levels in pinealectomized chicks: roles on development of spinal deformity? *Biol Trace Elem Res.* 2006; 113(1): 67–75, doi: [10.1385/BTER:113:1:67](https://doi.org/10.1385/BTER:113:1:67), indexed in Pubmed: [17114816](https://pubmed.ncbi.nlm.nih.gov/17114816/).
  39. Turgut M, Yenisey C, Uysal A, et al. The effects of pineal gland transplantation on the production of spinal deformity and serum melatonin level following pinealectomy in the chicken. *Eur Spine J.* 2003; 12(5): 487–494, doi: [10.1007/s00586-003-0528-9](https://doi.org/10.1007/s00586-003-0528-9), indexed in Pubmed: [12687443](https://pubmed.ncbi.nlm.nih.gov/12687443/).
  40. Vriend J, Reiter RJ. Melatonin, bone regulation and the ubiquitin-proteasome connection: a review. *Life Sci.* 2016; 145: 152–160, doi: [10.1016/j.lfs.2015.12.031](https://doi.org/10.1016/j.lfs.2015.12.031), indexed in Pubmed: [26706287](https://pubmed.ncbi.nlm.nih.gov/26706287/).
  41. Witt-Enderby PA, Radio NM, Doctor JS, et al. Therapeutic treatments potentially mediated by melatonin receptors: potential clinical uses in the prevention of osteoporosis, cancer and as an adjuvant therapy. *J Pineal Res.* 2006; 41(4): 297–305, doi: [10.1111/j.1600-079X.2006.00369.x](https://doi.org/10.1111/j.1600-079X.2006.00369.x), indexed in Pubmed: [17014686](https://pubmed.ncbi.nlm.nih.gov/17014686/).
  42. Zhang L, Chang M, Beck CA, et al. Analysis of new bone, cartilage, and fibrosis tissue in healing murine allografts using whole slide imaging and a new automated histomorphometric algorithm. *Bone Res.* 2016; 4: 15037, doi: [10.1038/boneres.2015.37](https://doi.org/10.1038/boneres.2015.37), indexed in Pubmed: [26816658](https://pubmed.ncbi.nlm.nih.gov/26816658/).
  43. Zhu G, Ma B, Dong P, et al. Melatonin promotes osteoblastic differentiation and regulates PDGF/AKT signaling pathway. *Cell Biol Int.* 2020; 44(2): 402–411, doi: [10.1002/cbin.11240](https://doi.org/10.1002/cbin.11240), indexed in Pubmed: [31535749](https://pubmed.ncbi.nlm.nih.gov/31535749/).

# N-acetylcysteine protects against cuprizone-induced demyelination: histological and immunohistochemical study

S.H. El Sharouny<sup>1</sup>, M.H. Shaaban<sup>1</sup>, R.M. Elsayed<sup>2</sup>, A.W. Tahef<sup>2</sup>, M.K. Abd ElWahed<sup>2</sup> 

<sup>1</sup>Department of Anatomy and Embryology, Faculty of Medicine, Cairo University, Cairo, Egypt

<sup>2</sup>Department of Anatomy and Embryology, Faculty of Medicine, Fayoum University, Egypt

[Received: 8 March 2021; Accepted: 9 April 2021; Early publication date: 29 April 2021]

**Background:** Myelination is a sequential process that is tightly controlled by a number of intrinsic and extrinsic factors. Any central nervous system disease in which the neuronal myelin sheath is damaged is referred to as demyelinating disease. The present work was designed to study the histopathological, ultrastructural and immunohistochemical changes in rat brain, mainly corpus callosum (CC), following oral administration of cuprizone (CPZ), and the role of N-acetylcysteine (NAC) in reducing these changes.

**Materials and methods:** Demyelination was induced by CPZ administration for short (4 weeks) and long (8 weeks) periods. NAC was given concomitantly and sequentially for similar periods. Spontaneous recovery after cessation of CPZ followed by no medication was also investigated. At the end of each experimental period, both cerebral hemispheres were extracted and prepared for light and electron microscopic examination and immuno-histochemical study.

**Results:** The obtained results showed a direct proportion between the duration of CPZ administration and the severity of demyelination. The co-administration of CPZ and NAC, had a fair protective impact that was stronger than the sequential administration of the two drugs. Incomplete spontaneous remyelination was observed after cessation of CPZ, being more evident in short than in long period group, indicating that when CPZ administration is prolonged, remyelination is delayed.

**Conclusions:** In the light of the above results, it could be concluded that NAC has neuroprotective effects and has the potential to be a novel therapeutic approach for the treatment of demyelinating diseases such as multiple sclerosis; however, treatment should begin as soon as the disease manifests. (Folia Morphol 2022; 81, 2: 280–293)

**Key words:** cuprizone, N-acetylcysteine, demyelination, remyelination, corpus callosum, rats

## INTRODUCTION

Myelination is a process that is highly orchestrated by many intrinsic and extrinsic variables, step-by-step [19]. Many animal studies have shown that the neu-

ronal activity along axons modulates its degree of myelination [3]. Although the mechanism of myelin formation is not yet fully understood; it is modelled as a staged process, from differentiation of oligodendro-

Address for correspondence: Ass. Prof. M.K. Abd ElWahed, Anatomy and Embryology, Faculty of Medicine, Fayoum University, Egypt, e-mail: mahakhaled007@yahoo.com

This article is available in open access under Creative Common Attribution-Non-Commercial-No Derivatives 4.0 International (CC BY-NC-ND 4.0) license, allowing to download articles and share them with others as long as they credit the authors and the publisher, but without permission to change them in any way or use them commercially.

cyte (OL) progenitor cells to oligodendrocytes (OLs), followed by ensheathment of axons and ultimately maturation of the sheath [28].

Demyelinating disease is defined as any central nervous system (CNS) disease in which the neuronal myelin sheath is damaged [27]. Based on their pathogenesis, demyelinating CNS diseases can be categorised into: inflammatory diseases (e.g.: multiple sclerosis [MS] and acute-disseminated encephalomyelitis), viral infection, hypoxic-ischaemic types and demyelination caused by acquired metabolic disorders or focal compression of the brain [30]. Oligodendrocytes are vulnerable to oxidative stress-mediated damage, cytotoxicity, deprivation of the trophic factor and activation of apoptotic pathways [13]. Demyelination and inflammation are pathological features of MS and both are assumed to contribute to axon damage and consequently to cerebral atrophy that is prevalent in later stages of the disease [48]. MS demyelinating lesions are multifocal and spread in the brain affecting both white and grey matter. After demyelinating events, remyelination frequently occurs, but it is often incomplete. Consequently, understanding remyelination failure and designing strategies to restore myelin sheath is one of the challenges of MS science [22].

In MS pathogenesis, oxidative stress is a key factor that alleviates the migration of leukocytes, thereby leading to OLs damage and axonal injury. In the CNS of MS patients, reactive oxygen and nitrogen species are formed mainly by activated macrophages and microglia, the resident macrophage of the brain, and are responsible for demyelination and axon disruption. Various inflammatory and oxidative stress mediators such as cytokines and chemokines are secreted by activated microglia [6, 34].

Cuprizone (CPZ) is a copper-chelator of low molecular weight that affects the metabolism of cells and contributes to reversible demyelination in both grey and white matter [10]. Feeding with cuprizone results in the death of mature OLs, whereas other CNS cell types are not affected because oligodendroglia is more vulnerable to copper deficiency [59]. The toxic effect of CPZ on mature OLs results in the inhibition of the mitochondrial activity of the copper-dependent cytochrome oxidase and monoamine oxidase enzymes, resulting in mitochondrial dysfunction either through enlargement or clustering, this is followed by their apoptosis [2]. Oligodendrocytes death is thought to result from persistent mitochondrial stress brought on by both the toxic effect of the drug and

the inherent immune response [57]. Microglia and reactive astrocytes populate in the demyelination areas and secrete pro-inflammatory cytokines (e.g.: tumour necrosis factor- $\alpha$ , interleukin-1 $\beta$  and interferon- $\gamma$ ) that govern the demyelination process [56].

N-acetylcysteine (NAC) is an effective free radicals scavenger of reactive oxygen species (ROS) but its key function as a therapeutic antioxidant stems from its role as a cysteine and glutathione synthesis precursor [12, 14]. Previous studies provide evidence for the therapeutic potential of NAC in multiple psychiatric and neurological disorders and claimed that to its anti-oxidant, anti-inflammatory and anti-apoptosis effects [4, 6, 9, 16, 38, 46].

Recently, Zhou et al. 2020 [61] indicated that NAC boosts remyelination process via promoting OL survival in oxidative stress-related conditions through the increase in glutathione levels and upregulation of haem oxygenase-1 (HO-1), a cytoprotective enzyme, that play a fundamental role in OLs protection.

The aim of the this work is to investigate the possible therapeutic role of NAC in CPZ-induced demyelination in the brain, particularly corpus callosum, of male albino rat and to elucidate the possible spontaneous recovery (remyelination) after cessation of cuprizone.

## MATERIALS AND METHODS

### Material

**Chemicals.** Cuprizone (bis-cyclohexanone-oxal-dihydrazone) was supplied by Sigma-Aldrich Company in the form of powder, which was dissolved in distilled water and given orally by gastric gavage tube to the rats in a dose of 2 g/kg of body weight (bw) [39].

N-acetylcysteine was supplied by Sedico Company as effervescent instant granules 600 mg/mL, which were dissolved in distilled water and given orally by gastric gavage tube in a dose of 50 mg/kg bw [11]. The gastric gavage tube was left in position for 20 s to prevent regurgitation and ensure administration of the calculated doses.

**Animals.** Seventy adult male albino rats of Sprague Dawley strain, 4-months of age and weighing 150–250 g were used in the current study. They were obtained from the animal house, Faculty of Medicine, Cairo University and housed in metal cages, 5 rats/cage under standard laboratory and environmental conditions. The rats were used according to ethics of Animal Care and Use Committee (ACUC) of Cairo University.

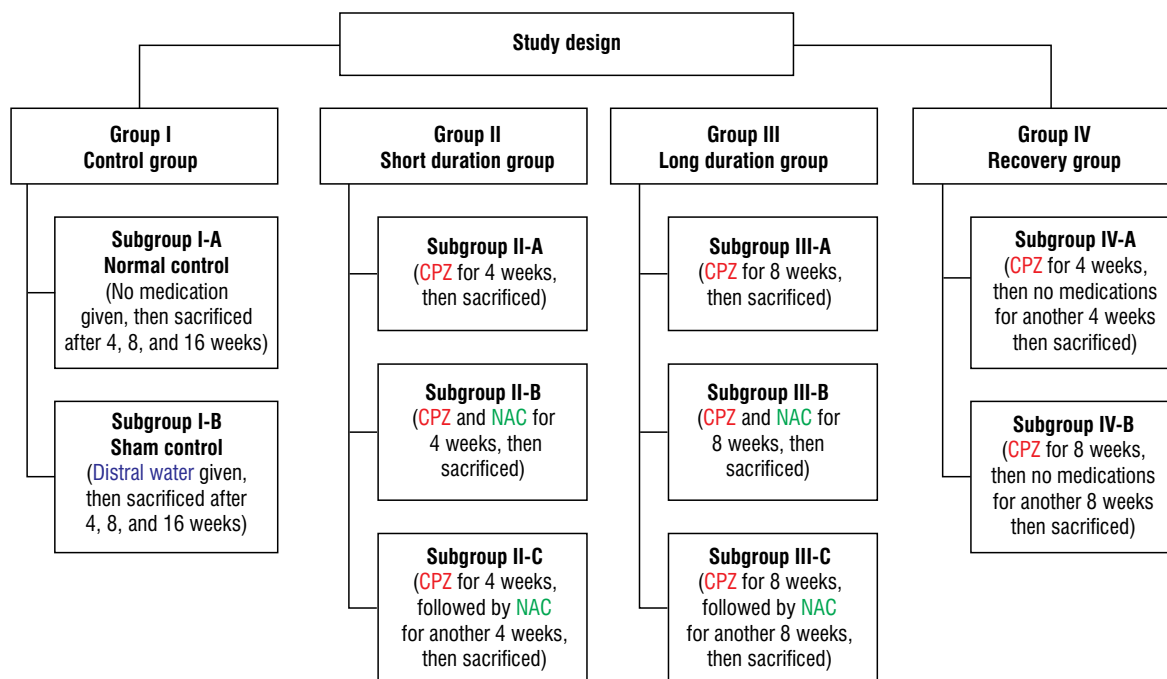


**Figure 1.** Flowchart of study design; CPZ — cuprizone; NAC — N-acetylcysteine.

**Experimental design.** Rats were divided into four groups:

- group I (Control group): comprised 30 rats and subdivided into two subgroups:
  - subgroup I-A (Normal control group): comprised 15 rats, they received no medications. Five rats were sacrificed after 4, 8 and 16 weeks respectively;
  - subgroup I-B (Sham control group): comprised 15 rats, they were given distilled water orally; daily for 4, 8 and 16 weeks respectively;
- group II (CPZ treated group, short duration): comprised 15 rats and divided into three subgroups as follows:
  - subgroup II-A: each rat received the calculated dose of CPZ orally; daily for 4 successive weeks;
  - subgroup II-B: each rat received the calculated doses of CPZ concomitant with NAC orally; daily for 4 successive weeks;
  - subgroup II-C: each rat received the calculated dose of CPZ daily orally for 4 successive weeks followed by the calculated dose of NAC orally; daily for another 4 successive weeks;
- group III (CPZ treated group, long duration): comprised 15 rats and subdivided into three subgroups; 5 rats each as follows:
  - subgroup III-A: each rat received the calculated dose of CPZ for 8 weeks;
  - subgroup III-B: each rat received the calculated doses of CPZ concomitant with NAC orally; daily for 8 successive weeks;
  - subgroup III-C: each rat received the calculated doses of CPZ followed by NAC orally; daily for 8 successive weeks;
- group IV (CPZ recovery group): comprised 10 rats and subdivided into two subgroups; 5 rats each:
  - subgroup IV-A: each rat received the calculated dose of CPZ daily orally for 4 successive weeks; then no medication received for another 4 successive weeks;
  - subgroup IV-B: each rat received the calculated dose of CPZ daily orally for 8 successive weeks; then no medication received for another 8 successive weeks (Fig. 1).

## Methods

At the end of the experimental period, the rats were sacrificed after anaesthetisation with 50 mL/kg subcutaneous injection of thiopental sodium and the brains were extracted and rinsed under distilled water to remove any surface blood, followed by immersion in ice-cold normal saline for 5 min then placed on cold metal plate, finally two cerebral hemispheres were sectioned along the sagittal suture and prepared for the following studies.

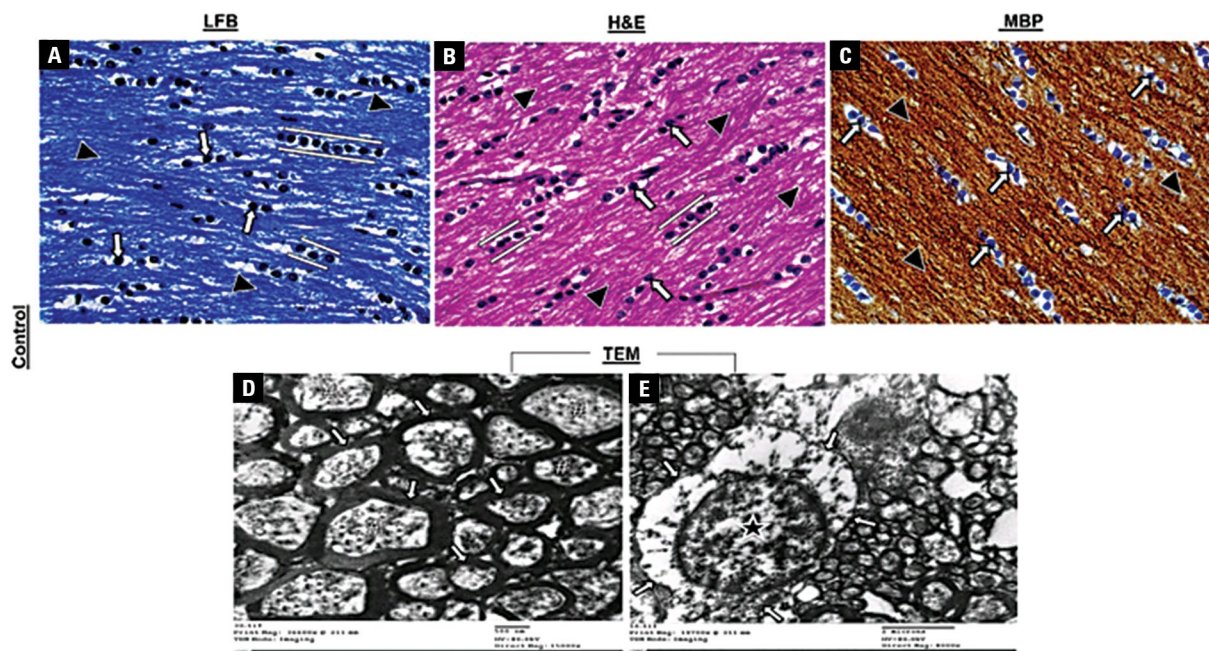


**Figure 2.** Myelinated nerve fibres of corpus callosum. Light microscopic examination of myelination in control groups; **A, B.** Densely packed, myelinated and parallel arranged fibres (▲). The oligodendrocytes nuclei (arrows) appear well defined, rounded, darkly stained and arranged in longitudinal rows parallel (bracketed by lines) to the nerve fibres that they myelinate; **C.** Strong positive myelin basic protein reaction of myelin fibres (▲) and oligodendrocytes nuclei (arrows). Electron microscopic examination; **D.** Variable sized densely packed axons (#), surrounded by thick dense myelin sheath (arrows) with electron lucent intact cytoplasm; **E.** Normal oligodendrocyte with oval dark nucleus (★), regular nuclear envelope, clumped chromatin and surrounded by electron lucent cytoplasm (arrows); **A.** Luxol fast blue stain (LFB)  $\times 400$ ; **B.** Haematoxylin and eosin stain (H&E)  $\times 400$ ; **C.** Myelin basic protein (MBP)  $\times 400$ ; **D.** Electron microscopic examination (TEM)  $\times 15000$ ; **E.** TEM  $\times 8000$ .

**Light microscopic examination.** The extracted brains were immersed in formalin 10%, for 2 days. Then washed under running tap water, and then embedded in paraffin. Sagittal sections of 7 microns thickness were made and stained with:

- luxol fast blue stain (LFB): to visualise the myelin in nerve sheath. Myelin stained blue while the nuclei and Nissl substance stained violet or red [26];
- haematoxylin and eosin stain (H&E): for standard histological examination [29].

**Immuno-histochemical study [45].** Myelin basic protein antibody (MBP-antibody) (Thermo Fischer, Labvision, USA): is an unconjugated rabbit polyclonal antibody. A positive myelin fibres reaction is visible as a brown precipitate under the microscope, and the nuclei appear light blue.

**Electron microscopic examination (TEM).** Freshly prepared sections from brain samples of each group were fixed in 4% glutaraldehyde. Then processed and examined to detect ultrastructure changes [23].

## RESULTS

**Myelinated nerve fibres of corpus callosum (CC).** Light microscopic examination of myelination in

control groups revealed densely packed, myelinated and parallel arranged fibres. The OLs nuclei appeared well defined, rounded, darkly stained and arranged in longitudinal rows parallel to the nerve fibres that they myelinate (Fig. 2A, B). The nerve fibres and OLs nuclei showed strong positive myelin basic protein reaction (Fig. 2C). TEM showed variable sized densely packed axons. Axons were seen surrounded by thick electron dense myelin sheath and electron lucent intact cytoplasm (Fig. 2D). The OL appeared ovoid with dark nucleus surrounded by regular nuclear envelope and contains clumped chromatin material beneath the nuclear envelope and throughout the nucleoplasm. It is seen surrounded by electron lucent cytoplasm (Fig. 2E).

**Concomitant administration of NAC protected from CPZ-induced demyelination more efficiently than the consecutive treatment by the two drugs.** Light microscopic examination of demyelination in **CPZ-treated group for 4 weeks** showed multiple areas of unpacked partially demyelinated nerve fibres with axonal disruption and splitting, partial loss of OLs nuclei, most of them appeared dispersed and showed faint staining and karyorrhexis, others appeared cir-

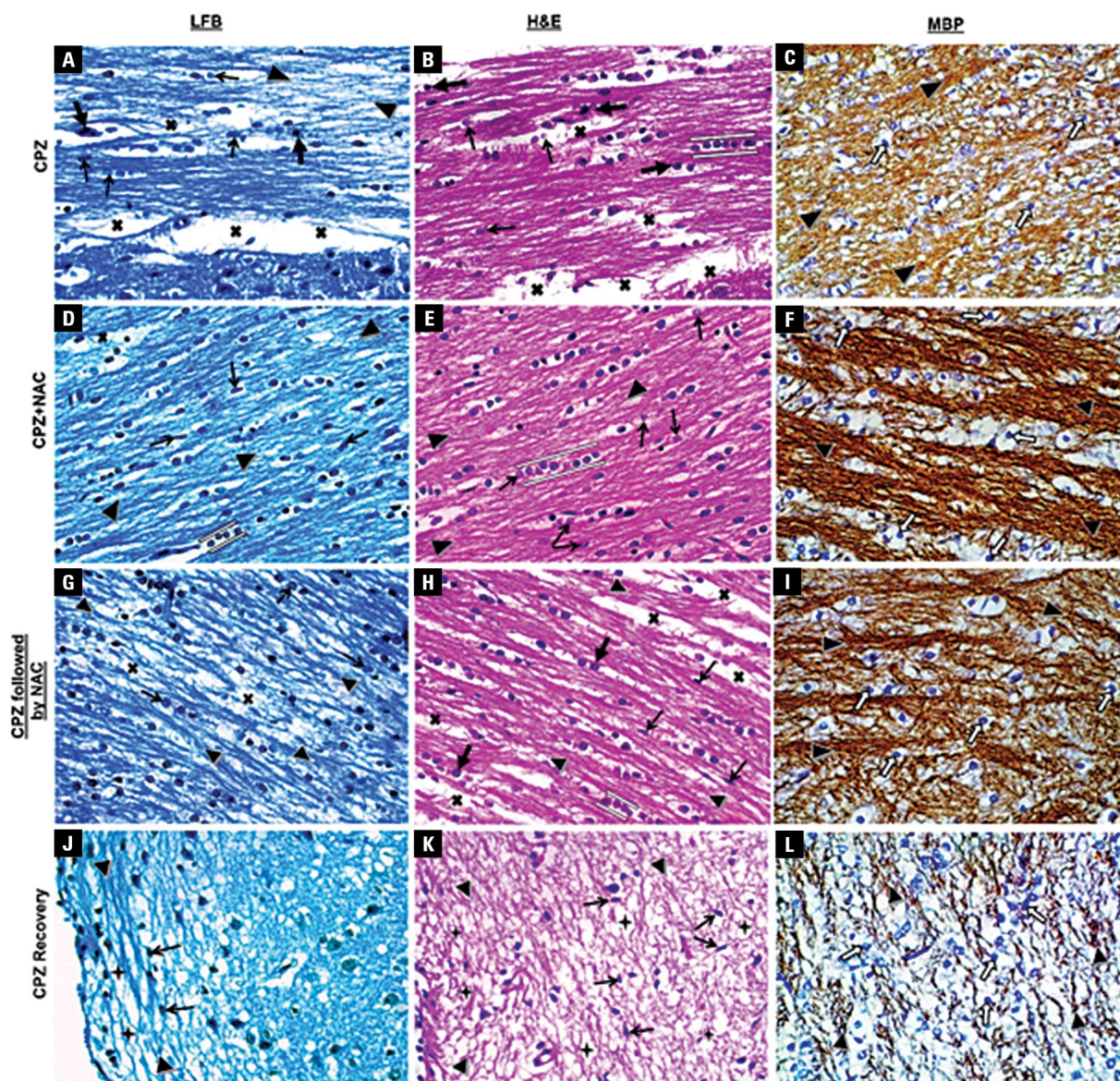


**Figure 3.** Concomitant administration of N-acetylcysteine (NAC) protects from cuprizone (CPZ)-induced demyelination more efficiently than the consecutive treatment by the two drugs. Light microscopic examination of demyelination in CPZ-treated group for 4 weeks; **A, B.** Multiple areas of unpacked partially demyelinated nerve fibres ( $\blacktriangle$ ) with axonal disruption and splitting (X), partial loss of oligodendrocytes nuclei, most of them appear dispersed and showing faint staining and karyorrhexis (thin arrows), others are circumscribed and darkly stained (thick arrows), few nuclei are seen oriented parallel to the nerve fibres (bracketed by lines); **C.** Moderate positive myelin basic protein reaction of myelin fibres ( $\blacktriangle$ ) and oligodendrocytes nuclei (arrows). CPZ and NAC treated group; **D.** Well-arranged, packed demyelinated nerve fibres ( $\blacktriangle$ ) with focal axonal disruption and fragmentation (X); **E.** Preserved disorganised oligodendrocytes nuclei with some of them arranged in linear rows (bracketed by lines). Most of them appear rounded and darkly stained with few flattened small sized nuclei showing faint staining and karyorrhexis (arrows); **F.** Strong myelin basic protein positive reaction of myelin fibres ( $\blacktriangle$ ) and positive oligodendrocytes nuclei (arrows) reaction. CPZ followed by NAC-treated group; **G, H.** Demyelinated unpacked nerve fibres ( $\blacktriangle$ ) with focal axonal splitting (X) and dispersed faintly stained oligodendrocyte nuclei (arrows). Oligodendrocyte nuclei are seen parallel to the nerve fibres (bracketed by lines). Most of them appear round and circumscribed with faint staining (thick arrows) and few appear flattened (thin arrows); **I.** Strong positive myelin basic protein reaction of myelin fibres ( $\blacktriangle$ ) and oligodendrocytes nuclei (arrows). Weak spontaneous remyelination is detected in the short duration (CPZ 4 weeks) recovery group after 4 weeks of CPZ cessation; **J, K.** Disorganised, fragmented, demyelinated nerve fibres ( $\blacktriangle$ ) with wide areas of vacuolation ( $\star$ ). Notable loss of oligodendrocytes nuclei with the remaining ones appear dispersed, flattened and of small size with faint staining (arrows); **L.** Weak myelin basic protein positive reaction of myelin fibres ( $\blacktriangle$ ) and moderate oligodendrocytes nuclei (arrows). A, D, G, J. Luxol fast blue stain (LFB)  $\times 400$ ; B, E, H, K. Haematoxylin and eosin stain (H&E)  $\times 400$ ; C, F, I, L. Myelin basic protein (MBP)  $\times 400$ .

cumscribed and darkly stained. Few nuclei are seen oriented parallel to the nerve fibres (Fig. 3A, B).

The nerve fibres and OLs nuclei showed moderate positive myelin basic protein reaction (Fig. 3C). CC

nerve fibres of **CPZ and NAC treated group** displayed that most of the nerve fibres exhibited fair myelination and appeared well arranged and packed. Few specimens showed focal axonal disruption and fragmentation. The OLs nuclei appeared preserved but disorganised. Some of them are seen oriented in linear rows parallel to the nerve fibres. The nuclei appeared rounded with darkly stained. Few nuclei appeared flattened and small in size with faint staining and karyorrhexis (Fig. 3D, E). The nerve fibres showed strong positive myelin basic protein reaction associated with positive OLs nuclei reaction (Fig. 3F). **CPZ followed by NAC-treated group** revealed demyelinated and unpacked nerve fibres with localized areas of axonal disruption and splitting. The OLs nuclei were preserved but dispersed. Some of them were seen oriented parallel to the nerve fibres. Most of the nuclei appeared rounded faintly stained (Fig. 3G, H). The nerve fibres showed moderate positive myelin basic protein reaction and positive OLs nuclei reaction (Fig. 3I). **Weak spontaneous remyelination was detected in the short duration (CPZ4Ws) recovery group after 4 weeks of CPZ cessation.** The CC nerve fibres of this recovery group appeared fragmented, demyelinated and disorganized with large cytoplasmic vacuoles being more evident near the periventricular region. Oligodendrocytes nuclei appeared of small size, rounded, darkly stained and dispersed, while others appeared flattened (Fig. 3J, K). The nerve fibres displayed weak positive myelin basic protein reaction and moderate positive OLs nuclei reaction (Fig. 3L).

Electron microscopic examination of the **CPZ-treated group for 4 weeks** revealed that the nerve fibres were unpacked with narrow gapping in between, multiple thin myelinated and scanty unmyelinated axons were seen. Few thick myelinated axons were also seen. Most of the myelin sheaths appeared redundant or irregular and displayed focal areas of lamellar splitting. Some axons showed axonal cytoplasmic degeneration, others showed inclusion bodies in their cytoplasm (Fig. 4A). The OLs in this group appeared ovoid containing dark nucleus with regular nuclear envelope and clumped chromatin both beneath the nuclear envelope and throughout the nucleoplasm. They were seen surrounded by multiple variable sized thin and thick myelinated axons with degenerated cytoplasm (Fig. 4B). The CC nerve fibres of **CPZ and NAC-treated group** were predominantly thin myelinated with few

well myelinated ones. Some of their myelin sheaths appeared redundant with splitting and showed variable degrees of axonal cytoplasmic degeneration and inclusion bodies (Fig. 4C). The OLs nuclei were ovoid and dark with regular nuclear envelope and surrounded by rarified cytoplasm. They were seen in close relation to the surrounding axons (Fig. 4D). The **CPZ followed by the NAC-treated group** displayed unpacked nerve fibres with narrow gaps in between. A lot of thin myelinated and unmyelinated axons were seen. The myelin sheaths appeared redundant with focal lamellar splitting. Variable degrees of cytoplasmic degeneration were seen (Fig. 4E). The OLs nuclei appeared ovoid and dark with regular nuclear envelope and clumped chromatin. The surrounding cytoplasm showed connection to multiple variable sized thin myelinated axons (Fig. 4F). **The CPZ-recovery group (4 weeks after CPZ cessation)** displayed unpacked axons with wide areas of gapping in between. The demyelination patches showed predominantly thin myelinated axons, few unmyelinated axons with rarified axonal cytoplasm. Myelin sheaths appeared irregular, split and abnormally folded. Rarified axonal cytoplasm with absence of inclusion bodies was observed (Fig. 4G). The OLs nuclei appeared ovoid and dark with regular nuclear envelope and clumped chromatin. The surrounding cytoplasm appeared electron lucent with multiple vacuoles and few abnormal folded myelin sheaths with no evidence of axonal connection (Fig. 4H).

**CPZ supplementation for long duration (8 weeks) produced massive demyelination and lessened the protective effects of NAC.** Light microscopic examination of demyelination in **CPZ-treated group for 8 weeks** revealed marked demyelination, fragmentation and complete disorganisation of CC nerve fibres. All OLs nuclei appeared disorganised and of small size, irregular shaped with faint staining and variable degrees of karyorrhexis and karyolysis (Fig. 5A, B). The nerve fibres showed negative myelin basic protein reaction with poor OLs nuclei reaction (Fig. 5C). **CPZ and NAC-treated group** showed that the CC nerve fibres appeared partially demyelinated and unpacked, with scanty areas of splitting in the myelin sheath and vacuolated cytoplasm. The OLs nuclei appeared preserved and arranged in linear rows between the unpacked nerve fibres. They appeared rounded, darkly stained apart from scanty nuclei which showed faint staining and others appeared flattened (Fig. 5D, E). The nerve fibres

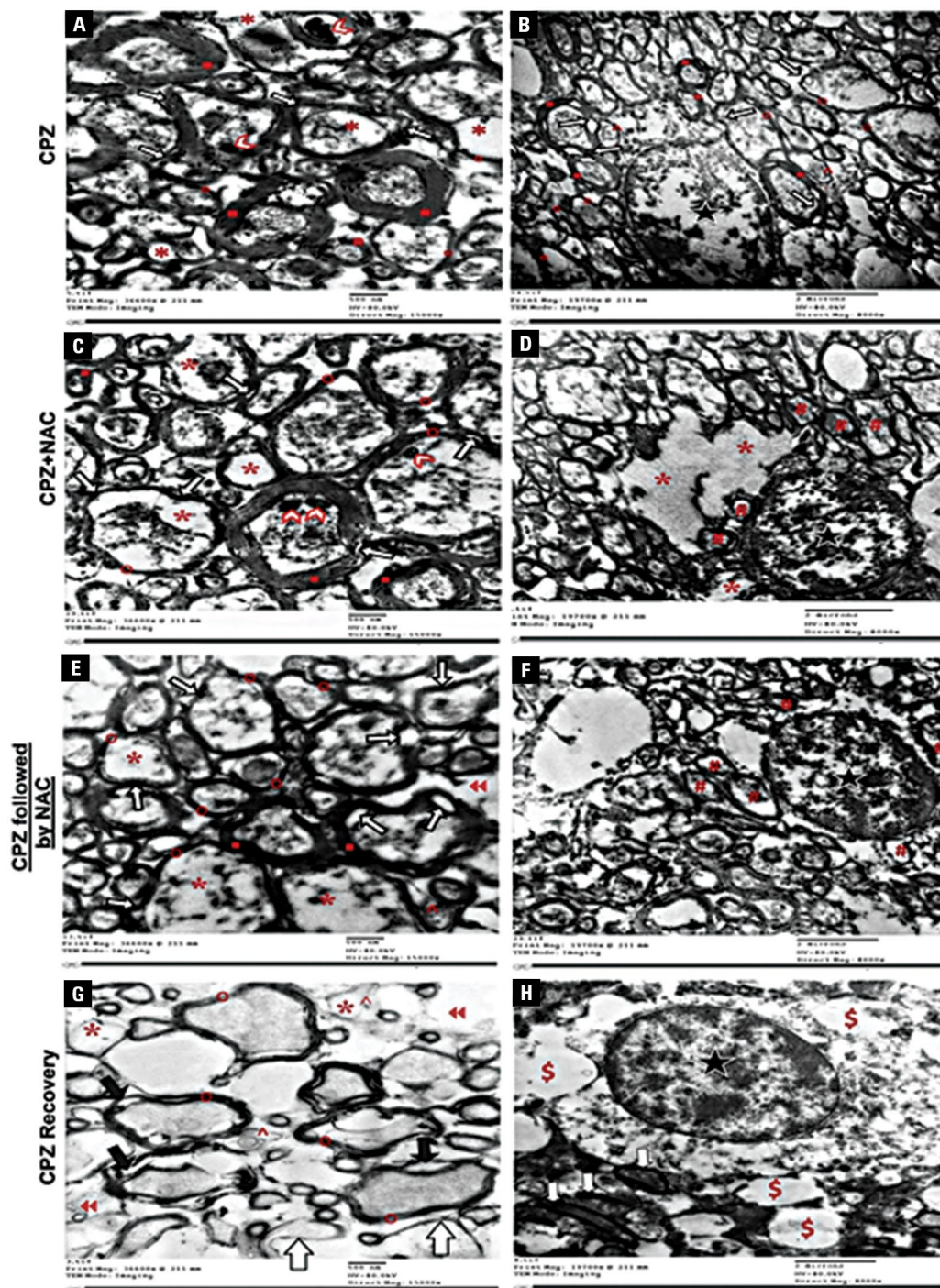


**Figure 4.** Electron microscopic examination of short duration cuprizone (CPZ)-treated group (4 weeks); **A.** Narrow gapping between unpacked thin myelinated (o) and thick myelinated (■) axons exhibiting redundant sheath (arrows) with some of them showing partial axonal degeneration (\*) and inclusion bodies (◀◀); **B.** Oligodendrocyte (★) containing dark nucleus surrounded by few thick myelinated axons (■) with redundant myelin sheath and focal areas of splitting (arrows), unmyelinated (∧) and multiple irregular thin myelinated (o) axons. CPZ and N-acetylcysteine (NAC)-treated group; **C.** Multiple thick myelinated (■) and thin myelinated (o) axons with some of them exhibiting split, redundant sheath (arrows) as well as degenerated axonal cytoplasm (\*) and inclusion bodies (◀◀); **D.** Ovoid, dark nucleus (★) surrounded by rarified cytoplasm (\*) and is adherent to the nearby axons (#). CPZ followed by the NAC-treated group; **E.** Unpacked axons with narrow gapping in between (◀◀). Multiple thin myelinated (o) and few unmyelinated (∧) axons are seen, few axons exhibit redundant split myelin sheath (arrows) and axonal cytoplasmic degeneration (\*); **F.** Ovoid, dark nucleus (★) with the surrounded cytoplasm displayed connection to multiple variable sized thin myelinated axons (#). The short duration CPZ-recovery group; **G.** Multiple thin myelinated (o) and few unmyelinated (∧) axons with rarified axonal cytoplasm (\*) and wide gaps in between (◀◀). The myelin sheaths are irregular with notable splitting (black arrows), abnormal folded myelin sheaths are seen (white arrows); **H.** Ovoid, dark nucleus (★), surrounded by electron lucent cytoplasm showing multiple vacuoles (\$) and abnormal folded myelin sheaths (white arrows) with no evidence of axonal connection. A, C, E, G. Electron microscopic examination (TEM) ×15000; B, D, F, H. TEM ×8000.

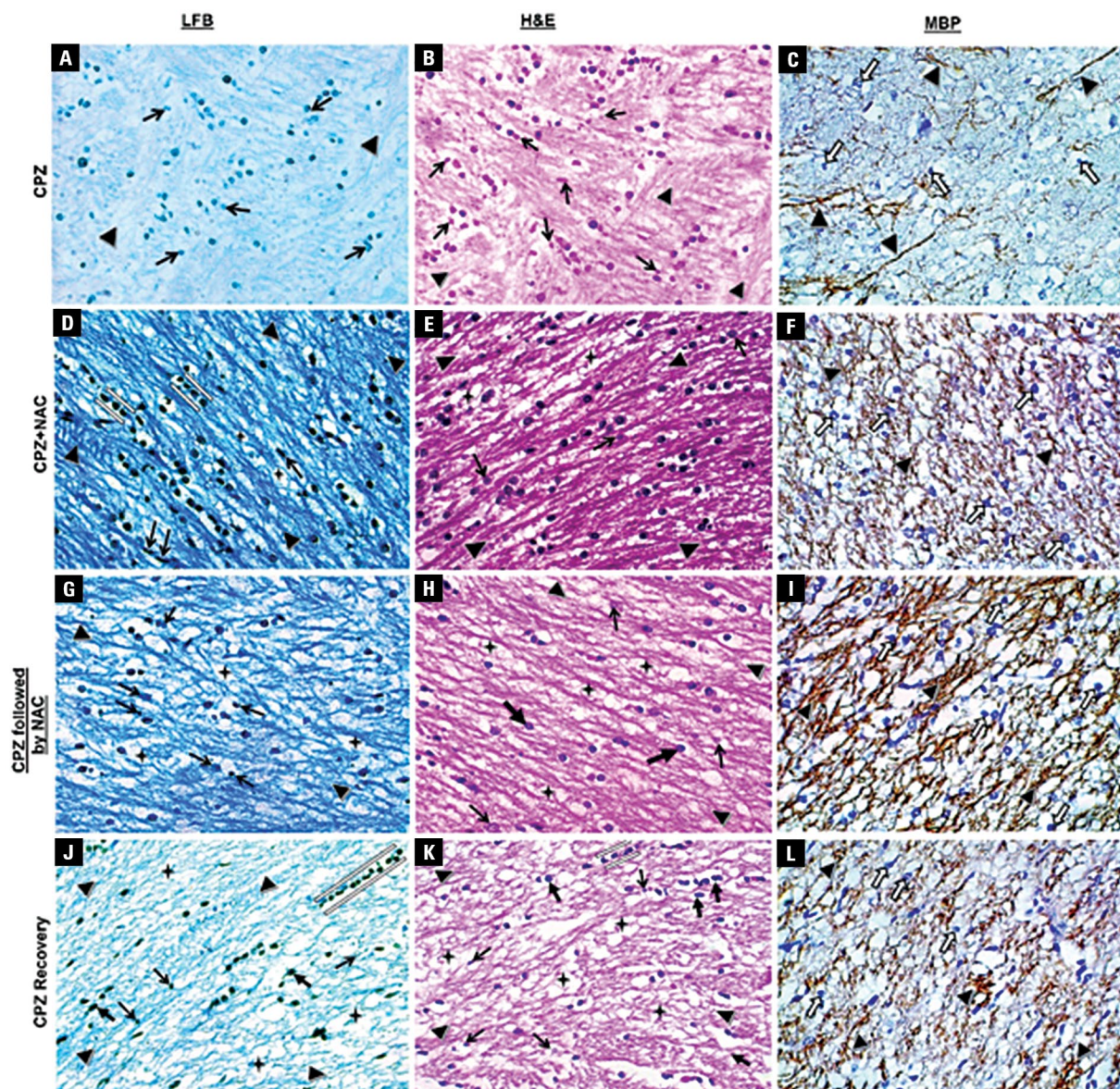


**Figure 5.** Cuprizone (CPZ) supplementation for long duration produces massive demyelination and lessens the protective effects of N-acetylcysteine (NAC). Light microscopic examination of demyelination in long duration CPZ-treated group (8 weeks); **A, B.** Markedly demyelinated, disorganised and fragmented nerve fibres ( $\blacktriangle$ ). Loss of oligodendrocytes nuclei with the remaining ones appear disorganised, of small size with variable degrees of karyorrhexis and karyolysis (arrows); **C.** Negative myelin basic protein reaction of myelin fibres ( $\blacktriangle$ ) and oligodendrocytes nuclei (arrows). CPZ and NAC treated group; **D, E.** Partially demyelinated unpacked nerve fibres ( $\blacktriangle$ ) with scanty areas of vacuolation ( $\star$ ). Most oligodendrocyte nuclei appear rounded, darkly stained with few displaying faint staining (arrows) and seen parallel to the nerve fibres (bracketed by lines) with few nuclei appear flattened (arrows); **F.** Weak positive myelin basic protein reaction of myelin fibres ( $\blacktriangle$ ) and moderate positive oligodendrocytes nuclei (arrows). CPZ followed by NAC-treated group; **G, H.** Unpacked diffusely demyelinated nerve fibres ( $\blacktriangle$ ) with axonal splitting and vacuolation ( $\star$ ). Dispersed oligodendrocyte nuclei, which appear rounded, circumscribed with faint staining (thick arrows) and few appear of small size and exhibit karyorrhexis and karyolysis (thin arrows); **I.** Positive reaction of oligodendrocytes nuclei (arrows) with weak positive myelin fibres ( $\blacktriangle$ ). Poor spontaneous remyelination is detected in the long duration (CPZ 8 weeks) recovery group after 8 weeks of CPZ cessation; **J, K.** Markedly disorganised demyelinated nerve fibres ( $\blacktriangle$ ) with diffuse vacuolation ( $\star$ ). The oligodendrocyte nuclei appear dark (thick arrows) and parallel aligned to nerve fibres (bracketed by lines), while others appear of small size with faint staining (thin arrows); **L.** Weak positive myelin basic protein reaction of myelin fibres ( $\blacktriangle$ ) and oligodendrocytes nuclei (arrows). A, D, G, J. Luxol fast blue stain (LFB)  $\times 400$ ; B, E, H, K. Haematoxylin and eosin stain (H&E)  $\times 400$ ; C, F, I, L. Myelin basic protein (MBP)  $\times 400$ .

showed weak positive myelin basic protein reaction with moderate positive OLs nuclei reaction (Fig. 5F). CPZ followed by NAC-treated group showed that

the CC nerve fibres appear diffusely demyelinated, unpacked and disorganised with wide areas of axonal fragmentation, splitting and cytoplasmic vacuolation.

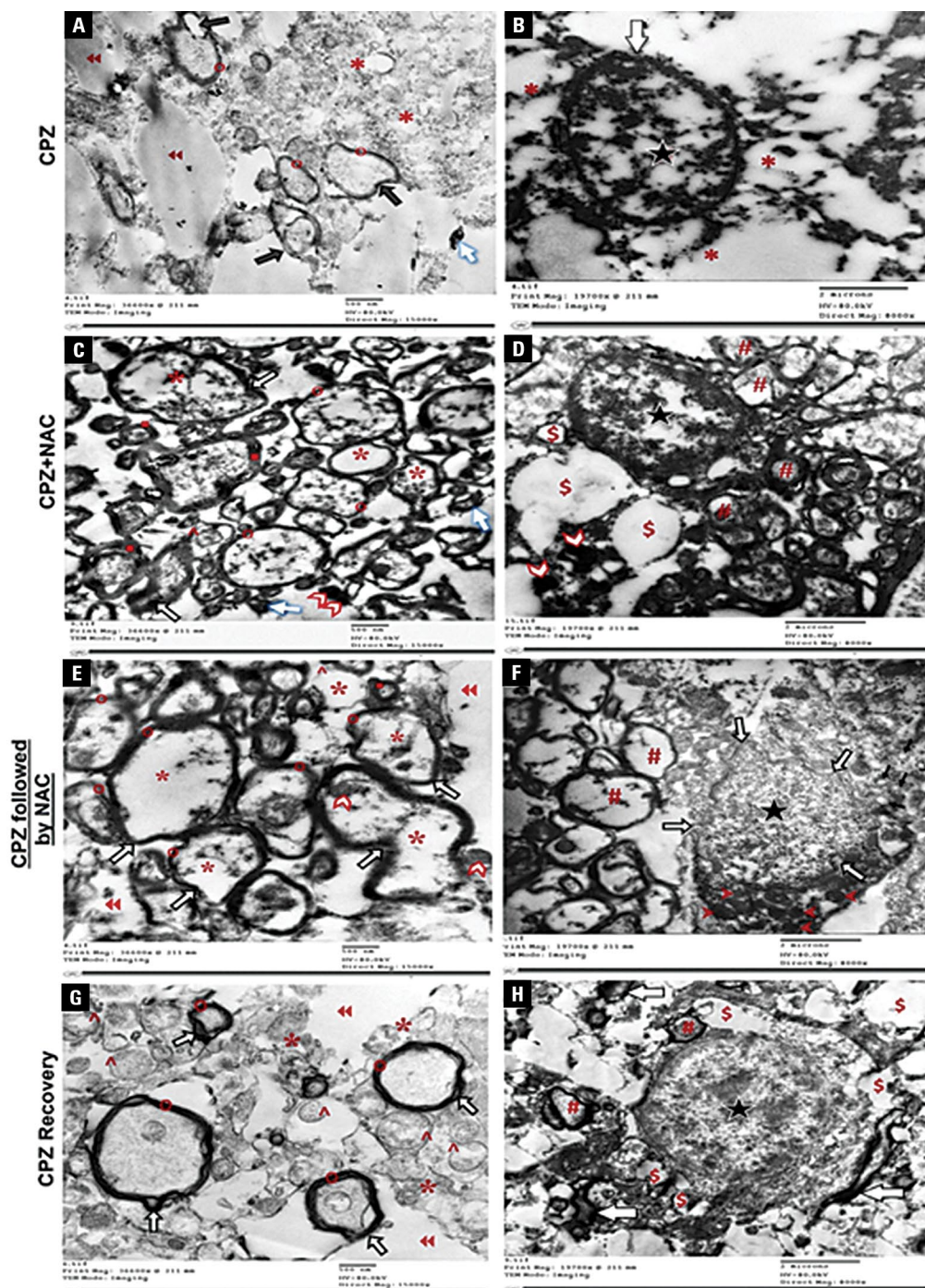


**Figure 6.** Electron microscopic examination cuprizone (CPZ)-treated group for 8 weeks; **A.** Scanty thin myelinated (o) axons with split redundant myelin sheath (arrows). Wide gaps of complete axonal loss (◀◀) containing extensive remnants of fragmented degenerated axons (\*) and folded collapsed myelin sheath (white arrows); **B.** Oval heterochromatic oligodendrocyte nucleus (★) with focal nuclear envelop indentation (white arrow) and surrounded by completely degenerated rarified cytoplasm (\*). CPZ and N-acetylcysteine (NAC) treated group; **C.** Irregularly arranged unpacked multiple thin myelinated (o), few myelinated (■) and unmyelinated (^) axons. Most axons showing redundant sheath (arrows) inclusion bodies (◁) and compact myelin sheath (white arrows); **D.** Ovoid, dark nucleus (★) with large cytoplasmic vacuoles (\$) and inclusion bodies (◁) and connection to demyelinated axons (#). CPZ followed by the NAC-treated group; **E.** Wide areas of irregularly arranged axons with gaps in between (◀◀). Multiple thin myelinated (o), few unmyelinated (^) axons almost all of them have irregular deformed myelin sheaths with diffuse axonal cytoplasmic degeneration (\*) and scanty inclusion bodies (◁); **F.** An ovoid nucleus (★) with irregular nuclear envelope (white arrows) and electron dense cytoplasm contain multiple mitochondria (◀), secretory granules (black arrows), and is seen connected to multiple thin myelinated axons (#). The CPZ-recovery group; **G.** Wide gapping (◀◀) between multiple thin myelinated (o) axons with irregular-split and tight-deformed myelin sheaths (arrows) and rarefied axonal cytoplasm (\*). Multiple fragmented unmyelinated axons (^) are seen; **H.** Rounded, dark nucleus (★) surrounded by vacuolated cytoplasm (\$) with multiple abnormal folded myelin sheaths (white arrows) and connected to few axons (#). A, C, E, G. Electron microscopic examination (TEM) ×15000; B, D, F, H. TEM ×8000.

Few nerve fibres appeared well arranged. Partial loss of OLs nuclei, with the remaining ones appearing dispersed. Some of them appeared rounded and circumscribed, Others appeared of small size with poor staining and karyolysis (Fig. 5G, H). The nerve fibres displayed weak positive myelin basic protein reaction and positive OLs nuclei reaction (Fig. 5I).

**Poor spontaneous remyelination was detected in the long duration (CPZ 8 weeks) recovery group after 8 weeks of CPZ cessation.** The nerve fibres of the long duration recovery group appeared markedly disorganised and demyelinated with diffuse poor staining and marked cytoplasmic vacuolation. Few OLs nuclei were seen parallel to the nerve fibres, most of them were dispersed and small sized with partial loss of their population. The nuclei exhibited dark and faint staining (Fig. 5J, K). The nerve fibres and OLs nuclei showed weak positive myelin basic protein reaction (Fig. 5L).

Electron microscopic examination of the **CPZ-treated group for 8 weeks** revealed massive axonal degeneration. The remaining axons were thin myelinated with split myelin sheath and wide gaps in between, these gaps contain remnants of fragmented degenerated axons and fragmented collapsed myelin sheaths (Fig. 6A). The OLs displayed oval heterochromatic nuclei with localised nuclear envelope indentation. Most OLs exhibited completely degenerated rarified cytoplasm (Fig. 6B). **CPZ and NAC-treated group** showed disorganised nerve fibres with narrow gaps in between. Multiple thin myelinated and unmyelinated axons were detected. Few specimens demonstrated multiple compact folded myelin sheath fragments and inclusion bodies (Fig. 6C). The OLs nuclei appeared ovoid and dark with regular nuclear envelope and clumped chromatin. The surrounding cytoplasm showed large vacuoles and inclusion bodies with close connection to the demyelinated axons (Fig. 6D). **CPZ followed by NAC-treated group** showed a lot of unpacked thin myelinated and demyelinated axons. Scanty myelinated small sized axons with irregular deformed myelin sheaths were seen. Axons displayed cytoplasmic rarefaction with scanty inclusion bodies (Fig. 6E). The OLs nuclei appeared ovoid and dark with irregular nuclear envelope and diffuse chromatin clumps. The surrounding cytoplasm appeared electron dense with abundant mitochondria and secretory granules. It was seen connected to multiple thin myelinated axons (Fig. 6F). **The CPZ-recovery group (after 8 weeks of CPZ cessation)** showed unpacked

axons with wide gaps in between. The demyelination patches showed predominantly multiple fragmented unmyelinated axons and scanty thin myelinated axons. Some myelin sheaths appeared irregular and split. Almost all axons showed cytoplasmic rarefaction (Fig. 6G). Oligodendrocytes nuclei appeared rounded, dark and surrounded by electron dense vacuolated cytoplasm that contains multiple abnormal folded myelin sheaths with evidence of connection to few axons (Fig. 6H).

## DISCUSSION

The development of animal models of human diseases is critical. Over the past 60 years, studies of MS and other demyelinating CNS disorders have closely followed this approach [35].

In the current study, CPZ intoxication model was used to induce CNS demyelination. That was in accordance with MacArthur and Papanikolaou (2014) [31], who stated that marked nerve demyelination in animals is induced by oral administration of CPZ, likewise, Vega-Riquer et al. (2019) [55] indicated that CPZ targets many enzymes such as ceruloplasmin, which impairs the activity of the copper dependent cytochrome oxidase, decreases oxidative phosphorylation and causes degenerative OL changes. Eventually, this cascade of events results in demyelination. Male albino rats were used in the present research to study the various aspects of demyelination in the CC, which was similar to other study by Franco et al. (2008) [17]. Hibbits et al. (2009) [24] and Steelman et al. (2012) [48] have documented that female rats are more resistant to CPZ-induced toxic demyelination, which could be due to potential hormonal and genetic influences.

In line with the current study, Skripuletz et al. (2011) [43] focused on the demyelinating effects of CPZ in the CC, as it is an OL-rich structure and the degree of demyelination may easily be achieved.

Systemic intoxication by CPZ was produced by daily administration of the drug for 4 and 8 week's durations to induce CC nerve demyelination, this was in agreement with Oakden et al. (2017) [39]. On the other hand, Taraboletti et al. (2017) [49] used CPZ fed mice model for 2 and 6 weeks and demyelination was observed at the third week and maximum demyelination reached at the 5<sup>th</sup> or 6 weeks. Administration of CPZ in subgroup III-A produced severe pathological changes more than in subgroup II-A indicating the presence of direct proportion between the duration

of administration and the severity of nerve demyelination, this was compatible with Zendedel et al. (2013) [59] who reported that partial demyelination of CC nerve fibres occurred after 2 weeks of CPZ intoxication, and called this process as (acute demyelination); while complete demyelination occurred after 5 to 6 weeks. On the other hand, Acs and Komoly (2012) [1] documented the incidence of severe demyelination after 3 weeks of CPZ administration associated with massive macrophage infiltration and astrocytosis in the demyelinated areas.

In the current model of CPZ intoxication, The examined groups illustrated variable degrees of axonal degeneration, loss of OLs and gapping between nerve fibres; these were in accordance with Freeman et al. (2015) [18]; Van Munster et al. (2015) [52]; Grothe et al. (2016) [21] and Vargas and Tyor (2017) [54]. These changes were more pronounced in subgroup III-A. Ultra-structurally, subgroup III-A revealed thin myelinated axons with axonal degeneration, fragmentation, axonal loss, fragmented collapsed myelin sheaths and OLs nuclear changes. Subgroup II-A, on the other hand, displayed mainly thick myelinated nerve fibres with redundant myelin sheaths and broken focal areas of splitting. Zendedel et al. (2013) [59] declared that demyelinated axons are more susceptible to damage due to the absence of trophic support from myelin sheaths, which are vital for maintaining axonal integrity. Craner et al. (2004) [8] reported a hypothesis of demyelination-related axonal damage, which could be due to the demyelinated axons' increased energy requirements to perform action potential, which could make demyelinated axons more prone to destructive processes.

In addition, gapping between the demyelinated nerve fibres in subgroup III-A were more than subgroups II-A, which was in accordance to a study made by Mierzwa et al. (2015) [33] who explained that the abnormal gaps between nerve fibres could slow information-processing speed, which is a common deficit in MS patients. Similar observations were clarified by Tobin et al. (2011) [51] and Hibbits et al. (2012) [25], who stated that CPZ induces extreme microglial phagocytosis of damaged myelin, and most cases of axons damage do not regenerate again.

Glutathione is an antioxidant that naturally exists in neurons that protects against oxidative harm. In the brain and the periphery of MS patients, glutathione levels have been found to be depleted [50]. Monti et al. (2020) [37] stated that, due to restricted antioxidants

such as glutathione, the brain of MS patients was susceptible to high oxidative stress. Cacciatore et al. (2012) [5] and Wu and Batist (2013) [58] demonstrated that direct administration of glutathione is difficult due to its poor absorption and stability, which limits its bioavailability. Therefore, in a trial to raise endogenous glutathione levels, NAC is used in current research. This was consistent with Skvarc et al. (2017) [44] who reported that NAC was a glutathione precursor with potent antioxidant, pro-neurogenesis and anti-inflammatory properties. likewise, Zhou et al. (2020) [61] clarified that NAC promoted murine OL survival in oxidative stress-related conditions through the elevation of glutathione levels and upregulation of HO-1, a cytoprotective enzyme, played a principle role in OL protection and consequently boosted remyelination.

In the present study, the combined administration of NAC with CPZ in subgroups II-B and III-B reduced CC demyelination changes as compared to subgroups II-C and III-C. NAC led to retrieving almost the normal histological architecture of corpus callosum nerve fibres and OLs population, which were pronounced in subgroup II-B more than subgroup III-B demonstrating a duration dependency. This was in line with Stanislaus et al. (2005) [47] who reported that NAC treatment decreased inflammatory monocyte/macrophage cells in the CNS of rats with acute encephalomyelitis. Similarly, Saraswathy et al. (2014) [42] revealed that NAC at doses of 100 and 200 mg/kg could protect the brain tissue against phenytoin-induced brain damage. In vitro studies have indicated that NAC can promote the survival of neurons and OLs by preventing a decrease in the expression of their myelin-related genes, potentially facilitating remyelination. NAC can also attenuate OL degeneration caused by lipopolysaccharide in the developing rat brain [40]. In addition to Mohammed et al. (2019) [36] who demonstrated that supplementation with NAC reduced both histopathological abnormalities and biochemical findings induced by doxorubicin in cerebral cortex of albino rats and Fan et al. (2020) [15] who suggested that NAC therapy reduced neuronal damage caused by neuroinflammation and apoptosis, which was linked to decreased dendritic spine atrophy and synapse deficits in animal model of depression.

With regard to group IV, in the current thesis, consecutive administration of CPZ and NAC showed partial improvement in demyelination events less than that observed in group III with co-administration of both drugs. This was supported by Cilio and Ferriero

(2010)'s [7] previous work in neonates suffering from hypoxic injury after intrauterine infection. Monti et al. (2020) [37] used NAC for 2 months in MS patients. However, those patients have neurological symptoms for years and it might be necessary to expand the duration of administration of NAC for several months or even years in order to observe its maximum effectiveness in symptom control.

Cuprizone recovery group in the present work showed incomplete spontaneous remyelination of corpus callosum nerve fibres being more evident in subgroup IV-A than in subgroup IV-B. In a previous work of Manrique-Hoyos et al. (2012) [32] they demonstrated that following cessation of CPZ supplementation for 5 weeks, animals showed an initial recovery of locomotor performance with partial remyelination, a finding which was in line with the current study. Similarly, Zhen et al. (2017) [60] demonstrated that removal of CPZ from the diet of animals enhances remyelination of CC. Poor remyelination was evident in subgroup IV-B following withdrawal of CPZ. Vana et al. (2007) [53] and Zendedel et al. (2013) [59] reported that when CPZ administration was prolonged, remyelination was delayed, a process called (chronic demyelination) where the number of damaged axons is high. Goldschmidt et al. (2009) [20] and Vega-Riquer et al. (2019) [55] suggested that remyelination was a transient phenomenon and remyelinated shadow plaques might be affected by new bouts of demyelination, which ultimately leads to incomplete myelin sheath repair.

The current immuno-histochemical study showed a decreased myelin basic protein reaction in CC nerve fibres and OLs nuclei over time. The myelin basic protein reaction was improved in subgroups II-B and II-C more than subgroups III-B and III-C. In addition, there was minimal improvement in subgroup IV-A with no notable improvement in subgroup IV-B. Similar findings were recorded by Pohl et al. (2011) [41] who documented progressive reduction of immune-labeling for MBP over time in the cerebellar white matter, brainstem, midbrain and spinal cord white and grey matter. In addition to widespread progressive vacuolation (status spongiosus) in white matter that was present at the onset of clinical signs and increased in size and number over time.

## CONCLUSIONS

In conclusion, administration of CPZ induced demyelination of CC nerve fibres with evidence of direct

proportion between the duration of CPZ administration and the severity of demyelination. The co-administration of CPZ and NAC had a fair protective impact that was stronger than the sequential administration of the two drugs. On the basis of these observations, NAC has neuroprotective effects and has the potential to be a novel therapeutic approach for the treatment of demyelinating disease such as multiple sclerosis; however, treatment should begin as soon as the disease manifests.

**Conflict of interest:** None declared

## REFERENCES

1. Acs P, Komoly S. Selective ultrastructural vulnerability in the cuprizone-induced experimental demyelination. *Ideggyogy Sz.* 2012; 65(7-8): 266–270, indexed in Pubmed: [23074847](#).
2. Acs P, Kipp M, Norkute A, et al. 17beta-estradiol and progesterone prevent cuprizone provoked demyelination of corpus callosum in male mice. *Glia.* 2009; 57(8): 807–814, doi: [10.1002/glia.20806](#), indexed in Pubmed: [19031445](#).
3. Auer F, Vagionitis S, Czopka T. Evidence for myelin sheath remodeling in the CNS revealed by in vivo imaging. *Curr Biol.* 2018; 28(4): 549–559.e3, doi: [10.1016/j.cub.2018.01.017](#), indexed in Pubmed: [29429620](#).
4. Bavarsad Shahripour R, Harrigan MR, Alexandrov AV. N-acetylcysteine (NAC) in neurological disorders: mechanisms of action and therapeutic opportunities. *Brain Behav.* 2014; 4(2): 108–122, doi: [10.1002/brb3.208](#), indexed in Pubmed: [24683506](#).
5. Cacciatore I, Baldassarre L, Fornasari E, et al. Recent advances in the treatment of neurodegenerative diseases based on GSH delivery systems. *Oxid Med Cell Longev.* 2012; 2012: 240146, doi: [10.1155/2012/240146](#), indexed in Pubmed: [22701755](#).
6. Cherry JD, Olschowka JA, O'Banion MK. Neuroinflammation and M2 microglia: the good, the bad, and the inflamed. *J Neuroinflammation.* 2014; 11: 98, doi: [10.1186/1742-2094-11-98](#), indexed in Pubmed: [24889886](#).
7. Cilio MR, Ferriero DM. Synergistic neuroprotective therapies with hypothermia. *Semin Fetal Neonatal Med.* 2010; 15(5): 293–298, doi: [10.1016/j.siny.2010.02.002](#), indexed in Pubmed: [20207600](#).
8. Craner MJ, Newcombe J, Black JA, et al. Molecular changes in neurons in multiple sclerosis: altered axonal expression of Nav1.2 and Nav1.6 sodium channels and Na<sup>+</sup>/Ca<sup>2+</sup> exchanger. *Proc Natl Acad Sci U S A.* 2004; 101(21): 8168–8173, doi: [10.1073/pnas.0402765101](#), indexed in Pubmed: [15148385](#).
9. Deepmala B, Slattery J, Kumar N, et al. Clinical trials of N-acetylcysteine in psychiatry and neurology: a systematic review. *Neurosci Biobehav Rev.* 2015; 55: 294–321, doi: [10.1016/j.neubiorev.2015.04.015](#), indexed in Pubmed: [25957927](#).
10. Denic A, Johnson AJ, Bieber AJ, et al. The relevance of animal models in multiple sclerosis research. *Pathophysiology.* 2011; 18(1): 21–29, doi: [10.1016/j.pathophys.2010.04.004](#), indexed in Pubmed: [20537877](#).

11. Dickey DT, Muldoon LL, Doolittle ND, et al. Effect of N-acetylcysteine route of administration on chemoprotection against cisplatin-induced toxicity in rat models. *Cancer Chemother Pharmacol.* 2008; 62(2): 235–241, doi: [10.1007/s00280-007-0597-2](https://doi.org/10.1007/s00280-007-0597-2), indexed in Pubmed: [17909806](https://pubmed.ncbi.nlm.nih.gov/17909806/).
12. Dodd S, Dean O, Copolov DL, et al. N-acetylcysteine for antioxidant therapy: pharmacology and clinical utility. *Expert Opin Biol Ther.* 2008; 8(12): 1955–1962, doi: [10.1517/14728220802517901](https://doi.org/10.1517/14728220802517901), indexed in Pubmed: [18990082](https://pubmed.ncbi.nlm.nih.gov/18990082/).
13. Dumont D, Noben JP, Moreels M, et al. Characterization of mature rat oligodendrocytes: a proteomic approach. *J Neurochem.* 2007; 102(2): 562–576, doi: [10.1111/j.1471-4159.2007.04575.x](https://doi.org/10.1111/j.1471-4159.2007.04575.x), indexed in Pubmed: [17442050](https://pubmed.ncbi.nlm.nih.gov/17442050/).
14. Elbini DI, Jallouli M, Annabi A, et al. A minireview on N-acetylcysteine: an old drug with new approaches. *Life Sci.* 2016; 151: 359–363, doi: [10.1016/j.lfs.2016.03.003](https://doi.org/10.1016/j.lfs.2016.03.003).
15. Fan C, Long Y, Wang L, et al. N-Acetylcysteine rescues hippocampal oxidative stress-induced neuronal injury suppression of p38/JNK signaling in depressed rats. *Front Cell Neurosci.* 2020; 14: 554613, doi: [10.3389/fncel.2020.554613](https://doi.org/10.3389/fncel.2020.554613), indexed in Pubmed: [33262689](https://pubmed.ncbi.nlm.nih.gov/33262689/).
16. Fernandes J, Gupta GL. N-acetylcysteine attenuates neuroinflammation associated depressive behavior induced by chronic unpredictable mild stress in rat. *Behav Brain Res.* 2019; 364: 356–365, doi: [10.1016/j.bbr.2019.02.025](https://doi.org/10.1016/j.bbr.2019.02.025), indexed in Pubmed: [30772427](https://pubmed.ncbi.nlm.nih.gov/30772427/).
17. Franco PG, Silvestroff L, Soto EF, et al. Thyroid hormones promote differentiation of oligodendrocyte progenitor cells and improve remyelination after cuprizone-induced demyelination. *Exp Neurol.* 2008; 212(2): 458–467, doi: [10.1016/j.expneurol.2008.04.039](https://doi.org/10.1016/j.expneurol.2008.04.039), indexed in Pubmed: [18572165](https://pubmed.ncbi.nlm.nih.gov/18572165/).
18. Freeman L, Garcia-Lorenzo D, Bottin L, et al. The neuronal component of gray matter damage in multiple sclerosis: A [<sup>11</sup>C]flumazenil positron emission tomography study. *Ann Neurol.* 2015; 78(4): 554–567, doi: [10.1002/ana.24468](https://doi.org/10.1002/ana.24468).
19. Gibson EM, Purger D, Mount CW, et al. Neuronal activity promotes oligodendrogenesis and adaptive myelination in the mammalian brain. *Science.* 2014; 344(6183): 1252304, doi: [10.1126/science.1252304](https://doi.org/10.1126/science.1252304), indexed in Pubmed: [24727982](https://pubmed.ncbi.nlm.nih.gov/24727982/).
20. Goldschmidt T, Antel J, König FB, et al. Remyelination capacity of the MS brain decreases with disease chronicity. *Neurology.* 2009; 72(22): 1914–1921, doi: [10.1212/WNL.0b013e3181a8260a](https://doi.org/10.1212/WNL.0b013e3181a8260a), indexed in Pubmed: [19487649](https://pubmed.ncbi.nlm.nih.gov/19487649/).
21. Grothe M, Lotze M, Langner S, et al. The role of global and regional gray matter volume decrease in multiple sclerosis. *J Neurol.* 2016; 263(6): 1137–1145, doi: [10.1007/s00415-016-8114-3](https://doi.org/10.1007/s00415-016-8114-3), indexed in Pubmed: [27094570](https://pubmed.ncbi.nlm.nih.gov/27094570/).
22. Gudi V, Gingele S, Skripuletz T, et al. Glial response during cuprizone-induced de- and remyelination in the CNS: lessons learned. *Front Cell Neurosci.* 2014; 8: 73, doi: [10.3389/fncel.2014.00073](https://doi.org/10.3389/fncel.2014.00073), indexed in Pubmed: [24659953](https://pubmed.ncbi.nlm.nih.gov/24659953/).
23. Hayat MA. Principles and Techniques of electron microscopy: Biological Applications. 4th ed. Cambridge University Press 2000: 37–59.
24. Hibbits N, Pannu R, Wu TJ, et al. Cuprizone demyelination of the corpus callosum in mice correlates with altered social interaction and impaired bilateral sensorimotor coordination. *ASN Neuro.* 2009; 1(3), doi: [10.1042/AN20090032](https://doi.org/10.1042/AN20090032), indexed in Pubmed: [19650767](https://pubmed.ncbi.nlm.nih.gov/19650767/).
25. Hibbits N, Yoshino J, Le TQ, et al. Astrogliosis during acute and chronic cuprizone demyelination and implications for remyelination. *ASN Neuro.* 2012; 4(6): 393–408, doi: [10.1042/AN20120062](https://doi.org/10.1042/AN20120062), indexed in Pubmed: [23025787](https://pubmed.ncbi.nlm.nih.gov/23025787/).
26. Kiernan JA. Dyes. In: Kiernan JA (eds). *Histological and Histochemical Methods: Theory and Practice.* 3rd ed. CRC Press 2000: 74–140.
27. Konopaske G, Dorph-Petersen KA, Sweet R, et al. Effect of chronic antipsychotic exposure on astrocyte and oligodendrocyte numbers in macaque monkeys. *Biol Psychiatry.* 2008; 63(8): 759–765, doi: [10.1016/j.biopsych.2007.08.018](https://doi.org/10.1016/j.biopsych.2007.08.018).
28. Kristensen TD, Mandl RCW, Jepsen JRM, et al. Non-pharmacological modulation of cerebral white matter organization: a systematic review of non-psychiatric and psychiatric studies. *Neurosci Biobehav Rev.* 2018; 88: 84–97, doi: [10.1016/j.neubiorev.2018.03.013](https://doi.org/10.1016/j.neubiorev.2018.03.013), indexed in Pubmed: [29550210](https://pubmed.ncbi.nlm.nih.gov/29550210/).
29. Llewellyn BD. Nuclear staining with alum hematoxylin. *Biotech Histochem.* 2009; 84(4): 159–177, doi: [10.1080/10520290903052899](https://doi.org/10.1080/10520290903052899), indexed in Pubmed: [19579146](https://pubmed.ncbi.nlm.nih.gov/19579146/).
30. Love S. Demyelinating diseases. *J Clin Pathol.* 2006; 59(11): 1151–1159, doi: [10.1136/jcp.2005.031195](https://doi.org/10.1136/jcp.2005.031195), indexed in Pubmed: [17071802](https://pubmed.ncbi.nlm.nih.gov/17071802/).
31. Macarthur J, Papanikolaou T. The Cuprizone Mouse Model. 2014. <http://www.msdiscovery.org/research-resources/animal-models/10993-cuprizone-mouse-model>.
32. Manrique-Hoyos N, Jürgens T, Grønborg M, et al. Late motor decline after accomplished remyelination: Impact for progressive multiple sclerosis. *Ann Neurol.* 2012; 71(2): 227–244, doi: [10.1002/ana.22681](https://doi.org/10.1002/ana.22681).
33. Mierzwa AJ, Marion CM, Sullivan GM, et al. Components of myelin damage and repair in the progression of white matter pathology after mild traumatic brain injury. *J Neuropathol Exp Neurol.* 2015; 74(3): 218–232, doi: [10.1097/NEN.000000000000165](https://doi.org/10.1097/NEN.000000000000165), indexed in Pubmed: [25668562](https://pubmed.ncbi.nlm.nih.gov/25668562/).
34. Miller E, Wachowicz B, Majsterek I. Advances in antioxidative therapy of multiple sclerosis. *Curr Med Chem.* 2013; 20(37): 4720–4730, doi: [10.2174/09298673113209990156](https://doi.org/10.2174/09298673113209990156), indexed in Pubmed: [23834174](https://pubmed.ncbi.nlm.nih.gov/23834174/).
35. Miller RH, Fyffe MS, Capriarello AC. Animal Models for the Study of Multiple Sclerosis In: Michael Conn P. (eds). *Animal Models for the Study of Human Disease.* 2nd ed. Academic Press 2017: 967–948.
36. Mohammed W, Radwan R, Elsayed H. Prophylactic and Ameliorative Effect of N-Acetylcysteine on Doxorubicin-Induced Neurotoxicity in Wister Rats. *Egypt J Basic Clin Pharmacol.* 2019; 9, doi: [10.32527/2019/101396](https://doi.org/10.32527/2019/101396).
37. Monti DA, Zabrecky G, Leist TP, et al. N-acetyl cysteine administration is associated with increased cerebral glucose metabolism in patients with multiple sclerosis: an exploratory study. *Front Neurol.* 2020; 11: 88, doi: [10.3389/fneur.2020.00088](https://doi.org/10.3389/fneur.2020.00088), indexed in Pubmed: [32117038](https://pubmed.ncbi.nlm.nih.gov/32117038/).
38. Muniroh M. Methylmercury-induced pro-inflammatory cytokines activation and its preventive strategy using anti-inflammation N-acetyl-L-cysteine: a mini-review. *Rev Environ Health.* 2020; 35(3): 233–238, doi: [10.1515/reveh-2020-0026](https://doi.org/10.1515/reveh-2020-0026), indexed in Pubmed: [32710722](https://pubmed.ncbi.nlm.nih.gov/32710722/).

39. Oakden W, Bock NA, Al-Ebraheem A, et al. Early regional cuprizone-induced demyelination in a rat model revealed with MRI. *NMR Biomed.* 2017; 30(9), doi: [10.1002/nbm.3743](https://doi.org/10.1002/nbm.3743), indexed in Pubmed: [28544286](https://pubmed.ncbi.nlm.nih.gov/28544286/).
40. Park D, Shin K, Choi EK, et al. Protective effects of N-acetyl-L-cysteine in human oligodendrocyte progenitor cells and restoration of motor function in neonatal rats with hypoxic-ischemic encephalopathy. *Evid Based Complement Alternat Med.* 2015; 2015: 764251, doi: [10.1155/2015/764251](https://doi.org/10.1155/2015/764251), indexed in Pubmed: [25918547](https://pubmed.ncbi.nlm.nih.gov/25918547/).
41. Pohl HBF, Porcheri C, Mueggler T, et al. Genetically induced adult oligodendrocyte cell death is associated with poor myelin clearance, reduced remyelination, and axonal damage. *J Neurosci.* 2011; 31(3): 1069–1080, doi: [10.1523/JNEUROSCI.5035-10.2011](https://doi.org/10.1523/JNEUROSCI.5035-10.2011), indexed in Pubmed: [21248132](https://pubmed.ncbi.nlm.nih.gov/21248132/).
42. Saraswathy GR, Maheswari E, Santhrani T, et al. N-acetyl-cysteine alleviates phenytoin-induced behavioral abnormalities in rats. *IJPSR.* 2014; 5(8): 3279–92.
43. Skripuletz T, Gudi V, Hackstette D, et al. De- and remyelination in the CNS white and grey matter induced by cuprizone: the old, the new, and the unexpected. *Histol Histopathol.* 2011; 26(12): 1585–1597, doi: [10.14670/HH-26.1585](https://doi.org/10.14670/HH-26.1585), indexed in Pubmed: [21972097](https://pubmed.ncbi.nlm.nih.gov/21972097/).
44. Skvarc DR, Dean OM, Byrne LK, et al. The effect of N-acetylcysteine (NAC) on human cognition: a systematic review. *Neurosci Biobehav Rev.* 2017; 78: 44–56, doi: [10.1016/j.neubiorev.2017.04.013](https://doi.org/10.1016/j.neubiorev.2017.04.013), indexed in Pubmed: [28438466](https://pubmed.ncbi.nlm.nih.gov/28438466/).
45. Snider DP. Adjuvant-free polyclonal antibody response manipulated by antibody-mediated antigen targeting In: Malik VS, Lillehoj EP, (eds). *Antibody Techniques*. 1st ed. Academic Press 1994: 49–70.
46. Song Q, Feng YB, Wang L, et al. COX-2 inhibition rescues depression-like behaviors via suppressing glial activation, oxidative stress and neuronal apoptosis in rats. *Neuropharmacology.* 2019; 160: 107779, doi: [10.1016/j.neuropharm.2019.107779](https://doi.org/10.1016/j.neuropharm.2019.107779), indexed in Pubmed: [31539536](https://pubmed.ncbi.nlm.nih.gov/31539536/).
47. Stanislaus R, Gilg AG, Singh AK, et al. N-acetyl-L-cysteine ameliorates the inflammatory disease process in experimental autoimmune encephalomyelitis in Lewis rats. *J Autoimmune Dis.* 2005; 2(1): 4, doi: [10.1186/1740-2557-2-4](https://doi.org/10.1186/1740-2557-2-4), indexed in Pubmed: [15869713](https://pubmed.ncbi.nlm.nih.gov/15869713/).
48. Steelman AJ, Thompson JP, Li J. Demyelination and remyelination in anatomically distinct regions of the corpus callosum following cuprizone intoxication. *Neurosci Res.* 2012; 72(1): 32–42, doi: [10.1016/j.neures.2011.10.002](https://doi.org/10.1016/j.neures.2011.10.002), indexed in Pubmed: [22015947](https://pubmed.ncbi.nlm.nih.gov/22015947/).
49. Taraboletti A, Walker T, Avila R, et al. Cuprizone intoxication induces cell intrinsic alterations in oligodendrocyte metabolism independent of copper chelation. *Biochemistry.* 2017; 56(10): 1518–1528, doi: [10.1021/acs.biochem.6b01072](https://doi.org/10.1021/acs.biochem.6b01072), indexed in Pubmed: [28186720](https://pubmed.ncbi.nlm.nih.gov/28186720/).
50. Tasset I, Agüera E, Sánchez-López F, et al. Peripheral oxidative stress in relapsing-remitting multiple sclerosis. *Clin Biochem.* 2012; 45(6): 440–444, doi: [10.1016/j.clin-biochem.2012.01.023](https://doi.org/10.1016/j.clin-biochem.2012.01.023), indexed in Pubmed: [22330938](https://pubmed.ncbi.nlm.nih.gov/22330938/).
51. Tobin JE, Xie M, Le TQ, et al. Reduced axonopathy and enhanced remyelination after chronic demyelination in fibroblast growth factor 2 (Fgf2)-null mice: differential detection with diffusion tensor imaging. *J Neuropathol Exp Neurol.* 2011; 70(2): 157–165, doi: [10.1097/NEN.0b013e31820937e4](https://doi.org/10.1097/NEN.0b013e31820937e4), indexed in Pubmed: [21343885](https://pubmed.ncbi.nlm.nih.gov/21343885/).
52. Van Munster CEP, Jonkman LE, Weinstein HC, et al. Gray matter damage in multiple sclerosis: Impact on clinical symptoms. *Neuroscience.* 2015; 303: 446–461, doi: [10.1016/j.neuroscience.2015.07.006](https://doi.org/10.1016/j.neuroscience.2015.07.006), indexed in Pubmed: [26164500](https://pubmed.ncbi.nlm.nih.gov/26164500/).
53. Vana AC, Flint NC, Harwood NE, et al. Platelet-derived growth factor promotes repair of chronically demyelinated white matter. *J Neuropathol Exp Neurol.* 2007; 66(11): 975–988, doi: [10.1097/NEN.0b013e3181587d46](https://doi.org/10.1097/NEN.0b013e3181587d46), indexed in Pubmed: [17984680](https://pubmed.ncbi.nlm.nih.gov/17984680/).
54. Vargas DL, Tyor WR. Update on disease-modifying therapies for multiple sclerosis. *J Investig Med.* 2017; 65(5): 883–891, doi: [10.1136/jim-2016-000339](https://doi.org/10.1136/jim-2016-000339), indexed in Pubmed: [28130412](https://pubmed.ncbi.nlm.nih.gov/28130412/).
55. Vega-Riquer J, Mendez-Victoriano G, Morales-Luckie R, et al. Five decades of cuprizone, an updated model to replicate demyelinating diseases. *Curr Neuropharmacol.* 2019; 17(2): 129–141, doi: [10.2174/1570159x15666170717120343](https://doi.org/10.2174/1570159x15666170717120343).
56. Voss EV, Škuljec J, Gudi V, et al. Characterisation of microglia during de- and remyelination: can they create a repair promoting environment? *Neurobiol Dis.* 2012; 45(1): 519–528, doi: [10.1016/j.nbd.2011.09.008](https://doi.org/10.1016/j.nbd.2011.09.008), indexed in Pubmed: [21971527](https://pubmed.ncbi.nlm.nih.gov/21971527/).
57. Wergeland S, Torkildsen Ø, Myhr KM, et al. The cuprizone model: regional heterogeneity of pathology. *APMIS.* 2012; 120(8): 648–657, doi: [10.1111/j.1600-0463.2012.02882.x](https://doi.org/10.1111/j.1600-0463.2012.02882.x), indexed in Pubmed: [22779688](https://pubmed.ncbi.nlm.nih.gov/22779688/).
58. Wu JH, Batist G. Glutathione and glutathione analogues; therapeutic potentials. *Biochim Biophys Acta.* 2013; 1830(5): 3350–3353, doi: [10.1016/j.bbagen.2012.11.016](https://doi.org/10.1016/j.bbagen.2012.11.016), indexed in Pubmed: [23201199](https://pubmed.ncbi.nlm.nih.gov/23201199/).
59. Zendedel A, Beyer C, Kipp M. Cuprizone-induced demyelination as a tool to study remyelination and axonal protection. *J Mol Neurosci.* 2013; 51(2): 567–572, doi: [10.1007/s12031-013-0026-4](https://doi.org/10.1007/s12031-013-0026-4), indexed in Pubmed: [23666824](https://pubmed.ncbi.nlm.nih.gov/23666824/).
60. Zhen W, Liu A, Lu J, et al. An alternative cuprizone-induced demyelination and remyelination mouse model. *ASN Neuro.* 2017; 9(4): 1759091417725174, doi: [10.1177/1759091417725174](https://doi.org/10.1177/1759091417725174), indexed in Pubmed: [28840755](https://pubmed.ncbi.nlm.nih.gov/28840755/).
61. Zhou J, Terluk MR, Basso L, et al. N-acetylcysteine provides cytoprotection in murine oligodendrocytes through heme oxygenase-1 activity. *Biomedicines.* 2020; 8(8), doi: [10.3390/biomedicines8080240](https://doi.org/10.3390/biomedicines8080240), indexed in Pubmed: [32717964](https://pubmed.ncbi.nlm.nih.gov/32717964/).

# Volumetric measurements of the subcortical structures of healthy adult brains in the Turkish population

H. Soysal<sup>1</sup> , N. Acer<sup>2</sup> , M. Özdemir<sup>3</sup> , Ö. Eraslan<sup>3</sup> 

<sup>1</sup>Department of Anatomy, Faculty of Dentistry, Ankara Yıldırım Beyazıt University, Ankara, Turkey

<sup>2</sup>Department of Anatomy, Faculty of Medicine, Arel University, Istanbul, Turkey

<sup>3</sup>Department of Radiology, Dışkapı Yıldırım Beyazıt Health Application and Research Centre, Medical Sciences University, Ankara, Turkey

[Received: 4 January 2021; Accepted: 5 March 2021; Early publication date: 22 March 2021]

**Background:** The interest in the morphological development of brain structures during childhood and adolescence arises from discussions on subcortical anomalies and sexual dimorphism, from adolescent changes in cognitive functions supported by cortical and subcortical structures to a wide range of childhood neuropsychiatric diseases. This study aims to investigate the subcortical structures regarding age/gender changes in the healthy adult human brain using web-based volBrain.

**Materials and methods:** In this study, 303 normal healthy adults (males and females) were examined using a 1.5 T unit with a 20-channel head coil.

**Results:** The volumes of white matter, grey matter, total brain, cerebrospinal fluid, and total intracranial volume were significantly higher in males than those in females. Our analysis revealed a significantly larger accumbens volume in females. With the age of less than or equal to 50 years, older males were found to have higher total lateral ventricle, putamen, thalamus, amygdala, cerebrum, white matter and grey matter volumes than females. In the age group of 50 years and older mean total volumes of thalamus, globus pallidus and accumbens were higher in females than those in males. Right hemisphere volumes in younger and older age groups were higher except for caudate volume in the older age group; the mean of caudate was significantly higher in females than those in males.

**Conclusions:** These conclusions might be important for the explanation of the effects of gender and age in cross-sectional structural magnetic resonance imaging studies. Also, knowing the volume changes of the subcortical structures can provide convenience about the prevention, diagnosis, and treatment of various neuromental disorders. (Folia Morphol 2022; 81, 2: 294–306)

**Key words:** cortical volume, subcortical nuclei, sex differences, magnetic resonance imaging, healthy adult brain, volBrain

Address for correspondence: Dr. H. Soysal, Department of Anatomy, Faculty of Dentistry, Ankara Yıldırım Beyazıt University, Ankara, Turkey, e-mail: handan\_soysal@hotmail.com

This article is available in open access under Creative Common Attribution-Non-Commercial-No Derivatives 4.0 International (CC BY-NC-ND 4.0) license, allowing to download articles and share them with others as long as they credit the authors and the publisher, but without permission to change them in any way or use them commercially.

## INTRODUCTION

Magnetic resonance imaging (MRI) allows examination of brain parts in a noninvasive way and *in vivo*. This is significant in studying the pathogenesis and pathophysiology of neurological disturbances [18]. There are many volumetric brain studies that show neuroanatomical disorders in MRI [14].

Previous studies have reported an increase in the volume of basal ganglia in schizophrenia [8]. However, new volumetric studies have reported a decrease in the volume of basal ganglia such as putamen, caudate, thalamus [17, 19, 32].

Autopsy studies show that brain weight decreases by at least 10% in men and women between the ages of 25–75, also in the age range of 50–75, the volume decreases by about 2% every decade [4].

The brain differs depending on age/gender. Variety can be measured *in vivo* with MRI. The volumetric MRI analyses indicate that age-associated volume reductions have been reported especially for basal ganglia such as the thalamus, caudate, putamen, globus pallidus (GP) [2, 22].

There are many studies about basal grey structures' volume depending on age and gender using different methods [17, 24, 25, 31, 32].

Studies on volume indicated a negative proportion among age, sex, and basal ganglia volumes [1]. Male caudate volume is higher than female [11].

There are many reports to support the effect of subcortical volumes in gender-specific neuropsychiatric disturbances (e.g. autism, schizophrenia, Parkinson's disease, attention deficit hyperactivity disorder, and addictions) [5, 35, 38].

Recently, different techniques have been studied for automatic or semi-automatic segmentations of subcortical structures, such as software for analysis and visualisation of functional magnetic resonance neuroimages [10], BrainVoyager [15], FreeSurfer [12, 41], Mristudio [21, 26] and statistical parametric maps [2] — software used to analyse the structural features of the human brain. volBrain is an automated method where the observer can perform fully automatic segmentation using a web-based application. Recently, volBrain has been used for a neuroimaging study of MRI data [23].

volBrain is an automatic and sturdy quantitative analysis system that also gives a result in a short time. In our study, we share the results of the MRI study on the effects of age on subcortical structures using volBrain. All participants consisted of 303 subjects aged from 12 to 84 years (113 men, 190 women).

## MATERIALS AND METHODS

### Participants

All participants provided written informed consent for the relevant studies and ethical approval was obtained from the Dışkapı Training and Research Hospital Clinical Research Ethics Committee. Research was conducted on human participants. All procedures performed in this study comply with the ethical standards of the institution. Approval was obtained from the Ethics Committee of Dışkapı Yıldırım Beyazıt Training and Research Hospital, indicating that the MRI used in the study were ethically and scientifically safe (Ethics Committee's decision date: 06.08.2018; Decision number: 53/05).

The study group consisted of healthy volunteers with no history of surgery or trauma of the brain, neurological or psychiatric disease, or substance abuse.

A mini-score assessment was performed in order to rule out psychiatric disease as well as cognitive impairment. Finally, our study group consisted of 303 participants. Participants included 113 men and 190 women with a mean age of 49 years (range: 12–84) and 42.5 years (range: 11–82), respectively. Informed consent was obtained from parent and/or legal guardian for human participants under the age of 18. Children under the age of 18 came to the hospital with their parents, and brain MRI radiographs were taken after obtaining informed consent from the parents.

### MRI protocol and segmentation method

Magnetic resonance imaging of the subcortical structures was acquired on a 1.5 T unit (Magnetom Aera, Siemens, Erlangen, Germany) with a 20-channel head coil. The subcortical volumetric assessment was conducted on sagittal oblique T1-weighted images obtained perpendicular to the long axis of the subcortical structures. A magnetisation prepared rapid acquisition gradient echo sequence (MP-RAGE) was used with the following parameters: repetition time = 2400 ms, echo time = 3.54 ms, field of view = 240 mm, slice thickness = 1.2 mm, voxel size = 1.3 × 1.3 × 1.2 mm.

Magnetic resonance imaging data processing and subcortical volumetric analyses were performed using volBrain (v.1.0, <http://volbrain.upv.es>), a free online MRI brain volumetry system. volBrain is a fully automated segmentation technique of which the algorithm is based on multi-atlas patch-based label fusion segmentation technology (Figs. 1, 2) [9, 23].

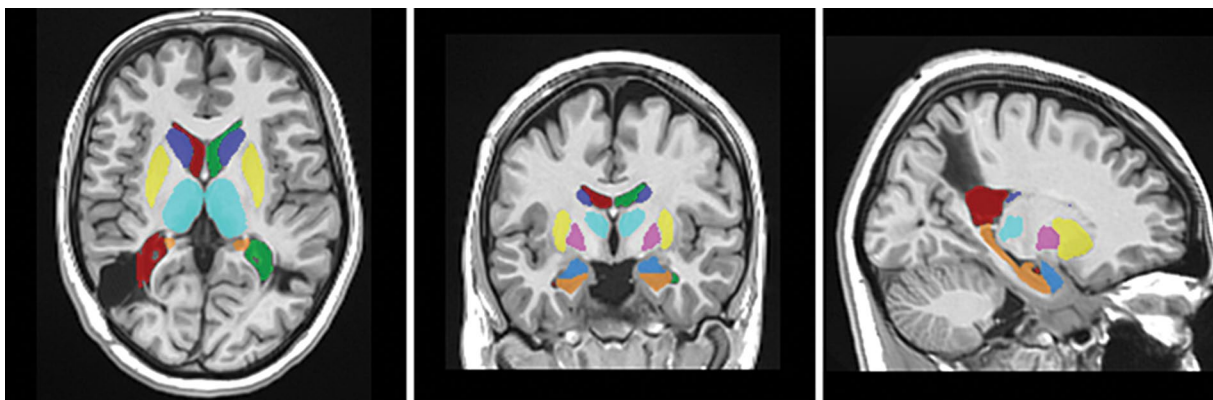


**Figure 1.** Fully-automated subcortical segmentation by volBrain.

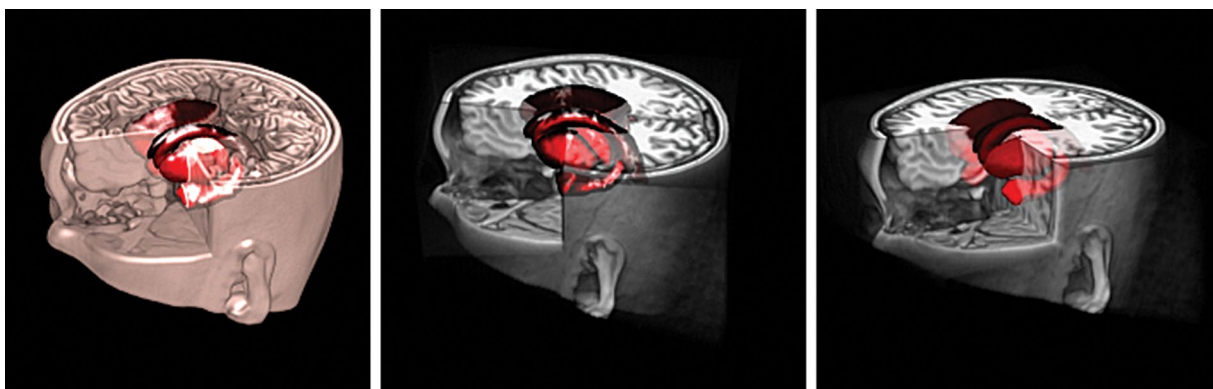


**Figure 2.** Three-dimensional visualisation of volBrain data.

### Statistical analysis

The distributions of age and volume measurements were examined by the Shapiro-Wilk's test and normality plots. All continuous variables were reported as median (range). Total and side volumes were also summarized by mean  $\pm$  standard deviation (mean  $\pm$  SD).

Genders were compared by the Mann-Whitney U test for age and volume measurements. Additionally, independent samples t-test was performed in comparison between males and females for normally distributed volumes in the oldest age group. The adjustment of age and total intracranial volume (TIC) was also applied for the comparisons of volumes by general linear model procedure. Intracranial volume (ICV) was used as a covariate to compare the volumes of males and females in age groups. The volumes of the left and right hemisphere of the brain were compared by the Wilcoxon test in males and females, separately. A p-value  $< 0.05$  was considered as statistically significant.

Statistical analyses were performed via IBM SPSS Statistics 22.0 (IBM Corp. Released 2013. IBM SPSS Statistics for Windows, Version 22.0. Armonk, NY: IBM Corp.).

## RESULTS

### Global effect of aging

The median age of men and women was 49 (range: 12–84) and 42.5 years (range: 11–82), respectively. There was no significant difference between men and women by age ( $p = 0.071$ ). The volumes of white matter (WM), grey matter (GM), total brain (TB), cerebrospinal fluid (CF), and TIC were significantly higher in males than females ( $p < 0.001$  for all, Table 1).

### Gender differences for subcortical nuclei

The univariate analysis revealed that the volumes of lateral ventricle (LV), putamen, GP, amygdala, cerebrum, WM, and GM were significantly higher in men ( $p < 0.05$ , Table 2). When the adjustment according

**Table 1.** Age and volume distributions in males and females

	Male (n = 113)	Female (n = 190)	Total (n = 303)
Age [years]*	49 (12–84)	42.5 (11–82)	45 (11–84)
Volumes [mm <sup>3</sup> ]**:			
White matter	530.16 (317.29–785.44)	477.73 (215.18–1,027.72)	493.35 (215.18–1,027.72)
Grey matter	719.07 (401.78–929.19)	661.45 (242.56–903.33)	681.21 (242.56–929.19)
Total brain	1,241.83 (862.18–1,548.87)	1,151.11 (644.70–1,475.80)	1,183.99 (644.70–1,548.87)
Cerebrospinal fluid	242.30 (101.99–518.05)	178.46 (62.79–596.96)	195.09 (62.79–596.96)
Total intracranial	1,494.78 (1,146.07–1,866.76)	1,329.50 (941.06–1653.44)	1,374.51 (941.06–1,866.76)

Data are shown as median (minimum–maximum); \*p = 0.071, \*\*p < 0.001

**Table 2.** Distribution of subcortical volumes in males and females

	Male		Female		P-value	Adj. p-value
	Mean ± SD	Median (min–max)	Mean ± SD	Median (min–max)		
LV	23.08 ± 18.04	16.96 (2.20–83.92)	13.48 ± 15.88	9.75 (2.09–149.93)	< 0.001	0.260
Caudate	7.01 ± 1.54	6.81 (4.39–18.92)	6.82 ± 0.97	6.75 (4.41–11.55)	0.354	0.265
Putamen	8.49 ± 1.69	8.31 (5.52–21.97)	8.07 ± 1.08	8.11 (3.60–13.41)	0.012	0.785
Thalamus	11.04 ± 2.13	11.07 (6.86–27.04)	10.69 ± 1.28	10.75 (6.51–14.64)	0.178	0.293
GP	2.39 ± 0.44	2.37 (1.27–5.10)	2.26 ± 0.35	2.27 (0.68–3.14)	0.021	0.276
Amygdala	1.77 ± 0.34	1.78 (0.44–2.60)	1.64 ± 0.31	1.68 (0.04–2.65)	< 0.001	0.635
Accumbens	0.66 ± 0.18	0.67 (0.04–1.08)	0.68 ± 0.16	0.68 (0.07–1.11)	0.347	< 0.001
Cerebrum	1,088.94 ± 119.37	1,090.01 (746.69–1,345.42)	998.02 ± 106.54	1,001.35 (607.16–1,308.94)	< 0.001	0.133
WM	474.60 ± 73.11	484.08 (288.09–701.24)	433.93 ± 72.21	429.58 (170.51–879.07)	< 0.001	0.144
GM	614.34 ± 74.20	609.66 (348.86–814.31)	564.09 ± 70.74	555.75 (214.27–795.99)	< 0.001	0.830

SD — standard deviation; LV — lateral ventricle; GP — globus pallidus; GM — grey matter; WM — white matter; Adj. p-value — p-value after total intracranial volume and age adjustment

to the age and TIC was applied, the only significant difference was in accumbens volume between males and females; it was found to be higher in women compared to males (p < 0.001) (Fig. 3).

**Side differences**

The right brain volumes were significantly lower for LV, putamen, accumbens and WM, and higher for caudate than those of the left brain in males. The right brain volumes were significantly lower for LV, putamen, thalamus, GP, amygdala, accumbens and WM, and higher for caudate and GM than those of the left volumes in females (Fig. 4, Table 3).

**Gender differences in the younger age group**

When the individuals with age less than or equal to 50 years were examined, males were found to have higher total LV, putamen, thalamus, amygdala, cerebrum, WM and GM volumes than females (p < 0.05,

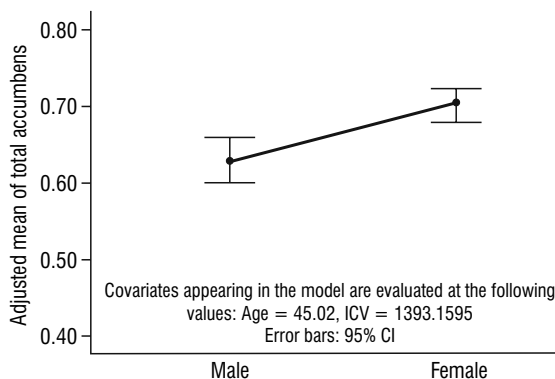


**Figure 3.** Intracranial volume (ICV)- and age-adjusted mean of total accumbens in males and females; CI — confidence interval.

Table 4). However, ICV-adjusted total accumbens mean in females was found to be higher than those in males (p = 0.008) (Fig. 5, Table 4).

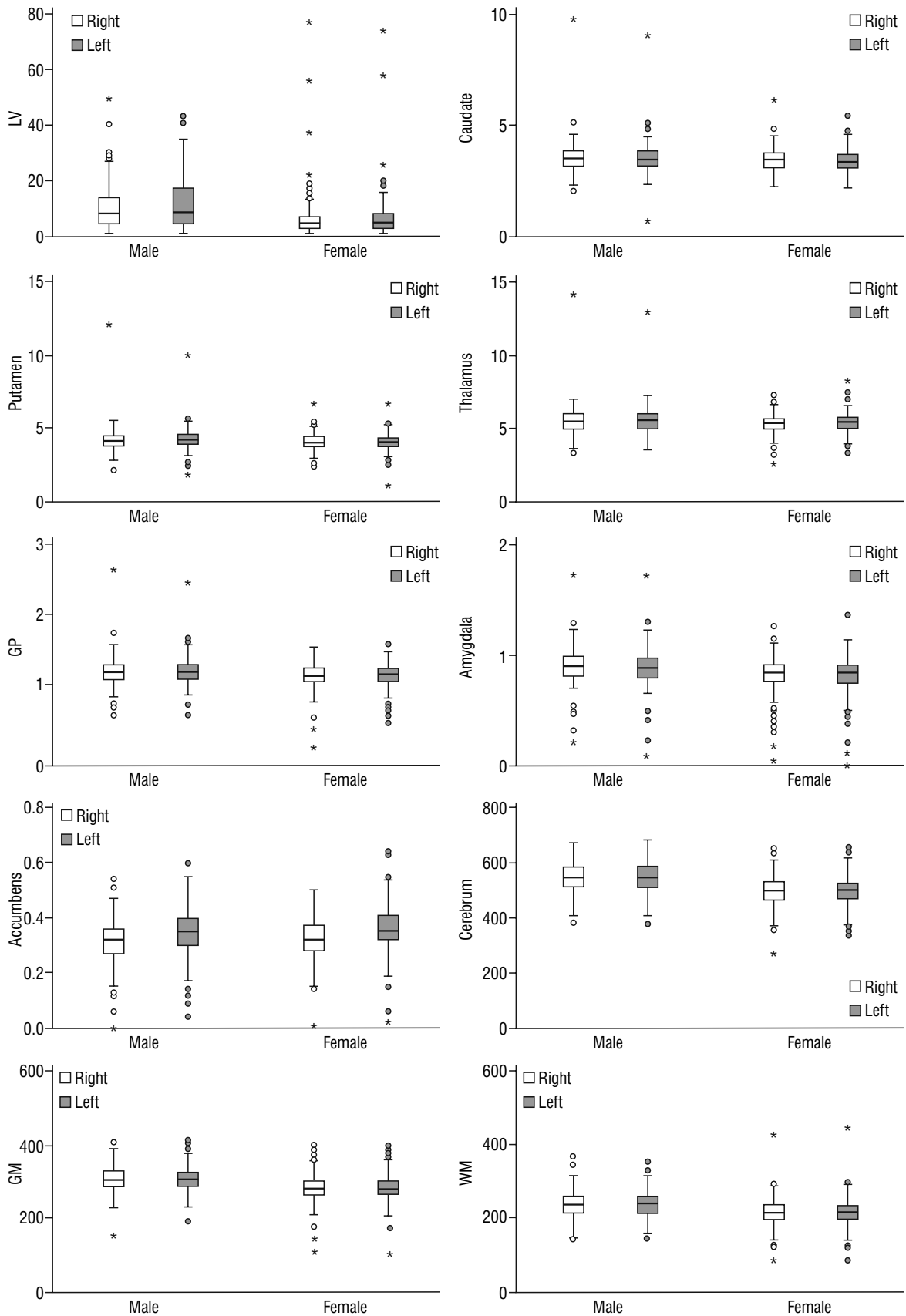


**Figure 4.** Distribution of right and left sides in males and females; LV — lateral ventricle; GM — grey matter; GP — globus pallidus; WM — white matter.

**Table 3.** Distribution of right and left sides in males and females

	Right		Left		P
	Mean $\pm$ SD	Median (min–max)	Mean $\pm$ SD	Median (min–max)	
<b>Male</b>					
LV	10.88 $\pm$ 8.69	8.38 (1.26–50.08)	12.20 $\pm$ 9.80	8.71 (0.94–43.26)	< 0.001
Caudate	3.53 $\pm$ 0.80	3.48 (1.98–9.84)	3.48 $\pm$ 0.79	3.44 (0.61–9.08)	0.010
Putamen	4.21 $\pm$ 0.94	4.11 (2.16–12.05)	4.28 $\pm$ 0.80	4.20 (1.89–9.92)	< 0.001
Thalamus	5.50 $\pm$ 1.13	5.49 (3.3–14.18)	5.54 $\pm$ 1.06	5.56 (3.49–12.85)	0.086
GP	1.19 $\pm$ 0.24	1.19 (0.57–2.65)	1.20 $\pm$ 0.22	1.19 (0.58–2.45)	0.639
Amygdala	0.90 $\pm$ 0.19	0.90 (0.22–1.73)	0.88 $\pm$ 0.20	0.89 (0.08–1.72)	0.061
Accumbens	0.31 $\pm$ 0.09	0.32 (0–0.54)	0.35 $\pm$ 0.10	0.35 (0.04–0.60)	< 0.001
Cerebrum	544.06 $\pm$ 61.08	546.91 (373.2–671.09)	544.88 $\pm$ 60.04	544.52 (373.49–681.72)	0.494
GM	307.43 $\pm$ 38.41	304.95 (154.96–408.61)	306.92 $\pm$ 36.67	305.37 (193.90–413.49)	0.176
WM	236.63 $\pm$ 37.87	240.00 (145.54–369.85)	237.96 $\pm$ 36.33	240.44 (142.55–351.79)	0.010
<b>Female</b>					
LV	6.35 $\pm$ 7.68	4.61 (0.91–77.38)	7.12 $\pm$ 8.35	5.10 (0.93–72.55)	< 0.001
Caudate	3.43 $\pm$ 0.49	3.40 (2.19–6.17)	3.39 $\pm$ 0.50	3.33 (2.10–5.39)	< 0.001
Putamen	4.01 $\pm$ 0.53	4.01 (2.49–6.69)	4.05 $\pm$ 0.57	4.08 (1.08–6.72)	< 0.001
Thalamus	5.30 $\pm$ 0.65	5.34 (2.69–7.30)	5.39 $\pm$ 0.68	5.42 (3.33–8.30)	< 0.001
GP	1.12 $\pm$ 0.18	1.12 (0.13–1.54)	1.14 $\pm$ 0.18	1.15 (0.46–1.59)	0.028
Amygdala	0.83 $\pm$ 0.15	0.84 (0.04–1.27)	0.82 $\pm$ 0.17	0.84 (0.00–1.37)	0.046
Accumbens	0.32 $\pm$ 0.08	0.32 (0.01–0.50)	0.36 $\pm$ 0.09	0.35 (0.02–0.64)	< 0.001
Cerebrum	498.57 $\pm$ 53.79	500.42 (269.6–652.79)	498.69 $\pm$ 52.41	499.91 (337.56–656.14)	0.689
GM	282.32 $\pm$ 35.83	279.21 (109.51–398.88)	281.77 $\pm$ 35.10	279.03 (104.76–397.11)	0.012
WM	216.24 $\pm$ 35.70	214.20 (84.72–430.87)	216.92 $\pm$ 35.59	216.41 (85.79–448.20)	0.021

SD — standard deviation; LV — lateral ventricle; GP — globus pallidus; GM — grey matter; WM — white matter

### Gender differences in the older age group

In individuals with age greater than 50 years, the univariate analyses resulted in the same as in the younger age group. The ICV-adjusted mean of total thalamus, GP and accumbens volumes were higher in women than in men ( $p < 0.05$ ) (Fig. 5, Table 4).

When left hemisphere volumes in the younger age group were analysed, males were found to have higher LV, putamen, thalamus, amygdala, cerebrum, WM and GM volumes than females ( $p < 0.05$ , Table 5). However, the ICV-adjusted accumbens mean in females was higher than that in males ( $p = 0.038$ ) (Fig. 6, Table 5). In the older age group, the univariate analyses resulted in the same as in the younger age group. The ICV-adjusted mean of thalamus, GP and accumbens volumes were higher in women than in men ( $p < 0.05$ ) (Fig. 6, Table 5).

Right hemisphere volumes in younger and older age groups were almost the same as left hemisphere volumes, except for caudate in the older age groups

(Table 6). The ICV-adjusted mean of caudate was significantly higher in women than in men ( $p = 0.019$ ) (Fig. 7, Table 6).

## DISCUSSION

In our study, we measured the subcortical structures' volumes in healthy adults between the ages of 20–86 and evaluated the data by age and gender.

There are many reports on the brain and subcortical structures' volumes in both sexes and different ages. The majority of these studies focused on the subcortical structures and examined age-related volume changes of various subcortical structures. It has been reported in various cross-sectional and longitudinal studies that the volumes of caudate, thalamus and putamen decrease with age [6, 13, 16, 29, 30, 32, 36, 39].

Walhovd et al. [36] studied the cortical and subcortical regions of 73 men and women (20–88 years old) using an automated segmentation technique.

**Table 4.** Distribution in males and females in younger and older age group ( $\leq 50$  years old and  $+50$  years old in total)

	Male		Female		P-value	Adj. p-value
	Mean $\pm$ SD	Median (min–max)	Mean $\pm$ SD	Median (min–max)		
<b>Younger age</b>						
LV	15.71 $\pm$ 12.65	11.27 (2.20–61.82)	10.84 $\pm$ 13.91	8.35 (2.09–149.93)	<b>0.001</b>	0.301
Caudate	7.46 $\pm$ 1.82	7.26 (4.39–18.92)	7.07 $\pm$ 1.01	6.97 (4.92–11.55)	0.122	0.563
Putamen	8.95 $\pm$ 2.03	8.71 (5.53–21.97)	8.43 $\pm$ 1.04	8.36 (3.60–13.41)	<b>0.030</b>	0.803
Thalamus	11.94 $\pm$ 2.31	11.59 (8.87–27.04)	11.18 $\pm$ 1.1	11.05 (6.51–14.64)	<b>0.002</b>	0.803
GP	2.48 $\pm$ 0.48	2.42 (1.27–5.10)	2.31 $\pm$ 0.38	2.35 (0.68–3.14)	0.057	0.681
Amygdala	1.84 $\pm$ 0.3	1.80 (0.87–2.60)	1.69 $\pm$ 0.32	1.72 (0.04–2.65)	<b>&lt; 0.001</b>	0.875
Accumbens	0.72 $\pm$ 0.18	0.73 (0.04–1.08)	0.72 $\pm$ 0.16	0.72 (0.07–1.11)	0.769	<b>0.008</b>
Cerebrum	1127.02 $\pm$ 104.65	1114.85 (873.65–1345.4)	1029.7 $\pm$ 97.57	1031.47 (607.16–1308.94)	<b>&lt; 0.001</b>	0.133
WM	488.91 $\pm$ 64.15	489.75 (360.10–701.24)	445.36 $\pm$ 73.99	436.82 (170.51–879.07)	<b>&lt; 0.001</b>	0.532
GM	638.11 $\pm$ 79.41	623.75 (348.86–814.31)	584.34 $\pm$ 73.66	579.80 (214.27–795.99)	<b>&lt; 0.001</b>	0.536
<b>Older age</b>						
LV	31.73 $\pm$ 19.63	27.27 (5.91–83.92)	18.1 $\pm$ 18.04	13.04 (3.11–114.58)	<b>&lt; 0.001</b>	0.068
Caudate	6.48 $\pm$ 0.89	6.55 (4.57–8.77)	6.39 $\pm$ 0.73	6.34 (4.41–8.17)	0.551	0.072
Putamen	7.95 $\pm$ 0.94	8.01 (5.52–10.13)	7.44 $\pm$ 0.83	7.52 (5.08–10.61)	<b>0.002</b>	0.594
Thalamus	9.99 $\pm$ 1.26	9.9 (6.86–12.68)	9.82 $\pm$ 1.09	9.99 (6.61–11.75)	0.433	<b>&lt; 0.001</b>
GP	2.28 $\pm$ 0.36	2.3 (1.48–3.38)	2.17 $\pm$ 0.24	2.17 (1.53–2.67)	0.066	<b>0.037</b>
Amygdala	1.7 $\pm$ 0.38	1.69 (0.44–2.52)	1.56 $\pm$ 0.28	1.61 (0.72–2.06)	<b>0.013</b>	0.123
Accumbens	0.59 $\pm$ 0.14	0.60 (0.12–0.87)	0.61 $\pm$ 0.14	0.63 (0.34–1.11)	0.502	<b>0.007</b>
Cerebrum	1044.27 $\pm$ 121	1058.10 (746.69–1328.12)	942.47 $\pm$ 99.16	939.27 (712.33–1173.36)	<b>&lt; 0.001</b>	0.176
WM	457.8 $\pm$ 79.79	452.80 (288.09–630.98)	413.88 $\pm$ 64.73	408.89 (245.55–582.04)	<b>0.001</b>	0.096
GM	586.47 $\pm$ 56.6	579.86 (458.6–740.8)	528.59 $\pm$ 48.23	534.87 (350.09–638.26)	<b>&lt; 0.001</b>	0.969

Bold measurements are significantly higher in females than those in males after total intracranial volume adjustment. SD — standard deviation; LV — lateral ventricle; GP — globus pallidus; WM — white matter; GM — grey matter; Adj. p-value — p-value after total intracranial volume adjustment

Except for pallidum, they showed age-related volume decrease in cortical grey matter, cerebral white matter, hippocampus, amygdala, thalamus, accumbens, caudate, putamen, pallidus, brainstem, cerebellar cortex and cerebellar white matter. They also found that advanced age was strongly associated with volumes of the thalamus and cortical grey matter, which showed a linear decline and curvilinear decline with age.

In our study, total thalamus, GP and accumbens volumes in patients older than 50 years were higher in women. In our findings, we did not find an age-related decrease in left thalamus volume in a similar age range (20–86 years) and a higher thalamus volume in men over the age of 50 years.

Alexander et al. [3] stated that putamen, caudate, accumbens and pallidum, all of which are related to emotional, motor behaviour and cognition, are blunted by aging. Basal ganglia reach a peak volume before the age of 20. The youngest participant in our

study was people aged 11–84 years were evaluated. Therefore, the basal ganglia did not go through an atrophy period.

Accumbens and pallidum volumes, which are reported as less stable in the literature than other subcortical structures [16], showed a minimal age effect on pallidum than other structures. Walhovd et al. [37] examined the effects of age on subcortical structures and they found great differences in putamen, thalamus and accumbens volume due to aging. Regions such as caudate and amygdala were not affected by aging.

In the subcortical regions such as caudate, pallidum and amygdala, a linear decrease in the age-related pattern is shown [13, 29, 30]. Pfefferbaum et al. [27] performed MRI studies in 55 men and 67 women (20–85 years), and showed that older age was related to a decrease in thalamus volume, and this decline increased with age (60+ years).

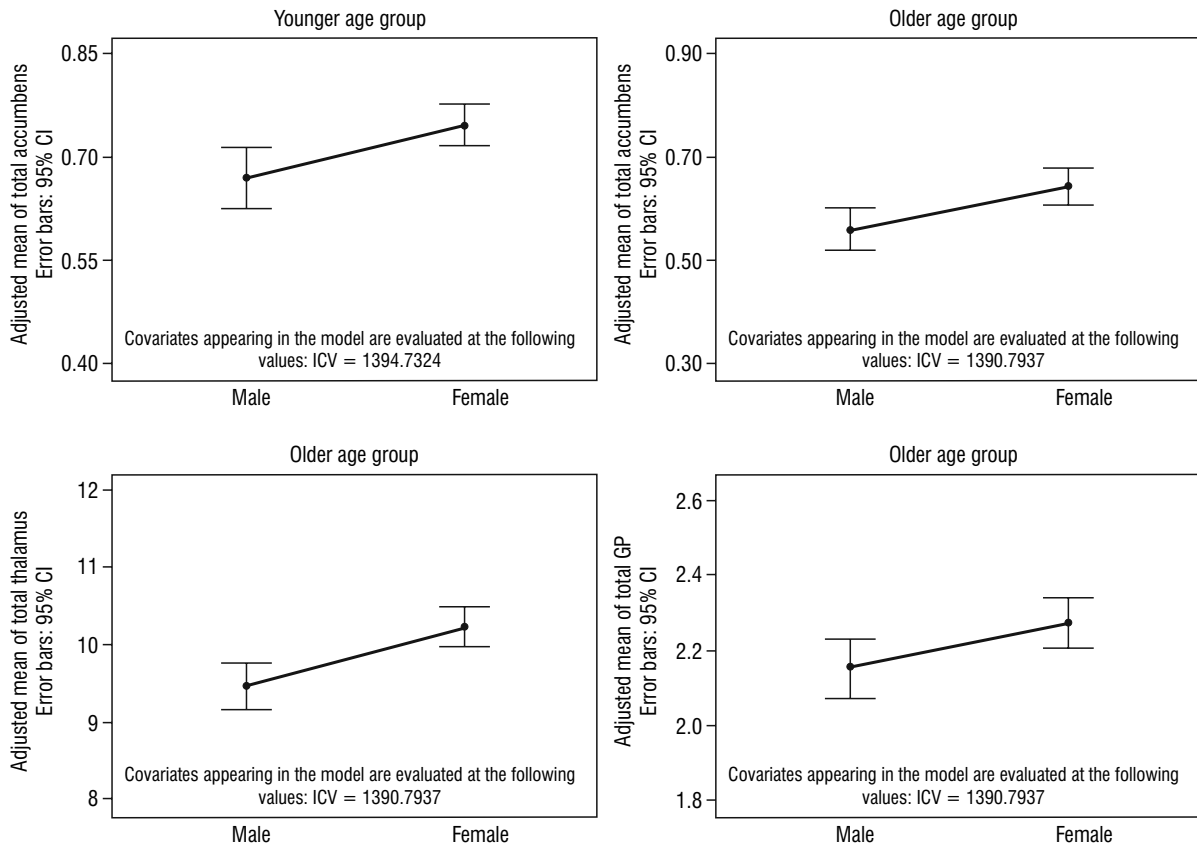


**Figure 5.** Intracranial volume (ICV)-adjusted mean of total accumbens, thalamus and globus pallidus (GP) volumes in males and females of younger and older age groups; CI — confidence interval.

Abedalahi and Hasanzadeh [1] calculated the caudate volume with the Cavalieri principle. This study was carried out in 120 normal human subjects (60 males, 60 females) divided into young (< 40 years) and older ( $\geq$  40 years) groups between the ages of 15–65. The volume of caudate nucleus showed a significant negative correlation with age. Goodre et al. [16] showed that there was a stronger correlation between the age and the structural volume for the hippocampus, amygdala and accumbens in the older group (60–85 years) than the middle-aged (35–60 years) group. Similarly, in our study, 303 normal people (113 men, 190 women) aged 11–84 were divided into young ( $\leq$  50 years old) and elderly (> 50 years old) groups. There was a significant negative correlation between the young group with the volume of the accumbens and the old group with the volume of the thalamus, GP, and accumbens.

Thalamic volumetric analyses showed that thalamus volumes were smaller in the elderly than younger adults using cross-sectional and automated technique studies [6, 36]. Cherubini et al. [6] found that age

showed strong correlation in both striatal structures and thalamic volume. In our study, gender differences in cortical grey matter concentration were greater in patients aged 50 years and older than in the younger age group; LV, putamen, thalamus, amygdala, cerebrum, WM and GM volumes of men were higher than women. However, women had significantly higher accumbens volume. Unlike our findings, Wang et al. [39] stated in their study that the volume of accumbens decreased with increasing age. The effect of gender on the volume of subcortical structures may play an important role because basal ganglia have high-density sex steroid receptors [34]. In this period, age and gender interaction showed that the right putamen and right pallidum in men had a marked age progression.

In general, male brains were found to have larger GM, WM, and subcortical structures than women. As a result of the correction of the total intracranial volume, we found that women had a larger volume of accumbens. In addition, in the male group only, we found a significant large volume effect on the

**Table 5.** Distribution in males and females in younger and older age group ( $\leq 50$  years old and  $+50$  years old) in left hemisphere

Left hemisphere	Male		Female		P-value	Adj. p-value
	Mean $\pm$ SD	Median (min–max)	Mean $\pm$ SD	Median (min–max)		
<b>Younger age</b>						
LV	8.37 $\pm$ 7.31	5.61 (0.94–35.01)	5.65 $\pm$ 6.89	4.40 (0.93–72.55)	<b>0.003</b>	0.256
Caudate	3.69 $\pm$ 0.94	3.61 (0.61–9.08)	3.53 $\pm$ 0.50	3.49 (2.53–5.39)	0.119	0.520
Putamen	4.50 $\pm$ 0.94	4.43 (1.89–9.92)	4.23 $\pm$ 0.56	4.19 (1.08–6.72)	<b>0.008</b>	0.800
Thalamus	5.99 $\pm$ 1.15	5.91 (3.49–12.85)	5.65 $\pm$ 0.60	5.63 (3.82–8.30)	<b>0.003</b>	0.947
GP	1.24 $\pm$ 0.24	1.20 (0.58–2.45)	1.17 $\pm$ 0.19	1.20 (0.46–1.59)	0.167	0.464
Amygdala	0.91 $\pm$ 0.19	0.91 (0.08–1.31)	0.84 $\pm$ 0.18	0.86 (0–1.37)	<b>&lt; 0.001</b>	0.900
Accumbens	0.38 $\pm$ 0.10	0.37 (0.04–0.60)	0.38 $\pm$ 0.09	0.37 (0.02–0.63)	0.578	<b>0.038</b>
Cerebrum	563.46 $\pm$ 53.99	555.28 (434.27–681.72)	514.43 $\pm$ 47.27	514.91 (337.56–656.14)	<b>&lt; 0.001</b>	0.219
WM	244.64 $\pm$ 31.60	245.31 (179.41–351.79)	222.43 $\pm$ 36.28	219.81 (85.79–448.20)	<b>&lt; 0.001</b>	0.651
GM	318.82 $\pm$ 39.49	310.69 (193.90–413.49)	291.99 $\pm$ 36.38	290.19 (104.76–397.11)	<b>&lt; 0.001</b>	0.554
<b>Older age</b>						
LV	16.70 $\pm$ 10.48	14.91 (2.38–43.26)	9.69 $\pm$ 9.98	6.44 (1.34–58.48)	<b>&lt; 0.001</b>	0.088
Caudate	3.23 $\pm$ 0.46	3.27 (2.29–4.33)	3.16 $\pm$ 0.39	3.12 (2.10–4.27)	0.393	0.227
Putamen	4.02 $\pm$ 0.50	4.04 (2.51–5.16)	3.73 $\pm$ 0.42	3.77 (2.58–5.26)	<b>0.001</b>	0.857
Thalamus	5.02 $\pm$ 0.64	4.95 (3.53–6.38)	<b>4.93 <math>\pm</math> 0.56</b>	<b>4.99 (3.33–6.11)</b>	0.440	<b>0.002</b>
GP	1.15 $\pm$ 0.19	1.14 (0.72–1.66)	<b>1.09 <math>\pm</math> 0.13</b>	<b>1.09 (0.67–1.32)</b>	<b>0.046</b>	<b>0.047</b>
Amygdala	0.83 $\pm$ 0.21	0.82 (0.22–1.72)	0.78 $\pm$ 0.15	0.79 (0.20–1.01)	0.082	0.168
Accumbens	0.31 $\pm$ 0.08	0.32 (0.09–0.53)	<b>0.33 <math>\pm</math> 0.08</b>	<b>0.33 (0.19–0.64)</b>	0.423	<b>0.016</b>
Cerebrum	523.09 $\pm$ 59.90	532.08 (373.49–662.49)	471.08 $\pm$ 49.77	471.04 (350.15–588.37)	<b>&lt; 0.001</b>	0.301
WM	230.14 $\pm$ 40.10	227.97 (142.55–316.04)	207.24 $\pm$ 32.37	205.90 (122.11–292.40)	<b>0.001</b>	0.126
GM	292.95 $\pm$ 27.39	289.34 (230.94–371.23)	263.84 $\pm$ 24.02	265.02 (171.92–317.10)	<b>&lt; 0.001</b>	0.675

Bold measurements are significantly higher in females than those in males after total intracranial volume adjustment. SD — standard deviation; LV — lateral ventricle; GP — globus pallidus; WM — white matter; GM — grey matter; Adj. p-value — p-value after total intracranial volume adjustment

right caudate volume compared to the contralateral structures of the brain hemisphere.

Ruigrok et al. [32] found that the TB volume was on average 8–15% higher in males than females. Wang et al. [39] reported that the volume of the right putamen, right pallidum, and right thalamus decreased faster in males, whereas the volume of the left thalamus, bilateral hippocampus and amygdala follow a quadratic model in males and a linear decline model in females. In our study, in men, LV, putamen, accumbens and WM volumes in the right brain were significantly lower than the left brain and higher than the left brain for caudate volume.

Xu et al. [40] found that males had atrophy due to aging in the basal ganglia of the left hemisphere and also the volume of the thalamus and brain in the left hemisphere was significantly smaller than the right hemisphere. Brain atrophy with aging in male patients was higher than female patients. We found

left hemisphere volumes in males from both younger and older age group were higher for LV, putamen, thalamus, amygdala, cerebrum, WM and GM volumes than in females. However, accumbens volume mean in females was higher than that in males. Nevertheless, right hemisphere volumes in younger and older age groups were almost the same as left hemisphere volumes, except caudate in the older age group. The mean volume of caudate was significantly higher in women than in men.

Goodro et al. [16] found that left and right thalamus volume decreased faster than women. Similarly, in our study, the volumes of thalamus in women and men were different in the left and right thalamus. In women between the ages of 20–86, the left thalamic volume was higher than in men.

Although our MRI research cannot identify the mechanism that leads to volume differences due to age, it can provide additional information for the

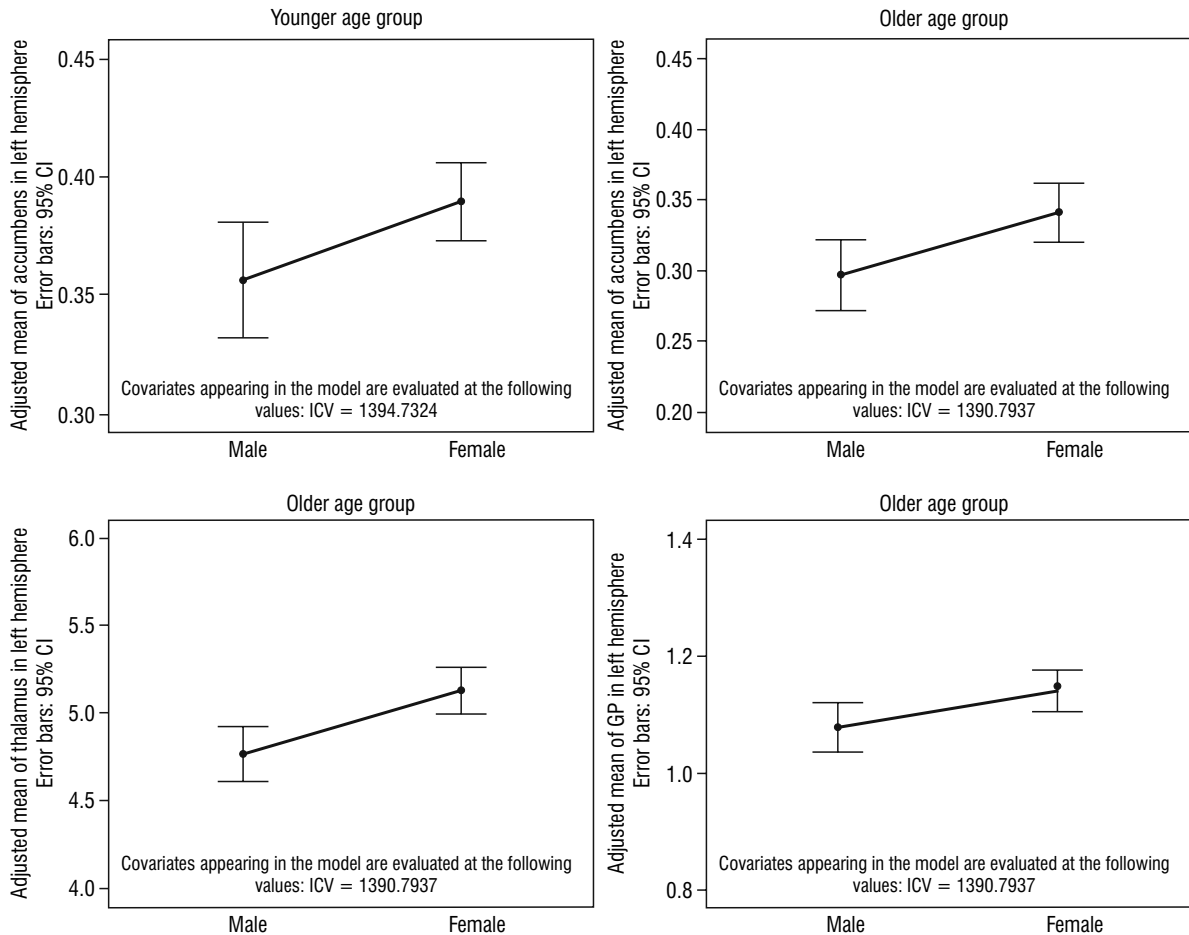


**Figure 6.** Intracranial volume (ICV)-adjusted mean of left hemisphere accumbens, thalamus and globus pallidus (GP) volumes in males and females of younger and older age groups; CI — confidence interval.

possible mechanism of sex-dependent volume differences in basal ganglia when associated with advanced software technology. Volume analysis of the nucleus accumbens helps in the evaluation of neurodegenerative diseases. In this context, our results are of importance for gender-dependent nucleus accumbens volume increase.

Compared to women, men have been found to perform worse in the ongoing response task and visual-spatial learning and planning task, especially in older ages [7, 28]. However, some studies have not reported age and gender effects or different aging effects on cognition in men and women [20, 33].

In this study, we used an automated and reliable analysis to address volumetric changes [23]. We presented a new method, namely, volBrain. It can be used in place of other volume techniques. volBrain has several advantages for brain imaging researchers. In addition, it is less tiring software that can get very

fast results in the treatments and clinical studies in neurological disorders.

The main limitation of our study is that it is not a longitudinal study. More participants and more studies are needed to confirm the findings of this study. Another limitation is that it is not done using manual volumetry.

volBrain can be used to measure volumes of other anatomical areas of the body using radiological images. We believe that our results will provide additional information to volumetric studies evaluating the development, pathology and abnormalities of subcortical structures.

The results of the study demonstrated that in the age group of 50 years or less, males were found to have higher total LV, putamen, thalamus, amygdala, cerebrum, WM and GM volumes than females. In the age group over 50 years, the means of total thalamus, GP, and accumbens volumes were higher in females than those in males.

**Table 6.** Distribution in males and females in younger and older age group ( $\leq 50$  years old and  $+50$  years old) in right hemisphere

Right hemisphere	Male		Female		p-value	Adj. p-value
	Mean $\pm$ SD	Median (min–max)	Mean $\pm$ SD	Median (min–max)		
<b>Younger age</b>						
LV	7.34 $\pm$ 5.72	5.50 (1.26–28.33)	5.19 $\pm$ 7.12	4.19 (0.91–77.38)	<b>0.001</b>	0.370
Caudate	3.77 $\pm$ 0.95	3.70 (1.98–9.84)	3.55 $\pm$ 0.52	3.51 (2.19–6.17)	0.055	0.635
Putamen	4.45 $\pm$ 1.16	4.29 (2.16–12.05)	4.19 $\pm$ 0.50	4.14 (2.52–6.69)	0.052	0.812
Thalamus	5.95 $\pm$ 1.25	5.78 (3.60–14.18)	5.53 $\pm$ 0.58	5.51 (2.69–7.30)	<b>&lt; 0.001</b>	0.686
GP	1.24 $\pm$ 0.26	1.20 (0.59–2.65)	1.14 $\pm$ 0.20	1.14 (0.13–1.54)	<b>0.015</b>	0.907
Amygdala	0.93 $\pm$ 0.14	0.90 (0.47–1.29)	0.85 $\pm$ 0.16	0.86 (0.04–1.27)	<b>0.001</b>	0.857
Accumbens	0.34 $\pm$ 0.09	0.34 (0–0.54)	0.35 $\pm$ 0.08	0.34 (0.01–0.50)	0.859	<b>0.002</b>
Cerebrum	563.56 $\pm$ 53.68	559.56 (413.08–671.09)	514.07 $\pm$ 49.95	515.50 (269.60–652.79)	<b>&lt; 0.001</b>	0.220
WM	244.28 $\pm$ 34.36	245.42 (151.33–369.85)	221.72 $\pm$ 36.41	220.98 (84.72–430.87)	<b>&lt; 0.001</b>	0.653
GM	319.28 $\pm$ 41.18	317.76 (154.96–408.61)	292.35 $\pm$ 37.48	289.57 (109.51–398.88)	<b>&lt; 0.001</b>	0.528
<b>Older age</b>						
LV	15.03 $\pm$ 9.73	12.58 (3.31–50.08)	8.39 $\pm$ 8.26	6.04 (1.54–56.10)	<b>&lt; 0.001</b>	0.058
Caudate	3.25 $\pm$ 0.45	3.23 (2.25–4.44)	3.22 $\pm$ 0.35	3.20 (2.31–4.01)	0.697	0.019
Putamen	3.93 $\pm$ 0.46	3.98 (2.91–4.97)	3.70 $\pm$ 0.43	3.70 (2.49–5.35)	<b>0.005</b>	0.383
Thalamus	4.97 $\pm$ 0.67	4.92 (3.30–6.31)	4.89 $\pm$ 0.55	4.99 (3.28–5.75)	0.651	<b>0.001</b>
GP	1.14 $\pm$ 0.19	1.15 (0.57–1.73)	1.09 $\pm$ 0.12	1.09 (0.82–1.35)	0.058	<b>0.046</b>
Amygdala	0.87 $\pm$ 0.22	0.86 (0.22–1.73)	0.79 $\pm$ 0.14	0.81 (0.30–1.05)	<b>0.025</b>	0.181
Accumbens	0.27 $\pm$ 0.07	0.28 (0–0.42)	0.28 $\pm$ 0.07	0.29 (0.14–0.48)	0.660	<b>0.005</b>
Cerebrum	521.18 $\pm$ 61.75	527.69 (373.20–665.65)	471.39 $\pm$ 49.61	471.10 (362.18–584.99)	<b>&lt; 0.001</b>	0.098
WM	227.66 $\pm$ 40.11	224.25 (145.54–314.94)	206.64 $\pm$ 32.48	204.41 (123.44–289.64)	<b>0.002</b>	0.075
GM	293.52 $\pm$ 29.65	290.40 (227.66–369.58)	264.75 $\pm$ 24.42	268.09 (178.17–321.15)	<b>&lt; 0.001</b>	0.729

Bold measurements are significantly higher in females than those in males after total intracranial volume adjustment. SD — standard deviation; LV — lateral ventricle; GP — globus pallidus; WM — white matter; GM — grey matter; Adj. p-value — p-value after total intracranial volume adjustment

## CONCLUSIONS

In conclusion, the results of recent research show that brain cortical structures and volume loss of subcortical nuclei are a common finding in a number of neuropsychiatric problems. The data obtained in this study are normal brain data according to age and gender of the adult Turkish population. It can be useful in clinical applications and cognitive disorders of many neuropsychiatric diseases.

## Acknowledgements

The authors thank the Department of Radiology of Dışkapı Training and Research Hospital for providing the raw data, the Ethics Committee for approving the permits, all contributing authors, and the faculty members of the Department of Foreign Languages, Erciyes University for the English editing, to Ankara Yıldırım Beyazıt University Department of Biostatistics for statistical analysis.

**Conflict of interest:** None declared

## REFERENCES

1. Abedalahi A, Hasanzadeh H. MRI based morphometry of caudate nucleus in normal. Persons. Archives of advances in biosciences. J Paramedical Sci. 2013; 42(2): 70–75.
2. Acer N, Bastepe-Gray S, Sagiroglu A, et al. Diffusion tensor and volumetric magnetic resonance imaging findings in the brains of professional musicians. J Chem Neuroanat. 2018; 88: 33–40, doi: [10.1016/j.jchemneu.2017.11.003](https://doi.org/10.1016/j.jchemneu.2017.11.003), indexed in Pubmed: [29113947](https://pubmed.ncbi.nlm.nih.gov/29113947/).
3. Alexander GE, DeLong MR, Strick PL. Parallel organization of functionally segregated circuits linking basal ganglia and cortex. Annu Rev Neurosci. 1986; 9: 357–381, doi: [10.1146/annurev.ne.09.030186.002041](https://doi.org/10.1146/annurev.ne.09.030186.002041), indexed in Pubmed: [3085570](https://pubmed.ncbi.nlm.nih.gov/3085570/).
4. Allen JS, Bruss J, Brown CK, et al. Normal neuroanatomical variation due to age: the major lobes and a parcellation of the temporal region. Neurobiol Aging. 2005; 26(9): 1245–1260, doi: [10.1016/j.neurobiolaging.2005.05.023](https://doi.org/10.1016/j.neurobiolaging.2005.05.023), indexed in Pubmed: [16046030](https://pubmed.ncbi.nlm.nih.gov/16046030/).
5. Bourque M, Dluzen DE, Di Paolo T. Neuroprotective actions of sex steroids in Parkinson's disease. Front

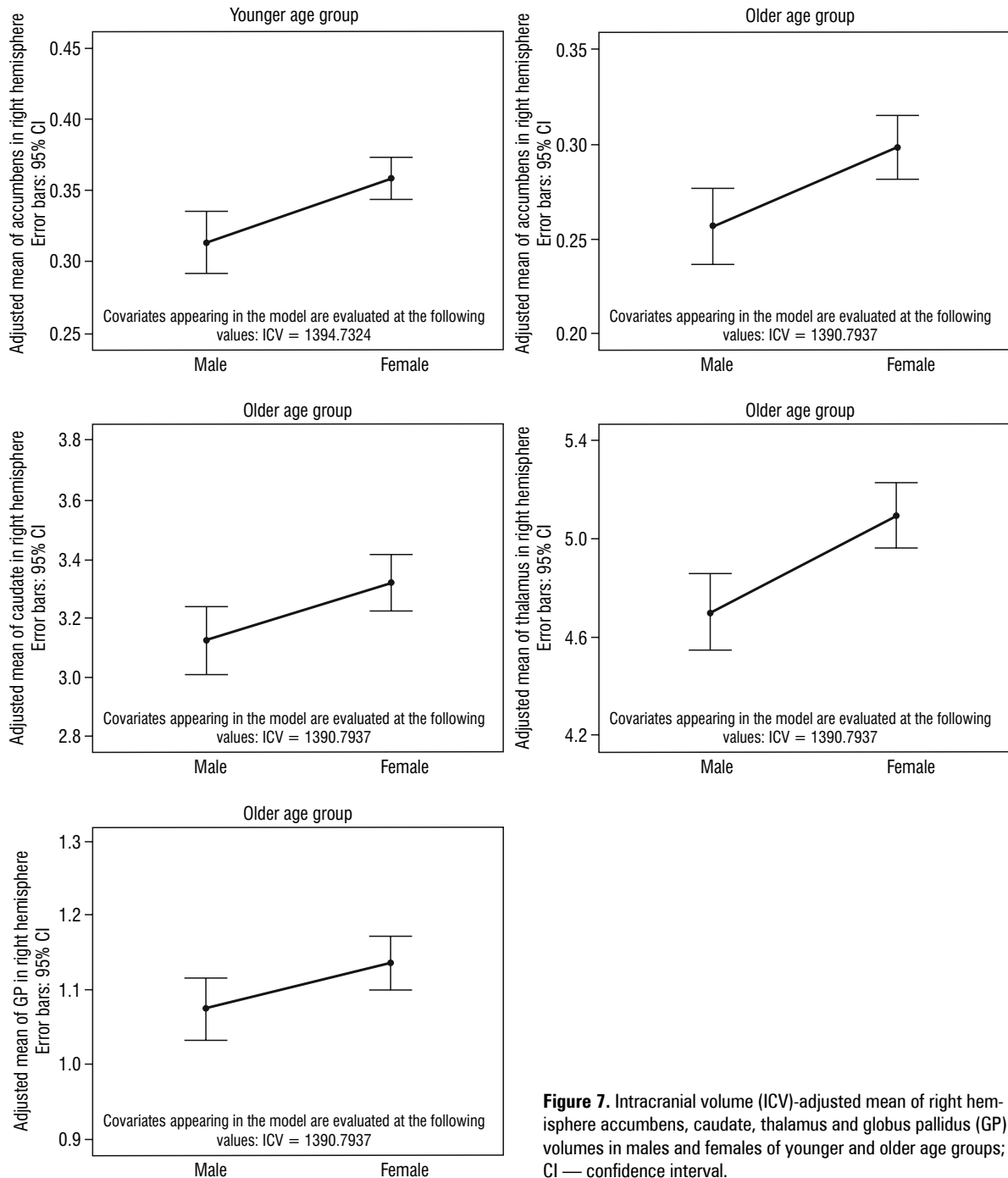


**Figure 7.** Intracranial volume (ICV)-adjusted mean of right hemisphere accumbens, caudate, thalamus and globus pallidus (GP) volumes in males and females of younger and older age groups; CI — confidence interval.

Neuroendocrinol. 2009; 30(2): 142–157, doi: [10.1016/j.ynfe.2009.04.014](https://doi.org/10.1016/j.ynfe.2009.04.014), indexed in Pubmed: [19410597](https://pubmed.ncbi.nlm.nih.gov/19410597/).

6. Cherubini A, Pérán P, Caltagirone C, et al. Aging of subcortical nuclei: microstructural, mineralization and atrophy modifications measured in vivo using MRI. *Neuroimage*. 2009; 48(1): 29–36, doi: [10.1016/j.neuroimage.2009.06.035](https://doi.org/10.1016/j.neuroimage.2009.06.035), indexed in Pubmed: [19540925](https://pubmed.ncbi.nlm.nih.gov/19540925/).

7. Clark CR, Paul RH, Williams LM, et al. Standardized assessment of cognitive functioning during development and aging using an automated touchscreen battery. *Arch*

*Clin Neuropsychol*. 2006; 21(5): 449–467, doi: [10.1016/j.acn.2006.06.005](https://doi.org/10.1016/j.acn.2006.06.005), indexed in Pubmed: [16904862](https://pubmed.ncbi.nlm.nih.gov/16904862/).

8. Corson PW, Nopoulos P, Miller DD, et al. Change in basal ganglia volume over 2 years in patients with schizophrenia: typical versus atypical neuroleptics. *Am J Psychiatry*. 1999; 156(8): 1200–1204, doi: [10.1176/ajp.156.8.1200](https://doi.org/10.1176/ajp.156.8.1200), indexed in Pubmed: [10450260](https://pubmed.ncbi.nlm.nih.gov/10450260/).

9. Coupé P, Manjón JV, Fonov V, et al. Patch-based segmentation using expert priors: application to hippocampus and ventricle segmentation. *Neuroimage*. 2011; 54(2):

- 940–954, doi: [10.1016/j.neuroimage.2010.09.018](https://doi.org/10.1016/j.neuroimage.2010.09.018), indexed in Pubmed: [20851199](https://pubmed.ncbi.nlm.nih.gov/20851199/).
10. Cox RW. AFNI: what a long strange trip it's been. *Neuroimage*. 2012; 62(2): 743–747, doi: [10.1016/j.neuroimage.2011.08.056](https://doi.org/10.1016/j.neuroimage.2011.08.056), indexed in Pubmed: [21889996](https://pubmed.ncbi.nlm.nih.gov/21889996/).
  11. Filipek PA, Richelme C, Kennedy DN, et al. The young adult human brain: an MRI-based morphometric analysis. *Cereb Cortex*. 1994; 4(4): 344–360, doi: [10.1093/cercor/4.4.344](https://doi.org/10.1093/cercor/4.4.344), indexed in Pubmed: [7950308](https://pubmed.ncbi.nlm.nih.gov/7950308/).
  12. Fischl B. FreeSurfer. *Neuroimage*. 2012; 62(2): 774–781, doi: [10.1016/j.neuroimage.2012.01.021](https://doi.org/10.1016/j.neuroimage.2012.01.021), indexed in Pubmed: [22248573](https://pubmed.ncbi.nlm.nih.gov/22248573/).
  13. Fjell AM, Westlye LT, Grydeland H, et al. Critical ages in the life course of the adult brain: nonlinear subcortical aging. *Neurobiol Aging*. 2013; 34(10): 2239–2247, doi: [10.1016/j.neurobiolaging.2013.04.006](https://doi.org/10.1016/j.neurobiolaging.2013.04.006), indexed in Pubmed: [23643484](https://pubmed.ncbi.nlm.nih.gov/23643484/).
  14. Gilbert A, Keshavan M. MRI structural findings in schizophrenia. *Revista Brasileira de Psiquiatria*. 2001; 23(suppl 1): 15–18, doi: [10.1590/s1516-44462001000500006](https://doi.org/10.1590/s1516-44462001000500006).
  15. Goebel R. BrainVoyager -- past, present, future. *Neuroimage*. 2012; 62(2): 748–756, doi: [10.1016/j.neuroimage.2012.01.083](https://doi.org/10.1016/j.neuroimage.2012.01.083), indexed in Pubmed: [22289803](https://pubmed.ncbi.nlm.nih.gov/22289803/).
  16. Goodro M, Sameti M, Patenaude B, et al. Age effect on subcortical structures in healthy adults. *Psychiatry Res*. 2012; 203(1): 38–45, doi: [10.1016/j.psychres.2011.09.014](https://doi.org/10.1016/j.psychres.2011.09.014), indexed in Pubmed: [22863654](https://pubmed.ncbi.nlm.nih.gov/22863654/).
  17. Huang X, Pu W, Li X, et al. Decreased left putamen and thalamus volume correlates with delusions in first-episode schizophrenia patients. *Front Psychiatry*. 2017; 8: 245, doi: [10.3389/fpsy.2017.00245](https://doi.org/10.3389/fpsy.2017.00245), indexed in Pubmed: [29209237](https://pubmed.ncbi.nlm.nih.gov/29209237/).
  18. Igual L, Soliva JC, Hernández-Vela A, et al. A fully-automatic caudate nucleus segmentation of brain MRI: application in volumetric analysis of pediatric attention-deficit/hyperactivity disorder. *Biomed Eng Online*. 2011; 10: 105, doi: [10.1186/1475-925X-10-105](https://doi.org/10.1186/1475-925X-10-105), indexed in Pubmed: [22141926](https://pubmed.ncbi.nlm.nih.gov/22141926/).
  19. Jiji S, Smitha KA, Gupta AK, et al. Segmentation and volumetric analysis of the caudate nucleus in Alzheimer's disease. *Eur J Radiol*. 2013; 82(9): 1525–1530, doi: [10.1016/j.ejrad.2013.03.012](https://doi.org/10.1016/j.ejrad.2013.03.012), indexed in Pubmed: [23664648](https://pubmed.ncbi.nlm.nih.gov/23664648/).
  20. Kavé G, Shrira A, Palgi Y, et al. Formal education level versus self-rated literacy as predictors of cognitive aging. *J Gerontol B Psychol Sci Soc Sci*. 2012; 67(6): 697–704, doi: [10.1093/geronb/gbs031](https://doi.org/10.1093/geronb/gbs031), indexed in Pubmed: [22421808](https://pubmed.ncbi.nlm.nih.gov/22421808/).
  21. Kocaman H, Acer N, Köseoğlu E, et al. Evaluation of intracerebral ventricles volume of patients with Parkinson's disease using the atlas-based method: A methodological study. *J Chem Neuroanat*. 2019; 98: 124–130, doi: [10.1016/j.jchemneu.2019.04.005](https://doi.org/10.1016/j.jchemneu.2019.04.005), indexed in Pubmed: [30986488](https://pubmed.ncbi.nlm.nih.gov/30986488/).
  22. Madan CR, Kensinger EA. Age-related differences in the structural complexity of subcortical and ventricular structures. *Neurobiol Aging*. 2017; 50: 87–95, doi: [10.1016/j.neurobiolaging.2016.10.023](https://doi.org/10.1016/j.neurobiolaging.2016.10.023), indexed in Pubmed: [27939959](https://pubmed.ncbi.nlm.nih.gov/27939959/).
  23. Manjón JV, Coupé P. volBrain: An Online MRI brain volumetry system. *Front Neuroinform*. 2016; 10: 30, doi: [10.3389/fninf.2016.00030](https://doi.org/10.3389/fninf.2016.00030), indexed in Pubmed: [27512372](https://pubmed.ncbi.nlm.nih.gov/27512372/).
  24. Morey RA, Petty CM, Xu Y, et al. A comparison of automated segmentation and manual tracing for quantifying hippocampal and amygdala volumes. *Neuroimage*. 2009; 45(3): 855–866, doi: [10.1016/j.neuroimage.2008.12.033](https://doi.org/10.1016/j.neuroimage.2008.12.033), indexed in Pubmed: [19162198](https://pubmed.ncbi.nlm.nih.gov/19162198/).
  25. Morey RA, Selgrade ES, Wagner HR, et al. Scan-rescan reliability of subcortical brain volumes derived from automated segmentation. *Hum Brain Mapp*. 2010; 31(11): 1751–1762, doi: [10.1002/hbm.20973](https://doi.org/10.1002/hbm.20973), indexed in Pubmed: [20162602](https://pubmed.ncbi.nlm.nih.gov/20162602/).
  26. Palancı Ö, Kalaycıoğlu A, Acer N, et al. Volume calculation of brain structures in migraine disease by using mrstudio. *NeuroQuantology*. 2018; 16(10): 8–13, doi: [10.14704/nq.2018.16.10.1692](https://doi.org/10.14704/nq.2018.16.10.1692).
  27. Pfefferbaum A, Rohlfing T, Rosenbloom MJ, et al. Variation in longitudinal trajectories of regional brain volumes of healthy men and women (ages 10 to 85 years) measured with atlas-based parcellation of MRI. *Neuroimage*. 2013; 65: 176–193, doi: [10.1016/j.neuroimage.2012.10.008](https://doi.org/10.1016/j.neuroimage.2012.10.008), indexed in Pubmed: [23063452](https://pubmed.ncbi.nlm.nih.gov/23063452/).
  28. Proust-Lima C, Amieva H, Letenneur L, et al. Gender and education impact on brain aging: a general cognitive factor approach. *Psychol Aging*. 2008; 23(3): 608–620, doi: [10.1037/a0012838](https://doi.org/10.1037/a0012838), indexed in Pubmed: [18808250](https://pubmed.ncbi.nlm.nih.gov/18808250/).
  29. Raz N, Lindenberger U. Only time will tell: cross-sectional studies offer no solution to the age-brain-cognition triangle: comment on Salthouse (2011). *Psychol Bull*. 2011; 137(5): 790–795, doi: [10.1037/a0024503](https://doi.org/10.1037/a0024503), indexed in Pubmed: [21859179](https://pubmed.ncbi.nlm.nih.gov/21859179/).
  30. Raz N, Lindenberger U, Rodrigue KM, et al. Regional brain changes in aging healthy adults: general trends, individual differences and modifiers. *Cereb Cortex*. 2005; 15(11): 1676–1689, doi: [10.1093/cercor/bhi044](https://doi.org/10.1093/cercor/bhi044), indexed in Pubmed: [15703252](https://pubmed.ncbi.nlm.nih.gov/15703252/).
  31. Rijpkema M, Everaerd D, van der Pol C, et al. Normal sexual dimorphism in the human basal ganglia. *Hum Brain Mapp*. 2012; 33(5): 1246–1252, doi: [10.1002/hbm.21283](https://doi.org/10.1002/hbm.21283), indexed in Pubmed: [21523857](https://pubmed.ncbi.nlm.nih.gov/21523857/).
  32. Ruigrok ANV, Salimi-Khorshidi G, Lai MC, et al. A meta-analysis of sex differences in human brain structure. *Neurosci Biobehav Rev*. 2014; 39: 34–50, doi: [10.1016/j.neubiorev.2013.12.004](https://doi.org/10.1016/j.neubiorev.2013.12.004), indexed in Pubmed: [24374381](https://pubmed.ncbi.nlm.nih.gov/24374381/).
  33. Silver H, Goodman C, Gur RC, et al. 'Executive' functions and normal aging: selective impairment in conditional exclusion compared to abstraction and inhibition. *Dement Geriatr Cogn Disord*. 2011; 31(1): 53–62, doi: [10.1159/000322568](https://doi.org/10.1159/000322568), indexed in Pubmed: [21150204](https://pubmed.ncbi.nlm.nih.gov/21150204/).
  34. Taber KH, Murphy DD, Blurton-Jones MM, et al. An update on estrogen: higher cognitive function, receptor mapping, neurotrophic effects. *J Neuropsychiatry Clin Neurosci*. 2001; 13(3): 313–317, doi: [10.1176/jnp.13.3.313](https://doi.org/10.1176/jnp.13.3.313), indexed in Pubmed: [11514636](https://pubmed.ncbi.nlm.nih.gov/11514636/).
  35. Volkow ND, Wang GJ, Fowler JS, et al. Addiction circuitry in the human brain. *Annu Rev Pharmacol Toxicol*. 2012; 52: 321–336, doi: [10.1146/annurev-pharmtox-010611-134625](https://doi.org/10.1146/annurev-pharmtox-010611-134625), indexed in Pubmed: [21961707](https://pubmed.ncbi.nlm.nih.gov/21961707/).
  36. Walhovd KB, Fjell AM, Reinvang I, et al. Effects of age on volumes of cortex, white matter and subcortical structures. *Neurobiol Aging*. 2005; 26(9): 1261–1270, doi: [10.1016/j.neurobiolaging.2005.05.020](https://doi.org/10.1016/j.neurobiolaging.2005.05.020), indexed in Pubmed: [16005549](https://pubmed.ncbi.nlm.nih.gov/16005549/).
  37. Walhovd KB, Westlye LT, Amlien I, et al. Consistent neuroanatomical age-related volume differences across multiple samples. *Neurobiol Aging*. 2011; 32(5): 916–932, doi: [10.1016/j.neurobiolaging.2009.05.013](https://doi.org/10.1016/j.neurobiolaging.2009.05.013), indexed in Pubmed: [19570593](https://pubmed.ncbi.nlm.nih.gov/19570593/).
  38. Wang Y, Xu Q, Li S, et al. Gender differences in anomalous subcortical morphology for children with ADHD. *Neurosci Lett*. 2018; 665: 176–181, doi: [10.1016/j.neulet.2017.12.006](https://doi.org/10.1016/j.neulet.2017.12.006), indexed in Pubmed: [29217259](https://pubmed.ncbi.nlm.nih.gov/29217259/).
  39. Wang Y, Xu Q, Luo J, et al. Effects of age and sex on subcortical volumes. *Front Aging Neurosci*. 2019; 11(259): 1–12, doi: [10.3389/fnagi.2019.00259](https://doi.org/10.3389/fnagi.2019.00259), indexed in Pubmed: [31616285](https://pubmed.ncbi.nlm.nih.gov/31616285/).
  40. Xu J, Kobayashi S, Yamaguchi S, et al. Gender effects on age-related changes in brain structure. *AJNR Am J Neuroradiol*. 2000; 21(1): 112–118.
  41. Zheng F, Li C, Zhang D, et al. Study on the sub-regions volume of hippocampus and amygdala in schizophrenia. *Quant Imaging Med Surg*. 2019; 9(6): 1025–1036, doi: [10.21037/qims.2019.05.21](https://doi.org/10.21037/qims.2019.05.21), indexed in Pubmed: [31367556](https://pubmed.ncbi.nlm.nih.gov/31367556/).

# Evaluation of olfactory bulb volume and olfactory sulcus depth development with 3 Tesla magnetic resonance imaging in childhood

B. Güney<sup>1</sup>, N. Çullu<sup>1</sup>, M.Y. Özdemir<sup>1</sup>

Department of Radiology, Muğla Sıtkı Koçman University Medical Faculty, Muğla, Turkey

[Received: 15 December 2020; Accepted: 1 February 2021; Early publication date: 1 March 2021]

**Background:** This study aimed to reveal the change in olfactory bulb volume (OBV) and olfactory sulcus depth (OSD) in healthy Turkish paediatric individuals between 1 month and 18 years of age with 3 Tesla magnetic resonance imaging (MRI), taking into account different age groups and gender factors.

**Materials and methods:** In this retrospective study, 190 paediatric individuals who underwent cranial MRI were evaluated. Healthy paediatric cases were divided into four groups as infantile period (first 24 months when cerebral myelination was completed), early childhood (2–6 years), childhood (6–12 years) and adolescence (12–18 years). OBV and OSD measurements were performed on coronal T2-weighted brain MRI by 3 Tesla magnetic resonance scan. The mean, right and left OBVs and OSDs were used for evaluation.

**Results:** The mean age was  $9.9 \pm 7.5$  months for the infantile period,  $4.5 \pm 1.3$  years for early childhood,  $9.3 \pm 1.7$  years for childhood and  $15.2 \pm 1.7$  years for adolescence. Mean, right and left OBV was found to be slightly larger in male children than in female children ( $p = 0.015$ ,  $p = 0.033$  and  $p = 0.010$ , respectively). There was no statistical difference between the genders for mean, right and left OSD ( $p = 0.559$ ,  $p = 0.536$  and  $p = 0.598$ , respectively). Among the age groups, the values of the 3<sup>rd</sup> and 4<sup>th</sup> groups in terms of mean, right and left OBV were higher than in the other two groups ( $p < 0.001$ ). In terms of OSD, mean, right and left values were higher in group 2, 3 and 4 than in group 1 ( $p < 0.001$ ).

**Conclusions:** These data differ by paediatric age group and gender for the development of OBV and OSD. Normal values for the paediatric age group and gender should be calculated to detect olfactory dysfunction. (Folia Morphol 2022; 81, 2: 307–313)

**Key words:** paediatric age, bulbus olfactorius, olfactory sulci, 3 Tesla magnetic resonance

## INTRODUCTION

The sense of smell is one of the five senses that have an important function in human life, and the olfactory bulb (OB) is considered to be the most im-

portant transmission station in processing the sense of smell. Anatomical structures of the sense of smell begin to develop early in the human foetus. There are studies and anatomical atlases on the development

Address for correspondence: Dr. B. Güney, Assistant Professor, Muğla Sıtkı Koçman University Medical Faculty, Department of Radiology, tel: +90 533 4911152, fax: +90 252 2111345, e-mail: bunyaminguney@mu.edu.tr

This article is available in open access under Creative Common Attribution-Non-Commercial-No Derivatives 4.0 International (CC BY-NC-ND 4.0) license, allowing to download articles and share them with others as long as they credit the authors and the publisher, but without permission to change them in any way or use them commercially.

and anatomical change of the primordial olfactory bulb, which was first observed anatomically in a 41-day (4.5 week) embryo in the foetal development period, from gestation to birth [2, 13, 15, 17]. However, the number of studies on the anatomical development and change of the olfactory bulb in the paediatric period is limited. In a study conducted by Schneider and Floemer [18] about the maturation of the olfactory bulb in the postnatal period, they found that olfactory bulb showed a similar maturation parallel to the maturation of the cerebral white matter until the end of the second year, when the myelination and maturation of the cerebral white matter was completed. In this study, it was found that the olfactory bulbs took the adult shape at the end of the postnatal 24 months [18]. The first study on the anatomical development and change of olfactory bulb volume (OBV) in the paediatric age group was conducted by Hummel et al. [10]. A positive relationship was found between increased OBV and increased olfactory function in this study performed in children aged 1 to 17 years. It was found that both OBV and olfactory function increased with age.

Another parameter used in evaluating olfactory functions is the depth of the olfactory sulcus. Some diseases such as major depression, anxiety disorder, Behçet's disease, Parkinson's and Alzheimer's disease have been shown to reduce the depth of the olfactory sulcus and cause a decrease in the sense of smell [1, 5, 11]. There are limited studies on the change of OBV and olfactory sulcus depth (OSD) with age in paediatric cases [16]. OBV and OSD are known to vary with age [4, 10]. The age-related change and normal values of both OBV and OSD in healthy paediatric individuals are not clearly known.

This study aimed to reveal the change of OBV and OSD over time in healthy Turkish paediatric individuals between 1 month and 18 years of age with 3 Tesla magnetic resonance imaging (MRI) taking into account different age groups and gender factors.

## MATERIALS AND METHODS

After being approved by the Ethics Committee of our University, the research was started retrospectively in the Radiology Department. Only children with normal brain MRI were included in the study. Paediatric individuals with any brain abnormality (developmental anomaly, myelination disorder, maturation disorder, etc.) or disease were excluded from

the study. While evaluating the patients, the patient files registered in the hospital information system were taken as basis. Those with a genetic disease in their family, those with suspected congenital neurometabolic disease, chronic diseases such as diabetes mellitus and hypertension, and asthma patients were excluded from the study. Patients who had MRI examination for control purposes and patients with nonspecific symptoms and no pathology were included in the study. The cases had nonspecific complaints such as headache and dizziness in order of frequency. No disease was detected in these paediatric individuals and no disease developed during clinical follow-up in our hospital.

In this study, 190 paediatric individuals who underwent cranial MRI between 2017 and 2019 were evaluated retrospectively. Cases with good image resolution and no motion artefact were included in the study, while cases with poor image resolution and artefacts were excluded. Ninety-five of our cases were females and 95 were males. Healthy paediatric cases were divided into four groups according to their age and gender: group 1: infantile period (1–24 months), group 2: early childhood (2–6 years), group 3: childhood (7–12 years) and group 4: adolescence (13–18 years); group A consisting of 95 females; group B consisting of 95 males. The study was conducted on the basis of and in accordance with the Declaration of Helsinki. OBV and OSD measurements were made on T2-weighted brain MRIs in the coronal plane (Fig. 1) obtained on a 3 Tesla MR (Magnetom Skyra, Siemens, Germany) device. Our imaging parameters were 256 × 256 matrix and 22 cm field of view (FOV), repetition time (TR): 3500 ms, echo time (TE): 75 ms, excitation number (NEX): 2, and a slice thickness of 4 mm. OBV and OSD measurements were made by two experienced radiologists who had no knowledge of the cases.

Volumetric measurement of OBV was made using three-dimensional Slicer software (3D Slicer software ver. 4.2.2-1, <http://www.slicer.org>). The Slicer volumetric measurement programme is a free open source software package developed by Harvard University and approved for medical research. After dividing the olfactory bulb into sections with appropriate threshold values in the coronal image, separate MR numbers were assigned to each image with the Slicer software. Region of interest was adjusted to not exceed the anatomical contours of the bulb. After each slice containing the relevant OB sections was revealed, a 3D graphical model of the OB was creat-

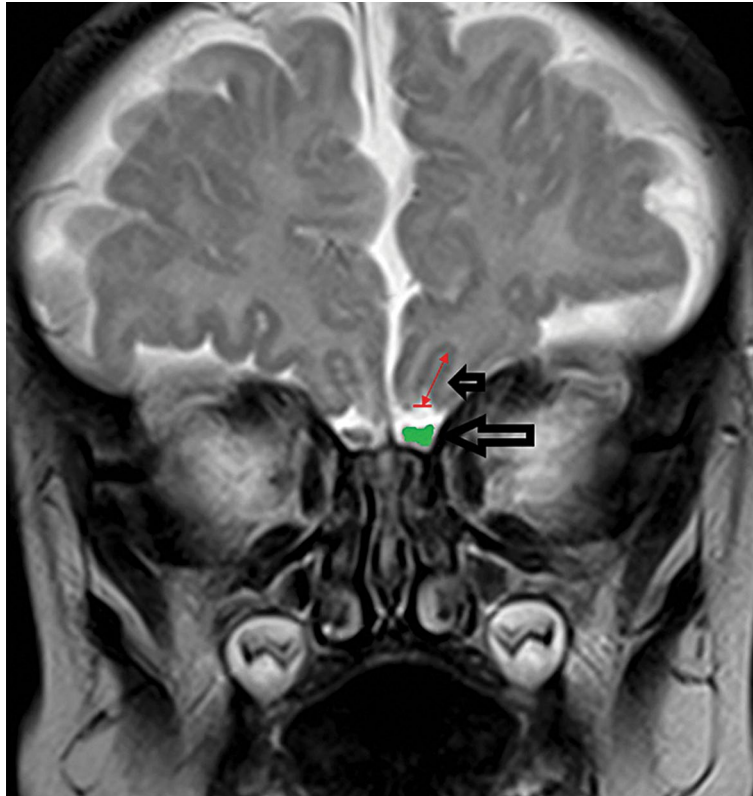


**Figure 1.** The coronal T2-weighted image shows the olfactory bulb volume measurement and the olfactory sulcus depth measurement. A measurement example of olfactory sulcus depth (small hollow arrow) and a measurement example of olfactory bulb surface area (large hollow arrow).

ed and volume calculation was made. Intra-observer variability was set at less than 5%.

#### Ethics Committee approval and consent to participate

Ethics Committee approval was given by Muğla Sıtkı Koçman University Human Research Ethics Committee. Ethics Committee Number: 200236.

Approval was obtained from the parent or legal guardian of each case participating in the study.

#### Statistical analysis

IBM SPSS version 20.0 software (IBM Corp, Armonk, NY, USA) was used for statistical evaluation and normal distribution was checked using Kolmogorov-Smirnov test. Data are presented as mean  $\pm$  standard deviation. Statistical comparisons of the right and left OBV values and the depth of the right and left olfactory sulcus were made using the paired t test. Independent-sample t test was used to evaluate the statistical differences between groups formed by considering gender, while one-way ANOVA test was

used to evaluate the statistical differences between groups formed according to age. Multiple comparisons were made with the Tukey test and a p value of 0.05 was considered statistically significant.

## RESULTS

A total of 190 patients (95 males, 95 females) were included in the study. The mean age was  $9.9 \pm 7.5$  months for the infantile period,  $4.5 \pm 1.3$  years for early childhood,  $9.3 \pm 1.7$  years for childhood and  $15.2 \pm 1.7$  years for adolescence. The OBV was  $42.03 \pm 5.96$  (range 29.2–57.6)  $\text{mm}^3$  on the right and  $42.33 \pm 6.06$  (range 28.8–62.4)  $\text{mm}^3$  on the left side. There was no statistical difference between right and left side OBV ( $p > 0.167$ ). Mean, right and left OBV was found to be slightly larger in male children than female children ( $p = 0.015$ ,  $p = 0.033$  and  $p = 0.010$ , respectively) (Table 1). OSD values were  $8.34 \pm 0.92$  mm on the right and  $8.32 \pm 0.89$  mm on the left. There was no statistical difference between right and left in terms of OSD ( $p > 0.481$ ). There was no statistical difference between the genders

**Table 1.** The distribution of age, mean, left and right olfactory bulb volume (OBV) and olfactory sulcus depth (OSD) according to sex

	Group A (n = 95)	Group B (n = 95)	P
OBV [mm <sup>3</sup> ]:			
Mean	41.15 ± 5.32	43.20 ± 6.15	0.015
Right	41.11 ± 5.67	42.95 ± 6.14	0.033
Left	41.20 ± 5.35	43.45 ± 6.52	0.010
OSD [mm]:			
Mean	8.37 ± 0.92	8.29 ± 0.87	0.559
Right	8.38 ± 0.93	8.30 ± 0.92	0.536
Left	8.36 ± 0.93	8.30 ± 0.85	0.598

for mean, right and left OSD ( $p = 0.559$ ,  $p = 0.536$  and  $p = 0.598$ , respectively) (Table 1).

The distributions of mean OBV and OSD according to age groups are given in Table 2. Among the age groups, the values of the 3<sup>rd</sup> and 4<sup>th</sup> groups in terms of mean, right and left OBV were higher than the other two groups ( $p < 0.001$ ) (Table 2). In terms of OSD, mean, right and left values were higher in group 2, 3 and 4 than group 1 ( $p < 0.001$ ) (Table 2).

## DISCUSSION

There are several important results of our study. First, in the paediatric age group, the OBV increases as the age increases, but the most significant volume increase is in the 7–12 age group. Second, OSD is lower in the infantile patient group (1–24 months) compared to other paediatric age groups. After 3 years of age, there is no statistically significant change in the depth of the olfactory sulcus until the

age of 18. Third, there was no statistically significant difference in OSD measurements based on gender in the normal healthy paediatric population, but OBV was slightly larger in male children than in female children.

Magnetic resonance imaging method has been used successfully in adults to analyse the normal anatomy of OBs [4, 6, 12, 20, 23]. In the study conducted by Schneider and Floemer [18], cranial MRI examinations of 121 paediatric cases aged between 1 and 19.6 years were retrospectively re-evaluated in order to detect the maturation of the OB. Three anatomical patterns have been described defining different anatomical shapes for the olfactory bulb. Whatever the anatomical shape of the OBs, they found that the gradual rearrangement of the peripheral neuronal layers and central structures of the bulb resulted in an adult-like appearance in all children at the end of the second year at the latest, in parallel with the maturation changes of the cerebral white matter [18]. Therefore, in our study, we grouped paediatric individuals of the first 2 years of age separately. However, we found that OBV increased minimally in paediatric individuals aged 3–6 years compared to the first 2-year-old case group. We found the OSD to be lower in the first 2-year-old paediatric group compared to the other three paediatric groups. This finding supports this study by Schneider and Floemer [18] on olfactory maturation.

In a study conducted by Croy et al. [3] on 27 depressed female individuals, 15 of whom were maltreated during childhood, the OBV measured in individuals who were maltreated during childhood was found to be lower than those who were not exposed to child-

**Table 2.** The distribution of age, mean, left and right olfactory bulb volume (OBV) and olfactory sulcus depth (OSD) according to age group.

	0–2 years (n = 40)	3–6 years (n = 50)	7–12 years (n = 50)	13–18 years (n = 50)
Age [years]	9.9 ± 7.5	4.5 ± 1.3	9.3 ± 1.7	15.2 ± 1.7
OBV [mm <sup>3</sup> ]:				
Mean	37.75 ± 4.27	39.26 ± 5.95	44.85 ± 5.01 <sup>ab</sup>	44.96 ± 5.72 <sup>ab</sup>
Right	37.70 ± 4.60	39.08 ± 5.98	44.72 ± 4.80 <sup>ab</sup>	44.88 ± 6.07 <sup>ab</sup>
Left	37.80 ± 4.34	39.44 ± 6.31	44.98 ± 5.55 <sup>ab</sup>	45.03 ± 5.81 <sup>ab</sup>
OSD [mm]:				
Mean	7.54 ± 0.93	8.56 ± 0.78 <sup>a</sup>	8.30 ± 1.39 <sup>a</sup>	8.60 ± 0.78 <sup>a</sup>
Right	7.48 ± 0.96	8.58 ± 0.78 <sup>a</sup>	8.49 ± 0.71 <sup>a</sup>	8.64 ± 0.82 <sup>a</sup>
Left	7.60 ± 0.95	8.53 ± 0.81 <sup>a</sup>	8.45 ± 0.74 <sup>a</sup>	8.56 ± 0.77 <sup>a</sup>

Data are n of participants, mean ± standard deviation; <sup>a</sup> $p < 0.001$  compared with 0–2 years group (one-way ANOVA-Tukey test); <sup>b</sup> $p < 0.001$  compared with 3–6 years group (one-way ANOVA-Tukey test)

**Table 3.** Comparison of olfactory bulb volume (OBV) and olfactory sulcus depth (OSD) studies in healthy paediatric cases

First author	Year	Country	Measurement method	N	Age	Magnetic field	OBV [mm <sup>3</sup> ]	OSD [mm]
Hummel T.	2011	France	AMIRA 3-D visualisation and modelling system (Visage Imaging, Carlsbad, USA)	87	1–17 years	1.5 Tesla	M: 21–98 R: 68; L: 71  F: 21–121 R: 66; L: 65	No measurement
Sahin S.	2020	Turkey	Semi-automatically method, Philips workstation	90	3–17 years	1.5 Tesla	M: 32.7–98.6 R: 64; L: 65.3  F: 31.8–99.6 R: 67.1; L: 72	R: 8.85 (min 6, max 13.6)  L: 8.8 (min 1.8, max 16)
Our study	2020	Turkey	3D Slicer software (3D Slicer software ver. 4.2.2-1, USA)	190	1 month–17 years	3 Tesla	M: 30.1–62.4 R: 41.11; L: 41.20  F: 29.2–55.2 R: 42.95; L: 43.45	R: 8.34 ± 0.92 L: 8.32 ± 0.89

F — females; M — males; L — left; R — right

hood maltreatment [3]. In the first hypothesis they put forward for this result they suggests that major stress exposure in childhood affects neurogenesis in human OB, as previously demonstrated in animal studies [7]. For these reasons, we think that, as in our study, it is important to know the normal OBV and OSD measurement intervals in paediatric individuals to determine the connection between the abnormalities that may occur in adulthood and the paediatric period.

In a study conducted by Hummel et al. [9] on 87 paediatric individuals aged between 1 and 17 years without olfactory dysfunction (mean:  $8 \pm 5.5$  years, 46 boys and 41 girls), it was found that OBV and olfactory function increased with age. In this study, OBVs of male children (left:  $71 \text{ mm}^3$ , right:  $68 \text{ mm}^3$ ) were found to be larger than female children (left:  $65 \text{ mm}^3$ , right:  $66 \text{ mm}^3$ ). It was also found that for both boys and girls, the right and left OBVs gradually increased from the age of 1 year. According to the study, the mean OBV for 1 year old boys is: left:  $65$ , right:  $64 \text{ mm}^3$ ; mean OBV for girls: left:  $61$ , right:  $62 \text{ mm}^3$ . When the mean OBV was evaluated in 17-year-old paediatric individuals, in boys: left:  $79 \text{ mm}^3$ , right:  $77 \text{ mm}^3$ ; in girls: left:  $73 \text{ mm}^3$ , right:  $71 \text{ mm}^3$ . As a result of our study, OBV was found to be slightly higher in boys compared to girls, similar to the study of Hummel et al. [9]. However, although OBV increased gradually with age, it was found that the statistically more significant increase in OBV was between the ages of 7–12, regardless of gender.

In studies conducted in patients with congenital anosmia and psychiatric disorders such as schizophrenia or psychosis, OSD was found to be lower than normal [9, 14, 21, 22]. Although standard values for

the depth of the olfactory sulcus have been published mostly for adults, few studies have published standard values for the paediatric age group. In the study conducted by Smitka and Hummel [19] on 40 normosmic children aged between 6 and 18 years, it was found that OSD was 8 mm and above in all children over 9 years old. It was stated that the recommended cut-off value of 8 mm, which indicates anosmia, can be used safely for children aged 9 years and older, and different limit values should be considered for children aged 8 years and younger. In the study conducted by Huart et al. [8] in 106 individuals (36 anosmic individuals and 70 healthy individuals) aged between 7 and 79 years, sulcus depth below 8 mm was found to be an important indicator for the development of anosmia [8].

The first study in the literature examining the age-related change of both OSD and OBV in healthy paediatric individuals was conducted by Şahin et al. [16]. A total of 90 paediatric patients aged between 3 and 17 years were included in this study and a 1.5 Tesla MRI device was used [16]. Our study is fundamentally different from 3 aspects according to the study of Şahin et al. [16]. The first is that healthy paediatric individuals in the 1 month–2 years age group were included in the study and the study was conducted with 190 individuals, the second is the use of 3 Tesla MRI device and the third is that the OBV measurement method was different. Thus, the change in OBV and OSD in all paediatric age groups between 1 month and 17 years was examined. Studies including OSD and OBV measurements of healthy paediatric individuals in the literature are summarised comparatively in Table 3.

According to our research, our study is the first study to separately show the development and change of the olfactory sulcus depth for four separate periods after birth until the age of 18 in healthy paediatric individuals. It was found that OSD gradually increased with age in both healthy male and female individuals in the paediatric age group. The infantile group (0–24 months) had the lowest OSD and the mean OSD in this group was found to be less than 8 mm. For patients aged 3 years and older, mean OSD was over 8 mm for each age group. Another difference between our study and other studies is that the images were obtained with a 3 Tesla MR scanner. We think that we may have obtained more accurate results since 3 T MRI provide clearer and thinner-slice images with higher resolution.

#### Limitations of the study

Our study had some limitations. The first of these is that our study was retrospective and there was no evaluation of olfactory function. In addition, inter-observer variability was not taken into account in our study. Another limitation is that some of the individuals participating in the study were very young and the patient backgrounds were obtained from the hospital information system.

### CONCLUSIONS

In conclusion, there are still very few studies showing the development of OBV and OSD with age and time changes considering gender for normal healthy paediatric individuals. We think that more studies should be done on this subject, since these data show differences in both the paediatric age group and adults according to age and that OBV and OSD can be an indicator of the development of olfactory dysfunction. Therefore, within the paediatric age group, normal values should be calculated considering age and gender.

**Conflict of interest:** None declared

### REFERENCES

- Asal N, Bayar Muluk N, Inal M, et al. Olfactory bulb volume and olfactory sulcus depth in psychotic patients and patients with anxiety disorder/depression. *Eur Arch Otorhinolaryngol.* 2018; 275(12): 3017–3024, doi: [10.1007/s00405-018-5187-x](https://doi.org/10.1007/s00405-018-5187-x), indexed in Pubmed: [30382395](https://pubmed.ncbi.nlm.nih.gov/30382395/).
- Azoulay R, Fallet-Bianco C, Garel C, et al. MRI of the olfactory bulbs and sulci in human fetuses. *Pediatr Radiol.* 2006; 36(2): 97–107, doi: [10.1007/s00247-005-0030-0](https://doi.org/10.1007/s00247-005-0030-0), indexed in Pubmed: [16341529](https://pubmed.ncbi.nlm.nih.gov/16341529/).
- Croy I, Negoias S, Symmank A, et al. Reduced olfactory bulb volume in adults with a history of childhood maltreatment. *Chem Senses.* 2013; 38(8): 679–684, doi: [10.1093/chemse/bjt037](https://doi.org/10.1093/chemse/bjt037), indexed in Pubmed: [24051351](https://pubmed.ncbi.nlm.nih.gov/24051351/).
- Çullu N, Yeniçeri İÖ, Güney B, et al. Evaluation of olfactory bulb volume and olfactory sulcus depth by 3 T MR. *Surg Radiol Anat.* 2020; 42(9): 1113–1118, doi: [10.1007/s00276-020-02484-w](https://doi.org/10.1007/s00276-020-02484-w), indexed in Pubmed: [32377954](https://pubmed.ncbi.nlm.nih.gov/32377954/).
- Doğan A, Bayar Muluk N, Asal N, et al. Olfactory bulb volume and olfactory sulcus depth in patients with Beçet's disease. *J Laryngol Otol.* 2018; 132(12): 1088–1092, doi: [10.1017/S0022215118002141](https://doi.org/10.1017/S0022215118002141), indexed in Pubmed: [30558688](https://pubmed.ncbi.nlm.nih.gov/30558688/).
- Held P, Seitz J, Fründ R, et al. MRI detection of olfactory bulb and tract. *J Neuroradiol.* 2000; 27(2): 112–118.
- Hitoshi S, Maruta N, Higashi M, et al. Antidepressant drugs reverse the loss of adult neural stem cells following chronic stress. *J Neurosci Res.* 2007; 85(16): 3574–3585, doi: [10.1002/jnr.21455](https://doi.org/10.1002/jnr.21455), indexed in Pubmed: [17668856](https://pubmed.ncbi.nlm.nih.gov/17668856/).
- Huart C, Meusel T, Gerber J, et al. The depth of the olfactory sulcus is an indicator of congenital anosmia. *Am J Neuroradiol.* 2011; 32(10): 1911–1914.
- Hummel T, Damm M, Vent J, et al. Depth of olfactory sulcus and olfactory function. *Brain Res.* 2003; 975(1-2): 85–89, doi: [10.1016/s0006-8993\(03\)02589-7](https://doi.org/10.1016/s0006-8993(03)02589-7), indexed in Pubmed: [12763595](https://pubmed.ncbi.nlm.nih.gov/12763595/).
- Hummel T, Smitka M, Puschmann S, et al. Correlation between olfactory bulb volume and olfactory function in children and adolescents. *Exp Brain Res.* 2011; 214(2): 285–291, doi: [10.1007/s00221-011-2832-7](https://doi.org/10.1007/s00221-011-2832-7), indexed in Pubmed: [21842188](https://pubmed.ncbi.nlm.nih.gov/21842188/).
- Hummel T, Urbig A, Huart C, et al. Volume of olfactory bulb and depth of olfactory sulcus in 378 consecutive patients with olfactory loss. *J Neurol.* 2015; 262(4): 1046–1051, doi: [10.1007/s00415-015-7691-x](https://doi.org/10.1007/s00415-015-7691-x), indexed in Pubmed: [25712545](https://pubmed.ncbi.nlm.nih.gov/25712545/).
- Iida Y, Naito M, Asahina N, et al. Magnetic resonance imaging of the olfactory apparatus. *Arch Otolaryngol Head Neck Surg.* 1994; 120(8): 869–872, doi: [10.1001/archotol.1994.01880320069015](https://doi.org/10.1001/archotol.1994.01880320069015), indexed in Pubmed: [8049051](https://pubmed.ncbi.nlm.nih.gov/8049051/).
- Müller F, O'Rahilly R. Olfactory structures in staged human embryos. *Cells Tissues Organs.* 2004; 178(2): 93–116, doi: [10.1159/000081720](https://doi.org/10.1159/000081720), indexed in Pubmed: [15604533](https://pubmed.ncbi.nlm.nih.gov/15604533/).
- Nishikawa Y, Takahashi T, Takayanagi Y, et al. Orbitofrontal sulcogyral pattern and olfactory sulcus depth in the schizophrenia spectrum. *Eur Arch Psychiatry Clin Neurosci.* 2016; 266(1): 15–23, doi: [10.1007/s00406-015-0587-z](https://doi.org/10.1007/s00406-015-0587-z), indexed in Pubmed: [25757375](https://pubmed.ncbi.nlm.nih.gov/25757375/).
- O'Rahilly R, Müller F, Bossy J, et al. [Atlas of the stages of development of the nervous system in the intact human embryo]. *Arch Anat Histol Embryol.* 1982; 65: 57–76, indexed in Pubmed: [6764349](https://pubmed.ncbi.nlm.nih.gov/6764349/).
- Sahin S, Baykan AH, Altunisik E, et al. Quantitative analysis of healthy olfactory sulcus depth, olfactory tract length and olfactory bulb volume in the paediatric population: a magnetic resonance study. *Folia Morphol.* 2021; 80(1): 33–39, doi: [10.5603/FM.a2020.0125](https://doi.org/10.5603/FM.a2020.0125), indexed in Pubmed: [33084007](https://pubmed.ncbi.nlm.nih.gov/33084007/).
- Sarnat HB, Flores-Sarnat L. Olfactory development, part 2: neuroanatomic maturation and dysgeneses. *J Child Neurol.* 2017; 32(6): 579–593, doi: [10.1177/0883073816685192](https://doi.org/10.1177/0883073816685192), indexed in Pubmed: [28424008](https://pubmed.ncbi.nlm.nih.gov/28424008/).

18. Schneider JF, Floemer F. Maturation of the olfactory bulbs: MR imaging findings. *AJNR Am J Neuroradiol.* 2009; 30(6): 1149–1152, doi: [10.3174/ajnr.A1501](https://doi.org/10.3174/ajnr.A1501), indexed in Pubmed: [19279285](https://pubmed.ncbi.nlm.nih.gov/19279285/).
19. Smitka M, Hummel T. The depth of the olfactory sulcus in normosmic children and adolescents. *Neuropediatrics.* 2015; 46(S 01): WS07-1, doi: [10.1055/s-0035-1550753](https://doi.org/10.1055/s-0035-1550753).
20. Suzuki M, Takashima T, Kadoya M, et al. MR imaging of olfactory bulbs and tracts. *AJNR Am J Neuroradiol.* 1989; 10(5): 955–957, indexed in Pubmed: [2505540](https://pubmed.ncbi.nlm.nih.gov/2505540/).
21. Takahashi T, Nakamura Y, Nakamura K, et al. Altered depth of the olfactory sulcus in first-episode schizophrenia. *Prog Neuropsychopharmacol Biol Psychiatry.* 2013; 40: 167–172, doi: [10.1016/j.pnpbp.2012.10.001](https://doi.org/10.1016/j.pnpbp.2012.10.001), indexed in Pubmed: [23063493](https://pubmed.ncbi.nlm.nih.gov/23063493/).
22. Turetsky BI, Moberg PJ, Quarmley M, et al. Structural anomalies of the peripheral olfactory system in psychosis high-risk subjects. *Schizophr Res.* 2018; 195: 197–205, doi: [10.1016/j.schres.2017.09.015](https://doi.org/10.1016/j.schres.2017.09.015), indexed in Pubmed: [28974405](https://pubmed.ncbi.nlm.nih.gov/28974405/).
23. Yousem DM, Geckle RJ, Bilker WB, et al. Olfactory bulb and tract and temporal lobe volumes. Normative data across decades. *Ann N Y Acad Sci.* 1998; 855: 546–555, doi: [10.1111/j.1749-6632.1998.tb10624.x](https://doi.org/10.1111/j.1749-6632.1998.tb10624.x), indexed in Pubmed: [9929650](https://pubmed.ncbi.nlm.nih.gov/9929650/).

# The evaluation of cerebral venous normal anatomy and variations by phase-contrast cranial magnetic resonance venography

E. Doğan<sup>1</sup>, M. Apaydın<sup>2</sup>

<sup>1</sup>Department of Radiology, Faculty of Medicine, Muğla Sıtkı Koçman University, Muğla, Turkey

<sup>2</sup>Department of Radiology, İzmir Atatürk Education and Research Hospital, İzmir, Turkey

[Received: 5 January 2020; Accepted: 5 February 2021; Early publication date: 1 March 2021]

**Background:** The aim of our study was to determine the ability of the phase-contrast-cranial magnetic resonance venography (PC-CMRV) technique to detect cranial anatomy, variations, thrombosis, to reveal the deficits of the technique and to discuss the reasons for these deficits on a physics basis.

**Materials and methods:** Phase-contrast's detection rates of anatomic variations and physiological filling defects (FDs) were evaluated in 136 patients and compared with the time-of-flight technique magnetic resonance imaging (MRI) and cadaveric studies.

**Results:** The dominance correlation between the three evaluated sinuses (transverse sinus [TS], sigmoid sinus, jugular vein) which originated from different embryological buds was statistically significant and the right vessel chain was dominant. PC is inadequate to show some vessels like inferior sagittal sinus (anatomically, this vessel is approximately present in 100% of the cases, but it was only visualised in 41.2% of the patients in PC-MRI). Visualisation of major veins was sufficient. PC-MRI created physiological FDs in 27.2% (72.3% middle, 10.3% inner, 17% outer part) of the patients. The FDs were concentrated in the middle part and not observed in the dominant sinus.

**Conclusions:** The defects of visualisation are present due to the PC's technique. It can be misdiagnosed as agenesis or thrombosis. PC creates a high incidence of physiologic FDs in TS. The results are not reliable, especially if FDs are in the middle part or non-dominant side. (Folia Morphol 2022; 81, 2: 314–323)

**Key words:** magnetic resonance, venography, dural sinuses, phase contrast, arachnoid granulations

## INTRODUCTION

Cranial magnetic resonance venography (CMRV) is the basic imaging method in the evaluation of venous sinuses, since it is a non-invasive and non-irradiating technique [10]. Time-of-flight (TOF) and phase-contrast

(PC) are the techniques used in CMRV [26]. CMRV is the most common method used in scientific research to evaluate venous variations [22]. Our study is one of the first studies performed with the PC technique using a 1.5 Tesla magnetic resonance imaging (MRI) machine.

---

Address for correspondence: Ass. Prof. E. Doğan, Muğla Sıtkı Koçman University Education and Research Hospital, Department of Radiology, 228 sok. Obam sitesi No:15 Kötekli/Menteşe, Muğla, Turkey, tel: +90 5066619794, fax: +90 2522123599, e-mail: dr\_e\_dogan@hotmail.com; emrahdogan@mu.edu.tr

This article is available in open access under Creative Common Attribution-Non-Commercial-No Derivatives 4.0 International (CC BY-NC-ND 4.0) license, allowing to download articles and share them with others as long as they credit the authors and the publisher, but without permission to change them in any way or use them commercially.

According to literature, right chain vascular structures are remarkably dominant. Why is that? Transverse sinus (TS) and sigmoid sinus (SS) originate from the posterior plexus, jugular vein (JV) originates from the anterior cardinal vein (ACV). The correlation between these embryological structures can be determined by comparison of dominance [17]. Can the embryological mechanisms be explained by evaluating the correlation of vascular structures originating from different embryological buds? Is the embryological mechanism independent or interdependent?

Venography is a technique mostly used to detect thrombosis. Filling defects (FDs) are the main diagnostic finding in CMRV, but it can also be seen as physiological except for thrombosis [4, 22]. The percentage of these defects had been evaluated in previous studies [1, 2, 4]; however, the points where the defect is located on the TS are not specified. In which segments are FDs common? Which physical and physiological mechanisms can be associated with these FDs?

The aim of our study was to determine the ability of the PC-CMRV technique to detect cranial anatomy, variations, thrombosis, to reveal the deficits of the technique and to discuss the reasons for these deficits on a physics basis.

## MATERIALS AND METHODS

### Patients

Ethics committee approval was obtained for this study with document number 0945/7. Two hundred fourteen patients who had CMRV were chosen for the preliminary exam. Patients with a history of operation, thrombosis, ischaemic change, tumour, congenital anomalies, small vessel disease and demyelinating diseases were excluded from the study. All subjects were followed up for two years to exclude thrombosis.

Finally, 136 patients were included in the study: 50 males and 86 females; mean age ( $\pm$  standard deviation [SD]),  $48.7 \pm 16.3$  years, range: 18–93 years. Males' mean age ( $\pm$  SD) was  $47.6 \pm 12.9$  years; range between 19 and 86 years. Females' mean age ( $\pm$  SD) was  $50.6 \pm 13.7$  years; range between 18 and 93 years. All our patients were in the adult age group. CMRV and conventional MRI's (CMRI) of all the patients were evaluated by one experienced radiologist and one neuroradiologist and evaluated together again in case of a discrepancy.

### Imaging examinations

A 1.5-tesla PHILIPS (The New Intera Nova, Philips medical system, Best, Netherlands) device was used for scanning. CMRV examinations were performed using the three dimensional (3D) PC technique without applying any saturation band. Maximum intensity projections (MIPs) were created at the MR operating console for the 3D CMRV dataset. The standard parameters that were used were as follows: field of view = matrix  $230/70 = 256 \times 256$ , slice 160, thickness = 1, Col = 1, TR/TE: 16/6.8. The images were obtained with axial sections in 3D/FFE sequence. The last images were created with a velocity encoding (VENC) method by applying bipolar gradients sequentially along the cardinal directions (x-, y-, and z-).

### Image analysis

The images obtained with the picture archiving and communication system (PACS) were scanned in different projections for various veins in each patient. All veins were evaluated in raw images and 3D MIP images obtained by PC technique.

Parameters: dominances of TS, SS and JV were determined according to gender. Measurements were taken 1 cm from the torcular herophili for the TS, 1 cm from the TS junction for the SS, 1 cm from the SS junction for the JV [6, 20]. If there was a difference greater than 1/5 between the sinuses, the larger side was evaluated as dominant.

In addition, superior sagittal sinus (SSS), inferior sagittal sinus (ISS), straight sinus (StS), internal cerebral vein (ICV), Galen vein (GV), basal vein of Rosenthal (BVOR), occipital vein (OV), Labbe vein (LV) and Trolard vein (TrIV) were evaluated bilaterally. All vein's PC visualisation rates were compared with anatomical cadaveric studies and we found the real visualisation. The bilateral TS was divided into three equal parts (I: Inner part, II: Middle part, III: Outer part) and physiological FDs' percentages were calculated.

### Statistical analysis

The obtained data were enrolled and tabulated using the Office Excel (Microsoft) data recording system. The data were analysed using statistical software (SPSS, IBM). All continuous variables were expressed as counts and averages were calculated (mean  $\pm$  SD). Percentages were calculated for qualitative values. Pearson and chi-square analysis were used for com-

**Table 1.** Transverse sinus (TS), sigmoid sinus (SS), jugular vein (JV) dominances according to gender and side

SINUS	R-dominant		L-dominant		C-dominant	
	Number	Percentage	Number	Percentage	Number	Percentage
<b>TS</b>						
Female	30	34.88%	25	29.06%	31	36.04%
Male	22	44.00%	12	24.00%	16	32.00%
Total	52	38.23%	37	27.95%	47	32.35%
<b>SS</b>						
Female	31	36.04%	25	29.07%	30	34.88%
Male	23	46.00%	13	26.00%	14	28.00%
Total	54	39.70%	38	27.95%	44	32.35%
<b>JV</b>						
Female	27	31.40%	20	23.25%	39	45.34%
Male	19	38.00%	10	20.00%	21	42.00%
Total	46	33.82%	30	22.06%	60	44.12%

parisons. The p value < 0.05 was accepted as statistically significant. Kendal Tau B test was performed in the non-parametric correlation analysis.

## RESULTS

Dominances of TS, SS and JV were evaluated:

- for TS: Right (R)-dominance was found in 52 (38.23%), left (L)-dominance in 37 (27.95%), co-dominance in 47 (32.35%) of the patients;
- for SS: R-dominance was found in 54 (39.70%), L-dominance in 38 (27.95%), co-dominance in 44 (32.35%) of the patients;
- for JV: R-dominance was found in 46 (33.82%), L-dominance in 30 (22.06%), co-dominance in 60 (44.12%) of the patients.

According to gender:

- for males; TS: R-dominance was found in 20 (44.00%), L-dominance in 12 (24.00%), co-dominance in 16 (32.00%) of the patients; SS: R-dominance was found in 23 (46.00%), L-dominance in 13 (26.00%), co-dominance in 14 (28.00%) of the patients; JV: R-dominance was found in 19 (38.00%), L-dominance in 10 (20.00%), co-dominance in 21 (42.00%) of the patients;
- for females; TS: R-dominance was found in 30 (34.88%), L-dominance in 25 (29.06%), co-dominance in 31 (36.04%); SS: R-dominance was found in 31 (36.04%), L-dominance in 25 (29.07%), co-dominance in 30 (34.88%) of the patients; JV: R-dominance was found in 27 (31.40%), L-dominance in 20 (23.25%), co-dominance in 39 (45.34%) of patients.

The TS, SS and JV's dominances' prevalence and frequency according to gender group are demonstrated in Table 1.

There was no statistically significant difference according to gender (TS:  $p = 0.567$ ; SS:  $p = 0.507$ ; JV:  $p = 0.726$ ).

Kendal Tau B correlation analysis was applied to evaluate the relationship between TS, SS and JV dominance. The dominance relationship between the three evaluated sinuses on the right and left separately was statistically significant. The strongest correlation ( $r_b: 0.945$ ) was found between left TS and left SS. The lowest level of relationship ( $r_b: 0.791$ ) was found between left TS and left JV. Tau B correlation between sinuses is demonstrated in Table 2.

All patients had SSS. However, SSS was completely visualised in 132 (97.06%) patients. In 4 (2.94%) patients, the anterior part of the SSS was not seen. ISS were visualised in 56 (41.17%) of the patients (32 [37.21%] females, 24 [48.00%] males). StV, ICV and GV were visualised in all of the patients. BVOR was seen in 130 (95.59%) and OC in 11 (8.09%) of the patients. The percentages of detection of venous structures in the study are demonstrated in Table 3.

The existence of TrIV and LV were coded (as '+' present, '-' absent).

For TrIV: R+L+ was found in 28 (20.59%), R+L- in 30 (22.06%), R-L+ in 23 (16.91%), R-L- in 55 (40.44%) of the patients.

According to gender:

**Table 2.** Dominance correlations of the transverse sinus (TS), sigmoid sinus (SS), jugular vein (JV) sinuses with Kendal Tau B test

Dominancy	Compared sinuses	Tau-B correlation coefficient	Probability value
Right dominant	ST and SS	$\tau_b: 0.877$	p: 0.000
	ST and VJ	$\tau_b: 0.877$	p: 0.000
Left dominant	ST and SS	$\tau_b: 0.945$	p: 0.000
	ST and VJ	$\tau_b: 0.791$	p: 0.000
Co-dominant	ST and SS	$\tau_b: 0.836$	p: 0.000
	ST and VJ	$\tau_b: 0.836$	p: 0.000

**Table 3.** Phase contrast visualisation ratio in cranial venous vessels

Anatomic localisation	Present		Absent	
	Number	Percentage	Number	Percentage
SSS:	136	100%	0	0%
Complete	132	97.06%		
Incomplete	4	2.94%		
ISS:	56	41.17%	80	58.83%
Female	32	37.21%	54	62.79%
Male	24	48.00%	26	52.00%
SV	136	100%	0	0
ICV	136	100%	0	0
GV	136	100%	0	0
BVOR	130	95.59%	6	4.41%
OV	11	8.09%	125	91.91%

SSS — superior sagittal sinus; ISS — inferior sagittal sinus; SV — straight sinus vein; ICV — internal cerebral vein; GV — Galen vein; BVOR — basal vein of Rosenthal; OV — occipital vein

— for females, R+L+ was found in 17 (19.77%), R+L- in 19 (22.09%), R-L+ in 13 (15.12%), R-L- in 37 (43.02%) of the patients;

— for males, R+L+ was found in 11 (22.00%), R+L- in 11 (22.00%), R-L+ in 10 (20.00%), R-L- in 18 (36.00%) of the patients.

For LV: R+L+ was found in 73 (53.67%), R+L- in 27 (19.85%), R-L+ in 21 (15.44%), R-L- in 15 (11.03%) of the patients.

According to gender:

— for females, R+L+ was found in 49 (56.98%), R+L- in 17 (19.77%), R-L+ in 10 (11.63%), R-L- in 10 (11.63%) of the patients;

— for males, R+L+ was found in 24 (48.00%), R+L- in 10 (20.00%), R-L+ in 11 (22.00%), R-L- in 5 (10.00%) of the patients.

There was no statistical difference according to gender ( $p = 0.153$  for TrIV and  $p = 0.060$  for LV). Bilaterally, TrIV and LV visualisation rates according to the gender are demonstrated in Table 4.

Finally, physiological FDs in the TS were evaluated. They were present in 37 of 136 patients (27.2%). Ten of these patients had FDs in more than one segment. In total 47 FDs were determined. Thirty-four of them were in the middle segments.

Two (1.48%) patients had FDs in the right outer part: one (0.74%) partial and one (0.74%) complete. Both of them were in the non-dominant sinuses. Fifteen (11.03%) FDs were in the middle part of the right TS: 13 (9.55%) were partial and 2 (1.48%) complete. Thirteen were in the non-dominant sinuses, whereas two in the co-dominant sinuses. Two (1.48%) patients had FDs in the right inner part: one (0.74%) partial and one (0.74%) complete. Both of them were in the non-dominant sinuses. Three (2.21%) patients had FDs in the left inner part: two (1.48%) partial and one (0.74%) complete. Three of them were in non-dominant sinuses. Nineteen (13.97%) were in the middle part of the left TS: 16 (11.76%) partial and three (2.21%) complete. Sixteen were in the non-dominant

**Table 4.** Phase contrast visualisation ratio of Trolard and Labbe veins

Veins	R+L+		R+L-		R-L+		R-L-	
	Number	Percentage	Number	Percentage	Number	Percentage	Number	Percentage
<b>Trolard</b>								
Female	17	19.77%	19	22.09%	13	15.12%	37	43.02%
Male	11	22.00%	11	22.00%	10	20.00%	18	36.00%
Total	28	20.59%	30	22.06%	23	16.91%	55	40.44%
<b>Labbe</b>								
Female	49	56.98%	17	19.77%	10	11.63%	10	11.63%
Male	24	48.00%	10	20.00%	11	22.00%	5	10.00%
Total	73	53.67%	27	19.85%	21	15.44%	15	11.03%

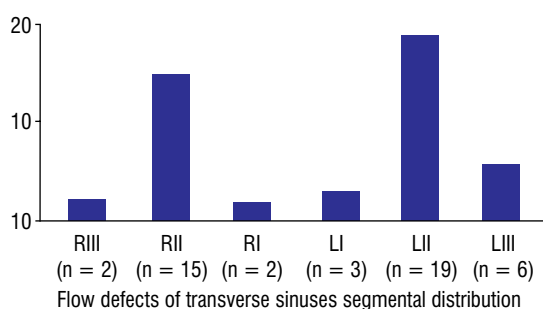


**Figure 1.** Segmental distribution of filling defects in transverse sinuses; R — right; L — left.

sinuses, whereas three in the co-dominant sinuses. Six (4.41%) were in the outer part of the left TS: one (0.74%) partial and five (3.67%) complete. Five were in the non-dominant sinuses, whereas one in the co-dominant sinuses. There was no FD in the dominant sinuses. The FDs according to segments were demonstrated in Figure 1.

**DISCUSSION**

The dominance of the cerebral venous vessels is crucial before the radical neck dissection, excision of tumours invading the TS, SS, JV or glomus jugular tumours that may require ligation of the internal JVs [8]. In this study, TS, SS, and JV's dominances were found as right dominance (44%), co-dominance (32%) and left dominance (24%) (Fig. 2). Although the percentages change, the order didn't change for both anatomic and radiological studies as well as this study [4, 5, 16]. Why right dominance is more visualized than left? We can find the answer to this question in the hypotheses belonging to the embryological development period. The superior vena cava originates from the right ACV together with the right



**Figure 2.** Venous sinuses are dominant in right (arrow: sigmoid sinus; arrowhead: transverse sinus; cut arrowhead: jugular vein).

JV. The caudal part of the left ACV largely regresses in the development process. If it does not regress, an anomaly called double vena cava occurs. ACVs merge with the posterior plexus which gives origin to TS and SS. Earlier joins coinciding with the regression process on the left, possibly lead to recessive left vessel chain. ACV regression on the left side influences not only JV but also TS and SS [17, 28]. This study revealed that if the TS was dominant, the SS and JV were also dominant on the same side [26]. It showed that ipsilateral embryological buds move together. This information supports the hypothesis above.

Since the use of oral contraceptives and pregnancy is associated with cranial venous thrombosis, the use of CMRV is more common in women [22]. In our study, the majority of our patients were females

(86 females, 50 males). There was no statistically significant gender-related difference between the TS, SS and JV dominances ( $p = 0.567$  for TS,  $p = 0.507$  for SS,  $p = 0.726$  for JV). The results of Goyal et al. [14] were similar.

Phase contrast's venous detection rates were evaluated and compared with anatomic studies. SSS was found at a rate of 100%. This finding is similar to the literature [1, 2, 4]. SSS develops from the marginal sinus. Partial fusion defect at the attachment point of the marginal sinus to the foramen cecum causes a partial growth defect anteriorly. This situation is called partial split sinus (PSS) [2]. In Kaplan and Browder's cadaveric series, PSS prevalence was found as 6% [14]. In our study, PSS variant of the SSS was observed at a rate of 2.94%. The signal loss may occur in the anterior section because the flow is going in the same direction as the artery, when an inferior saturation band is used to prevent arterial flow in TOF images [20]. In comparison with cadaveric studies, the percentage values are lower in our study. Its mean is that there is no signal loss due to PC technique in this area, unlike TOF.

In radiological studies, the presence of the ISS was noted between 33% and 43% [9, 18]. In our study, it was found at a rate of 41.17% (Fig. 3). In this case, it is necessary to look at the cadaveric studies. According to these ones, ISS was not detected in only 1% of the cases. To sum up, normally ISS is present but devices' visualisation and technique aren't adequate to show this vessel [13]. We looked at a study performed with more primitive device (0.35-tesla low-resolution) conducted by Sharma to explain more clearly the effect of device quality on venous visualisation. Visualisation rates with the low-tesla device of ISS, BVOR, ICV are respectively 11%, 34%, 60%.

In this study, many vascular structures that we visualised could not be sufficiently imaged. We can say that the lower the quality of the device, the poorer the visualisation [23]. Visualisation of minor venous vessel with 3T, 5T and 7T devices probably will be higher than our study. It is open to further research.

In our study, BVOR was detected at a rate of 95.58%. It was not observed unilaterally in five and bilaterally in one of the patients. In Ayanzen's TOF research, BVOR was detected in 91% of the patients. Our data are close to these findings [4]. We didn't find a cadaveric study to compare the percentage of basal vein [13]. StS, ICV and GV were detected in all of the patients. Results of other studies were similar to

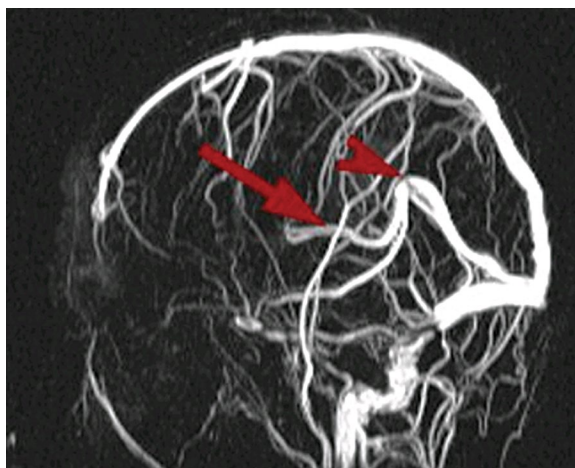


**Figure 3.** Internal cerebral veins (arrow) and Galen vein (arrow-head) in maximum intensity projections images.

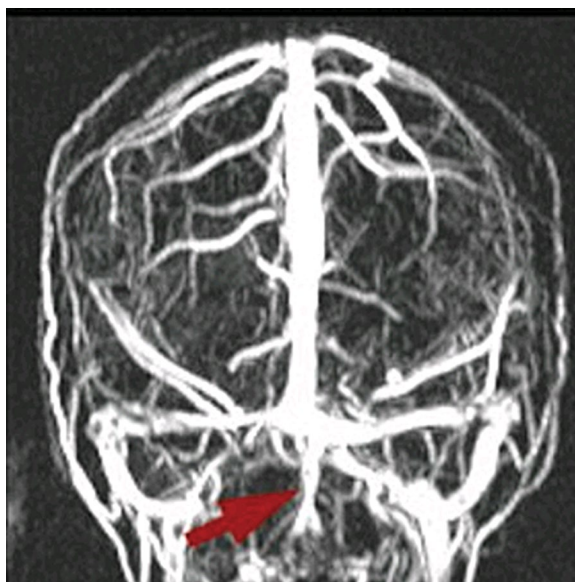


**Figure 4.** Occipital veins in posterior view of maximum intensity projections images (arrow).

ours [4, 23]. When FDs are found in 100% visualised veins, it should be accepted primarily as pathological.

It has been reported that the OV is more prominent in patients with thrombosis [24]. If the TS and SS are hypoplastic, the OV is used as an alternative outflow pathway [20]. In our study, the OV detection rate with PC was found as 8.09%. OV prevalence is between 4% and 35.5% according to data from reviewed anatomic and radiological TOF studies by Goyal et al. [11]. Our results were included in the aforementioned interval (Fig. 4).

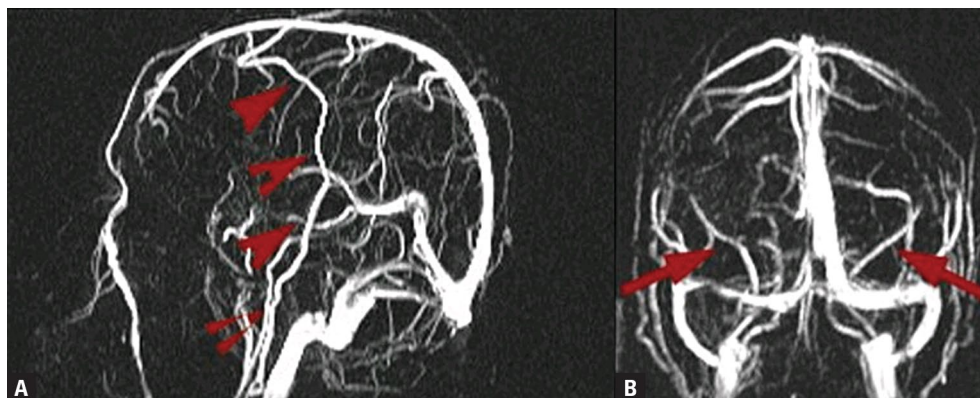


**Figure 5.** Trolard vein (arrowheads) and Labbe veins (arrows).

Trolard and Labbe veins form the main venous communicant anastomotic network. The LV provides the connection between the Sylvian veins and the posterior group, whereas the TrIV provides the connection between the SSS and the Sylvian veins. For this reason, it is also named as Trolard-Labbe circle. For example, when JV ligation is performed, if this network is not fully developed, venous infarct is probable. The LV should be preserved in temporal lobectomies and surgical interventions for epilepsy. Isolated thrombosis in LV, TrIV and related infarct cases have been reported in the literature [7, 22]. The angiographic studies elaborating information about these veins are present too [25]. Returning to our main subject, after we indicated why the LV and TrIV should be fully visualized and their clinical importance; our technique's detecting rate of LV and TrIV is close to other anatomical and radiological studies [1, 2, 4]. In addition, during our study, we noticed that there was no study according to gender regarding LV and TrIV, and we added it as a subtopic to the paper. There was no statistically significant difference ( $p = 0.153$  for TrIV and  $p = 0.060$  for LV) according to gender (Fig. 5A, B).

Conventional MRI evaluation can give useful findings about thrombosis, but it is not adequate in the final diagnosis. In MRI; the intensity of the thrombus changes according to the period. What is the weaknesses of CMRI and CMRV? Thrombus due to effect of deoxyhaemoglobin appears isointense at T1 and hypointense at T2 in the first 5 days. During this period, the hypointensity of the thrombus at T2 makes it impossible to be detected in CMRI. Thus, venous thrombus can only be detected by angiography [22]. Since 7% of deaths due to venous thrombosis hap-

pens in this period, it is important for the patient to be diagnosed early. Unfortunately, diagnosis is usually delayed for 7 days [20]. In these early days, where CMRI does not show any benefit and there is a risk of mortality, misleading sinus FDs are more important. Patients are mostly diagnosed within 5–15 days. This phase is also called the methaemoglobin phase. During this period, the thrombus T1 and T2 are hyperintense [22]. T1 hyperintensity is reflected as hyperintense in TOF technique also. Deleting of the flow void leads to interpreting the CMRV as normal. This situation is not seen in the PC technique. In this period PC is superior to TOF [20]. After 15 days, re-canalisation phase (chronic phase) starts [22]. In the chronic phase, pathways form within the thrombus. There is also dural enhancement accompanying capillary formation. Thus, it leads to a false negative result in contrast-enhanced MRI angiographic evaluation [20]. In this period, it cannot be mentioned that contrast enhanced MR angiography, which is accepted to be more advantageous than non-contrast CMRV, is superior to TOF and PC. It will be useful to evaluate CMRV FDs by comparing them with CMRI. Each technique has its pros and cons according to the period. It will be useful to evaluate CMRV images together with CMRI to prevent FDs from causing false diagnosis. In the early period, contrast enhanced MRI angiography, digital subtraction angiography in selected cases can be used for diagnosis [21].

Time-of-flight technique is used overwhelmingly in the CMRV examinations. The reason why PC research is rarely used is the long time according to TOF scanning [26]. Before mentioning the physical mechanisms of FDs, let's briefly talk about the general points of the techniques. Phase shift is undesirable in

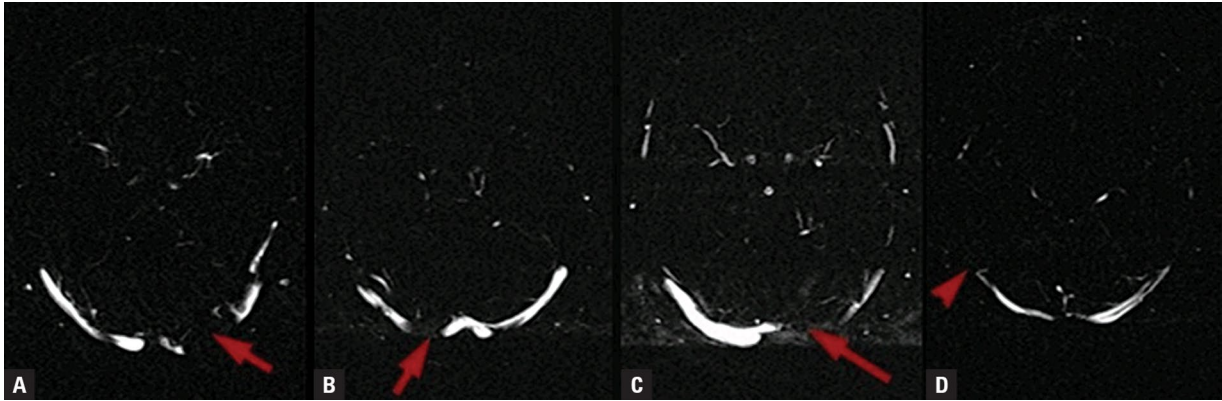


**Figure 6.** Physiological filling defects of transverse sinus; **A.** Filling defect of left inner and middle segments (arrow); **B.** Filling defects of right inner segment (arrow); **C.** Filling defect of left inner and middle segments (arrow); **D.** Filling defect of right outer segment (arrowhead).

TOF; therefore, “phase compensation technique” is used to prevent this. Phase shift that we want to prevent in TOF constitutes the basic of imaging in PC. In this technique, images are taken in pairs (phase shift) while operating in (+) and (–) gradient directions. Fixed textures are removed from the image with “image subtraction”; thus, only vascular structures are made visible. The technique is not sensitive to saturation due to flow; consequently, vascular structures with slow blood flow are better visualised in PC than in TOF. In addition, functional information such as flow direction and speed can be obtained with this technique [15]. PC’s background suppression feature and anatomic detailing are superior to TOF’s ones [26, 29].

Phase contrast has many disadvantages. The duration is long in PC and the eddy current effect is evident. It is sensitive to turbulence, spin saturation and intervoxel dephasing. It is also affected by intrinsic factors of the nucleus. Gradient imperfection secondary to inappropriate setting is creating aliasing artefacts in the flow direction as well. Gradient performance is directly related to device quality. There are many biomedical engineering articles in the literature about PC gradient settings. It is necessary to predict the appropriate gradient phase in advance [26].

Apart from this, there are some factors that cause FDs independent from the technique. This group consists of arachnoid granules (AG) and fibrotic bands located in the sinuses [20]. SSS and TSs are the most common places where AGs are seen. The majority of them are located between the middle and lateral parts in the TS (92%) [3, 12, 27]. Apart from the prominent eddy current effect due to PC technique, AG contributes to the formation of FD with mechanical effects

[3, 27]. Fibrotic bands can make mechanical barrier effect too, but it is rarely seen [20].

The FD were detected in the centre (R2–L2) at the rate of 72.3%, in the inner part (R3–L1) at the rate of 10.3%, in the outer part (R1–L3) at the rate of 17% in TS (Fig. 6). All the disadvantages resulting from intrinsic nuclear factors mentioned above are present in all of the segments. Gradient effects are more pronounced on sharp turns in the segments R3–L1 and R1–L3 (outer and inner parts of TS). Besides, when the eddy current effect and the over mentioned physical barrier effects (AG) are added, a complex set of causes creates artefacts in corners and central segments [19, 26, 29].

The movements of the spins in the presence of magnetic field gradients change the phase of the MR signal. These effects occur if blood flow goes a long way in the imaging volume, such as the TS. Phase shifts created by this movement cause artefacts in the phase coding direction and degrade image quality. This physical effect is more pronounced in PC than TOF [29]. The intrinsic nuclear factors contribute also to cause L2–R2 (middle parts of right and left TS) mid-point artefacts. Since the flow continues on a linear line, it will not be affected by the gradient effect’s refraction. The AGs is considered as the primary flow defect factor in the middle part. AGs are concentrated between the middle and lateral segments. When blood crosses a physiological barrier like AG, the eddy current effect is towards the part where the blood is going, not where it comes from. Considering the anatomical point where AGs are concentrated, this area exactly corresponds to the middle part of the sinus [29]. Due to the fact that the venous sinuses

are structures that don't have a muscularis mucosa that can expand according to the flow rate and they don't contain valves, two-way flow is possible and reverse flow is more pronounced in the middle section according to the hydro physics rules [22, 29]. Add to this, the venous sinuses that are connected to the right atrium by a relatively short vascular way without valves, are affected by diastolic contractions [28]. Another question is why physiological FDs are not usually detected in the SSS in MRI? Two theorems can be put forward for this. The first is the flow rate. The TS is the main portal, collecting all venous blood. It is connected to the superior vena cava via the SS and JV. It is clear that SSS and other minor veins have lower flow rate. The second reason is the presence of AGs. Despite AGs are abundant in the SSS, giant AGs are found in the TS; thus, eddy current effects of giant AGs can be more prominent [22, 29].

The FDs were in the non-dominant or co-dominant TSs. No FD was found in the dominant TS. Since the non-dominant sinus percentage was higher on the left side, the frequency of FDs was higher on the left side too (right 40.4%, left 59.6%). To conclude, a FD in the dominant sinus should be primarily interpreted as thrombosis in PC studies. Physio pathologically, in recessive sinuses, eddy currents are sharper. When the diameter of the sinus is narrow, the number of spins per unit area decreases. The space-occupying effects of AGs become more pronounced.

The FD rates with TOF technique that were found by Ayanzen et al. [4], Alper et al. [2] and Ahmet et al. [1] are 31%, 24% and 10.8%, respectively. In our study, the rate that was found is 27%. We can say that our FD rates are similar to other TOF and PC studies.

The study has some limitations. The tests have not been confirmed with anatomic specimen.

## CONCLUSIONS

This study is the first to assess the performance of PC technique by using normal anatomic and variations data. It is also the first time that dominances were correlated for explaining embryologic movements during the development of this region. Our results showed that the right vessel group was mostly dominant and found statistically significant correlations between the dominances of TS, SS and JV originating from different embryological buds. Left ACV regression also affects the posterior plexus during superior vena cava's embryological develop-

ment at right. Our article supports this embryological theorem. The visualization degree of major veins in PC were sufficient but it was inadequate for determining some vessels like ISS (anatomic presence was approximately 100%, visualisation was only 41.2%). In comparison with our device, low-tesla device's visualisation of vessels is poorer. The higher the quality of the device, the higher the visualisation rate. FDs observed in the veins normally visualised should be primarily considered as thrombosis. For the first time, TS's FDs was evaluated according to segments in PC and causes of FD's were discussed based on physiopathology. Indeed, PC creates a high proportion of physiological FDs in TS. Results should not be trusted, especially if FDs are present in the middle part or non-dominant side. In the middle segment, defects are primarily related to slow flow and AG while eddy current artefacts affected the corner parts. TOF and PC are similar to create FDs. Let's remind, the research has been done in normal patients and concerns the PC's ability to demonstrate normal anatomy and its variations. PC may be superior for showing thrombosis because of the above mentioned physical rules. This topic will be the subject of future research.

## Declarations

This is a retrospective study. Approval was obtained from İzmir Atatürk Training and Research Hospital with 0945/7 before the study. The data were obtained from the PACS system and no illegal or prohibited data was included in the study.

During the study, the programmes purchased by Muğla Sıtkı Koçman University and İzmir Atatürk Education and research hospital were used legally.

**Conflict of interest:** None declared

## REFERENCES

1. Ahmed MS, Imtiaz S, Shazlee MK, et al. Normal variations in cerebral venous anatomy and their potential pitfalls on 2D TOF MRV examination: Results from a private tertiary care hospital in Karachi. *J Pak Med Assoc.* 2018; 68(7): 1009–1013, indexed in Pubmed: [30317292](https://pubmed.ncbi.nlm.nih.gov/30317292/).
2. Alper F, Kantarci M, Dane S, et al. Importance of anatomical asymmetries of transverse sinuses: an MR venographic study. *Cerebrovasc Dis.* 2004; 18(3): 236–239, doi: [10.1159/000079960](https://doi.org/10.1159/000079960), indexed in Pubmed: [15273441](https://pubmed.ncbi.nlm.nih.gov/15273441/).
3. Apaydın F, Yalçınoğlu O, Yıldız A, et al. Arachnoid granulations in the transverse sinuses of a patient with ocular melanoma. *J Clin Neurosci.* 2003; 10(1): 132–134, doi: [10.1016/s0967-5868\(02\)00112-1](https://doi.org/10.1016/s0967-5868(02)00112-1).

4. Ayanzen RH, Bird RC, Keller PJ, et al. Cerebral MR Venography: Normal Anatomy and Potential Diagnostic Pitfalls. *Am J Neuroradiology*. 2000; 21(1): 74–78, indexed in Pubmed: [10669228](#).
5. Browning H. The confluence of dural venous sinuses. *Am J Anat*. 1953; 93(3): 307–329, doi: [10.1002/aja.1000930302](#), indexed in Pubmed: [13104335](#).
6. Canedo-Antelo M, Baleato-González S, Mosqueira AJ, et al. Radiologic Clues to Cerebral Venous Thrombosis. *Radiographics*. 2019; 39(6): 1611–1628, doi: [10.1148/rq.2019190015](#), indexed in Pubmed: [31589585](#).
7. Cullen S, Demengie F, Ozanne A, et al. The anastomotic venous circle of the base of the brain. *Interv Neuroradiol*. 2005; 11(4): 325–332, doi: [10.1177/159101990501100404](#), indexed in Pubmed: [20584444](#).
8. Durgun B, Ilglt ET, Cizmeli MO, et al. Evaluation by angiography of the lateral dominance of the drainage of the dural venous sinuses. *Surg Radiol Anat*. 1993; 15(2): 125–130, doi: [10.1007/BF01628311](#), indexed in Pubmed: [8367790](#).
9. Farb RI, Scott JN, Willinsky RA, et al. Intracranial venous system: gadolinium-enhanced three-dimensional MR venography with auto-triggered elliptic centric-ordered sequence-initial experience. *Radiology*. 2003; 226(1): 203–209, doi: [10.1148/radiol.2261020670](#), indexed in Pubmed: [12511691](#).
10. Ferro JM, Aguiar de Sousa D. Cerebral venous thrombosis: an update. *Curr Neurol Neurosci Rep*. 2019; 19(10): 74, doi: [10.1007/s11910-019-0988-x](#), indexed in Pubmed: [31440838](#).
11. Goyal G, Singh R, Bansal N, et al. Anatomical variations of cerebral MR venography: is gender matter? *Neuro-intervention*. 2016; 11(2): 92–98, doi: [10.5469/neuro-int.2016.11.2.92](#), indexed in Pubmed: [27621945](#).
12. Haroun AA, Mahafza WS, Al Najar MS. Arachnoid granulations in the cerebral dural sinuses as demonstrated by contrast-enhanced 3D magnetic resonance venography. *Surg Radiol Anat*. 2007; 29(4): 323–328, doi: [10.1007/s00276-007-0211-7](#), indexed in Pubmed: [17483869](#).
13. Ivashchuk RG, Tubbs S. *Anatomy, imaging and surgery of intracranial dural venous sinuses*, 1st ed. Elsevier Book, Seattle, Washington 2020: 29–35.
14. Kaplan HA, Browder J. Atresia of the rostral superior sagittal sinus: substitute parasagittal venous channels. *J Neurosurg*. 1973; 38(5): 602–607, doi: [10.3171/jns.1973.38.5.0602](#), indexed in Pubmed: [4711634](#).
15. Konez O. Manyetik rezonans görüntüleme [Turkish Book]. 1st Ed. Nobel tıp kitap evleri ltd, Istanbul 1995: 12–95.
16. Manara R, Mardari R, Ermani M, et al. Transverse dural sinuses: incidence of anatomical variants and flow artefacts with 2D time-of-flight MR venography at 1 Tesla. *Radiol Med*. 2010; 115(2): 326–338, doi: [10.1007/s11547-010-0480-9](#), indexed in Pubmed: [20058094](#).
17. Manjila S, Bazil T, Thomas M, et al. A review of extraaxial developmental venous anomalies of the brain involving dural venous flow or sinuses: persistent embryonic sinuses, sinus pericranii, venous varices or aneurysmal malformations, and enlarged emissary veins. *Neurosurg Focus*. 2018; 45(1): E9, doi: [10.3171/2018.5.FOCUS18107](#), indexed in Pubmed: [29961384](#).
18. Mattle HP, Wentz KU, Edelman RR, et al. Cerebral venography with MR. *Radiology*. 1991; 178(2): 453–458, doi: [10.1148/radiology.178.2.1987608](#), indexed in Pubmed: [1987608](#).
19. Ozsvath RR, Casey SO, Lustrin ES, et al. Cerebral venography: comparison of CT and MR projection venography. *Am J Roentgenol*. 1997; 169(6): 1699–1707, doi: [10.2214/ajr.169.6.9393193](#), indexed in Pubmed: [9393193](#).
20. Provenzale JM, Kranz PG. Dural sinus thrombosis: sources of error in image interpretation. *Am J Roentgenol*. 2011; 196(1): 23–31, doi: [10.2214/AJR.10.5323](#), indexed in Pubmed: [21178043](#).
21. Rizzo L, Crasto SG, Rudà R, et al. Cerebral venous thrombosis: role of CT, MRI and MRA in the emergency setting. *Radiol Med*. 2010; 115(2): 313–325, doi: [10.1007/s11547-010-0493-4](#), indexed in Pubmed: [20091136](#).
22. Sajjad ZM. and MRV in cerebral venous thrombosis. *J Pak Med Assoc*. 2006; 56(11): 523–526, indexed in Pubmed: [17183982](#).
23. Sharma UK, Sharma K. Intracranial MR venography using Low-Field magnet: normal anatomy and variations in nepalese population. *J Nepal Med Assoc*. 2012; 52(186): 61–65, doi: [10.31729/jnma.3](#).
24. Shin HS, Choi DS, Baek HJ, et al. The oblique occipital sinus: anatomical study using bone subtraction 3D CT venography. *Surg Radiol Anat*. 2017; 39(6): 619–628, doi: [10.1007/s00276-016-1767-x](#), indexed in Pubmed: [27796494](#).
25. Silva PS, Vilarinho A, Carvalho B, et al. Anatomical variations of the vein of Labbé: an angiographic study. *Surg Radiol Anat*. 2014; 36(8): 769–773, doi: [10.1007/s00276-014-1264-z](#), indexed in Pubmed: [24531417](#).
26. Surendrababu N, Livingstone RS. Variations in the cerebral venous anatomy and pitfalls in the diagnosis of cerebral venous sinus thrombosis: Low field MR experience. *Indian J Med Sci*. 2006; 60(4): 135–142, doi: [10.4103/0019-5359.24677](#).
27. Trimble CR, Harnsberger HR, Castillo M, et al. “Giant” arachnoid granulations just like CSF?: NOT!! *Am J Neuroradiol*. 2010; 31(9): 1724–1728, doi: [10.3174/ajnr.A2157](#), indexed in Pubmed: [20581064](#).
28. Tubbs RS, Goren O, McBain L. *Anatomy, Imaging and Surgery of the Intracranial Dural Venous Sinuses*, 1st Ed. Elsevier Book, Seattle, Washington 2020: 1–7.
29. Wang J, Wang J, Sun J, et al. Evaluation of the anatomy and variants of internal cerebral veins with phase-sensitive MR imaging. *Surg Radiol Anat*. 2010; 32(7): 669–674, doi: [10.1007/s00276-010-0669-6](#), indexed in Pubmed: [20422190](#).

# Extracranial guiding structures for navigation to specific topographical sectors of the equine neopallium: an anatomical investigation performing three-dimensional distance measurements in adult warm-blooded horses

F. Heun<sup>1</sup>, L. Böing<sup>1</sup>, J. Theunert<sup>2</sup>, H. Gasse<sup>1</sup>

<sup>1</sup>Institute of Anatomy, University of Veterinary Medicine Hannover, Hannover, Germany

<sup>2</sup>Faculty II — Mechanical Engineering and Bio Process Engineering, University of Applied Sciences and Arts, Hannover, Germany

[Received: 5 March 2021; Accepted: 29 April 2021; Early publication date: 17 May 2021]

**Background:** This basically anatomical study focuses on two items; firstly, the establishment of a system for the cartographic subdivision of the neopallium; secondly, the topographical correlation of extracranial landmarks and intracranial sites on the neopallium.

**Materials and methods:** The surface of the neopallium was subdivided into 15 sectors with reference to a newly introduced pattern of Primary Sulci. The topographical link between extracranial landmarks and certain intracranial sites (i.e. neopallium sectors) was elaborated by using a simple stereotactic device and a computer-assisted measurement device. Measurements were performed between points on the head's outer surface and on the isolated brain.

**Results and Conclusions:** The introduction of an anatomical three-dimensional coordinate system was an essential key issue for this investigation. This setting facilitated the measurements and calculations of the so-called indirect distances that were characterised by their alignment along the three orthogonal axes ( $x$ ,  $y$ ,  $z$ ) of the anatomical coordinate system. The inter-individual comparison (16 adult horses [*Equus caballus*]) of the indirect distances revealed that each sector centre lay within a distinct morphometric residence area. The measured and calculated data also showed that each sector centre could be assigned to its proper extracranial landmark that — in comparison with other landmarks — was best suited for the optimal allocation of the sector centre point. (Folia Morphol 2022; 81, 2: 324–335)

**Key words:** brain cartography, encephalometry, craniometry, landmark

## INTRODUCTION

The equine telencephalon recently attracted major scientific attention in veterinary medicine [16, 24, 34]; however, stereotactic manoeuvres were performed in dogs [30], but not in horses (*Equus caballus*). Ac-

cordingly, our morphometric study was designed to elucidate the topographical relations between extracranial landmarks and intracranial sites on the neopallium. Previously, the applicability and usefulness of such extra-intra measurements and calculations

Address for correspondence: Dr. F. Heun, Institute of Anatomy, University of Veterinary Medicine Hannover, Bischofsholer Damm 15, D-30173 Hannover, Germany, e-mail: frederik.heun@tiho-hannover.de

This article is available in open access under Creative Common Attribution-Non-Commercial-No Derivatives 4.0 International (CC BY-NC-ND 4.0) license, allowing to download articles and share them with others as long as they credit the authors and the publisher, but without permission to change them in any way or use them commercially.

were demonstrated in the field of equine craniometry [7] with special emphasis on the so-called indirect distances in a three-dimensional coordinate system.

Data from numerous equine craniometric studies [7, 10, 18, 19, 22, 25, 26], various imaging procedures [2, 12, 16, 32, 33] and some electrophysiological approaches [1, 3, 6] are currently available. However, they appear limited in their methodical scope because a topographical link is missing between the two subjects of interest, i.e. skull (head surface) and brain. Kramer et al. [20] used extracranial landmarks for a surgical approach to the brain; Wijnberg et al. [35] used extracranial landmarks for the placement of electrodes for electroencephalography, but a comprehensive cartographic guideline is still not available.

This may, in part, be due to the lack of a uniform reference system for the horse's head, and — in particular — to the very complex and heterogeneous surface architecture of the equine neopallium [4, 9, 24]. The recently elaborated cartographic pattern subdividing the surface of the equine neopallium [5, 13] was applied in this study as a promising tool to combine both, landmarks on the head and distinct sites on the brain's surface, for a comprehensive description of the topographical extra-intra relations. In order to allow the unanimous identification of the sulci (i.e. their courses and depths; cartographic pattern) the isolation of the brain from the cranial cavity was assumed to be indispensable at the present early state of this pilot study.

## MATERIALS AND METHODS

### Specimens

The heads of 16 adult warm-blooded horses were fixed by perfusion with 10% formalin via the left A. carotis communis shortly after euthanasia. The horses had been euthanized by medical staff at the Clinic for Horses (University of Veterinary Medicine Hannover, Hannover, Germany) to be used in the dissection courses of the Institute of Anatomy at the same university. No animals were exclusively euthanized for this study. All related procedures were carried out in accordance with the German Federal Law, i.e. the Protection of Animals Act (Tierschutzgesetz §4, §7, §7a) as well as the Directive of the European Parliament and of the Council for the Protection of Animals Used for Experimental and other Scientific Purposes (2010/63/EU). The project was reported to and approved by the Animal Welfare Officer of the University

of Veterinary Medicine Hannover, Hannover, Germany (TVO-2018-V-70 of 4 September 2018).

### Settings

The heads were frozen and longitudinally cut 15 mm to the right side of the median plane (to avoid damage to the left hemisphere). Then, the left half was placed on the stereotactic apparatus (the section plane lying on a specimen table). A simple stereotactic apparatus was built as previously described in detail [13]. Briefly, the specimen table was flexibly connected with a fixed base plate; hence, it could be lifted and adjusted to standardized angles (0 and 90 degrees). It also had scaled guide bars (mm units) on its sides and, therefore, could be shifted precisely back and forth and side to side. Additionally, a drill machine was mounted in a stable vertical position above the specimen table (wood drill bit with a diameter of 3 mm).

To ensure a uniform positioning of the different heads on the specimen table, the establishing of a uniform extracranial reference line (like for example the Frankfurt line in human medicine) was indispensable. Hence, the Hannover line was established: This ran along the crista facialis and extended to the head's caudal end. Accordingly, the head was placed in such a way that the Hannover line was always parallel to the longitudinal margin of the specimen table.

A three-dimensional anatomical coordinate system (Fig. 1) was established by using three extracranial reference planes, i.e. firstly, the horizontal plane called Hannover plane (at the level of the Hannover line); secondly, the transverse plane cutting the foramen supraorbitale; thirdly, the median plane. These planes were orthogonal, and all met in the so-called zero point of the head (ZP) and represented the three spatial axes: x, y and z (Fig. 1).

This setting allowed drilling at different angles (i.e. 90 degrees in the lateral view and 0 degrees in the dorsal view) and at different sites, i.e. at the so-called drilling points (D). The drilling points were topographically related to palpable anatomical landmarks, i.e. foramen supraorbitale, crista facialis, arcus zygomaticus, margo orbitalis, median plane. Three drilling points were placed parallel to the Hannover line, three parallel to the median plane (Fig. 2). This stereotactic drilling at the selected extracranial drilling points (D) yielded intracranial target points (T) at the internal surface of the calvaria and on the brain.

On the carefully removed brain, the facies convexa of the neopallium was subdivided into 15 sectors

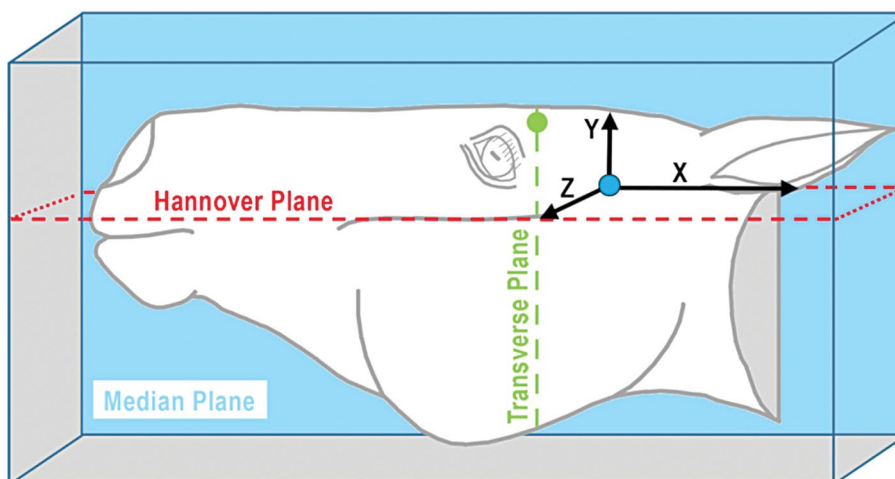


**Figure 1.** Graphical representation of the left half of an equine head. The horizontal Hannover plane (red dashed line) follows the crista facialis. The transverse plane (green dashed line) cuts the foramen supraorbitale (green dot); both are orthogonal to the third plane that is the median plane. In the median plane, all the three planes meet in the zero point of the head (blue dot). The arrows indicate the directions of the three spatial axes (x, y, z) of the anatomical coordinate system.

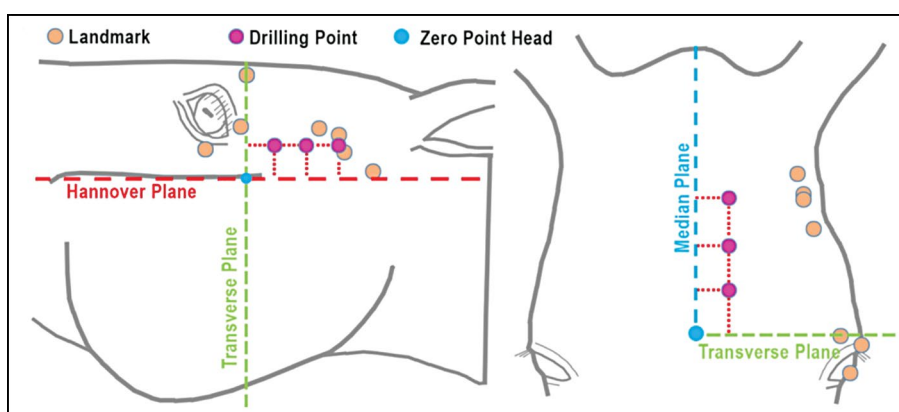


**Figure 2.** Sketch of an equine head in lateral and dorsal view. The three reference planes, i.e. Hannover plane (red), transverse plane (green) and median plane (blue), meet in the zero point of the head (blue point). The landmarks are osseous points which are easy to identify, and the drilling points are deduced from these landmarks. The red dotted lines mark the uniform distances between the respective drilling points and the reference planes.

(Fig. 3), as previously described [5, 13]. The sectors were delineated by the primary sulci and by auxiliary lines topographically related to the primary sulci. The centre of each sector was designated as the sector centre point (SCP). Additionally, the rostral pole (RP) and the caudal pole (CP) of the neopallium were marked (Fig. 3).

#### Measurements and calculations

Measurements were performed on the outside of the head (craniometry) and — after brain removal from the cranial cavity — on the surface of the isolated brain (encephalometry) using the scales of

the moveable specimen table of the stereotactic apparatus that was shifted in either the longitudinal or transversal direction. Measurements on the macerated skulls (craniometry) were performed by using the Faro® Fusion measurement device (Faro Europe, Stuttgart, GER) together with the operating software DELCAM PowerINSPECT (DELCAM, Birmingham, UK) as previously described [7, 22, 26].

The measured distances (Table 1) — designated as indirect distances — were strictly aligned parallel to the x-, y- and z-axes of the head/skull/brain in accordance with the anatomical coordinate system (Fig. 1). On the isolated brain, the longitudinal

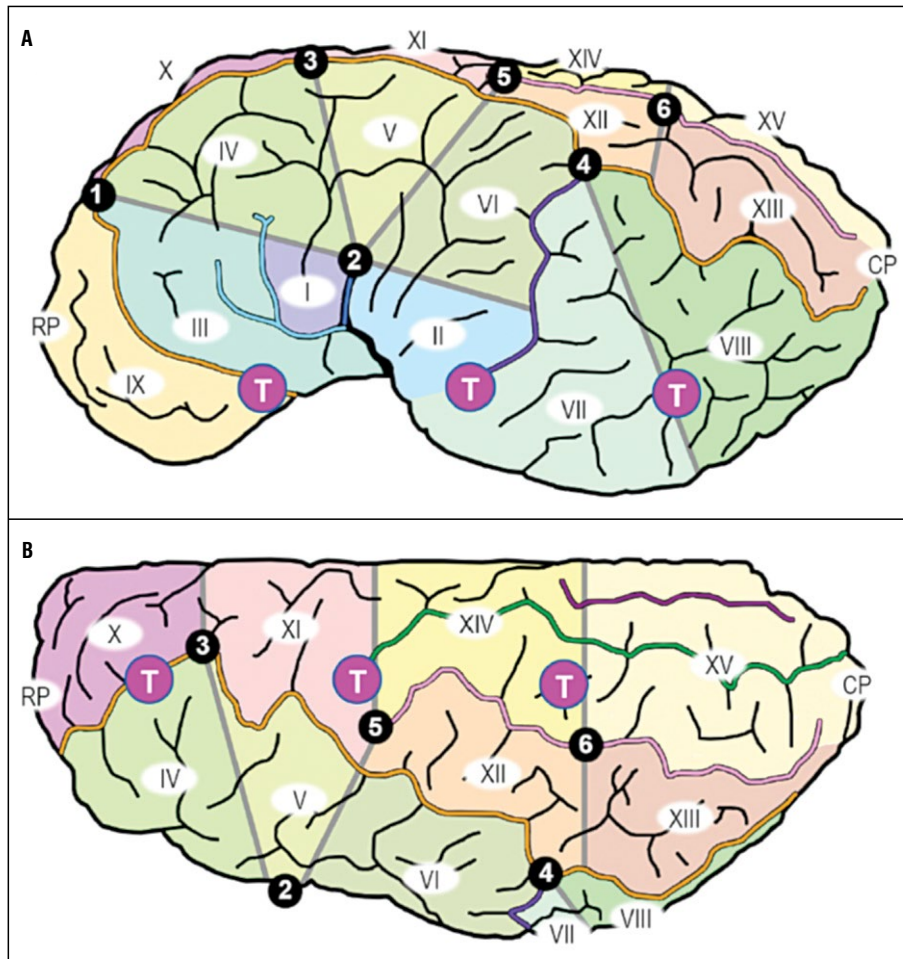


**Figure 3.** Graphical representation of 15 sectors (I–XV) of the equine neopallium. **A.** Lateral view (90° angle); **B.** Dorsal view (0° angle). The numbering of the sectors starts rostral and caudal to the fissura sylvia (sectors I and II) and then continues in a bow-like order in topographical relation to the primary sulci. The sectors are delineated by the primary sulci (colour-coded in accordance with Lang et al. [24]) and by auxiliary lines (grey). The auxiliary lines are related to standard orientation points (1–6, black) defined as follows: (1) the rostral point on the sulcus presylvius/sulcus coronalis; (2) the dorsal end of the fissura sylvia; (3) the most medial point on the sulcus coronalis/sulcus suprasylvius; (4) the intersection of the sulcus suprasylvius and the sulcus obliquus; (5) the rostral end of the sulcus ectomarginalis; (6) the point on the sulcus ectomarginalis halfway between point (5) and the caudal pole of neopallium. The rostral pole (RP) and caudal pole (CP) of the neopallium and the target points (T) are also marked. Colour-coding of each sulcus (S.): orange — S. presylvius/S. coronalis/S. suprasylvius; dark blue — F. sylvia; light blue — S. diagonalis; purple — S. obliquus; pink — S. ectomarginalis; green — S. marginalis; red — S. endomarginalis.

**Table 1.** Compilation of measured indirect distances between points of interest on the outside of the head and skull (craniometry), of measured indirect distances between points on the surface of the isolated brain (encephalometry) and of calculated distances between extra- and intracranial points

Measurements on head and macerated skull	Measurements on isolated neopallium	Calculations of extra-intra distances
From – To	From – To	From – To
L – D	T – SCP	L – SCP
ZP – L	T – RP	ZP – SCP
ZP – D	T – CP	ZP – CP
		ZP – RP

L — landmark on head/skull; D — drilling point on head/skull; T — target point on brain; ZP — zero point of head; SCP — sector centre point on neopallium; RP — rostral pole of neopallium; CP — caudal pole of neopallium

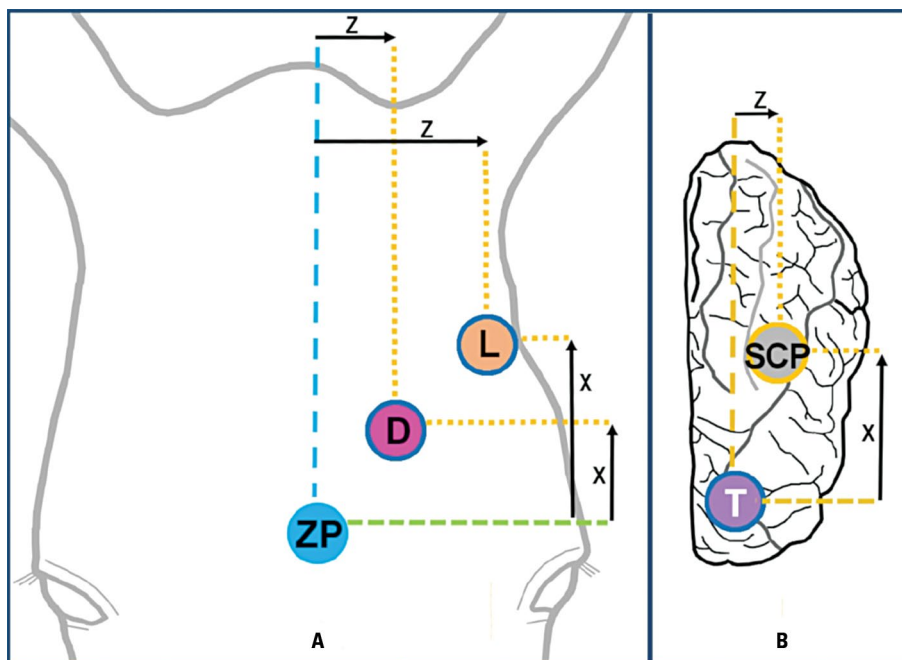


**Figure 4.** Graphical representation of the measurement of indirect distances in dorsal view; **A.** Extracranial measurement between the zero point head (ZP) and an extracranial landmark (L) or a drilling point (D); **B.** Measurement between a target point (T) and a sector centre point (SCP) on the neopallium of the isolated brain. The indirect distances indicate how far away one point is from another in the caudal direction (x-axis) or in the lateral direction (z-axis). The direction of each indirect distance is aligned with the axes of the coordinate system. A direct distance (not shown here) would indicate the shortest, i.e. direct way between two points and, hence, would run obliquely in most cases.

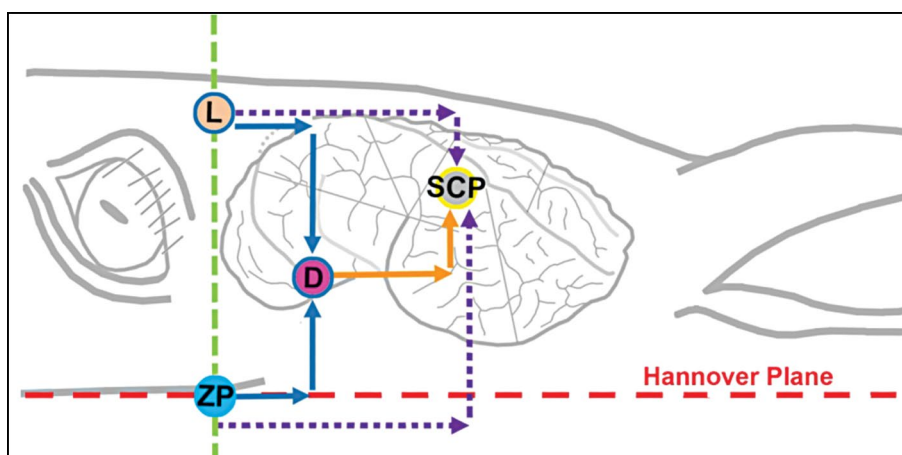


**Figure 5.** Graphical representation of the three steps for determining the extra-intra distances between extracranial points on the head/skull and intracranial sector centre points (SCP) on the brain; lateral view. Even though the encephalometry was performed on the isolated brain, the head and the brain were mounted together in this sketch to better visualise the entire procedure. Step 1: The two reference planes (Hannover plane [red] and transverse plane [green]) mark the position of the zero point head (ZP). Starting there (or at a landmark [L]), the indirect distance to the drilling point (D) was measured extracranially (blue arrows). Step 2: The indirect distance to a selected SCP was measured on the isolated brain, starting from the target point (T; identical with D in this lateral view) on the brain (orange arrows). Step 3: The distance between the extracranial L or ZP and the SCP on the neopallium was calculated (purple arrows).

axis was recognized by the target points that lay on a line parallel to the Hannover line and median plane of the head/skull, respectively; the zero point was an essential reference point (Fig. 4).

Determining the indirect distances between extracranial landmarks or the zero point head (ZP) and

sites on the brain (SCPs) — “extra-intra distances” — was performed in three steps:

- Step 1 (craniometry): the indirect distance between an extracranial landmark (or the ZP) and an extracranial drilling point was measured on the skull (Fig. 5, blue arrows);

- Step 2 (encephalometry): the indirect distance between a target point on the neopallium and a selected SCP was measured on the isolated brain (Fig. 5, yellow arrows);
- Step 3 (calculation): the indirect distance between the extracranial landmark (or the ZP) and the SCP was calculated by means of simple arithmetic addition or subtraction, depending on the topographical relation (Fig. 5, purple dotted arrows).

Finally, for the metric and arithmetic data of all 16 horses (Table 2), the mean values, the standard deviations and the differences between the longest and shortest indirect distances were calculated using Microsoft® Excel® 2016 (Microsoft Corporation, Redmond, WA, USA). Diagrams displaying the positions of the SCP in the coordinate system were generated with Microsoft Excel and subsequently graphically supplemented (Adobe Photoshop CS6 Extended 13.0.1; Adobe Systems, San Jose, CA, USA) to high-light distinct sites (Fig. 6).

## RESULTS

All SCP were always located dorsal and caudal to the zero point head (ZP), i.e. caudal to the foramen supraorbitale and dorsal to the Hannover plane. The rostral pole of the neopallium lay on average on the same transverse plane as the ZP. In the inter-individual comparison, the topographical relations between the SCPs of the neopallium and the ZP varied. However, a common basic pattern of localisation was obvious, meaning that each of the 15 SCPs (I-XV) — if compared in the 16 horses — had its position within a certain limited residence area (Fig. 6; see colour-coded areas).

These topographical relations between the SCPs of the neopallium and the ZP were visualised by using the mean values of the respective indirect distances mentioned above and by projecting their mean localisations onto the surface of the head (Figs. 7, 8). This allowed identifying the so-called mean localisation of each SCP with reference to the three reference planes.

The values of the indirect distances between extracranial landmarks and SCPs on the neopallium showed inter-individually variable characteristics, depending on the spatial axis and the selected landmark. Certain landmarks and the indirect distances related to them showed the least inter-individual differences, depending on the spatial axis (Table 2) and on the selected SCP. Such landmarks, one for each SCP in the respective spatial axis, are recommended as the

guiding structure to the respective SCP. With reference to these guiding structures, each SCP could be located in an area smaller than 23 mm in diameter. The calculated indirect distances between landmarks and the SCPs other than those listed in Table 2 showed more inter-individual differences; these data (not listed here) are available on request.

Considering the longitudinal axis (Table 2), one landmark, i.e. the most dorsal and caudal point on the arcus zygomaticus, is particularly recommended to be used as the most suitable guiding structure to SCP I and all subsequent caudal SCPs. As for SCPs located further rostrally, other landmarks (Table 2) are recommended because the indirect distances starting from these landmarks showed smaller inter-individual differences. In the vertical axis (Table 2), the porus acusticus externus is particularly recommended for most of the ventral, dorsal and laterocaudal SCPs because the indirect distances related to these showed the least inter-individual differences. In contrast, the most ventral point on the margo orbitalis is recommended as the guiding structure for lateral SCPs (Table 2). The median plane was a suitable guiding structure for the indirect distances in the transversal direction (z-axis; Table 2). However, the foramen supraorbitale is also recommended, e.g. as the guiding structure to the SCPs near the fissura sylvia (Table 2).

## DISCUSSION

Measurements and calculations of distances between extracranial landmarks and specific sites on the brain require appropriate anatomical reference systems in combination with an adequate stereotactic device to facilitate, firstly, the standardized and reproducible placement and probing/drilling on the head and, secondly, the reproducible placement of the isolated brain for the purpose of measurements on the neopallium.

The stereotactic apparatus used in this study differed from those that had been applied previously on pigs [27], cattle [21] or dogs [17, 30]. In those settings, a frame was attached to the intact head and the drill bit or probe was movably attached to it. Our setting was simpler and yet effective because it overcame the initial challenge in terms of uniform specimen positioning by using heads cut in the paramedian plane. This had several advantages. Firstly, it allowed removal of the brain (for separate measurements); secondly, it allowed adjusting of the median plane of the stereotactic system (i.e. the

**Table 2.** Compilation of selected indirect distances between an extracranial landmark and a sector centre point (SCP, I–XV) of the neopallium or the rostral/caudal pole of the neopallium (RP, CP) in a longitudinal (x-axis), vertical (y-axis) and transverse (z-axis) direction. Considering each SCP, the indirect distance that showed the least differences in the inter-individual comparison of the 16 horses is listed. The difference between the maximum and minimum value of the indirect distance represents the diameter of the morphometric residence area of the respective SCP. A negative sign indicates that the SCP lies rostral (x-axis), ventral (y-axis) or medial (z-axis) of the extracranial landmark

Extracranial landmark	SCP	M [mm]	SD [mm]	Max–Min [mm]
<b>Indirect distances along the longitudinal axis (x-axis)</b>				
Caudodorsal point on arcus zygomaticus	I	–47	5	14
Caudodorsal point on arcus zygomaticus	II	–29	5	16
Porus acusticus externus	III	–75	4	13
Most rostral point on margo orbitalis	IV	95	5	15
Caudodorsal point on arcus zygomaticus	V	–32	4	15
Caudodorsal point on arcus zygomaticus	VI	–18	5	15
Caudodorsal point on arcus zygomaticus	VII	–11	5	18
Caudodorsal point on arcus zygomaticus	VIII	9	6	19
Most rostral point on margo orbitalis	IX	80	4	14
Most ventral point on margo orbitalis	X	47	6	22
Porus acusticus externus	XI	–38	5	14
Caudodorsal point on arcus zygomaticus	XII	–3	5	16
Caudodorsal point on arcus zygomaticus	XIII	17	4	15
Caudodorsal point on arcus zygomaticus	XIV	1	5	18
Caudodorsal point on arcus zygomaticus	XV	23	4	14
Porus acusticus externus	RP	–102	5	18
Caudodorsal point on arcus zygomaticus	CP	35	4	13
<b>Indirect distances along the vertical axis (y-axis)</b>				
Most ventral point on margo orbitalis	I	25	6	17
Porus acusticus externus	II	30	5	15
Foramen supraorbitale	III	–43	6	18
Most ventral point on margo orbitalis	IV	51	6	18
Porus acusticus externus	V	63	5	17
Porus acusticus externus	VI	49	4	17
Most ventral point on margo orbitalis	VII	9	6	18
Porus acusticus externus	VIII	24	5	21
Most ventral point on margo orbitalis	IX	13	7	22
Foramen supraorbitale	X	–10	5	15
Porus acusticus externus	XI	73	4	14
Porus acusticus externus	XII	58	6	22
Most caudal point on arcus zygomaticus	XIII	11	6	22
Porus acusticus externus	XIV	65	5	18
Porus acusticus externus	XV	53	5	16
Porus acusticus externus	RP	38	5	13
Porus acusticus externus	CP	36	4	14
<b>Indirect distances along the transverse axis (z-axis)</b>				
Foramen supraorbitale	I	–33	4	12
Foramen supraorbitale	II	–27	5	14
Median plane	III	40	6	18
Most dorsal point on arcus zygomaticus	IV	–50	4	13

→

**Table 2 (cont.).** Compilation of selected indirect distances between an extracranial landmark and a sector centre point (SCP, I–XV) of the neopallium or the rostral/caudal pole of the neopallium (RP, CP) in a longitudinal (x-axis), vertical (y-axis) and transverse (z-axis) direction. Considering each SCP, the indirect distance that showed the least differences in the inter-individual comparison of the 16 horses is listed. The difference between the maximum and minimum value of the indirect distance represents the diameter of the morphometric residence area of the respective SCP. A negative sign indicates that the SCP lies rostral (x-axis), ventral (y-axis) or medial (z-axis) of the extracranial landmark

Extracranial landmark	SCP	M [mm]	SD [mm]	Max–Min [mm]
Foramen supraorbitale	V	–41	4	11
Caudodorsal point on arcus zygomaticus	VI	–30	4	14
Median plane	VII	56	4	14
Median plane	VIII	49	4	14
Median plane	IX	34	3	12
Median plane	X	13	3	13
Median plane	XI	17	3	12
Median plane	XII	36	4	14
Median plane	XIII	40	3	11
Median plane	XIV	17	4	14
Caudodorsal point on arcus zygomaticus	XV	–60	4	13
Median plane	RP	18	4	14
Caudodorsal point on arcus zygomaticus	CP	–62	5	15

N = 16; M — mean; SD — standard deviation; Max–Min — difference between longest and shortest indirect distance

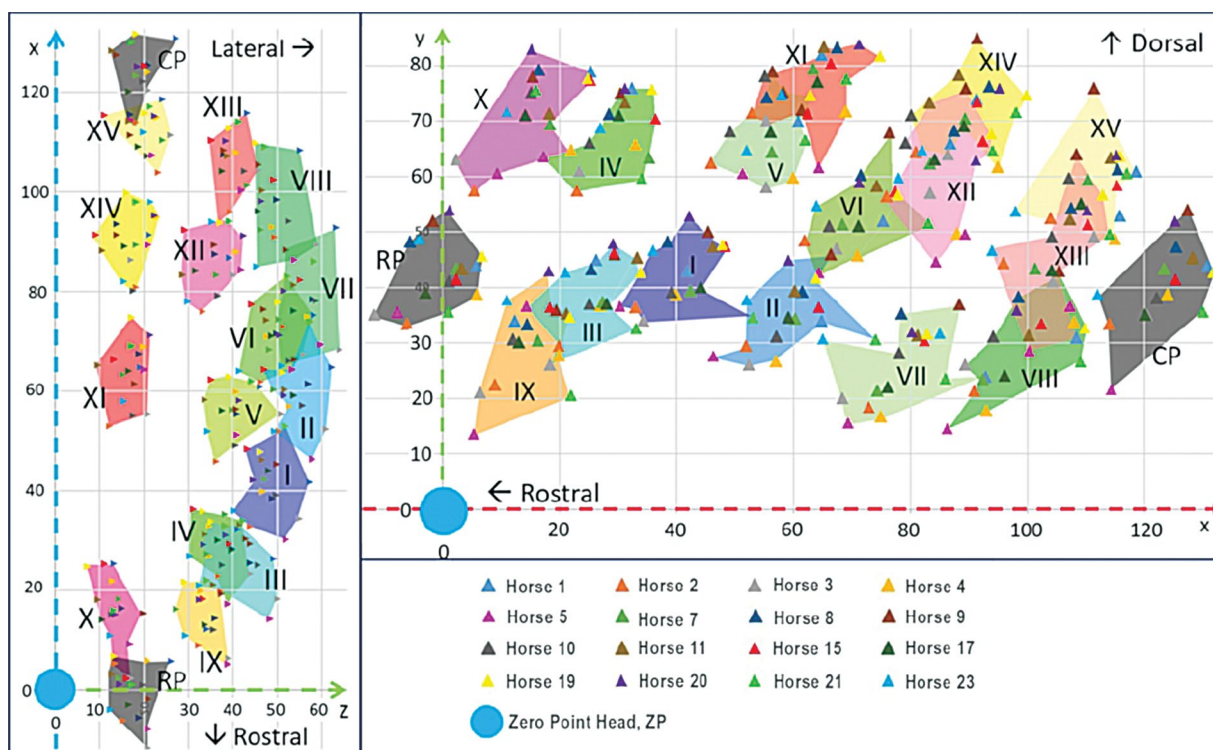


**Figure 6.** Localisation of the sector centre points (SCP) of the neopallium of 16 horses in a synoptic graphical representation to display their topographical relations to the zero point head (ZP, blue dot) in a lateral view and dorsal view (scale: mm). The Hannover plane (red, dashed line) the transverse plane (green, dashed) and the median plane (blue, dashed) correspond with the axes of the anatomical coordinate system and they meet in the ZP; the ZP of all 16 horses are superimposed to establish a uniform reference point in this synopsis. Starting from this point, the SCPs (I–XV) and the rostral pole (RP) and caudal pole (CP) were then positioned to scale according to their indirect distances (the diagram was created with MS Excel and modified with Adobe Photoshop). The outlines of the coloured fields express the positional variations in the SCPs (coloured triangles) in the inter-individual comparison of the 16 horses (residence areas).

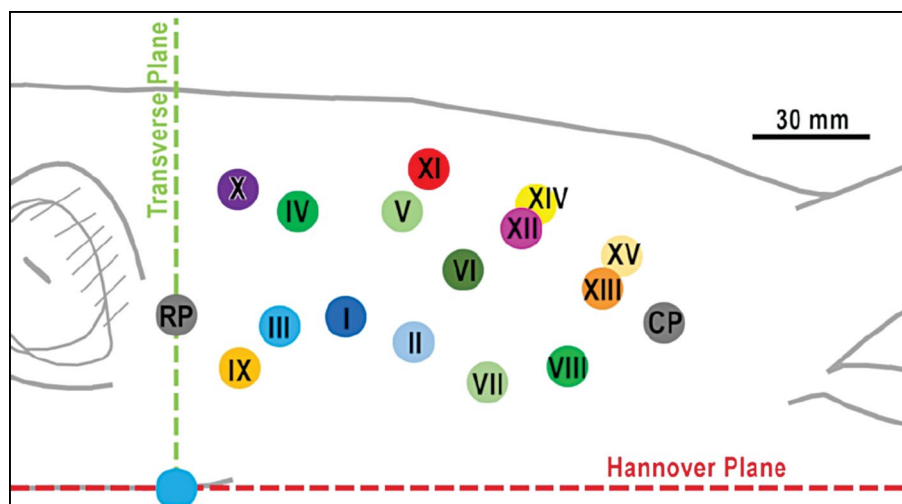


**Figure 7.** Graphical projection of the mean localisations of the sector centre points (SCPs, I–XV) of the left neopallium onto the head surface in a lateral view. Two of the three standard reference planes (Hannover plane [red] and transverse plane [green]) and the zero point head (blue dot) were used as reference points for the projection onto the head surface. Using the positions of the individual SCPs of all 16 horses, the mean localisation of each SCP was calculated and projected onto the head surface and drawn to scale; RP — rostral pole; CP — caudal pole of the neopallium.

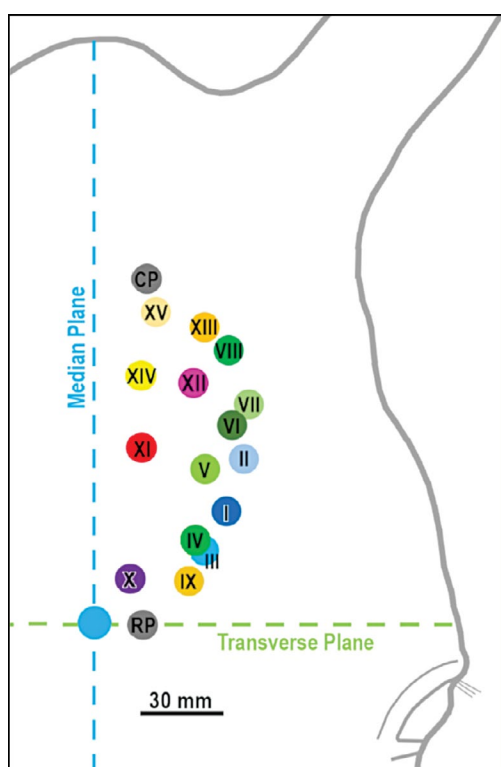


**Figure 8.** Graphical projection of the mean localisations of the sector centre points (SCPs, I–XV) of the left neopallium onto the head surface in a dorsal view. Two of the three standard reference planes (median plane [blue] and transverse plane [green]) and the zero point head (blue dot) were used as reference points for the projection onto the head surface. Using the positions of the individual SCPs of all 16 horses, the mean localisation of each SCP was calculated and projected onto the head surface and drawn to scale; RP — rostral pole; CP — caudal pole of the neopallium.

specimen table) with the paramedian plane of the specimen (i.e. the cutting surface of the head and brain); thirdly, it allowed adjusting the specimens along the table's scaled margins that represented the x-axis and y-axis of the stereotactic and anatomical coordinate system. Head and brain, though separated from each other, bore identical marks (i.e. external drilling points and target points on the neopallium), which were identically aligned along the Hannover plane and the median plane [13], i.e. two of the three reference planes.

The three established orthogonal planes formed the basis for the three-dimensional-navigation, for the measurements of the horse's head and brain, and for the distance calculations. In human medicine, similar patient-related coordinate systems and reference planes (like the Frankfurt plane) are commonly used in imaging or surgery [14, 29].

Previous systems for orientation appeared less suitable for this study because they referred to two planes only instead of three [31] or were only used for the examination of the brain [16], i.e. without reference to extracranial landmarks.

The zero point of the head (ZP) within our anatomical coordinate system was a valuable morphometric feature as it could be easily projected onto the surface of the head in the lateral and in the dorsal view. Previously, such central reference points had been used in equine craniometry [11]; however,

to calculate virtually instead of physically palpable points and — as such — were not suitable to serve as anatomical guiding structure. The position of the ZP was deduced from the combination of the three designated orthogonal standard planes and, hence, could be regarded as a proportional parameter that partially adjusted imbalances related to individual variations in size and shape of the head and brain.

The distinct, appropriately narrow allocation and designation of sites on the neopallium was challenged by the complex gyration pattern, which is known to be extremely heterogeneous in the equine brain [9, 23, 24]. The subdivision of the *facies convexa* into 15 sectors, in accordance with the recently introduced cartographic mapping system [5, 13], was the key element for the objective and reproducible orientation on the neopallium. Hence, the use of isolated brain specimens for the unanimous determination of these sectors was regarded as an indispensable technical prerequisite; this method was preferred instead of computer tomography and/or magnetic resonance imaging at this initial state of our study. Such imaging procedures are of course in the scope of future investigations now that the basic topographic extra-intra relations (skull vs. brain) and the neopallium's cartographic pattern (sectors) have been principally elucidated.

The morphometric procedure applied here highlighted the topography of the equine brain *in situ* because, for the first time, extracranial landmarks were topographically linked to selected cerebral surface structures in horses (extra-intra calculations/measurements). The immanent biological variability of both, skull and neopallium [24], commonly influences the results of any morphometric procedure. To exclude growth-related differences, only adult horses (> 5 years) were used in this study, bearing in mind that age-related differences in equine skulls have not been detected in horses older than 5 years [7]. In terms of this, our pool of specimens (adult, warm-blooded horses) was homogeneous.

Considering that morphometric data of two biologically variable systems (skull and neopallium) were linked in this study, one could not expect to find a certain SCP in the precisely identical spot in different horses. Yet, the comparison of data revealed that each SCP was localised in a limited space, i.e. the residence area. This finding is in line with general morphometric principles that apply in a three-dimensional system [7, 26]. Consequently, the residence area is regarded as a valuable descriptive tool of allocation of the SCPs.

Several extracranial landmarks on the equine head had been recommended [7, 20, 28, 36] and were examined in this study. However, our data emphasized that one particular landmark is not equally suitable for all sites on the neopallium in general. Rather, the choice of a distinct, specific landmark (i.e. the guiding structure) is recommended for the most precise navigation to the requested target site (SCP): the lists of selected data of indirect distances presented here and in the much more comprehensive data set including direct distances [13] are also proposed to be used as manuals of reference, indicating the appropriate guiding structure for accurate manoeuvres to an SCP.

The cartographic system of sectors [5, 13] is emphasized as a useful supplementary means for the distinct descriptive allocation of investigated sites in the case that certain techniques like, e.g. previously performed diagnostic electroencephalographic procedures [36], imaging studies [16] or surgery [20] should be further developed and elaborated for the application in horses. For example, the area that was electrophysiologically [3, 6] or histologically [8, 15] identified as the motor cortex is very likely to be partially located in sector XI of the neopallium.

## CONCLUSIONS

The elaborated map of standardised sectors on the neopallium was an effective tool to overcome the orientation problems caused by the heterogeneous surface architecture of the equine brain. The proposed sectors were adequately small enough to perform the distinct and unanimous allocation and designation of targeted sites on the brain. The coordinate system specifically elaborated for the equine head facilitated the topographical, metric linkage of extracranial, palpable landmarks and the neopallium's surface sectors. The choice of the appropriate landmarks on the head's outer surface enabled the reproducible navigation towards the different sectors. The presented anatomical data are supposed to represent a substantially sound basis for studies by means of diagnostic imaging systems like computed tomography or magnetic resonance imaging.

## Acknowledgements

We would like to thank our native speaker, Mrs. Frances Sherwood-Brock, who most meticulously revised the English manuscript.

**Conflict of interest:** None declared

## REFERENCES

- Adrian ED. The somatic receiving area in the brain of the shetland pony. *Brain*. 1946; 69(1): 1–8, doi: [10.1093/brain/69.1.1](https://doi.org/10.1093/brain/69.1.1).
- Arencibia A, Vazquez JM, Ramirez JA, et al. Magnetic resonance imaging of the normal equine brain. *Vet Radiol Ultrasound*. 2001; 42(5): 405–409, doi: [10.1111/j.1740-8261.2001.tb00959.x](https://doi.org/10.1111/j.1740-8261.2001.tb00959.x), indexed in Pubmed: [11678560](https://pubmed.ncbi.nlm.nih.gov/11678560/).
- Arloing MS. Détermination des points excitables du manteau de l'hémisphère des animaux solipèdes. Application a la topographie cérébrale. *Association française pour l'avancement des sciences*. 1879; 7: 995–1001.
- Böhme G. (ed.) Nickel R, Schummer A, Seiferle E. *Lehrbuch der Anatomie der Haustiere, Band IV: Nervensystem, Sinnesorgane, endokrine Drüsen* (4th ed.). Parey, Stuttgart, Germany 2004.
- Böing L. Die arterielle Vaskularisation der Gehirnoberfläche beim adulten Warmblutpferd: Anatomische Untersuchung unter Berücksichtigung des tierartspezifischen Furchungsmusters des Neopalliums (doctoral dissertation). University of Veterinary Medicine, Hannover 2020. [https://elib.tiho-hannover.de/receive/tiho\\_mods\\_00001263](https://elib.tiho-hannover.de/receive/tiho_mods_00001263).
- Breazile JE, Swafford BC, Biles DR. Motor cortex of the horse. *Am J Vet Res*. 1966; 27(121): 1605–1609, indexed in Pubmed: [5971615](https://pubmed.ncbi.nlm.nih.gov/5971615/).
- Brucker P. Morphometrische Untersuchung des Hirnschädels vom Pferd mit einem computergestützten 3-dimensionalen Messsystem (doctoral dissertation). Cuvillier Verlag, Göttingen 2015. [https://elib.tiho-hannover.de/receive/etd\\_mods\\_00000427](https://elib.tiho-hannover.de/receive/etd_mods_00000427).
- Cozzi B, De Giorgio A, Peruffo A, et al. The laminar organization of the motor cortex in monodactylous mammals: a comparative assessment based on horse, chimpanzee, and macaque. *Brain Struct Funct*. 2017; 222(6): 2743–2757, doi: [10.1007/s00429-017-1369-3](https://doi.org/10.1007/s00429-017-1369-3), indexed in Pubmed: [28210850](https://pubmed.ncbi.nlm.nih.gov/28210850/).
- Dexler H. Beiträge zur Kenntniss des feineren Baues des Zentralnervensystems der Ungulaten. *Gegenbaurs Morphologisches Jahrbuch*. 1904; 32: 288–389.
- Driesch A. vd. A guide to the measurement of animal bones from archaeological sites. *Pea Mus Bull 1*. Harvard University, Cambridge, Mass 1978.
- Evander RL. Craniometry of the equidae part I: two-dimensional shape analysis. *Paludicola*. 2008; 7(1): 1–13.
- Ferrell EA, Gavin PR, Tucker RL, et al. Magnetic resonance for evaluation of neurologic disease in 12 horses. *Vet Radiol Ultrasound*. 2002; 43(6): 510–516, doi: [10.1111/j.1740-8261.2002.tb01041.x](https://doi.org/10.1111/j.1740-8261.2002.tb01041.x), indexed in Pubmed: [12502103](https://pubmed.ncbi.nlm.nih.gov/12502103/).
- Heun F. Morphometrische Untersuchung der topographischen Beziehungen zwischen externen Landmarks am Kopf und kartographischen Mustern des Neopalliums bei adulten Warmblutpferden (doctoral dissertation). University of Veterinary Medicine, Hannover 2020. [https://elib.tiho-hannover.de/receive/tiho\\_mods\\_00001268](https://elib.tiho-hannover.de/receive/tiho_mods_00001268).
- Hofmann E, Fimmers R, Schmid M, et al. Landmarks of the Frankfurt horizontal plane : Reliability in a three-dimensional Cartesian coordinate system. *J Orofac Orthop*. 2016; 77(5): 373–383, doi: [10.1007/s00056-016-0045-1](https://doi.org/10.1007/s00056-016-0045-1), indexed in Pubmed: [27502792](https://pubmed.ncbi.nlm.nih.gov/27502792/).
- Hummel G. Die Feinstruktur der motorischen GroBhirnrinde des Pferdes. *Zbl Vet Med C*. 1976; 5: 35–53.
- Johnson PJ, Janvier V, Luh WM, et al. Equine stereotaxic population average brain atlas with neuroanatomic correlation. *Front Neuroanat*. 2019; 13: 89, doi: [10.3389/fnana.2019.00089](https://doi.org/10.3389/fnana.2019.00089), indexed in Pubmed: [31636547](https://pubmed.ncbi.nlm.nih.gov/31636547/).
- Kani Y, Cecere TE, Lahmers K, et al. Diagnostic accuracy of stereotaxic brain biopsy for intracranial neoplasia in dogs: Comparison of biopsy, surgical resection, and necropsy specimens. *J Vet Intern Med*. 2019; 33(3): 1384–1391, doi: [10.1111/jvim.15500](https://doi.org/10.1111/jvim.15500), indexed in Pubmed: [30990928](https://pubmed.ncbi.nlm.nih.gov/30990928/).
- Komosa M, Moliński K, Godynicki S. The variability of cranial morphology in modern horses. *Zoolog Sci*. 2006; 23(3): 289–298, doi: [10.2108/zsj.23.289](https://doi.org/10.2108/zsj.23.289), indexed in Pubmed: [16603822](https://pubmed.ncbi.nlm.nih.gov/16603822/).
- Krahmer R. Messungen am Kopfskelett des Pferdes. Ein Beitrag zur Bedeutung der Kraniologie (doctoral dissertation). Karl-Marx-University, Leipzig 1963.
- Kramer J, Coates JR, Hoffman AG, et al. Preliminary anatomic investigation of three approaches to the equine cranium and brain for limited craniectomy procedures. *Vet Surg*. 2007; 36(5): 500–508, doi: [10.1111/j.1532-950X.2007.00297.x](https://doi.org/10.1111/j.1532-950X.2007.00297.x), indexed in Pubmed: [17614932](https://pubmed.ncbi.nlm.nih.gov/17614932/).
- Kuhla B, Bellmann O, Metges CC. Technical note: An apparatus for catheterization of the lateral brain ventricle in Holstein cows. *J Dairy Sci*. 2010; 93(12): 5837–5841, doi: [10.3168/jds.2010-3431](https://doi.org/10.3168/jds.2010-3431), indexed in Pubmed: [21094756](https://pubmed.ncbi.nlm.nih.gov/21094756/).
- Lang A, Brucker P, Ludwig M, et al. The challenge of extra-intra craniometry: a computer-assisted three-dimensional approach on the equine skull. *Folia Morphol*. 2017; 76(3): 458–472, doi: [10.5603/FM.a2016.0082](https://doi.org/10.5603/FM.a2016.0082), indexed in Pubmed: [28026847](https://pubmed.ncbi.nlm.nih.gov/28026847/).
- Lang A, Sherwood-Brock F, Gasse H. Hermann Dexler's "Beiträge zur Kenntnis des feineren Baues des Zentralnervensystems der Ungulaten." An annotated English translation of the original German article; Part V: Telenkephalon – adult stages. Hannover 2018a. [https://doi.org/10.15487/tiho.4\\_2018.1/5](https://doi.org/10.15487/tiho.4_2018.1/5) (2018).
- Lang A, Wirth G, Gasse H. Review of the surface architecture of the equine neopallium: Principle elements of a cartographic pattern of sulci revisited and further elaborated. *Anat Histol Embryol*. 2018; 47(4): 280–297, doi: [10.1111/ahel.12355](https://doi.org/10.1111/ahel.12355), indexed in Pubmed: [29542168](https://pubmed.ncbi.nlm.nih.gov/29542168/).
- Löffler K. Untersuchungen über die Wachstumsverhältnisse der Kopfknochen des Pferdes (doctoral dissertation). Hessische Ludwigs-Universität, Giessen 1919.
- Ludwig M. Computergestützte Craniometrie beim Pferd unter Berücksichtigung altersabhängiger Lageverschiebungen osteologischer Landmarks. (doctoral dissertation). Cuvillier Verlag, Göttingen 2015. [https://elib.tiho-hannover.de/receive/etd\\_mods\\_00000406](https://elib.tiho-hannover.de/receive/etd_mods_00000406).
- Marcilloux JCA. Stereotaxic apparatus for the study of the central nervous structures in the pig. *Brain Res Bull*. 1989; 22: 591–597, doi: [10.1016/0361-9230\(89\)90118-4](https://doi.org/10.1016/0361-9230(89)90118-4).
- Mysinger PW, Redding RW, Vaughan JT, et al. Electroencephalographic patterns of clinically normal, sedated, and tranquilized newborn foals and adult horses. *Am J Vet Res*. 1985; 46(1): 36–41, indexed in Pubmed: [3970440](https://pubmed.ncbi.nlm.nih.gov/3970440/).
- Park JA, Lee JS, Koh KS, et al. Using the zygomatic arch as a reference line for clinical applications and anthropological studies. *Surg Radiol Anat*. 2019; 41(5): 501–505, doi: [10.1007/s00276-018-2162-6](https://doi.org/10.1007/s00276-018-2162-6), indexed in Pubmed: [30552488](https://pubmed.ncbi.nlm.nih.gov/30552488/).

30. Rossmeisl JH, Andriani RT, Cecere TE, et al. Frame-based stereotactic biopsy of canine brain masses: technique and clinical results in 26 cases. *Front Vet Sci.* 2015; 2: 20, doi: [10.3389/fvets.2015.00020](https://doi.org/10.3389/fvets.2015.00020), indexed in Pubmed: [26664949](https://pubmed.ncbi.nlm.nih.gov/26664949/).
31. Stoll M, Ros K, Vogt C, et al. The hemisphere model: a new description of directions for head radiographs in the horse. *Pferdeheilkunde.* 2011; 27(2): 115–118.
32. Stuckenschneider K. Magnetresonanztomographische Untersuchungen der Gehirnregion gesunder und neurologisch erkrankter Pferde mit einer Feldstärke von 3 Tesla. (doctoral dissertation). Cuvillier Verlag, Göttingen 2013. [https://elib.tiho-hannover.de/receive/etd\\_mods\\_00000668](https://elib.tiho-hannover.de/receive/etd_mods_00000668).
33. Stuckenschneider K, Hellige M, Feige K, et al. 3-Tesla magnetic resonance imaging of the equine brain in healthy horses - Potentials and limitations. *Pferdeheilkunde.* 2014; 30(6): 657–670, doi: [10.21836/Pem20140605](https://doi.org/10.21836/Pem20140605).
34. van der Ree M, Wijnberg I. A review on epilepsy in the horse and the potential of Ambulatory EEG as a diagnostic tool. *Vet Q.* 2012; 32(3-4): 159–167, doi: [10.1080/01652176.2012.744496](https://doi.org/10.1080/01652176.2012.744496), indexed in Pubmed: [23163553](https://pubmed.ncbi.nlm.nih.gov/23163553/).
35. Wijnberg ID, van der Ree M, van Someren P. The applicability of ambulatory electroencephalography (AEEG) in healthy horses and horses with abnormal behaviour or clinical signs of epilepsy. *Vet Q.* 2013; 33(3): 121–131, doi: [10.1080/01652176.2013.842075](https://doi.org/10.1080/01652176.2013.842075), indexed in Pubmed: [24111950](https://pubmed.ncbi.nlm.nih.gov/24111950/).
36. Williams DC, Aleman M, Holliday TA, et al. Qualitative and quantitative characteristics of the electroencephalogram in normal horses during spontaneous drowsiness and sleep. *Vet Intern Med.* 2008; 22(3): 630–638, doi: [10.1111/j.1939-1676.2008.0096.x](https://doi.org/10.1111/j.1939-1676.2008.0096.x), indexed in Pubmed: [18466241](https://pubmed.ncbi.nlm.nih.gov/18466241/).

# Arterial hypertension and remodelling of the right ventricle

A. Kosiński<sup>1</sup>, G.M. Piwko<sup>1</sup>, R. Kamiński<sup>1</sup>, E. Nowicka<sup>1</sup>, A. Kaczyńska<sup>1</sup>,  
M. Zajączkowski<sup>1</sup>, K. Czerwiec<sup>1</sup>, M. Gleinert-Rożek<sup>1</sup>, K. Karnecki<sup>2</sup>, T. Gos<sup>2</sup>

<sup>1</sup>Department of Clinical Anatomy, Gdansk Medical University, Gdansk, Poland

<sup>2</sup>Department of Forensic Medicine, Gdansk Medical University, Gdansk, Poland

[Received: 19 December 2020; Accepted: 11 March 2021; Early publication date: 13 April 2021]

**Background:** In the case of long-term and physiological loads (e.g. during pregnancy or regular athletics training), reversible morphological changes occur in the heart — cardiomyocytes undergo hypertrophy; however, this is not accompanied by impairment of left ventricular function or myocyte metabolism. However, in the course of various pathological processes, as time goes by, gradually permanent morphological changes occur. These changes are referred to as remodelling of the heart muscle, which, regardless of the primary cause, can lead to the development of chronic heart failure.

**Materials and methods:** The study was performed on post-mortem material of 35 human hearts obtained from forensic sections and anatomopathological sections of people who died of non-cardiac causes (mainly traffic accidents, suicide attempts, strokes, acute infections); material was fixed in a 4% formalin solution. The hearts were subjected to macro- and microscopic assessment. During microscopic assessment the features of remodelling were evaluated.

**Results and Conclusions:** In vivo and echocardiographic tests, as well as macroscopic evaluation of post-mortem material, suggest the presence of some kind of right ventricular muscle remodelling; however, classic microscopic observations, presented in this study, do not provide such unambiguous evidence. Thus, the question arises: why and how the right ventricular function is disturbed, sometimes at early stages of arterial hypertension. (Folia Morphol 2022; 81, 2: 336–342)

**Key words:** heart, human, changes, hypertensive

## INTRODUCTION

Various pathological factors, both external and intracardiac, can negatively affect the effectiveness of the heart. In return, the organ reacts to these factors by changes in its structure and function, which are aimed at ensuring efficient work in altered, sometimes adverse conditions. In the time of well-being, the heart has a wide range of compensation mechanisms. In the case of short-term physiological loads,

the heart muscle mainly uses the mechanisms of:

a) homeometric regulation — an increase in contractility without changing the sarcomere length (Anrep effect) and an increase in contractility with an increase in heart rate (Bowditch effect) [1];  
b) heterometric regulation — an increase in contractility associated with an increase in the length of sarcomeres (Frank-Starling law) [14]. In the case of long-term and physiological loads (e.g. during pregnancy

Address for correspondence: Dr. G.M. Piwko, Department of Clinical Anatomy, ul. Dębinki 1, 80–210 Gdańsk, Poland, tel: +48 58 349 14 20, e-mail: grzegorz.piwko@gumed.edu.pl

This article is available in open access under Creative Common Attribution-Non-Commercial-No Derivatives 4.0 International (CC BY-NC-ND 4.0) license, allowing to download articles and share them with others as long as they credit the authors and the publisher, but without permission to change them in any way or use them commercially.

or regular athletics training), reversible morphological changes also occur in the heart — cardiomyocytes undergo hypertrophy: however, this is not accompanied by impairment of left ventricular (LV) function or myocyte metabolism [7, 12, 20]. In the course of various pathological processes, as time passes, the basic compensatory mechanisms become exhausted, and gradually lead to permanent morphological changes [4, 10, 27]. Within the myocardium, the proportions and correlation between myocytes, fibroblasts and endothelial cells are disturbed. In the literature, the above changes are referred to as remodelling of the LV heart muscle, which, regardless of the primary cause (hypertension, hypertrophic cardiomyopathy, valvular heart disease, ischaemic disease, etc.), can lead to the development of chronic heart failure, or right ventricular (RV) hypertrophy with all its adverse consequences when appropriate factors affect right ventricle by causing pulmonary hypertension (e.g. chronic obstructive pulmonary disease, idiopathic pulmonary hypertension, chronic thromboembolic pulmonary hypertension, mitral valve insufficiency, etc.).

Due to the increasing prevalence of hypertension in overall population, this group of patients (almost 60% of the population > 59 years of age) is particularly at risk. Additionally, if we take into account the fact that only about 26% of treated patients manage to achieve the intended therapeutic effect, it is not surprising that hypertension and its complications, as a basic risk factor for the development of cardiovascular diseases and acute incidents, is — indirectly — the main cause of death in developed countries. Most of the available scientific studies assessing remodelling of the heart are focused on morphological changes within the left ventricle, which is directly affected by the pathological triggers of this remodelling, e.g. hypertension or cardiomyopathy, which apparently lead to asymmetrical hypertrophy of its walls (interventricular septal wall in comparison to the inferior wall) [19]. Similarly the right ventricle becomes a target of remodelling during pulmonary hypertension of different origins.

Right ventricular hypertrophy due to pulmonary hypertension has got higher attention of the scientists since last few years. However little do we know about already observed, but still sparsely described phenomenon of “cross-remodelling”, in this case, within the right ventricle during arterial hypertension [9].

In this study, looking for anatomical exponents of myocardial remodelling within the RV musculature in people with hypertension, we have set ourselves the

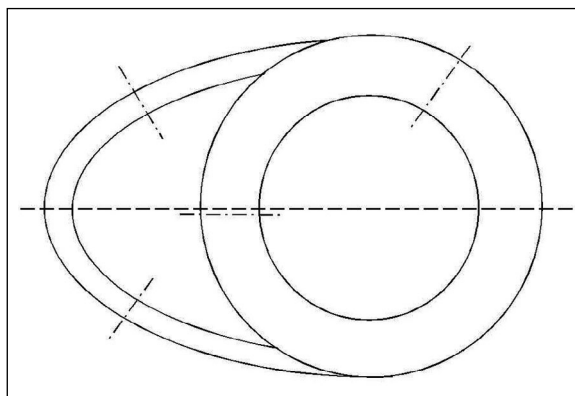


**Figure 1.** The scheme of heart opening cut (dashed line) and heart walls cuts for measurements (dashed-dot lines).

goal of answering the question whether myocardial remodelling may also involve structures that are not directly affected by the causative agent.

## MATERIALS AND METHODS

The material for this study consisted of 35 human hearts from forensic sections and anatomopathological sections of people who died of non-cardiac causes (e.g. traffic accidents, suicide attempts, strokes, acute infections). All hearts were instantly fixed in a solution of formalin and ethanol. The control group (CG) consisted of 13 hearts (6 female [F]/7 male [M]; weight (mean  $\pm$  standard deviation [SD]):  $317.7 \pm 35.15$  g; age (average  $\pm$  SD):  $50.9 \pm 16.8$  years) from persons in whom no cardiovascular disease has been diagnosed in vivo and no obvious pathological changes were found in post-mortem assessment. The study group (SG) consisted of 22 hearts (10 F/12 M; weight [mean  $\pm$  SD]:  $533.2 \pm 68.34$  g; age [average  $\pm$  SD]:  $51.7 \pm 16.8$  years) from people with a history of arterial hypertension and LV hypertrophy found during anatomopathological examination. The protocol was approved by the Independent Bioethics Commission for Research of the Medical University of Gdansk (consent no. NKBBN/165/2018 dated 12 April 2018).

The material was subjected to macro- and microscopic assessment. The right ventricle cavity was opened with a long axis cut along the acute margin from the tricuspid ring to the apex of the right ventricle. Similarly, the left ventricle cavity was opened with a cut along the oblique margin. In addition, the interventricular septum (IVS) was dissected along the long axis, in its frontal plane, in its mid-antero-posterior dimension (Fig. 1). After opening the hearts, the ven-

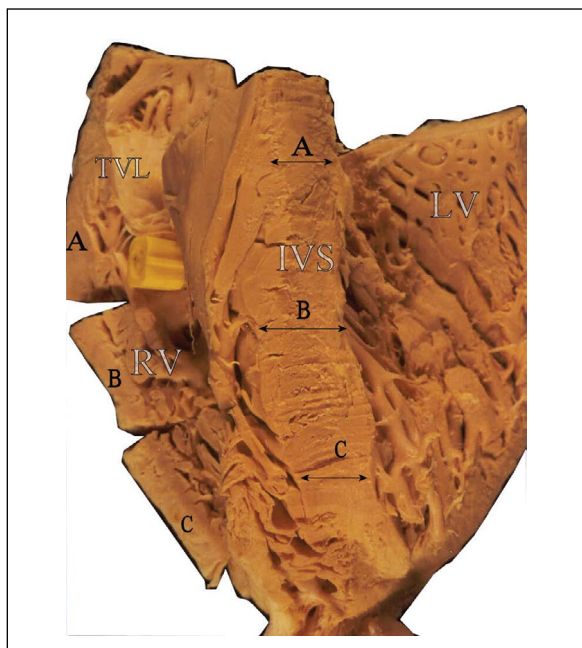


**Figure 2.** Opened heart and incisions of the walls to take measurements; LV — left ventricle, RV — right ventricle; IVS — interventricular septum; TVL — tricuspid valve leaflet; A, B, C — measurements of heart walls thickness at appropriate levels.

tricular septum was divided into four equal sections, thus determining three levels: A, B and C. At these levels, halfway between the acute margin and the septum (RV) and between the oblique margin and the septum (LV) incisions of the heart walls were made and the thickness of both RV walls, LV inferior wall and IVS were measured. The measurements were designated as dimensions A, B and C, respectively (Fig. 2).

The specimens for microscopic assessment were taken from: RV posterior wall (1 × 1 cm), IVS (covering the entire IVS section) and a fragment from the LV inferior wall (1 × 1 cm). Seven hearts were randomly selected for this stage of the study from each group (the control group and the study group). In order to reveal various types of tissue within the heart wall, the preparations were subjected to Masson staining with Goldner modification, which allows simultaneous assessment of connective, adipose tissues, and myocardial muscle cells. The preparations were evaluated in the Opta-Tech MN 800 light microscope (Opta-Tech, Poland), with Moticam 2000 2.0M camera (Motic Incorporation Ltd., Hong Kong) and Leica MZ8/MPS60 (Leica Microsystems Ltd., Switzerland) photographic adapter with the use of Motic Images Plus 2.0 software (version 2.0 2006 Motic China Group Co., Ltd.)

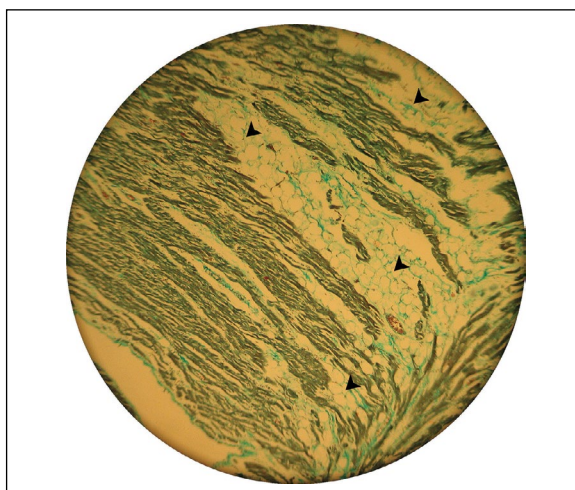


**Figure 3.** Right ventricle myocardium infiltration by adipose tissue (arrows) (male I.71; Mason-Goldner staining; 62.5×).

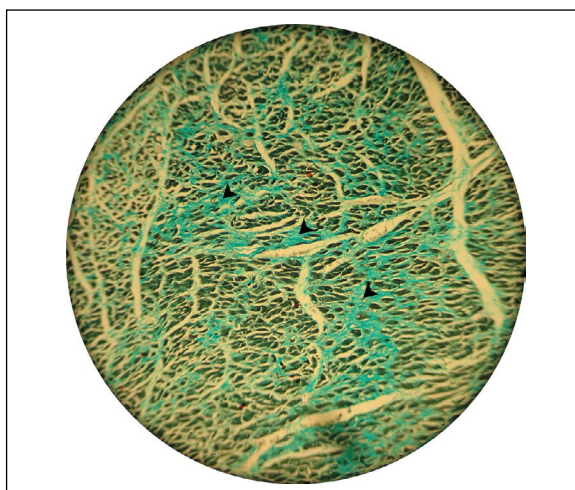


**Figure 4.** Interstitial fibrosis (arrows) of interventricular septum myocardium (male I.71; Mason-Goldner staining; 62.5×).

During microscopic assessment the following features were evaluated: 1) cardiomyocyte thickness, 2) infiltration of the muscular layer of the heart wall by adipose tissue, which penetrates between the muscle fibre strands, thus separating them from each other (Fig. 3), 3) disturbance of the proportion between the amount of muscle tissue and connective tissue, occurring in the form of clusters; its excessive growth is referred to as interstitial myocardial fibrosis (Fig. 4).

#### Statistical analysis

Statistical analysis was performed using Fisher's test and Student's t-test for mean of small samples.

The significance of differences between the results obtained from the qualitative observations of microscopic changes was confirmed using the non-parametric Mann-Whitney U test for two independent groups. P values < 0.05 were considered statistically significant. The software used to perform analyses was Statistica 9.0 package from StatSoft.

## RESULTS

### Macroscopic evaluation

#### Inferior wall of the left ventricle

Individual dimensions of the inferior wall of the left ventricle, which is the target of systemic hypertension, in SG hearts were significantly larger than those of CG. It is noteworthy that these differences were larger related to dimensions A and B, and slightly smaller (but still statistically significant) for dimension C. At level A, the thickness of the LV inferior wall in CG hearts was on average  $10.28 \pm 1.24$  mm, while in hearts with hypertrophy this average was  $14.26 \pm 2.35$  mm ( $p < 0.000003$ ). Dimension B averaged  $10.01 \pm 0.95$  mm in CG and  $13.27 \pm 2.06$  mm in SG ( $p < 0.00001$ ). Dimension C was  $8.71 \pm 1.20$  mm in CG and  $10.34 \pm 2.40$  mm in SG ( $p < 0.05$ ), respectively.

As the effect of the above changes, also the difference in proportions between individual dimensions of the LV inferior wall was noticeable. While there were no differences between the two groups in the A/B and B/C ratios, in hearts with hypertrophy the A/C ratio was significantly higher ( $p < 0.05$ ) than in CG. This implies a greater disproportion between dimensions A and C in SG (Table 1).

Assessing the shape of the cross-sectional plane along the long axis of the LV inferior wall, some differences in the geometry of this cross-section were observed. Namely, in CG dimensions A and B were similar and dominated over dimension C, which meant that in this group of hearts the cross-section of the LV inferior wall between the levels of the valve attachment (A) and the base of the papillary muscle (B) had a rectangular shape, and below it, towards the apex of left ventricle, it gradually decreased, giving the last segment a trapezoidal shape. In SG, on the other hand, the highest thickness occurred at level A, and then downwards gradually decreased. Therefore, the whole cross-section of the inferior wall assumed the shape of an inverted trapezoid (Table 2).

#### Interventricular septum

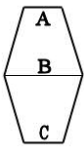
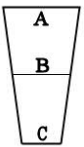
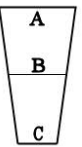
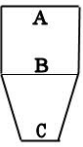
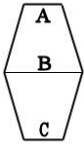
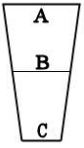
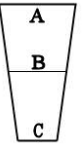
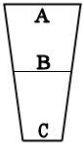
Same as the LV inferior wall, in terms of individual dimensions A, B and C, the thickness of IVS of

**Table 1.** Comparison of the ratios of the individual dimensions of the inferior wall of the left ventricle in the hearts of control group (CG) and study group (SG)

	A/B	B/C	A/C
CG	1.031	1.162	1.199
SG	1.044	1.467	1.521
p	0.28	0.11	<b>0.047</b>

A/B, B/C, A/C — relations of the individual dimensions, p — level of statistical significance

**Table 2.** Schematic representation of the shape of longitudinal section of each of the walls of the heart in control group (CG) and study group (SG)

	IVS	RV anterior wall	RV posterior wall	LV inferior wall
CG				
SG				

IVS — interventricular septum, RV — right ventricle, LV — left ventricle, CG — control group, SG — study group, A, B, C — levels at which the thickness of the myocardium has been measured

hearts from the SG was significantly greater than that of CG hearts. The average dimension A in CG was  $10.6 \pm 1.20$  mm, while in SG it was  $13.4 \pm 2.15$  mm ( $p = 0.0001$ ). Dimension B was  $11.6 \pm 1.18$  mm and  $15.93 \pm 2.52$  mm in groups CG and SG, respectively ( $p < 0.0001$ ). Dimension C averaged  $9.91 \pm 1.52$  mm in CG, and  $12.25 \pm 2.67$  mm in SG ( $p = 0.006$ ).

However, despite such a significant differentiation between individual dimensions in both groups, the comparison of ratios of these dimensions (A/B, B/C, A/C) did not show statistically significant deviations. It seems that hypertrophy of the heart muscle within the septum occurs evenly at all its levels, leading to a proportional increase in all measured IVS dimensions (Table 3).

#### Anterior wall of the right ventricle

As in the case of the in LV inferior wall, significant differences in the thickness of the muscle between both groups were also observed within the anterior wall of the right ventricle. The RV anterior wall

**Table 3.** Comparison of the ratios of the individual dimensions of the interventricular septum in the hearts of control group (CG) and study group (SG)

	A/B	B/C	A/C
CG	0.917	1.192	1.093
SG	0.843	1.260	1.066
p	0.09	0.07	0.68

A/B, B/C, A/C — relations of the individual dimensions; p — level of statistical significance

**Table 4.** Comparison of the ratios of the individual dimensions of the anterior wall of the right ventricle in the hearts of control group (CG) and study group (SG)

	A/B	B/C	A/C
CG	1.406	1.360	1.866
SG	1.274	1.351	1.761
p	0.62	0.97	0.97

A/B, B/C, A/C — relations of the individual dimensions; p — level of statistical significance

**Table 5.** Comparison of the ratios of the individual dimensions of the posterior wall of the right ventricle in the hearts of control group (CG) and study group (SG)

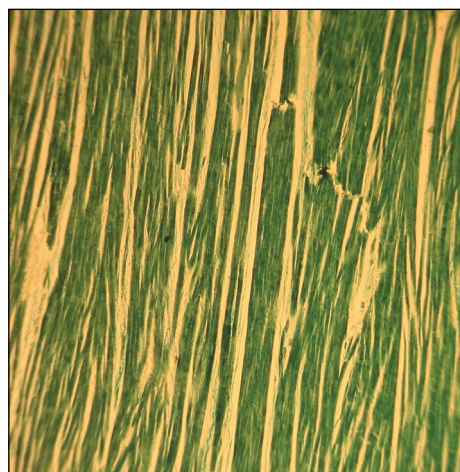
	A/B	B/C	A/C
CG	1.097	1.514	1.676
SG	1.142	1.384	1.462
p	0.76	0.94	0.72

A/B, B/C, A/C — relations of the individual dimensions; p — level of statistical significance

average thickness at level A was  $4.35 \pm 0.63$  mm in CG, while in SG  $5.35 \pm 1.00$  mm ( $p < 0.001$ ). The average dimension B was  $3.18 \pm 0.72$  mm in CG and  $4.19 \pm 1.16$  mm in SG ( $p < 0.005$ ). Dimension C, measured near the apex of the right ventricle, was on average  $2.37 \pm 0.40$  mm and  $3.20 \pm 1.20$  mm in CG and SG, respectively ( $p < 0.05$ ).

No statistically significant differences were noted between the two groups assessing the proportions between individual dimensions (Table 4).

The thickness of the anterior wall at individual levels was typical in all hearts with the largest dimension A, intermediate B and the smallest dimension C. Therefore, the longitudinal section through this wall gives the shape of a triangle, with the base pointing towards the base of the heart, and the top pointing towards the apex of the right ventricle. This image was the same for both groups of hearts (Table 2).

**Figure 5.** Microscopic view of a healthy myocardium of interventricular septum (male 1.24; Mason-Goldner staining; 62.5 $\times$ ).

### Posterior wall of the right ventricle

Within the RV posterior wall, statistically significant differences were also noted for individual dimensions A, B and C. The average dimension A in CG was  $4.27 \pm 0.89$  mm, while in SG it was  $5.11 \pm 1.28$  mm ( $p < 0.05$ ). Dimension B was  $3.93 \pm 0.69$  mm and  $4.73 \pm 1.17$  mm, in CG and SG, respectively ( $p < 0.05$ ). In CG the dimension C averaged  $2.68 \pm 0.81$  mm, and in SG  $3.38 \pm 1.18$  mm ( $p < 0.05$ ).

Again, despite the differences observed, comparing the ratios of these dimensions (A/B, B/C, A/C) in both groups did not reveal any statistically significant deviations (Table 5).

The posterior wall of the right ventricle in its longitudinal section had, like the RV anterior wall, the shape of an inverted triangle, resulting directly from its dimensions and their proportions (Table 2).

### Microscopic evaluation

In the CG, the average thickness of cardiomyocytes within the RV and LV free walls as well as IVS was  $10 \mu\text{m}$ . In 1 (14.3%) case, fat infiltration into the muscular layer of the RV wall was observed. This phenomenon did not occur in the remaining examined walls of this heart, nor in any of the walls of other hearts in this group (Fig. 5). Also in 1 (14.3%) case (same heart), interstitial fibrosis was noted, which was present in all its walls (RV, LV and IVS). Other hearts in this group did not show this pathology. In the vast majority of cases, the muscle fibre arrangement was regular. Only in 3 hearts (2 hearts — RV wall, 1 heart

**Table 6.** Table of microscopic observations — frequency [%] of morphological features of remodelling of the heart muscle in control group and study group

Group	Adipose tissue infiltrating myocardium [%]			Interstitial fibrosis [%]			Average myocytes thickness [ $\mu\text{m}$ ]		
	RV	IVS	LV	RV	IVS	LV	RV	IVS	LV
CG	14.3	0	0	14.3	14.3	14.3	10	10	10
SG	14.3	0	0	14.3	0	14.3	10	13.5	14

CG — control group, no hypertrophy; SG — study group, with myocardial hypertrophy; RV — posterior wall of the right ventricle; IVS — interventricular septum; LV — inferior wall of the left ventricle

— IVS; 28.6% and 14.3%, respectively), incidents of area-limited disturbance of the cardiomyocytes co-axial arrangement could be observed.

In the SG with macroscopic hypertrophy of the heart muscle, apart from the assessment of cardiomyocyte thickness, the results of microscopic observations did not differ much from those obtained in the assessment of CG. Within free walls of the RV, in all cases, the average diameter was 10  $\mu\text{m}$ . Within the remaining cardiac walls (IVS and LV), cardiomyocytes most often reached a diameter ranging 12–15  $\mu\text{m}$ . In one of the examined hearts in SG, the presence of adipose tissue was observed only in the RV musculature (14.3%). The other walls of this heart, as well as other walls of remaining hearts, did not show the presence of this feature. Interstitial fibrosis was observed in the same heart, also within RV (14.3%), and in the second heart, only in the muscle of the left ventricle (14.3%). The other walls in these 2 cases, as well as other hearts, also did not show the presence of this feature. Despite the myocardial hypertrophy found at the stage of macroscopic examination, microscopic examination did not show any disturbance of the spatial arrangement of muscle fibres in any of these hearts (Table 6).

## DISCUSSION

Remodelling of the heart muscle is a phenomenon quite well known and described. The natural course and final effect of this remodelling at organ, tissue and cellular levels may look different depending on the initiating factor. There are many reports focusing on a single heart chamber myocardial remodelling, e.g.: LV muscle under the influence of ischaemic disease and myocardial infarction [8, 21], valvular defects of the left arterial and atrioventricular outlet [15], cardiomyopathy [13], arterial hypertension [18]; RV musculature in chronic pulmonary hypertension of various aetiologies [11] or chronic obstructive pulmonary disease [2].

However, only recent years have resulted in reports of researchers who drew attention to the fact that in the

heart, which is obviously one inseparable whole, there is a possibility of adverse phenomena within the myocardial cavity seemingly unrelated to a given aggravating factor.

Research conducted by Tadic et al. [23–25] has shown a clear correlation between the occurrence of arterial hypertension and remodelling of the RV muscle, which leads to impairment of its function. The above observations were also reflected in the work conducted by Cuspidi et al. [5, 6] and other researchers [3, 26].

Interestingly, changes indicating this remodelling were observed not only in the group of patients with arterial hypertension, but also at earlier stages of the disease [17], and even in the group of patients with arterial blood pressure classified as “normal high” [16, 22].

The above studies were based on *in vivo* echocardiographic assessment of right ventricle morphology and function. Our study seems to partially confirm these observations on the sectional material.

It may be argued that statistically significant changes in the thickness of the free wall of the right heart ventricle do not go hand in hand with evident cardiomyocyte hypertrophy. However, if we take into account the fact that although the thickness of the RV free walls in SG compared to CG was significantly greater, it still remained within the accepted echocardiographic norms (up to 5 mm), exceeding them only at level A.

It can be suspected that in SG the phenomenon occurring in the RV musculature is a result of regulatory and/or compensatory processes occurring in the myocardium as a whole and may be equivalent to physiological hypertrophy observed within the LV muscle in conditions of its increased physiological load (e.g. practicing sports, pregnancy). This thesis is supported by the fact that microscopic examination revealed no evidence of permanent, irreversible remodelling of the RV muscle.

As the authors of this study we are aware of its undoubted limitation of the small size of the groups,

which limits both the possibility of formulating fully convincing conclusions and the effectiveness of statistical methods. Unfortunately, the selection of material originating from people burdened only with hypertension (in order to eliminate other known factors that can lead to muscle remodelling of any of the walls of the heart) and who died of non-cardiovascular causes is an extremely problematic task. Difficulties associated with obtaining this type of selected material is extremely difficult and time-consuming and affected its limited number.

## CONCLUSIONS

Although in vivo echocardiographic tests as well as our macroscopic evaluation of post-mortem material suggest such suspicions, based on the results of the study (primarily the microscopic observations), it was not possible to answer the question of whether the RV muscle remodelling is evident during hypertension. Instead of a simple, unambiguous answer, the question arises: why and how the RV systolic and diastolic function is disturbed, sometimes at a very early stage of the development of arterial hypertensive disease. Confirmation of this requires further research, possibly reaching deeper into the ultrastructure of the cardiomyocyte.

**Conflict of interest:** None declared

## REFERENCES

- Anrep GV, Häusler H. The coronary circulation: I. The effect of changes of the blood-pressure and of the output of the heart. *J Physiol.* 1928; 65(4): 357–373, doi: [10.1113/jphysiol.1928.sp002481](https://doi.org/10.1113/jphysiol.1928.sp002481), indexed in Pubmed: [16993957](https://pubmed.ncbi.nlm.nih.gov/16993957/).
- Biernacki W, Flenley DC, Muir AL, et al. Pulmonary hypertension and right ventricular function in patients with COPD. *Chest.* 1988; 94(6): 1169–1175, doi: [10.1378/chest.94.6.1169](https://doi.org/10.1378/chest.94.6.1169), indexed in Pubmed: [3191757](https://pubmed.ncbi.nlm.nih.gov/3191757/).
- Cicala S, Galderisi M, Caso P, et al. Right ventricular diastolic dysfunction in arterial systemic hypertension: analysis by pulsed tissue Doppler. *Eur J Echocardiogr.* 2002; 3(2): 135–142, doi: [10.1053/euje.2001.0124](https://doi.org/10.1053/euje.2001.0124), indexed in Pubmed: [12114098](https://pubmed.ncbi.nlm.nih.gov/12114098/).
- Cohn JN. Structural basis for heart failure. Ventricular remodeling and its pharmacological inhibition. *Circulation.* 1995; 91(10): 2504–2507, doi: [10.1161/01.cir.91.10.2504](https://doi.org/10.1161/01.cir.91.10.2504), indexed in Pubmed: [7743609](https://pubmed.ncbi.nlm.nih.gov/7743609/).
- Cuspidi C, Sampieri L, Angioni L, et al. Right ventricular wall thickness and function in hypertensive patients with and without left ventricular hypertrophy: echo-Doppler study. *J Hypertens Suppl.* 1989; 7(6): S108–S109, doi: [10.1097/00004872-198900076-00050](https://doi.org/10.1097/00004872-198900076-00050), indexed in Pubmed: [2534401](https://pubmed.ncbi.nlm.nih.gov/2534401/).
- Cuspidi C, Valerio C, Sala C, et al. Prevalence and correlates of left atrial enlargement in essential hypertension: role of ventricular geometry and the metabolic syndrome: the Evaluation of Target Organ Damage in Hypertension study. *J Hypertens.* 2005; 23(4): 875–882, doi: [10.1097/01.hjh.0000163158.14493.23](https://doi.org/10.1097/01.hjh.0000163158.14493.23), indexed in Pubmed: [15775794](https://pubmed.ncbi.nlm.nih.gov/15775794/).
- D'Andrea A, Caso P, Scarafile R, et al. Biventricular myocardial adaptation to different training protocols in competitive master athletes. *Int J Cardiol.* 2007; 115(3): 342–349, doi: [10.1016/j.ijcard.2006.03.041](https://doi.org/10.1016/j.ijcard.2006.03.041), indexed in Pubmed: [16959340](https://pubmed.ncbi.nlm.nih.gov/16959340/).
- Dong L, Mintz GS, Witzensbichler B, et al. Comparison of plaque characteristics in narrowings with ST-elevation myocardial infarction (STEMI), non-STEMI/unstable angina pectoris and stable coronary artery disease (from the ADAPT-DES IVUS Substudy). *Am J Cardiol.* 2015; 115(7): 860–866, doi: [10.1016/j.amjcard.2015.01.008](https://doi.org/10.1016/j.amjcard.2015.01.008), indexed in Pubmed: [25661569](https://pubmed.ncbi.nlm.nih.gov/25661569/).
- Franco V. Right ventricular remodeling in pulmonary hypertension. *Heart Fail Clin.* 2012; 8(3): 403–412, doi: [10.1016/j.hfc.2012.04.005](https://doi.org/10.1016/j.hfc.2012.04.005), indexed in Pubmed: [22748902](https://pubmed.ncbi.nlm.nih.gov/22748902/).
- Grajek S. Patofizjologia przebudowy serca. In: Szyszka A (ed.). *Przebudowa serca.* ViaMedica, Gdańsk 2002: 1–30.
- Harrison A, Hatton N, Ryan JJ. The right ventricle under pressure: evaluating the adaptive and maladaptive changes in the right ventricle in pulmonary arterial hypertension using echocardiography (2013 Grover Conference series). *Pulm Circ.* 2015; 5(1): 29–47, doi: [10.1086/679699](https://doi.org/10.1086/679699), indexed in Pubmed: [25992269](https://pubmed.ncbi.nlm.nih.gov/25992269/).
- Kamiński L, Płońska E, Szyszka A, et al. [Echocardiographic examination of cardiac structure and function in male athletes of static and dynamic disciplines]. *Pol Merkur Lek.* 2006; 20(117): 274–278, indexed in Pubmed: [16780253](https://pubmed.ncbi.nlm.nih.gov/16780253/).
- Latus H, Gummel K, Klingel K, et al. Focal myocardial fibrosis assessed by late gadolinium enhancement cardiovascular magnetic resonance in children and adolescents with dilated cardiomyopathy. *J Cardiovasc Magn Reson.* 2015; 17: 34, doi: [10.1186/s12968-015-0142-0](https://doi.org/10.1186/s12968-015-0142-0), indexed in Pubmed: [25976093](https://pubmed.ncbi.nlm.nih.gov/25976093/).
- Limbourg P, Wende W, Henrich H, et al. [Frequency potentiation and Frank-Starling mechanism in canine ventricle under sinus node rhythm and ventricular pacing]. *Pflugers Arch.* 1971; 322(3): 250–263, doi: [10.1007/BF00602073](https://doi.org/10.1007/BF00602073), indexed in Pubmed: [5099687](https://pubmed.ncbi.nlm.nih.gov/5099687/).
- Park JiY, Ryu SK, Choi JW, et al. Association of inflammation, myocardial fibrosis and cardiac remodelling in patients with mild aortic stenosis as assessed by biomarkers and echocardiography. *Clin Exp Pharmacol Physiol.* 2014; 41(3): 185–191, doi: [10.1111/1440-1681.12206](https://doi.org/10.1111/1440-1681.12206), indexed in Pubmed: [24471798](https://pubmed.ncbi.nlm.nih.gov/24471798/).
- Pedrinelli R, Canale ML, Giannini C, et al. Abnormal right ventricular mechanics in early systemic hypertension: a two-dimensional strain imaging study. *Eur J Echocardiogr.* 2010; 11(9): 738–742, doi: [10.1093/ejechoard/jeq059](https://doi.org/10.1093/ejechoard/jeq059), indexed in Pubmed: [20472915](https://pubmed.ncbi.nlm.nih.gov/20472915/).
- Pedrinelli R, Canale ML, Giannini C, et al. Right ventricular dysfunction in early systemic hypertension: a tissue Doppler imaging study in patients with high-normal and mildly increased arterial blood pressure. *J Hypertens.* 2010; 28(3): 615–621, doi: [10.1097/hjh.0b013e328334f181](https://doi.org/10.1097/hjh.0b013e328334f181), indexed in Pubmed: [20191674](https://pubmed.ncbi.nlm.nih.gov/20191674/).
- Puchades R, Ruiz-Nodar JM, Blanco F, et al. An analysis of cardiac remodeling in the elderly population. EPICARDIAN study. *Rev Esp Cardiol.* 2010; 63(8): 989–991, doi: [10.1016/s1885-5857\(10\)70193-6](https://doi.org/10.1016/s1885-5857(10)70193-6), indexed in Pubmed: [20738944](https://pubmed.ncbi.nlm.nih.gov/20738944/).
- Rodrigues JCL, Amadu AM, Dastidar AG, et al. Prevalence and predictors of asymmetric hypertensive heart disease: insights from cardiac and aortic function with cardiovascular magnetic resonance. *Eur Heart J Cardiovasc Imaging.* 2016; 17(12): 1405–1413, doi: [10.1093/ehjci/jev329](https://doi.org/10.1093/ehjci/jev329), indexed in Pubmed: [26705488](https://pubmed.ncbi.nlm.nih.gov/26705488/).
- Schannwell CM, Zimmermann T, Schneppenheim M, et al. Left ventricular hypertrophy and diastolic dysfunction in healthy pregnant women. *Cardiology.* 2002; 97(2): 73–78, doi: [10.1159/000057675](https://doi.org/10.1159/000057675), indexed in Pubmed: [11978952](https://pubmed.ncbi.nlm.nih.gov/11978952/).
- Schuleri KH, Centola M, Evers KS, et al. Cardiovascular magnetic resonance characterization of peri-infarct zone remodeling following myocardial infarction. *J Cardiovasc Magn Reson.* 2012; 14: 24, doi: [10.1186/1532-429X-14-24](https://doi.org/10.1186/1532-429X-14-24), indexed in Pubmed: [22510220](https://pubmed.ncbi.nlm.nih.gov/22510220/).
- Tadic M, Cuspidi C, Pencic B, et al. High-normal blood pressure impacts the right heart mechanics: a three-dimensional echocardiography and two-dimensional speckle tracking imaging study. *Blood Press Monit.* 2014; 19(3): 145–152, doi: [10.1097/MBP.0000000000000043](https://doi.org/10.1097/MBP.0000000000000043), indexed in Pubmed: [24695214](https://pubmed.ncbi.nlm.nih.gov/24695214/).
- Tadic M, Cuspidi C, Pencic B, et al. Relationship between right ventricular remodeling and heart rate variability in arterial hypertension. *J Hypertens.* 2015; 33(5): 1090–1097, doi: [10.1097/HJH.0000000000000511](https://doi.org/10.1097/HJH.0000000000000511), indexed in Pubmed: [25668353](https://pubmed.ncbi.nlm.nih.gov/25668353/).
- Tadic M, Ivanovic B, Celic V, et al. Are the metabolic syndrome, blood pressure pattern, and their interaction responsible for the right ventricular remodeling? *Blood Press Monit.* 2013; 18(4): 195–202, doi: [10.1097/MBP.0b013e3283631af4](https://doi.org/10.1097/MBP.0b013e3283631af4), indexed in Pubmed: [23777905](https://pubmed.ncbi.nlm.nih.gov/23777905/).
- Tadic M, Ivanovic B, Celic V, et al. The impact of metabolic syndrome, recently diagnosed diabetes and hypertension on right ventricular remodeling. Is there difference between risk factors? *Clin Exp Hypertens.* 2014; 36(5): 295–301, doi: [10.3109/10641963.2013.810235](https://doi.org/10.3109/10641963.2013.810235), indexed in Pubmed: [23865506](https://pubmed.ncbi.nlm.nih.gov/23865506/).
- Tumuklu MM, Erkorkmaz U, Ocal A. The impact of hypertension and hypertension-related left ventricle hypertrophy on right ventricle function. *Echocardiography.* 2007; 24(4): 374–384, doi: [10.1111/j.1540-8175.2007.00419.x](https://doi.org/10.1111/j.1540-8175.2007.00419.x), indexed in Pubmed: [17381646](https://pubmed.ncbi.nlm.nih.gov/17381646/).
- Weber KT, Sun Y, Guarda E. Structural remodeling in hypertensive heart disease and the role of hormones. *Hypertension.* 1994; 23(6 Pt 2): 869–877, doi: [10.1161/01.hyp.23.6.869](https://doi.org/10.1161/01.hyp.23.6.869), indexed in Pubmed: [8206620](https://pubmed.ncbi.nlm.nih.gov/8206620/).

# Venous drainage of the heart of the red fox (*Vulpes vulpes*)

Y. Akbulut<sup>1</sup>, G. Kirbař Dođan<sup>1</sup>, İ. Takcı<sup>1</sup>, S. Dalga<sup>1</sup>, E.E. Erkiłiç<sup>2</sup>, E. Uzlu<sup>2</sup>

<sup>1</sup>Department of Anatomy, Faculty of Medicine, Kafkas University, Kars, Turkey

<sup>2</sup>Department of Internal Medicine, Faculty of Veterinary Medicine, University of Kafkas, Kars, Turkey

[Received: 2 January 2021; Accepted: 5 March 2021; Early publication date: 9 April 2021]

**Background:** This study was carried out to reveal the coronary venous system of the red fox (*Vulpes vulpes*) heart. The hearts used in the study were obtained from six red foxes that were brought to the Kafkas University Wildlife Rescue and Rehabilitation Centre after serious injuries due to firearms or traffic accidents and could not be saved despite all interventions.

**Materials and methods:** Latex was injected from the cranial vena cava and caudal vena cava to expose the coronary vasculature. Hearts were photographed after dissection.

**Results:** It was determined that venous drainage of the red fox heart was provided by the great cardiac vein, middle cardiac vein, right cardiac veins, and the smallest cardiac veins. The strongest of these veins was determined to be the paraconal interventricular vein with a diameter of  $3.03 \pm 0.44$  mm. It was determined that the paraconal interventricular vein was accompanied by a strong vein with a diameter of  $2.09 \pm 0.43$  mm in five of six fox hearts examined. It was observed that left atrial oblique vein participated in the formation of the coronary sinus in four hearts, and the great cardiac vein, middle cardiac vein, and the left marginal ventricular vein were seen to be drained into the coronary sinus in the other two hearts. It was determined that the paraconal interventricular vein and middle cardiac vein collected the venous blood of septum interventriculare via septal veins in all hearts.

**Conclusions:** In this study, the smallest cardiac veins were clearly identified for the first time, and the myocardial bridge was revealed in a wild animal for the first time. (Folia Morphol 2022; 81, 2: 343–349)

**Key words:** red fox, cardiac veins, coronary sinus, heart

## INTRODUCTION

The red fox (*Vulpes vulpes*), which is the largest member of the true foxes and the most abundant wild species of the carnivores, can be found across the entire Northern Hemisphere from the Arctic Circle to North Africa, North America, and Eurasia. It is listed

as a least concern species by the International Union for Conservation of Nature [15].

The great cardiac vein, the middle cardiac vein, the right cardiac veins, and the smallest cardiac veins comprise the coronary venous system of the heart, which is the centre of circulatory system. The great

Address for correspondence: Dr. Y. Akbulut, Department of Anatomy, Faculty of Veterinary Medicine, Kafkas University, 36100, Kars, Turkey, e-mail: yalcinakbulut@kafkas.edu.tr

This article is available in open access under Creative Common Attribution-Non-Commercial-No Derivatives 4.0 International (CC BY-NC-ND 4.0) license, allowing to download articles and share them with others as long as they credit the authors and the publisher, but without permission to change them in any way or use them commercially.

cardiac vein, which collects the venous blood from the auricular surface, reaches the coronary sinus (CS) as the paraconal interventricular vein in the paraconal interventricular groove and the left circumflex vein in the coronary groove [10–12]. The middle cardiac vein in the subsinuosal interventricular groove on the atrial surface of the heart rises to the base from the apex of the heart along with the interventricularis subsinuosal artery, and opens to the CS. The CS is dilated at the terminal end of the great coronary vein. It is approximately 2 cm and 5 to 8 mm in diameter. The CS opens into the right atrium ventral to the termination of the caudal vena cava. The great cardiac vein and middle cardiac vein terminate at the CS, which is constituted by the great cardiac vein. Although the origin of the right cardiac veins varies considerably, they usually open directly into the right atrium. The smallest cardiac veins are found in all parts of the heart, and these veins carry more venous blood to the right atrium and the right ventricle [8, 10–12, 17].

There have been several studies concerning venous circulation of the heart in different animal species [4, 9, 14, 23]. However, there have been no studies concerning this topic in the red fox. The aim of this study was to describe the venous system of the red fox heart. We think this first study on the red fox heart could be a reference for future anatomical studies on the veins of domestic or wild carnivorous animal hearts.

## MATERIALS AND METHODS

Conditional permission was obtained from the Kafkas University Animal Experiments Local Ethics Committee (KAU-HADYEK/2018-028, Kars, Turkey) to conduct this study. With this conditional permission, an application was submitted to the Ministry of Agriculture and Forestry, General Directorate of Nature Conservation and National Parks. This study was approved (21264211-288.04-2575700/05.09.2018). Perfusion was performed under general anaesthesia. For premedication xylazine (Rompun; Bayer, Istanbul, Turkey) was used at a dose of 1 mg/kg. Subsequently, 10 mg/kg cyclohexanol (Ketalar; Parke-Davis, Istanbul, Turkey) were injected to achieve 45 minutes of general anaesthesia. The coronary veins of the hearts were washed with 0.9% saline, and then coloured-latex (ZPK-582-G Educational Scientific Products Ltd. West Sussex, UK) was injected via the caudal and cranial vena cava [5]. Latex-treated (red fabric dyed latex applied to arteries and blue coloured fabric-dyed latex

to veins) hearts were kept at room temperature for 1 day and fixed in 10% formaldehyde for 10 days. Six red fox hearts (3 female and 3 male) of unknown age were used in this study.

The weight of the foxes ranged 7.35–8.68 kg. The hearts were carefully dissected and photographed with a Kodak M320 camera. The diameters of all vessels were measured from where they originated. Electronic digital callipers (BTS, UK) were used to measure the hearts' characteristics. The terminology of this study was based on the *Nomina Anatomica Veterinaria* [13].

## RESULTS

Length and diameter of the CS were measured as  $21.13 \pm 3.55$  mm and  $4.24 \pm 2.41$  mm, respectively. The great cardiac vein, middle cardiac vein and left atrial oblique vein were found to be drained to the CS in four hearts. The great cardiac vein, middle cardiac vein and left marginal ventricular vein were found to be drained to the CS in two hearts, as well (Figs. 1B; 2B). Furthermore, arteries and veins forming the blood circulation of the heart often accompanied each other (Fig. 1A, B).

The great cardiac vein was found started as the paraconal interventricular vein in the incisura apices cordis where paraconal interventricular groove and subsinuosal interventricular groove intersected. Diameter of the paraconal interventricular vein in the paraconal interventricular groove was  $3.03 \pm 0.44$  mm. The paraconal interventricular artery accompanied the great cardiac vein from the starting point (Fig. 1A). In all cases, the vein that drains the majority of the cardiac vein was the great cardiac vein. The great cardiac vein passed over the circumflex branch of the left coronary artery in four specimens (Fig. 1A) and passed under in two specimens. Five to seven collateral branches less than 1 mm in diameter from the right ventricle were drained to paraconal interventricular vein in three hearts (Figs. 1A, 2A, 3B). The left proximal collateral vein with a diameter of  $1.45 \pm 0.60$  mm, the left distal collateral vein with a diameter of  $1.50 \pm 0.51$  mm and 5–10 thin collateral branches below 1 mm in diameter from the left ventricle were drained to paraconal interventricular vein. This result showed that paraconal interventricular vein collected mostly venous blood from the left ventricle. Seven to eleven septal branches were found to be drained to paraconal interventricular vein, as well. In three of the hearts, a strong vein with a diameter of

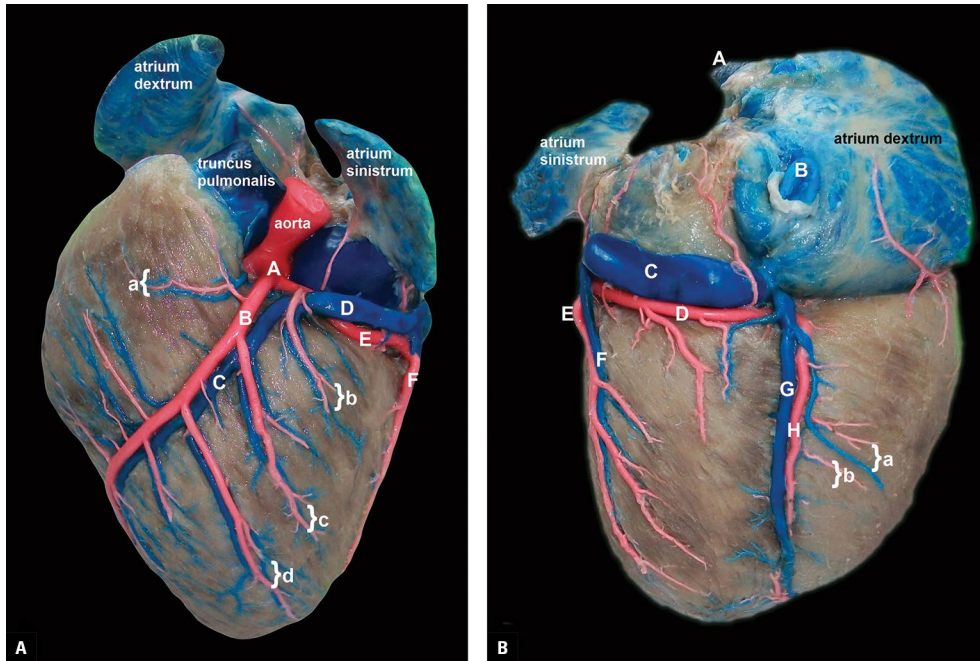


**Figure 1. A.** Cardiac veins and arteries in auricular surface of red fox heart; A — left coronary artery; B — paraconal interventricular artery; C — paraconal interventricular vein; D — left circumflex vein; E — left circumflex artery; F — left marginal ventricular artery; a — left conal vein and artery, b — left proximal ventricular vein and artery, c — left proximal collateral vein and artery, d — left distal collateral vein and artery; **B.** Cardiac veins and arteries in atrial surface of red fox heart; A — cranial vena cava; B — caudal vena cava; C — coronary sinus; D — left circumflex artery; E — left marginal ventricular artery; F — left marginal ventricular vein; G — middle cardiac vein, H — subsinuosal interventricular artery, a — right proximal collateral vein and artery, b — right distal collateral vein and artery.

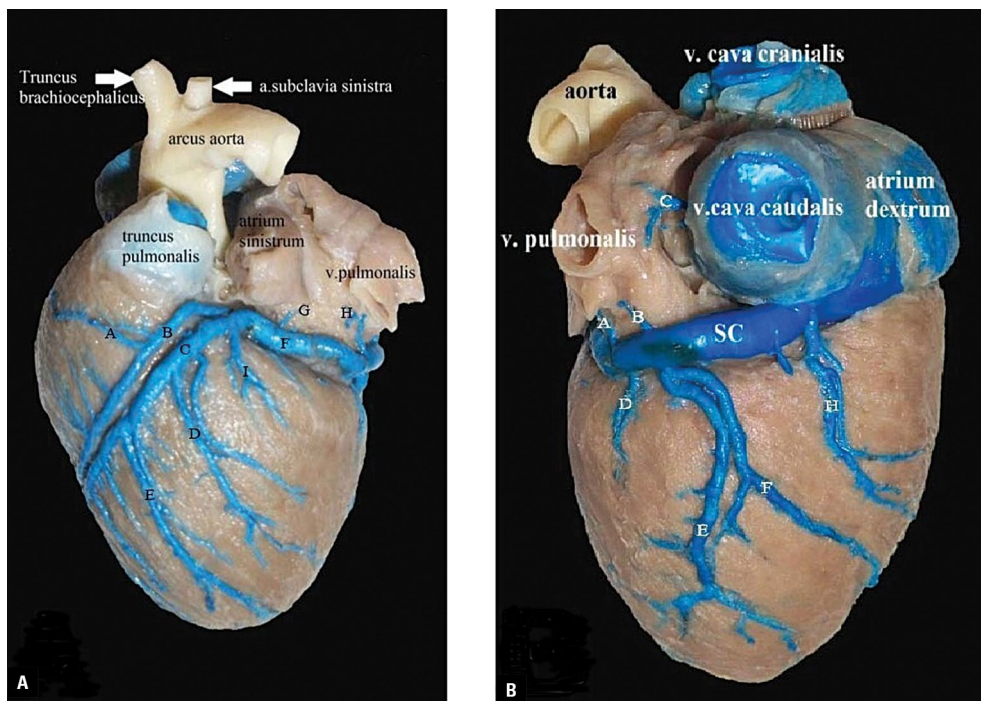


**Figure 2. A.** The great cardiac vein in the red fox; A — left conal vein; B — a strong vein; C — paraconal interventricular vein; D — left collateral proximal vein; E — left collateral distal vein; F — left circumflex vein; G — left atrial proximal vein; H — left atrial oblique vein; I — angular vein; **B.** The middle cardiac vein in the red fox; A — left atrial proximal vein; B — left atrial oblique vein; C — branch opens into the caudal vena cava; D — left proximal ventricular vein; E — left marginal ventricular vein; F — left distal ventricular vein; H — middle cardiac vein; SC — coronary sinus.

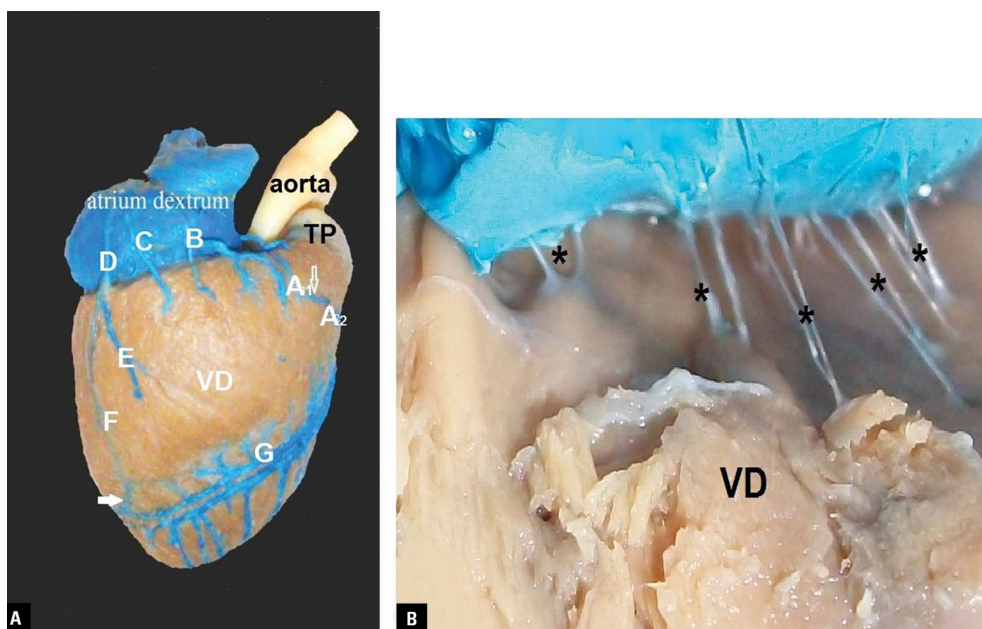


**Figure 3. A.** The right cardiac veins in the right ventricle of red fox heart; A<sub>1,2</sub> — left and right conal vein; B — right proximal ventricular vein; C — right distal ventricular vein; D, E, F — right marginal ventricular vein; G — paraconal interventricular vein; VD — right ventricle; TP — truncus pulmonalis; arrow — anastomosis; **B.** The smallest cardiac veins (\*) in the right ventricle of red fox heart (B); VD — right ventricle.

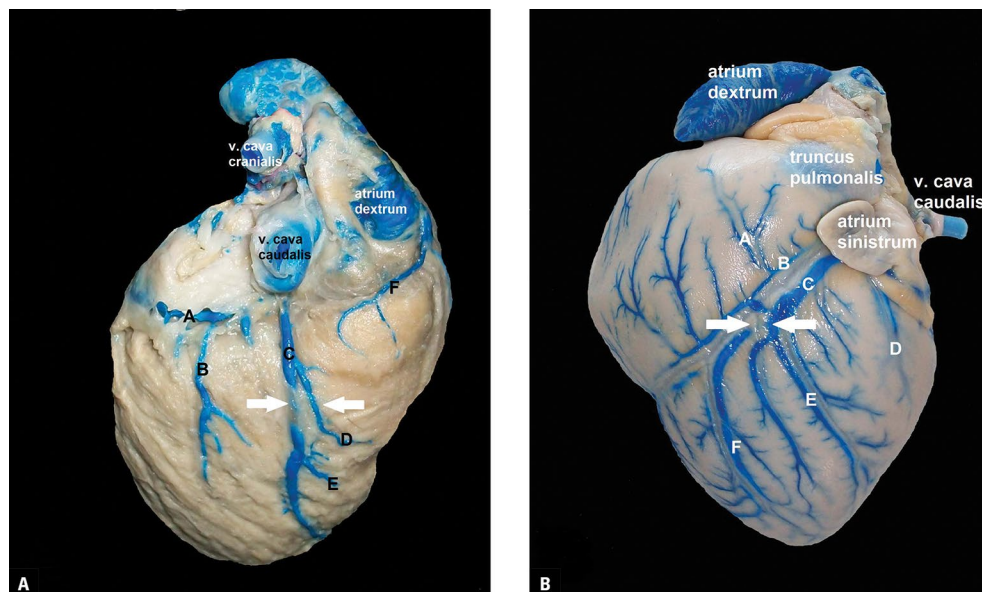


**Figure 4. A.** Myocardial bridge (arrow) on subsinuosal interventricular vein; A — coronary sinus; B — left distal ventricular vein; C — subsinuosal interventricular vein; D — right collateral proximal vein; E — right collateral distal vein; F — right distal ventricular vein; **B.** Myocardial bridge (arrow) on paraconal interventricular vein; A — left conal vein; B — a strong vein; C — paraconal interventricular vein; D — right proximal ventricular vein; E — right collateral proximal vein; F — right collateral distal vein.

2.09 ± 0.43 mm, which was not mentioned in *Nomina Anatomica Veterinaria* [13], which was parallel to the paraconal interventricular vein was found. This strong vein only collected venous blood from the right ventricle. The diameter of paraconal interventricular

vein decreased to 3.13 ± 0.05 mm in hearts with this strong vein (Figs. 2A, 3A, 4B). The great cardiac vein continued as a left circumflex vein with a diameter of 3.51 ± 0.09 mm in the coronary groove and ended by draining to the CS. In the coronary groove of the

left circumflex vein,  $1.21 \pm 0.12$  mm diameter left atrial oblique vein and 2–3 atrial branches smaller than 1 mm in diameter from the left atrium were found to be drained (Fig. 2A, B). In addition, the left distal ventricular vein, left marginal ventricular vein and left proximal ventricular vein drained to left circumflex vein from the upper part of the left ventricle (Figs. 1A, B; 2A, B). In only one heart, the left marginal ventricular vein and left distal ventricular vein were opened with a common root to the left circumflex vein. The diameter of the middle cardiac vein in this heart decreased to 1.87 mm (Fig. 2B). The paraconal interventricular vein was found to be anastomosed with right marginal ventricular vein, right conal vein, right proximal ventricular vein and subsinuosal interventricular vein (Fig. 3A).

The diameter of the left marginal ventricular vein, which collects the venous blood of the upper 1/3 of the atrial side of the heart, was  $1.54 \pm 0.35$  mm. This vein found to be drained to the left circumflex vein in two hearts and to the CS in four hearts. The left marginal ventricular vein did not make an anastomosis with either the great cardiac vein or the middle cardiac vein (Figs. 1B, 2B).

The angular vein, which carries venous blood from the proximal part of the left ventricle, was joined at the point where the paraconal interventricular vein passes into the left circumflex vein (Fig. 3A). Angular vein was absent in two hearts (Fig. 1A).

The middle cardiac vein was determined to be drained to the CS by collecting venous blood from the right ventricle, left ventricle and interventricular septum of the hearts. The middle cardiac vein started as the subsinuosal interventricular vein in the subsinuosal interventricular groove and its diameter was  $2.09 \pm 1.12$  mm. The artery of the same name accompanied the subsinuosal interventricular vein in the groove (Figs. 1B, 2B). The middle cardiac vein was a smaller vein than the great cardiac vein due to the small number of collateral and septal veins pouring into the middle cardiac vein and their small diameters. The diameters of the right distal collateral vein and the right distal collateral vein that drained the subsinuosal interventricular vein were measured as  $1.30 \pm 0.28$  mm and  $1.42 \pm 0.38$  mm, respectively (Figs. 1B, 2B).

The right cardiac veins was found consisted of the right distal ventricular vein, the right marginal ventricular vein, the right proximal ventricular vein, and the right conal vein and drained the venous blood

of upper 2/3 of the right ventricle to the right atrium. The right and left conal veins made anastomosis in all hearts. In three hearts, right marginal ventricular vein was found to be anastomosed with paraconal interventricular vein (Fig. 3A). Among the right cardiac veins, the longest branch was right marginal ventricular vein and the thickest branch was right proximal ventricular vein (Fig. 3A).

Although different sizes of the smallest cardiac veins were detected in the right ventricle and right atrium of the fox hearts, these small veins were not found in other parts of the heart (Fig. 3B). Myocardial bridges were detected, one on the paraconal interventricular vein and the other on the subsinuosal interventricular vein (Fig. 4A, B).

## DISCUSSION

Although there are several studies [2, 3, 16, 19] on the venous systems of the domestic carnivorous animals' hearts, there is only one study on the wild animals [18], which is built on the macroanatomical features of a tiger heart that died in a local ZOO. For the first time, with this study, the veins of the red fox heart were examined extensively.

We determined that the venous drainage of the red fox heart was provided by the great cardiac vein, the middle cardiac vein, the right cardiac veins, and the smallest cardiac veins. These findings are similar to those reported in Van cats [2], domestic cats [3], and dogs [19].

A study conducted by Piffer et al. [19] in adult dogs shows that the CS is mostly a continuation of the great cardiac vein, and it is formed by the great cardiac vein, the middle cardiac vein, the left atrial oblique vein and the left marginal ventricular vein. In our study, it was determined that the left distal ventricular vein participates in the formation of the CS in a heart in addition to the aforementioned veins. Unlike the Tuj sheep [4] and Roe deer [14], we determined that the left atrial oblique vein participated in the formation of the CS in the red fox.

The great cardiac vein was identified as the longest cardiac vein, as reported in the literature [2, 3], and the names were given according to the grooves it lies in. Similar to the Van cat [2], the red fox had a strong vein running parallel to the great cardiac vein, and this vein changed its dimensions due to the interventricular paraconal artery.

In our study, we found that the great cardiac vein passed over the circumflex branch of the left coronary

artery in four hearts and passed under in two of the hearts. However, Maric et al. [16] reported that the great cardiac vein in both humans and dogs reaches the coronary groove, and the greatest cardiac vein crosses over the circumflex branch of the coronary artery (65% in humans and 95% in canines), or passed under the left coronary artery (12.5% in humans and 2.5% in canines) or the circumflex branch (22.5% in humans and 2.5% in canines).

The great cardiac vein opened directly to the end of the coronary groove, and the venous blood of the interventricular septum together with the great cardiac vein were findings consistent with the literatures [2, 3, 16, 19]. An anastomosis between the paraconal interventricular vein and the subsinuosal interventricular vein has been identified in domestic cats [3] and dogs [19], whereas no anastomosis was observed between the two veins or conal veins in the Van cat [2]. However, in our study, an anastomosis was detected between the paraconal interventricular vein and the subsinuosal interventricular vein, and between the paraconal interventricular vein and the right marginal ventricular vein and amongst the conal veins.

Nickel et al. [17] have reported that, except for the right conal vein, other veins formed the right cardiac vein opening into the right atrium either directly or via a common vessel in cats. Aksoy et al. [2] found that the right cardiac veins opened to the right atrium with a common root in three of six materials in Van cats, whereas the right conical vein, the right proximal ventricular vein, the right marginal ventricular vein, and the right distal ventricular vein formed the right semicircumflex vein. Contrary to this information, we did not find any vein similar to the right semicircumflex vein. In our study, we determined that the right cardiac veins directly opened to the right atrium separately.

Besoluk and Tipirdamaz [6] reported that the smallest cardiac veins are available in all parts of the heart except the left ventricle in the Angora goat, while it is available only in the right atrium and right ventricle in the Akkaraman sheep. Kabak and Onuk [14] have stated that the Roe deer only had the right atrium and right ventricle of the heart. The distributions of the smallest cardiac veins in the red fox are consistent with the findings of the Akkaraman sheep [6] and the Roe deer [14].

Dursun et al. [7] investigated the dog hearts and reported the existence of myocardial bridges at intervals on the atrial and auricular surfaces. In our study,

only one myocardial bridge was observed on these surfaces. The myocardial bridge has been reported to occur in a range of 75–100%, especially in ruminants [1, 20–22], but this rate was found only 33% in our study. Accordingly, it can be argued that some disorders related to the myocardial bridges, including death, are unlikely to be seen in the red fox.

## CONCLUSIONS

To summarise, this is the first study that clearly demonstrates the configuration of the cardiac vessels of the red fox and compares them with the cardiac vessels of the other carnivores. The myocardial bridge was found for the first time in a wild animal with this study. Studies exhibiting the macroanatomical structures of the vessels of the red fox hearts can be extended and thus the emerged findings may contribute to future venous studies of other wildlife.

**Conflict of interest:** None declared

## REFERENCES

1. Akbulut Y, Demiraslan Y, Aslan K, et al. The Coronary Arteries and Myocardial Bridges in Zavot-Breed Cattle. *Kafkas Univ Vet Fak Derg.* 2014; 20: 287–293, doi: [10.9775/kvfd.2013.10066](https://doi.org/10.9775/kvfd.2013.10066).
2. Aksoy G, Karadag H, Ozudogru Z. Morphology of the venous system of the heart in the van cat. *Anat Histol Embryol.* 2003; 32(3): 129–133, doi: [10.1046/j.1439-0264.2003.00444.x](https://doi.org/10.1046/j.1439-0264.2003.00444.x), indexed in Pubmed: [12823097](https://pubmed.ncbi.nlm.nih.gov/12823097/).
3. Aksoy G, Karadag H, Soyguder Z. A macroanatomic investigation on the cardiac veins in the domestic cat. *J Health Sci Univ Firat.* 2001; 15: 315–324.
4. Aksoy G, Ozmen E, Kurtul İ, et al. The Venous Drainage of the Heart in the Tuj Sheep. *Kafkas Univ Vet Fak Derg.* 2009; 15: 279–286, doi: [10.9775/kvfd.2009.015-a](https://doi.org/10.9775/kvfd.2009.015-a).
5. Aycan K, Bilge A. The investigation on the vascular system anatomy using plastic injection and corrosion method. *J Faculty Med Univ Erciyes.* 1984; 6: 545–552.
6. Besoluk K, Tipirdamaz S. Comparative macroanatomic investigations of the venous drainage of the heart in Akkaraman sheep and Angora goats. *Anat Histol Embryol.* 2001; 30(4): 249–252, doi: [10.1046/j.1439-0264.2001.00327.x](https://doi.org/10.1046/j.1439-0264.2001.00327.x), indexed in Pubmed: [11534331](https://pubmed.ncbi.nlm.nih.gov/11534331/).
7. Dursun N, Asti NR, Tipirdamaz S, et al. Macroscopic and microscopic investigations on the myocardial bridges in domestic animals. *S U Vet Fak Derg.* 1992; 8: 12–17.
8. Dursun N. *Veteriner Anatomi.* 12th ed. Medisan, Ankara, Turkey 2008.
9. Esperança Pina JA, Correia M, O'Neill JG, et al. Morphology of the veins draining the coronary sinus of the dog. *Acta Anat (Basel).* 1981; 109(2): 122–128, doi: [10.1159/000145374](https://doi.org/10.1159/000145374), indexed in Pubmed: [7018158](https://pubmed.ncbi.nlm.nih.gov/7018158/).
10. Evans HE. *Miller's anatomy of the dog.* 3rd ed. Saunders, Philadelphia, PA, USA 1993.

11. Ghoshal NG. Carnivore heart and arteries. In: Sisson and Grossman's the Anatomy of the Domestic Animals, 5th ed., Philadelphia and London 1975.
12. Ghoshal NG, Koch T, Popesko P. The venous drainage of the domestic animals. Saunders, Philadelphia 1981.
13. International Committee on Veterinary Gross Anatomical Nomenclature. Nomina Anatomica Veterinaria (NAV), 5th ed, World Association of Veterinary Anatomists, Hannover, Columbia, Gent, Sapporo, 2005.
14. Kabak M, Onuk B. Macroanatomic Investigations on the Venous Drainage of the Heart in Roe Deer (*Capreolus capreolus*). Kafkas Univ Vet Fak Derg. 2012; 18: 957–963, doi: [10.9775/kvfd.2012.6841](https://doi.org/10.9775/kvfd.2012.6841).
15. Macdonald DW, Reynolds JC. *Vulpes vulpes*. International Union for Conservation of Nature Red List of Threatened Species. 2008, doi: [10.2305/iucn.uk.2008.rlts.t23062a9412884.en](https://doi.org/10.2305/iucn.uk.2008.rlts.t23062a9412884.en).
16. Marić I, Bobinac D, Ostojić L, et al. Tributaries of the human and canine coronary sinus. Acta Anat (Basel). 1996; 156(1): 61–69, indexed in Pubmed: [8960300](https://pubmed.ncbi.nlm.nih.gov/8960300/).
17. Nickel R, Schummer A, Seiferle E. The anatomy of the domestic animals. Vol. 3: The circulatory system, the skin, and the cutaneous organs of domestic mammals. Verlag Paul Parey, Berlin, Germany 1981.
18. Perez W, Lima M. Brief description of the cardiac anatomy in a tiger (*Panthera tigris*, Linnaeus, 1758): a case report. Veterinárni Medicína. 2008; 52(No. 2): 83–86, doi: [10.17221/2054-vetmed](https://doi.org/10.17221/2054-vetmed).
19. Piffer CR, Piffer MI, Santi FP, et al. Anatomic observations of the coronary sinus in the dog (*Canis familiaris*). Anat Histol Embryol. 1994; 23(4): 301–308, doi: [10.1111/j.1439-0264.1994.tb00479.x](https://doi.org/10.1111/j.1439-0264.1994.tb00479.x), indexed in Pubmed: [7887481](https://pubmed.ncbi.nlm.nih.gov/7887481/).
20. Santos JW, Bombonato PP, Beletti ME, et al. Carneiro e Silva FO. Myocardial bridges in the bovine of Conchim race. Braz J Vet Res Anim Sci. 2000; 37: 35–43.
21. Severino RS, Bombonato PP. Occurrence of myocardial bridges in Gir, Guzera, Nelore and Indubrasil bovines. Braz J Vet Res Anim Sci. 1992; 29: 15–30.
22. Shinjo SK, Oba-Shinjo SM, Prates NE. Bovine myocardial bridge morphology and association with coronary atherosclerosis. Braz J Morphol Sci. 2004; 21: 95–98.
23. Yadm ZA. Origin, course and distribution of the venae cordis in the donkey. (*Equus asinus*). Assiut Vet Med J. 1993; 28.2(56): 15–26, doi: [10.21608/avmj.1993.186369](https://doi.org/10.21608/avmj.1993.186369).

# The evaluation of morphology of renal pelvicalyceal system's and infundibulopelvic anatomy of kidney's lower pole in post-mortem series

R. Çiçek<sup>1</sup>, G. Dünder<sup>2</sup>, K. Gökçen<sup>3</sup>, G. Gökçe<sup>4</sup>, E.Y. Gültekin<sup>4</sup>

<sup>1</sup>Department of Urology, Malatya Training and Research Hospital, Malatya, Turkey

<sup>2</sup>Department of Urology, University of Health Sciences, Bursa Yuksek Ihtisas Training and Research Hospital, Bursa, Turkey

<sup>3</sup>Department of Urology, Bahçeşehir University, Medical Park Göztepe Hospital, Istanbul, Turkey

<sup>4</sup>Department of Urology, Cumhuriyet University, Faculty of Medicine, Sivas, Turkey

[Received: 11 March 2021; Accepted: 28 March 2021; Early publication date: 13 April 2021]

**Background:** Urinary system stones are frequently encountered in the community. Together with technological developments, introduction of new treatment procedures such as extracorporeal shock wave lithotripsy, percutaneous nephrolithotomy and retrograde intrarenal surgery has further reduced morbidity, mortality and hospitalisation time of patients. In order to maximise success and to reduce complications of these procedures, it is necessary to evaluate anatomy and morphological differences of kidney collector system before the procedure. This study was conducted for the purpose of determining the morphology of the kidney collector system and the negative anatomic factors of the lower pole in autopsy cases performed in our institution.

**Materials and methods:** Eighty two kidney units obtained from 41 autopsy cases conducted in Faculty of Medicine Department of Forensic Medicine, Sivas Cumhuriyet University between September 2017 and September 2018 were included in the study. Percentages were found as 78% for intrarenal pelvis, 13.4% for borderline pelvis, 6.1% for extrarenal pelvis and 2.4% for pelvic nonexistence. When pelvicalyceal anatomy was evaluated, percentages were found as 32.9% for bicalyceal, 26.8% for tricalyceal, 20.7% for multicalyceal, and 19.5% for unclassified calyceality. When it was evaluated according to opening of calyces into the renal pelvis based on Sampaio classification, percentages were found as 30.5% for AI, 17.1% for type II, 28% for BI, 18.3% for BII, and 6.1% for unevaluated part. Infundibular lengths of kidney's lower pole were detected as under 3 cm in 39% and over 3 cm in 61% of all cases. Infundibulopelvic angles of kidney's lower pole were measured as under 70° in 42.7% and over 70° in 57.3% of all cases.

**Results:** In our study, there was no statistically significant difference between the right and left kidneys in terms of collecting system morphology and lower pole's negative anatomical factors. Only infundibular length which is one of the collecting system morphology and lower pole's negative anatomical factors were statistically shorter in females than males. There was no difference in terms of other parameters.

Address for correspondence: Dr. G. Dünder, Department of Urology, University of Health Sciences, Bursa Yuksek Ihtisas Training and Research Hospital, Bursa, Turkey, tel: +90 5052464648, e-mail: dr@gokcedundar.com

The institution where the work was conducted: Cumhuriyet University, Faculty of Medicine, Sivas, Turkey.

This article is available in open access under Creative Common Attribution-Non-Commercial-No Derivatives 4.0 International (CC BY-NC-ND 4.0) license, allowing to download articles and share them with others as long as they credit the authors and the publisher, but without permission to change them in any way or use them commercially.

*Conclusions:* In conclusion, the findings of this study are largely consistent with the results of similar studies. This reveals that renal collecting system morphology and negative anatomic factors in the lower pole collecting system in human are roughly similar. In clinical practice, pre-treatment computed tomography and, if necessary, magnetic resonance urography evaluation of the lower pole negative anatomic factors may contribute to gain preliminary information about both the clearance of stone fragments especially after shock wave lithotripsy and retrograde intrarenal surgery procedures and perioperative complications proactively. (*Folia Morphol* 2022; 81, 2: 350–358)

**Key words:** **infundibulopelvic angle, infundibulopelvic anatomy, kidney anatomy, post-mortem morphology, kidney morphology, urology**

## INTRODUCTION

It is known that the intrarenal calyceal system may vary from person to person [19]. So much so that the possibility of both kidneys being symmetrical in the same person is only 37% [26].

Various studies have been carried out from past to present to define the kidney morphology. In a study by Ningthoujam et al. [19], where the renal collecting system was evaluated according to the shape and number of calyces, calyceal structures were discussed in four categories: bicalyceal, tricalyceal, multicalyceal and unclassifiable.

Sampaio and Mandarim-De-Lacerda [26] classified the renal collecting system in four different forms according to the openings of the major calyces. According to this type of classification:

- A1: The collecting system is comprised of the combination of the upper and lower calyx groups, and the middle calyx group opens to either the upper or lower, or both collecting systems;
- All: Similar to type A1, but one or both upper and lower calyx groups open to the middle calyx;
- B1: The middle pole of the kidney opens to the renal pelvis independently;
- BII: The minor calyces of the middle pole of the kidney open to the renal pelvis independently.

In another study, Bruce et al. [4] classified the renal pelvis and divided it into four groups as intrarenal, borderline, extrarenal, and absence of renal pelvis. Although it is believed that this may increase the predisposition to stone formation, since urinary stasis will be greater in the kidneys with extrarenal pelvis, surgical procedures can be performed more easily in collector systems with such morphology [2].

Lifetime risk of stone formation is 20% in adult white males, and 5–10% in females. Lower calyceal

stones constitute 25–35% of the kidney stones [21]. In the treatment of kidney lower pole stones, shock wave lithotripsy (SWL), percutaneous nephrolithotomy (PNL) and retrograde intrarenal surgery (RIRS) methods are used depending on the size [16]. Factors reducing success for SWL are accepted as the stone's resistance to shock waves (calcium oxalate, monohydrate, cystine stones), narrow infundibulopelvic angle, long lower pole calyx, narrow infundibulum, and long distance from the skin to the stone [17]. In recent years, RIRS has become the treatment option especially for stones smaller than 2 cm for which SWL has failed [8]. However, there are not many studies assessing the effect of the anatomical structure of the lower pole of the kidney on the success of the RIRS method for kidney lower pole stones. In a study conducted on this subject, preoperative and postoperative first year data were evaluated via the intravenous urography method, and it was concluded that the infundibulopelvic angle, infundibular length and infundibular width of the lower pole of the kidney, especially the infundibular width of the lower pole of the kidney out of three parameters, played a significant role in the clearance of stone fragments [13].

The current study aimed to reveal the anatomy and differences of the renal collecting system in forensic autopsy cases performed in the Department of Forensic Medicine of Cumhuriyet University Faculty of Medicine and also to specify the frequency of negative factors particularly encountered in the surgery of kidney lower pole stones by measuring the kidney lower pole infundibulopelvic anatomy.

## MATERIALS AND METHODS

Our research was conducted in forensic autopsies at Cumhuriyet University Application and Research

Hospital, Department of Forensic Medicine between September 2017 and September 2018, with the approval of Cumhuriyet University Clinical Research Ethics Committee, dated 11.07.2017 and numbered 2017-07/32. Autopsy cases with previous kidney surgery and trauma history were not included in the study.

The anatomy of the collecting system was photographed and assessed in 82 kidney units obtained from 41 autopsy cases included in the study according to exclusion criteria.

The kidneys and the proximal segment of the ureter of the autopsy cases, whose thorax and abdominal cavity were opened with an incision made from the chin to the pubis, were removed by the autopsy officers. After the kidneys were washed under tap water, an incision was made with a sharp knife in a coronal direction to cover the renal pelvis and ureter, dividing them into two parts. To evaluate the morphology of the pelvicalyceal system and lower infundibulopelvic anatomy, the kidneys lying on a flat surface were photographed in an upright position by placing a measuring ruler next to them.

The photographs were digitally evaluated and grouped according to Bruce et al. [4], Sampaio and Mandarim-De-Lacerda [26] and Ningthoujam et al. [19] classifications in terms of pelvic anatomy (Fig. 1).

Then, the lower calyx infundibulum length and infundibulopelvic angles were measured based on the study by Elbahnasy et al. [6] using the AutoCAD (Version 2016, Autodesk Inc.) programme in digital environment by taking the ruler in the photograph as a reference. The infundibulopelvic angle is the internal angle at the intersection of the ureteropelvic axis and the axis passing through the centre of the lower infundibulum, and the length of the infundibulum was obtained by measuring the distance from the base of the lower calyx group to the lower edge of the renal pelvis. The measurement method is given in Figure 2. Based on a similar study, the infundibulopelvic angle was categorized as above and below 70 degrees, and the infundibulum length value was categorised in centimetres as above and below 3 cm (Fig. 2) [13].

### Statistical analysis

The data obtained in our study were uploaded onto the IBM SPSS Statistics for Windows (Version 24.0, IBM Corp.) software. The majority of the data used in the study consists of categorical data. Chi-

-square analysis was preferred owing to the presence of categorical variables in the evaluation of the data. Cramer's V coefficient was used as a correction factor in  $2 \times 2$   $\chi^2$  analyses. Normal analyses were carried out for other nxm-mesh structures. The confidence level in the tests was considered as 95%.

## RESULTS

The age range of 42 autopsy cases included in the study was 23–75, and the mean age was  $49.34 \pm 16.81$  years. Eleven (26.8%) of the cases were female, 30 (73.2%) were male.

When the pelvicalyceal anatomy of the right and left kidneys were compared according to the classification of Ningthoujam [19], bicalyceal and tricalyceal anatomy was found to be more on the left side and multicalyceal anatomy on the right side; however, the difference was statistically insignificant ( $p = 0.068$ ) [19].

Since no morphological features could be defined that would enable it to be included in any group, Sampaio and Mandarim-De-Lacerda [26] evaluation could not be performed in five of our autopsy cases; therefore, the Sampaio classification was evaluated in 77 kidney units. When the right and left kidneys were compared according to this classification, used for the anatomical classification of the renal collecting system, the difference was found to be statistically insignificant ( $p = 0.559$ ). However, it was discovered that type BI defined by Sampaio and Mandarim-De-Lacerda [26] in his study, in which the middle pole of the kidney opened independently to the renal pelvis, consisted of the combination of the upper and lower calyx groups of the renal collecting system on the left side (34.1%), and that type AI, in which the middle calyx group opened into the upper, lower or both collecting systems, was more on the right side (29.3%).

When the right and left kidneys were compared according to the Bruce classification [4], which evaluated the pelvis morphology, the difference was found to be insignificant ( $p = 0.950$ ). In the current study, the incidence of intrarenal pelvis was found to be 78%, borderline 13.4%, extrarenal pelvis 6.1% and the rate of absence of pelvis was 2.4%. Findings belonging to these classifications are summarised in Table 1.

When the infundibulum lengths of the right and left kidneys in our study were compared as  $< 3$  cm and  $\geq 3$  cm, the difference was found to be insignificant ( $p = 0.651$ ). When the infundibulopelvic angles

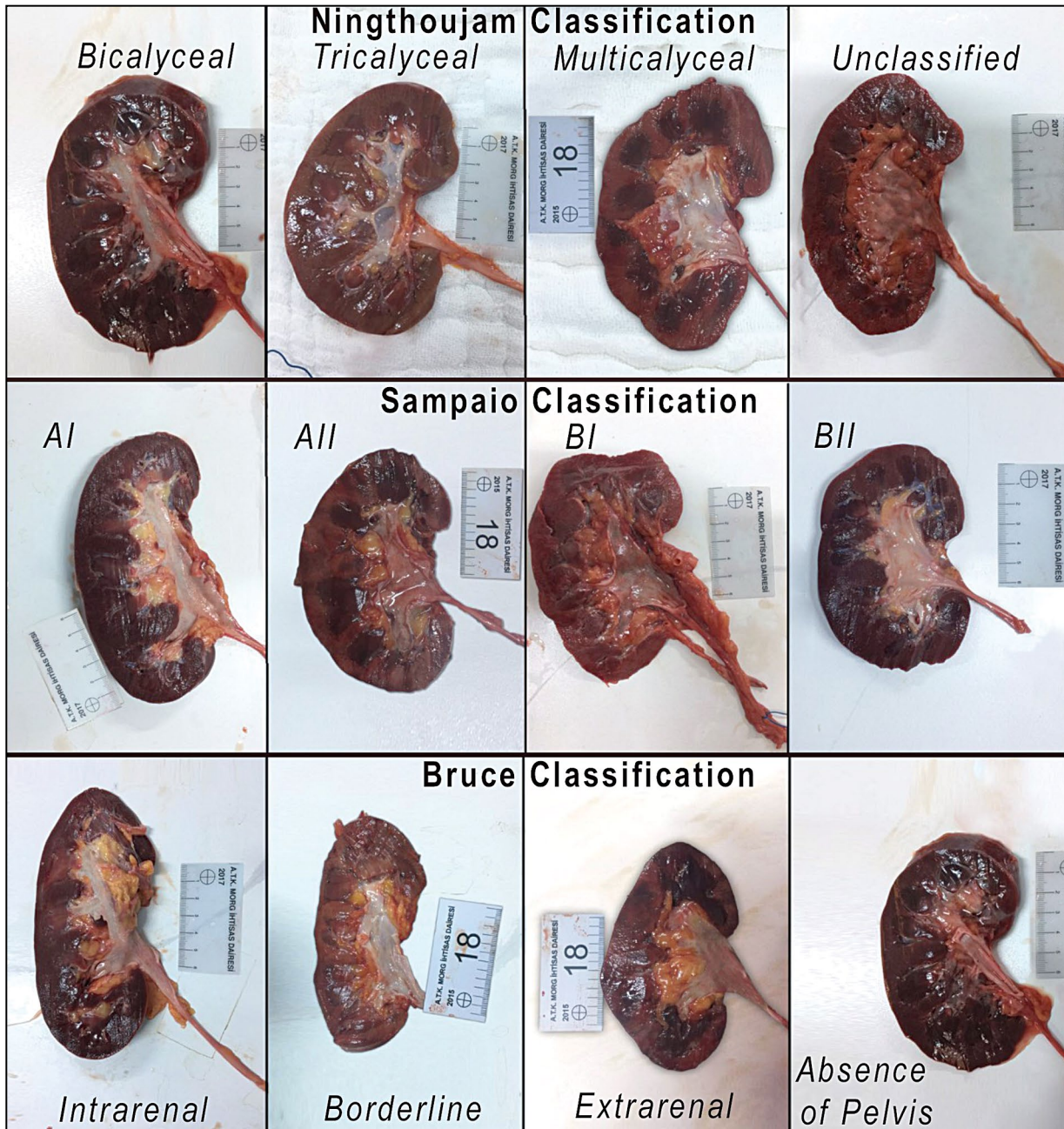


**Figure 1.** Ningthoujam classification, where the shapes and numbers of calyces are evaluated, evaluating the openings of major calyces Sampaio classification, Bruce classification, where the main pelvis morphology is evaluated.

of the right and left kidneys were compared as  $< 70^\circ$  and  $\geq 70^\circ$ , the difference was statistically insignificant ( $p = 0.503$ ) (Table 2).

When the renal collecting system was compared in males and females according to the Ningthoujam classification, the difference was found to be insignificant ( $p = 0.698$ ). However, it was seen that the rate of bicalyceal anatomy was higher in males (35%) and the rate of tricalyceal anatomy was higher in females (36.4%). When the anatomical structure of the renal

collecting system was compared between genders according to the Sampaio classification, no significant difference was observed ( $p = 0.932$ ) When the pelvic morphologies of males and females were compared according to the Bruce classification, the difference was found to be insignificant ( $p = 0.322$ ) (Table 3).

When the infundibular lengths were compared between males and females, it was seen that the infundibular length of less than 3 cm was more frequent in females, and the infundibular length of 3 cm and

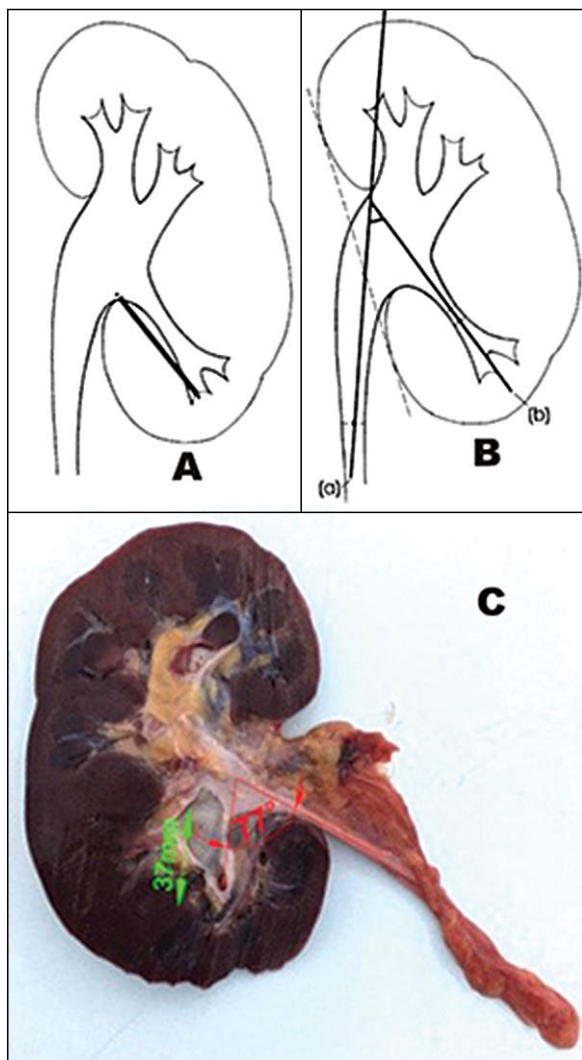


**Figure 2.** Lower calyx infundibulum length (A) and infundibulopelvic angle (B) measurement, measurement image of a kidney in this study (C).

above was more frequent in males ( $p = 0.024$ ). When the infundibulopelvic angles measured in autopsy cases were compared by gender, although infundibulopelvic angles of  $70^\circ$  and above (66.7%) were more frequent in males and below  $70^\circ$  in females (54.5%), there was no statistically significant difference in terms of infundibulopelvic angle according to gender ( $p = 0.081$ ) (Table 4).

## DISCUSSION

In our study, in autopsy cases, infundibular length and infundibulopelvic angle, which are among the pelvicalyceal anatomy and negative anatomical factors of the kidney lower pole, were measured and evaluated.

It has been reported that it would be more accurate to evaluate pelvicalyceal morphology in the cadaver, since superposition of the cross-calyx structures over each other in radiological evaluations may lead to incorrect evaluations [1].

In a study by filling polyester into the collecting system in 140 cadavers, the most common calyceal morphology was reported to be type AI and AII according to their own classification [26]. Similar results were obtained in an analogous study on cadavers [1]. In contrast, another study on 170 kidney units demonstrated that there were more type BI and BII. Even though the numerical difference is not much significant, it was found that the number of type AI and AII was higher in our study, similar to the finding of Sampaio Mandarim-De-Lacerda [26] and Anjana et al. [1] studies (Table 5) [18].

Evaluation of calyx openings according to the Sampaio classification can be important for clinicians. For example, Anjana et al. [1] report that, when endoscopy is attempted with flexible nephroscopy in kidneys with AI type calyceal morphology, the existing anatomy may make it difficult for the device to pass, and also clearing the stone fragments will be easier after SWL in kidneys with type BII morphology where minor calyces open directly to the renal pelvis.

According to the Bruce classification, renal pelvis is divided into four categories as intrarenal, borderline, extrarenal, and absence of renal pelvis. In most studies, same classification is used. In a recent study conducted by Krishnaveni et al. [15] on 44 cadavers, it was reported that the extrarenal pelvis was found at a rate of 31.8%. It has been determined that extrarenal pelvis emerges as a result of the branching of the ureteric bud before reaching the metanephric blastema in the embryological period [22]. When the morphology of the renal pelvis was evaluated in our research, 78% intrarenal, 13.4% borderline, 6.1% extrarenal and 2.4% absence of renal pelvis were observed. Moreover, there was no statistically significant change in the rate of pelvis morphology seen in the right-left kidney ( $p = 0.950$ ).

In a study by Anjana et al. [1], the most common position of the renal pelvis was reported to be intrarenal (79%) according to the Bruce classification, and the extrarenal pelvis and absence of renal pelvis were observed only in the right kidney. In our study, the ratio of right and left difference in renal pelvis morphology is similar to the results of analogical study [9]. Various different figures were reported in studies

**Table 1.** Kidney side — Ningthoujam, Sampaio, and Bruce classification comparison

Ningthoujam classification	Bicalyceal	Tricalyceal	Multicalyceal	Unclassifiable	p	p	
Left	15 (36.6%)	15 (36.6%)	5 (12.2%)	6 (14.6%)	0.031	0.068	
Right	12 (29.3%)	7 (17.1%)	12 (29.3%)	10 (24.4%)	0.652		
Total	27 (32.9%)	22 (26.8%)	17 (20.7%)	16 (19.5%)	0.289		
p	0.564	0.088	0.09	0.317			
Sampaio classification	O*	AI**	AII***	BI****	BI*****	p	p
Left	2 (4.9%)	13 (31.7%)	7 (17.1%)	14 (34.1%)	5 (12.2)	0.011	0.559
Right	3 (7.3%)	12 (29.3%)	7 (17.1%)	9 (22%)	10 (24.4)	0.222	
Total	5 (6.1%)	25 (30.5%)	14 (17.1%)	23 (28%)	15 (18.3)	0.004	
p	0.655	0.841	1	0.297	0.197		
Bruce classification	Intrarenal	Borderline	Extrarenal	Absent	p	p	
Left	33 (80.5%)	5 (12.2%)	2 (4.9%)	1 (2.4%)	< 0.001	0.950	
Right	31 (75.6%)	6 (14.6%)	3 (7.3%)	1 (2.4%)	< 0.001		
Total	64 (78%)	11 (13.4%)	5 (6.1%)	2 (2.4%)	< 0.001		
p	0.803	0.763	0.655	1			

\*O: Those that could not be evaluated.

\*\*AI: The collecting system consists of the combination of the upper and lower calyx groups, and the middle calyx group opens to the upper, lower, or both collecting systems.

\*\*\*AII: Similar to type AI, but one or both of the upper and lower calyx groups open to the middle calyx.

\*\*\*\*BI: The middle pole of the kidney opens to the renal pelvis independently.

\*\*\*\*\*BI: The minor calyces of the middle pole of the kidney open to the renal pelvis independently.

Absent — renal pelvis absence

**Table 2.** Kidney side — infundibulum lengths and infundibulopelvic angle comparison

Infundibulum lengths	< 3 cm	≥ 3 cm	p	p
Left	15 (36.6%)	26 (63.4%)	0.086	0.651
Right	17 (41.5%)	24 (58.5%)	0.274	
Total	32 (39%)	50 (61%)	0.047	
Infundibulopelvic angle	< 70°	≥ 70°	p	p
Left	19 (46.3%)	22 (53.7%)	0.639	0.503
Right	16 (39%)	25 (61%)	0.160	
Total	35 (42.7%)	47 (57.3%)	0.185	

regarding the extrarenal pelvis ratio, and they vary between 5% and 31.8% [1, 3, 9, 15]. In our study, the rate of extrarenal pelvis was found as 6.1% (Table 6).

When collecting systems in 107 kidney units obtained from cadavers were evaluated and it was revealed in a study that 38% of kidneys had bicalyceal, 26% had tricalyceal, 33% had middle pole minor calyces draining into upper and lower major calyces, and in 8%, all minor calyces drained into the renal pelvis without forming a major calyx [7]. Furthermore, the authors also demonstrated that the renal pelvis was generally formed by the combination of two or three major calyces. In another study performed in

2005 by evaluating 100 cadavers (80 fetuses and 20 adults) and 100 selected intravenous urography images in India, the researchers observed 20% bicalyceal, 40% tricalyceal, 30% multicalyceal, and 10% non-evaluable calyceal structure in cadavers, and found 22% bicalyceal, 51% tricalyceal, 15% multicalyceal and 12% non-evaluable calyceal structures in intravenous urography [19]. In this study, it is seen that tricalyceal structure is more frequent in both cadaver kidneys and intravenous urography evaluations. A study reports the bicalyceal, tricalyceal and multicalyceal rates as 27.3%, 20.4% and 52.3%, respectively [15]. In another study on 100 cadaver kidneys, calyceal morphology was reported as 35% bicalyceal, 27% tricalyceal, 23% multicalyceal, and 15% non-evaluable [1].

Even though the rate of multicalyceal structure is reported more often in some studies, it is visible that the bicalyceal type is the most common type in this study, as in the study by Anjana et al. (Table 7) [1].

In parallel with the developments in kidney stone treatment in recent years, the prominence of endoscopic surgery such as SWL, PNL, and RIRS requires a better understanding of the pelvicalyceal anatomy. Negative anatomical factors belonging to both pelvicalyceal morphology and the lower kidney pole

**Table 3.** Gender — Ningthoujam, Sampaio, and Bruce classification comparison

Ningthoujam classification	Bicalyceal	Tricalyceal	Multicalyceal	Unclassifiable	p	p	
Female	6 (27.3%)	8 (36.4%)	4 (18.2%)	4 (18.2%)	0.572	0.698	
Male	21 (35%)	14 (23.3%)	13 (21.7%)	12 (20%)	0.343		
Total	27 (32.9%)	22 (26.8%)	17 (20.7%)	16 (19.5%)	0.289		
Sampaio classification	O*	AI**	AII***	BI****	BI*****	p	p
Female	2 (9.1%)	7 (31.8%)	4 (18.2%)	6 (27.3%)	3 (13.6%)	0.418	0.932
Male	3 (5%)	18 (30%)	10 (16.7%)	17 (28.3%)	12 (20%)	0.016	
Total	5 (6.1%)	25 (30.5%)	14 (17.1%)	23 (28%)	15 (18.3%)	0.004	
Bruce classification	Intrarenal	Borderline	Extrarenal	Absent	p	p	
Female	15 (68.2%)	5 (22.7%)	2 (9.1%)	0 (0%)	0.002	0.322	
Male	49 (81.7%)	6 (10%)	3 (5%)	2 (3.3%)	< 0.001		
Total	64 (78%)	11 (13.4%)	5 (6.1%)	2 (2.4%)	< 0.001		

\*O: Those that could not be evaluated.

\*\*AI: The collecting system consists of the combination of the upper and lower calyx groups, and the middle calyx group opens to either the upper or lower, or both collecting systems.

\*\*\*AII: Similar to type AI, but one or both of the upper and lower calyx groups open to the middle calyx.

\*\*\*\*BI: The middle pole of the kidney opens to the renal pelvis independently.

\*\*\*\*\*BI: The minor calyces of the middle pole of the kidney open to the renal pelvis independently.

Absent — renal pelvis absence

**Table 4.** Gender — infundibulum lengths and infundibulopelvic angle comparison

Infundibulum lengths	< 3 cm	≥ 3 cm	p	p
Female	13 (59.1%)	9 (40.9%)	0.394	0.024*
Male	19 (31.7%)	41 (68%)	0.005	
Total	32 (39%)	50 (61%)	0.047	
Infundibulopelvic angle	< 70°	≥ 70°	p	p
Female	12 (54.5%)	10 (45.5%)	0.670	0.081
Male	20 (33.3%)	40 (66.7%)	0.035	
Total	32 (39.0%)	50 (61%)	0.094	

\*Statistically significant

(infundibulopelvic length, infundibulopelvic angle) affect the clearance of stone fragments after RIRS, PNL and SWL.

Clinically, it is asserted that preoperative evaluation of lower calyceal group anatomy is necessary for optimal treatment of lower calyceal stones with

SWL, PNL and ureteroscopy, and that it is difficult to standardize this evaluation with intravenous urography, and instead, spiral computed tomography is more appropriate today [20].

In a study which evaluated the effect of lower pole calyx anatomy on the clearance of stone fragments after SWL, it was emphasized that the infundibulopelvic angle above 70° and the infundibulum length less than 50 mm had a significant effect on the SWL results [11]. In a similar study, it was reported that factors such as infundibulum length and infundibulopelvic angle significantly influenced stone clearance after SWL, wide infundibulopelvic angle or short and wide infundibulum were positive factors affecting stone clearance independently from the infundibulopelvic angle, and that these factors could be important in ureteroscopy [6]. There are other studies on this subject that gave similar results [24, 28]. Some studies also show that the negative anatomy of the

**Table 5.** Summary of the studies evaluating the opening of the major calyces and our findings

	Number of kidney	AI*	AII**	BI***	BI****	P
Current study	77	32.4%	18.2%	29.9%	19.5%	0.186
Sampaio and Mandarin-De-Lacerda [26]	140	45%	17%	21%	16%	< 0.001
Bruce et al. [4]	170	33.5%	13.5%	34.7%	18.2%	< 0.001
Anjana et al. [1]	100	38%	12%	29%	20%	0.002

\*AI: The collecting system consists of the combination of the upper and lower calyx groups, and the middle calyx group opens to either the upper or lower or both collecting systems.

\*\*AII: Similar to type AI, but one or both of the upper and lower calyx groups open to the middle calyx.

\*\*\*BI: The middle pole of the kidney opens to the renal pelvis independently.

\*\*\*\*BI: The minor calyces of the middle pole of the kidney open to the renal pelvis independently.

**Table 6.** The summary of studies evaluating pelvis morphology and our results

	Number of kidney	Intrarenal	Borderline	Extrarenal	Renal pelvis absence	P
Current study	82	78%	13.5	6.1%	2.4%	< 0.001
Krishnaveni et al. [15]	44	68.18%	–	31.82%	–	0.016
Anjana et al. [1]	100	79%	13%	5%	3%	< 0.001
Gandhi and Chavan [9]	196	48.5%	20.9%	21.9%	8.7%	< 0.001

**Table 7.** The summary of studies evaluating the shapes and numbers of calyces and our results

	Number of kidney	Bicalyceal	Tricalyceal	Multicalyceal	Unclassifiable	P
Current study	82	32.9%	26.8%	20.7%	19.5%	0.289
Anjana et al. [1]	100	35%	27%	23%	15%	0.020
Krishnaveni et al. [15]	44	27.3%	20.4%	52.3%	–	0.025
Ningthoujam et al. [19] (cadaver data)	200	20%	40%	30%	10%	< 0.001

lower calyx has no effect on stone clearance after SWL [5, 25].

A study carried out in our country reported that positive anatomical factors of the kidney lower pole, especially an infundibulopelvic angle above 45°, positively affected the stone clearance after RIRS [23]. In a study, in which the effect of pyelocaliceal anatomy on the success of flexible ureteroscopy was evaluated, when the infundibulopelvic angle was above 90°, the success rate was 87.5%, when between 30–90°, 74.3%, and when below 30°, it was 0% in lower pole calyx stones. The success rate was 88.2% when the infundibular length was less than 3 cm, and 61.1% when longer [10].

A study which investigated the relationship of stone size with infundibulum length, infundibulopelvic angle and infundibular stenosis in patients that underwent RIRS due to lower calyx stones revealed that there was no relationship between stone size and these anatomical features, but infundibulum length and infundibular stenosis make RIRS application difficult [12]. In a study in 2015, it was stressed that infundibulum length, infundibulopelvic angle and stone size did not pose an obstacle to success for RIRS in lower calyx stones, but infundibular width of  $\geq 5$  mm significantly affected this success [13]. In a study which compared the anatomy of the collecting system and the stone-free rate in lower pole stones that underwent RIRS, stone size, long infundibulum and infundibulopelvic angle, below 30° were shown to statistically significantly affect the stone-free rate negatively, whereas the infundibular width did not change it [14].

In a recent similar study conducted in our country, when the infundibulopelvic angle, infundibulum length, infundibular height and stone size were considered, the most important factor affecting the success of RIRS was shown to be the infundibulopelvic angle, and stone size and infundibular height, while not as important as infundibulopelvic angle, were shown to affect RIRS success [27].

## CONCLUSIONS AND RECOMMENDATIONS

The most important result in our study, where the measurements of the collecting system morphologies and lower pole negative anatomical factors were examined in the renal coronal sections of autopsy cases, is that there are more cases with lower pole infundibulum lengths of  $\geq 3$  cm, and this is more common in males.

The results obtained in our study are substantially similar to the results of similar studies conducted both in our country and in different parts of the world. This reveals that the morphology of the renal collecting system in humans and adverse anatomical factors in the lower pole collecting system are found in roughly similar proportions. Thus, in clinical practice, the evaluation of lower pole negative anatomical factors with computed tomography and, if necessary, with magnetic resonance urography before the treatment may not only contribute to obtaining information about both perioperative complications and the clearance of stone fragments especially after SWL and RIRS but also taking measures accordingly.

**Conflict of interest:** None declared

## REFERENCES

- Anjana TSR, Muthian E, Thiagarajan S, et al. Gross morphological study of the renal pelvicalyceal patterns in human cadaveric kidneys. *Indian J Urol.* 2017; 33(1): 36–40, doi: [10.4103/0970-1591.194782](https://doi.org/10.4103/0970-1591.194782), indexed in Pubmed: [28197028](https://pubmed.ncbi.nlm.nih.gov/28197028/).
- Arzoz-Fabregas M, Ibarz-Servio L, Blaco-Casares FJ. Can infundibular height predict the clearance of lower pole stone after extracorporeal shockwave lithotripsy? *J Urol.* 2009; 35: 140–150.
- Brant WE, Helms CA. *Fundamentals of diagnostic radiology.* 4nd ed. Williams & Wilkins, Lippincott 2012: 817–830.
- Bruce SJ, Warmsley R, Ross JA. *The abdominal cavity in manual of surgical anatomy.* 5th ed. E and S Livingstone Ltd., Edinburgh 1967: 391–403.
- Danuser H, Müller R, Descoedres B, et al. Extracorporeal shock wave lithotripsy of lower calyx calculi: how much is treatment outcome influenced by the anatomy of the collecting system? *Eur Urol.* 2007; 52(2): 539–546, doi: [10.1016/j.eururo.2007.03.058](https://doi.org/10.1016/j.eururo.2007.03.058), indexed in Pubmed: [17400366](https://pubmed.ncbi.nlm.nih.gov/17400366/).
- Elbahnasy AM, Shalhav AL, Hoenig DM, et al. Lower caliceal stone clearance after shock wave lithotripsy or ureteroscopy: the impact of lower pole radiographic anatomy. *J Urol.* 1998; 159(3): 676–682, indexed in Pubmed: [9474124](https://pubmed.ncbi.nlm.nih.gov/9474124/).
- Fine J, Ken EN. The arteries of the human kidney. *J Anat.* 1966; 100: 881–894.
- Fuchs AM, Fuchs GJ. Retrograde intra-renal surgery for calculus disease: new minimally invasive treatment approach. *J Endourol.* 1990; 4: 337–345.
- Gandhi KR, Chavan S. Revisiting the morphology of pelvicalyceal system in human cadaveric kidneys with a systematic review of literature. *Asian J Urol.* 2019; 6(3): 249–255, doi: [10.1016/j.ajur.2018.12.006](https://doi.org/10.1016/j.ajur.2018.12.006), indexed in Pubmed: [31297316](https://pubmed.ncbi.nlm.nih.gov/31297316/).
- Geavlete P, Multescu R, Geavlete B. Influence of pyelocaliceal anatomy on the success of flexible ureteroscopic approach. *J Endourol.* 2008; 22(10): 2235–2239, doi: [10.1089/end.2008.9719](https://doi.org/10.1089/end.2008.9719), indexed in Pubmed: [18937587](https://pubmed.ncbi.nlm.nih.gov/18937587/).
- Ghoneim IA, Ziada AM, Elkatib SE. Predictive factors of lower caliceal stone clearance after extracorporeal shock wave lithotripsy (ESWL): A focus on infundibulopelvic anatomy. *Eur Urol.* 2005; 48: 296–302.
- Grasso M, Ficazzola M. Retrograde ureteropyeloscopy for lower pole caliceal calculi. *J Urol.* 1999; 162(6): 1904–1908, doi: [10.1016/s0022-5347\(05\)68065-2](https://doi.org/10.1016/s0022-5347(05)68065-2), indexed in Pubmed: [10569534](https://pubmed.ncbi.nlm.nih.gov/10569534/).
- Hakan K, Yurdaer K, Yakup K, et al. Unfavorable anatomical factors influencing the success of retrograde intra-renal surgery for lower pole renal calculi. *Urology J.* 2015; 12: 2065–2066.
- Jessen JP, Honeck P, Knoll T, et al. Flexible ureterorenoscopy for lower pole stones: influence of the collecting system's anatomy. *J Endourol.* 2014; 28(2): 146–151, doi: [10.1089/end.2013.0401](https://doi.org/10.1089/end.2013.0401), indexed in Pubmed: [24083332](https://pubmed.ncbi.nlm.nih.gov/24083332/).
- Krishnaveni C, Kulkarni R, Kishore Kumar BN. A study of renal calyces by using barium contrast. *Int J Anat Res.* 2014; 2: 369–374.
- Lingerman JE, Matlaga BR, Evan AP. *Surgical management of upper urinary tract calculi.* Wein AJ, Kavoussi LR, Nowick AC, Partin AW, Peters CA (Eds), *Campbell-Walsh Urology.* 10th ed. Elsevier Saunders, Philadelphia 2012: 1431–1507.
- Manikandan R, Gall Z, Gunendran T, et al. Do anatomic factors pose a significant risk in the formation of lower pole stones? *Urology.* 2007; 69(4): 620–624, doi: [10.1016/j.urology.2007.01.005](https://doi.org/10.1016/j.urology.2007.01.005), indexed in Pubmed: [17445636](https://pubmed.ncbi.nlm.nih.gov/17445636/).
- Marroig B, Favorito LA, Fortes MA. Lower pole anatomy and mid-renal-zone classification applied to flexible ureteroscopy: experimental study using human three-dimensional endocasts. *Surg Radiol Anat.* 2015; 37: 1243–1249.
- Ningthoujam DD, Chongtham RD, Sinam SS. Pelvi-calyceal pattern in foetal and adult human kidneys. *J Anat Soc India.* 2005; 54: 1–11.
- Pace KT, Weir MJ, Harju M, et al. Individual patient variation and inter-rater reliability of lower calyceal infundibular width on routine intravenous pyelography. *BJU Int.* 2003; 92(6): 607–609, doi: [10.1046/j.1464-410x.2003.04452.x](https://doi.org/10.1046/j.1464-410x.2003.04452.x), indexed in Pubmed: [14511044](https://pubmed.ncbi.nlm.nih.gov/14511044/).
- Pearle MS, Lotan Y. Urinary lithiasis, etiology, epidemiology, and pathogenesis. In Wein AJ (Ed). *Campbell-Walsh Urology.* 10th ed. Elsevier Saunders, Philadelphia 2012: 1257–1287.
- Pollack HM, McClennan BL. *Clinical Urography.* 2nd ed. Vol. 1. W.B. Saunders Company, Philadelphia 2000: 764–892.
- Resorlu B, Oguz U, Resorlu EB, et al. The impact of pelvicaliceal anatomy on the success of retrograde intrarenal surgery in patients with lower pole renal stones. *Urology.* 2012; 79(1): 61–66, doi: [10.1016/j.urology.2011.06.031](https://doi.org/10.1016/j.urology.2011.06.031), indexed in Pubmed: [21855968](https://pubmed.ncbi.nlm.nih.gov/21855968/).
- Ruggera L, Beltrami P, Ballario R, et al. Impact of anatomical pielocaliceal topography in the treatment of renal lower calyces stones with extracorporeal shock wave lithotripsy. *Int J Urol.* 2005; 12(6): 525–532, doi: [10.1111/j.1442-2042.2005.01101.x](https://doi.org/10.1111/j.1442-2042.2005.01101.x), indexed in Pubmed: [15985072](https://pubmed.ncbi.nlm.nih.gov/15985072/).
- Sahinkanat T, Ekerbicer H, Onal B, et al. Evaluation of the effects of relationships between main spatial lower pole calyceal anatomic factors on the success of shock-wave lithotripsy in patients with lower pole kidney stones. *Urology.* 2008; 71(5): 801–805, doi: [10.1016/j.urology.2007.11.052](https://doi.org/10.1016/j.urology.2007.11.052), indexed in Pubmed: [18279941](https://pubmed.ncbi.nlm.nih.gov/18279941/).
- Sampaio FJ, Mandarim-De-Lacerda CA. Anatomic classification of the kidney collecting system for endourologic procedures. *J Endourol.* 1988; 2(3): 247–251, doi: [10.1089/end.1988.2.247](https://doi.org/10.1089/end.1988.2.247).
- Sari S, Ozok HU, Topaloglu H, et al. The association of a number of anatomical factors with the success of retrograde intrarenal surgery in lower calyceal stones. *Urol J.* 2017; 14(4): 4008–4014, indexed in Pubmed: [28670667](https://pubmed.ncbi.nlm.nih.gov/28670667/).
- Sumino Y, Mimata H, Tasaki Y, et al. Predictors of lower pole renal stone clearance after extracorporeal shock wave lithotripsy. *J Urol.* 2002; 168(4 Pt 1): 1344–1347, doi: [10.1097/01.ju.0000025513.35145.28](https://doi.org/10.1097/01.ju.0000025513.35145.28), indexed in Pubmed: [12352389](https://pubmed.ncbi.nlm.nih.gov/12352389/).

# Anatomical variations of the hepatic artery: a closer view of rare unclassified variants

A. Imam<sup>1</sup> , C. Karatas<sup>1</sup>, N. Mecit<sup>1</sup>, A. Durur Karakaya<sup>2</sup>, T. Yildirimoglu<sup>1</sup>, M. Kalayoglu<sup>1</sup>, T. Kanmaz<sup>1</sup>

<sup>1</sup>Liver Transplantation Department, Koc University Hospital, Istanbul, Turkey

<sup>2</sup>Radiology Department, Koc University Hospital, Istanbul, Turkey

[Received: 21 August 2020; Accepted: 1 February 2021; Early publication date: 1 March 2021]

**Background:** Defining the hepatic artery anatomy is of great importance for both surgeons and radiologists. Michel classification was designed to classify hepatic artery variations. Nevertheless, there are variations that do not fit into this classification. In this study, we aim to define the incidence of all variations in a healthy liver donor by reviewing their computed tomography (CT) scan with special emphasis on variations that do not fit in any of the Michel classes.

**Materials and methods:** A retrospective analysis of CT scan of donors and potential liver donors who were evaluated by triphasic CT scan. The CT scans were reviewed independently by a radiologist and two transplant surgeons. Cases that did not fit in any of the Michel classes were classified as class 0.

**Results:** Out of 241 donors, 210 were classified within the Michel classification, of which 60.9% were class I and 9.1% class II. Thirty-one (12.9%) donors classified as class 0. Of which, nine, three, two and three had replaced right hepatic artery from pancreaticoduodenal artery, gastroduodenal artery, aorta and coeliac artery, respectively. Two and six donors had accessory right hepatic artery from pancreaticoduodenal artery and gastroduodenal artery, respectively. Segment 4 artery originated from left and right hepatic artery in 56.8% and 31.9%, respectively.

**Conclusions:** A great caution should be taken when evaluating the hepatic artery anatomy, clinicians should anticipate and be familiar with the rare unclassified variations of the hepatic artery. (Folia Morphol 2022; 81, 2: 359–364)

**Key words:** anatomical variations, computed tomography, hepatic artery, replaced right hepatic artery, gastroduodenal artery, pancreaticoduodenal artery

## INTRODUCTION

The anatomical variation of the coeliac trunk and its branches may affect the surgical approach of several organs such as stomach, duodenum, pancreas, gallbladder and most importantly the liver [16]. Hepatic artery variations were described in 55% of cadavers by Michel [see 5].

In 1995, Michel classification was established, with 10 different classes that described the hepatic artery anatomy and its variations [11]. These variations are of great importance for the transplant, laparoscopic, hepatobiliary, trauma surgeons and interventional radiologists [1, 13]. There are several reports in the literature regarding hepatic artery variations that do not fit in Michel classification [3, 6, 8, 10].

Address for correspondence: A. Imam, MD, Topkapı, Koç Üniversitesi Hastanesi, Davutpaşa Cd. No:4, Zeytinburnu/İstanbul, 34010, Turkey, tel: +90 850 250 8 250, fax: +90 212 311 34 10, e-mail: ash\_imam04@hotmail.com

This article is available in open access under Creative Common Attribution-Non-Commercial-No Derivatives 4.0 International (CC BY-NC-ND 4.0) license, allowing to download articles and share them with others as long as they credit the authors and the publisher, but without permission to change them in any way or use them commercially.

**Table 1.** The distribution of cases in each class of Michel classification and the segment 4 artery origin in each class

	Class										
	I	II	III	IV	V	VI	VII	VIII	IX	X	0*
<b>Number</b>	<b>147</b>	<b>22</b>	<b>18</b>	<b>1</b>	<b>11</b>	<b>1</b>	<b>1</b>	<b>7</b>	<b>2</b>	<b>0</b>	<b>31</b>
S4 artery — RHA	50	13	1	0	6	1	1	1	0	0	4
S4 artery — LHA	84	7	17	1	5	0	0	5	2	0	16
S4 artery — PHA	0	1	0	0	0	0	0	0	0	0	1
S4 artery — Coeliac	0	0	0	0	0	0	0	0	0	0	4
S4 artery not seen	11	1	0	0	0	0	0	1	0	0	6
Other S4 artery	L and R S4 artery	0	0	0	0	0	0	0	0	0	AS4-GDA

\*The cases that did not fit in any of the Michel classes. S4 artery — segment 4 hepatic artery; RHA — right hepatic artery; LHA — left hepatic artery; PHA — proper hepatic artery; L — left; R — right; AS4 — accessory segment 4 artery; GDA — gastroduodenal artery

In this article, we describe the anatomical variation of the hepatic artery of donors and potential liver donors that had a triphasic computed tomography (CT) scan for anatomical evaluation, with special emphasis on variations that were not described by Michel.

## MATERIALS AND METHODS

Institutional review board approval was obtained and waived the need for informed consent. A retrospective analysis of prospectively collected data of all liver donors and potential donors during a 2 years period in our transplant centre. All the arterial vascular anatomy was prospectively collected.

The CT scans of the donors were independently reviewed by two transplant surgeons and a senior radiologist using Myrian studio software by Intrase.

### The CT protocol

The donors were subjected to a triple phase multi-detector CT scan using Siemens SOMATOM Definition Flash. An un-enhanced, hepatic venous, arterial and portal venous phases were obtained.

At a rate of 3.0 mL/s, a 1.5 mL/kg of 300 mg/mL non-ionic iodinated contrast using a pressure injector was administered intravenously with an 18–20 gauge peripheral access catheter in the arm to all donors. After setting the trigger to a 100 Hounsfield Unit, the region of interest cursor was placed in the aorta just above the dome of the diaphragm.

The unenhanced and hepatic venous phases included the whole abdominal organ while the arterial, and portal phases were directed to the liver.

### Arterial classification

Donors who had a low-quality CT scan were excluded from the study.

The patients were classified according to Michel classification. Those who did not meet any of Michel classification subtypes were classified as class 0. Additional detailed description of the class 0 type was given.

## RESULTS

Out of the 263 donors and potential liver donors that have been evaluated in the study period, 241 were included in the study. The remaining 22 donors were excluded due to low quality CT scan. 210 patients met Michel classification subtypes of which 147 (60.9%) were class I which is the most common. The second most common variation was class II with 22 (9.1%) donors, followed by class III, 18 (7.5%) donors. Table 1 demonstrates the number of patients in all classes.

Thirty-one (12.9%) donors did not fit in any of the classes of Michel classification and were classified as class 0 (Table 2). Of which, 9, 2, 3 and 6 had replaced right hepatic artery (RRHA) from pancreaticoduodenal artery (PDA) (Fig. 1), accessory right hepatic artery (ARHA) from PDA, RRHA from gastroduodenal artery (GDA) (Fig. 2), ARHA from GDA, respectively (Table 3). Two donors had an RRHA directly from the aorta (Figs. 3, 4), three donors had RRHA from the coeliac artery (Fig. 5), and one had ARHA from coeliac artery. Additional variations include two left hepatic arteries (LHA) from the proper hepatic artery (PHA) which was demonstrated in five donors. One case had a hepatic trunk that originated from the superior mesenteric artery (SMA) with accessory LHA from the left gastric artery and another case had an accessory segment four artery from the GDA. Table 2 demonstrates class 0 variation in detail.

It's worth mentioning that some donors share more than one unclassified variation.

**Table 2.** The characteristic of all class 0 (unclassified) cases

	RHA-PHA	ARHA-PDA	RRHA-PDA	ARHA-GDA	RRHA-GDA	RRHA-Coeliac	ARHA-Coeliac	RRHA-Aorta	Others
LHA-PHA	0	1	4*	3*	1	2	1	0	0
ALHA-LGA	0	0	1	1	2	0	0	0	0
RLHA-LGA	0	1	3	2	0	1	0	2	0
Two LHA-PHA	4	0	1	0	0	0	0	0	0
Other	0	0	0	0	0	0	0	0	2

\*One patient had ARHA from GDA (small branch) and RRHA from PDA (main branch). LHA — left hepatic artery; RHA — right hepatic artery; PHA — proper hepatic artery; LGA — left gastric artery; ALHA — accessory left hepatic artery; RLHA — replaced left hepatic artery; ARHA — accessory right hepatic artery; RRHA — replaced right hepatic artery; PDA — pancreaticoduodenal artery; GDA — gastroduodenal artery



**Figure 1.** Computed tomography three-dimensional view: replaced right hepatic artery from pancreaticoduodenal artery (red arrow).

Segment 4 artery (S4) was also studied (Tables 1, 3). In 19 patients, S4 could not be visualised.

In general, 137 (56.8%) donors had S4 from the LHA, 77 (31.9%) from the right hepatic artery (RHA), 2 from the PHA, and four from the coeliac artery. One donor had a S4 from both LHA and RHA. And one case had accessory S4 from the GDA.

## DISCUSSION

The standard hepatic artery anatomy with the left and right hepatic artery arising from the common hepatic artery after giving of the gastroduodenal artery is present in up to 55% of the population [11].



**Figure 2.** Computed tomography coronal view: replaced right hepatic artery (red arrow) from the gastroduodenal artery (yellow arrow).

Determining the hepatic artery variation is of utmost importance for the surgeon and the interventional radiologist [1, 13].

In our study, we found that the standard anatomy is present in 60.9% of the healthy donors, which is similar to what was previously described in the literature [4].

From embryological point of view, there are four primitive splanchnic branches arises from aorta early during the embryo development. Those branches are connected by longitudinal anastomosis in their roots. Some of the branches disappear later during the embryo development. The common hepatic artery originates from this longitudinal anastomosis. Disappearance or retention of parts of this plexus could give numerous anatomical variations [12, 17].

**Table 3.** The anatomical details of replaced and accessory right hepatic artery cases that originate from the gastroduodenal artery

	ARHA-GDA	RRHA-GDA	LHA-PHA	ALHA-LGA	RLHA-LGA	S4-L	S4-R	S4 not seen
1	*				*		*	
2	*				*		*	
3	*			*		*		
4	*		*					*
5	*		*					*
6		*		*				*
7		*		*		*		
8		*				*		

LHA — left hepatic artery; PHA — proper hepatic artery; LGA — left gastric artery; ALHA — accessory left hepatic artery; RLHA — replaced left hepatic artery; ARHA — accessory right hepatic artery; RRHA — replaced right hepatic artery; GDA — gastroduodenal artery; S4-L — segment 4 artery from the left hepatic artery; S4-R — segment 4 artery from the right hepatic artery

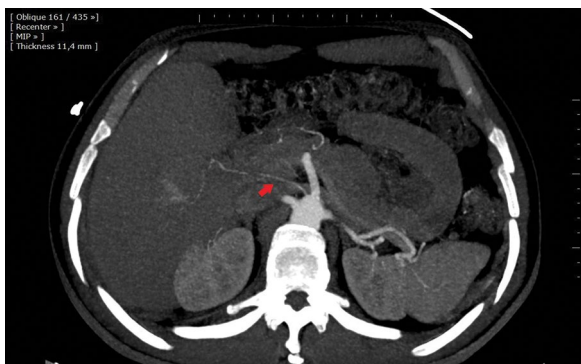


**Figure 3.** Computed tomography axial view: replaced right hepatic artery from the aorta (red arrow).

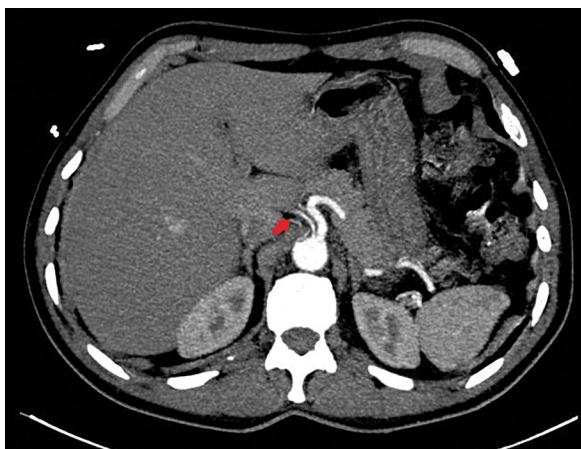


**Figure 4.** Computed tomography axial view: replaced right hepatic artery from the aorta (red arrow) (additional view).

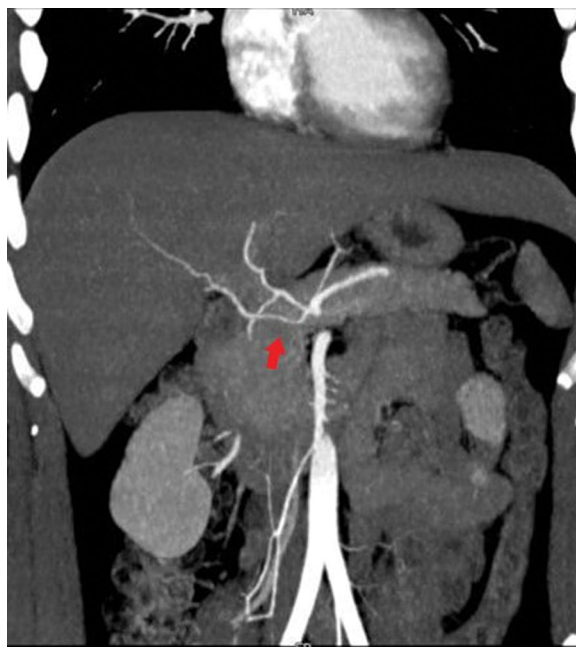


**Figure 5.** Computed tomography coronal view: replaced right hepatic artery from the coeliac artery (red arrow).

One of the most widely accepted classification of the hepatic artery anatomical variation is Michel classification, which includes 10 classes [11]. In our

study, 12.9% of the population did not fit in any of the classes of Michel classification and were classified as class 0. This relatively high incidence shows the value of identifying those variants. For example, in our sample we found that 9 (3.7%) cases have either replaced or accessory RHA from the GDA, these variations were barely mentioned in the literature and were limited to case reports [15]. Identifying these findings may be critical in the setting of liver transplantation when performing liver procurement, since this branch can be preserved by harvesting the GDA with its branches and keeping the RRHA or

ARHA intact. Thus, minimizing the number of arterial anastomosis and, in turn, decreasing the chance of arterial complications.

Furthermore, this variation may be of great importance for interventional radiologists especially when performing trans-arterial chemoembolisation for hepatocellular carcinoma, since this aberrant branch may feed the tumour [9]. Moreover, a great caution should be taken when embolising the GDA as a result of bleeding, due to the risk of cutting off the blood supply to the right segments of the liver in case of RRHA.

Another variation that is usually misclassified as class III or VI is when the RRHA or ARHA originate from the PDA or when they both share a common trunk. The importance of this variation arises when performing pancreaticoduodenectomy or when performing angiographic embolisation of the rare PDA pseudoaneurysm [7]. In case of pancreaticoduodenectomy as a result of a tumour, it is important to identify the arterial variations and their relation to the tumour in order to perform a safe surgery and to avoid vascular complications [14]. Alternatively, it may be better to subclassify this variant as class III p or class VI p when the RRHA or ARHA originate from the PDA.

An additional variant is the RRHA directly from the aorta, this variant may be important when performing angiography and trans-arterial chemoembolisation for hepatocellular carcinoma [2], since it may be challenging to access this artery. Similarly, the significance of this variation emerges during liver harvest in the setting of cadaveric donation because it may be confusing to the surgeon if he is not familiar with this rare variation.

Another rare variation is a case that had a hepatic trunk that originated from the SMA with accessory LHA from the left gastric artery, this variation may make pancreaticoduodenectomy procedure more challenging and may increase the vascular complication rate as was reported by Ye et al. [18].

In this study, we also focused on identifying the root of the S4 hepatic artery (middle hepatic artery). Turning back to the literature including Michel classification, limited data is documented regarding the segment 4 arterial supply, and Michel classification didn't include the S4 artery variation. It is worth noting that S4 hepatic artery determination is very important in the setting of live donor liver donation. For instance, when performing left lateral segmentectomy, there might be a high probability of sacrificing

it in case it arises from the left hepatic artery and, in turn, a higher chance of complications to the donor. On the contrary, when a right hepatectomy is to be performed, the arterial blood supply to segment 4 may be affected if the S4 artery originates from the right hepatic artery [4].

We believe that adding an additional class to Michel classification, with class 0 as a non-conventional variation, may help both the radiological and surgical team to develop a common language and make the surgeon or the interventional radiologist more alert, and fully prepared for these anatomical variations during the procedure.

A limitation of this study is that it included both donors and potential donors so a correlation with operative findings is not possible. An additional limitation is that it did not include the hepatic duct or portal vein variations.

## CONCLUSIONS

A meticulous pre-procedure imaging revision for identification of the hepatic artery variation and keeping in mind the possibility of non-conventional variations that were described in this study is a key for performing a successful procedure with minimal complications.

## Acknowledgements

The assistance provided by Riham Imam in technical editing of the manuscript is greatly appreciated.

**Conflict of interest:** None declared

## REFERENCES

- Balachandran A, Darden DL, Tamm EP, et al. Arterial variants in pancreatic adenocarcinoma. *Abdom Imaging*. 2008; 33(2): 214–221, doi: [10.1007/s00261-007-9235-z](https://doi.org/10.1007/s00261-007-9235-z), indexed in Pubmed: [17435979](https://pubmed.ncbi.nlm.nih.gov/17435979/).
- Cazejust J, Bessoud B, Colignon N, et al. Hepatocellular carcinoma vascularization: from the most common to the lesser known arteries. *Diagn Interv Imaging*. 2014; 95(1): 27–36, doi: [10.1016/j.diii.2013.04.015](https://doi.org/10.1016/j.diii.2013.04.015), indexed in Pubmed: [23978434](https://pubmed.ncbi.nlm.nih.gov/23978434/).
- Ciyiltepe H, Cetin D, Aday U, et al. Rare hepatic artery anomaly (Michel type unclassified) in a patient who underwent radical gastrectomy for gastric cancer: a case report. *Bezmialem Science*. 2017; 5(3): 142–144, doi: [10.14235/bs.2017.1104](https://doi.org/10.14235/bs.2017.1104).
- Favelier S, Germain T, Genson PY, et al. Anatomy of liver arteries for interventional radiology. *Diagn Interv Imaging*. 2015; 96(6): 537–546, doi: [10.1016/j.diii.2013.12.001](https://doi.org/10.1016/j.diii.2013.12.001), indexed in Pubmed: [24534562](https://pubmed.ncbi.nlm.nih.gov/24534562/).
- Goss C. Blood supply and anatomy of the upper abdominal organs with a descriptive atlas. By N.A. Michels. xiv + 581

- pages, 172 figures. \$24.00. J. B. Lippincott Company, Philadelphia, 1955. *Anat Rec.* 1960; 137(2): 153–154, doi: [10.1002/ar.1091370211](https://doi.org/10.1002/ar.1091370211).
6. Hlaing KP, Othman F. Complex pattern of a variant hepatic artery. *Singapore Med J.* 2012; 53(9): e186–e188, indexed in Pubmed: [23023911](https://pubmed.ncbi.nlm.nih.gov/23023911/).
  7. Imam R, Khalayleh H, Khoury D, et al. Rupture of an idiopathic aneurysm of the inferior pancreaticoduodenal artery leading to an intra-abdominal bleeding. *J Acute Care Surg.* 2020; 10(1): 33–35, doi: [10.17479/jacs.2020.10.1.33](https://doi.org/10.17479/jacs.2020.10.1.33).
  8. Johnson PB, Cawich SO, Shah S, et al. Vascular supply to the liver: a report of a rare arterial variant. *Case Rep Radiol.* 2013; 2013: 969327, doi: [10.1155/2013/969327](https://doi.org/10.1155/2013/969327), indexed in Pubmed: [24159405](https://pubmed.ncbi.nlm.nih.gov/24159405/).
  9. Liang Y, Li E, Min J, et al. Rare anatomic variation of the right hepatic artery and accessory right hepatic artery supplying hepatocellular carcinoma: A case report and literature review. *Medicine (Baltimore).* 2017; 96(39): e8144, doi: [10.1097/MD.00000000000008144](https://doi.org/10.1097/MD.00000000000008144), indexed in Pubmed: [28953651](https://pubmed.ncbi.nlm.nih.gov/28953651/).
  10. Mehta V, Dave V, Suri RK, et al. Quadrifurcation of the hepatic artery proper in conjunction with double right gastric arteries. *Singapore Med J.* 2012; 53(10): e211–e213, indexed in Pubmed: [23112032](https://pubmed.ncbi.nlm.nih.gov/23112032/).
  11. Michels NA. Newer anatomy of the liver and its variant blood supply and collateral circulation. *Am J Surg.* 1966; 112(3): 337–347, doi: [10.1016/0002-9610\(66\)90201-7](https://doi.org/10.1016/0002-9610(66)90201-7), indexed in Pubmed: [5917302](https://pubmed.ncbi.nlm.nih.gov/5917302/).
  12. Morita M. Reports and conception of three anomalous cases on the area of the celiac and the superior mesenteric arteries. *Igaku Kenkyu.* 1936; 5: 159–172.
  13. Munshi IA, Fusco D, Tashjian D, et al. Occlusion of an aberrant right hepatic artery, originating from the superior mesenteric artery, secondary to blunt trauma. *Trauma.* 2000; 48(2): 325–326, doi: [10.1097/00005373-200002000-00025](https://doi.org/10.1097/00005373-200002000-00025), indexed in Pubmed: [10697098](https://pubmed.ncbi.nlm.nih.gov/10697098/).
  14. Padilla Valverde D, Villarejo Campos P, Villanueva Liñán J, et al. [Radiological-surgical methods to identify celiac-mesenteric anomalies of the hepatic artery before duodenopancreatectomy]. *Cir Esp.* 2013; 91(2): 103–110, doi: [10.1016/j.ciresp.2012.04.012](https://doi.org/10.1016/j.ciresp.2012.04.012), indexed in Pubmed: [23219204](https://pubmed.ncbi.nlm.nih.gov/23219204/).
  15. Polguy M, Podgórski M, Hogendorf P, et al. Variations of the hepatobiliary vasculature including coexistence of accessory right hepatic artery with unusually arising double cystic arteries: case report and literature review. *Anat Sci Int.* 2014; 89(3): 195–198, doi: [10.1007/s12565-013-0219-5](https://doi.org/10.1007/s12565-013-0219-5), indexed in Pubmed: [24310410](https://pubmed.ncbi.nlm.nih.gov/24310410/).
  16. Prakash, Rajini T, Mokhasi V, et al. Coeliac trunk and its branches: anatomical variations and clinical implications. *Singapore Med J.* 2012; 53(5): 329–331, indexed in Pubmed: [22584973](https://pubmed.ncbi.nlm.nih.gov/22584973/).
  17. Tandler J. Über die Varietäten der Arteria coeliaca und deren Entwicklung. *Beiträge und Referate zur Anatomie und Entwicklungsgeschichte.* 1904; 25(2): 473–500, doi: [10.1007/bf02300762](https://doi.org/10.1007/bf02300762).
  18. Ye Z, Ye S, Zhou D, et al. A rare variation of celiac trunk and hepatic artery complicating pancreatico-duodenectomy: A case report and literature review. *Medicine (Baltimore).* 2017; 96(48): e8969, doi: [10.1097/MD.00000000000008969](https://doi.org/10.1097/MD.00000000000008969), indexed in Pubmed: [29310402](https://pubmed.ncbi.nlm.nih.gov/29310402/).

# Hexafurcated coeliac trunks, trifurcated common hepatic artery, and a new variant of the arc of Bühler

B.A. Manta<sup>1</sup>, M.C. Rusu<sup>1</sup>, A.M. Jianu<sup>2</sup>, A.C. Ilie<sup>3</sup>

<sup>1</sup>Division of Anatomy, Department 1, Faculty of Dental Medicine, “Carol Davila” University of Medicine and Pharmacy, Bucharest, Romania

<sup>2</sup>Department of Anatomy and Embryology, Faculty of Medicine, “Victor Babeș” University of Medicine and Pharmacy, Timisoara, Romania

<sup>3</sup>Department of Functional Sciences, Discipline of Public Health, Faculty of Medicine, “Victor Babeș” University of Medicine and Pharmacy, Timisoara, Romania

[Received: 1 January 2021; Accepted: 8 February 2021; Early publication date: 1 March 2021]

**Background:** The coeliac trunk (CT) is well-known as trifurcated into the left gastric (LGA), common hepatic (CHA) and splenic (SA) arteries.

**Materials and methods:** Scarce reports indicate that the CT could appear quadri-, penta-, hexa-, or even heptafurcated. Reports of CTs with six branches (hexafurcated CT) are few, less than ten. The hexafurcated CT variant was documented by a retrospective study of 93 computed tomography angiograms.

**Results:** Two hexafurcated CTs were found. In one case an arc of Bühler was added to the inferior phrenic arteries, LGA, CHA and SA. In the second case the dorsal pancreatic artery was added to the other five branches. That arc of Bühler descended in front of the aorta to connect with the origin of the third jejunal artery. The CHA in that second case was trifurcated into the left and right hepatic arteries, and the gastroduodenal artery; the proper hepatic artery was absent.

**Conclusions:** Although the hexafurcated CT, as well as the trifurcated CHA, are rarely occurring and reported anatomic variants, this doesn't mean they could not be encountered during surgical or interventional procedures, which they would complicate if not recognised. Moreover, the arc of Bühler, the embryonic remnant, was not reported previously to insert into the CT as an additional branch of it. (Folia Morphol 2022; 81, 2: 365–371)

**Key words:** aorta, computed tomography, hepatic artery, splenic artery, superior mesenteric artery, arc of Bühler, portal vein

## INTRODUCTION

The coeliac trunk (CT) is the first ventral branch of the abdominal aorta, commonly emerging at the level of the 12<sup>th</sup> thoracic vertebra, beneath the aortic hiatus of the diaphragm [20]. The CT usually trifur-

cates to form the *tripus Halleri*, sending off the left gastric artery (LGA), common hepatic artery (CHA) and splenic artery (SA) [21]. Panagouli et al. (2013) [17] defined the type III of CT variation in which additional branches of the CT occur. These authors

Address for correspondence: A.M. Jianu, MD, PhD, Ass. Prof., “Victor Babeș” University of Medicine and Pharmacy, Department of Anatomy and Embryology, 2 Eftimie Murgu Square, 300041, Timisoara, Romania, tel: 0040/0256204250, e-mail: adelina.jianu@gmail.com; adelina.jianu@umft.ro

All the authors have equally contributed to the manuscript.

This article is available in open access under Creative Common Attribution-Non-Commercial-No Derivatives 4.0 International (CC BY-NC-ND 4.0) license, allowing to download articles and share them with others as long as they credit the authors and the publisher, but without permission to change them in any way or use them commercially.

documented a prevalence of 1.06% of this type of anatomic variations of the CT [17]. Different patterns of such additional branches include the inferior phrenic arteries, left (LIPA) and right (RIPA), or the dorsal pancreatic artery (DPA) [4].

To the authors' knowledge, eight hexafurcated patterns of the CT were previously reported [1, 2, 5, 6, 8, 18, 19]. A different study reported a prevalence of 4% for the hexafurcated CT, but this results just from a meeting abstract [25]. In these reports different arteries with specific patterns of distribution were added to the three normal branches of the CT to increase their number to six.

We hereby report a new pattern of hexafurcated CT in which one of the additional branches was not an artery with a specific target tissue, but it was a previously unreported variant of the arc of Bühler. The Bühler's arc is a rare direct retropancreatic anastomosis between the CT and the superior mesenteric artery (SMA) or their branches [15]. Different other coeliacomesenteric anastomotic paths are more distanced from the aorta than the arc of Bühler, being either anastomoses of the superior and inferior pancreaticoduodenal arteries, or anastomoses of the DPA and the SMA, or one of its branches (middle colic artery, inferior pancreaticoduodenal arteries) [14, 15]. To the authors' knowledge, an insertion of the arc of Bühler into a jejunal artery was not reported previously.

## MATERIALS AND METHODS

The anatomic variants of CT hexafurcation reported here were found during a targeted retrospective study of 93 computed tomography angiograms of 44 male and 49 female cases, with ages from 48 to 72 years old. The computed tomographic exams consisted in injecting an iodine radiocontrast agent in the left brachial vein (100 mL, with 6 mL/s flow), followed by 50 mL iodine radiocontrast agent (Ultravist 370 mg/mL) in the brachial vein, and by 20 mL saline medium. The computed tomography was performed with a 32-slice scanner (Siemens Multislice Perspective Scanner), using a 0.6 mm collimation and reconstruction of 0.75 mm thickness with 50% overlap for multiplanar, maximum intensity projection, and three-dimensional (3D) volume rendering technique [22]. The specific arterial anatomy was documented using the Horos software and its 3D volume rendering application.

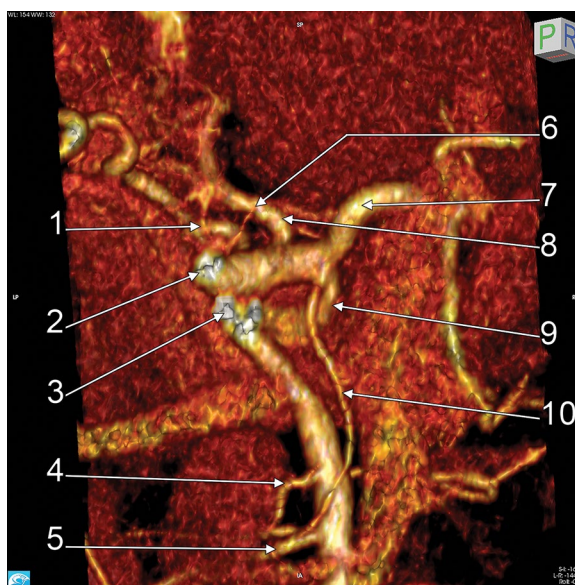


**Figure 1.** Case 1. Hexafurcated coeliac trunk and superior mesenteric artery. Three-dimensional volume rendering; 1 — left inferior phrenic artery; 2 — coeliac trunk origin; 3 — superior mesenteric artery; 4 — first jejunal artery; 5 — third jejunal artery; 6 — right inferior phrenic artery; 7 — common hepatic artery; 8 — left gastric artery; 9 — splenic artery; 10 — arc of Bühler.

## RESULTS

In the 93 computed tomography angiograms that were studied were found two cases (Case 1: male, 60 years old; Case 2: male, 50 years old) (2.15%) with hexafurcated CTs. In both cases, five of the CT branches were the inferior phrenic arteries, LGA, CHA and SA. The sixth branch of the CT was in Case 1 an arc of Bühler and in Case 2 — the DPA.

### Case 1

The CT origin was on the anterior side of the abdominal aorta at the level of the upper third of the 1<sup>st</sup> lumbar vertebra. The SMA origin was 1.37 cm below, at the level of the middle third of the 1<sup>st</sup> lumbar vertebra. The calibre of the CT at its origin was 5.46 mm, while the calibre of the SMA was 6.63 mm.

There were found six branches emerging from the CT, three of these being collateral (LIPA, RIPA, LGA), and the other three, terminal branches (CHA, SA, arc of Bühler) (Fig. 1).

At 2.07 mm from the aortic insertion of the CT the two inferior phrenic arteries (LIPA, RIPA) emerged independently from the superior side of the CT, being separated between by a distance of 2.28 mm. The in-

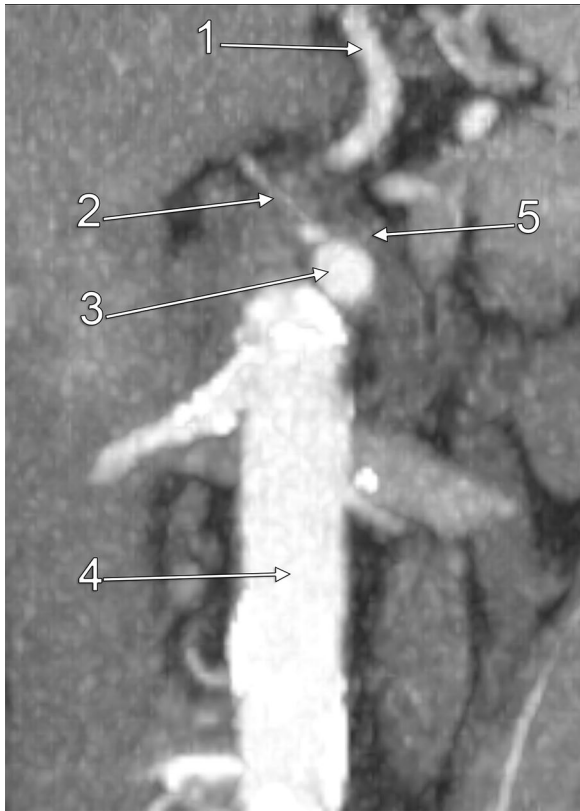


**Figure 2.** Case 1. Hexafurcated coeliac trunk. Coronal maximum intensity projection slice demonstrating the independent coeliac origins of the inferior phrenic arteries; 1 — left gastric artery; 2 — right inferior phrenic artery; 3 — coeliac trunk; 4 — aorta; 5 — left inferior phrenic artery.

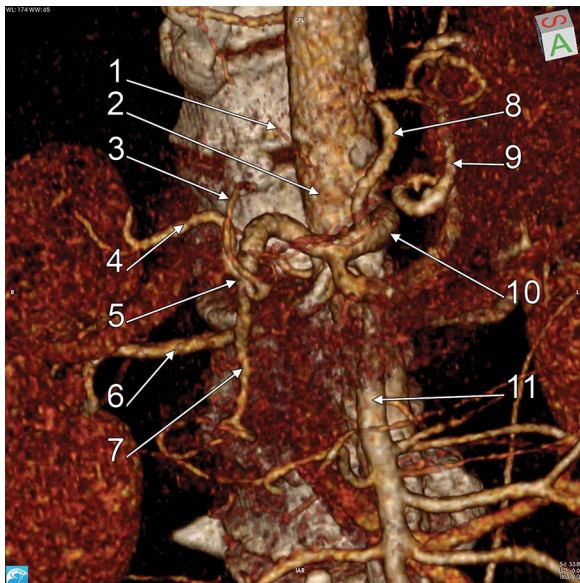


**Figure 3.** Case 1. Hexafurcated coeliac trunk. Right antero-inferior view of the trifurcated common hepatic artery. Three-dimensional volume rendering; 1 — right inferior phrenic artery; 2 — aorta; 3 — left hepatic artery; 4 — right hepatic artery; 5 — trifurcation of the common hepatic artery; 6 — right renal artery; 7 — gastroduodenal artery; 8 — left gastric artery; 9 — coiled splenic artery; 10 — coeliac trunk; 11 — superior mesenteric artery.

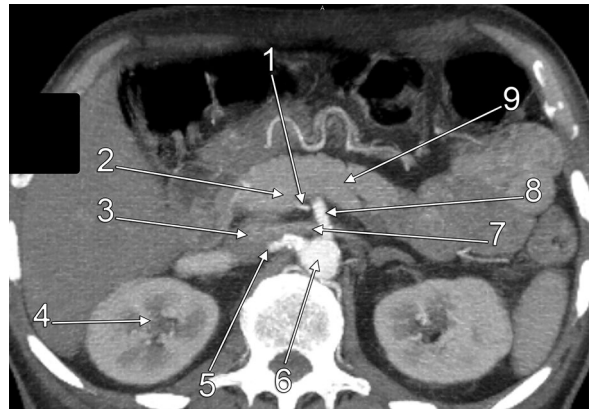


**Figure 4.** Case 1. Hexafurcated coeliac trunk. Axial maximum intensity projection slice through the lower third of the 1<sup>st</sup> lumbar vertebra; 1 — arc of Bühler; 2 — portal vein; 3 — inferior vena cava; 4 — right kidney; 5 — right renal artery; 6 — aorta; 7 — left renal vein; 8 — superior mesenteric artery; 9 — pancreas.

ferior phrenic arteries further ascended and diverged, to enter each within the pillar of the diaphragm on that side (Fig. 2).

The LGA emerged from the superior side of the CT at 1.36 cm distally to the origin of the inferior phrenic arteries. The LGA had an initial calibre of 4.37 mm. It sent off oesophageal branches and further continued to distribute on the lesser gastric curvature.

The CT further arched anterior and to the right and trifurcated terminally at 1.84 cm in front of the abdominal aorta, still at the level of the upper third of the 1<sup>st</sup> lumbar vertebra. It sent off the CHA, directed superiorly to the right, the SA, directed inferiorly to the left, and a posterior branch which further proved being an arc of Bühler. The CHA further trifurcated in front of the portal vein into the RHA, LHA and GDA (Fig. 3). Thus, the proper hepatic artery (PHA) lacked in this case (absent PHA). The SA continued towards the spleen, crossing in front of the SMA and coiling superior to the pancreas and posterior to the stomach.

The sixth branch of the CT was an arc of Bühler which descended from the terminal trifurcation of the CT (Fig. 1). The diameter of the arc of Bühler was 3.65 mm. It descended initially applied on the posterior side of the portal vein, antero-medial to the inferior vena cava, and crossing anteriorly over the left renal vein (Fig. 4). Then it continued posterior to the superior mesenteric vein. In its course, that arc of Bühler was paralleling the SMA on its right posterior side. Inferiorly, the arc of Bühler crossed the posterior side of the SMA below the level of origin of the first jejunal artery (distributed to the duodenojejunal

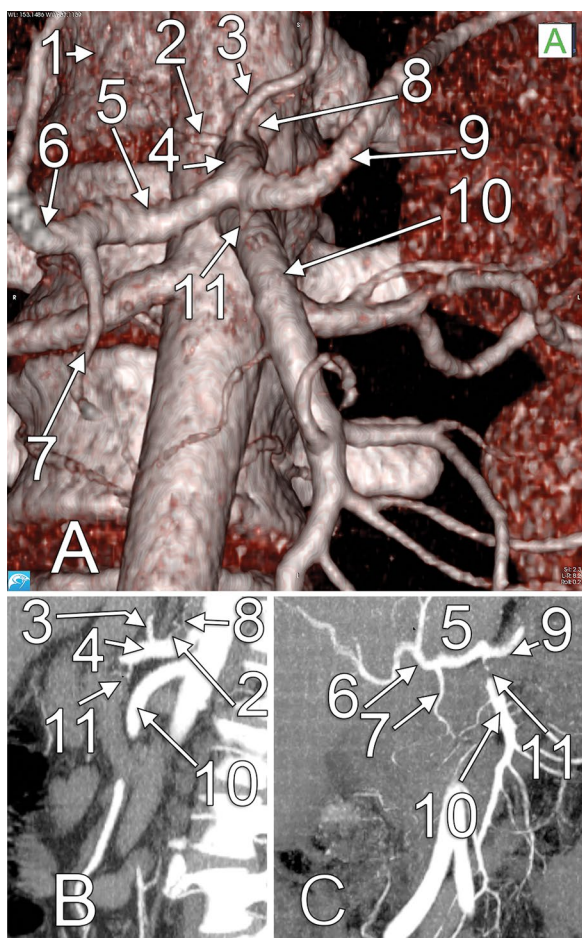


**Figure 5.** Case 2. Hexafurcated coeliac trunk. **A.** Three-dimensional volume rendering, anterior view; **B.** Sagittal maximum intensity projection slice through the coeliac trunk; **C.** Coronal maximum intensity projection slice through the terminal end of the coeliac trunk; 1 — 12<sup>th</sup> thoracic vertebra; 2 — right inferior phrenic artery; 3 — left gastric artery; 4 — coeliac trunk; 5 — common hepatic artery; 6 — proper hepatic artery; 7 — gastroduodenal artery; 8 — left inferior phrenic artery; 9 — splenic artery; 10 — superior mesenteric artery; 11 — dorsal pancreatic artery.

flexure) and ended into the segment of origin of the 3<sup>rd</sup> jejunal artery (Fig. 1). The 2<sup>nd</sup> and the 3<sup>rd</sup> jejunal arteries left the SMA by a common trunk of origin.

#### Case 2

In this second case the CT origin was on the anterior side of the abdominal aorta at the level of the lower third of the 12<sup>th</sup> thoracic vertebra. The SMA origin was 1.58 cm below, at the level of the upper third of the 1<sup>st</sup> lumbar vertebra. The calibre of the CT at its origin was 4.51 mm, while the calibre of the SMA was 6.34 mm.

There were found six branches emerging from the CT, three of these being collateral (LIPA, RIPA,

LGA), and the other three, terminal branches (CHA, SA, DPA) (Fig. 5).

The LGA emerged from the superior side of the CT at 2.38 cm distally to the origin of the CT.

The CT further trifurcated terminally at 3.19 cm in front of the abdominal aorta, at the level of the middle third of the 1<sup>st</sup> lumbar vertebra. It sent off the CHA, directed to the right, the SA, directed to the left, and the descending DPA. The CHA further divided into the GDA and PHA in front of the portal vein.

## DISCUSSION

### Hexafurcated coeliac trunks

Few authors previously reported, or described, hexafurcations of the CT [1, 2, 5, 6, 8, 18, 19, 25]. Moreover, there are certain flaws of these reports, as documented in Table 1. A single previous study used computed tomography angiograms, but that meeting abstract did not indicate the arterial pattern of those hexafurcations but reported a 4% prevalence of the variant [25]. There were six previous reports of hexafurcated CTs resulted after [1, 2, 5, 6, 18, 19], but only one [1] came with an accurate proof of the evidence of all those six branches of the CT. To these poor previous evidences of hexafurcated CTs was added a review paper in which the variant was depicted just by a drawing [8]. It is therefore considered that the evidence presented here is the second convincing one.

The hereby reported variants of hexafurcation of the CT could be regarded as resulted from a LIPA + RIPA + LGA + CHA + SA pentafurcation pattern to which was added either the DPA, or an arc of Bühler. Such pentafurcated patterns were reported only twice previously [13, 19].

### The arc of Bühler and novelty of the present variant

Anatomic variations of the CT and SMA are explained by the Mac Kay arc theory and by the longitudinal ventral anastomosis described by Julius Tandler in 1904 [15, 26]. According to Mac Kay's theory, the distribution of the embryonic aorta branches is metameric [15]. Each metamere gives rise to three pairs of branches which unite in an arch, posterior, lateral and anterior or visceral [15]. Further, the visceral arches evolve to metameric single median digestive arteries [15]. The 10<sup>th</sup> metameric artery will form the LGA, the 11<sup>th</sup> metameric artery will form the SA, the 12<sup>th</sup> one forms the CHA and the 13<sup>th</sup> one — the SMA [14, 15]. These embryonic arteries are united by

**Table 1.** Previously reported or described hexafurcations of the coeliac trunk

Author(s), year	Method	Anatomical pattern	Observations
Çiçekcibaşı et al. (2005) [6]	Dissection	LIPA, RIPA, LGA, CHA, SA, LGEA	Case report of a CMT; in the figures it is not clear whether, or not, the LGEA has indeed a gastric distribution
Gielecki et al. (2005) [8]	Review paper	LIPA, RIPA, LGA, CHA, SA, ASRHA	A schema depicts the variant
Chitra (2010) [5]	Dissection	LIPA, RIPA, LGA, CHA, SA, duodenal branch	1/50 cadavers (2%) was reported with hexafurcated CT but there is no figure to support the finding
Paraskevas and Raikos (2011) [18]	Dissection	LIPA, ALSA, LGA, CHA, SA, AJA	Case report, the CHA is not depicted in the figures, nor is the target loop of the AJA
Srivastava (2012) [25]	Computed tomography	–	Meeting abstract only, a prevalence of 4% of the hexafurcation of the CT is reported but the pattern is obscure
Alashkham (2012) [2]	Dissection	LIPA, RIPA, LGA, CHA, SA, aberrant branch for pancreas and duodenum	The inferior phrenic arteries emerging the CT do not appear in the image presented by the author
Agarwal et al. (2016) [1]	Dissection	LIPA, RIPA, LGA, CHA, SA, DPA	The hexafurcation of the CT is accurately demonstrated in the figure
Pinal-Garcia et al. (2018) [19]	Dissection	(a) LIPA, RIPA, LGA, CHA, SA, DPA (b) LIPA, LMSA, RIPA, LGA, CHA, SA	Hexafurcation of the CT was found in 1.4% (2 from 140 cases) but it was not proofed by any figure

AJA — accessory jejunal artery; ALSA — accessory left suprarenal artery; ASRHA — accessory superior right hepatic artery; CHA — common hepatic artery; CMT — coeliacomesenteric trunk; CT — coeliac trunk; DPA — dorsal pancreatic artery; LGA — left gastric artery; LGEA — left gastroepiploic artery; LIPA — left inferior phrenic artery; LMSA — left middle suprarenal artery; RIPA — right inferior phrenic artery; SA — splenic artery

Tandler's longitudinal anastomosis located in front of the aorta [15, 26]. However, although the arc of Bühler is regarded as a vestige of Tandler's anastomosis between the CT and the SMA, its embryogenesis closely relates to the DPA [15]. Thus because the DPA could emerge either the SA, or the SMA, and if both origins are maintained, the arc of Bühler is configured [15]. In the variant reported here (Case 1) the upper origin of the DPA was translated to the CT itself, the lower origin — to the third jejunal artery, but both were maintained to configure a retropancreatic arc of Bühler. In Case 2, the origin of the DPA was translated from the SA to the CT itself, but an inferior insertion onto the SMA lacked.

In a recent review of the literature, Michalinos et al. [15] concluded that "Despite its importance, knowledge on the Bühler's arc is still incomplete". Indeed, the report presented here adds such knowledge, by demonstrating that the arc of Bühler could insert in the CT as one of the six branches of a hexafurcation.

Michalinos et al. (2019) [15] documented that Grabbe and Bücheler (1980) [9] determined the diameter of the arc of Bühler being 2–7 mm. The respective authors found the arc of Bühler with a prevalence of 4.11% (14/340 cases). Later, Saad et al. (2005) [23], also documented by Michalinos et al. (2019) [15], found the diameter of the arc of Bühler being 1.5–2.5 mm. But those later authors found the respective anastomosis in 4/120 angiograms, thus

with a prevalence of 3.3%. In the case reported here the diameter of the arc of Bühler was of 3.65 mm, which corresponds to the measurements of Grabbe and Bücheler [9], but is larger than the values of Saad et al. [23]. The arc of Bühler could use as collateral path of blood flow between the CT and SMA, if one of these two main arteries is obstructed [15]. A direct CT insertion of the arc of Bühler would equally supply the branches of the CT from the SMA, if the CT is obstructed. However, a jejunal insertion of the arc of Bühler could not ensure a good haemodynamic support of the SMA, if this later artery is obstructed. It should also be emphasized that when the arc of Bühler acts as a shunt, either it could steal blood from different collateral branches of the CT and SMA, or it could facilitate the development of aneurysms by local increase of the arterial pressure [15].

#### Trifurcated common hepatic artery: absent proper hepatic artery

Song et al. (2010) [24] evaluated the arterial anatomy on computed tomography angiograms of 5002 patients. From what was observed, the variant of the RHA and LHA originating directly from the CHA which is reported here (absent PHA, Case 1) was not found among that large lot of cases, although those authors got evidence to present and discuss the absent CHA variants [24]. A recent study by Ekingen et al. [7] on the specific variation of the PHA was performed on 671 multidetector computed tomography angiog-

raphy images. The authors classified as type 2 the RHA+LHA+GDA originated from the CHA, with absent PHA (trifurcation of CHA) morphology [7], which is similar to the findings reported here in Case 1. Ekingen et al. (2020) [7] found this type 2 morphology in 8.94% of cases, while the normal anatomy of the PHA was encountered in just 43.52% of their cases. They quoted Gurgacz et al. (2011) [10] for reporting a trifurcated CHA, but that trifurcated CHA had not a RHA+LHA+GDA pattern, it had instead the LHA+GDA+right gastric artery pattern, which is different equally from the variant reported here, and from Ekingen's type 2. Moreover, while Ekingen et al. (2020) [7] did not indicate whether, or not, the cases with trifurcated CHA added multiple branching patterns of the CT, hereby is reported a hexafurcated CT with a trifurcated CHA. At the opposite end of the spectrum of such variations, Badagabettu et al. (2016) [3] reported an absent CT with a trifurcated CHA with a RHA+LHA+GDA pattern. Hiatt et al. (1994) [11] documented the previous reports of Kemeny et al. (1986) [12] and, respectively, Niederhuber and Ensminger (1983) [16], who reported the RHA+LHA+GDA pattern of the CHA trifurcation, but regarded that pattern as "a subtype of the normal scheme" [11]. As quoted by Hiatt et al. [11], the respective authors documented a prevalence of 9%, and, respectively, 14%, of the trifurcated CHA.

## CONCLUSIONS

In conclusion, additional branches of the CT are exposed at risk during surgical and interventional procedures, if not accurately documented. Available literature resources in such cases are still poor and in various instances insufficiently documented. Nevertheless, finding a rare arterial variant does not mandatory imply it is the only variant which occurred in that territory.

**Conflict of interest:** None declared

## REFERENCES

1. Agarwal S, Pangtey B, Vasudeva N. Unusual variation in the branching pattern of the celiac trunk and its embryological and clinical perspective. *J Clin Diagn Res.* 2016; 10(6): AD05–AD07, doi: [10.7860/JCDR/2016/19527.8064](https://doi.org/10.7860/JCDR/2016/19527.8064), indexed in Pubmed: [27504274](https://pubmed.ncbi.nlm.nih.gov/27504274/).
2. Alashkham A. Anomalies of the celiac axis. *AXIS.* 2012; 4: 1–4.
3. Badagabettu SN, Padur AA, Kumar N, et al. Absence of the celiac trunk and trifurcation of the common hepatic artery: a case report. *J Vasc Bras.* 2016; 15(3): 259–262, doi: [10.1590/1677-5449.004016](https://doi.org/10.1590/1677-5449.004016), indexed in Pubmed: [29930600](https://pubmed.ncbi.nlm.nih.gov/29930600/).
4. Bergman RA, Tubbs RS, Shoja MM. *Bergman's comprehensive encyclopedia of human anatomic variation.* John Wiley & Sons, Hoboken, New Jersey 2016.
5. Chitra R. Clinically relevant variations of the coeliac trunk. *Singapore Med J.* 2010; 51(3): 216–219, indexed in Pubmed: [20428743](https://pubmed.ncbi.nlm.nih.gov/20428743/).
6. Çiçekbaşı AE, Uysal II, Seker M, et al. A rare variation of the coeliac trunk. *Ann Anat.* 2005; 187(4): 387–391, doi: [10.1016/j.aanat.2005.02.011](https://doi.org/10.1016/j.aanat.2005.02.011), indexed in Pubmed: [16163851](https://pubmed.ncbi.nlm.nih.gov/16163851/).
7. Ekingen A, Tuncer MC, Ertuğrul Ö. Investigation of proper hepatic artery and gastroduodenal artery variations by multidetector computed tomography angiography method. *Acta Chir Belg.* 2020; 120(2): 102–115, doi: [10.1080/00015458.2019.1570744](https://doi.org/10.1080/00015458.2019.1570744), indexed in Pubmed: [30714485](https://pubmed.ncbi.nlm.nih.gov/30714485/).
8. Gielecki J, Zurada A, Sonpal N, et al. The clinical relevance of coeliac trunk variations. *Folia Morphol.* 2005; 64(3): 123–129, indexed in Pubmed: [16228946](https://pubmed.ncbi.nlm.nih.gov/16228946/).
9. Grabbe E, Bücheler E. [Bühler's anastomosis (author's transl)]. *Rofo.* 1980; 132(5): 541–546, doi: [10.1055/s-2008-1056615](https://doi.org/10.1055/s-2008-1056615), indexed in Pubmed: [6451503](https://pubmed.ncbi.nlm.nih.gov/6451503/).
10. Gurgacz AM, Horbaczewska A, Klimek-Piotrowska W, et al. Variations in hepatic vascularisation: lack of a proper hepatic artery. Two case reports. *Folia Morphol.* 2011; 70(2): 130–134, indexed in Pubmed: [21630235](https://pubmed.ncbi.nlm.nih.gov/21630235/).
11. Hiatt JR, Gabbay J, Busuttill RW. Surgical anatomy of the hepatic arteries in 1000 cases. *Ann Surg.* 1994; 220(1): 50–52, doi: [10.1097/0000658-199407000-00008](https://doi.org/10.1097/0000658-199407000-00008), indexed in Pubmed: [8024358](https://pubmed.ncbi.nlm.nih.gov/8024358/).
12. Kemeny MM, Hogan JM, Goldberg DA, et al. Continuous hepatic artery infusion with an implantable pump: problems with hepatic artery anomalies. *Surgery.* 1986; 99(4): 501–504, indexed in Pubmed: [3952672](https://pubmed.ncbi.nlm.nih.gov/3952672/).
13. Krishna Chaitanya K, Sharada H. Pentafurcation of the celiac trunk. *Anat Physiol.* 2012; 2(2), doi: [10.4172/2161-0940.s7-001](https://doi.org/10.4172/2161-0940.s7-001).
14. McNulty JG, Hickey N, Khosa F, et al. Surgical and radiological significance of variants of Bühler's anastomotic artery: a report of three cases. *Surg Radiol Anat.* 2001; 23(4): 277–280, doi: [10.1007/s00276-001-0277-6](https://doi.org/10.1007/s00276-001-0277-6), indexed in Pubmed: [11694975](https://pubmed.ncbi.nlm.nih.gov/11694975/).
15. Michalinos A, Schizas D, Ntourakis D, et al. Arc of Bühler: the surgical significance of a rare anatomical variation. *Surg Radiol Anat.* 2019; 41(5): 575–581, doi: [10.1007/s00276-018-2168-0](https://doi.org/10.1007/s00276-018-2168-0), indexed in Pubmed: [30552487](https://pubmed.ncbi.nlm.nih.gov/30552487/).
16. Niederhuber JE, Ensminger WD. Surgical considerations in the management of hepatic neoplasia. *Semin Oncol.* 1983; 10(2): 135–147, indexed in Pubmed: [6306833](https://pubmed.ncbi.nlm.nih.gov/6306833/).
17. Panagouli E, Venieratos D, Lolis E, et al. Variations in the anatomy of the celiac trunk: A systematic review and clinical implications. *Ann Anat.* 2013; 195(6): 501–511, doi: [10.1016/j.aanat.2013.06.003](https://doi.org/10.1016/j.aanat.2013.06.003), indexed in Pubmed: [23972701](https://pubmed.ncbi.nlm.nih.gov/23972701/).
18. Paraskevas GK, Raikos A. Multiple aberrant coeliac trunk ramifications. *Singapore Med J.* 2011; 52(7): e147–e149, indexed in Pubmed: [21808947](https://pubmed.ncbi.nlm.nih.gov/21808947/).

19. Pinal-Garcia DF, Nuno-Guzman CM, Gonzalez-Gonzalez ME, et al. The celiac trunk and its anatomical variations: a cadaveric study. *J Clin Med Res.* 2018; 10(4): 321–329, doi: [10.14740/jocmr3356w](https://doi.org/10.14740/jocmr3356w), indexed in Pubmed: [29511421](https://pubmed.ncbi.nlm.nih.gov/29511421/).
20. Rusu MC, Manta BA. Novel anatomic variation: heptafurcation of the celiac trunk. *Surg Radiol Anat.* 2018; 40(4): 457–463, doi: [10.1007/s00276-018-1995-3](https://doi.org/10.1007/s00276-018-1995-3), indexed in Pubmed: [29497808](https://pubmed.ncbi.nlm.nih.gov/29497808/).
21. Rusu MC, Manta BA. Pentafurcated celiac trunk. *Ann Vasc Surg.* 2021; 70: 567.e1–567.e6, doi: [10.1016/j.avsg.2020.08.007](https://doi.org/10.1016/j.avsg.2020.08.007), indexed in Pubmed: [32795653](https://pubmed.ncbi.nlm.nih.gov/32795653/).
22. Rusu MC, Măru N, Rădoi PM, et al. Trifurcated external carotid artery and complete gamma-loop of its maxillary branch. *Surg Radiol Anat.* 2019; 41(2): 231–234, doi: [10.1007/s00276-018-2142-x](https://doi.org/10.1007/s00276-018-2142-x), indexed in Pubmed: [30483866](https://pubmed.ncbi.nlm.nih.gov/30483866/).
23. Saad WE, Davies MG, Sahler L, et al. Arc of buhler: incidence and diameter in asymptomatic individuals. *Vasc Endovascular Surg.* 2005; 39(4): 347–349, doi: [10.1177/153-857440503900407](https://doi.org/10.1177/153-857440503900407), indexed in Pubmed: [16079944](https://pubmed.ncbi.nlm.nih.gov/16079944/).
24. Song SY, Chung JW, Yin YHu, et al. Celiac axis and common hepatic artery variations in 5002 patients: systematic analysis with spiral CT and DSA. *Radiology.* 2010; 255(1): 278–288, doi: [10.1148/radiol.09090389](https://doi.org/10.1148/radiol.09090389), indexed in Pubmed: [20308464](https://pubmed.ncbi.nlm.nih.gov/20308464/).
25. Srivastava AK, Sehgal G, Sharma P, et al. Various types of branching patterns of celiac trunk. *The FASEB Journal.* 2012; 26(S1), doi: [10.1096/fasebj.26.1\\_supplement.722.5](https://doi.org/10.1096/fasebj.26.1_supplement.722.5).
26. Tandler J. Über die Varietäten der Arteria coeliaca und deren Entwicklung. *Anat Hefte (Beiträge und Referate zur Anatomie und Entwicklungsgeschichte).* 1904; 25(2): 473–500, doi: [10.1007/bf02300762](https://doi.org/10.1007/bf02300762).

# Topographic location and branching pattern of the superior mesenteric artery with its clinical relevance: a cadaveric study

S. Nigah<sup>1</sup>, A. Patra<sup>1</sup>, S. Chumbar<sup>2</sup>, P. Chaudhary<sup>1</sup>

<sup>1</sup>Department of Anatomy, All India Institute of Medical Sciences, Bathinda (PB), India

<sup>2</sup>Department of Forensic Medicine, GGS Medical College, Faridkot, India

[Received: 7 January 2021; Accepted: 22 February 2021; Early publication date: 22 March 2021]

**Background:** The topographic location of the superior mesenteric artery (SMA) and its branching pattern are usually arbitrary in textbooks. This study, therefore, aims to provide topographic information of SMA with reference to the vertebral bodies, ventral branches of aorta and branching pattern of SMA.

**Materials and methods:** The study was conducted on 35 embalmed adult human cadavers. We performed detailed dissection of the SMA to topographically locate its origin in respect to vertebral level and other ventral branches of the abdominal aorta. We have categorised the branching pattern of SMA into three different types depending upon the number of arterial pedicles, traced from proximal to distal to look into their anastomoses and formation marginal artery of Drummond.

**Results:** Vertebral level of origin of SMA varied between the lower third of twelfth thoracic vertebra (T12) and lower third of first lumbar vertebra (L1), most commonly arose at the level of the lower third of L1 (77.14%). The average distances between the origin of SMA and coeliac trunk (CT), inferior mesenteric artery (IMA) and aortic bifurcation were 1.84 cm, 6.67 cm and 10.39 cm, respectively. Depending on the branching pattern, type A was found in 29 (82.85%) cases, type B in 5 (14.28%) and type C in 1 (2.85%). In 2 cases (both of type B), the marginal artery was incomplete.

**Conclusions:** The most common topography of origin of the SMA was opposite the lower third of L1. The coeliac-superior mesenteric relationship was most consistent than between any other two points on the abdominal aorta; 85% of the SMAs were concentrated within a space of 1.00 cm (0.60–1.50 cm) from the CT. Type A branching pattern was most commonly seen in our study population. (Folia Morphol 2022; 81, 2: 372–378)

**Key words:** aortic bifurcation, coeliac artery, inferior mesenteric artery, superior mesenteric artery, topography

## INTRODUCTION

Three unpaired arteries arise from the ventral surface of the aorta, coeliac trunk (CT), superior mesenteric artery (SMA) and inferior mesenteric artery (IMA). The branches arising from these three arteries

solely cater the derivatives of foregut, midgut and hindgut, respectively [20]. Usually, SMA originates from the anterior surface of the aorta 1 cm below the CT, at the level of the L1/2 intervertebral disc, posterior to the body of the pancreas. It then descends abruptly

Address for correspondence: Dr. A. Patra, Ass. Prof., Department of Anatomy, All India Institute of Medical Sciences, Bathinda (PB), India, tel: +91-8580481455, e-mail: apurba.cnm03@gmail.com

This article is available in open access under Creative Commons Attribution-Non-Commercial-No Derivatives 4.0 International (CC BY-NC-ND 4.0) license, allowing to download articles and share them with others as long as they credit the authors and the publisher, but without permission to change them in any way or use them commercially.

downwards anterior to the left renal vein, the uncinate process of the pancreas and the horizontal part of the duodenum, and runs within the root of the mesentery of the small intestine up to the ileocecal junction in the right iliac fossa. Here it ends by giving branches to the ileum and form an anastomosis with a branch of the ileocolic artery in most of the cases [17]. The artery gives off several branches which include; the inferior pancreaticoduodenal artery from the posterior aspect, jejunal and ileal branches from the left surface and middle colic, right colic and ileocolic branches from the right surface [26]. The colic branches of SMA (right colic, middle colic and ileocolic) anastomoses with each other and with the colic branch of IMA (left colic) to form the marginal artery of Drummond which supplies the large gut. Discontinuous marginal artery due to the failure of the anastomosis [2, 16] may lead to infarction injury to the colon. Left colic flexure is the most common site of such vascular injury. Topographical features of the ventral aortic branches including SMA have been reported, to a limited extent. The values given in the standard textbooks are usually arbitrary and no degrees of variation mentioned. With such background, the present study was undertaken to provide statistical information on the points of origin of the SMA with reference to the level of vertebral bodies and intervertebral discs, inter distances between the origin of SMA and the CT, inferior mesenteric Artery and aortic bifurcation. Anatomical knowledge regarding the branching pattern of SMA is very crucial for operating surgeons while mobilising them during surgery. Unfortunately, very few studies are available on this issue. So, we aimed to study its branching pattern, the formation of anastomotic chain between them in relation to the supplying area prone to infarction injury of the colon and categorise the findings accordingly.

## MATERIALS AND METHODS

Thirty five adult cadavers of north Indian origin and aged between 45 to 65 years with a mean age of  $55.84 \pm 7.74$  years were examined in this study. The relatively small number of females (5) in the study sample did not call for separate records on sex differences. The cadavers were obtained from the gross anatomy dissecting room of the Department of Anatomy. Dissection carried out after ethical approval was obtained from the Institutional Ethical Committee. The cadavers were of north Indian origin and formalin embalmed. A midline incision was given starting

from the xiphoid process to symphysis pubis. Skin and fascia were reflected laterally following the method of Cunningham's practical manual for dissection [18]. The greater omentum, coils of small intestine with its mesentery and large intestine were identified. The transverse colon with greater omentum was reflected superiorly over the costal margin to get a better and clear view of the coils of the small intestine. The coils of the jejunum and ileum were seen attached firmly to the posterior abdominal wall through the root of the mesentery. These coils were reflected laterally and moved to the left side of the abdomen without undue stretch so that the right side of the mesentery faces anteriorly. Peritoneum on the right side of the mesentery was removed to expose the branches of SMA. SMA was seen lying along the root of the mesentery and branches arising from it were distributed between the two layers of the mesentery to supply the coils of the intestine. Once the routine dissection of the abdomen was advanced sufficiently to dispose the abdominal aorta and its branches, a pin with a small head was inserted into the vertebral column through the centre of the origin of each unpaired visceral branch and also at the level of bifurcation of the abdominal aorta into the common iliac arteries. The pins were hammered into the vertebral column very carefully to insert the pin in the transverse plane and to avoid the error of an oblique insertion. The distance between the four pins was then measured using digital vernier callipers (Mitutoyo 12"/300 mm, Japan) with least count of 0.01 mm and recorded as inter arterial distances. The measurements were taken from the centre of one pin-head to the centre of the next pin-head (Fig. 1). The measurements were repeated 3 times by the same observer and the mean was taken as final for further analysis. The inter arterial distances thus obtained were statistically analysed using the Microsoft Office Excel software version 16.0 for Windows 10.

Superior mesenteric artery with its branches was traced from proximal to distal up to the level of formation of marginal artery of Drummond. Depending upon the number of arterial pedicles, Mane and Shinde [13] categorised the branching pattern of SMA into three types. In the present study, we followed the same classification of branching pattern:

- type A: usual pattern with three arterial pedicles. middle colic artery (MCA), right colic artery (RCA) and ileocolic artery (ICA) arising independently;

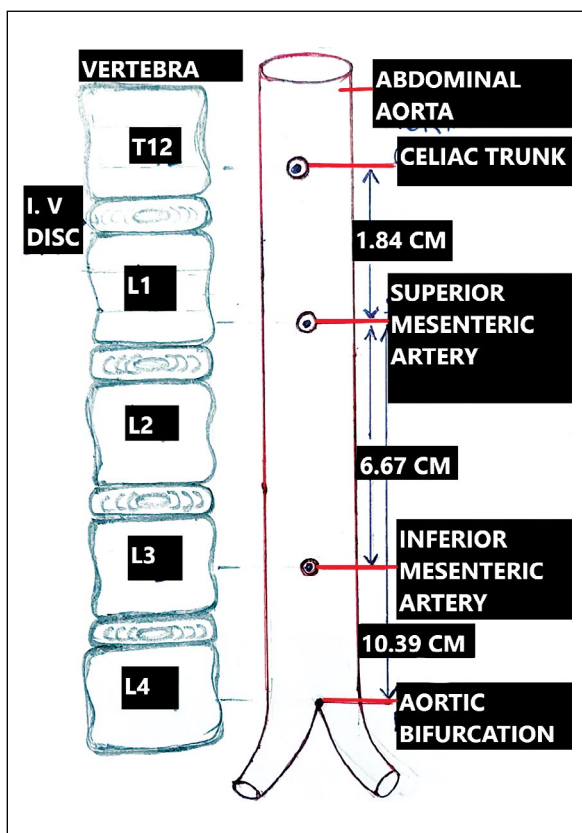


**Figure 1.** Location of the unpaired ventral branches of the abdominal aorta and its bifurcation in relation to the vertebral bodies and measurements of inter arterial distances. The average distances between the origin of superior mesenteric artery and coeliac trunk, inferior mesenteric artery and aortic bifurcation were  $1.84 \pm 0.43$  cm,  $6.67 \pm 1.13$  cm and  $10.39 \pm 1.23$  cm, respectively.

- type B: two arterial pedicles. MCA and RCA arising as a common stem;
- type C: two arterial pedicles. The common stem of MCA and RCA with branches of MCA arise individually.

After documenting the branching pattern, the abdominal viscera were removed and the abdominal aorta was stripped off from the front of the vertebral column, the vertebral level of the second pin determining the level of origin of SMA was recorded in relation to the vertebral body. The twelfth rib was identified and traced medially to identify the T12 vertebra and thus subsequent vertebral levels in the cadaver. To locate the origin of the SMA in accordance to the vertebral level, the vertebral bodies were divided into upper, middle and lower thirds and the intervertebral discs were considered equivalent to the height of the one-third of a vertebral body.

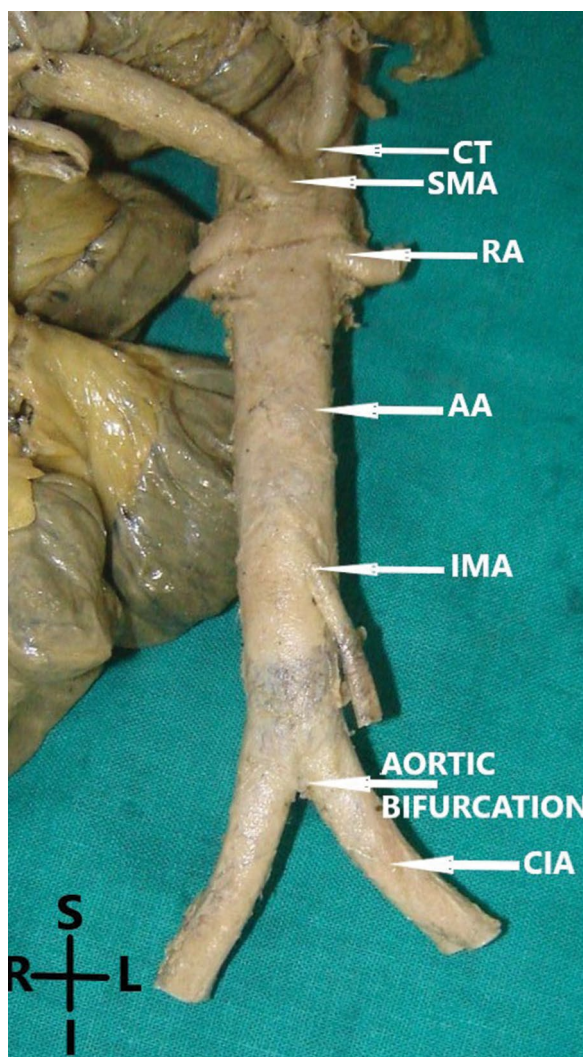


**Figure 2.** Chronology of emergence of ventral branches from aorta with close approximation of coeliac trunk (CT) and superior mesenteric artery (SMA); RA — renal artery; AA — abdominal aorta; IMA — inferior mesenteric artery; CIA — common iliac artery.

## RESULTS

In the present study, a total of 35 human cadavers aged 45 to 65 years were dissected. SMA with its branches was studied to identify the topographic location of SMA and its branching pattern.

In all the cadavers, SMA was seen arising from the abdominal aorta as a separate ventral branch and coeliac-mesenteric trunk (CMT) was absent. In two specimens there was a close approximation (inter arterial distance  $< 0.05$  cm) of coeliac and superior mesenteric vessels, but their topographical integrity was not hampered as they emerged from the aorta (Fig. 2). Chronologically, SMA was 2<sup>nd</sup> in origin in all the cases after the origin of CT.



**Figure 3.** Type A: usual pattern with three arterial pedicles. Middle colic artery (MCA), right colic artery (RCA) and ileocolic artery (ICA) arising independently from the aorta (specimen no: 11R).

**Vertebral topography of origin.** The origin of SMA was studied in respect to the vertebral level of thoracolumbar region and ranged between the lower third of T12 to lower third of L1 vertebra, a spread of 5 intervals (4 vertebral thirds and 1 intervertebral disc). In 27 (77.14%) cases it was arising at the level of the lower third of L1, in 5 (14.28%) cases at the upper third of L1 and in 3 (8.57%) cases at the lower third of T12. So, the mean level of origin was opposite the lower third of L1.

**Inter arterial distance of origin (in cm).** Measurements were taken to document the distances of the site of origin of SMA from CT, IMA and bifurcation of the aorta.

- inter-distance between SMA and CT: the mean distance between SMA and CT was found to be  $1.84 \pm 0.43$  cm (1.30–2.10 cm). Two (5.71%) cases were found in close approximation (distance  $\leq 0.5$  cm), 30 (85.71%) cases concentrated between 0.60 cm and 1.50 cm and in 3 (8.57%) cases it was more than 1.50 cm;
- between SMA and IMA: points of origin ranged from 4.30 cm to 8.00 cm; the mean interval was  $6.67 \pm 1.13$  cm, there was a marked concentration of the variates (34%) between 5.60 cm to 6.50 cm followed by a space of 2.50 cm (5.50 cm to 8.00 cm);
- between SMA and aortic bifurcation: SMA ranged from 8.30 cm to 11.90 cm above the bifurcation; the mean interval was  $10.39 \pm 1.23$  cm.

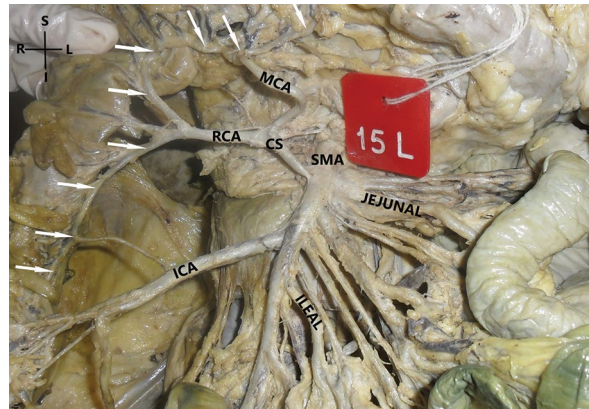


**Figure 4.** Type B: two arterial pedicles. Middle colic artery (MCA) and right colic artery (RCA) arising as a common stem (CS). Arrows showing the formation of marginal artery of Drumond by anastomoses among the branches of ileocolic artery, RCA and MCA (specimen no: 15L).

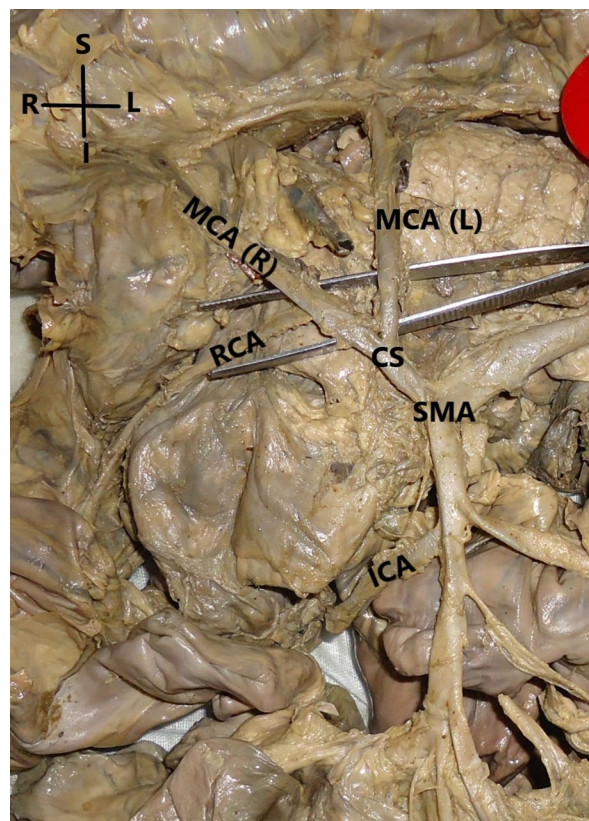


**Figure 5.** Type C: two arterial pedicles. Common stem of middle colic artery (MCA) and right colic artery (RCA) with branches of MCA arise individually and RCA arises from one of the branches of MCA (right branch of MCA).

**Branching pattern.** Pattern of distribution was categorised into three different types depending upon the number of arterial pedicles. type A (Fig. 3)

was found in 29 (82.85%) cases, type B (Fig. 4) in 5 (14.28%) and type C (Fig. 5) in 1 (2.85%). In most of the cases, the anastomotic chain was completely formed except in 2 cases (type B) where the left branch of MCA did not reach up to the left colic flexure, thus failed to anastomose with the ascending branch of the left colic artery (Fig. 4).

## DISCUSSION

Anatomical knowledge about the topographic location of SMA and its branches can help in preventing iatrogenic injuries during abdominal surgeries, specifically during laparoscopic procedures. Keeping in view the importance of the topographic location of SMA and its branching pattern, our observations were discussed and correlated with the study of earlier workers.

The abdominal vessels, especially the CT and the SMA, frequently show diverse anomalies in their origin and course; thus, these arteries are studied with great interest. Several anatomic and radiological studies have described the variations in origin of the ventral branches of the abdominal aorta [14]. CT and SMA may rarely arise as common trunk from the ventral surface of the abdominal aorta, called as the CMT. The incidence of CMT was reported to be low ranging from 0.40% to 2.70% [25]. No obvious cause of CMT was seen in any of the specimens, SMA was 2<sup>nd</sup> in chronological order of origin from the abdominal aorta after CT.

In the present study, the vertebral levels of origin of SMA were found between the lower third of T12 and lower third of L1. In most of the cases (77.14%) the point of origin of SMA was at the level of the lower third of L1, followed by the upper third of L1 (14.28%) and lower third of T12 (8.57%). The mean level of origin occurred opposite the lower third of L1. This level corresponded to that obtained by George [7] in the Canadian population and Heidsieck [8] in the German population. Adachi [1] and Taniguchi [24] found the mean vertebral level of origin of SMA at the middle third of L1. In all of these means cluster opposite the lower two-thirds of the L1. This was a sharp contrast with the findings of Corsy and Aubert [4] who gave the mean of location opposite the disc between the T12 and L1.

Kao et al. [10] studied 24 SMA angiograms to determine the level of origin of SMA. They found SMA to arise below the level of the pedicle of T12 in 4 (16.60%) cases, above the level of the pedicle of

L1 in 4 (16.60%) cases, at the level of the pedicle of L1 in 11 (45.80%) cases and below the level of the pedicle of L1 in 5 (21.00%) cases. So, the vertebral levels of origin of SMA are almost in consonance with our findings.

Topographic location of SMA in relation to the ventral branches of the aorta was studied by few authors. In most of the studies, the origin of the artery was located in relation to the CT. In the present study, we have measured the distances between the origin of SMA and CT, IMA and bifurcation of the abdominal aorta to locate the SMA more consistently.

Superior mesenteric artery was found 1.84 cm distal to the CT and the distance ranged from 1.30 cm to 2.10 cm. whereas, in a study done by Songur et al. [21], the distance ranged from 1.20 cm to 1.60 cm, almost in agreement with our study.

George [7] studied 94 cadavers in which the mean distance between SMA and celiac trunk was 1.6 cm ranging from 0.50 cm to 3.10 cm.

Heidsieck [8] measured this distance in 98 cadavers and SMA was found 1.40 cm distal to the CT and the distance ranged from 0.50 cm to 3.00 cm. Such differences may be attributed to the method of study adopted by different authors, built of the cadavers understudy and ethnicity.

We found the inter-distance between the origin of SMA and IMA to be 6.67 cm ranging from 4.3 cm to 8.00 cm whereas, Songur et al. [21], found the distance ranging from 4.97 cm to 6.60 cm. Heidsieck [8] examined 93 cadavers and found the mean inter distance to be 7.50 cm ranging from 5.00 cm to 10.00 cm.

George [7] measured the distance between the origins of the SMA and IMA in 95 cadavers, the mean distance was 7.10 cm, ranging from 4.20 cm to 10.30 cm.

Very few works have reported the topographic location of SMA in relation to the aortic bifurcation. We found SMA 10.39 cm (range 8.30–11.90 cm) proximal to the bifurcation. According to a case reported by Yoo et al. [27], the distance between SMA and bifurcation of the aorta was 12.50 cm and located at the level of the body of L1.

Comparing these inter arterial distances statistically, less variability was observed in the coeliac-superior mesenteric relationship than between any other two points on the abdominal aorta; 85.71% of the superior mesenteric vessels were concentrated within a small space of 1 cm (0.60–1.00 cm) from the CT.

In two instances, the CT and SMA arose in very close approximation ( $< 0.5$  cm), almost at the same level.

The coeliac and SMA have a striking consistency in topographic position in the adult human body. The low cervical origins in embryonic life and subsequent caudal "migration" during intrauterine development may be considered for such a phenomenon. Tandler [23] have shown that the arteries arising from the ventral aspect of the aorta to supply the stomach and intestines undergo progressive shifting in segmental levels until their definitive site have been reached. The coeliac artery migrates from a point opposite the fourth cervical nerve to the level of the 12<sup>th</sup> thoracic segment. The superior mesenteric artery, from the 1<sup>st</sup> thoracic to the 1<sup>st</sup> lumbar segment; the inferior mesenteric, however, descends from the 12<sup>th</sup> thoracic to the third lumbar segment. The adult levels are usually attained by the time the embryo is 17.00 mm in length. Thus, it is apparent that the final sites of these vessels are subject to variation. The striking differences in descent demonstrated by the coeliac and superior mesenteric arteries in contrast to the inferior mesenteric are readily explained by the proportionately greater alterations involving the upper part of the alimentary tract. Although the exact mechanism of this migration has not been established, Felix [6] believed that it was due to unequal growth of dorsal and ventral walls of the aorta, an actual shifting of the ventral branches when compared with the dorsal segmental vessels.

Depending upon the number of arterial pedicles we have divided SMA into three categories. We documented type A (three arterial pedicles) as the most common (79%) pattern of arrangement. According to Decker et al. [5], three arterial pedicles (type A) was seen in 23.8%, two arterial pedicles (type B) with RCA arose from the ileocolic seen in 22.70% and from MCA seen in 21.50% of cases. Igiri et al. [9], studied the pattern of distribution of branches of SMA in the Nigerian population. They had divided population into three groups:

- group A: classical three arterial trunks with 6–7 jejuno-ileal branches (60%);
- group B: three arterial trunks with appendicular artery arising directly from ICA (26.70%);
- group C: two arterial trunks with RCA from the ileocolic artery (13.30%).

Nelson et al. [15] found that RCA and MCA arose separately from SMA in 34% and 58% of the cas-

es, respectively. Whereas, in 40% RCA originated as a common stem.

Variations in the branching and distributions of the SMA are not uncommon phenomena [3, 11, 15, 19]. Branches of SMA (MCA, RCA, ICA) anastomose with each other to form a continuous arterial chain, which sends twigs to supply the large intestine up to the level of the junction between the right 2/3<sup>rd</sup> and left 1/3<sup>rd</sup>. If these branches fail to anastomose, then the continuity of the chain breaks and thus making large intestine prone to ischaemia. Igiri et al. [9], reported that the branches of RCA and ICA were not anastomosing in group C pattern of SMA. This was similar to earlier researchers who also reported discontinuous marginal artery due to the ICA failing to anastomose with the RCA [14, 22]. In the present study, the marginal artery supplying the ascending colon up to the right colic flexure was continuous in all the cases.

Left colic flexure is very crucial (watershed region) regarding its arterial supply and more prone to ischaemic injury, as it receives dual blood supply from the terminal branches of SMA and the IMA. In the context of ischaemia, the splenic flexure is sometimes referred to as Griffith's point. Most of the authors believe that the left colic flexure is often poorly supplied as in this part the vascular continuity of the arterial arcades (Riolan's arcade) is usually interrupted [17, 18]. Contrary to what is believed by most authors, Lorenzini et al. [12] studied 2000 angiograms of mesenteric arteries and reported the left flexure to be very well supplied while the descending colon results to be poorly supplied.

Basmajian et al. [2] reported discontinuous marginal artery in about 50% of cases over splenic flexure due to failure of anastomoses between RCA (branch of SMA) and LCA (branch of IMA). According to Steward and Rankin [22], the RCA may originate from the MCA or ICA, and a large branch, the Arc of Riolan, may occasionally connect the stem of the SMA with the LCA on the posterior abdominal wall.

In the present study, we found two cases, both of type B variety where the left branch of MCA failed to reach the LCA resulting in a discontinuous marginal artery. In such cases LCA serves as an end artery making the splenic flexure prone to ischaemic injury, especially accidental ligation/ cauterization of the small branches of LCA during hemicolectomy may make aggravate the situation.

## CONCLUSIONS

The mean location of the origin of the SMA was opposite the lower third of L1. Less variability was observed in the coeliac-superior mesenteric relationship than between any other two points on the abdominal aorta; 85% of the superior mesenteric vessels were concentrated within a space of 1.00 cm (0.60–1.50 cm) from the CT. Type A branching pattern was most commonly seen in our study population. Variations in the branching pattern of SMA are clinically very important for laparoscopic surgeons and interventional radiologists to prevent iatrogenic injury to these vessels.

**Conflict of interest:** None declared

## REFERENCES

- Adachi B. Anatomie der Japaner I. Das Arterien system der Japaner. Band II Kaiserlich-Japanischen Universitätzu Kyoto, Kyoto Maruzen 1928: 20–71.
- Basmajian JV, Slonecker CE. Mesenteric vessels, Duodenum, and Pancreas. Grant's Method of Anatomy. 11th ed. William & Wilkins, Baltimore 1980: 172–173.
- Benton RS, Cotter WB. A hitherto undocumented variation of the inferior mesenteric artery in man. *Anat Rec.* 1963; 145: 171–173, doi: [10.1002/ar.1091450208](https://doi.org/10.1002/ar.1091450208), indexed in Pubmed: [13967564](https://pubmed.ncbi.nlm.nih.gov/13967564/).
- Corsy E, Aubert A. Artères de l'intestin grêle et des colons. *Bibliogr Anat.* 1913; 23: 221.
- Decker GAG, du Plessis DJ. Lee McGregor's: A Synopsis of Surgical Anatomy. 12th ed. Varghese Publishing House, Bombay : 226–228.
- Felix W. In: Keibel F, Mall FP. Manual of human embryology. Vol. 2, Chapter 19. JB Lippincott Co., Philadelphia 1912.
- George R. Topography of the unpaired visceral branches of the abdominal aorta. *J Anat.* 1935; 69(Pt 2): 196–205, indexed in Pubmed: [17104532](https://pubmed.ncbi.nlm.nih.gov/17104532/).
- Heidsieck E. Zur Skeletopie der grossen Äste der Bauchorta. *Anat Anz.* 1928; 66: 6–24.
- Igiri AO, Ekong MB, Egemba GO, et al. The pattern of arrangement and distribution of the superior mesenteric artery in a Nigerian population. *Int J Morphol.* 2010; 28: 33–36.
- Kao G, Whittington R, Coia L. Anatomy of the celiac axis and superior mesenteric artery and its significance in radiation therapy. *Int J Radial Oncol Biol Phys.* 1993; 25(1): 131–134, doi: [10.1016/0360-3016\(93\)90155-o](https://doi.org/10.1016/0360-3016(93)90155-o), indexed in Pubmed: [8416869](https://pubmed.ncbi.nlm.nih.gov/8416869/).
- Koizumi M, Horiguchi M. Accessory arteries supplying the human transverse colon. *Acta Anat (Basel).* 1990; 137(3): 246–251, doi: [10.1159/000146827](https://doi.org/10.1159/000146827), indexed in Pubmed: [2349869](https://pubmed.ncbi.nlm.nih.gov/2349869/).
- Lorenzini L, Bertelli L, Lorenzi M. La disposizione arteriosa nel territorio della flessura colica sinistra [Arterial supply in the left colonic flexure]. *Ann Ital Chir.* 1999; 70(5): 691–698, indexed in Pubmed: [10692789](https://pubmed.ncbi.nlm.nih.gov/10692789/).
- Mane D, Shinde D. A Morphometric study of superior mesenteric artery and its implication in laparoscopic Surgery. *Int J Med Res Rev.* 2015; 3(4): 372–377, doi: [10.17511/ijmrr.2015.i4.070](https://doi.org/10.17511/ijmrr.2015.i4.070).
- Michels NA, Siddharth P, Kornblith PL, et al. The variant blood supply to the descending colon, rectosigmoid and rectum based on 400 dissections. Its importance in regional resections: A review of medical literature. *Dis Colon Rectum.* 1965; 8: 251–278, doi: [10.1007/BF02617894](https://doi.org/10.1007/BF02617894), indexed in Pubmed: [14323715](https://pubmed.ncbi.nlm.nih.gov/14323715/).
- Nelson T, Pollak R, Jonasson O, et al. Anatomic variants of the celiac, superior mesenteric, and inferior mesenteric arteries and their clinical relevance. *Clin Anat.* 1988; 1(2): 75–91, doi: [10.1002/ca.980010202](https://doi.org/10.1002/ca.980010202).
- Oran I, Yesildag A, Memis A. Aortic origin of right hepatic artery and superior mesenteric origin of splenic artery: two rare variations demonstrated angiographically. *Surg Radiol Anat.* 2001; 23(5): 349–352, doi: [10.1007/s00276-001-0349-7](https://doi.org/10.1007/s00276-001-0349-7), indexed in Pubmed: [11824137](https://pubmed.ncbi.nlm.nih.gov/11824137/).
- Romanes GJ. The abdominal cavity. Cunningham's Manual of Practical Anatomy. Thorax and Abdomen. 5th ed. Oxford University Press, London 2000: 135–136.
- Romanes GJ. Cunningham's Manual of Practical Anatomy. Thorax and Abdomen. 5th ed. Oxford University Press, London 2004: 137.
- Sato O, Matsumoto I, Kondoh K. Middle mesenteric artery encountered during abdominal aortic aneurysm surgery. *Jpn J Vasc Surg.* 2007; 16(7): 799–801.
- Schoenwolf GC, Bleyl SB, Brauer PR, Francis-West PH. Development of the gastrointestinal tract. Larsen's Human Embryology, 4th ed. Churchill Livingstone Elsevier, Philadelphia 2009: 441–442.
- Songür A, Toktaş M, Alkoç O, et al. Abdominal Aorta and Its Branches: Morphometry - Variations In Autopsy Cases. *Eur J Gen Med.* 2010; 7(3): 321–325, doi: [10.29333/ejgm/82876](https://doi.org/10.29333/ejgm/82876).
- Steward JA., Rankin FW. Blood supply of the large intestines: its surgical consideration. *Arch Surg.* 1933; 26(5): 843–891, doi: [10.1001/archsurg.1933.01170050113008](https://doi.org/10.1001/archsurg.1933.01170050113008).
- Tandler J. Zur Entwicklungsgeschichte der menschlichen Darmarterien. *Anat Hefte. Beiträge und Referate zur Anatomie und Entwicklungsgeschichte.* 1903; 23(1): 188–210, doi: [10.1007/bf02109984](https://doi.org/10.1007/bf02109984).
- Taniguchi J. Beitrag zur Topographie der grossen Aste der Bauchorta. *Folia Anat Jpn.* 1931; 9(3-4): 201–214, doi: [10.2535/ofaj1922.9.3-4\\_201](https://doi.org/10.2535/ofaj1922.9.3-4_201).
- Tanuma K, Kitazawa M, Itonaga T, et al. Four cases with the splenic artery of abnormal origin. *Kaibogaku Zasshi.* 1986; 61(2): 130–137.
- Williams PL, Bannister LH, Berry MM. Gray's anatomy. 38th ed. Churchill Livingstone, London 1995: 1553–1554.
- Yoo SJ, Ku MJ, Cho SS, et al. A case of the inferior mesenteric artery arising from the superior mesenteric artery in a Korean woman. *J Korean Med Sci.* 2011; 26(10): 1382–1385, doi: [10.3346/jkms.2011.26.10.1382](https://doi.org/10.3346/jkms.2011.26.10.1382), indexed in Pubmed: [22022194](https://pubmed.ncbi.nlm.nih.gov/22022194/).

# Glutamate receptor antagonist suppresses the activation of nesfatin-1 neurons following refeeding or glucose administration

S. Serter Kocoglu<sup>1</sup>, C. Oy<sup>2</sup>, Z. Halk<sup>2</sup>, C. Cakır<sup>2</sup>, Z. Minbay<sup>2</sup>, O. Eyigor<sup>2</sup>

<sup>1</sup>Department of Histology and Embryology, Balikesir University School of Medicine, Balikesir, Turkey

<sup>2</sup>Department of Histology and Embryology, Bursa Uludag University School of Medicine, Bursa, Turkey

[Received: 10 December 2020; Accepted: 3 March 2021; Early publication date: 22 March 2021]

**Background:** Nesfatin-1 is a newly identified satiety peptide that has regulatory effects on food intake and glucose metabolism, and is located in the hypothalamic nuclei, including the supraoptic nucleus (SON). In this study, we have investigated the hypothesis that nesfatin-1 neurons are activated by refeeding and intraperitoneal glucose injection and that the glutamatergic system has regulatory influences on nesfatin-1 neurons in the SON.

**Materials and methods:** The first set of experiments analysed activation of nesfatin-1 neurons after refeeding as a physiological stimulus and the effectiveness of the glutamatergic system on this physiological stimulation. The subjects were randomly divided into three groups: fasting group, refeeding group and antagonist (CNQX + refeeding) group. The second set of experiments analysed activation of nesfatin-1 neurons by glucose injection as a metabolic stimulus and the effectiveness of the glutamatergic system on this metabolic stimulation. The subjects were randomly divided into three groups: saline group, glucose group and antagonist (CNQX + glucose) group.

**Results:** Refeeding significantly increased the number of activated nesfatin-1 neurons by approximately 66%, and intraperitoneal glucose injection activated these neurons by about 55%, compared to the fasting and saline controls. The injections of glutamate antagonist (CNQX) greatly decreased the number of activated nesfatin-1 neurons.

**Conclusions:** This study suggested that nesfatin-1 neurons were activated by peripheral and/or metabolic signals and that this effect was mediated through the glutamatergic system. (Folia Morphol 2022; 81, 2: 379–386)

**Key words:** CNQX, glucose, glutamate, nesfatin-1, refeeding

## INTRODUCTION

Nesfatin-1 is an 82 amino acid peptide that has modulating effects in regulating food intake, body weight and gluconeogenesis [11, 41]. NUCB2/nesfatin-1 is widely expressed in peripheral tissues and the

central nervous system [51]. Nesfatin-1 is expressed in the hypothalamic nuclei which are involved with the regulation of food intake including the paraventricular nucleus (PVN), arcuate nucleus (ARC), supraoptic nucleus (SON), lateral hypothalamic area (LHA), zona

Address for correspondence: Asst. Prof. S. Serter Koçoğlu, PhD, Balikesir University Faculty of Medicine, Department of Histology and Embryology, Balikesir, Turkey, Postal code: 10000, tel: +90 (266) 612 10 10, fax: +90 (266) 612 14 17, e-mail: serter\_bio@hotmail.com

This article is available in open access under Creative Common Attribution-Non-Commercial-No Derivatives 4.0 International (CC BY-NC-ND 4.0) license, allowing to download articles and share them with others as long as they credit the authors and the publisher, but without permission to change them in any way or use them commercially.

incerta, and the solitary tract [11, 23, 41, 43, 44]. NUCB2/nesfatin-1 has also shown to be expressed in the periphery such as the gastric mucosa, adipose tissue, ovaries, testes, uterus, epididymis, cardiomyocytes and pancreatic beta cells [41]. Surprisingly, NUCB2/nesfatin-1 immunoreactivity was found to be 10 times higher in the gastric mucosa than in the brain [15]. The inhibitory effects on food intake of nesfatin-1 have been studied and it has also been shown to influence the regulation of cardiac functions, lipid metabolism, glucose homeostasis and reproductive functions [5]. It has been shown that intracerebroventricular injection of nesfatin-1 into the 3<sup>rd</sup> and 4<sup>th</sup> ventricles reduces food intake in mice and rats [29, 35, 44, 49].

Immunohistochemically, the expression of transcription factors such as c-Fos, phosphorylated CREB or phosphorylated STATs (phosphorylated signal transducers and transcription activators) are used as markers for determining neuronal activity changes [1, 4, 20, 52]. Nesfatin-1 injection to the 3<sup>rd</sup> ventricle has been shown to cause c-Fos expression, especially in the PVN and the nucleus of the solitary tract [11, 29]. The expression of c-Fos in these nuclei shows the anorectic signalling mechanism of nesfatin-1 [11].

Glucose sensitive neurons include glucose homeostasis and glucoprivic feeding. Recently, these neurons have received more attention due to their regulatory effects on appetite [51]. Nesfatin-1 inhibits food intake by increasing the number of the glucose sensitive neurons in the hypothalamus (dorsal vagal complex) [51]. Nesfatin-1 participates in blood glucose regulation. Subcutaneous injection of nesfatin-1 reduces the glucose levels in the blood during the oral glucose tolerance test. However, intracerebroventricular injection of nesfatin-1 does not reduce glucose levels in the blood [28]. This finding suggests that the glycaemic effect of nesfatin-1 may be peripheral. Co-injection of insulin and nesfatin-1 increased the phosphorylation of AKT kinase in liver, skeletal muscle and adipose tissue. As a result, GluT4 expression increased to increase glucose uptake [15].

Glutamate is the major excitatory amino acid neurotransmitter in the mammalian central nervous system [7, 8]. Glutamate plays an important role in the regulation of the neuroendocrine systems and the hypothalamus-pituitary-endocrine system axis by acting on many neuroendocrine and peptidergic neurons localised in the hypothalamus [7, 8, 40]. Glutamate-mediated neurotransmission occurs via metabotropic

and ionotropic glutamate receptors [22]. Ionotropic glutamate receptors are classified according to their agonists: N-methyl-D-aspartate (NMDA),  $\alpha$ -amino-3-hydroxy-5-methyl-4-isoxazolepropionic acid (AMPA) and 2-carboxy-3-carboxymethyl-4-isopropenylpyrrolidine (kainate) receptors [22, 27, 45]. NMDA receptors are composed of subunits named GluN1, GluN2A-D and GluN3A-B [9, 24]. These receptors have a critical function in excitatory synaptic transmission, plasticity and neurotoxicity [10, 30, 36–38].

Despite the many publications describing the mechanisms of action of nesfatin-1, there are no data about the peripheral and central control systems which play a role in the regulation of nesfatin-1 neuron activation. In this study, we analysed the effects of glutamatergic receptor antagonist (6-cyano-7-nitroquinoline-2,3-dione [CNQX]) on the activation of nesfatin-1 neurons following refeeding or glucose administration.

## MATERIALS AND METHODS

### Animals

All animal experiments were carried out in accordance with the National Institute of Health Guide for the Care and Use of Laboratory Animals and approved by the Experimental Ethics Committee of Bursa Uludag University (Date: 01.03.2016, No: HDP(T)-2016/25). Sixty-day-old male Sprague-Dawley rats (200–250 g) (n = 30), obtained from the Bursa Uludag University Laboratory Animal Breeding, Usage and Research Centre, were used in this study. Animals were kept in a light- and temperature-controlled facility (12:12 h light-dark cycle with lights off at 7:00 am and at 21°C) with water freely available.

### Experimental groups

#### ***Experiment 1: Suppressive effect of glutamate receptor antagonist (CNQX) on nesfatin-1 neuronal activation induced by refeeding***

The animals were divided into three groups (n = 5 per group). After a 48-h fasting period, the refeeding group was allowed to eat ad libitum for 2 h, while the fasting group was unfed and the antagonist group was injected intraperitoneally with non-NMDA glutamate antagonist (CNQX) (2 mg/kg CNQX in 300  $\mu$ L distilled water, DW) 15 min before the 2-h refeeding period. After the 48-h fasting, refeeding was started at 9:00 am at the beginning of the dark period of the dark-light cycle and the animals were allowed to feed for 2 h. Also, the CNQX injections were performed at 9:00 am.

### **Experiment 2: Suppressive effect of glutamate receptor antagonist (CNQX) on nesfatin-1 neuronal activation induced by glucose injection**

The animals were divided into three groups ( $n = 5$  per group). After a 48-h fasting period, the control group received saline (400  $\mu$ L saline, intraperitoneally [ip]), the glucose group was injected with glucose (2 g/kg glucose in 400  $\mu$ L saline, ip) and the antagonist group was injected with non-NMDA glutamate antagonist (2 mg/kg CNQX in 400  $\mu$ L saline, ip) 15 min before the glucose injection. The dosage of glucose injection was determined by referring the previous reports in the literature [21, 46, 47].

#### **Tissue preparation**

All injections were performed between 9:00 and 11:00 am and 90 min after injection, the animals were deeply anaesthetised with ether and fixed by trans-cardiac perfusion with 4% paraformaldehyde (PFA) in 0.13 M Sorenson's phosphate buffer, pH 7.4 (300 mL/animal). Brains and brainstems were carefully removed and post-fixed overnight in the same fixative at +4°C. Five series of brain sections with a thickness of 40  $\mu$ m were taken along the rostral-caudal axis of the hypothalamus with a vibratome and collected into Tris-HCl buffer (0.05 M, pH 7.6). The brain sections were washed 3 times with Tris-HCl buffer (0.05 M, pH 7.6) and then stored at -20°C in cryoprotectant until use.

#### **Immunohistochemistry**

Tris-HCl buffer was used for all washing steps. Primary and secondary antibodies were diluted in blocking buffer (10% normal horse serum, 0.2% Triton X-100, and 0.1% sodium azide in Tris-HCl buffer) for 2 h in order to prevent non-specific binding. Following 2-h incubation in blocking buffer, sections were transferred into rabbit anti-c-Fos antibody solution at a dilution of 1/20 000 (Chemicon, Billerica, MA, USA). The sections were incubated in donkey anti-rabbit IgG (1/300 dilution, Jackson Immuno-Research Laboratories, West Grove, PA, USA) for 2 h, processed with avidin-biotin complex according to the manufacturer's instructions (ABC Elite Standard Kit, Vector Laboratories, Burlingame, CA, USA) for 1 h and stained with diaminobenzidine (DAB) solution (25 mg DAB, 2 g nickel ammonium sulphate, 2.5  $\mu$ L hydrogen peroxide in 100 mL Tris-HCl buffer). After washing, the sections were secondarily blocked with 10% normal horse serum, and incubated in rabbit

anti-nesfatin-1 antibody (1/20 000 dilution, H-060-50, Phoenix Pharmaceuticals, Inc., USA) overnight at room temperature. This step was followed by secondary antibody incubation using biotin conjugated donkey anti-rabbit IgG (1/400 dilution, Jackson ImmunoResearch Labs, West Grove, PA, USA) for 2 h. DAB (25 mg DAB, 2.5  $\mu$ L hydrogen peroxide in 50 mL Tris-HCl buffer) was used for visualisation of the immunochemical complex. Double-stained sections were then transferred into Tris-HCl buffer, washed, mounted on glass slides, dried and coverslipped with DPX.

c-Fos antibodies used in this study have been used in many reports in the literature as well as in our previous studies [17, 42]. Nesfatin-1 antibody specificity was shown in previous studies in the literature [6].

#### **Cell counting**

Sections were analysed and photographed with Olympus BX-50 photomicroscope attached to a CCD camera (Olympus DP71, CCD colour camera, 1.5 million pixels, Olympus Corporation, Japan). Sections between the coordinates determined according to the rat brain atlas (bregma -0.48 mm and -1.44 mm SON) were used for double immunohistochemical labelling [39]. Cross sections taken at five different levels at the same coordinate and at equal distance for each animal in the rostrocaudal plane were used for cell counting. All nesfatin-1-positive cells, with and without c-Fos-positive nuclei neurons in the SON were counted bilaterally and blindly in every fourth section between the stereotaxic coordinates of bregma -0.48 mm — bregma -1.44 mm. Then the percentage of c-Fos-positive nesfatin-1 neurons to all nesfatin neurons was calculated within each animal in dual indirect immunoperoxidase-labelled sections.

#### **Statistical analysis**

The percentage of the c-Fos positivity in nesfatin-1 positive cells is expressed as mean  $\pm$  standard deviation. The significance of differences between the groups was assessed with ANOVA test. The level of statistical significance was set at  $p < 0.05$ . Statistical data analysis was performed with IBM SPSS, 23.0.

## **RESULTS**

The agonist and antagonist injections did not cause adverse reactions or mortality during the experiments.

Nesfatin-1 positivity was visualized by brown reaction product with chromogen in the cytoplasm and

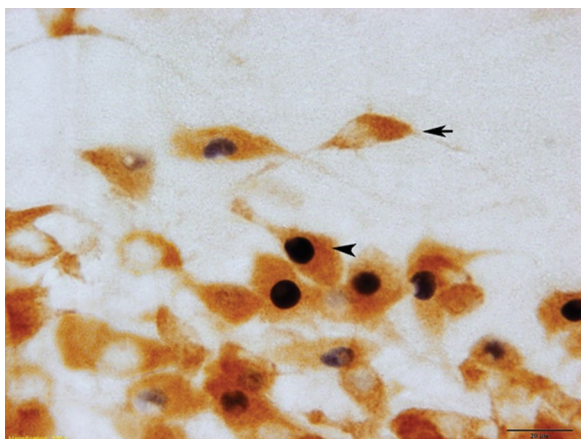


**Figure 1.** Representative c-Fos-positive and c-Fos-negative nesfatin-1 neurons. The arrow-head indicates c-Fos positivity (black) in the nucleus of a nesfatin-1-positive (brown) neuron. The arrow indicates a representative c-Fos-negative nesfatin-1 neuron.

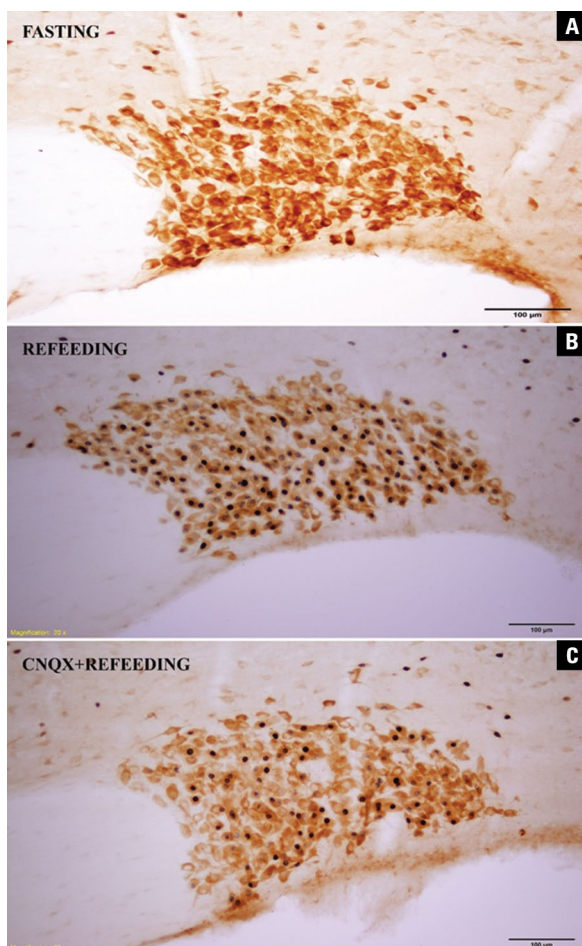


**Figure 2.** Effect of CNQX, a non-N-methyl-D-aspartate (NMDA) glutamate antagonist, in subjects stimulated by refeeding after fasting. Double-immunohistochemical staining of c-Fos and nesfatin-1 in supra-optic nucleus after 48 h fasting (A), after 2 h refeeding following 48 h fasting (B) and CNQX-treated subjects before feeding (C).

**Table 1.** The percentages of c-Fos-positive nesfatin-1 neurons relative to all nesfatin-1 neurons in all groups (mean  $\pm$  standard deviation). P values pertain to the comparison with the refeeding and glucose-injected groups

	c-Fos expression (%)	
	Nesfatin-1 neurons	P
Fasting	1.00 $\pm$ 0.94	= 0.00
Refeeding	66.65 $\pm$ 9.82	
CNQX + refeeding	25.15 $\pm$ 17.22	< 0.009
Glucose control	1.13 $\pm$ 0.66	< 0.01
Glucose	55.7 $\pm$ 21.46	
CNQX + glucose	6.32 $\pm$ 9.60	< 0.01

CNQX — 6-cyano-7-nitroquinoxaline-2,3-dione

c-Fos positivity by blue/black reaction product in the nuclei (Fig. 1). After the 48-h fasting, refeeding and ip glucose injection significantly increased the number of c-Fos-expressing nesfatin-1 neurons, compared with the fasting and saline controls. These effects were also blocked by antagonist injection (CNQX).

#### Refeeding induced c-Fos expression in nesfatin-1 neurons and CNQX reduced the number of active nesfatin-1 neurons

After refeeding for 2 h following 48 h fasting, c-Fos-immunoreactive neurons were observed abundantly in the SON, PVN.

The 2-h refeeding after 48-h fasting caused a significant increase in the number of c-Fos-positive nesfatin-1 neurons compared with the fasting group. These effects were also blocked by antagonist (CNQX). In the refeeding group, about 66% of nesfatin-1 neurons localised in the SON were c-Fos-positive, whereas this ratio was 1% in the fasting group ( $p = 0.000$ ). The ratio of the activated nesfatin-1 neurons was reduced to 25% after CNQX injection ( $p = 0.009$ ). The number of nesfatin-1 neurons expressing c-Fos immunoreactivity was significantly (66 times) greater under refeeding, compared with fasting conditions (Figs. 2, 4A, Table 1).

#### Glucose induced c-Fos expression in nesfatin-1 neurons and CNQX reduced the number of active nesfatin-1 neurons

After glucose injection following 48 h fasting, c-Fos-immunoreactive neurons were observed abundantly in the SON, PVN.

The glucose injection after 48-h fasting significantly increased the number of c-Fos-positive nesfatin-1

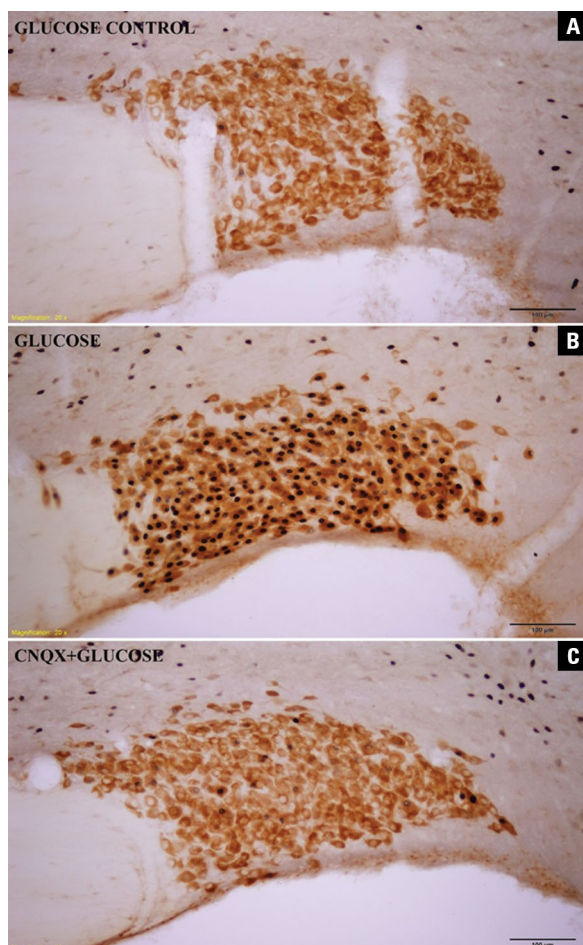


**Figure 3.** Effect of CNQX, a non-N-methyl-D-aspartate (NMDA) glutamate antagonist, in subjects stimulated by glucose injection. Double-immunohistochemical staining of c-Fos and nesfatin-1 in supraoptic nucleus, after 48 h fasting; saline injection (**A**), glucose injection (**B**) and CNQX-treated subjects before glucose injection (**C**).

neurons compared with the control group. These effects were also blocked by antagonist (CNQX). The glucose injection activated about 55% of c-Fos-positive neurons (55%, significantly more than in the control group: 1%,  $p = 0.01$ ). The ratio of the activated nesfatin-1 clearly decreased after antagonist injection (CNQX) (6%,  $p = 0.01$ ).

The number of c-Fos-expressing nesfatin-1 neurons was significantly increased following glucose injections when compared with saline conditions. The number of glucose-activated nesfatin-1 neurons was significantly reduced if CNQX was pre-injected (Figs. 3, 4B, Table 1).

## DISCUSSION

Nesfatin-1 is a newly identified peptide that has regulatory effects on food and water intake, energy

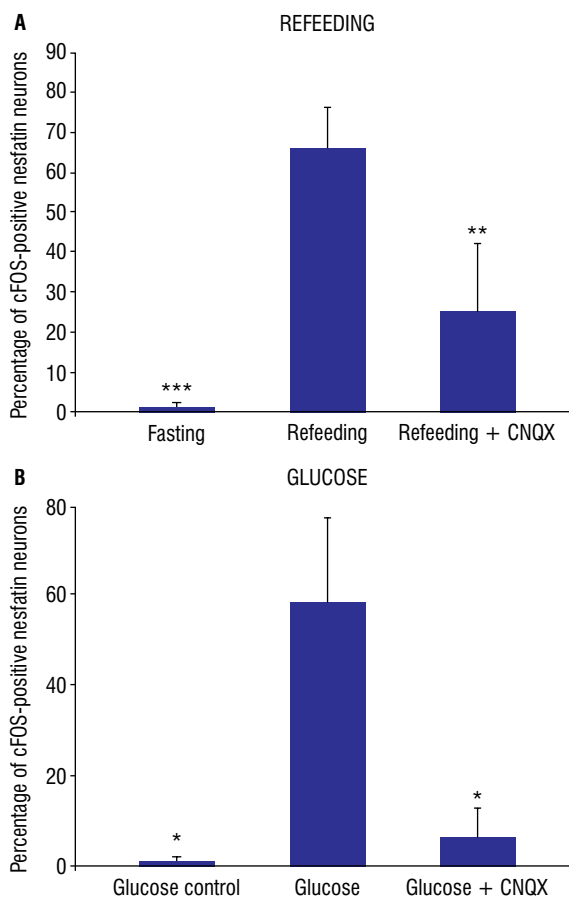


**Figure 4.** The percentages of c-Fos-positive nesfatin-1 neurons relative to all nesfatin-1 neurons. Effect of 6-cyano-7-nitroquinoxaline-2,3-dione (CNQX), a non-N-methyl-D-aspartate (NMDA) glutamate antagonist, in subjects stimulated by refeeding after fasting. There were significant differences between fasting-refeeding (\*\*\*)  $p < 0.001$  groups and refeeding-antagonist groups (\*\*\*)  $p < 0.01$  (**A**). Effect of CNQX, a non-NMDA glutamate antagonist, in subjects stimulated by glucose injection. There were significant differences between glucose control-glucose and glucose-antagonist (CNQX + glucose) groups (\* $p < 0.05$ ) (**B**).

consumption, cardiovascular and gastrointestinal functions, anxiety and depression and reproductive functions [41]. Although there is some literature on the effects of nesfatin-1 neurons in the target cells and organs, no experimental studies have been found on central neurotransmitter systems. In the present study, we investigated the hypothesis that nesfatin-1 neurons are activated by refeeding and glucose injection as peripheral and metabolic factors and that the glutamatergic system has regulatory influences on nesfatin-1 neurons in the SON.

The regulatory effects related to neurogenesis, apoptosis, neurite development and synapse formation of glutamate, the main excitatory neurotransmitter

of the central nervous system, on the hypothalamic neuroendocrine systems, is intensively investigated [12–14, 32]. Glutamate is the dominant excitatory transmitter in neuroendocrine regulation in the hypothalamus. There were large amounts of glutamate in boutons making synaptic contact with neuroendocrine neurons in the arcuate, paraventricular, and supraoptic nuclei. The immunohistochemical studies showed that high level glutamate-immunoreactive terminals were present in the SON. Glutamate is also one of the major excitatory neurotransmitters in the SON [31]. In our laboratories we showed that kainic acid activates oxytocinergic neurons through non-NMDA glutamate receptors in the SON and PVN [34]. Our immunohistochemical studies showed that systemic administration of ionotropic non-NMDA and NMDA glutamate receptor agonists directly or indirectly activate neuronostatin neurons at different rates [42]. Also, we detected increased number of c-Fos positive nesfatin-1 neurons in kainic acid, AMPA and NMDA injected subjects in the SON [18]. In addition, expression of the ionotropic glutamate receptors has been demonstrated with fluorescence microscopy on nesfatin-1 neurons in the SON [18]. In the present study, after refeeding and glucose injection, c-Fos-immunoreactive neurons were observed abundantly in the SON. We analysed the SON for the effects of the glutamatergic system on nesfatin-1 neurons induced by refeeding and glucose injection.

The anorexigenic effect after injection into brain ventricles of nesfatin-1 has been studied in various animal groups such as rats [25, 44, 50], mice [3, 16], pigs [26] and goldfish [19], and it has been found to have a strong anorexigenic effect. Inhibition of dark phase food intake after third ventricle injection of nesfatin-1 has been described [35]. Low dose injection into the 4<sup>th</sup> ventricle of nesfatin-1 has been shown to reduce food intake in the first 4 h and suppress cumulative food intake in the 5<sup>th</sup> h [43]. Intracerebroventricular injection of nesfatin-1 has been shown to reduce water intake as well as food intake [48]. In the SON, refeeding has been shown to activate the number of nesfatin-1-immunoreactive neurons and mRNA expression of NUCB2 [23]. Refeeding after fasting also increased the number of c-Fos-positive nesfatin-1 neurons in the SON [23]. Our results not only confirmed this previous report by showing that activation of the nesfatin-1 neurons was caused by refeeding after fasting, but also that this activation was significantly suppressed by the administration

of the AMPA/kainate receptor antagonist CNQX. This result suggests that the regulatory effect of glutamate on nesfatin-1 neurons is unique. In our previous study, we showed that 2-h refeeding after 48-h fasting induced pSTAT5 expression in the neuronostatin neurons in the anterior hypothalamic periventricular nucleus and this expression was significantly suppressed by glutamate receptor antagonist (CNQX) [42]. This information supports that a peripheral factor, such as refeeding, was effective in regulating the functions of nesfatin-1 neurons and that this effect was mediated through the glutamatergic system.

CNQX application to the fasting group was considered while designing the presented study. But in preliminary experiments, c-fos positivity was only 1% in nesfatin neurons in the fasting group. We did not use this group because we predicted that CNQX administration before fasting would not significantly change the activation of nesfatin neurons.

The hypothalamus plays an important role in regulating food intake and glucose homeostasis [33]. Glucose is the primary fuel for the brain and enters the central nervous system with the high-affinity glucose transporter (GLUT) type 1 [2]. Glucosensitive and glucoresponsive neurons are found in the hypothalamic nuclei and participate in glucose homeostasis [33]. Glucose-sensitive neurons are glucose-activated or glucose-inhibited neurons. Glucose-sensitive neurons are found in the hypothalamic nuclei such as ARC, PVN, SON, VMH, and lateral hypothalamus, and respond to blood glucose changes [33]. Neuronal activation of the hypothalamic nuclei after glucose infusion has been demonstrated using the c-Fos as the neuronal activation marker. The number of c-Fos-positive neurons peaks in 90 min after stimulus as a response to acute physiological stimuli. After intracarotid glucose injection, c-Fos, immunoreactive neurons are detected in PVN and VMH. The number of c-Fos-positive neurons in ARC and PVN was significantly higher than in the saline group [33]. We not only found that glucose injection after fasting dramatically increased the number of c-Fos immunoreactive-nesfatin-1 neurons in the SON but also determined that the number of active nesfatin-1 neurons was significantly reduced after glutamate receptor antagonist (CNQX) injections. This information suggests that nesfatin-1 neurons are glucose sensitive neurons and glutamatergic system regulates this mechanism.

In the present study, the increase in the number of activated nesfatin-1 neurons was observed to be

about 66-fold with refeeding and 55-fold with glucose injection after fasting. These results suggest that refeeding and/or glucose injection after fasting led to activation of nesfatin-1 neurons and this activation was mediated by the intracellular pathway with c-Fos. This data also supports the possibility of an intracellular pathway using c-Fos as the transcription factor, has a role in the regulation of the physiological activities of nesfatin-1 neurons. Furthermore, the number of activated nesfatin-1 neurons was significantly suppressed by glutamate receptor antagonist (CNQX) application. To our knowledge, this is the first report that has shown the regulatory effect of glutamatergic system on nesfatin-1 neurons. Our previous studies supports that glutamate receptor antagonist (CNQX) can reach the central nervous system and affect the neuronal activation [13, 18, 34, 42]. Also, our data showed that nesfatin-1 neurons express glutamate receptor subunits [18]. Taken together, we can suggest that glutamatergic signals may reach the nesfatin-1 neurons directly. Another possibility of course is that an indirect mechanism involving glutamate-receptive interneurons may play a role in the regulation of nesfatinergic system.

It is important to implicate that the immunohistochemistry is limited to the detectable levels of the proteins that are analysed in this study. Our results only include the nesfatin-1 neurons that can be identified by immunohistochemistry, and the numbers provided in this study only represents these neurons.

## CONCLUSIONS

In conclusion, this study demonstrated that refeeding and glucose intake highly selectively activates nesfatin-1 neurons in the SON. This activation suggests that nesfatin-1 neurons in the SON may play a role in the regulation of feeding behaviour and glucose metabolism. The results also demonstrated that glutamate antagonist CNQX can specifically block this activation, suggesting that this effect was mediated through the glutamatergic system.

**Conflict of interest:** None declared

## REFERENCES

- Altarejos JY, Montminy M. CREB and the CREB co-activators: sensors for hormonal and metabolic signals. *Nat Rev Mol Cell Biol.* 2011; 12(3): 141–151, doi: [10.1038/nrm3072](https://doi.org/10.1038/nrm3072), indexed in Pubmed: [21346730](https://pubmed.ncbi.nlm.nih.gov/21346730/).
- Alvarsson A, Stanley SA. Remote control of glucose-sensing neurons to analyze glucose metabolism. *Am J Physiol Endocrinol Metab.* 2018; 315(3): E327–E339, doi: [10.1152/ajpendo.00469.2017](https://doi.org/10.1152/ajpendo.00469.2017), indexed in Pubmed: [29812985](https://pubmed.ncbi.nlm.nih.gov/29812985/).
- Atsuchi K, Asakawa A, Ushikai M, et al. Centrally administered nesfatin-1 inhibits feeding behaviour and gastroduodenal motility in mice. *Neuroreport.* 2010; 21(15): 1008–1011, doi: [10.1097/WNR.0b013e32833f7b96](https://doi.org/10.1097/WNR.0b013e32833f7b96), indexed in Pubmed: [20827224](https://pubmed.ncbi.nlm.nih.gov/20827224/).
- Balazs R. Trophic effect of glutamate. *Curr Top Med Chem.* 2006; 6(10): 961–968, doi: [10.2174/15680260677323700](https://doi.org/10.2174/15680260677323700).
- Blanco AM, Velasco C, Bertucci JI, et al. Nesfatin-1 regulates feeding, glucosensing and lipid metabolism in rainbow trout. *Front Endocrinol (Lausanne).* 2018; 9: 484, doi: [10.3389/fendo.2018.00484](https://doi.org/10.3389/fendo.2018.00484), indexed in Pubmed: [30210451](https://pubmed.ncbi.nlm.nih.gov/30210451/).
- Brailoiu GC, Dun SL, Brailoiu E, et al. Nesfatin-1: distribution and interaction with a G protein-coupled receptor in the rat brain. *Endocrinology.* 2007; 148(10): 5088–5094, doi: [10.1210/en.2007-0701](https://doi.org/10.1210/en.2007-0701), indexed in Pubmed: [17627999](https://pubmed.ncbi.nlm.nih.gov/17627999/).
- Brann DW. Glutamate: a major excitatory transmitter in neuroendocrine regulation. *Neuroendocrinology.* 1995; 61(3): 213–225, doi: [10.1159/000126843](https://doi.org/10.1159/000126843), indexed in Pubmed: [7898626](https://pubmed.ncbi.nlm.nih.gov/7898626/).
- Brann D, Mahesh V. Excitatory amino acids: function and significance in reproduction and neuroendocrine regulation. *Front Neuroendocrinol.* 1994; 15(1): 3–49, doi: [10.1006/frne.1994.1002](https://doi.org/10.1006/frne.1994.1002).
- Collingridge GL, Olsen RW, Peters J, et al. A nomenclature for ligand-gated ion channels. *Neuropharmacology.* 2009; 56(1): 2–5, doi: [10.1016/j.neuropharm.2008.06.063](https://doi.org/10.1016/j.neuropharm.2008.06.063), indexed in Pubmed: [18655795](https://pubmed.ncbi.nlm.nih.gov/18655795/).
- Cull-Candy S, Brickley S, Farrant M. NMDA receptor subunits: diversity, development and disease. *Curr Opin Neurobiol.* 2001; 11(3): 327–335, doi: [10.1016/s0959-4388\(00\)00215-4](https://doi.org/10.1016/s0959-4388(00)00215-4), indexed in Pubmed: [11399431](https://pubmed.ncbi.nlm.nih.gov/11399431/).
- Dong J, Guan HZ, Jiang ZY, et al. Nesfatin-1 influences the excitability of glucosensing neurons in the dorsal vagal complex and inhibits food intake. *PLoS One.* 2014; 9(6): e98967, doi: [10.1371/journal.pone.0098967](https://doi.org/10.1371/journal.pone.0098967), indexed in Pubmed: [24906120](https://pubmed.ncbi.nlm.nih.gov/24906120/).
- Eyigor O, Centers A, Jennes L. Distribution of ionotropic glutamate receptor subunit mRNAs in the rat hypothalamus. *J Comp Neurol.* 2001; 434(1): 101–124, doi: [10.1002/cne.1167](https://doi.org/10.1002/cne.1167), indexed in Pubmed: [11329132](https://pubmed.ncbi.nlm.nih.gov/11329132/).
- Eyigor O, Minbay Z, Cavusoglu I. Activation of orexin neurons through non-NMDA glutamate receptors evidenced by c-Fos immunohistochemistry. *Endocrine.* 2010; 37(1): 167–172, doi: [10.1007/s12020-009-9284-x](https://doi.org/10.1007/s12020-009-9284-x), indexed in Pubmed: [20963566](https://pubmed.ncbi.nlm.nih.gov/20963566/).
- Eyigor O, Minbay Z, Cavusoglu I, et al. Localization of kainate receptor subunit GluR5-immunoreactive cells in the rat hypothalamus. *Brain Res Mol Brain Res.* 2005; 136(1-2): 38–44, doi: [10.1016/j.molbrainres.2005.01.015](https://doi.org/10.1016/j.molbrainres.2005.01.015), indexed in Pubmed: [15893585](https://pubmed.ncbi.nlm.nih.gov/15893585/).
- Fan XT, Tian Z, Li SZ, et al. Ghrelin receptor is required for the effect of nesfatin-1 on glucose metabolism. *Front Endocrinol (Lausanne).* 2018; 9: 633, doi: [10.3389/fendo.2018.00633](https://doi.org/10.3389/fendo.2018.00633), indexed in Pubmed: [30405536](https://pubmed.ncbi.nlm.nih.gov/30405536/).
- Goebel M, Stengel A, Wang L, et al. Central nesfatin-1 reduces the nocturnal food intake in mice by reducing meal size and increasing inter-meal intervals. *Peptides.* 2011; 32(1): 36–43, doi: [10.1016/j.peptides.2010.09.027](https://doi.org/10.1016/j.peptides.2010.09.027), indexed in Pubmed: [20933030](https://pubmed.ncbi.nlm.nih.gov/20933030/).
- Gok-Yurtseven D, Kafa IM, Minbay Z, et al. Glutamatergic activation of A1 and A2 noradrenergic neurons in the rat brain stem. *Croat Med J.* 2019; 60(4): 352–360, indexed in Pubmed: [31483121](https://pubmed.ncbi.nlm.nih.gov/31483121/).
- Gok Yurtseven D, Serter Kocoglu S, Minbay Z, et al. Immunohistochemical evidence for glutamatergic regulation of nesfatin-1 neurons in the rat hypothalamus. *Brain Sci.* 2020; 10(9), doi: [10.3390/brainsci10090630](https://doi.org/10.3390/brainsci10090630), indexed in Pubmed: [32932902](https://pubmed.ncbi.nlm.nih.gov/32932902/).
- Gonzalez R, Kerbel B, Chun A, et al. Molecular, cellular and physiological evidences for the anorexigenic actions of nesfatin-1 in goldfish. *PLoS One.* 2010; 5(12): e15201, doi: [10.1371/journal.pone.0015201](https://doi.org/10.1371/journal.pone.0015201), indexed in Pubmed: [21151928](https://pubmed.ncbi.nlm.nih.gov/21151928/).
- Hoffman GE, Lyo D. Anatomical markers of activity in neuroendocrine systems: are we all 'fos-ed out'? *J Neuroendocrinol.* 2002;

- 14(4): 259–268, doi: [10.1046/j.1365-2826.2002.00775.x](https://doi.org/10.1046/j.1365-2826.2002.00775.x), indexed in Pubmed: [11963822](https://pubmed.ncbi.nlm.nih.gov/11963822/).
21. Huo L, Gamber K, Greeley S, et al. Leptin-dependent control of glucose balance and locomotor activity by POMC neurons. *Cell Metab.* 2009; 9(6): 537–547, doi: [10.1016/j.cmet.2009.05.003](https://doi.org/10.1016/j.cmet.2009.05.003), indexed in Pubmed: [19490908](https://pubmed.ncbi.nlm.nih.gov/19490908/).
  22. Kew JNC, Kemp JA. Ionotropic and metabotropic glutamate receptor structure and pharmacology. *Psychopharmacology (Berl.)*. 2005; 179(1): 4–29, doi: [10.1007/s00213-005-2200-z](https://doi.org/10.1007/s00213-005-2200-z), indexed in Pubmed: [15731895](https://pubmed.ncbi.nlm.nih.gov/15731895/).
  23. Kohno D, Nakata M, Maejima Y, et al. Nesfatin-1 neurons in paraventricular and supraoptic nuclei of the rat hypothalamus coexpress oxytocin and vasopressin and are activated by refeeding. *Endocrinology*. 2008; 149(3): 1295–1301, doi: [10.1210/en.2007-1276](https://doi.org/10.1210/en.2007-1276), indexed in Pubmed: [18048495](https://pubmed.ncbi.nlm.nih.gov/18048495/).
  24. Köles L, Wirkner K, Illes P. Modulation of ionotropic glutamate receptor channels. *Neurochem Res.* 2001; 26(8-9): 925–932, doi: [10.1023/a:1012380416876](https://doi.org/10.1023/a:1012380416876), indexed in Pubmed: [11699944](https://pubmed.ncbi.nlm.nih.gov/11699944/).
  25. Könczöl K, Pintér O, Ferenczi S, et al. Nesfatin-1 exerts long-term effect on food intake and body temperature. *Int J Obes (Lond)*. 2012; 36(12): 1514–1521, doi: [10.1038/ijo.2012.2](https://doi.org/10.1038/ijo.2012.2), indexed in Pubmed: [22290539](https://pubmed.ncbi.nlm.nih.gov/22290539/).
  26. Lents CA, Barb CR, Hausman GJ, et al. Effects of nesfatin-1 on food intake and LH secretion in prepubertal gilts and genomic association of the porcine NUCB2 gene with growth traits. *Domest Anim Endocrinol.* 2013; 45(2): 89–97, doi: [10.1016/j.domaniend.2013.06.002](https://doi.org/10.1016/j.domaniend.2013.06.002), indexed in Pubmed: [23820242](https://pubmed.ncbi.nlm.nih.gov/23820242/).
  27. Lerma J, Paternain AV, Rodríguez-Moreno A, et al. Molecular physiology of kainate receptors. *Physiol Rev.* 2001; 81(3): 971–998, doi: [10.1152/physrev.2001.81.3.971](https://doi.org/10.1152/physrev.2001.81.3.971), indexed in Pubmed: [11427689](https://pubmed.ncbi.nlm.nih.gov/11427689/).
  28. Li Z, Gao L, Tang H, et al. Peripheral effects of nesfatin-1 on glucose homeostasis. *PLoS One.* 2013; 8(8): e71513, doi: [10.1371/journal.pone.0071513](https://doi.org/10.1371/journal.pone.0071513), indexed in Pubmed: [23967220](https://pubmed.ncbi.nlm.nih.gov/23967220/).
  29. Maejima Y, Sedbazar U, Suyama S, et al. Nesfatin-1-regulated oxytocinergic signaling in the paraventricular nucleus causes anorexia through a leptin-independent melanocortin pathway. *Cell Metab.* 2009; 10(5): 355–365, doi: [10.1016/j.cmet.2009.09.002](https://doi.org/10.1016/j.cmet.2009.09.002), indexed in Pubmed: [19883614](https://pubmed.ncbi.nlm.nih.gov/19883614/).
  30. Mayer ML. Structural biology of glutamate receptor ion channel complexes. *Curr Opin Struct Biol.* 2016; 41: 119–127, doi: [10.1016/j.sbi.2016.07.002](https://doi.org/10.1016/j.sbi.2016.07.002), indexed in Pubmed: [27454049](https://pubmed.ncbi.nlm.nih.gov/27454049/).
  31. Meeker RB, Greenwood RS, Hayward JN. Glutamate is the major excitatory transmitter in the supraoptic nuclei. *Ann N Y Acad Sci.* 1993; 689: 636–639, doi: [10.1111/j.1749-6632.1993.tb55614.x](https://doi.org/10.1111/j.1749-6632.1993.tb55614.x), indexed in Pubmed: [8103978](https://pubmed.ncbi.nlm.nih.gov/8103978/).
  32. Meeker RB, McGinnis S, Greenwood RS, et al. Increased hypothalamic glutamate receptors induced by water deprivation. *Neuroendocrinology.* 1994; 60(5): 477–485, doi: [10.1159/000126784](https://doi.org/10.1159/000126784), indexed in Pubmed: [7531299](https://pubmed.ncbi.nlm.nih.gov/7531299/).
  33. Miñana-Solis MD, Angeles-Castellanos M, Buijs RM, et al. Altered Fos immunoreactivity in the hypothalamus after glucose administration in pre- and post-weaning malnourished rats. *Nutr Neurosci.* 2010; 13(4): 152–160, doi: [10.1179/147683010X12611460764246](https://doi.org/10.1179/147683010X12611460764246), indexed in Pubmed: [20670470](https://pubmed.ncbi.nlm.nih.gov/20670470/).
  34. Minbay FZ, Eyigor O, Cavusoglu I. Kainic acid activates oxytocinergic neurons through non-nmda glutamate receptors. *Int J Neurosci.* 2006; 116(5): 587–600, doi: [10.1080/00207450600592123](https://doi.org/10.1080/00207450600592123), indexed in Pubmed: [16644519](https://pubmed.ncbi.nlm.nih.gov/16644519/).
  35. Oh-I S, Shimizu H, Satoh T, et al. Identification of nesfatin-1 as a satiety molecule in the hypothalamus. *Nature.* 2006; 443(7112): 709–712, doi: [10.1038/nature05162](https://doi.org/10.1038/nature05162), indexed in Pubmed: [17036007](https://pubmed.ncbi.nlm.nih.gov/17036007/).
  36. Ozawa S, Kamiya H, Tsuzuki K. Glutamate receptors in the mammalian central nervous system. *Prog Neurobiol.* 1998; 54(5): 581–618, doi: [10.1016/s0301-0082\(97\)00085-3](https://doi.org/10.1016/s0301-0082(97)00085-3), indexed in Pubmed: [9550192](https://pubmed.ncbi.nlm.nih.gov/9550192/).
  37. Pachernegg S, Strutz-Seeböhm N, Hollmann M. GluN3 subunit-containing NMDA receptors: not just one-trick ponies. *Trends Neurosci.* 2012; 35(4): 240–249, doi: [10.1016/j.tins.2011.11.010](https://doi.org/10.1016/j.tins.2011.11.010), indexed in Pubmed: [22240240](https://pubmed.ncbi.nlm.nih.gov/22240240/).
  38. Paoletti P. Molecular basis of NMDA receptor functional diversity. *Eur J Neurosci.* 2011; 33(8): 1351–1365, doi: [10.1111/j.1460-9568.2011.07628.x](https://doi.org/10.1111/j.1460-9568.2011.07628.x), indexed in Pubmed: [21395862](https://pubmed.ncbi.nlm.nih.gov/21395862/).
  39. Paxinos G, Watson C. *The rat brain in stereotaxic coordinates.* Acad Press, London 2009.
  40. Samson WK, Zhang JV, Avsian-Kretschmer O, et al. Neuronostatin encoded by the somatostatin gene regulates neuronal, cardiovascular, and metabolic functions. *J Biol Chem.* 2008; 283(46): 31949–31959, doi: [10.1074/jbc.M804784200](https://doi.org/10.1074/jbc.M804784200), indexed in Pubmed: [18753129](https://pubmed.ncbi.nlm.nih.gov/18753129/).
  41. Schalla MA, Stengel A. Current understanding of the role of nesfatin-1. *J Endocr Soc.* 2018; 2(10): 1188–1206, doi: [10.1210/je.2018-00246](https://doi.org/10.1210/je.2018-00246), indexed in Pubmed: [30302423](https://pubmed.ncbi.nlm.nih.gov/30302423/).
  42. Serter Kocoglu S, Gok Yurtseven D, Cakir C, et al. Glutamatergic activation of neuronostatin neurons in the periventricular nucleus of the hypothalamus. *Brain Sci.* 2020; 10(4), doi: [10.3390/brainsci10040217](https://doi.org/10.3390/brainsci10040217), indexed in Pubmed: [32268550](https://pubmed.ncbi.nlm.nih.gov/32268550/).
  43. Stengel A, Goebel M, Taché Y. Nesfatin-1: a novel inhibitory regulator of food intake and body weight. *Obes Rev.* 2011; 12(4): 261–271, doi: [10.1111/j.1467-789X.2010.00770.x](https://doi.org/10.1111/j.1467-789X.2010.00770.x), indexed in Pubmed: [20546141](https://pubmed.ncbi.nlm.nih.gov/20546141/).
  44. Stengel A, Goebel M, Wang L, et al. Central nesfatin-1 reduces dark-phase food intake and gastric emptying in rats: differential role of corticotropin-releasing factor2 receptor. *Endocrinology.* 2009; 150(11): 4911–4919, doi: [10.1210/en.2009-0578](https://doi.org/10.1210/en.2009-0578), indexed in Pubmed: [19797401](https://pubmed.ncbi.nlm.nih.gov/19797401/).
  45. Tse YC, Yung KK. Cellular expression of ionotropic glutamate receptor subunits in subpopulations of neurons in the rat substantia nigra pars reticulata. *Brain Res.* 2000; 854(1-2): 57–69, doi: [10.1016/s0006-8993\(99\)02292-1](https://doi.org/10.1016/s0006-8993(99)02292-1), indexed in Pubmed: [10784107](https://pubmed.ncbi.nlm.nih.gov/10784107/).
  46. Üner A, Gonçalves GHM, Li W, et al. The role of GluN2A and GluN2B NMDA receptor subunits in AgRP and POMC neurons on body weight and glucose homeostasis. *Mol Metab.* 2015; 4(10): 678–691, doi: [10.1016/j.molmet.2015.06.010](https://doi.org/10.1016/j.molmet.2015.06.010), indexed in Pubmed: [26500840](https://pubmed.ncbi.nlm.nih.gov/26500840/).
  47. Üner AG, Keçik O, Quaresma PGF, et al. Role of POMC and AgRP neuronal activities on glycaemia in mice. *Sci Rep.* 2019; 9(1): 13068, doi: [10.1038/s41598-019-49295-7](https://doi.org/10.1038/s41598-019-49295-7), indexed in Pubmed: [31506541](https://pubmed.ncbi.nlm.nih.gov/31506541/).
  48. Yosten GLC, Redlinger L, Samson WK. Evidence for a role of endogenous nesfatin-1 in the control of water drinking. *J Neuroendocrinol.* 2012; 24(7): 1078–1084, doi: [10.1111/j.1365-2826.2012.02304.x](https://doi.org/10.1111/j.1365-2826.2012.02304.x), indexed in Pubmed: [22375892](https://pubmed.ncbi.nlm.nih.gov/22375892/).
  49. Yosten GLC, Samson WK. Nesfatin-1 exerts cardiovascular actions in brain: possible interaction with the central melanocortin system. *Am J Physiol Regul Integr Comp Physiol.* 2009; 297(2): R330–R336, doi: [10.1152/ajpregu.90867.2008](https://doi.org/10.1152/ajpregu.90867.2008), indexed in Pubmed: [19474390](https://pubmed.ncbi.nlm.nih.gov/19474390/).
  50. Yosten GLC, Samson WK. The anorexigenic and hypertensive effects of nesfatin-1 are reversed by pretreatment with an oxytocin receptor antagonist. *Am J Physiol Regul Integr Comp Physiol.* 2010; 298(6): R1642–R1647, doi: [10.1152/ajpregu.00804.2009](https://doi.org/10.1152/ajpregu.00804.2009), indexed in Pubmed: [20335376](https://pubmed.ncbi.nlm.nih.gov/20335376/).
  51. Yuan JH, Chen Xi, Dong J, et al. Nesfatin-1 in the lateral parabrachial nucleus inhibits food intake, modulates excitability of glucosensing neurons, and enhances UCP1 expression in brown adipose tissue. *Front Physiol.* 2017; 8: 235, doi: [10.3389/fphys.2017.00235](https://doi.org/10.3389/fphys.2017.00235), indexed in Pubmed: [28484396](https://pubmed.ncbi.nlm.nih.gov/28484396/).
  52. Zhao JB, Zhang Y, Li GZ, et al. Activation of JAK2/STAT pathway in cerebral cortex after experimental traumatic brain injury of rats. *Neurosci Lett.* 2011; 498(2): 147–152, doi: [10.1016/j.neulet.2011.05.001](https://doi.org/10.1016/j.neulet.2011.05.001), indexed in Pubmed: [21596098](https://pubmed.ncbi.nlm.nih.gov/21596098/).

# The effect of hyperglycaemia on the macrophages in the cell culture

E.R. Megawati<sup>1</sup> , N. Meutia<sup>1</sup>, L.D. Lubis<sup>2</sup>

<sup>1</sup>Department of Physiology, Faculty of Medicine, Universitas Sumatera Utara, Medan, Indonesia

<sup>2</sup>Department of Histology, Faculty of Medicine, Universitas Sumatera Utara, Medan, Indonesia

[Received: 11 December 2020; Accepted: 27 January 2021; Early publication date: 23 February 2021]

**Background:** The availability of glucose in tissue has a role in macrophages polarisation into an inflammatory phenotype. The overnutrition condition such as hyperglycaemia induces macrophage infiltration especially the inflammatory macrophages. The aim of this study was to analyse the effect of hyperglycaemia condition on cytokines production by human monocytes-derived macrophages.

**Materials and methods:** Monocyte cells obtained from peripheral blood mononuclear cells isolation from donors were incubated for 6 days in 37°C, 5% CO<sub>2</sub>. On day 4, the stimulating factors such as lipopolysaccharide (LPS) and interferon gamma were added to activate monocytes into macrophages. Then, on day 6, two doses of glucose; either normal or high doses along with low or high dose of LPS were given for 24 h, followed by collecting the culture media and cells then stored at –80°C until assayed.

**Results:** There was a significant difference in tumour necrosis factor alpha (TNF- $\alpha$ ) levels among groups, with highest level found in group with high-dose glucose plus high-dose LPS. However, the concentration of interleukin-6 (IL-6) among groups was not significantly different.

**Conclusions:** Macrophages treated with high-dose glucose plus high-dose LPS significantly increased production of TNF- $\alpha$ , but not of IL-6. (Folia Morphol 2022; 81, 2: 387–393)

**Key words:** glucose, interleukin-6 (IL-6), lipopolysaccharides (LPS), macrophages, tumour necrosis factor alpha (TNF- $\alpha$ )

## INTRODUCTION

Macrophage is one of innate immune cells that responds immediately to any invaders or cell debris. Macrophages have pathogen recognition receptors (PRRs) on its surface that can recognise pathogen-associated molecular patterns (PAMPs) or endogenous danger-associated molecular patterns (DAMPs) [7]. To bind to those molecules, macrophages are equipped with toll like receptors (TLR). NOD like-receptors (NLRs), the HIN-200 receptor family, and RIG-1-like

receptor (RLRs) are also types of PRRs that can be found in macrophages which are located in the cytoplasm and act as stressor signals when pathogen is found in the cytoplasm [6].

Macrophages also have role to maintain tissue homeostasis [14], by polarising into two types of subpopulations, depending on the microenvironment they are exposed to [2]. The classical or proinflammatory macrophages are known as M1 and the alternative or anti-inflammatory macrophages as M2 [3].

Address for correspondence: Dr. E.R. Megawati, Jalan dr. T. Mansur No. 5 Kampus USU Medan 20155 Sumatera Utara, Indonesia, tel: +62618211045, fax: +62618216264, e-mail: eka3@usu.ac.id

This article is available in open access under Creative Common Attribution-Non-Commercial-No Derivatives 4.0 International (CC BY-NC-ND 4.0) license, allowing to download articles and share them with others as long as they credit the authors and the publisher, but without permission to change them in any way or use them commercially.

The imbalance of the M1/M2 ratio occurs in chronic inflammation condition such as insulin resistance, cardiovascular disease, obesity, tumour development, and autoimmune disease [3].

Macrophage infiltration also increases in the metabolically active tissue during overnutrition condition that leads to proinflammatory environment and is marked by the increase in tumour necrosis factor alpha (TNF- $\alpha$ ), interleukin (IL)-1 $\beta$ , and inducible nitric oxide synthase (iNOS) secretion. In type 2 diabetes mellitus, macrophages involve in progressivity of the disease by altering metabolic pattern [5]. In obese patients, the M1 macrophages infiltrate the enlarged fat cells of adipose tissue and results in production of abundance of inflammatory cytokines such as TNF- $\alpha$  and IL-6. These contribute to the decrease in insulin sensitivity and the ability of glucose uptake in fat cells [6].

In the presence of interferon gamma (IFN- $\gamma$ ) and lipopolysaccharide (LPS), macrophages will rapidly activate their glycolytic pathway. Then, the abundance of glucose uptake and utilisation lead to the increases in IL-6 and IL-1 $\beta$  secretion. Hence, the availability of glucose in a tissue may shift macrophages' polarization into an inflammatory phenotype [14]. In diabetes, the M1 macrophages persistently lead to diabetic neuropathy by over production of protease, cytokines and reactive oxygen species (ROS). These molecules induce oxidative stress and myelin degradation and neuronal damage. M1 macrophages may also change pancreatic cells functions and cause insulin resistance [1]. The M1 proinflammatory macrophages may produce, release and respond to cytokines and chemokines in its environment such as TNF- $\alpha$ , IL-6, IL-1, and monocyte chemoattractant protein (MCP)-1. On the other hand, if the environments do not need the dominancy of proinflammatory macrophages, they adapt to the M2 macrophages. The anti-inflammatory macrophages M2 then allow the resolution of inflammation. The anti-inflammatory cytokines and the growth factors that are released by M2, such as the antagonist receptor IL-1, IL-10, and transforming growth factor beta, induce the decrease in the pro-inflammatory factors and then reduce the macrophages activation. The decrease in macrophages activation marked the end of acute inflammation. But, if the process is hampered, the resolution of inflammation cannot be achieved and chronic inflammation occurs [4].

The hyperglycaemic condition may activate monocyte and increase the expression of pro inflammatory

macrophages (M1 phenotype), even if there is no tissue damage or infection [4]. Previous study showed that hyperglycaemic mice induced by streptozotocin had vast infiltration of macrophages and developed into a systemic proinflammatory state shown by the increase in IL-6, IL-1 $\beta$ , TNF- $\alpha$ , and IL-8 [10]. In an in vitro study, human monocytes and macrophages exposed to high levels of glucose also underwent transformation into inflammatory macrophages and the same situation apparently also can be observed in patients with hyperglycaemia [15].

The aim of the study was to analyse the effect of hyperglycaemia condition in the environment of the macrophage cell culture.

## MATERIALS AND METHODS

### Subject recruitment

The blood donors for this study were three females and one male with an average age of 20 years, body weight  $64.5 \pm 8.44$  kg, height  $161.5 \pm 1.66$  cm, and body mass index  $25.20 \pm 3.30$  kg/m<sup>2</sup>. All participants were screened for eligible criteria, such as not having any infection and metabolic diseases in 1 month before and also signed the informed consent after being explained about the study procedures. All procedures of this study were approved by the Ethical Committee of Human Studies, Faculty of Medicine and Adam Malik General Hospital, Medan. This study was conducted in the Research Laboratory of Faculty of Medicine, Universitas Sumatera Utara, Medan, Indonesia between July and October 2019.

### Isolation of PBMCs

Fifty millilitres of blood was withdrawn from a vein and collected in EDTA-containing Vacutainer tubes. The peripheral blood mononuclear cells (PBMCs) of buffy coat were collected by gradient centrifugation using Lymphoprep™ (Stemcell, Axis-Shield, Dundee, UK), according to the manufacturer's instruction.

### Isolation of monocytes

Monocytes were isolated from PBMCs by using EasySep™ negative monocyte isolation kit (Stemcell™ Technologies, Vancouver, Canada). Briefly, the PBMCs were treated with antibody and platelet removal before selected with magnet beads and incubate in an EasySep Magnet (Stemcell™ Technologies, Vancouver, Canada) according to the manufacturer's procedures.

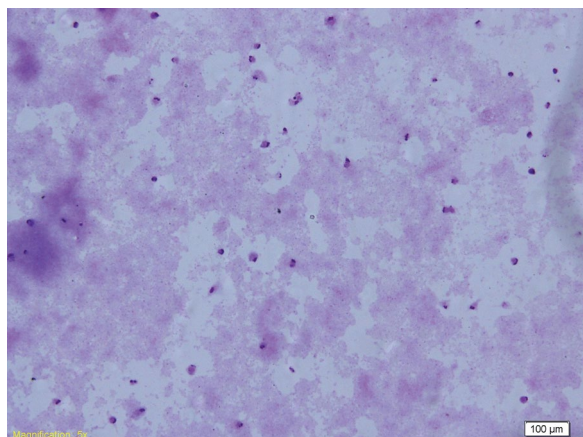


**Figure 1.** Normal glucose 10 × 10.

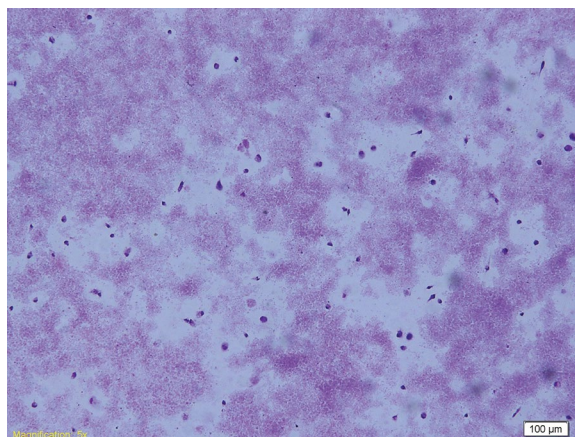


**Figure 3.** High glucose 10 × 10.

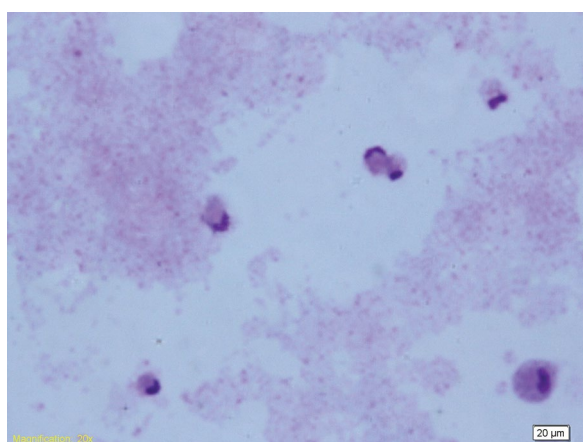


**Figure 2.** Normal glucose 10 × 40.

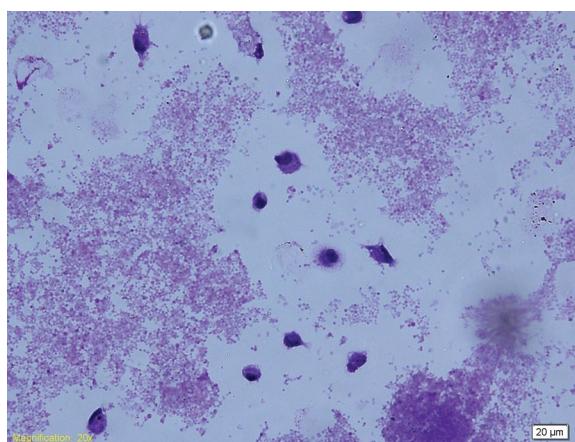


**Figure 4.** High glucose 10 × 40.

### Culture of monocytes

Monocytes were cultured in RPMI 1640 (Gibco, Waltham, MA, USA) supplemented with 10% foetal bovine serum (FBS; Sigma, St. Louis, MO, USA), 1% penicillin-streptomycin (Gibco, Waltham, MA, USA) and 1% L-glutamine (Gibco, Waltham, MA, USA) at 37°C in a 5% CO<sub>2</sub> humidified incubator. Recombinant human M-CSF/CSF1 (ABclonal Technology, Woburn, MA, USA) at the concentration of 50 ng/mL was used to direct macrophage differentiation. Cells were incubated for 6 day in 37°C, 5% CO<sub>2</sub>. The monocytes seeded in 24 wells culture plates (Iwaki tissue culture treated polystyrene microplate, Asahi Glass Co., Japan). On day 4, fresh media were added with lipopolysaccharide (LPS; 10 ng/mL) from *E. coli* (O26:B6) (Sigma, St. Louis, MO, USA) and IFN- $\gamma$  (50 ng/mL) (Stemcell™ Technologies, Vancouver,

Canada) to differentiate macrophage into M1 macrophages. On day 6, all media were removed and replaced with serum-free complete media (SF-CM).

### Glucose stimulation

The macrophages were divided into five groups; two were supplemented with two doses of glucose (Sigma, St. Louis, MO, USA) (7 mM as normal dose [ND-Glu] and 35 mM as high dose [HD-Glu]). This concentration is based on the diabetes diagnosis by World Health Organization [16] and doubling the dosage will resemble the diabetes state in patients [4]. The other three groups besides having the two doses of glucose were also supplemented with LPS (low dose 100 ng/mL [LD-LPS] and high doses 2  $\mu$ g/mL [HD-LPS]). The control group was treated with SF-CM. The treatments were given for 24 h after day 6. Then

the culture media and cells were harvested and frozen at  $-80^{\circ}\text{C}$  until assayed.

### Giemsa staining

The coverslips that previously put inside the wells were discarded and left dry in room temperature. Then fixed with 98% methanol for 1 min and bathed with Giemsa (diluted with distilled water, 1:1 vol/vol) for 5 min. In the final step, the coverslips were washed with distilled water and left to dry then mounted onto slides. The Giemsa staining of macrophages stimulated with normal dose of glucose is seen in Figures 1 and 2 and in high dose of glucose in Figures 3 and 4, with  $10 \times 10$  and  $10 \times 40$  magnification.

### Analysis of cytokines production

Human Pico Kine ELISA kits (My BioSource Inc., San Diego, CA, USA) were used to analyse the concentration of TNF- $\alpha$  and IL-6 according to manufacturer's protocols. The assays were performed in duplicates. The intra-assay coefficient of variation was  $< 11\%$ .

### Statistical analysis

All data are presented as mean  $\pm$  standard deviation. All data were normally distributed after analysed using Shapiro-Wilk test, then were analysed with one way ANOVA and followed by Bonferroni post hoc test. The  $p$  value  $< 0.05$  was considered statistically significant. All data were statistically analysed using SPSS software version 17.0.

## RESULTS

### The production of TNF- $\alpha$

Test of homogeneity of variances with Levene's test showed that there were significant differences in variance with  $p$ -value = 0.001, then one way ANOVA Welch test showed that the data were significantly different among groups with  $p$  value = 0.004 ( $p < 0.05$ ). The Robust Test of Equality of Means showed the  $p$  value = 0.29 ( $p > 0.05$ ) (equals variances assumed), so the analysis was continued with the Bonferroni post hoc test to find which groups were significantly different.

As can be seen in Table 1, the levels of TNF- $\alpha$  were significantly different among groups with  $p = 0.004$ , the group treated with normal dose of glucose had lowest TNF- $\alpha$  concentration ( $40.67 \pm 9.94$  pg/mL), while in the group treated with high dose of glucose plus high dose of LPS had highest TNF- $\alpha$  concentration ( $2150.22 \pm 1379.77$  pg/mL).

This study showed that macrophages treated with normal dose or high dose of glucose and/or stimulated with low dose or high dose of LPS had higher concentration of TNF- $\alpha$  compared to the treated macrophages. Then, after being analysed with the Bonferroni post hoc test, it was shown that there are significant differences in TNF- $\alpha$  concentration within groups; Control vs. HD-Glu+HD-LPS (mean differences [MD] =  $-2107.34$  pg/mL;  $p = 0.015$ ), ND-Glu vs. HD-Glu+HD-LPS (MD =  $-1943.53$  pg/mL;  $p = 0.009$ ), and HD-Glu vs. HD-Glu+HD-LPS (MD =  $-2095.69$  pg/mL,  $p = 0.002$ ). It means that high dose of glucose plus high dose of LPS resulted in an increase in TNF- $\alpha$  production (Table 2).

### The production of IL-6

This study showed that the lowest concentration of IL-6 were found in the group treated with a high dose of glucose ( $43.37 \pm 16.29$  pg/mL), whereas the highest concentration was found in the group treated with a high dose of glucose plus a high dose of LPS ( $59.66 \pm 16.72$  pg/mL). But after being analysed with one way ANOVA test, the concentrations of IL-6 were not significantly different ( $p = 0.742$ ; Table 3).

### The macrophages staining

This study also performed the Giemsa staining of macrophages with normal-dose and high-dose glucose. The figures are shown with  $10 \times 10$  and  $10 \times 40$  magnification (Figs. 1–4).

## DISCUSSION

We observed that the highest level of TNF- $\alpha$  was found in the HD-Glu+HD-LPS group, and the lowest was found in the control group ( $p = 0.004$ ). This finding is similar to previous study that compared the production of proinflammatory cytokines in macrophages that stimulated with LPS to the non-stimulated macrophages. The previous study showed that the production of TNF- $\alpha$ , MCP-1, IL-6 and IL-1 $\beta$  was significantly higher in stimulated macrophages compared to control [1]. Previous study also showed that THP-1 macrophage cultured in high glucose concentration (15 mM) with or without LPS stimulation displayed higher concentration of TNF- $\alpha$  compared to normal glucose (5 mM) or osmotic control group [4]. Furthermore, activated macrophages that were stimulated with hyperglycaemia and hypoxia condition were shown to upregulate TNF- $\alpha$ , IL-6 and IL-1 gene expression [9]. Another study on diabetic rats induced

**Table 1.** The TNF- $\alpha$  level among groups

Groups	TNF- $\alpha$ [pg/mL]	P value
Control	42.88 $\pm$ 22.85	0.004*
ND-Glu	40.67 $\pm$ 9.94	
HD-Glu	54.43 $\pm$ 26.93	
ND-Glu+HD-LPS	915.09 $\pm$ 804.02	
HD-Glu+LD-LPS	979.49 $\pm$ 8226.84	
HD-Glu+HD-LPS	2150.22 $\pm$ 1379.77	

Values are mean  $\pm$  standard deviation (n = 4). TNF- $\alpha$  — tumour necrosis factor alpha; Control — serum-free media only; ND-Glu — normal-dose glucose, 7 mM; HD-Glu — high-dose glucose, 35 mM; LD-LPS — low-dose lipopolysaccharides, 100 ng/mL; HD-LPS — high-dose lipopolysaccharides, 2  $\mu$ g/mL; \*p < 0.05 (the one way ANOVA test)

**Table 3.** The IL-6 level among groups

Groups	IL-6 [pg/mL]	P value
Control	55.16 $\pm$ 23.19	0.742
ND-Glu	49.52 $\pm$ 29.28	
HD-Glu	43.37 $\pm$ 16.29	
ND-Glu+HD-LPS	53.06 $\pm$ 20.45	
HD-Glu+LD-LPS	52.08 $\pm$ 23.85	
HD-Glu+HD-LPS	59.66 $\pm$ 16.72	

Values are mean  $\pm$  standard deviation (n = 4). IL-6 — interleukin-6; Control — serum-free media only; ND-Glu — normal-dose glucose, 7 mM; HD-Glu — high-dose glucose, 35 mM; LD-LPS — low-dose lipopolysaccharides, 100 ng/mL; HD-LPS — high-dose lipopolysaccharides, 2  $\mu$ g/mL; \*p < 0.05 (the one way ANOVA test)

**Table 2.** The post hoc test of tumour necrosis factor alpha level among groups

Groups	Mean differences	95% confidence interval		P value
		Lower bound	Upper bound	
Control vs. ND-Glu	-163.81	1852.16	1524.53	1.00
Control vs. HD-Glu	-11.65	1661.18	1637.88	1.00
Control vs. HD-Glu+LD-LPS	-936.61	2841.33	968.09	1.00
Control vs. ND-Glu+HD-LPS	-872.21	2776.92	1032.50	1.00
Control vs. HD-Glu+HD-LPS	-2107.34	4012.05	202.63	0.015*
ND-Glu vs. HD-Glu	-152.16	1241.94	1546.27	1.00
ND-Glu vs. HD-Glu+LD-LPS	-772.80	2461.15	915.54	1.00
ND-Glu vs. ND-Glu+HD-LPS	-708.40	2396.74	979.95	1.00
ND-Glu vs. HD-Glu+HD-LPS	-1943.53	3631.87	255.18	0.009*
HD-Glu vs. HD-Glu+LD-LPS	-924.96	2574.49	724.56	1.00
HD-Glu vs. ND-Glu+LD-LPS	-860.56	2510.09	788.97	1.00
HD-Glu vs. HD-Glu+HD-LPS	-2095.69	3745.22	446.16	0.002*
HD-Glu+LD-LPS vs. ND-Glu+HD-LPS	64.41	1840.30	1968.12	1.00
HD-Glu+LD-LPS vs. HD-Glu+HD-LPS	-1170.72	3075.43	733.99	1.00
ND-Glu+HD-LPS vs. HD-Glu+HD-LPS	-1235.13	3139.84	669.58	1.00

Control — serum-free media only; ND-Glu — normal-dose glucose, 7 mM; HD-Glu — high-dose glucose, 35 mM; LD-LPS — low-dose lipopolysaccharides, 100 ng/mL; HD-LPS — high-dose lipopolysaccharides, 2  $\mu$ g/mL; \*p < 0.05 (Bonferroni post hoc test)

by streptozotocin also shown an increase in TNF- $\alpha$  and overexpression of inflammatory genes, such as TNF- $\alpha$ , COX-2 and iNOS [11].

Differences in TNF- $\alpha$  concentration was observed among groups; Control vs. HD-Glu+HD-LPS, ND-Glu vs. HD-Glu+HD-LPS, and HD-Glu vs. HD-Glu+HD-LPS with p value of 0.015, 0.009, and 0.002 (p < 0.05), respectively. The macrophages with high-dose glucose plus high-dose LPS produced significantly higher levels of TNF- $\alpha$  compared to the serum free medium (control), or to the macrophages with normal or high-dose glucose.

The TNF- $\alpha$ , IFN- $\gamma$ , or the recognition of LPS are the Th1 (T helper 1) cytokines that can trigger the polar-

ization of proinflammatory M1 macrophages. The activity of these M1 macrophages will then increase the expression of IL-12, IL-23, and the production of TNF, IL-1 $\beta$  and IL-6, and also ROS via activation of nicotinamide adenine dinucleotide phosphate (NADPH) oxidase system. The function of this action is to remove pathogens during infection that results in ROS-mediated tissue damage and declined wound healing [8]. It also has been known that the circulating LPSs bind with LPS binding protein (LBP) and are caught by CD14 surface scavenging receptor. This signal activates TLR that initiates the phosphorylation cascade mediated by different kinase enzymes. The result of this signal is releasing transcription

factor — nuclear factor kappa B from its inhibitor I $\kappa$ B — and translocating it to the nucleus. The effect of this cascade is increasing the expression of inflammatory genes such as TNF, antibiotic peptides and NADPH oxidase that produce the reactive oxygen intermediate [13].

We observed that the highest level of IL-6 was found in HD-Glu+HD-LPS and the lowest was found in HD-Glu, but the differences were not significant ( $p > 0.05$ ). This study showed that the IL-6 production was not changed by glucose and/or LPS stimulation. This result is in contrary to previous study that analysed the differences in cytokine production among type 2 diabetes patients and diabetic peripheral neuropathy patients; the macrophages from patients with type 2 diabetes produced significantly higher level of IL-6 when compared to control and diabetic peripheral neuropathy patients [1]. Another study also showed that THP-1 macrophages produced higher level of IL-6 when stimulated with high glucose and LPS, compared to control group. The concentration of normal glucose in that study was 5 mM and the high glucose was 15 mM [4]. It means that M1 macrophages are more metabolically active in hyperglycaemic conditions, and promote obesity associated insulin resistance [12]. The difference between this finding and those studies is the dose being used. In addition, the dramatically increased IL-6 gene expression was seen after 17 h of activation and stimulation with hyperglycaemic along with hypoxia [9], whereas in this study the concentration of IL-6 was analysed after 24 h of stimulation. Similar results were also found in the previous study of monocyte-derived macrophages exposed to high glucose (15 mM) that showed no significant differences in TNF- $\alpha$  production when compared to the normal glucose (5 mM) or hyperosmotic (glucose free) conditions [15].

The limitation of this study is we did not perform the immunophenotypic assessment that is useful to identify and count the percentage of cells. Anyhow, we identify the cells using the cytomorphology and the number of cells with improved Neubauer chamber.

## CONCLUSIONS

Finally, this study concluded that macrophages which were stimulated with a high dose of glucose plus a high dose of LPS significantly increased the TNF- $\alpha$  production. On the other hand, different dosages of glucose and LPS stimulation to the macrophages cell cultures did not change the production of IL-6.

## Acknowledgements

This study was supported by Ministry of Research and Technology and Higher Education Republic of Indonesia under the research grants of TALENTA Universitas Sumatera Utara Year 2019 with contract number 4167/UN5.1.R/PPM/2017, on April 1<sup>st</sup>, 2019.

**Conflict of interest:** None declared

## REFERENCES

- Alvarado-Vázquez PA, Grosick RL, Moracho-Vilrriales C, et al. Cytokine production capabilities of human primary monocyte-derived macrophages from patients with diabetes mellitus type 2 with and without diabetic peripheral neuropathy. *J Pain Res.* 2019; 12: 69–81, doi: [10.2147/JPR.S186372](https://doi.org/10.2147/JPR.S186372), indexed in Pubmed: [30588081](https://pubmed.ncbi.nlm.nih.gov/30588081/).
- Arnold CE, Gordon P, Barker RN, et al. The activation status of human macrophages presenting antigen determines the efficiency of Th17 responses. *Immunobiology.* 2015; 220(1): 10–19, doi: [10.1016/j.imbio.2014.09.022](https://doi.org/10.1016/j.imbio.2014.09.022), indexed in Pubmed: [25454489](https://pubmed.ncbi.nlm.nih.gov/25454489/).
- Figueroa LA, Abarca-Vargas R, García Alanis C, et al. Comparison between Peritoneal Macrophage Activation by Extract and LPS and/or Interleukins. *Biomed Res Int.* 2017; 2017: 4602952, doi: [10.1155/2017/4602952](https://doi.org/10.1155/2017/4602952), indexed in Pubmed: [29279849](https://pubmed.ncbi.nlm.nih.gov/29279849/).
- Grosick R, Alvarado-Vazquez PA, Messersmith AR, et al. High glucose induces a priming effect in macrophages and exacerbates the production of pro-inflammatory cytokines after a challenge. *J Pain Res.* 2018; 11: 1769–1778, doi: [10.2147/JPR.S164493](https://doi.org/10.2147/JPR.S164493), indexed in Pubmed: [30237731](https://pubmed.ncbi.nlm.nih.gov/30237731/).
- Hameed I, Masoodi SR, Mir SA, et al. Type 2 diabetes mellitus: From a metabolic disorder to an inflammatory condition. *World J Diabetes.* 2015; 6(4): 598–612, doi: [10.4239/wjd.v6.i4.598](https://doi.org/10.4239/wjd.v6.i4.598), indexed in Pubmed: [25987957](https://pubmed.ncbi.nlm.nih.gov/25987957/).
- Hirayama D, Iida T, Nakase H. The phagocytic function of macrophage-enforcing innate immunity and tissue homeostasis. *Int J Mol Sci.* 2017; 19(1), doi: [10.3390/ijms19010092](https://doi.org/10.3390/ijms19010092), indexed in Pubmed: [29286292](https://pubmed.ncbi.nlm.nih.gov/29286292/).
- Kelly B, O'Neill LAJ. Metabolic reprogramming in macrophages and dendritic cells in innate immunity. *Cell Res.* 2015; 25(7): 771–784, doi: [10.1038/cr.2015.68](https://doi.org/10.1038/cr.2015.68), indexed in Pubmed: [26045163](https://pubmed.ncbi.nlm.nih.gov/26045163/).
- Momtazi-Borojeni AA, Abdollahi E, Nikfar B, et al. Curcumin as a potential modulator of M1 and M2 macrophages: new insights in atherosclerosis therapy. *Heart Fail Rev.* 2019; 24(3): 399–409, doi: [10.1007/s10741-018-09764-z](https://doi.org/10.1007/s10741-018-09764-z), indexed in Pubmed: [30673930](https://pubmed.ncbi.nlm.nih.gov/30673930/).
- Morey M, O'Gaora P, Pandit A, et al. Hyperglycemia acts in synergy with hypoxia to maintain the pro-inflammatory phenotype of macrophages. *PLoS One.* 2019; 14(8): e0220577, doi: [10.1371/journal.pone.0220577](https://doi.org/10.1371/journal.pone.0220577), indexed in Pubmed: [31415598](https://pubmed.ncbi.nlm.nih.gov/31415598/).
- Niu S, Bian Z, Tremblay A, et al. Broad infiltration of macrophages leads to a proinflammatory state in streptozotocin-induced hyperglycemic mice. *J Immunol.* 2016; 197(8): 3293–3301, doi: [10.4049/jimmunol.1502494](https://doi.org/10.4049/jimmunol.1502494), indexed in Pubmed: [27619992](https://pubmed.ncbi.nlm.nih.gov/27619992/).

11. Pan Y, Wang Yi, Cai Lu, et al. Inhibition of high glucose-induced inflammatory response and macrophage infiltration by a novel curcumin derivative prevents renal injury in diabetic rats. *Br J Pharmacol.* 2012; 166(3): 1169–1182, doi: [10.1111/j.1476-5381.2012.01854.x](https://doi.org/10.1111/j.1476-5381.2012.01854.x), indexed in Pubmed: [22242942](https://pubmed.ncbi.nlm.nih.gov/22242942/).
12. Riemann S, Klüter H, Gratchev A, et al. Hyperglycemia induces mixed M1/M2 cytokine profile in primary human monocyte-derived macrophages. *Immunobiology.* 2017; 222(10): 952–959, doi: [10.1016/j.imbio.2016.07.006](https://doi.org/10.1016/j.imbio.2016.07.006), indexed in Pubmed: [27492721](https://pubmed.ncbi.nlm.nih.gov/27492721/).
13. Roitt IM, Delves PJ. *Roitts's Essential Immunology*. 10th ed. Blackwell Science 2001: 1–494.
14. Thapa B, Lee K. Metabolic influence on macrophage polarization and pathogenesis. *BMB Reports.* 2019; 52(6): 360–372, doi: [10.5483/bmbrep.2019.52.6.140](https://doi.org/10.5483/bmbrep.2019.52.6.140).
15. Torres-Castro I, Arroyo-Camarena ÚD, Martínez-Reyes CP, et al. Human monocytes and macrophages undergo M1-type inflammatory polarization in response to high levels of glucose. *Immunol Lett.* 2016; 176: 81–89, doi: [10.1016/j.imlet.2016.06.001](https://doi.org/10.1016/j.imlet.2016.06.001), indexed in Pubmed: [27269375](https://pubmed.ncbi.nlm.nih.gov/27269375/).
16. World Health Organization (WHO). *Global report on diabetes*. 2016. <https://www.who.int/publications/item/9789241565257>.

# Morphological structure of the tongue of the European badger (*Meles meles*)

A. Haligur<sup>1</sup>, S. Ozkadif<sup>1</sup>, A. Alan<sup>2</sup>, M. Haligur<sup>3</sup>

<sup>1</sup>Department of Anatomy, Ceyhan Veterinary Faculty, Cukurova University, Ceyhan-Adana, Turkey

<sup>2</sup>Department of Anatomy, Veterinary Faculty, Erciyes University, Kayseri, Turkey

<sup>3</sup>Department of Pathology, Ceyhan Veterinary Faculty, Cukurova University, Ceyhan-Adana, Turkey

[Received: 26 November 2020; Accepted: 27 January 2021; Early publication date: 1 March 2021]

**Background:** This study aimed to reveal the morphological aspects of the tongue and investigate the histologic and scanning electron microscopic (SEM) findings of the papillae on the tongue of the European badger.

**Materials and methods:** Two adult European badgers were used as material. The tongues of the European badgers were removed via the dissection method, and morphometric measurements were taken. The tongues were fixed in 10% buffered formalin solution for histological examination, and the SEM procedure was applied to the tongues.

**Results:** Three types of papillae were observed on the tongues: filiform, fungiform, vallate papillae. The different shapes (hook or conical structures) of filiform papillae were observed on the whole tongue. Fungiform papillae were found scattered in filiform papillae. Six vallate papillae were found on the dorsal face of the middle and root of the tongues. In the root of the tongue, the lingual tonsil was observed in the lentiform shape.

**Conclusions:** The authors believe that this research will provide contributions to morphological knowledge about the tongue of the badger, which is a poorly known species. (Folia Morphol 2022; 81, 2: 394–399)

**Key words:** badger, morphology, papillae, scanning electron microscopic (SEM), wild animal

## INTRODUCTION

The European badger (*Meles meles*) belongs to the order Carnivora of the Mustelidea subfamily and is found all around the world [3, 16]. The badger population in Turkey is endangered, and therefore these animals are protected through an international agreement with BERN and CITES [18].

The diet of the badger consists of larvae, pupae, and adults of different species of insects, as well as other small animals such as snails, frogs, reptiles, mice, and small rabbits. It consumes more herbal

nutrients than other carnivore species. The badger uses its tongue similar to Carnivora [17].

Many studies have been conducted to investigate the tongue of different animals using scanning electron microscopic (SEM), histological, morphological or functional analyses. Among the animals investigated are the civet cat [19], silver fox [14], porcupine [1, 15], mice [21], Asian black bear and panther [5], bush dog [8], Japanese badger [24] and mongoose [12, 20]. The aim of this study was to determine the possible scanning electron microscopic (SEM), histo-

Address for correspondence: Dr. S. Ozkadif, Department of Anatomy, Ceyhan Veterinary Faculty, Cukurova University, Ceyhan-Adana, Turkey, tel: +90 322 613 35 07, fax: +90 322 613 35 07, e-mail: semaerten80@gmail.com

This article is available in open access under Creative Common Attribution-Non-Commercial-No Derivatives 4.0 International (CC BY-NC-ND 4.0) license, allowing to download articles and share them with others as long as they credit the authors and the publisher, but without permission to change them in any way or use them commercially.

logical and morphological changes in the papillae and tongue of the European badger. These results were compared with other studies in the literature to emphasize the morphologic and microscopic diversities among species. This study is also hoped to contribute to improving our current knowledge related to the badger.

## MATERIALS AND METHODS

This study was performed with permission from the General Directorate of Nature Conservation and National Parks of the Ministry of Forestry and Water Affairs (permission number: 38002405-445.05-177733). Also this study was accepted by the local Ethics Committee for animal experiments of the Cukurova University (decision number: 2017/6-5).

In this study, two dead adult European badgers (*Meles meles*) (2 females [9.21–11.72 kg]) were used as materials. This animals died by traffic accident in Ceyhan region. Classic dissection method was made and the tongue was removed from the head. Morphometric measurements were taken from the tongue by using a digital calliper. The methods used in tissue processing are described below.

### Histological procedure

After the tongue of European badgers had been cleaned with physiological saline solution and examined anatomically, the appropriate sized parts of the tongue were fixed in 10% formaldehyde for 24 hours in order to preserve the tissue structure in the nearest living state and facilitate getting thin sections by increasing hardness. Tissue samples were washed to remove formaldehyde and passed through a series of low to high alcohol grades to remove water. After paraffin embedding, the blocks were cut transversely into 5  $\mu\text{m}$  sections and stained with haematoxylin and eosin (H&E) for general histological examination. After staining, it was dehydrated by passing through alcohol series, cleared in xylene and mounted with entellan. The slides were examined histologically using light microscope (Lyca) and photographed with Lyca digital camera.

### SEM procedure

First of all, trimmed specimens (0.5  $\times$  0.5 cm) were washed twice with 0.1 M (pH 7.4) phosphate buffer solution and then were kept in 2.5% glutaraldehyde solution for 2 days at 4°C. After that period, the tissues were kept in 1% osmium tetroxide ( $\text{OsO}_4$ ) for

1 hour. The tissues were passed through sequential acetone series and dried with critical point drying. They were coated with gold by using Polaron SC7620 Sputter Coater and finally the images were taken with LEICA LEO 440 trade scanning electron microscopy in various magnifications.

## RESULTS

### Morphological findings

The tongue of the badger is elongated with an oval flat apex (Fig. 1). In this study, the tongue was examined in three parts: the tip, middle and root. The length of the tongue from the tip to the root was measured as 8.4 cm and 8.7 cm. The thickness was 0.128–0.172 cm at the tip, 1.326–1.393 cm at the centre, and 1.667–1.701 cm at the root. The width of the tongue was 2.315–2.394 cm at the tip and 2.669–2.704 cm at the root. Accordingly, a significant expansion of the tongue was observed.

There were six vallate papillae on the tongue. The vallate papilla was seen as irregular; so, it was not in a V shape. It was determined that the cranial first two of these papillae were prominent, and the last papillae was less pronounced. Especially in the middle part of the midline near the corpus, fungiform papillae were visualised in the external aspect. Filiform papillae were found along with the entire tongue. On both lateral sides of the tongue, it was seen that the shape of the filiform papillae changed in the caudal 1/3 plane. In the caudal part of the tongue, filiform papillae were present but the number and shape were more pronounced and less in number than in the apex. Foliate papillae were not observed in any part of the tongue.

### Histological findings

Filiform papillae were composed of stratified squamous epithelium (Fig. 2A). The dorsal surface of the papillae was observed to have prominent keratinisation structure. Fungiform papillae were observed among the filiform papillae (Fig. 2B). Conical and hook-shaped papillae were found in sections taken from the root of the tongue (Fig. 2C). These were localised between the filiform papillae. There were several taste buds covered with squamous epithelium (Fig. 2D). The top of the vallate papillae was seen to slightly collapse inwards, forming a wide encircling groove. The vallate papillae were found to be surrounded by several papillary projections.

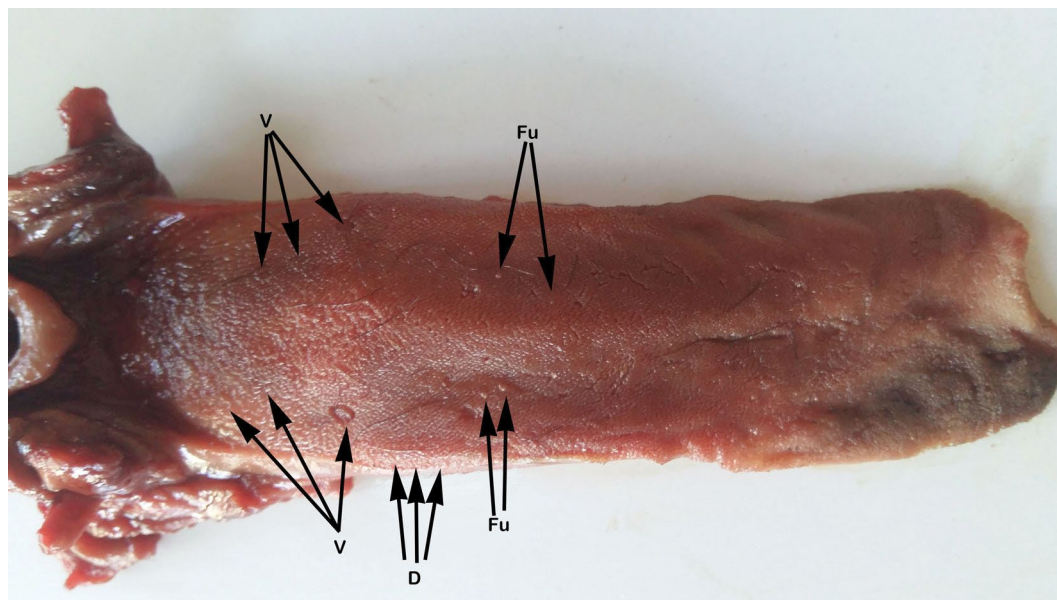


**Figure 1.** The general appearance of the dorsal surface of European badger tongue; D — differentiated filiform papillae; Fu — fungiform papillae, V — vallate papillae.

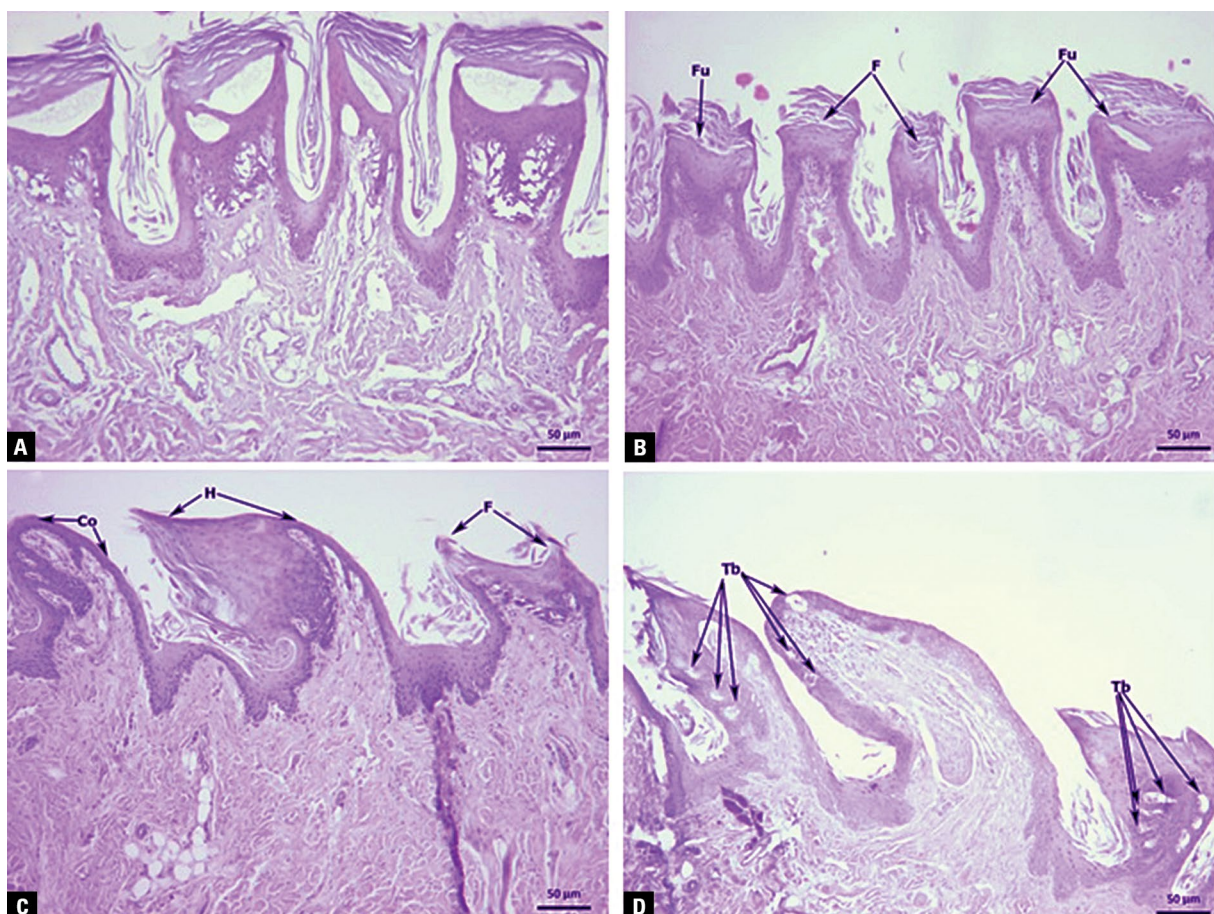


**Figure 2. A–D.** Histological sections of different regions of the tongue; **A.** Filiform papillae in the apex tongue, H&E, bar = 50 µm; **B.** Fungiform and filiform papillae in the middle of the tongue; F — filiform papillae (arrows); Fu — fungiform papillae (arrows), H&E, bar = 50 µm; **C.** Appearance of the different papillae on the root of the tongue; Co — conic papillae (arrows); F — filiform papillae (arrows); H — hook-shaped papilla (arrow); H&E, bar = 50 µm; **D.** Fungiform papillae on the middle tongue; Tb — taste buds (arrows), H&E, bar = 50 µm.

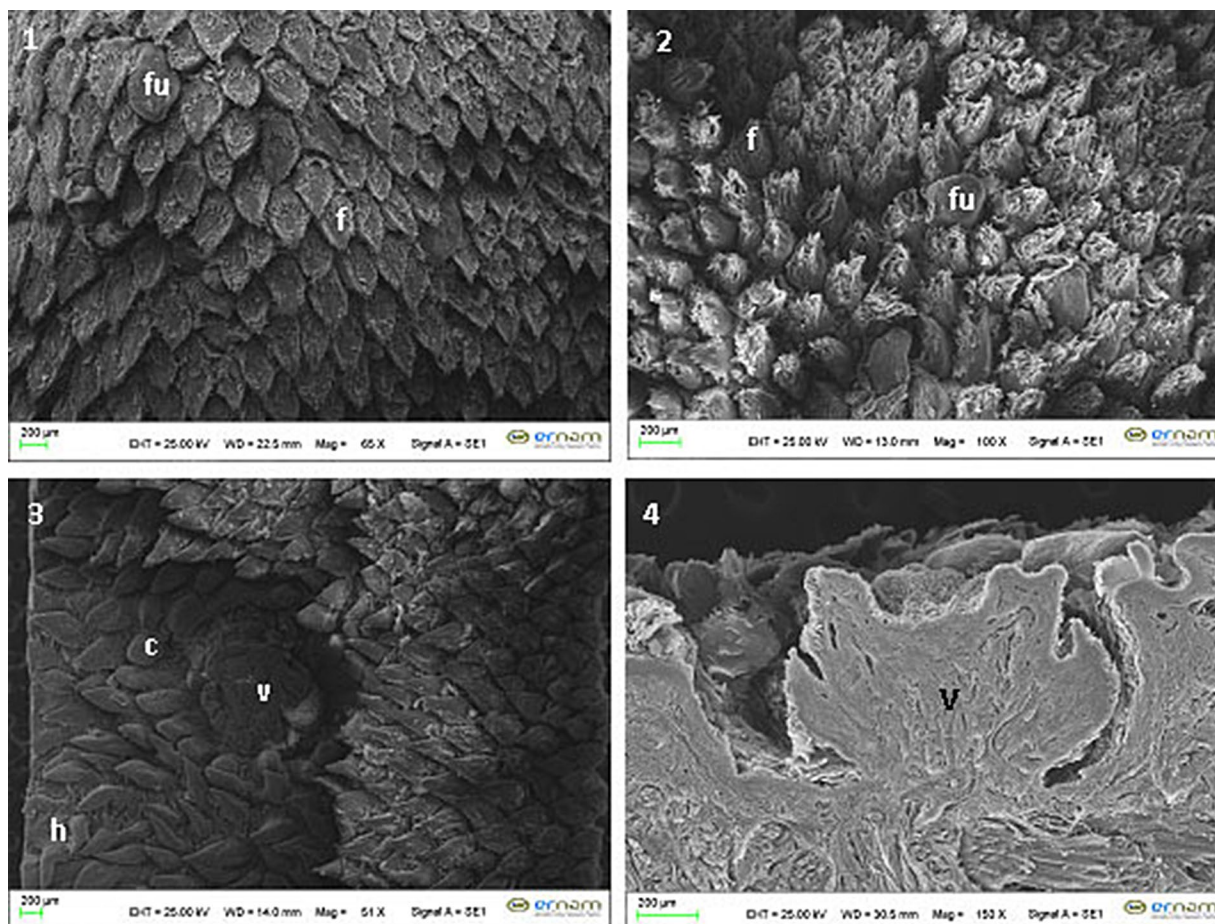


**Figure 3.** The tip of tongue and general appearance of the dorsal surface papillae; **1.** Localisation of the papillae fungiformes and scattered within the filiform papillae; fu — fungiform papillae; f — filiform papillae, SEM magnification 65 $\times$ , bar = 200  $\mu$ m; **2.** General aspect of the middle of the tongue; fu — fungiform papillae; f — filiform papillae, SEM magnification 100 $\times$ , bar = 200  $\mu$ m; **3.** Marked vallate papillae and surrounding structure; c — conic papillae; h — hook shape papillae; v — vallate papillae; SEM magnification 51 $\times$ , bar = 200  $\mu$ m; **4.** Longitudinal section of the vallate papillae; v — vallate papillae, SEM magnification 150 $\times$ , bar = 200  $\mu$ m.

### SEM findings

In the SEM analyses of the tongues, the filiform (Fig. 3/1, 2-f), fungiform (Fig. 3/1, 2-fu) and vallate papillae (Fig. 3/3, 4-v) were identified. In addition to these main papillae, hook (Fig. 3/3-h) and conical papillae (Fig. 3/3-c) were seen on the dorsal surface of the European badger tongue.

The examination of the SEM images of both European badgers revealed that the dorsal surface of the filiform papillae of the middle was flattened. These papillae were observed to approach the caudal of the tongue, and looked like an arrow. The cranial part of the papillae was flat on the dorsal surface of the tongue. The number of filiform papillae was decreased toward the back of the tongue. However, these papillae were fewer than in the remaining parts of the tongue. In the same area, some of the filiform papillae were observed to have gland ducts.

Fungiform papillae were found scattered. Especially in the middle tongue, fungiform papillae were higher in number than filiform papillae, and they had an irregular ovoid shape. In addition, fungiform papillae were extensively located on the 1/3 middle part of the tongue bilateral but they were not seen at the end of the tongue.

The vallate papillae were mostly found on the dorsal face of the middle and end of the tongue. A total of six vallate papillae were seen and four of these structures differed from the others. These four vallate papillae were faintly observed while the remaining two were marked. The top of the vallate papillae collapsed inwards, and their edges were fragmented. Papillae foliate were not observed, but the lateral edges of the tongue were differentiated in terms of filiform papillae, which did not contain a ductal structure. At the root of the tongue

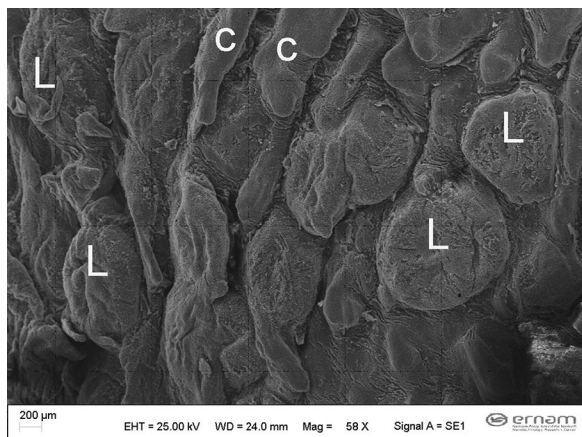


**Figure 4.** General appearance of the dorsal surface of papillae and lingual tonsillae on the root of the tongue; C — conic papillae; L — lentiform structure of lingual papillae; SEM magnification 58 $\times$ , bar = 200  $\mu$ m.

were lentiform-shaped structures of lingual tonsillae (Fig. 4). These structures were located under the epiglottis and arranged in a sequential “U” shape.

## DISCUSSION

The position of the papillae, structure, shape and length of the tongue vary among animal species. The length of the tongue was reported to be approximately 9 cm for young lions [22], 7–8 cm for the silver fox [14], raccoon dog and fox [7], 20 cm for tigers [6], 7–7.5 cm for the Japanese badger [24], 12.3 cm for pumas [11] and in 6–7 cm for porcupines [1, 15]. In this study, the length of the European badger tongue was measured as 8.4–8.7 cm. It was also found that the length of the tongue differed from the other species, which was considered to be due to the habitat.

In the silver fox [14], puma [11], tiger [6], young lion [22] and Carnivora [8, 13], the filiform papillae are found from the apex linguae to the radix linguae on the dorsal surface of the tongue. In addition, these papillae are seen on the ventral surface of the tongue, especially lateral edges, in the tiger [6], puma [11], young lion [22] and silver fox [14]. These papillae are located on the median channel of the dorsal surface of the tongue and have a similar shape to the hook of a meerkat [9]. These papillae have different types (bifurcated, papule-like, cylindrical, conical and blunt) in pumas [11]. In porcupines [15] they have two different shapes (one flat and the other cylindrical). On the margin of the tiger tongue, filiform papillae are divided into hemispherical, horny-shaped, giant

club-shaped, conical, hoe-shaped or bifid types in the different parts of the tongue [6]. The current study was carried out with the European badger and revealed the presence of filiform papillae on the whole surface of the tongue (mostly at the tip and middle tongue). These papillae were similar both in terms of type and location to the meerkat [9], raccoon dog and fox tongue [7]. In the present study, another finding related to the filiform papillae was the presence of keratinized areas in these papillae, which is consistent with the finding reported by Selim and Samir [20]. In addition, unlike the Japanese badger [24], these papillae were detected in a small number in the root of the tongue (in hook, conic and filiform shapes). The epithelial structures of the filiform papillae in the European badger were similar to those of young lions [22].

In contrast to the literature [6, 20], in this study, the fungiform papillae were located in the posterior (tip) part of the tongue. Moreover, these papillae were generally observed on both sides of the middle part of the tongue. The shape of the fungiform papillae is reported to be flat at the upper surface in the silver fox [14], and smooth and dome-like in the Japanese badger [24]. These papillae are located on the apex and lateral region of the tongue and have a mushroom-like shape in squirrels [23] and a hemispherical or horn shape on the margin of the tongue in the tiger [6]. In this study, different from the literature [2, 10, 14, 23], the fungiform papillae were found to have an irregular ovoid shape, and were extensively observed after the 1/3 middle part of the European badger tongue bilaterally. A few taste buds were found at the top of the fungiform papillae in the Japanese badger [24]. In this study, some of the buds were seen on both the upper and ventrolateral surfaces of the fungiform papillae as different from the Japanese badger [24].

The number of vallate papillae varies according to species; e.g. four for the silver fox [14] and puma [11], six for the civet cat [19] and Japanese badger [24], 7–8 for the Asian black bear and 5–9 for lion [4], 4 for tigers [6] and 28 for porcupines [1]. In the present study, the number of papillae was six as in the civet cat [19] and Japanese badger [24]. The vallate papillae are in a “V” shape in other species of animals; however, in the European badger, they were not regularly shaped, similar to the case observed in the raccoon dog and fox [7]. While the location of the papillae was similar to that of other animals, they had

a different distribution. In addition, while the cranial first two filiform papillae were quite prominent, the others were not as pronounced in the European badger. This is another finding that differentiates the European badger tongue from the other animal species.

In the literature, it is that the civet cat [19] has two foliate papillae and from 4–5 laminae occur in silver fox [14]. Foliate papillae are not present in young lions [22], pumas [11] and tigers [6]. In this study, foliate papillae were not seen. The bilateral edges of the root tongue were similar to those of the Japanese badger [24] reported by Yoshimura.

## CONCLUSIONS

In conclusion, this study shows that the number and position of papillae in the tongue of wild animals differ between wild species. The authors believe that the anatomic, histological and SEM findings of the data obtained from the present study will contribute to the literature.

## Acknowledgements

This study was supported by Cukurova University Scientific Research Projects (Number: TSA-2017-8852).

**Conflict of interest:** None declared

## REFERENCES

- Atalar O, Karan M. The light and scanning electron microscopic structure of papilla vallatae in the porcupine (*Hystrix cristata*). *J Anim Vet Adv*. 2011; 10: 3069–3073, doi: [10.3923/javaa.2011.3069.3073](https://doi.org/10.3923/javaa.2011.3069.3073).
- Can M, Atalgin S, Ates S, et al. Scanning electron microscopic study on the structure of the lingual papillae of the Karacabey Merino sheep. *Eur J Vet Sci*. 2016; 32(3): 130–130, doi: [10.15132/eurasianjvetsci.2016318389](https://doi.org/10.15132/eurasianjvetsci.2016318389).
- Demirsoy A. Yasamın temel kuralları. Omurgalılar/Amniyota (sürüngenler, kuşlar ve memeliler) Cilt-III/Kısım-II. Meteksan, Ankara, Turkey 2003: 758.
- Emura S, Hayakawa D, Chen H, et al. and gross study on the lingual surface of the lion, *Panthera leo*. *Mar Mammal Sci*. 2003; 43(1): 45–50, doi: [10.11238/mammalianscience.43.45](https://doi.org/10.11238/mammalianscience.43.45).
- Emura S, Hayakawa D, Chen H, et al. Morphology of the dorsal lingual papillae in the newborn panther and Asian black bear. *Okajimas Folia Anat Jpn*. 2001; 78(5): 173–177, doi: [10.2535/ofaj1936.78.5\\_173](https://doi.org/10.2535/ofaj1936.78.5_173), indexed in Pubmed: [11915359](https://pubmed.ncbi.nlm.nih.gov/11915359/).
- Emura S, Hayakawa D, Chen H, et al. Morphology of the lingual papillae in the tiger. *Okajimas Folia Anat Jpn*. 2004; 81(2-3): 39–43, doi: [10.2535/ofaj.81.39](https://doi.org/10.2535/ofaj.81.39), indexed in Pubmed: [15455727](https://pubmed.ncbi.nlm.nih.gov/15455727/).
- Emura S, Okumura T, Chen H, et al. Morphology of the lingual papillae in the raccoon dog and fox. *Okajimas Folia Anat Jpn*. 2006; 83(3): 73–76, doi: [10.2535/ofaj.83.73](https://doi.org/10.2535/ofaj.83.73), indexed in Pubmed: [17154050](https://pubmed.ncbi.nlm.nih.gov/17154050/).
- Emura S, Tamada A, Hayakawa D, et al. Morphology of the dorsal lingual papillae in the bush dog (*Speothos venaticus*). *Okajimas Folia Anat Jpn*. 2000; 77(5): 137–141, doi: [10.2535/ofaj1936.77.5\\_137](https://doi.org/10.2535/ofaj1936.77.5_137), indexed in Pubmed: [11218710](https://pubmed.ncbi.nlm.nih.gov/11218710/).
- Erdoğan S, Lima M, Pérez W. Anatomical and Scanning Electron Microscopic Study of the Tongue in the Meerkat (*Suricata suricatta*, Schreber, 1776). *Anat Histol Embryol*. 2016; 45(1): 51–59, doi: [10.1111/ah.12170](https://doi.org/10.1111/ah.12170), indexed in Pubmed: [25588707](https://pubmed.ncbi.nlm.nih.gov/25588707/).
- Erdoğan S, Pérez W. Anatomical and scanning electron microscopic studies of the tongue and lingual papillae in the chital deer (*Axis axis*, Erxleben 1777). *Acta Zoologica*. 2013; 95(4): 484–492, doi: [10.1111/azo.12044](https://doi.org/10.1111/azo.12044).
- Erdoğan S, Villar S, König HE, et al. Papillary architecture of the lingual surface in the puma (*Puma concolor*). *Anat Histol Embryol*. 2018; 47(1): 51–57, doi: [10.1111/ah.12323](https://doi.org/10.1111/ah.12323), indexed in Pubmed: [29152772](https://pubmed.ncbi.nlm.nih.gov/29152772/).
- Iwasaki S, Miyata K. Fine structure of the dorsal epithelium of the mongoose tongue. *J Anat*. 1990; 172: 201–212.
- Iwasaki S, Miyata K. Fine structure of the filiform papilla of beagle dogs. *J Morphol*. 1989; 201(3): 235–242, doi: [10.1002/jmor.1052010303](https://doi.org/10.1002/jmor.1052010303), indexed in Pubmed: [2478716](https://pubmed.ncbi.nlm.nih.gov/2478716/).
- Jackowiak H, Godynicki S. The scanning electron microscopic study of lingual papillae in the silver fox (*Vulpes vulpes fulva*, Desmarest, 1820). *Ann Anat*. 2004; 186(2): 179–183, doi: [10.1016/s0940-9602\(04\)80037-2](https://doi.org/10.1016/s0940-9602(04)80037-2).
- Karan M, Yılmaz S, Aydın A. Morphology of the filiform lingual papillae in porcupine (*Hystrix cristata*). *Anat Histol Embryol*. 2011; 40(2): 100–103, doi: [10.1111/j.1439-0264.2010.01045.x](https://doi.org/10.1111/j.1439-0264.2010.01045.x), indexed in Pubmed: [21105901](https://pubmed.ncbi.nlm.nih.gov/21105901/).
- Kuru M. Omurgalı hayvanlar. Palme, Ankara, Turkey 1999: 672.
- Ozen AS, Ulucay I. Kütahya ili Meles meles Linnaeus, 1758 (Mammalia: Carnivora)'ın bazı ekolojik, biyolojik ve taksonomik özellikleri. *DPÜ Fen Bilimleri Enstitüsü Dergisi*. 2010; 21: 9–20.
- Pamukoglu N, Demir E. Porsuğun (Meles meles) Günlük Besinindeki Böcekler. *Cent ent Stud Misc Pap*. 2001; 74: 4–7.
- Sarma K, Sarma M, Kalita SN. Gross anatomical and biometrical studies on the tongue of an adult small Indian civet cat. *Isr J Vet Med*. 2009; 64: 36–38.
- Selim A, Samir R. Light and scanning electron microscope studies of the tongue of the egyptian mongoose (*Herpestes ichneumon*). *J Cytol Histol*. 2018; 9: 499, doi: [10.4172/2157-7099.1000499](https://doi.org/10.4172/2157-7099.1000499).
- Toprak B. Light and scanning microscopic structure of filiform papillae in mice. *Vet Arhiv*. 2006; 76: 555–562.
- Toprak B, Ulusoy Y. Macroscopic and light microscopic structure of lingual papillae on the tongue of a young lion (*Panthera leo*). *Isr J Vet Med*. 2011; 66: 114–117.
- Unsaldi E. Sincaplarda (*Sciurus vulgaris*) Papillae Fungiformes'in Makroskopik ve Işık Mikroskopik Yapısı. *Kafkas Univ Vet Fak*. 2009, doi: [10.9775/kvfd.2009.530](https://doi.org/10.9775/kvfd.2009.530).
- Yoshimura K, Shindo J, Kageyama I. Light and scanning electron microscopic study on the tongue and lingual papillae of the Japanese badgers, Meles meles anakuma. *Okajimas Folia Anat Jpn*. 2009; 85(4): 119–127, doi: [10.2535/ofaj.85.119](https://doi.org/10.2535/ofaj.85.119), indexed in Pubmed: [19408581](https://pubmed.ncbi.nlm.nih.gov/19408581/).

# Structural and functional adaptation of the lingual papillae of the Egyptian fruit bat (*Rousettus aegyptiacus*): specific adaptive feeding strategies

R.M. Kandyel<sup>1</sup>, M.M.A. Abumandour<sup>2</sup> , S.F. Mahmoud<sup>3</sup>, M. Shukry<sup>4</sup>, N. Madkour<sup>2</sup>, A. El-Mansi<sup>5, 6</sup>, F.A. Farrag<sup>7</sup>

<sup>1</sup>Department of Zoology, Faculty of Science, Tanta University, Tanta, Egypt

<sup>2</sup>Department of Anatomy and Embryology, Faculty of Veterinary Medicine, Alexandria University, Alexandria, Egypt

<sup>3</sup>Department of Biotechnology, College of Science, Taif University, Taif, Saudi Arabia

<sup>4</sup>Department of Physiology, Faculty of Veterinary Medicine, Kafrelsheikh University, Kafrelsheikh, Egypt

<sup>5</sup>Department of Biology, Faculty of Science, King Khalid University, Abha, Saudi Arabia

<sup>6</sup>Department of Zoology, Faculty of Science, Mansoura University, Mansoura, Egypt

<sup>7</sup>Department of Anatomy and Embryology, Faculty of Veterinary Medicine, Kafrelsheikh University, Kafrelsheikh, Egypt

[Received: 19 February 2021; Accepted: 28 March 2021; Early publication date: 28 April 2021]

**Background:** The current investigation was aimed to clarify the correlations between the feeding strategy and lingual structure of the Egyptian fruit bat captured from the Egyptian east desert.

**Materials and methods:** The current work was performed on 12 adult Egyptian fruit bats that were observed grossly and with the help of the stereo, light, and scanning electron microscope. There were three types of the lingual papillae: one mechanical (filiform) and two gustatory (fungiform and circumvallate).

**Results:** There were seven subtypes of filiform papillae recognised on the seven lingual regions. There were few fungiform papillae distributed among the filiform papillae on the lingual tip and two lateral parts of apex and body while fungiform papillae were completely absent in the median part. There were three circumvallate papillae. The central bulb of circumvallate papillae was surrounded by one layer of two segmented circular pad. The lingual tip had cornflower-like and diamond-shaped filiform papillae.

**Conclusions:** Histochemical results revealed that the lingual glands showed a stronger Alcian Blue (AB)-positive reaction and gave dark blue colour, while the reaction for the periodic acid-Schiff (PAS)-stain was negative. Also, the glands exhibited a blue colour as an indication of positive AB reactivity with combined AB-PAS staining. (Folia Morphol 2022; 81, 2: 400–411)

**Key words:** Egyptian fruit bat, lingual papillae, scanning electron microscope (SEM), histology, histochemical examination

---

Address for correspondence: M.M.A. Abumandour, Ass. Prof., Department of Anatomy and Embryology, Faculty of Veterinary Medicine, Alexandria, Egypt, Post Box: 22785, tel: +20 1000322937, fax: +20 452960450, e-mail: m.abumandour@yahoo.com; R.M. Kandyel, Lecture in Department of Zoology, Faculty of Science, Tanta University, Egypt, e-mail: r\_kandyel@science.tanta.edu.eg

This article is available in open access under Creative Common Attribution-Non-Commercial-No Derivatives 4.0 International (CC BY-NC-ND 4.0) license, allowing to download articles and share them with others as long as they credit the authors and the publisher, but without permission to change them in any way or use them commercially.

## INTRODUCTION

The bats were classified as the second-largest mammalian order (after rodent), and organized into two suborders: mega-chiropters and micro-chiropters [52]. The bats are arboreal animals [6] and the only mammalian-species naturally capable of flight [60]. Egyptian fruit bat belongs to *Chiroptera* order, *Mega-chiroptera* suborder, *Pteropodidae* family, *Rousettus* genus *Rousettus aegyptiacus* species [1, 6]. The *Rousettus aegyptiacus* species had six subspecies, the only subspecies that live in Egypt is *Rousettus aegyptiacus aegyptiacus*. The feeding habit of the *Pteropodidae* family depends on fruit, flowers, nectar, and pollen, so these animals are classified as frugivorous species.

There are some studies on the effect of the feeding system on increasing the viability and corresponding adaptations of the structure of organs in vertebrates [4, 28]. Generally, there are different feeding styles reported in different bat species: the blood suckling bats, insectivorous bats, and frugivorous bats [25]. Physiologically, to know the preservation tools of any vertebrate species, you must know its lingual structure [4, 14]. The tongue is the most important structure that was modified with the distinctive nutritional ability, behaviour, and different types of available food particles [15]. Moreover, the lingual structure is modified to have different functions [4, 51]. Furthermore, the lingual papillae are the most structures on the tongue that are most adaptable to the feeding mechanism [2].

The current investigation was prepared to give a complete morphological description of the lingual papillary system of the Egyptian fruit bat (*Rousettus aegyptiacus*) grossly and by the aid of the stereo, light, and scanning electron microscope (SEM). Then, the results were compared with the previous reports in other bat-species.

## MATERIALS AND METHODS

### Collection of bat samples

The present investigation was carried out on 12 tongues from adult Egyptian fruit bats (*Rousettus aegyptiacus*). The Egyptian fruit bats (*Rousettus aegyptiacus*) were collected from the fruit farms in the Siwa Oasis, Egypt. This study was performed in compliance with the animal care and handling rules and was approved by the Ethics Committee on Animal Experiments of the Department of Veterinary Sciences, University of Alexandria. The animals were

euthanized by deep halothane inhalation, and the tongues were quickly transferred for stereo and electron microscope lab. The anatomical terms followed the *Nomina Anatomica Veterinaria* [47].

### Gross and stereomicroscopic morphological examination

Four tongues from adult Egyptian fruit bats (*Rousettus aegyptiacus*) were used to describe the lingual papillary system. After euthanasia, tongues were dissected, separated, examined, and photographed using a camera (Canon IXY 325, Japan) grossly, and under a stereoscopic Zeiss Stemi 2000-C microscope (Carl Zeiss, Jena, Germany).

### Scanning electron microscopic examination

Four tongues from adult Egyptian fruit bats (*Rousettus aegyptiacus*) were fixed in (2% formaldehyde, 1.25% glutaraldehyde in 0.1 M sodium cacodylate buffer, pH~7.2) at 4°C. After fixation, samples were washed in 0.1 M sodium cacodylate containing 5% sucrose, processed through tannic acid, and finally dehydrated in ascending grades of ethanol [4]. The samples were then critical point dried in Polaron apparatus (E3000 CPD), attached to stubs with colloidal carbon, and coated with gold-palladium in a sputtering device (Pelco model 3 sputter coater 91000). Specimens were examined and photographed using a JEOL SEM (JSM-6510LV, Japan) operating at 15 kV, at the Faculty of Science, Alexandria University.

### Histological and histochemical investigations

Four specimens of the Egyptian fruit bat (*Rousettus aegyptiacus*) tongue were dissected out and fixed in 10% formaldehyde for 48 hours at (pH 7.4), dehydrated in graded series of ethanol, cleared with xylene, and immersed in melted paraffin wax. Five- $\mu$ m cutting sections were prepared. Then, samples were sectioned in 5 microns using Leica rotatory microtome (RM 20352035; Leica Microsystems, Wetzlar, Germany) and stained by haematoxylin and eosin according to Suvarna et al. [58] to demonstrate the general histological structure. Extra sections were stained by Masson's trichrome [21, 39] to visualise collagen and muscle fibres.

For histochemical studies, some sections were taken and stained by Alcian Blue (AB) [57] for acidic mucin; periodic acid-Schiff (PAS) [27] for neutral mucin, and double stain of AB (pH = 2.5), and PAS (AB-PAS) technique for acidic and neutral mucin [45].

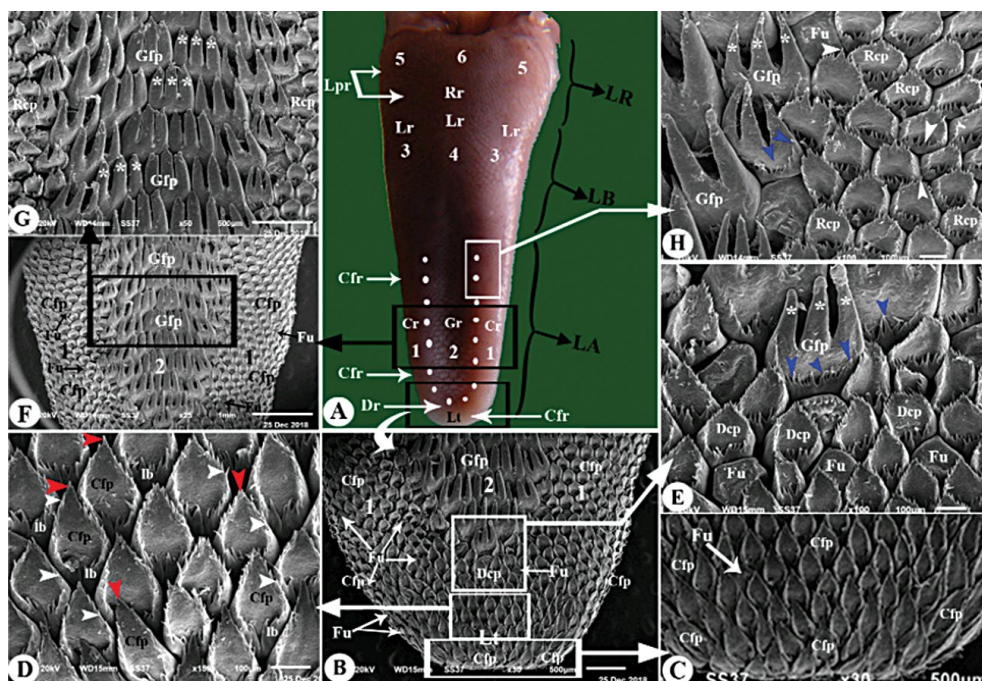


**Figure 1.** Gross morphological image of the tongue (A) and scanning electron microscope images (B–H) of the lingual apex of the Egyptian fruit bat. Panel A shows the lingual regions: lingual apex (LA) with its lingual tip (Lt), two lateral (1) and median parts (2) and lingual body (LB) with its two lateral (3) and median parts (4); lingual root (Lr) with its two lateral (5) and median parts (6). The seven regions of the filiform papillae: region of cornflower filiform papillae (Cfr); region of diamond filiform papillae (Dr); region of giant filiform papillae (Gr); region of round and rectangular filiform papillae (Cr); region of leaf-like filiform papillae (Lr); region of rosette-like filiform papillae (Rr) and region of long pointed filiform papillae (Lpr). Panels B–H show the cornflower filiform papillae (Cfp) with the posterior pointed process (red arrowheads) and numerous processes (white arrowheads) on two elevated lateral borders that bent on the base (lb); diamond filiform papillae (Dcp); giant filiform papillae (Gfp); round and rectangular filiform papillae (Rcf), leaf-like filiform papillae (Lfp) fungiform papillae (Fu).

These sections were examined and photographed under a bright field light microscope (Olympus BX 50 compound microscope).

## RESULTS

Grossly, the short tongue from the adult Egyptian fruit bat (*Rousettus aegyptiacus*) was divided into three parts; lingual apex (anterior free part), lingual body (middle part), and lingual root (posterior part). The dorsal lingual surface had three lingual papillary types; one mechanical that was described as filiform, and two gustatory that were described as a fungiform and circumvallate papillae. By SEM perceptions, the shape, size, number, dispersion, direction and terminology of lingual papillae was species-specific. Their position, shape, size, number, and direction of the papillae and their very own functions were locale explicit as per the feeding propensities, mechanism of mastication, and sorts of sustenance particles. There were three main directions of all lingual papillae: posterior, posterior-median or median. The ventral lingual surface was connected to the sublingual floor

by the lingual frenulum leaving a long free end of the tongue to encourage the opportunity for lingual movement. The dorsal surface of the lingual root was characterised by the presence of three circumvallate papillae.

Generally, the lingual papillae were located on the lateral region taken the posteriorly or medioposteriorly or medially directions, while that located on the median region and the lingual tip were took the posterior orientation toward the pharynx and the lingual root. The papillae on the lateral region took the different orientations to help in the collected food particles in the median region of the tongue.

### Gross anatomical observations

Macroscopically, the protrusible prolonged tongue of the Egyptian fruit bats (*Rousettus aegyptiacus*) was ended with a round lingual apex and had two round lateral borders (Figs. 1A, 2A, 3A). In addition, every region of the tongue (apex, body, and root) was subdivided into a median and two lateral parts (Figs. 1A, 2A, 3A).

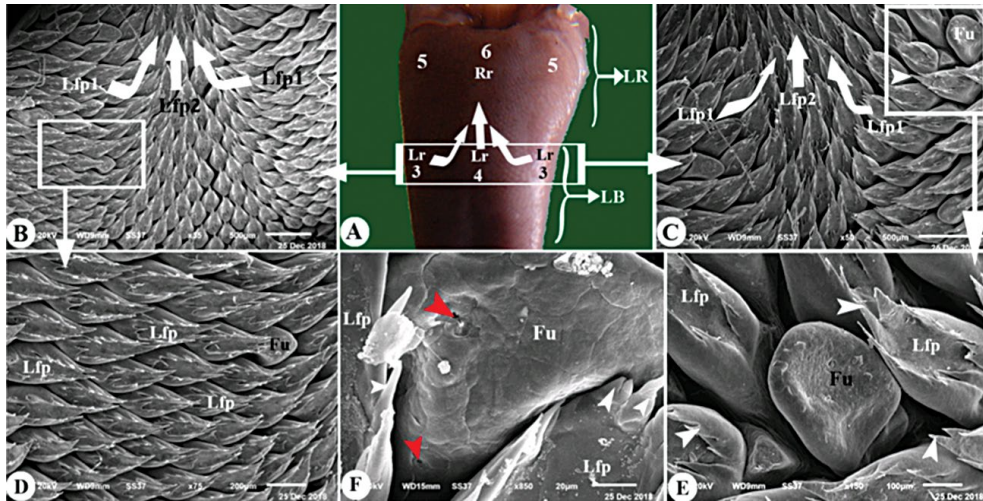


**Figure 2.** Gross morphological image of the lingual body and root (A) scanning electron microscope images (B–F) of the posterior part of the lingual body of the Egyptian fruit bat; Panel A shows lingual body (LB) and its two lateral (3) and median parts (4) with the region of leaf-like filiform papillae (Lr). Lingual root (LR) and its two lateral (5) and median parts (6) with region of rosette-like filiform papillae (Rr). Panels B–F show the region of leaf-like filiform papillae (Lfp1) of medioposteriorly direction on the lateral region of lingual body; region of leaf-like filiform papillae (Lfp2) of posterior direction on the median region of the lingual body. Leaf-like filiform papillae (Lfp): the processes on the margin of leaf-like filiform papillae (white arrowheads) and taste pores (red arrowheads) on the fungiform papillae (Fu).

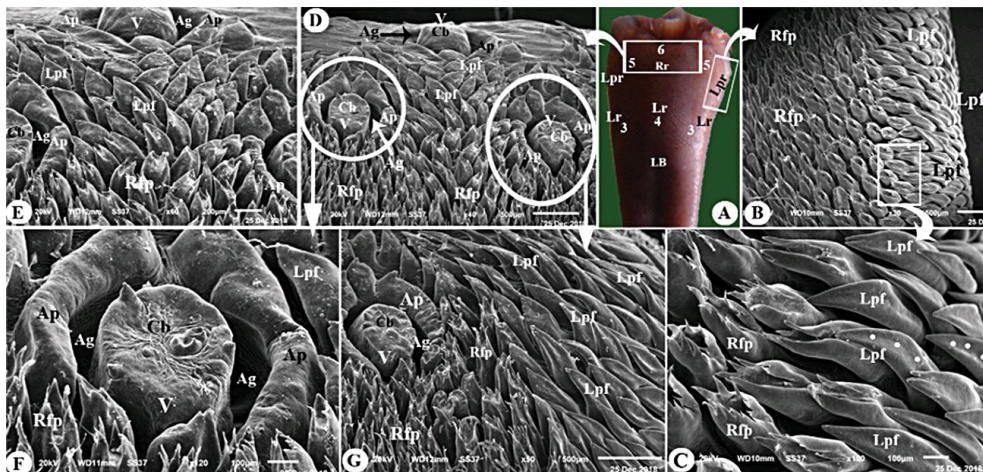


**Figure 3.** Gross morphological image of the lingual body and root (A) and scanning electron microscope images (B–G) of the lingual root of the Egyptian fruit bat; Panel A shows lingual body (LB) and its two lateral (3) and median parts (4) with the region of leaf-like filiform papillae (Lr). Lingual root (LR) and its two lateral (5) and median parts (6) with the region of rosette-like filiform papillae (Rr) and region of long pointed filiform papillae (Lpr). Panels B–G show the long pointed filiform papillae (Lpf) with the groove on its dorsal surface (white dotted line); circumvallate papillae (V) with central bulb (Cb) and surrounded by a continuous deep groove (Ag) that is surrounded by one layer of two segmented circular annular pad (Ap).

The tongue was narrow at the anterior rostral tip, while it was broad at the lingual root. The tongue length was  $1.1 \pm 0.2$  cm yet reach  $0.44 \pm 0.2$  cm wide at its centre part. There were seven subtypes of papillae that were disseminated on seven papillary regions (Figs. 1A, 2A, 3A; Cfr, Dr, Gr, Cr, Lr, Rr, LPr).

### Scanning electron microscopy

The anterior lingual region was subdivided into four U-shaped regions: lingual tip, two lateral regions, and median region (Fig. 1A, B and F; 1, 2, 3 and Lt). There were two types of lingual papillae: mechanical and gustatory papillae.

### Mechanical filiform lingual papillae

There were seven subtypes of filiform papillae that were recognised on the tongue of Egyptian fruit bats and described as follows:

**Cornflower-like filiform papillae** (Fig. 1B–D; Cfp). Filiform papillae of this type took a posterior direction and were located on the dorsal surface of the rostral part of the lingual tip and the rostral and two lateral borders of the tongue. These papillae had apex caudally with an elongated, posteriorly directed process, and wide base rostrally and elongated body with two elevated lateral borders that bent on the base. In addition there were 8–12 posteriorly directed small, pointed processes on each lateral border (Fig. 1D; white and red arrowheads).

**Diamond-shaped conical filiform papillae** (Fig. 1B, E; Dcp). These diamond-shaped conical filiform papillae were posteriorly directed and located on the dorsal surface of the median part of the lingual apex (just rostral to the region of trifold filiform papillae). These papillae had elongated apex caudally with an elongated posterior process, wide base rostrally and diamond-shaped body with non-elevated serrated borders that were curved rostrally on the base. In addition, non-elevated serrated borders had 30–32 posteriorly directed small, pointed processes.

**Trifold (Giant) filiform papillae** (Fig. 1B, E–H; Gfp). The trifold filiform papillae were located on the dorsal surface of the median region of the lingual apex and the anterior part of the lingual body. The organization of papillae was observed as they overlapped on each other and each papilla had a wide rectangular smooth body carrying 18–22 small pointed posteriorly directed anterior processes (Fig. 1E, 1H; blue arrowheads). While the papillar body was ended posteriorly by three posteriorly directed, large finger-like posterior processes (Fig. 1E, G, H; white\*).

**Round or rectangular conical filiform papillae** (Fig. 1G, H; Rcp). These papillae were located on the dorsal surface of two lateral regions of the lingual apex (the area around the region of the trifold papillae) and the anterior part of the lingual body. Each papilla carried 26–28 posteriorly directed processes that arose from all borders of the papillae (Fig. 1H; white arrowheads).

**Leaf-like filiform papillae** (Fig. 2; Lfp). These papillae had a different orientation; the laterally situated papillae took the median direction, while that located near the median region took the posteromedian direction, but the median situated papillae took the

posterior direction (Fig. 2B, 2C; Lfp1, Lfp2). These leaf-like filiform papillae were located on all dorsal surface of the posterior part of the lingual body; each papilla had an ovoid-shaped body that carried 14–16 posteriorly directed processes that originated from all borders (Fig. 2C–F; white arrowheads).

**Rosette-like filiform papillae** (Fig. 3; Rfp). These papillae were located on the dorsal surface of the median part and the areas of the two lateral parts near the median part of the lingual root till the beginning of the triangular region of the circumvallate papillae. Each papilla had a round base and body with an apex that terminated by posteriorly directed numerous small processes forming a basket-like shape (Fig. 3C; Rfp).

**Long pointed filiform papillae** (Fig. 3; Lpf). These papillae were located on the lateral border (Fig. 3B, C; Lpf), in addition to the triangular area of circumvallate papillae (Fig. 3D, E; Lpf) and the small area posterior to the triangular area (Fig. 3F, G; Lpf). The papillae that were situated on the lateral border took the median direction while that on the lateral region took the posteromedian direction, but those located on the triangular area of the circumvallate papillae took the posterior direction. Each papilla overlapped the other in the form of the long pointed tongue-shaped papilla without any secondary processes, with a central groove (Fig. 3C; dotted line).

### Gustatory lingual papillae

The gustatory papillae were recorded with characteristic position, dispersion, and number all through the entire tongue length. These papillae were the fungiform and circumvallate papillae, and described as follows.

**Fungiform papillae.** There were scanty numbers of the fungiform papillae randomly distributed among the filiform papillae on the lingual tip (Fig. 1B, C, E; Fu) and the two lateral parts of the lingual apex and body (Fig. 1F; Fu). While the fungiform papillae were completely absent in the median lingual part (region of trifold filiform papillae and leaf-like filiform papillae and the median region of the lingual root). There was one shape of the fungiform papillae, they had quadrilateral appearance. The dorsal surface of the fungiform papillae had micro-ridges and micro-scales in addition to the one or two small depressions for taste pores (Fig. 2F; red arrowheads).

**Circumvallate papillae** (Fig. 3D–G; V). There were three rounded circumvallate papillae distributed on

the posterior part of the lingual root that took the triangular arrangement; its base was directed rostrally with two laterally located papillae while its apex was directed posteriorly with one median located papilla. Each papilla consisted of a round central bulb surrounded by a continuous deep papillary groove (Fig. 3D–G; cb, Ag). The central round bulb was surrounded by one layer of two segmented circular annular pad laterally, but from the rostral and posterior side it was not surrounded by this circular pad (Fig. 3D–G; Ap). The dorsal surface of the central bulb had an irregular surface with microtubercles, microfolds, microgrooves, and numerous taste buds (Fig. 3F).

#### Light microscopic examination

Histological observation of the tongue of the Egyptian fruit bat (*Rousettus aegyptiacus*) cleared three types of lingual papillae (filiform, circumvallate, and fungiform papillae) with different subtypes and densities that distributed over the whole dorsal lingual surface of the tongue. Each papilla was covered by a keratinised multilayered stratified squamous epithelium and supported by connective tissue core, and underneath the lamina propria and muscle fibre layers. The lingual apex showed numerous filiform papillae that were widely dispersed over the dorsal surface, their tips were pointed posteriorly (Fig. 4A, B). Dense connective tissue rich with collagen fibres and blood vessels penetrated deeply into the core of the papillae and continued with the underneath connective tissue layer (Fig. 4C).

At the lingual body, the dorsal epithelium showed numerous fungiform papillae with a quadrilateral appearance. Their epithelium was covered by a thin detached keratin layer and containing few taste buds (Fig. 4D–F). The three triangularly arranged circumvallate papillae covered the dorsal surface of the lingual root. The papillae were covered with a keratinised mucosal surface (Fig. 5A, B). They were also supported by collagen connective tissue fibres and skeletal muscle bundles. Collagen fibres, lymphoid cells, and blood vessels occupied the connective tissue layer and were supported by an underlying layer of muscle fibres arranged in many directions. Abundant fatty cells were seen between the bundles of muscle fibres (Fig. 5C).

Histochemical results revealed that the lingual glands displayed a stronger AB-positive reaction and gave dark blue colour (Fig. 6A, B), while the reaction for the PAS-stain was negative (Fig. 6C, D). In addition,

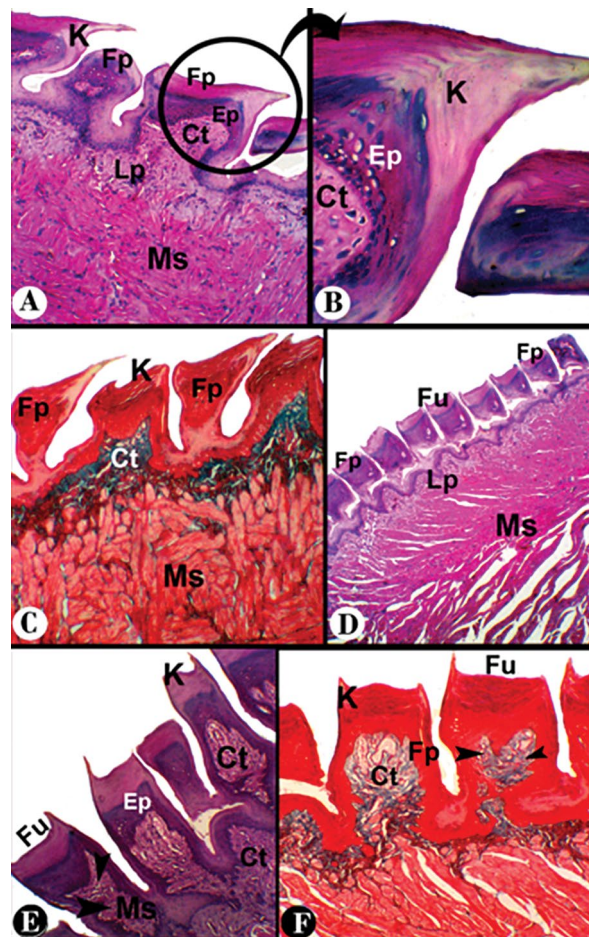


**Figure 4.** Histological image of the lingual apex (A–C) and body (D–F) of the Egyptian fruit bat; Panel A represent the dorsal view of the lingual apex of the Egyptian fruit bat (*Rousettus aegyptiacus*), panel B represents the higher magnification of the filiform papillae (Fp); haematoxylin and eosin. Panel C represents the Masson's trichrome stain of the lingual apex to clear the collagen connective tissue (Ct). Panel D represents the dorsal view of the lingual body of the Egyptian fruit bat (*Rousettus aegyptiacus*), and panel E represents the higher magnification of the dorsal view of the lingual body of the Egyptian fruit bat (*Rousettus aegyptiacus*); haematoxylin and eosin. Panel F represents the Masson's trichrome stain of the lingual body of the Egyptian fruit bat (*Rousettus aegyptiacus*). Filiform papillae (Fp) with a thick keratinised layer (K), the dorsal epithelium (Ep), lamina propria (Lp), connective tissue core (Ct), muscles (Ms), fungiform papillae (Fu), and the black arrowheads refer to the taste buds in the fungiform papillae.

the glands exhibited a blue colour as an indication of positive AB reactivity with combined AB-PAS staining (Fig. 6E, F).

## DISCUSSION

The variations of the feeding mechanism with the different available feeding particles were reflected on the position, structure, number, shape, nomination and, orientation of the lingual papillae [2, 4, 14, 19, 26].

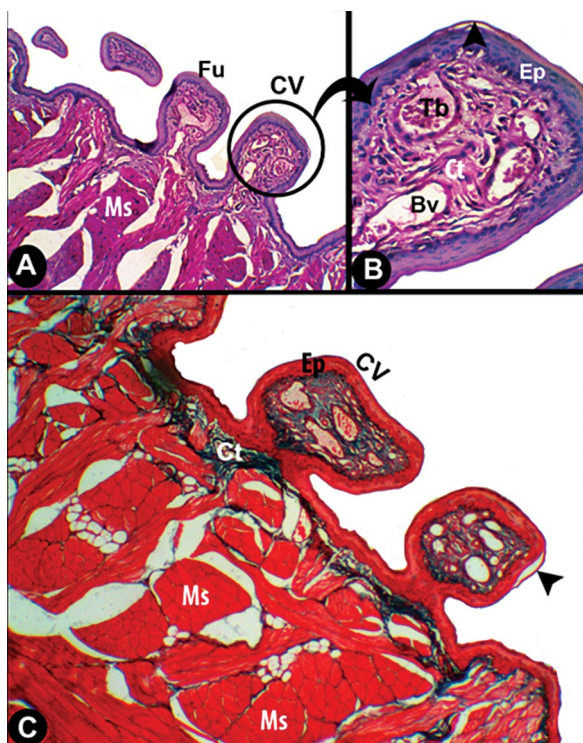


**Figure 5.** Histological image of the lingual root (A–C) of the Egyptian fruit bat; Panel A represents the dorsal view of the lingual root of the Egyptian fruit bat (*Rousettus aegyptiacus*), panel B represents the higher magnification of the circumvallate papillae (CV); haematoxylin and eosin stain. Panel C represent the Masson's trichrome (Alcian Blue) stain of the lingual root to clear the collagen connective tissue (Ct). The dorsal epithelium (Ep), connective tissue core (Ct), lingual muscles (Ms), circumvallate papillae (CV) with a keratinised layer (black arrowhead), taste bud (Tb), and blood vessel (Bv).

The common example for the adaptation of the different bat-species to the different feeding mechanism with the feeding on different food particles during the flying lead to the species-variations in the morphological appearance of the lingual papillae, as appeared in the previously published data [4, 7, 15, 44, 51, 55] and confirmed by the current study on the two bat-species of the different feeding mechanism. The mammalian tongue exhibited numerous morphological adaptations to perform numerous functions including the food particles collection, manipulation, and direction of the food particles towards the oesophagus [4, 28].

The tongue of the Egyptian fruit bat (*Rousettus aegyptiacus*) was described as subdivided into three regions, lingual apex, body, and root, similar to those reported in all vertebrate species [4, 7, 14, 23, 28]. Moreover, in the Egyptian fruit bat, there was a sub-

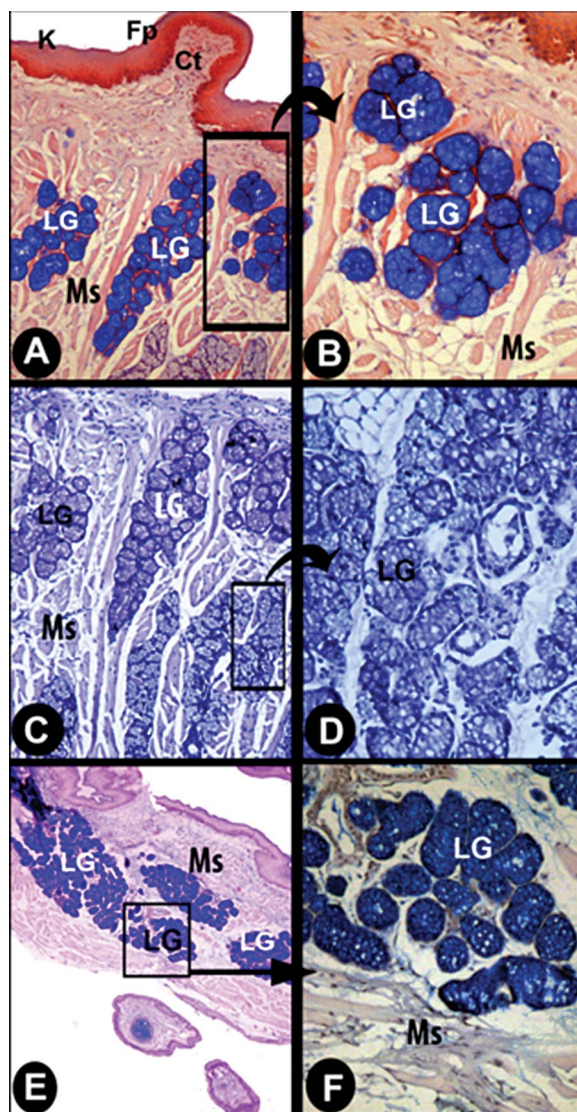


**Figure 6.** Transverse histological image of the lingual root (A–F) of the Egyptian fruit bat; Panels A and B represent the transverse sections of the tongue of the Egyptian fruit bat (*Rousettus aegyptiacus*) showing a positive acidic mucin reaction of the lingual glands (LG); Alcian Blue (AB) stain. Panels C and D represent the transverse sections of the tongue of the Egyptian fruit bat (*Rousettus aegyptiacus*) showing a negative neutral mucin reaction of the lingual glands (LG); periodic acid-Schiff (PAS) stain. Panels E and F represent the transverse sections of the tongue of the Egyptian fruit bat (*Rousettus aegyptiacus*) showing a positive AB reaction and a negative PAS reaction of the lingual glands (LG); AB-PAS stain. Circumvallate papillae (CV), keratinised layer (K), and connective tissue core (Ct), lingual gland (LG), and lingual muscles (Ms).

division of these three regions into two lateral and single median parts. In addition, the anterior lingual region was subdivided into four U-shaped regions: lingual tip, two lateral regions and median region. Also, these subdivision parts were carrying lingual papillae of different

shape, orientation, nomination, and function, similar to that observed by Abumandour et al. [4], El-Mansi et al. [15] and Massoud and Abumandour [41].

Morphologically, most researchers focused on the description of the lingual papillae due to their direct relationship with the feeding style of each species and available food particles [28]. Functionally, the papillary system was adapted and this appears in the structure, number, appearance, orientation, and dispersion of the lingual papillae [4]. The present description confirmed that the lingual papillae can be classified functionally into mechanical and gustatory papillae according to their specific function [4, 7, 15, 19, 34]. Moreover, these papillae were described as three types in Egyptian fruit bat (*Rousettus aegyptiacus*): one mechanical papilla that was described as filiform and two gustatory papillae that were described as fungiform and circumvallate. These findings were similar to that reported in some bats species [19, 43, 49, 51]. On the other hand, Abumandour et al. [4] and El-Mansi et al. [15] observed the presence of four types of lingual papillae: two mechanical and two gustatory in Egyptian fruit bat (*Rousettus aegyptiacus*). However Masuko et al. [43] observed the presence of two types of lingual papillae; filiform and fungiform in hematophagous bats.

The lingual filiform papillae had species-specific and region-specific characterisation and were described as the lingual papillae structure adapted to the feeding mechanism and the available food particles. For that reason, the filiform papillae had a characteristic appearance and functional adaptation and this appears in their characteristic shape, subdivision, number, directions, and positions [2]. Functionally, the subdivision of the filiform papillary system is the most important classification of due to their important role in food particles intake and transportation [2, 4, 15]. The anatomical subdivision of the lingual filiform was reported previously in the published articles especially in bat [2]. The filiform papillary system was subdivided into seven subtypes as reported in the current work in the Egyptian fruit bat (*Rousettus aegyptiacus*), similar to that findings of Park and Hall [48] in bat; however, some authors observed six subtypes in Egyptian fruit bat (*Rousettus aegyptiacus*) [4] and Japanese long-fingered bats [37]. Five subtypes were noted in lesser dog-faced fruit and nectarivorous bats [19, 43], and four subtypes were reported in frugivorous bats [43, 46] and Egyptian fruit bat (*Rousettus aegyptiacus*) [15]. Three subtypes

were observed by Pastor et al. [51], Jackowiak et al. [34], and Park and Lee [49].

Another factor affecting the anatomical subdivision of the filiform papillae is the geographical distribution of the bats. This adaptation appears in some cases. The first case is the little red flying-fox bat that feeds on nectar, so its filiform papillary system adapted by the presence of numerous long giant pointed filiform papillae on the lingual apex [8, 12], while when subjected to the migration to research on food particles other than nectar-feeding, the filiform papillary system modified to depend on the feeding on fruit instead of nectar-feeding [13]. The second case is the Egyptian fruit bat caught from the fruit farms in the Nile Delta of Egypt, which had the filiform papillary system divided into six subtypes [2, 4], whereas that caught from the fruit farms in the Siwa Oasis of Egypt in the current study carried seven subtypes. Moreover the bat caught from Japan had five subtypes, the bat caught from Saudi Arabia carried four subtypes only [15], and that caught from Poland had only three subtypes [34]. The third case was observed in the filiform papillary system on the lingual tip; the current study reported that the Egyptian fruit bat carried cornflower filiform papillae, while in the Egyptian fruit bat caught from Poland, the lingual tip had numerous small filiform papillae [34], and in that caught from Japan, the lingual tip had numerous scales-like filiform papillae [20]. The current findings agree with previously published data [2, 15, 62] that the anatomical shape, distribution, and nomination of the lingual papillae had characteristic features that reflected on the evolutionary taxonomic status of the bat species [15, 63].

The gustatory fungiform papillae were subjected to three main classifications. The first classification is according to their function and had three types of the gustatory papillae, as in that shown in the current work in Egyptian fruit bat (*Rousettus aegyptiacus*). The same results were described by Abumandour and El-Bakary [4], El-Mansi et al. [15], Massoud and Abumandour [41] and Abumandour and El-Bakary [3]. The second one is named the mechanical papilla and does not have any taste buds; this type has not been recorded in any bat species, but was noted in other species, such as donkey [40]. The third one is the mixed type in which some papillae had taste buds and other do not have any in the same animal, as was shown in Australian Megachiroptera [7]. The second classification is according to the distribution of these papillae, as described by Chung and Kwun [9].

The first one described that these papillae were found on the entire lingual length [49] in bats, but the second one described that these papillae were found on the lingual boundaries [50] in *S. species*; however, the third one described that these papillae were found on the lingual tip and side edge areas, as observed in fruit bat [4, 19] and flying squirrel [17], while the fourth one noted the presence of these papillae at the lingual centre and tip as reported in bank vole and Japanese grass vole [24, 31]. Moreover, the present study described that the scanty numbers of these papillae were found on the lingual tip and the two lateral parts of the lingual apex and body, while these papillae were completely absent in the median lingual part, similar to that described by Abumandour and El-Bakary [4]. The third classification is according to the shape of these papillae. From the previously published data, all species had only one shape that differs from species to species. The present study observed the quadrilateral shape, similar to that described by El-Mansi et al. [15] in Egyptian fruit bat captured from Saudi Arabia, while that captured from Egypt had the dome-shaped fungiform papillae, as reported by Massoud and Abumandour [41]; the round fungiform papillae were recorded by El-Bakary and Abumandour [14] in the Egyptian Water Buffalo (*Bubalus bubalis*), the elliptical shape [49], the dome-shaped fungiform papillae [17] in the flying squirrel, the mushroom shape [38], the discoid fungiform observed by El-Mansi et al. [15] in Egyptian tomb bat, and the fungus shape fungiform observed by Dinc et al. [11] in the rat. While in Egyptian fruit bat observed the presence of two shapes of the fungiform papillae: rectangular and round [4].

According to the previously published articles, there are species variations in the number, shape, distribution, position, and shape of its lingual dorsal surface with taste buds. The most characteristic point is the number of the circumvallate papillae that differ from the completely absent to more than 20 papillae. The circumvallate papillae are completely absent in the blood-drinking *Desmodus rotundus* and haematophagous bats [25, 43], but the presence of only one circumvallate papilla has been observed in some mammalian species [16, 42]. Moreover, the most common number is the presence of two papillae as reported in common European bat [51], Korean greater horseshoe bat [56], lesser dog-faced fruit and flying fox [18, 19], free-tailed bat [26], and Korean long-fingered bats [50]. However, we found the presence of three circumval-

late papillae in the present study in Egyptian fruit bat (*Rousettus aegyptiacus*), similar to that described by Abumandour et al. [4], El-Mansi et al. [15], Jackowiak et al. [34], and Massoud et al. [41] in Egyptian fruit bat [18, 19], in frugivorous bats [7], in *S. australis* and *Pteropus* [46], in *E. wahlbergi*, and the long-eared hedgehog (*H. auritus*) [42]. Moreover, four circumvallate papillae were described by Masuko et al. [43] in long-nosed bat and frugivorous and nectarivorous bats [7] as well as in Australian Megachiroptera (*N. Robinsoni*). However, there were some mammalian species that carried several circumvallate lingual papillae, such as deer [64] and buffalo [14].

The circumvallate papillae had a round central bulb encircled by a continuous deep groove in Egyptian fruit bat (*Rousettus aegyptiacus*), similar to that described by Abumandour et al. [4], Ciuccio et al. [10] and El-Mansi et al. [15]. Moreover, the present investigation described that the central round bulb was encircled only by one layer of two segmented circular annular pad laterally but, from the rostral and posterior side, not surrounded by this circular pad. There was some variation in the number of pad layers surrounding the circumvallate papillae; the presence of only one layer of the annular pad was observed in mouse, rat and other rodents [29, 30], and primates [36], while the two layers of the pad were observed in some bat species [4, 50].

The dorsal surface of the circumvallate papillae had an irregular surface by the SEM observations. The same findings were described by Aboelnour et al. [4] and El-Mansi et al. [15] in Egyptian fruit bat and in the rabbit [3]. However, the smooth papillary surface was recorded in fox [32].

The triangular arrangement of the circumvallate papillae was a characteristic appearance that appeared in some mammalian species. The present examination on the two bat species of various feeding habits had this triangular arrangement of the circumvallate papillae, like that revealed in fruit bat [4, 15, 18, 34, 41, 46], Egyptian long-eared hedgehog [42], and the Persian squirrel [53].

The obtained histological findings showed that the dorsal surface of the tongue was covered with a thick keratinised multilayered stratified squamous epithelial layer that covered all the dorsal surface with its papillae, similar results were recorded by Abumandour and El-Bakary [4], El-Mansi [15] and Massoud and Abumandour [41] in the Egyptian fruit bat (*Rousettus aegyptiacus*).

The obtained histological findings showed that there were numerous taste buds in both fungiform and circumvallate papillae in the Egyptian fruit bat (*Rousettus aegyptiacus*) tongue. The taste buds were also recorded in most bat species: in the Egyptian tomb bat (*Taphozous perforatus*) [16] and in the Egyptian fruit bat (*Rousettus aegyptiacus*) [15, 41].

The present results corresponding with that reported by Goździewska-Harłajczuk et al. [23], Jackowski et al. [34], and Iwasaki et al. [30] that the presence of the taste buds was related to the process of chemoreception of the gland secretion of the tongue. Furthermore, the description of the lingual glands in the current work matched with the obtained results of Akbari et al. [5], Goździewska-Harłajczuk [22], Jarrar et al. [35], and Tandler et al. [59].

In vertebrate animals, the lingual gland secretions act as a lubricant that assists in moistening the food particles, then facilitates food movements, transport, and swallowing [33, 54, 61]. The current histochemical results revealed that the lingual glands showed a stronger AB-positive reaction and gave dark blue colour, while the reaction for the PAS-stain was negative. This negative reaction with PAS-stain was similar to that noted by Massoud and Abumandour [41]. The current study reported that the glands give a blue colour as an indication of positive AB reactivity with combined AB-PAS staining, while Massoud and Abumandour [41] reported the AB positive granules with blue colour stain of the acidic mucins.

#### Funding

Taif University Researchers Supporting Project number (TURSP-2020/138), Taif University, Taif, Saudi Arabia.

#### Acknowledgements

The authors would like to express their gratitude to the Anatomy and Embryology Department, Faculty of Veterinary Medicine, Alexandria University for providing technical and administrative support. Also, we are indebted to the Zoology Department, Faculty of Science, Tanta University. We deeply thank Taif University Researchers Supporting Project number (TURSP-2020/138), Taif University, Taif, Saudi Arabia.

**Conflict of interest:** None declared

#### REFERENCES

1. Aboelnour A, Noreldin AE, Massoud D, et al. Retinal characterization in the eyes of two bats endemic in the Egyptian fauna, the Egyptian fruit bat (*Rousettus aegyptiacus*) and insectivorous bat (*Pipistrellus kuhlii*), using the light microscope and transmission electron microscope. *Microsc Res Tech.* 2020; 83(11): 1391–1400, doi: [10.1002/jemt.23530](https://doi.org/10.1002/jemt.23530), indexed in Pubmed: [33405350](https://pubmed.ncbi.nlm.nih.gov/33405350/).
2. Abumandour M. Morphological Comparison of the Filiform Papillae of New Zealand White Rabbits (*Oryctolagus cuniculus*) as Domestic Mammals and Egyptian Fruit Bat (*Rousettus aegyptiacus*) as Wild Mammals Using Scanning Electron Microscopic Specimens. *Int J Morphol.* 2014; 32(4): 1407–1417, doi: [10.4067/s0717-95022014000400045](https://doi.org/10.4067/s0717-95022014000400045).
3. Abumandour MMA, El-Bakary RMA. Anatomic reference for morphological and scanning electron microscopic studies of the New Zealand white rabbits tongue (*Oryctolagus cuniculus*) and their lingual adaptation for feeding habits. *J Morphol Sci.* 2013; 30(4): 1–12.
4. Abumandour MMA, El-Bakary RMA. Morphological and scanning electron microscopic studies of the tongue of the Egyptian fruit bat (*Rousettus aegyptiacus*) and their lingual adaptation for its feeding habits. *Vet Res Commun.* 2013; 37(3): 229–238, doi: [10.1007/s11259-013-9567-9](https://doi.org/10.1007/s11259-013-9567-9), indexed in Pubmed: [23709139](https://pubmed.ncbi.nlm.nih.gov/23709139/).
5. Akbari G, Babaei M, Hassanzadeh B. Morphological study of the European hedgehog (*Erinaceus europaeus*) tongue by SEM and LM. *Anat Sci Int.* 2018; 93(2): 207–217, doi: [10.1007/s12565-017-0391-0](https://doi.org/10.1007/s12565-017-0391-0), indexed in Pubmed: [28160234](https://pubmed.ncbi.nlm.nih.gov/28160234/).
6. Altringham JD, McOwat T, Hammond L. Bats: biology and behaviour. Oxford University Press, Oxford 1996.
7. Birt P, Hall L, Smith G. Ecomorphology of the Tongues of Australian Megachiroptera (Chiroptera: Pteropodidae). *Austr J Zool.* 1997; 45(4): 369, doi: [10.1071/zo97005](https://doi.org/10.1071/zo97005).
8. Boland DJ. Forest Trees of Australia. Thomas Nelson, Melbourne 1984.
9. Chung YW, Kwun HS. A morphological study on the tongues of the vertebrates. I. Comparative macroscopic and microscopic observations. *J Catholic Medical College (Korean).* 1977; 30: 531–555.
10. Ciuccio M, Estecondo S, Casanave EB. Scanning electron microscopy study of the dorsal surface of the tongue of *Dasypus hybridus* (Mammalia, Xenarthra, Dasypodidae). *Int J Morphol.* 2010; 28(2), doi: [10.4067/s0717-95022010000200007](https://doi.org/10.4067/s0717-95022010000200007).
11. Dinç G, Girgin A, Yllmaz S. Ratlarda papilla fungiformis'in prenatal ve postnatal gelişimi. *Fırat Üniv Sağlık Bil Derg.* 1995; 9(2): 161–163.
12. Eby P. Finger-winged night workers: managing forests to conserve the role of grey-headed flying foxes as pollinators and seed dispersers. In: Lunney D. (ed.). Conservation of Australia's Forest Fauna. Royal Zoological Society of New South Wales, Mosman 1991: 91–100.
13. Eby P. The biology and management of flying foxes in New South Wales. New South Wales National Parks and Wildlife Service, Report No. 18, 1995.
14. El-Bakary NER, Abumandour MMA. Morphological studies of the tongue of the Egyptian water buffalo (*Bubalus bubalis*) and their lingual papillae adaptation for its feeding habits. *Anat Histol Embryol.* 2017; 46(5): 474–486, doi: [10.1111/ahp.12292](https://doi.org/10.1111/ahp.12292), indexed in Pubmed: [28833390](https://pubmed.ncbi.nlm.nih.gov/28833390/).
15. El-Mansi A, Al-Kahtani MA, Abumandour M. Comparative phenotypic and structural adaptations of tongue and gastrointestinal tract in two bats having different

- feeding habits captured from Saudi Arabia: Egyptian fruit bat (*Rousettus aegyptiacus*) and Egyptian tomb bat (*Taphozous perforatus*). *Zoologischer Anzeiger*. 2019; 281: 24–38, doi: [10.1016/j.jcz.2019.05.005](https://doi.org/10.1016/j.jcz.2019.05.005).
16. El-Sharaby AA, El-Gendy SA, Alsafy MA, et al. Morphological variations of the vallate papillae in some mammalian species. *Anat Sci Int*. 2014; 89(3): 161–170, doi: [10.1007/s12565-013-0215-9](https://doi.org/10.1007/s12565-013-0215-9), indexed in Pubmed: [24242871](https://pubmed.ncbi.nlm.nih.gov/24242871/).
  17. Emura S, Tamada A, Hayakawa D, et al. SEM study on the dorsal lingual surface of the flying squirrel, *Petaurista leucogenys*. *Ann Anat - Anatomischer Anzeiger*. 1999; 181(5): 495–498, doi: [10.1016/s0940-9602\(99\)80033-8](https://doi.org/10.1016/s0940-9602(99)80033-8).
  18. Emura S, Hayakawa D, Chen H, et al. SEM study on the dorsal lingual surface of the large flying fox, *Pteropus vampyrus*. *Okajimas Folia Anat Jpn*. 2002; 79(4): 113–119, doi: [10.2535/ofaj.79.113](https://doi.org/10.2535/ofaj.79.113), indexed in Pubmed: [12484446](https://pubmed.ncbi.nlm.nih.gov/12484446/).
  19. Emura S, Hayakawa D, Chen H, et al. SEM study on the dorsal lingual surface of the lesser dog-faced fruit bat, *Cynopterus brachyotis*. *Okajimas Folia Anat Jpn*. 2001; 78(4): 123–128, doi: [10.2535/ofaj1936.78.4\\_123](https://doi.org/10.2535/ofaj1936.78.4_123), indexed in Pubmed: [11774747](https://pubmed.ncbi.nlm.nih.gov/11774747/).
  20. Emura S, Okumura T, Chen H. Morphology of the lingual papillae in the Egyptian rousette bat (*Rousettus aegyptiacus*). *Okajimas Folia Anat Jpn*. 2012; 89(3): 61–66, doi: [10.2535/ofaj.89.61](https://doi.org/10.2535/ofaj.89.61), indexed in Pubmed: [23429050](https://pubmed.ncbi.nlm.nih.gov/23429050/).
  21. Gewily DI, Mahmoud FA, Saber SA, et al. Ultrastructural comparison between the tongue of two reptilian species endemic in Egyptian fauna; Bosc's fringe-toed lizard *Acanthodactylus boskianus* and Sinai fan-fingered gecko *Ptyodactylus guttatus*. *Microsc Res Tech*. 2021; 84(9): 1977–1991, doi: [10.1002/jemt.23753](https://doi.org/10.1002/jemt.23753), indexed in Pubmed: [33720486](https://pubmed.ncbi.nlm.nih.gov/33720486/).
  22. Goździewska-Harłajczuk K, Klećkowska-Nawrot J, Nowaczyk R, et al. Biological aspect of the surface structure of the tongue in the adult red kangaroo (*Macropus rufus*): light and scanning electron microscopy. *Biologia*. 2016; 71(6): 174–178, doi: [10.1515/biolog-2016-0082](https://doi.org/10.1515/biolog-2016-0082).
  23. Goździewska-Harłajczuk K, Klećkowska-Nawrot J, Barszcz K, et al. Biological aspects of the tongue morphology of wild-captive WWCP rats: a histological, histochemical and ultrastructural study. *Anat Sci Int*. 2018; 93(4): 514–532, doi: [10.1007/s12565-018-0445-y](https://doi.org/10.1007/s12565-018-0445-y), indexed in Pubmed: [29948977](https://pubmed.ncbi.nlm.nih.gov/29948977/).
  24. Grandi D, Arcari ML, Azalli G. Ultrastructural aspects of the lingual papillae in the gerbil (*Meriones unguiculatus*). *Ital J Anat Embryol*. 1994; 99: 201–217.
  25. Greenbaum IF, Phillips CJ. Comparative anatomy and general histology of tongues of long-nosed bats (*Leptonycteris sanborni* and *L. nivalis*) with reference to infestation of oral mites. *J Mammal*. 1974; 55(3): 489–504, indexed in Pubmed: [4851092](https://pubmed.ncbi.nlm.nih.gov/4851092/).
  26. Gregorin R. Comparative morphology of the tongue in free-tailed bats (Chiroptera, Molossidae). *Iheringia. Série Zoologia*. 2003; 93(2): 213–221, doi: [10.1590/s0073-47212003000200014](https://doi.org/10.1590/s0073-47212003000200014).
  27. Humason GL. Animal tissue techniques. Animal tissue techniques, 1962.
  28. Iwasaki Si. Evolution of the structure and function of the vertebrate tongue. *J Anat*. 2002; 201(1): 1–13, doi: [10.1046/j.1469-7580.2002.00073.x](https://doi.org/10.1046/j.1469-7580.2002.00073.x), indexed in Pubmed: [12171472](https://pubmed.ncbi.nlm.nih.gov/12171472/).
  29. Iwasaki S, Yoshizawa H, Kawahara I. Study by scanning electron microscopy of the morphogenesis of three types of lingual papilla in the mouse. *Acta Anat (Basel)*. 1996; 157(1): 41–52, doi: [10.1159/000147865](https://doi.org/10.1159/000147865), indexed in Pubmed: [9096741](https://pubmed.ncbi.nlm.nih.gov/9096741/).
  30. Iwasaki S, Yoshizawa H, Kawahara I. Study by scanning electron microscopy of the morphogenesis of three types of lingual papilla in the rat. *Anat Rec*. 1997; 247(4): 528–541, doi: [10.1002/\(SICI\)1097-0185\(199704\)247:4<528::AID-AR12>3.0.CO;2-R](https://doi.org/10.1002/(SICI)1097-0185(199704)247:4<528::AID-AR12>3.0.CO;2-R), indexed in Pubmed: [9096793](https://pubmed.ncbi.nlm.nih.gov/9096793/).
  31. Jackowiak H, Godynicki S. The distribution and structure of the lingual papillae on the tongue of the bank vole *Clethrionomys glareolus*. *Folia Morphol*. 2005; 64(4): 326–333, indexed in Pubmed: [16425161](https://pubmed.ncbi.nlm.nih.gov/16425161/).
  32. Jackowiak H, Godynicki S. The scanning electron microscopic study of lingual papillae in the silver fox (*Vulpes vulpes fulva*, Desmarest, 1820). *Ann Anat*. 2004; 186(2): 179–183, doi: [10.1016/S0940-9602\(04\)80037-2](https://doi.org/10.1016/S0940-9602(04)80037-2), indexed in Pubmed: [15125050](https://pubmed.ncbi.nlm.nih.gov/15125050/).
  33. Jackowiak H, Ludwig M. Light and scanning electron microscopic study of the structure of the ostrich (*Strutio camelus*) tongue. *Zoolog Sci*. 2008; 25(2): 188–194, doi: [10.2108/zsj.25.188](https://doi.org/10.2108/zsj.25.188), indexed in Pubmed: [18533750](https://pubmed.ncbi.nlm.nih.gov/18533750/).
  34. Jackowiak H, Trzecielińska-Lorych J, Godynicki S. The microstructure of lingual papillae in the Egyptian fruit bat (*Rousettus aegyptiacus*) as observed by light microscopy and scanning electron microscopy. *Arch Histol Cytol*. 2009; 72(1): 13–21, doi: [10.1679/aohc.72.13](https://doi.org/10.1679/aohc.72.13), indexed in Pubmed: [19789409](https://pubmed.ncbi.nlm.nih.gov/19789409/).
  35. Jarrar BM, Taib N. Histochemical characterization and distribution of mucosubstances and enzyme activity in the lingual salivary glands of the one-humped camel (*Camelus dromedarius*). *Revue d'élevage et de médecine vétérinaire des pays tropicaux*. 1989; 41(1): 63–71.
  36. Kobayashi K, Kumakura M, Yoshimura K, et al. Comparative morphological studies on the stereo structure of the lingual papillae of selected primates using scanning electron microscopy. *Ann Anat*. 2004; 186(5-6): 525–530, doi: [10.1016/S0940-9602\(04\)80101-8](https://doi.org/10.1016/S0940-9602(04)80101-8), indexed in Pubmed: [15646287](https://pubmed.ncbi.nlm.nih.gov/15646287/).
  37. Kobayashi S, Shimamura A. Comparative anatomical observations of the tongue of the Japanese long-fingered bats, *Miniopterus schreibersi fuliginosus*. *Okajimas Folia Anat Jpn*. 1982; 58(4-6): 923–932, doi: [10.2535/ofaj1936.58.4-6\\_923](https://doi.org/10.2535/ofaj1936.58.4-6_923), indexed in Pubmed: [7122024](https://pubmed.ncbi.nlm.nih.gov/7122024/).
  38. Kurtul I, Atalgın SH. Scanning electron microscopic study on the structure of the lingual papillae of the Saanen goat. *Small Ruminant Res*. 2008; 80(1-3): 52–56, doi: [10.1016/j.smallrumres.2008.09.003](https://doi.org/10.1016/j.smallrumres.2008.09.003).
  39. Luna LG. Routine staining procedures. Manual of histologic staining methods of the Armed Forces Institute of Pathology. Blakiston Division, McGraw-Hill, New York 1968: 33–46.
  40. Mahmoud MMAE, Ahmed EZ, Rudolf L, et al. Morphological characteristics of the tongue and its papillae in the donkey (*Equus asinus*): a light and scanning electron microscopical study. *Ann Anat Anatomischer Anzeiger*. 2002; 184(5): 473–480, doi: [10.1016/s0940-9602\(02\)80081-4](https://doi.org/10.1016/s0940-9602(02)80081-4).
  41. Massoud D, Abumandour MMA. Anatomical features of the tongue of two chiropterans endemic in the Egyptian fauna; the Egyptian fruit bat (*Rousettus aegyptiacus*) and insectivorous bat (*Pipistrellus kuhlii*). *Acta Histochem*. 2020; 122(2): 151503, doi: [10.1016/j.acthis.2020.151503](https://doi.org/10.1016/j.acthis.2020.151503), indexed in Pubmed: [31955907](https://pubmed.ncbi.nlm.nih.gov/31955907/).

42. Massoud D, Abumandour MMA. Descriptive studies on the tongue of two micro-mammals inhabiting the Egyptian fauna; the Nile grass rat (*Arvicanthis niloticus*) and the Egyptian long-eared hedgehog (*Hemiechinus auritus*). *Microsc Res Tech*. 2019; 82(9): 1584–1592, doi: [10.1002/jemt.23324](https://doi.org/10.1002/jemt.23324), indexed in Pubmed: [31225934](https://pubmed.ncbi.nlm.nih.gov/31225934/).
43. Masuko TS, et al. Comparative Scanning Electron Microscopic Study of the Lingual Papillae in Three Species of Bats (*Carollia perspicillata*, *Glossophaga soricina* and *Desmodus rotundus*). *Microsc Microanal*. 2007; 13(Suppl 2): 280–281.
44. Morrison DW. Efficiency of food utilization by fruit bats. *Oecologia*. 1980; 45(2): 270–273, doi: [10.1007/BF00346469](https://doi.org/10.1007/BF00346469), indexed in Pubmed: [28309539](https://pubmed.ncbi.nlm.nih.gov/28309539/).
45. Mowry RW. Alcian blue technics for the histochemical study of Alcian carbohydrates. *J Histochem Cytochem*. 1956; 4: 407–411.
46. Mqokeli BR, Downs CT. Palatal and lingual adaptations for frugivory and nectarivory in the Wahlberg's epauletted fruit bat (*Epomophorus wahlbergi*). *Zoomorphology*. 2012; 132(1): 111–119, doi: [10.1007/s00435-012-0170-3](https://doi.org/10.1007/s00435-012-0170-3).
47. Nomina Anatomica Veterinaria N. International Committee on Veterinary Gross Anatomical Nomenclature and authorized by the general assembly of the world Association of veterinary Anatomist. Knoxville, 3rd Ed. Ghent. Published by the Editorial Committee Hanover (Germany), Ghent (Belgium), Columbia, MO (USA), Rio de Janeiro (Brazil). 2017.
48. Park H, Hall E. The gross anatomy of the tongues and stomachs of eight new world bats. *Trans Kans Acad Sci (1903-)*. 1951; 54(1): 64–72, doi: [10.2307/3626255](https://doi.org/10.2307/3626255).
49. Park J, Lee JH. Comparative Morphology of the Tongue of *Miniopterus schreibersi fuliginosus* and *Pipistrellus savii*. *Applied Microscopy*. 2009; 39(3): 267–276.
50. Park J, Lee JH. Morphological Study on the Dorsal Lingual Papillae of *Sorex caecutiens* Laxmann. *Korean J Microscopy*. 2009; 39(2): 106–106.
51. Pastor JF, Moro JA, Verona JA, et al. Morphological study by scanning electron microscopy of the lingual papillae in the common European bat (*Pipistrellus pipistrellus*). *Arch Oral Biol*. 1993; 38(7): 597–599, doi: [10.1016/0003-9969\(93\)90125-6](https://doi.org/10.1016/0003-9969(93)90125-6), indexed in Pubmed: [7690226](https://pubmed.ncbi.nlm.nih.gov/7690226/).
52. Prothero DR. The Princeton field guide to prehistoric mammals. Vol. 112. Princeton University Press 2016.
53. Sadeghinezhad J, Tootian Z, Javadi F. Anatomical and histological structure of the tongue and histochemical characteristics of the lingual salivary glands in the Persian squirrel (*Sciurus anomalus*). *Anat Sci Int*. 2018; 93(1): 58–68, doi: [10.1007/s12565-016-0367-5](https://doi.org/10.1007/s12565-016-0367-5), indexed in Pubmed: [27565979](https://pubmed.ncbi.nlm.nih.gov/27565979/).
54. Schwenk K. Morphology of the tongue in the tuatara, *Sphenodon punctatus* (Reptilia: Lepidosauria), with comments on function and phylogeny. *J Morphol*. 1986; 188(2): 129–156, doi: [10.1002/jmor.1051880202](https://doi.org/10.1002/jmor.1051880202), indexed in Pubmed: [29945355](https://pubmed.ncbi.nlm.nih.gov/29945355/).
55. Sharma R, Vidyadaran MK, Zulkifli I, et al. Ecomorphological implications of the microstructures on the tongue of the fawn roundleaf bat, *Hipposideros cervinus* (Chiroptera: Hipposideridae). *Austr J Zool*. 1999; 47(4): 405, doi: [10.1071/zo98051](https://doi.org/10.1071/zo98051).
56. Son SW, Lee HJ, Lee JH. Ultrastructural observations of the lingual papillae of the Korean greater horseshoe bat, *Rhinolophus ferrumequinum korai*. *Kyungnam Univ J Basic Sci Res Int (Korean)*. 2000; 14: 65–72.
57. Spicer SS, Meyer DB. Histochemical differentiation of acid mucopolysaccharides by means of combined aldehyde fuchsin-alcian blue staining. *Am J Clin Pathol*. 1960; 33(5\_ts): 453–460, doi: [10.1093/ajcp/33.5\\_ts.453](https://doi.org/10.1093/ajcp/33.5_ts.453).
58. Suvarna SK, Layton C, Bancroft JD. Bancroft's Theory and Practice of Histological Techniques, Expert Consult: Online and Print, 7: Bancroft's Theory and Practice of Histological Techniques. Churchill Livingstone Elsevier, Churchill Livingstone 2013.
59. Tandler B, Toyoshima K, Seta Y, et al. Ultrastructure of the salivary glands in the midtongue of the common vampire bat, *Desmodus rotundus*. *Anat Rec*. 1997; 249(2): 196–205, doi: [10.1002/\(SICI\)1097-0185\(199710\)249:2<196::AID-AR6>3.0.CO;2-W](https://doi.org/10.1002/(SICI)1097-0185(199710)249:2<196::AID-AR6>3.0.CO;2-W), indexed in Pubmed: [9335465](https://pubmed.ncbi.nlm.nih.gov/9335465/).
60. Wilson DE, Reeder DM. Mammal Species of the World. A Taxonomis and Geographic Reference. 2nd Ed. Smithsonian Institution Press, Washington 1993.
61. Winokur RM. The buccopharyngeal mucosa of the turtles (Testudines). *J Morphol*. 1988; 196(1): 33–52, doi: [10.1002/jmor.1051960105](https://doi.org/10.1002/jmor.1051960105), indexed in Pubmed: [3373540](https://pubmed.ncbi.nlm.nih.gov/3373540/).
62. Yoshimura K, Hama N, Shindo J, et al. Light and scanning electron microscopic study on the lingual papillae and their connective tissue cores of the Cape hyrax *Procavia capensis*. *J Anat*. 2008; 213(5): 573–582, doi: [10.1111/j.1469-7580.2008.00969.x](https://doi.org/10.1111/j.1469-7580.2008.00969.x), indexed in Pubmed: [18713236](https://pubmed.ncbi.nlm.nih.gov/18713236/).
63. Yoshimura K, Shindoh J, Kobayashi K. Scanning electron microscopy study of the tongue and lingual papillae of the California sea lion (*Zalophus californianus californianus*). *Anat Rec*. 2002; 267(2): 146–153, doi: [10.1002/ar.10093](https://doi.org/10.1002/ar.10093), indexed in Pubmed: [11997883](https://pubmed.ncbi.nlm.nih.gov/11997883/).
64. Zheng J, Kobayashi K. Comparative morphological study on the lingual papillae and their connective tissue cores (CTC) in reeves' muntjac deer (*Muntiacus reevesi*). *Ann Anat — Anatomischer Anzeiger*. 2006; 188(6): 555–564, doi: [10.1016/j.aanat.2006.05.014](https://doi.org/10.1016/j.aanat.2006.05.014), indexed in Pubmed: [17140149](https://pubmed.ncbi.nlm.nih.gov/17140149/).

# Histological analysis of spermatogenesis and the germ cell seasonal development within the testis of domesticated tree shrews (*Tupaia belangeri chinensis*)

J. Tang<sup>1, 2 \*</sup>, G. He<sup>1, 3 \*</sup>, Y. Yang<sup>1</sup>, Q. Li<sup>1</sup>, Y. He<sup>1</sup>, C. Yu<sup>1</sup>, L. Luo<sup>1</sup>

<sup>1</sup>School of Basic Medical Sciences, Kunming Medical University, Kunming, China

<sup>2</sup>Department of Medical Genetics and Prenatal Diagnosis, Kunming Maternity and Child Health Hospital, Kunming, China

<sup>3</sup>Clinical Laboratory, Yunnan Maternal and Child Health Care Hospital, Kunming, China

[Received: 1 March 2021; Accepted: 22 April 2021; Early publication date: 6 May 2021]

**Background:** This study aimed to address the lack of information on the male germ cell seasonal development of domesticated tree shrews (*Tupaia belangeri chinensis*).

**Materials and methods:** Testicular tissues were collected from 60 tree shrews ( $n = 5$  per month). The ultrastructures of the testes and spermatids were examined via transmission electron microscopy. Apoptosis of spermatogenic cells was measured through terminal deoxynucleotidyl transferase dUTP nick end labelling (TUNEL) staining. The expression of proliferation factors, namely, proliferating cell nuclear antigen (PCNA) and Ki67, in testicular tissues was assayed through immunohistochemistry.

**Results:** Spermatid ultrastructure showed seasonal differences, and spermatogenesis was relatively active in June and July and relatively stagnant from October to November. The percentage of TUNEL-positive germ cells was less during October and November, while greater in July than other phases. The number of PCNA-nucleus-positive germ cells was most in June and July, but with cytoplasm staining from October to November. Ki67 presented positive expression in the testes from April to September, with highest expression in June, but with no expression from October to March.

**Conclusions:** In summary, there are seasonal differences in tissue morphology related to spermatogenesis in domesticated tree shrews. PCNA expression and Ki67 expression are good indicators of seasonal differences in male germ cells. (Folia Morphol 2022; 81, 2: 412–420)

**Key words:** tree shrew, spermatogenic cell, seasonal differences, testis

## INTRODUCTION

Tree shrews (*Tupaia belangeri chinensis*), which belong to the family Tupaiidae, genus *Tupaia*, are

rat-sized mammals that live mainly in deciduous, evergreen and secondary forests in tropical and subtropical regions [30]. Whole-genome sequencing

Address for correspondence: Prof. L. Luo, No. 1168 Chunrong West Road, Yuhua Street, Chenggong, Kunming, China, tel +86 871-65922865, e-mail: luolan@kmmu.edu.cn

\*Equal contribution

This article is available in open access under Creative Common Attribution-Non-Commercial-No Derivatives 4.0 International (CC BY-NC-ND 4.0) license, allowing to download articles and share them with others as long as they credit the authors and the publisher, but without permission to change them in any way or use them commercially.

analysis has revealed that tree shrews are similar to humans with regard to histology, physiology, biochemistry, and nervous (brain function), metabolic and immune systems [8, 22, 24]. The tree shrew is small, has a short reproductive cycle, is easy to perform experiments on, is inexpensive to feed, and has other favourable characteristics, such as susceptibility to a wide range of human pathogenic viruses [32]. Thus, the tree shrew may be a good animal model for scientific experiments.

Studies have shown that the reproduction of sexually mature male wild tree shrews has obvious seasonality; the reproductive season lasts only from April to July each year [29]. In a previous study by Cao [4], highly active seminiferous epitheliums were observed in January and April. Regression of seminiferous tubules begins in July and there are extensive regressive changes in seminiferous epitheliums losing spermatogenic function in August and October. Similar seasonal changes in spermatozoa amount are shown in epididymis. However, recent studies have reported that artificial domestication can overcome the seasonal restrictions of tree shrew reproduction [14]. The seasonal reproduction pattern of this species has caused considerable uncertainty and unforeseen complications related to the reproducibility, stability and comparability of male reproductive medicine studies using the tree shrew as a model organism, which has restricted the use of the tree shrew as a model organism for reproduction research. However, there have been no studies on the seasonal differences in morphology or proliferation and apoptosis levels in domesticated tree shrew sperm.

Spermatogenesis is a complex process. Sperm matures through the mitosis of spermatogonia, meiosis of spermatocytes, and maturation of spermatids [9]. Spermatogenic cells proliferate often, develop continuously and have physiological significance in the process of spermatogenesis. Proliferating cell nuclear antigen (PCNA) is a cell cycle regulatory protein marker that is closely related to DNA synthesis and participates in the initiation of cell proliferation [26]. Ki67, another nuclear antigen related to cell proliferation, exists in the cell nucleus and participates in the mitotic prophase-to-metaphase transition and the maintenance of DNA structure [13, 23]. Therefore, the protein expression levels of PCNA and Ki67 in the testes are standard markers for the proliferation of spermatogenic cells [31]. Additionally, apoptosis of spermatogenic cells in the testes may contribute to seasonal differences in sperm [3].

The present study aimed to investigate whether there are seasonal differences in spermatogenesis in domesticated tree shrews. We examined 1) spermatids morphology using haematoxylin and eosin (HE) staining and transmission electron microscopy (TEM); 2) the frequency of apoptosis using a terminal deoxynucleotidyl transferase dUTP nick end labelling (TUNEL) assay; and 3) immunohistochemical staining of PCNA or Ki67 in testis collected from tree shrews in different seasons.

## MATERIALS AND METHODS

### Animals and treatment

Sixty 18-month-old healthy tree shrews, weighing 128–151 g, were obtained from the Animal Centre of Kunming Medical University and kept in a standard animal house with a temperature of 25°C and a humidity of 45% at 12 L:12 D (lights on at 08:00). Five tree shrews were randomly selected for the experiment every month. The study was approved by the Ethics Committee of Kunming Medical University (Kunming, China, No. KM16/17), and the experimental animals comply with the guidelines of the Chinese Ethics Committee.

The tree shrews were anaesthetized with isoflurane, and the testicles were quickly taken. A tissue block of about 2 mm was cut from one of the testicles and fixed with 2.5% glutaraldehyde for TEM. The rest of the testicles were fixed overnight with 10% neutral formaldehyde within 2 min after sampling, dehydrated in alcohol series, transparent in xylene, and embedded in conventional paraffin. The slice thickness was 5  $\mu$ m, and it was pasted on a glass slide pre-treated with Poly-L-Lysine, and the slice was baked at 60°C for 1 h, and stored at 4°C for later experiments.

### Histomorphological examination

Testicular sections were prepared as described above. The 5- $\mu$ m testicular sections were continuously sliced and stained with HE. The histological structure was then observed under a light microscope (Nikon 90i, Tokyo, Japan).

### Transmission electron microscopy

The 2 mm thick gonadal sections were fixed in 2.5% glutaraldehyde in 0.1 M phosphate buffer pH 7.4 for 3 h at 4°C and post fixed in 1% osmium tetroxide in 0.1 M phosphate buffer overnight at room temperature. Samples were then dehydrated in 75%,

85%, 95%, and 100% alcohols and in 100% acetone, and then embedded in an epoxy Spurr resin. Ultrathin sections of 50 nm were cut and stained with lead citrate-uranyl acetate, then observed by TEM (JEM-1000, JEOL, Tokyo, Japan).

#### Immunohistochemistry assay

The 5- $\mu$ m paraffin slices were baked 65°C for 30 min, dewaxed, and rehydrated in xylene, alcohol and distilled water. Afterward, antigen retrieval was conducted in a microwave oven. Endogenous peroxidase activity in sections was quenched by 3% hydrogen peroxide at room temperature for 30 min, and the sections were then blocked with 5% bovine serum for 15 min. The sections were incubated with diluted primary antibody (PCNA, ab29, 1:100 dilutions; Ki67, ab15580, 1:100 dilutions, Abcam, MA, USA) overnight at 4°C. Then, the section was immunohistochemistry (IHC) staining using MaxVision™ HRP-Polymer anti-Mouse/Rabbit IHC Kit (MXB Biotechnologies Inc., Fuzhou, China). The sections were counterstained with haematoxylin and rinsed in tap water. IHC micrographs were observed under a microscope (Nikon 90i). The PCNA and Ki67 protein nuclei show brown-yellow particles as a positive reaction.

#### TUNEL assay

The level of apoptosis-related DNA fragmentation in the testicular tissues was evaluated by TUNEL assay by using a commercially available kit (Roche, Indianapolis, IN, USA). The sections of 5- $\mu$ m paraffin tissue specimens were serially sectioned, and the standard method was applied according to the manufacturer's instructions. The sections were observed under a light microscope, and the cells in the testis exhibiting brown nuclear staining were considered positive for nuclear DNA fragmentation.

#### Statistical analysis

Statistical analyses were performed using GraphPad prism 6.0. Data were expressed as mean  $\pm$  standard deviation, and analysis of variance was done on non-parametric test. Student's t-test was performed for statistical analyses.  $P < 0.05$  was indicated statistical significance.

## RESULTS

#### Histological structures of the testes

The histological changes in the testes are shown in Figure 1. In January, most of the seminiferous tubules

could be observed at different developmental stages in testis tissue. Spermatogonia were attached to the basement membrane of seminiferous tubules, which was small size, lightly stained and with round nucleus. The primary spermatocytes was in the second and third layers, which was slender size, deeply stained, and with round nucleus. The secondary spermatocytes and round spermatids were near the centre of the lumen, these cells were smaller, lightly stained and with round nucleus. Some fully deformed or partly deformed spermatozoa and residues could be observed near the lumen. Deformed spermatozoa showed darker staining and had a superimposed fusiform shape, while the residue was lighter staining and of irregular shape (Fig. 1A). Compared with January, the number of deformed spermatozoa and its residue in the lumen of the thin tubules increased month by month from February to May (Fig. 1B–E). From June to July, spermatogonia, primary spermatocytes, secondary spermatocytes, round spermatids, a large number of deformed spermatozoa and its residue almost filled the lumen (Fig. 1F, G). From August to September, spermatogenic cells at different developmental stages were observed in the seminiferous tubules of testis tissue, but the number of deformed spermatozoa and its residue began to decrease month by month (Fig. 1H, I). In October, the arrangement of seminiferous tubules and spermatogenic cells in the testes became regular and compact and cavitation were present in part of the seminiferous tubules. Few deformed spermatozoa and its residue were observed (Fig. 1J). From November to December, the number of deformed spermatozoa and its residual increased compared with October, which was similar to the structure of seminiferous tubules in January (Fig. 1K, L).

#### Ultrastructure of the testicular tissue and sperm of tree shrews

The TEM images of the testicular tissue and spermatozoa ultrastructures are shown in Figure 2. In January, there were few free spermatozoa in the lumens of the seminiferous tubules. Some primary spermatocytes had shrunken nuclei, ruptured nuclear membranes, agglutination of organelles, and nearly round apoptotic bodies with enhanced electron density. A small number of primary spermatocytes presented putamen (Fig. 2F). Additionally, abnormal morphological features in sperm such as head mass loss, vacuolisation, and crooked tails were also observed (Fig. 2L, R). From February to July, the numbers

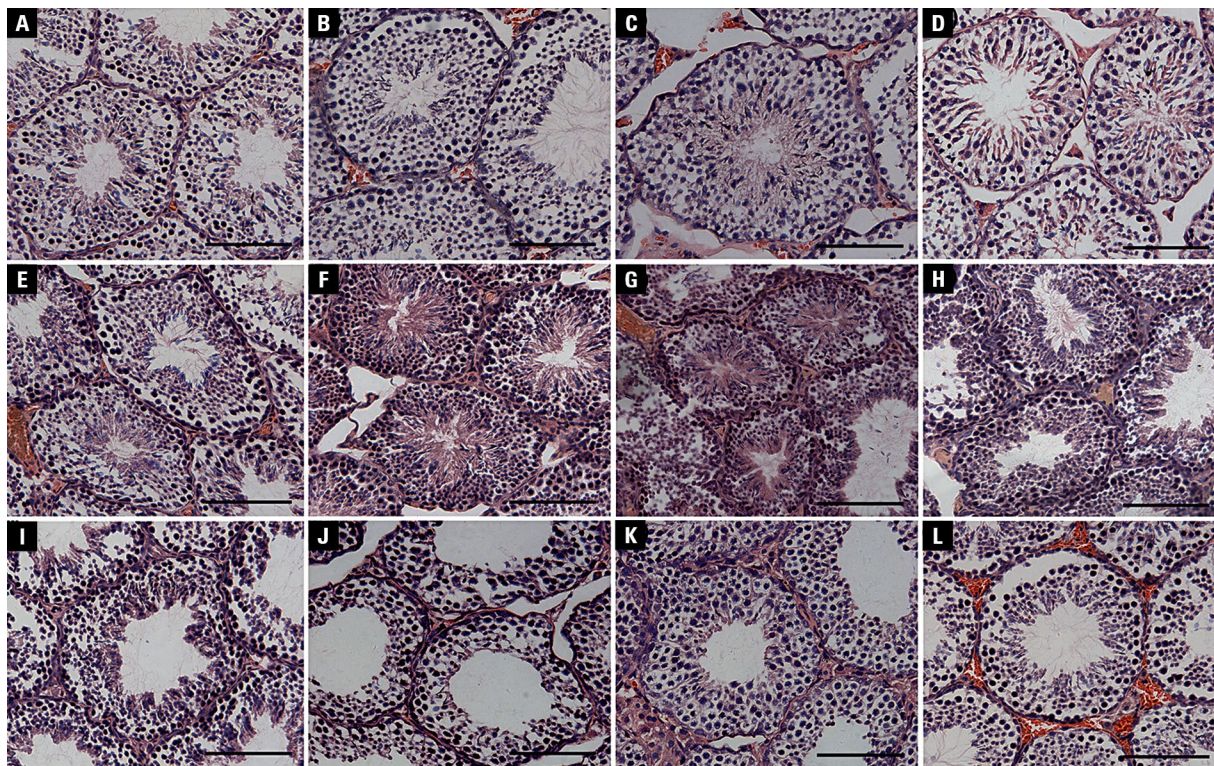


**Figure 1. A–L.** Morphological changes in the testis of the domesticated tree shrew. Haematoxylin–eosin staining of paraffin-embedded sections of testis from male tree shrew from January to December. Bar = 100  $\mu$ m.

of free spermatozoa in the lumens of seminiferous tubules gradually increased (Fig. 2G–I), and the deformed spermatozoa and free spermatozoa gradually returned to their normal forms (Fig. 2M–O).

In August/September, the chromatin of some primary sperm cells in the seminiferous tubules shrank, and the nuclear membranes disappeared (Fig. 2P). The numbers of free spermatozoa in the lumens of seminiferous tubules were significantly lower in August than in July (Fig. 2J). From September to December, the chromosomes of spermatogonia or primary spermatocytes gradually shrank, and apoptotic bodies with enhanced electron density appeared (Fig. 2D, E). The number of free sperm gradually decreased. Abnormally shaped sperm gradually appeared, including sperm with missing heads, vacuolisation, etc. (Fig. 2J, K).

#### IHC assay of PCNA and Ki67 expression in testicular tissues

Proliferating cell nuclear antigen-positive cells were found mainly in spermatogonia and primary spermatocytes in convoluted tubules. In the testicular tissues collected from June and July, PCNA

showed strong positive staining in the nucleus (Fig. 3A). In the testicular tissues collected from October and November, the expression of PCNA protein was observed in the cytoplasm instead of in the nucleus (Fig. 3B).

The Ki67 protein showed strong positive staining in spermatogonia and primary spermatocytes and weak positive staining in secondary spermatocytes and spermatids. In the testicular tissues collected from June and July, the cells with positive expression of the Ki67 protein were mainly spermatogonia, primary spermatocytes, and a small number of secondary spermatocytes (Fig. 3C). In the testicular tissues collected from October to March, Ki67-positive cells were not observed among any spermatogenic cells in the seminiferous tubules (Fig. 3D).

#### TUNEL assay of the testicular tissue and spermatids of tree shrews

As shown in Figure 4, testis sections were analysed using a TUNEL assay. Apoptosis of spermatogonia and primary spermatocytes was observed in the testicular tissue from January to September and December (Fig. 4A–I, L). The apoptosis rate was highest in July (Fig.

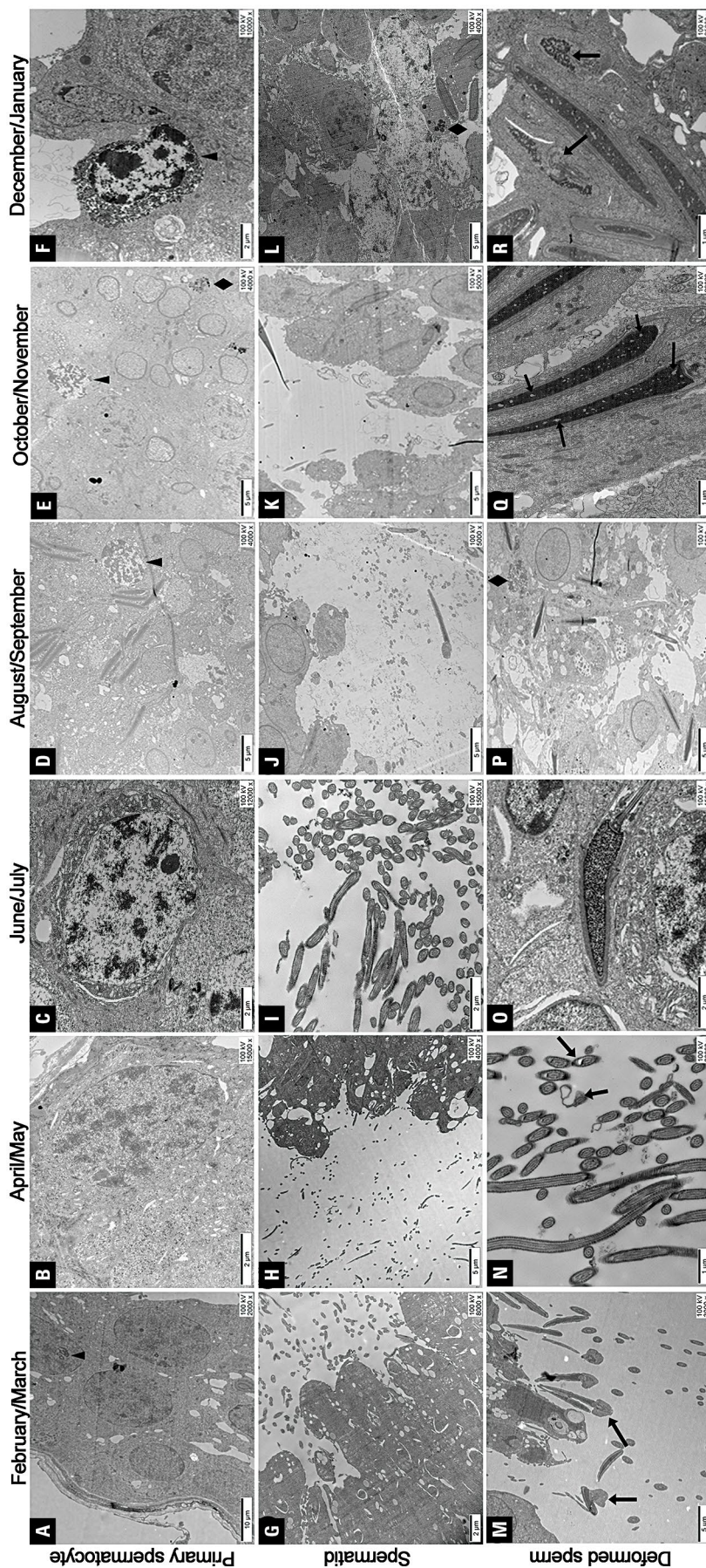


**Figure 2.** Electron micrographs of various germ cell types in the seminiferous tubules of the tree shrew during active spermatogenesis, as well as apoptosis during the regressive period; **A.** Putamen in primary spermatocytes from February/March; **B.** Normal primary spermatocytes from April/May; **C.** Normal primary spermatocytes from June/July; **D.** The chromosomes condense and the nuclear envelope disappears in primary spermatocytes from August/September; **E.** The chromosomes condense and the nuclear envelope disappears in primary spermatocytes from October/November; **F.** Apoptotic primary spermatocytes from December/January. The condensed chromatin in the apoptotic spermatocyte was localized to the periphery or to one side of the nucleus; **G–L.** Free spermatozoa in the lumens of seminiferous tubules; **M–R.** Abnormal morphological features in spermatozoa such as head mass loss, vacuolisation, and crooked tails were also observed in the regressive period; **O.** Normal spermatozoa; arrowhead — abnormal primary spermatocytes; arrow — abnormal spermatozoa; diamond — apoptotic round spermatids.

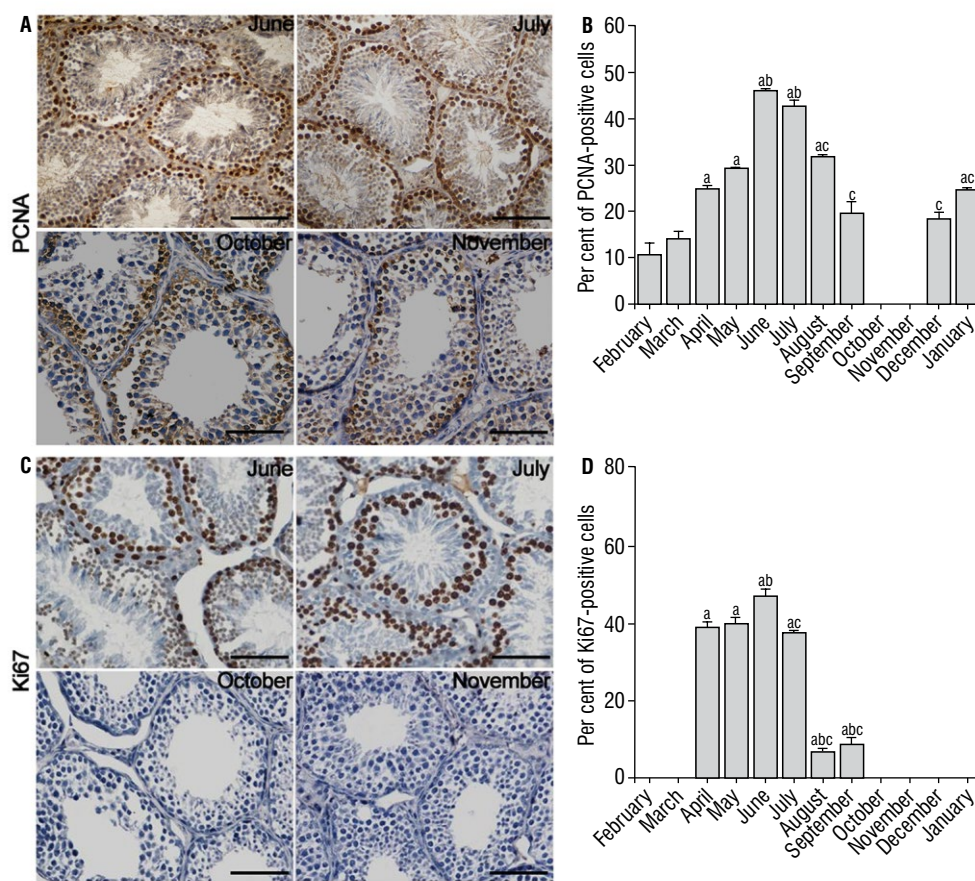


**Figure 3.** Immunostaining of proliferating cell nuclear antigen (PCNA) and Ki67 in the tree shrew testis; **A.** In June and July, in the spermatogenically active seminiferous epithelium, the nucleus of spermatogonia and primary spermatocytes had strong staining of PCNA with constant intensity. In October and November, the cytoplasm of spermatogonia and primary spermatocytes but not the nucleus is PCNA positive-staining; **B.** The rate of PCNA-positive cells of testis during the year (mean  $\pm$  standard deviation); **C.** In June and July, Ki67 expressed in spermatogonia, primary spermatocytes, and spermatids. In October and November, Ki67-positive cells were not detected in any spermatogenic cells in the seminiferous tubules of the tree shrews testis; **D.** The rate of Ki67-positive cells of testis during the year (mean  $\pm$  standard deviation); bar = 100  $\mu$ m; <sup>a</sup> $p < 0.05$  vs. February; <sup>b</sup> $p < 0.05$  vs. April; <sup>c</sup> $p < 0.05$  vs. June.

4M). No apoptotic spermatogenic cells were observed in the testes in October and November (Fig. 4J, K).

## DISCUSSION

To our knowledge, this is the first study showing the seasonal changes that occur in spermatids morphology and ultrastructural parameters in artificial tree shrews. We found seasonal differences in the microstructure of spermatids in domesticated tree shrews that were evident mainly at the late stage of spermatogenesis (i.e. the spermatids deformation stage).

From the perspective of sperm structure, sperm with abnormal morphologies were observed in the seminiferous tubules of domesticated tree shrew testes in months 1–5 and 8–12. Some sperm abnor-

malities can occur in the sperm head, such as head vacuolization and acrosome loss, while others can occur in the neck, body, or tail, such as tail crookedness and tail fracture. Studies have shown that sperm abnormalities often lead to declines in fertilisation potential [2, 18]. Sperm motility and sperm deformity are negatively correlated, and deformities in different parts of sperm have different effects on sperm motility and egg fertilisation ability [6, 20]. No abnormal sperm appeared from June to July. The findings indicate that the period from June to July is the period with the most orderly spermatogenesis in domesticated tree shrews, while the period from October to November is a period of relative stagnation. In wild tree shrews, Cao [4] found that highly active seminiferous epitheliums and typical cell associations in

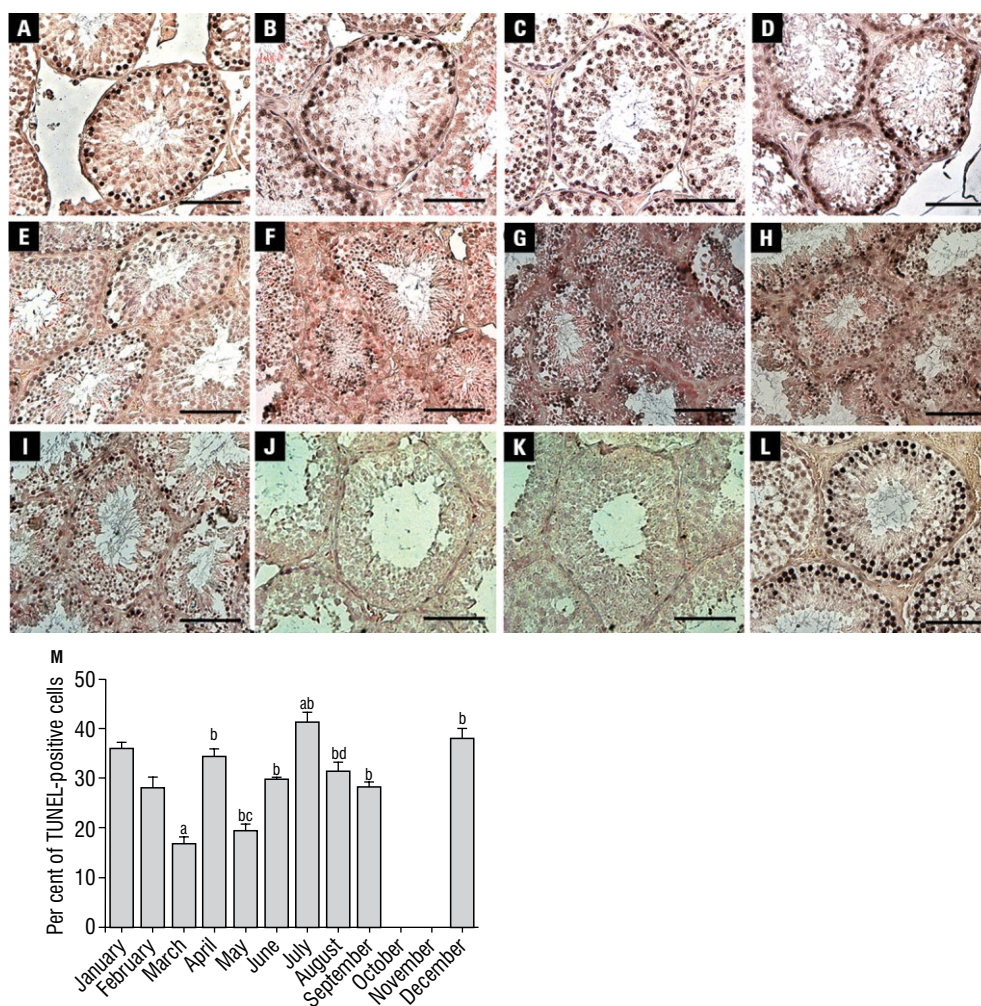


**Figure 4.** Apoptosis determined using terminal deoxynucleotidyl transferase dUTP nick end labelling (TUNEL) staining of seminiferous tubules of tree shrew; **A–L.** TUNEL staining of paraffin-embedded sections of testes from male tree shrew from January to December. Spontaneous apoptosis of germ cells appears in June and July with intensely stained spermatogonia and spermatocyte. No TUNEL-positive germ cells are observed in the testis of tree shrew from October and November; **M.** The rate of TUNEL-positive male germ cells per seminiferous tubule. Values are presented as mean  $\pm$  standard deviation; bar = 100  $\mu$ m; \* $p$  < 0.05 vs. February; <sup>b</sup> $p$  < 0.05 vs. March; <sup>c</sup> $p$  < 0.05 vs. April; <sup>d</sup> $p$  < 0.05 vs. June.

January and April. Regression of seminiferous tubules begins in July, and extensive regressive changes in seminiferous epitheliums losing spermatogenic function in August and October. Similar seasonal changes in spermatozoa amount are shown in epididymis [4]. Our data are slightly different from previous results [4, 16]. HE and TEM showed that the spermatogenesis cycle of domesticated tree shrews start later, with more vigorous spermatogenesis activity from June to July and the lowest in winter. This may be due to differences in living environment and female social stimulation. It is reported that captivity could alter activities of the neuroendocrine system, thereby control the reproduction [7].

We further assessed the protein levels of proliferation markers to determine the activation status

of germ cells. PCNA is expressed only in proliferating cells and its levels peak in the S phase of the cell cycle. Therefore, it is an important indicator for evaluation of cell proliferation [26]. Our IHC results showed that in June and July, PCNA was expressed in the nuclei of spermatogonia and primary spermatocytes in testicular tissue, suggesting that the spermatogenic cells were actively proliferating. The reason may be that the spermatogonia needed to undergo mitosis, as DNA replication occurs in S phase and also before meiosis in primary spermatocytes [28]. Interestingly, cytoplasmic PCNA staining was observed in October and November. Possibly, cytoplasmic PCNA localisation in tree shrew testis could be connected to a role of PCNA in apoptosis. This correlation pattern may be similar to that of humans,

which is important for survival of human neutrophils and HL-60 cells [5, 19]. The Ki67 protein was mainly expressed in spermatogonia, primary spermatocytes and spermatids. Higher expression intensity was observed in spermatogonia and primary spermatocytes than in other types of cells. In the M phase of spermatogonial mitosis, the Ki67 protein functions in organizing and binding DNA and participates in the disappearance and reconstruction of nucleoli [15, 25]. In addition, Ki67 protein was weakly expressed in secondary spermatocytes. We speculate that Ki67 protein expressed in spermatogonia and primary spermatocytes may not be completely degraded by the secondary spermatocyte and spermatid stages such that weak expression is still observed in these stages. From October to March, there is no immunostaining of spermatogenic cells with the Ki67 antibody in the testis. These are in accordance with the fact that the Ki67 protein immediately degrades after mitosis and that cell nuclei are generally Ki67 immunonegative during early G1- and G0-phase of the cell cycle [27].

Spontaneous apoptosis affects germ cell development. Therefore, in seasonally breeding animals, apoptosis may lead to changes in spermatogenesis [11]. In this study, the TUNEL results showed that apoptosis of spermatogonia, primary spermatocytes and small numbers of secondary spermatocytes and round spermatids occurred in the testicular tissue from January to September and December. Additionally, the TEM results showed that shell-shaped nucleoli were occasionally observed in primary spermatocytes in January and February. Since the nucleolus is where ribosomal RNA transcription and transformation take place, the proliferative activity of spermatogenic cells is reduced when the nucleolus becomes shell-shaped [21]. We further used the TUNEL method to examine the numbers, percentages and locations of apoptotic germ cells in seminiferous tubules in testicular sections. During the process of spermatogenesis (except October and November), TUNEL-positive germ cells were observed in seminiferous tubule from each month. Notably, the ratio of TUNEL-positive germ cells to total male germ cells is higher during active periods (July) than during other stages of spermatogenesis. Spermatogenesis is a very unique process involving not only the frequent division, proliferation and developmental differentiation of spermatogenic cells but also the continuous degradation of spermatogenic cells. The degeneration process of spermatogenic cells is mainly achieved through apoptosis [10, 12].

Apoptosis, a programmed cell death pathway, can eliminate damaged cells and cells with chromosomal abnormalities caused by meiotic or mitotic errors during the period when the proliferation rate of germ cells is elevated to ensure a sufficient number and quality of viable spermatogenic cells [1]. In addition, apoptosis may remove cells with PCNA-positive nuclei (such as spermatogonia and primary spermatocytes), thereby controlling the number of germ cells in the testes to respond to seasonal changes [17].

## CONCLUSIONS

In this study, we showed seasonal differences in spermatogenesis in domesticated tree shrews, active in June and July, inactive in October and November. Apoptosis of spermatogonia and primary spermatocytes were observed, but may not contribute to the germ-cell loss; sperm cells restored by cell proliferation in the next reproductive cycle.

## Acknowledgements

The authors thank Associate Professor Jingling Song from the Electron Microscopy Centre of Kunming Medical University for her help in testicular electron microscopy.

## Funding

This study was supported by grants from The Applied Basic Research Foundation of Yunnan Province Science and Technology Department and Kunming Medical University [No. 2018FE001(-187)].

**Conflict of interest:** None declared

## REFERENCES

1. Aitken RJ, Findlay JK, Hutt KJ, et al. Apoptosis in the germ line. *Reproduction*. 2011; 141(2): 139–150, doi: [10.1530/REP-10-0232](https://doi.org/10.1530/REP-10-0232), indexed in Pubmed: [21148286](https://pubmed.ncbi.nlm.nih.gov/21148286/).
2. Ben-Rafael Z, Farhi J, Feldberg D, et al. Folic acid treatment for men with idiopathic oligo-teratoasthenozoospermia before in vitro fertilization: the impact on sperm microstructure and fertilization potential. *Fertil Steril*. 2000; 73(1): 24–30, doi: [10.1016/S0015-0282\(99\)00461-6](https://doi.org/10.1016/S0015-0282(99)00461-6), indexed in Pubmed: [10632407](https://pubmed.ncbi.nlm.nih.gov/10632407/).
3. Blottner S, Hingst O, Meyer HH. Inverse relationship between testicular proliferation and apoptosis in mammalian seasonal breeders. *Theriogenology*. 1995; 44(3): 321–328, doi: [10.1016/0093-691x\(95\)00187-d](https://doi.org/10.1016/0093-691x(95)00187-d), indexed in Pubmed: [16727732](https://pubmed.ncbi.nlm.nih.gov/16727732/).
4. Cao XM. Seasonal changes in spermatogenesis of tree shrew (*Tupaia belangeri* Chinensis). *Zool Res*. 1989; 10(1): 15–21.
5. De Chiara A, Pederzoli-Ribeil M, Burgel PR, et al. Targeting cytosolic proliferating cell nuclear antigen in neutro-

- phil-dominated inflammation. *Front Immunol.* 2012; 3: 311, doi: [10.3389/fimmu.2012.00311](https://doi.org/10.3389/fimmu.2012.00311), indexed in Pubmed: [23181059](https://pubmed.ncbi.nlm.nih.gov/23181059/).
6. Donnelly ET, Lewis SE, McNally JA, et al. In vitro fertilization and pregnancy rates: the influence of sperm motility and morphology on IVF outcome. *Fertil Steril.* 1998; 70(2): 305–314, doi: [10.1016/s0015-0282\(98\)00146-0](https://doi.org/10.1016/s0015-0282(98)00146-0), indexed in Pubmed: [9696226](https://pubmed.ncbi.nlm.nih.gov/9696226/).
  7. DuRant S, Love AC, Belin B, et al. Captivity alters neuroendocrine regulators of stress and reproduction in the hypothalamus in response to acute stress. *Gen Comp Endocrinol.* 2020; 295: 113519, doi: [10.1016/j.ygcen.2020.113519](https://doi.org/10.1016/j.ygcen.2020.113519), indexed in Pubmed: [32470473](https://pubmed.ncbi.nlm.nih.gov/32470473/).
  8. Fan Yu, Huang ZY, Cao CC, et al. Genome of the Chinese tree shrew. *Nat Commun.* 2013; 4: 1426, doi: [10.1038/ncomms2416](https://doi.org/10.1038/ncomms2416), indexed in Pubmed: [23385571](https://pubmed.ncbi.nlm.nih.gov/23385571/).
  9. França LR, Avelar GF, Almeida FFL. Spermatogenesis and sperm transit through the epididymis in mammals with emphasis on pigs. *Theriogenology.* 2005; 63(2): 300–318, doi: [10.1016/j.theriogenology.2004.09.014](https://doi.org/10.1016/j.theriogenology.2004.09.014), indexed in Pubmed: [15626401](https://pubmed.ncbi.nlm.nih.gov/15626401/).
  10. Hsueh AJ, Eisenhauer K, Chun SY, et al. Gonadal cell apoptosis. *Recent Prog Horm Res.* 1996; 51: 433–55; discussion 455, indexed in Pubmed: [8701090](https://pubmed.ncbi.nlm.nih.gov/8701090/).
  11. Ito J, Meguro K, Komatsu K, et al. Seasonal changes in the spermatogenesis of the large Japanese field mice (*Apodemus speciosus*) controlled by proliferation and apoptosis of germ cells. *Anim Reprod Sci.* 2020; 214: 106288, doi: [10.1016/j.anireprosci.2020.106288](https://doi.org/10.1016/j.anireprosci.2020.106288), indexed in Pubmed: [32087913](https://pubmed.ncbi.nlm.nih.gov/32087913/).
  12. Jahnukainen K, Chrysis D, Hou Mi, et al. Increased apoptosis occurring during the first wave of spermatogenesis is stage-specific and primarily affects midpachytene spermatocytes in the rat testis. *Biol Reprod.* 2004; 70(2): 290–296, doi: [10.1095/biolreprod.103.018390](https://doi.org/10.1095/biolreprod.103.018390), indexed in Pubmed: [14522836](https://pubmed.ncbi.nlm.nih.gov/14522836/).
  13. Korgun ET, Celik-Ozenci C, Acar N, et al. Location of cell cycle regulators cyclin B1, cyclin A, PCNA, Ki67 and cell cycle inhibitors p21, p27 and p57 in human first trimester placenta and deciduas. *Histochem Cell Biol.* 2006; 125(6): 615–624, doi: [10.1007/s00418-006-0160-y](https://doi.org/10.1007/s00418-006-0160-y), indexed in Pubmed: [16491347](https://pubmed.ncbi.nlm.nih.gov/16491347/).
  14. Li B, Chen LI, Liu RW, et al. Preliminary discussions about laboratory breeding and management of tupaia belangeri chinensis. *Sci Tech Info.* 2008; 2008(35): 664.
  15. Liberal V, De Miguel MP, Henze M, et al. Reduced spermatogonial proliferation and decreased fertility in mice overexpressing cyclin E in spermatogonia. *Cell Cycle.* 2010; 9(20): 4222–4227, doi: [10.4161/cc.9.20.13544](https://doi.org/10.4161/cc.9.20.13544), indexed in Pubmed: [20962587](https://pubmed.ncbi.nlm.nih.gov/20962587/).
  16. Maeda S, Endo H, Kimura J, et al. Classification of the cycle of the seminiferous epithelium in the common tree shrew (*Tupaia glis*). *J Vet Med Sci.* 1996; 58(5): 481–484, doi: [10.1292/jvms.58.481](https://doi.org/10.1292/jvms.58.481), indexed in Pubmed: [8741615](https://pubmed.ncbi.nlm.nih.gov/8741615/).
  17. Müller R, Misund K, Holien T, et al. Targeting proliferating cell nuclear antigen and its protein interactions induces apoptosis in multiple myeloma cells. *PLoS One.* 2013; 8(7): e70430, doi: [10.1371/journal.pone.0070430](https://doi.org/10.1371/journal.pone.0070430), indexed in Pubmed: [23936203](https://pubmed.ncbi.nlm.nih.gov/23936203/).
  18. Nikolettos N, K pker W, Demirel C, et al. Fertilization potential of spermatozoa with abnormal morphology. *Hum Reprod.* 1999; 14 Suppl 1: 47–70, doi: [10.1093/humrep/14.suppl\\_1.47](https://doi.org/10.1093/humrep/14.suppl_1.47), indexed in Pubmed: [10573024](https://pubmed.ncbi.nlm.nih.gov/10573024/).
  19. Ohayon D, De Chiara A, Chapuis N, et al. Cytoplasmic proliferating cell nuclear antigen connects glycolysis and cell survival in acute myeloid leukemia. *Sci Rep.* 2016; 6: 35561, doi: [10.1038/srep35561](https://doi.org/10.1038/srep35561), indexed in Pubmed: [27759041](https://pubmed.ncbi.nlm.nih.gov/27759041/).
  20. Pereira R, S  R, Barros A, et al. Major regulatory mechanisms involved in sperm motility. *Asian J Androl.* 2017; 19(1): 5–14, doi: [10.4103/1008-682X.167716](https://doi.org/10.4103/1008-682X.167716), indexed in Pubmed: [26680031](https://pubmed.ncbi.nlm.nih.gov/26680031/).
  21. Romano FJ, Rossetti S, Conteduca V, et al. Role of DNA repair machinery and p53 in the testicular germ cell cancer: a review. *Oncotarget.* 2016; 7(51): 85641–85649, doi: [10.18632/oncotarget.13063](https://doi.org/10.18632/oncotarget.13063), indexed in Pubmed: [27821802](https://pubmed.ncbi.nlm.nih.gov/27821802/).
  22. Sanada T, Tsukiyama-Kohara K, Shin-I T, et al. Construction of complete *Tupaia belangeri* transcriptome database by whole-genome and comprehensive RNA sequencing. *Sci Rep.* 2019; 9(1): 12372, doi: [10.1038/s41598-019-48867-x](https://doi.org/10.1038/s41598-019-48867-x), indexed in Pubmed: [31451757](https://pubmed.ncbi.nlm.nih.gov/31451757/).
  23. Scholzen T, Gerdes J. The Ki-67 protein: from the known and the unknown. *J Cell Physiol.* 2000; 182(3): 311–322, doi: [10.1002/\(SICI\)1097-4652\(200003\)182:3<311::AID-JCP1>3.0.CO;2-9](https://doi.org/10.1002/(SICI)1097-4652(200003)182:3<311::AID-JCP1>3.0.CO;2-9), indexed in Pubmed: [10653597](https://pubmed.ncbi.nlm.nih.gov/10653597/).
  24. Shen P-Q, Zheng H, Liu RW. Progress and prospect in research on laboratory tree shrew in China. *Dongwuxue Yanjiu.* 2011; 32(1): 109–114, doi: [10.3724/SP.J.1141.2011.01109](https://doi.org/10.3724/SP.J.1141.2011.01109), indexed in Pubmed: [21341393](https://pubmed.ncbi.nlm.nih.gov/21341393/).
  25. Steger K, Aleithe I, Behre H, et al. The proliferation of spermatogonia in normal and pathological human seminiferous epithelium: an immunohistochemical study using monoclonal antibodies against Ki-67 protein and proliferating cell nuclear antigen. *Mol Hum Reprod.* 1998; 4(3): 227–233, doi: [10.1093/molehr/4.3.227](https://doi.org/10.1093/molehr/4.3.227), indexed in Pubmed: [9570268](https://pubmed.ncbi.nlm.nih.gov/9570268/).
  26. Strzalka W, Ziemienowicz A. Proliferating cell nuclear antigen (PCNA): a key factor in DNA replication and cell cycle regulation. *Ann Bot.* 2011; 107(7): 1127–1140, doi: [10.1093/aob/mcq243](https://doi.org/10.1093/aob/mcq243), indexed in Pubmed: [21169293](https://pubmed.ncbi.nlm.nih.gov/21169293/).
  27. Sun X, Kaufman PD. Ki-67: more than a proliferation marker. *Chromosoma.* 2018; 127(2): 175–186, doi: [10.1007/s00412-018-0659-8](https://doi.org/10.1007/s00412-018-0659-8), indexed in Pubmed: [29322240](https://pubmed.ncbi.nlm.nih.gov/29322240/).
  28. White-Cooper H, Doggett K, Ellis R. The evolution of spermatogenesis. *Sperm Biology.* 2009: 151–183, doi: [10.1016/b978-0-12-372568-4.00004-5](https://doi.org/10.1016/b978-0-12-372568-4.00004-5).
  29. Xiao-mei C. Seasonal changes in spermatogenesis of tree shrew (*Tupaia belangeri* Chinensis). *Zool Res.* 1989; 10(1): 15–21.
  30. Yao YG. Creating animal models, why not use the Chinese tree shrew (*Tupaia belangeri* chinensis)? *Zool Res.* 2017; 38(3): 118.
  31. Zhao WP, Wang HW, Liu J, et al. Positive PCNA and Ki-67 expression in the testis correlates with spermatogenesis dysfunction in fluoride-treated rats. *Biol Trace Elem Res.* 2018; 186(2): 489–497, doi: [10.1007/s12011-018-1338-6](https://doi.org/10.1007/s12011-018-1338-6), indexed in Pubmed: [29748930](https://pubmed.ncbi.nlm.nih.gov/29748930/).
  32. Zhong S, Zhang Sy, Xing Hj, et al. Revealing histological and morphological features of female reproductive system in tree shrew (*Tupaia belangeri*). *Zoomorphology.* 2017; 137(1): 191–199, doi: [10.1007/s00435-017-0374-7](https://doi.org/10.1007/s00435-017-0374-7).

# Comparing effects of L-carnitine and sildenafil citrate on histopathologic recovery from sciatic nerve crush injury in female albino rats

O.I. Zedan<sup>1</sup>, M.A. Bashandy<sup>1</sup>

Anatomy and Embryology Department, Faculty of Medicine, Menoufia University, Egypt

[Received: 24 February 2021; Accepted: 12 March 2021; Early publication date: 9 April 2021]

**Background:** The sciatic nerve is a peripheral nerve and is more vulnerable to compression with subsequent short- or long-term neuronal dysfunction. The current study was designed to elucidate the possible ameliorative effect of L-carnitine and sildenafil (SIL) on sciatic nerve crush injury. We sought to determine the effects of L-carnitine, a neuroprotective and a neuro-modulatory agent, and SIL citrate, a selective peripheral phosphodiesterases inhibitor, on modulating neuro-degenerative changes due to sciatic nerve compression.

**Materials and methods:** The comparative effect of L-carnitine (at an oral dose of 20 mg/kg/day) or SIL citrate (20 mg/kg/day orally) administration for 21 days was studied in a rat model of sciatic nerve compression. Sciatic nerve sections were subjected to biochemical, histological, ultrastructure, and immunohistochemical studies to observe the effects of these treatments on neurofilament protein.

**Results:** The sciatic nerve crush injury group (group II) showed a significant decrease in tissue catalase (CAT), superoxide dismutase (SOD) and increase in malondialdehyde (MDA) as compared to control group ( $p < 0.01$ ). Histological changes in the form of degenerated and vacuolated axoplasm with areas of nerve fibre loss and pyknotic nuclei were reported. The blood vessels were dilated, congested with areas of haemorrhage and mononuclear cell infiltration. Histo-morphometrically, a statistically significant reduction in the nerve fibres' number, mean axon cross-sectional area, myelin sheath thickness and a significant increase in collagen fibres' percentage ( $p < 0.05$ ) as compared to control group. Immunohistochemically, neurofilament protein was significantly downregulated as proved by a significant reduction in mean area per cent of neurofilament expression. L-carnitine ameliorated the studied parameters through its neuroprotective effect while SIL, a selective peripheral phosphodiesterases (PDE-5) inhibitor, improved crush injury parameters but with less extent than L-carnitine.

**Conclusions:** These findings indicate the valuable effects of L-carnitine administration compared to that of SIL citrate in alleviating the serious debilitating effects of sciatic nerve crush injury. Our results provide a new insight into the scope of neuroprotective and neuro-regenerative effects of L-carnitine in a sciatic nerve compression model. (Folia Morphol 2022; 81, 2: 421–434)

**Key words:** sciatic nerve, compression, L-carnitine, sildenafil citrate, histopathology, oxidative stress, immunohistochemistry

Address for correspondence: Dr. M.A. Bashandy, Anatomy and Embryology Department, Faculty of Medicine, Menoufia University, Shebin El-Kom, Egypt, e-mail: mannar.bashandi@med.menofia.edu.eg; a\_z491@yahoo.com

This article is available in open access under Creative Common Attribution-Non-Commercial-No Derivatives 4.0 International (CC BY-NC-ND 4.0) license, allowing to download articles and share them with others as long as they credit the authors and the publisher, but without permission to change them in any way or use them commercially.

## INTRODUCTION

It is vital for the characteristic morphology of the peripheral nerve bundle to remain intact for normal autonomic, motor, and sensory nerve functions. Peripheral nerves injury results in transient or long-term neuronal dysfunction, often leading to subsequent social and economic disability [37].

The various types of nerve injuries include compression (crush), stretch, and laceration [10]. Acute traumatic peripheral nerve injury induces tissue lesions at the damaged site, such as axonal degeneration, demyelination, multifocal loss of nerve fibres, oedema in the endoneurium as well as enhanced vascular permeability with axoplasmic flow block [8, 55]. Persistent nerve crushing can affect microcirculation which play main role in nerve regeneration, oxygen supply and maintain neural conduction [23]. Release of nerve compression (reperfusion) leads to release of nerve tissue pressure and subsequent redeposition of nutrients and oxygen in high pressure and enhances free radicals formation leading to lipid peroxidation and tissue damage [54, 71].

The chances of sensory function returning are still very poor even with expert surgical repair, and this may have subsequent adverse effects on motor function, particularly fine motor skills [34]. If medical treatment is not available, death can occur in the injured nerve cell, resulting in functional loss [47]. Various agents have been tested via experimental trials in an attempt to prevent this loss of motor function [13, 20].

Carnitine is an amine with vitamin-like characteristics and a non-amino acid structure [6]. There are two forms of carnitine: L-carnitine and its analogues. These have a protective effect against tissue ischaemia and subsequent reperfusion damage [55]. It is responsible for the transportation of fatty acids from the cytoplasm to the mitochondria, allowing adenosine triphosphate production via oxidative phosphorylation process [36]. It may also play a role in acetylcholine synthesis and release. Acetyl L-carnitine also plays a role in neuron repair and balances nerve growth factor expression in the central nervous system [63].

Researches have evaluated the neuroprotective effect of acetyl-L-carnitine in patients suffering from neuropathic pain, nerve function loss, and damaged sciatic nerve. Furthermore, marked improvement and symptom relief has been reported in these patients [14, 32, 55].

Pettegrew et al. [51] studied the neuromodulatory and neuroprotective effects of carnitine on

Alzheimer's disease, revealing its beneficial effects on cognitive function and neurodegeneration in these patients. L-carnitine has also been shown to possess analgesic [22] and antidepressant properties [11]. Moreover, L-carnitine has been reported to play a key role in treating diabetes-induced retinopathy and neuropathy as shown by a decrease in the level of L-carnitine in the sciatic nerve. Additionally, it exerts antiinflammatory activity by decreasing interleukin (IL)-6, IL-1 $\beta$ , and tumour necrosis factor alpha (TNF- $\alpha$ ) levels [69] and antifibrotic activity [46].

Sildenafil (SIL) is a selective peripheral phosphodiesterases (PDE-5) inhibitor and has been shown to have a therapeutic effect in improving erectile dysfunction by increasing the level of intracellular cGMP [25, 50]. Moreover, SIL also has a beneficial effect on several diseases [64] such as having peripheral antinociceptive properties, resulting in the accumulation of intracellular cGMP [30]. Additionally, it exacerbates the antinociceptive character of different analgesics such as morphine, celecoxib, and indomethacin via the nitric oxide-cyclic guanosine monophosphate (NO-cGMP) pathway [17, 44]. According to the American Heart Association [5], SIL increases the level of brain neurotransmitters that enhances stroke recovery. Furthermore, it can improve the neurological effects of brain neurotransmitters when administered to rats within 2–24 hours of stroke.

The present study was designed to elucidate the possible ameliorative effect of L-carnitine and SIL on sciatic nerve crush injury. To observe these effects, we conducted histological, ultrastructure, morphometric, and quantitative immunohistochemical studies in rats administered these agents.

## MATERIALS AND METHODS

### Animals

In this study, 65 adult female albino rats were obtained from the Menoufia University animal house located in the Faculty of Medicine. Each rat weighed approximately 200–220 g. The rats were housed in metal cages under suitable laboratory conditions (12 h light/dark cycle, with lights on from 07:00 to 19:00). The environment was maintained a temperature of  $22 \pm 2^\circ\text{C}$  during the experimental period. The rats had access to tap water and standard food *ad libitum*. The study was conducted in accordance with all international guidelines for animal care. All experimental protocols and animal care were approved by the Experimental Animal Ethics Committee, Menoufia

University, Shibin Elkom, Egypt. This experiment was prepared and designed according to guidelines approved by the Menoufia University Ethical Committee.

### Experimental design

The female rats were divided into four groups.

- **group I:** was designated as the control group, and was subdivided into four groups (n = 5 rats/group):
  - **subgroup IA,** in which rats did not receive any experimental treatment through the study duration;
  - **subgroup IB** (sham operation subgroup), in which the sciatic nerves were exposed on the right hindlimb of each rat without crushing;
  - **subgroup IC** (L-carnitine subgroup), in which rats were orally administered with L-carnitine (100 mg/kg/day) which was dissolved in distilled water for 21 days [6];
  - **subgroup ID** (SIL citrate subgroup), in this group rats were orally administered SIL citrate (20 mg/kg/day) which was dissolved in normal saline for 21 days [39];
- **group II** (sciatic nerve crush injury group): animals were subjected to sciatic nerve crush injury (n = 15);
- **group III** (L-carnitine-treated sciatic nerve crush injury group) animals were orally administered with L-carnitine at the same dosage and schedule as subgroup IC, and were subjected to sciatic nerve crush injury (n = 15);
- **group IV** (SIL citrate-treated sciatic nerve crush injury group) animals were administered with SIL citrate at the same dosage and schedule as subgroup ID, and were subjected to sciatic nerve crush injury (n = 15).

The duration of the experiment was 21 days. Twenty-four hours after the final dosages were administered, rats were anaesthetised with an overdose of phenobarbital via inhalation (200 mg/kg) then sacrificed by rapid cervical dislocation. The proximal segments of the sciatic nerve of the right hindlimb were obtained from each animal using scissors.

### Drugs and chemicals

**L-carnitine.** L-carnitine base (350 mg) was obtained in tablet form from MEPACO–MEDIFOOD (Arab Company of Pharmaceuticals and Medicinal Plants, Sharkeya, Egypt). Each tablet was dissolved in distilled water to obtain the required dose, and was used immediately subsequent to dilution.

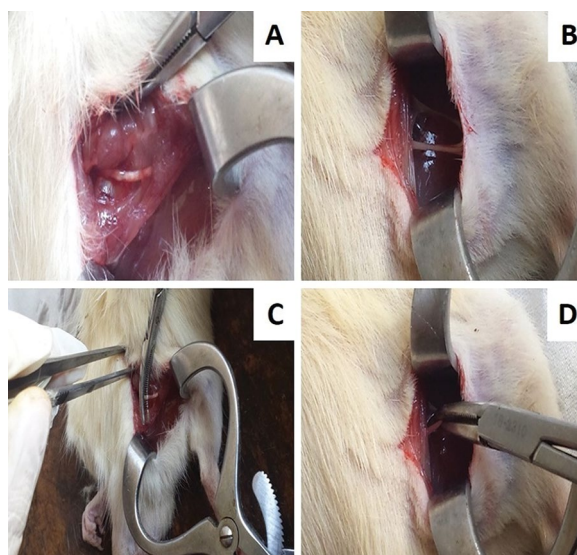


**Figure 1.** Exposure and compression of the sciatic nerve; **A, B.** Sciatic nerve exposure; **C, D.** Sciatic nerve compression.

**Sildenafil citrate.** SIL citrate (VIAGRA) was obtained in tablet form, and each tablet contained 50 mg of the active ingredient (Pharmaco-Vigilance Centre, Pfizer Pharmaceutical Company, Dokki, Egypt). The estimated dose was suspended in normal saline.

### Surgical procedure

Rats were anaesthetised before surgery via intraperitoneal injection of ketamine (100 mg/kg body weight) (Pfizer, New York, USA) and 10 mg/kg xylazine (Xyla-Ject, ADWIA Pharmaceuticals Co, El Obour City, Egypt) [53, 74].

Nerve crushing was performed on the right hind limb. The area of incision was shaved, and skin was sterilised with 10% povidone iodine. A 2-cm incision was then performed along the proximal half of the line between the greater trochanter and the knee joint. To expose the sciatic nerve, a splitting incision was made in the gluteal muscle. The vastus lateralis and biceps femoris muscle were then separated using artery forceps [53].

Nerve crush was performed by applying sustained pressure for 15 s to the exposed sciatic nerve with artery forceps, at an area 1 cm proximal to the sciatic nerve division into the tibial and common peroneal nerves. To confirm complete nerve crush injury with intact epineurium, a microprobe was used to elevate the nerve slightly and confirm the appearance of a clear area within the nerve, as shown in Figure 1. Finally, the skin incision was sutured, and rats were kept warm by placing them on a heating pad [53]. Each rat

received (10 mg/kg) kataflam (Novartis Pharmaceuticals Corporation, East Hanover, New Jersey, USA) via intramuscular injection for pain relief and (10 mg/kg) flumox (Egyptian Int. Pharmaceutical industries CO EIPICo, 10<sup>th</sup> Ramadan City, Egypt) via intramuscular injection to prevent secondary bacterial infection. The local antibiotic Biovitracin spray (Egyptian Company for Advanced Pharmaceuticals, Giza, Egypt) was also applied once daily in spray form (two puffs) to treat local infection. All medications were used for 5 days to facilitate healing. The right hind limb was obtained after animal scarifications and divided into two samples. The first was subjected to histological study and the second was kept in an Eppendorf tube and stored at  $-80^{\circ}\text{C}$  until the day of the experiment for biochemical study.

#### Evaluation methods

**Biochemical study.** The frozen sciatic nerve specimens were homogenized in cold 0.9% NaCl using glass homogenizer. The homogenates were centrifuged to obtain the supernatant fraction for catalase (CAT), superoxide dismutase (SOD) and malondialdehyde (MDA) determination [70]. Sciatic nerve tissue MDA levels were estimated using Mihara and Uchiyama [43] method based on estimating colour absorbance of complex result from MDA and thiobarbituric acid mixing in an acidic environment at 532 nm using turnable microplate reader (Molecular Devices, LLC, Sunnyvale, CA, USA). MDA values were expressed as nmol/g wet sciatic tissue.

Catalase levels in sciatic nerve tissue (CAT) were measured using Goth's [26] method which depend on measuring the absorbance of yellow coloured complex developed from ammonium molybdate and hydrogen peroxide at 405 nm. Tissue CAT result was expresses as U/mg protein. Tissue superoxide dismutase (SOD) was evaluated using Sun et al.'s [60] method. It depends on nitroblue tetrazolium reduction by  $\text{O}_2$  and measuring the absorbance of the resulting purple formazan molecule at 560 nm using turnable microplate reader (VERSA max). The final SOD activity was obtained by dividing SOD activity on total protein level and expressed as U/mg protein.

**Histology.** Sciatic nerve specimens were fixed in 10% formal saline for 24 h and then processed for paraffinization. The paraffin blocks were cut into slices (of 5  $\mu\text{m}$  thickness), and haematoxylin and eosin (H&E) staining was conducted to determine the general architecture of the sciatic nerve [59].

**Histochemistry.** Paraffin slices were stained with Masson trichrome (MT) stain to visualise collagen fibres [9].

**Immunohistochemistry.** The avidin-biotin-peroxidase method was used for immunohistochemical study of neurofilament protein expression. Paraffin-embedded tissue sections were placed on poly-L-lysine coated glass slides, followed by deparaffinization and rehydration in ethyl alcohol. To block endogenous peroxidase activity, the slides were incubated with 3% hydrogen peroxide in a humidity chamber for 10–15 min, then washed three times with phosphate buffered saline (PBS) for 10 min. Sciatic nerve sections were incubated with primary antibody (polyclonal rabbit anti-neurofilament-200, N4142, Sigma-Aldrich) for 1 h at  $4^{\circ}\text{C}$ . Primary antibody was diluted at 1:80 in PBS and kept in a humidity chamber. Sections were first incubated with secondary antibody (1:200, ab97055; Abcam, Cambridge, MA, USA) in PBS for 30 min at  $37^{\circ}\text{C}$  after washing 3 times. Then, section were incubated with the avidin-biotin-peroxidase complex (Universal Elite ABC kit PK-6200; Vectastain, Burlingame, CA, USA) for 30 min followed by rinsing with PBS. Sections were then stained with Vexation diaminobenzidine (DAB) (Kit HK153–5K; Biogenex, San Ramon, CA, USA) for 10 min to visualise the areas of antibody immunostaining. Finally, the sections were washed with tap water. The sections were counterstained with haematoxylin, dehydrated, cleared, and covered with glass mounted with Canada balsam (C1795, Sigma-Aldrich). The primary antibody was replaced by PBS and served as a negative control. Rat cerebral cortex was used as a positive control. Positive expression of neurofilament protein in the cytoplasm of the nerve fibres was indicated by a brown colour.

**Transmission electron microscopy (TEM).** Sciatic nerve was cut into small pieces (1  $\text{mm}^3$ ) and kept in 2.5% gluteraldehyde for 24 h for fixation. Using an ultra-microtome 0.5–1  $\mu\text{m}$ -slices were obtained as semithin sections and subjected to toluidine blue staining for analysis via light microscopy. The blocks were trimmed, and some areas were selected for ultrathin sections preparations. The blocks were encapsulated in a copper grid. Uranyl acetate and lead citrate stains were used for ultrathin sections staining, followed by examination using a TEM (Seo-Russia) in the Alexandria Medical Research Institute [9].

### Quantitative assessment

Image J software (version K.1.45) was used for measuring the following parameters:

- the number of myelinated axons (nerve fibre number);
- axon cross-sectional area;
- myelin sheath thickness in apparently non-degenerated nerve fibres;
- the percentage of collagen fibres;
- mean percentage of the area of positive neurofilament protein expression.

The quantitative measurements were performed by using a Leica DML B2/11888111 microscope contained Leica DFC450 camera and were evaluated and measured. For each of the chosen groups, five slides were selected from each specimen. Ten non-overlapping fields were picked up for measurement at a 40× magnification.

### Ethical approval

All relevant institutional, national, and international guidelines related to animal use and care was followed. All methods and strategies were managed according to the guidelines approved by the Animal Research Ethics Committee, Menoufia University, Faculty of Medicine.

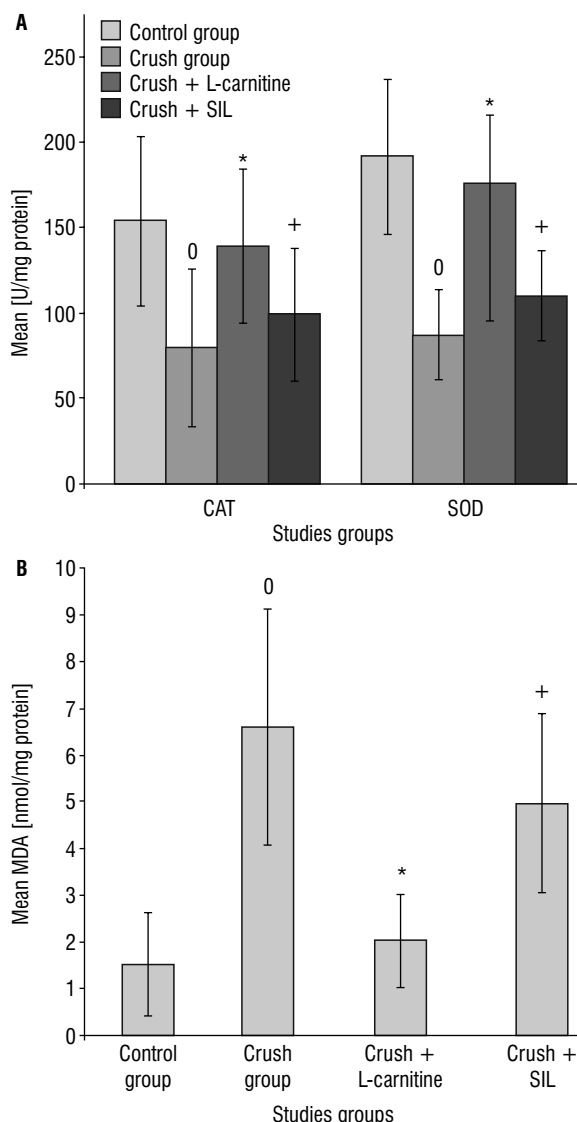
### Statistical analysis

Image analysis data were obtained, and their means  $\pm$  standard deviation (SD) were calculated and statistically analysed. The different groups were compared using various parameters using one-way analysis of variance (ANOVA) and then post-hoc Bonferroni test to determine statistical significance. Data were considered statistically significant and highly significant at  $p < 0.05$  and  $0.001$ , respectively. The results were listed in tables and plotted graphically.

## RESULTS

### Histochemical results

Oxidative enzymes' results in all studied groups are represented in Figure 2A, B. Compared with control group (group I), tissue CAT and SOD activities were significantly decreased ( $79.31 \pm 46$  vs.  $154.18 \pm 50$  U/mg protein and  $86.82 \pm 26.31$  vs.  $191.4 \pm 45$  U/mg protein, respectively) while MDA was significantly increased ( $6.61 \pm 2.51$  vs.  $1.53 \pm 1.1$  nmol/mg protein) in crush group (group II) ( $p < 0.05$ ) as compared to group I. After L-carnitine treatment, tissue CAT and SOD activities were significantly elevated ( $139.25 \pm 45$  vs.  $79.31 \pm 46$



**Figure 2. A.** A histogram revealing a significant decrease in catalase (CAT) and superoxide dismutase (SOD) level in group II as compared to control group ( $0p < 0.05$ ) and were significantly elevated in group III as compared to group II ( $*p < 0.05$ ); **B.** A histogram revealing a significant increase in the malondialdehyde (MDA) level in group II as compared to control group ( $0p < 0.05$ ) and declined significantly in group III as compared to group II ( $*p < 0.05$ ); SIL — sildenafil (+ $p < 0.05$ ).

and  $175.32 \pm 41$  vs.  $86.82 \pm 26.31$  U/mg protein, respectively) and MDA level declined significantly ( $2.06 \pm 0.98$  vs.  $6.61 \pm 2.51$  nmol/mg protein) as compared to group II ( $p < 0.05$ ). However, administering SIL also increased CAT and SOD activities ( $99.54 \pm 39$  vs.  $79.31 \pm 46$  and  $109.62 \pm 27$  vs.  $86.82 \pm 26.31$  U/mg protein, respectively) and decreased MDA activity ( $4.95 \pm 1.92$  vs.  $6.61 \pm 2.51$  nmol/mg protein) as compared to group II ( $*p < 0.05$ ); SIL — sildenafil (+ $p < 0.05$ ).

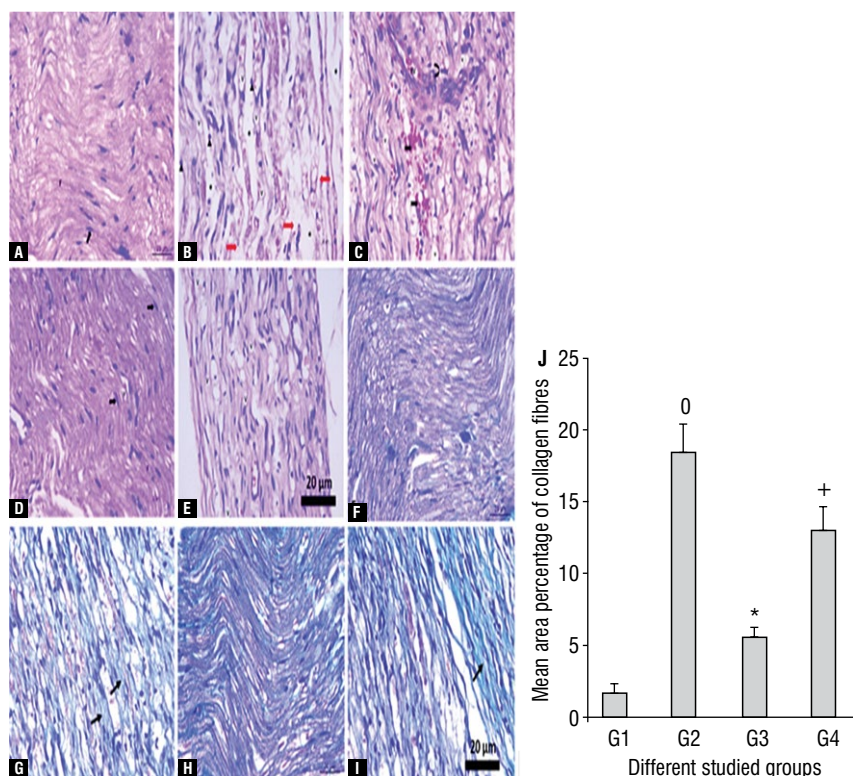


**Figure 3.** Representative photomicrographs of longitudinal rat sciatic nerve sections from each of the experimental groups; **A.** Control group I showing myelinated nerve fibres (F), with Schwann cell nuclei (arrow) between the fibres; **B.** Group II showing discontinuity of most nerve fibres (red arrow), with vacuolated axoplasm (V), some pyknotic nuclei (arrow head), and areas of nerve fibre loss (\*); **C.** Group II showing nerve fibres with widespread vacuolations (V), mononuclear cell infiltration (curved arrow), and dilated congested blood vessels (BV) with areas of haemorrhage (notched arrow); **D.** Group III showing regeneration of most of the nerve fibres (F). Some vacuolation (V) can be seen in the fibres with Schwann cell nuclei (arrow); **E.** Group IV showing widespread vacuolations (V) (haematoxylin and eosin staining, scale bar 20  $\mu$ m, 40 $\times$  magnification); **F.** Control group I showing minimal collagen fibres between the nerve axon. A marked increase in collagen fibres was observed in group II (**G**), a mild increase was observed in group III (**H**) and a moderate increase was observed in group IV (**I**) (Masson's trichrome staining, scale bar 20  $\mu$ m, 40 $\times$  magnification); **J.** Histogram demonstrating a significant increase in the percentage of collagen fibres in both groups II and IV when compared with that in control group I (0, + $p$  < 0.05). The percentage of collagen fibres was significantly reduced in group III compared with that in group II (\* $p$  < 0.05), and significantly decreased in group III compared to group IV (\* $p$  < 0.05).

### Histological results

H&E-stained longitudinal sections of the different studied groups were examined using light microscopy. In the control group (group I), the nerve fibres were parallel, and were packed together with Schwann cell nuclei between the nerve fibres (Fig. 3A). Sections from the sciatic nerve crush injury group (group II) showed various histological changes, including degenerated and vacuolated axoplasm with areas of nerve fibre loss with pyknotic nuclei. The other sections showed dilated and congested blood vessels with areas of haemorrhage and mononuclear cell infiltration (Fig. 3B, C).

Additionally, in the sections from the L-carnitine-treated sciatic nerve crush injury group (group III), regeneration and some vacuolation was observed in most nerve fibres, with Schwann cell nuclei observed between them (Fig. 3D). Moreover, in the SIL citrate-treat-

ed sciatic nerve crush injury group (group IV), most nerve fibres showed widespread vacuolation (Fig. 3E).

The longitudinal sciatic nerve sections from group I control rats showed minimal collagen fibres between nerve axons after MT staining (Fig. 3F). A marked increase in collagen fibres was observed in sections from group II compared to the group I control sections (Figs. 3G). A mild increase in collagen fibres was observed in group III (Fig. 3H), while a moderate increase in collagen was observed in group IV (Fig. 3I). A statistically significant increase in the percentage of collagen fibres ( $p$  < 0.05) was observed in both group II and group IV ( $18.33 \pm 2.51$  and  $13.0 \pm 1.65$ , respectively) compared with that in group I ( $1.67 \pm 0.58$ ). However, the percentage of collagen fibres significantly decreased in group III when compared with that in group IV ( $5.50 \pm 0.71$  vs.  $13.0 \pm 1.65$ ,  $p$  < 0.05).

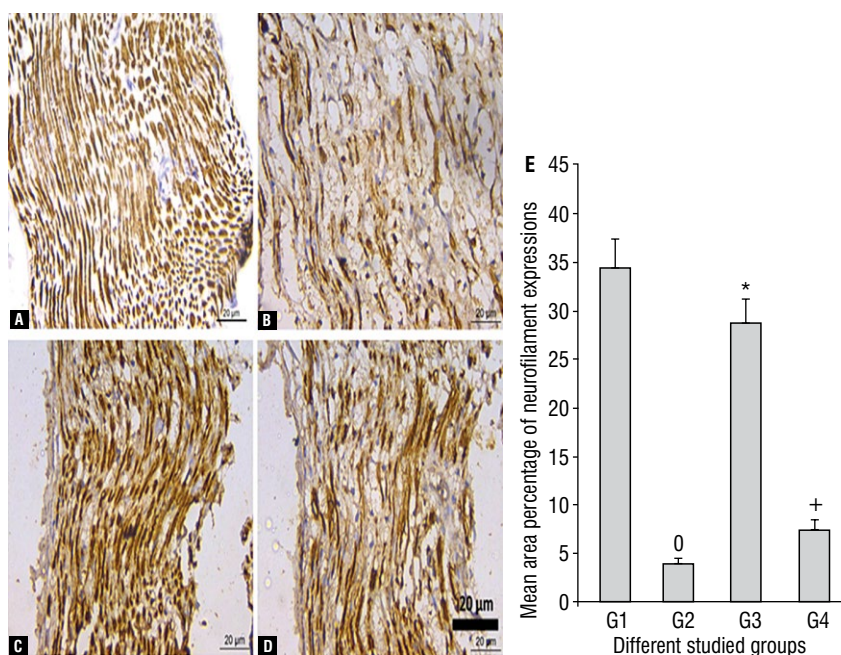


**Figure 4.** Representative neurofilament immunostaining in rat sciatic nerve sections from the different experimental groups. Immunostaining revealed that neurofilament protein expression was significantly downregulated in groups II and IV compared with the adult control group I ( $0, +p < 0.05$ ) (A, B, D, E), and also in group IV compared with group II ( $+p < 0.05$ ) (B, D, E). In contrast, a significant upregulation was observed in group III compared with that in group II ( $*p < 0.05$ ) (B, C, E) (scale bar 20  $\mu\text{m}$ , 40 $\times$  magnification).

Furthermore, the percentage of collagen fibres in group III was reduced compared with that in group II ( $5.50 \pm 0.71$  vs.  $18.33 \pm 2.51$ ,  $p < 0.05$ ) (Fig. 3J).

#### Immunohistochemical results

Immunohistochemical staining of the longitudinal sciatic nerve sections revealed that neurofilament protein was significantly downregulated in groups II and IV ( $3.80 \pm 0.52$  and  $7.40 \pm 0.89$ , respectively) compared with its expression in group I ( $34.40 \pm 3.1$ ) ( $p < 0.05$ ). Moreover, neurofilament protein was significantly downregulated in group IV compared with that in group II ( $p < 0.05$ ). In contrast, neurofilament protein was significantly upregulated in group III compared with its expression in group II ( $28.60 \pm 2.64$  vs.  $3.80 \pm 0.52$ ,  $p < 0.05$ ) (Fig. 4A–E).

#### Results of toluidine blue staining of semithin sections

Control group semithin sections stained with toluidine blue demonstrated that part of the nerve bundles were surrounded by perineurium. The myelinated nerve fibres had regular oval or rounded myelin sheaths, and were stained dark blue around the light blue-stained axons. The blood vessels could also be observed (Fig. 5A). Group II showed degenerative

changes in the myelin coat, with disintegrated myelin fragments completely covering normal fibre sections areas or compressing the axons. Few nerve fibres with thin myelin could be seen (Fig. 5B). Group III showed restoration of the normal appearance of myelin sheaths compared with the control group (Fig. 5C). Group IV had many myelinated nerve fibres with an irregular myelin sheath, with myelin in-folding and out-folding and degenerated axons (Fig. 5D).

There was a statistically significant reduction in the number of nerve fibres ( $p < 0.05$ ) in both groups II and IV ( $2.00 \pm 0.11$  and  $4.41 \pm 0.89$ , respectively) when compared with that in the control group ( $28.24 \pm 4.44$ ). However, the number of nerve fibres increased in group III compared with that in group II ( $24.29 \pm 1.89$  vs.  $2.00 \pm 0.11$ ,  $p < 0.05$ ). Moreover, the number of nerve fibres increased in group III when compared with that in group IV ( $24.29 \pm 1.89$  vs.  $4.41 \pm 0.89$ ,  $p < 0.05$ ) (Fig. 5E).

There was a statistically significant decrease in the mean axon cross-sectional area in groups II and IV ( $8.68 \pm 1.75$  vs.  $14.11 \pm 2.89 \mu\text{m}^2$ , respectively) compared with that in the control group ( $40.95 \pm 2.87 \mu\text{m}^2$ ,  $p < 0.05$ ). However, a significant reduction was observed in the mean axon cross-sectional area in group IV compared with that in group III

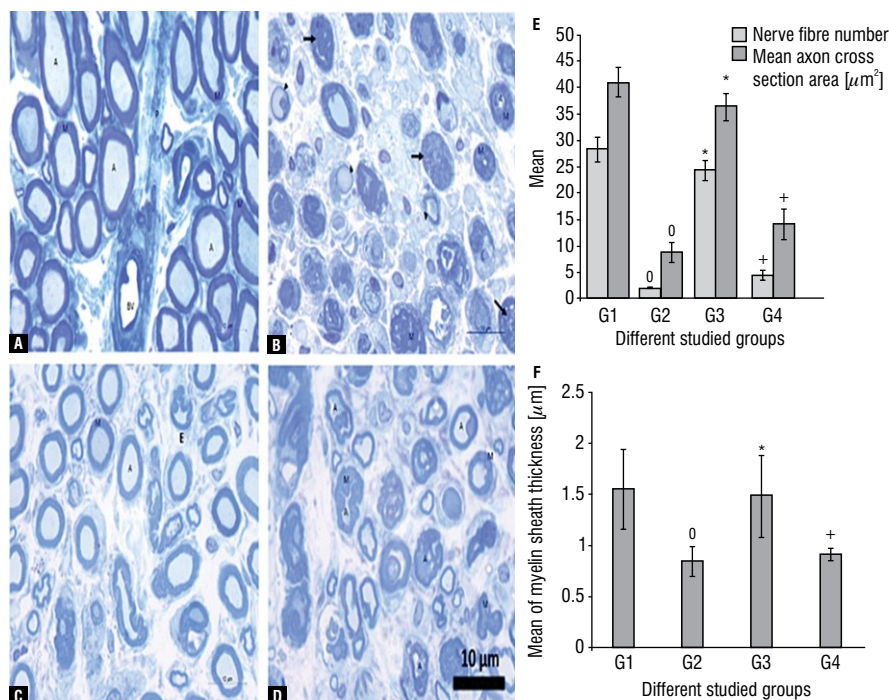


**Figure 5.** Representative photomicrographs of the stained semithin rat sciatic nerve sections from the different experimental groups; **A.** Control group I showing bundles of nerve fibres. The myelinated nerve fibres have regular myelin sheaths (M) stained dark blue around the axons (A). The perineurium surrounds the nerve bundles (P), and blood vessels (BV) can be seen; **B.** Degenerative changes of the myelin coat in group II, with disintegrated myelin fragments covering the sections with normal fibres (arrow) or compressing the axons (A). Some have thickened myelin (M) and some nerve fibres have thin myelin (arrowhead); **C.** Group III showing restoration of the normal appearance of myelin sheaths (M) and axons (A) in most myelinated nerve fibres; **D.** Group IV showing many myelinated nerve fibres with irregular myelin sheaths (M), with in-folding, out-folding, and degenerated axons (A) (Toluidine blue, scale bar 10 µm, 1000× magnification); **E.** Histogram for the number of nerve fibres and the mean axon cross-sectional area showing a significant reduction in the number of nerve fibres and the mean axon cross-sectional area in both group II and group IV compared to that in group I (0,  $p < 0.05$ ). There were also increased numbers of nerve fibres in group III compared to those in groups II and IV ( $*p < 0.05$ ). The mean axon cross-sectional area was increased in group III compared to group II ( $*p < 0.05$ ). However, a significant reduction in the mean axon cross-sectional area was observed in group IV compared to that in group III ( $+p < 0.05$ ); **F.** Histogram showing a significant reduction in the mean of myelin sheath thickness in group II and IV compared to that in group I (0,  $p < 0.05$ ). A significant increase in myelin sheath thickness was reported in group III compared to that in group II and IV ( $*p < 0.05$ ). However, a significant reduction in the mean of myelin sheath thickness was observed in group IV compared to that in group III ( $+p < 0.05$ ).

( $14.11 \pm 2.89$  vs.  $36.26 \pm 2.53 \mu\text{m}^2$ ,  $p < 0.05$ ). Moreover, there was a significant increase in the mean axon cross-sectional area in group III compared with that in group II ( $36.26 \pm 2.53$  vs.  $8.68 \pm 1.75 \mu\text{m}^2$ ,  $p < 0.05$ ) (Fig. 5E).

The thickness of the myelin sheath significantly decreased ( $p < 0.05$ ) in groups II and IV ( $0.84 \pm 0.14$ ,  $0.91 \pm 0.06 \mu\text{m}$  vs.  $1.55 \pm 0.39$ , respectively) as compared with the control group. Moreover, a highly significant increase ( $p < 0.05$ ) in myelin sheath thickness was reported in group III compared with that in group IV ( $1.84 \pm 0.4$  vs.  $0.91 \pm 0.06 \mu\text{m}$ , respectively). Additionally, there was a highly significant reduction ( $p < 0.05$ ) in myelin sheath thickness in group II compared with that in group III ( $0.84 \pm 0.14$  vs.  $1.48 \pm 0.40 \mu\text{m}$ , respectively) (Fig. 5F).

#### TEM analysis

Transmission electron microscopy analysis of the control group showed myelinated axons surrounded by a thick regular myelin sheath. The axoplasm contained mitochondria, neurofilaments, and microtubules. Axons were enclosed by Schwann cell cytoplasm, and the Schwann cell had a large nucleus with peripheral heterochromatin. Groups of unmyelinated nerve fibres were also observed (Fig. 6A).

Transmission electron microscopy examination of group II showed irregular and distorted myelin sheaths. The sheaths did not have a uniform thickness, and some had multiple vacuolations. Other myelin sheaths showed separation in the myelin sheath lamellae. Retracted degenerated myelinated axons with small vacuolation were observed in the

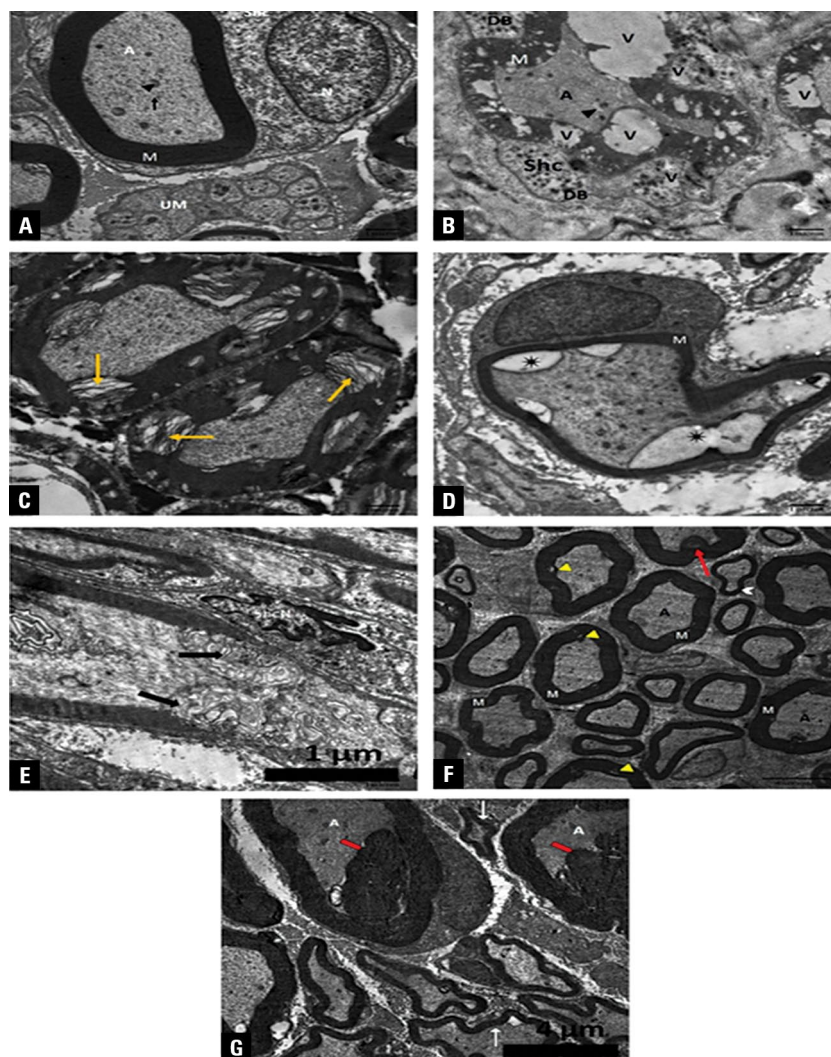


**Figure 6.** Representative electron micrographs of rat sciatic nerve sections from the different experimental groups; **A.** Cross-section of control group showing myelinated axons (A) ensheathed with a myelin sheath (M) of uniform thickness. The electron-dense dots present in the axons are neurotubules, neurofilaments (arrow), and mitochondria (arrow head). Schwann cells (Shc) have large nuclei (N) and enclose the myelinated nerve fibres. Unmyelinated nerve fibres are indicated (UM); **B.** Cross-section of the group II showing an irregular myelin sheath (M) with multiple vacuolations (V). These are enclosed by Schwann cells (Shc), which have vacuolated (V) cytoplasm and dense bodies (DB). We observed a compressed axon (A) with a small vacuolation (arrow head); **C.** Cross-section of the group II showing separation in the myelin sheath lamellae (yellow arrow); **D.** Cross-section of the group II with a thin and irregular myelin sheath (M) and axon retraction (\*); **E.** Longitudinal section of group II showing distortion of the myelin sheath (arrow) and an irregular indented Schwann cell nucleus (ShcN) with peripheral chromatin condensation; **F.** Cross-section from group III, showing that myelinated nerves appear nearly normal with a regular compact myelin sheath (M) and homogenous axoplasm (A). Some of the myelin sheaths have either splitting (yellow head arrow) or in-folding (red arrow), while others are thin and irregular (chevron arrow); **G.** Cross-section from group IV, showing an irregular myelin sheath (arrow) with focal thickening in some nerve fibres (red arrow) compressing the axons (A). (A–E, 17500× magnification) (F, G, 5000× magnification).

axoplasm (Fig. 6B–E). The Schwann cell nucleus was irregular and indented with peripheral chromatin condensation. In another section, the Schwann cell cytoplasm had multiple vacuolations and dense bodies (Fig. 6E, B).

Group III mostly demonstrated normal myelinated nerves with a regular compact myelin sheath and homogenous axoplasm. However, some nerve fibres still

had splitting in the myelin sheath (Fig. 6F). Group IV had some nerve fibres with irregular myelin sheaths, with focal thickening compressing the axons (Fig. 6G)

## DISCUSSION

Peripheral nervous system injuries are increasing in frequency, and pose a health hazard. Such injuries mostly affect young adults, resulting from traffic acci-

dents, falls, and surgery [42]. These injuries may lead to lifelong debilitating disability, potentially resulting in loss of organ functions [76]. Feng and Yuan [21] concluded that drugs can be a reliable method for obtaining acceptable functional recovery in crush injury, but that surgical repair is a more precise option for transection injury.

In a peripheral nerve crush injury, the mechanism of injury is unclear, as some nerve integrity is maintained. Emel et al. [19] have demonstrated that the possible mechanism of crush injury is due to mechanical compression, followed by oedema and ischaemia of the crushed nerve fibres. Moreover, enhanced arachidonic acid metabolism and both intracellular and extracellular endoperoxide accumulations occur at the lesion site as sequelae of morphological changes and deficient oxygen supply [73]. Zhang and Chopp [74] concluded that neurorepair processes (angiogenesis and neurogenesis) are activated in adults after the occurrence of various pathological conditions.

Sciatic nerve crush injury results in vasa nervosa damage and impairment of nerve blood flow if persistent compressive ischaemia lasts for long period [45]. The pathology of crush injury in sciatic nerve may be due to various factors such as endogenous chemical mediators' accumulation, apoptosis, free radical generation and ischaemia [59]. Oxidative stress gives rise to cellular damage with activating apoptosis. Free oxygen radicals (ROS) are the main source of lipid peroxidation (LPO) and induce oxidative stress by modulating antioxidant activities [52]. Various antioxidant enzymes as CAT, SOD and glutathione peroxidase (GSH) can be involved in detoxification of ROS. CAT and SOD are capable of scavenging peroxide and superoxide anions [12]. Therefore, their elevated level in tissue pointed to raised antioxidant activity [58]. Hence, during cell injury, there is a reduction in antioxidant enzymes activity such as SOD, CAT and GSH [62]. On the other hand, MDA and myeloperoxidase activity was reported to increase due to inflammatory reaction associated with tissue injury leading to direct membrane function impairment and indirect cellular component damage [71].

In the current study tissue CAT and SOD activities were significantly decreased in crushed group as compared to control group ( $p < 0.05$ ) while MDA was significantly increased ( $p < 0.05$ ). Our findings were in line with Kocaoglu et al. [38] who reported same findings. They explained that nerve compression induced blood brain barrier disruption and nerve

oedema with a decrease in peripheral nerve oxygen supply and morphological changes. The previous findings enhance arachidonic acid metabolism and permit unstable endoperoxides accumulation both extracellular and intracellular. Moreover, reperfusion after nerve compression causes free radical formation similar to ischaemia-reperfusion injury [73]. Nervous system injuries stimulate glutamate production, glutamate receptor activation and calcium ion accumulation with subsequent induction of ROS, hydrogen peroxide, and superoxide anion formation. Lipid peroxidation cascades are initiated by oxidative stress leading to cell membrane damage during the initial period after injury [18].

Light microscopic examination of the H&E sections from the specimen of nerve crush injury group showed degenerated and vacuolated axoplasm, with areas of nerve fibre loss and pyknotic nuclei. Other sections showed dilated and congested blood vessels with areas of haemorrhage and mononuclear cell infiltration. These findings were in accordance with those obtained by some researches [4, 40, 61]. These findings were supported by a significant reduction in the number of sciatic nerve fibres ( $p < 0.05$ ) in the sciatic nerve crush group compared to that in control group. This was reflected by the weak anti-neurofilament antibody expression observed in the crush group. Tomassoni et al. [63] reported the apparent loss of both myelinated and unmyelinated nerve fibres after nerve ligation. Moreover, Di Cesare Mannelli et al. [15] determined that more significant axonal degeneration and nerve trunk apoptosis, along with Schwann cells DNA fragmentation in the nuclei, were reported in the distal end of the nerve.

In the current study, MT staining revealed a significant increase in the perineurial and endoneurial collagen fibres in group II compared to those in group III and the control group ( $p < 0.05$ ). This can be attributed to fibrin deposition as a consequence of sciatic nerve injury, resulting in enhanced nerve damage, alteration of the composition of the extracellular matrix and the suppression of Schwann cell migration [16]. However, an inflammatory reaction with proinflammatory cytokines occurs due to fibrin deposition and macrophage accumulation. This may induce tissue injury, but its main role lies in mechanisms involved in tissue regeneration [49]. Moreover, other studies involving sciatic nerve crush injury have observed an increased number of endoneurial fibroblasts and an accumulation of connective tissue in the interfibre endoneurium [35].

In this manuscript, we observed misexpression and weak neurofilament expression in group II; there was strong neurofilament expression in the nerve fibres in group III. Additionally, the mean percentage of the area of neurofilament expression increased in a significant manner ( $p < 0.05$ ) in the control group compared to groups II and VI. Our results are in accordance with those obtained by Song et al. [58] who observed that a decrease in positive neurofilament expression in the nervous system microtubules was correlated with diabetes and various nerve injuries. This results from a disturbance in the synthesis and transport of neuronal substances, and therefore, the irregular activity in the nervous system.

The immunohistochemical findings from our study were supported by a significant increase in the number of sciatic nerve fibres ( $p < 0.05$ ) in group III compared to that in group II. These immunohistochemical findings are in line with those obtained by Khabiri et al. [33] who reported that olfactory ensheathing cells transplantation accelerates nerve axon myelination and regeneration following crush nerve injury. Omura et al. [48] concluded that neurofilament expression in sciatic nerve axons was correlated with early signs of nerve regeneration.

In the present study, TEM examination of the nerve crushed group showed irregular and distorted myelin sheaths with lamellar separation and degenerated myelinated axons. However, the Schwann cell nucleus was irregular and indented with peripheral chromatin condensation, while multiple vacuolations and dense bodies were reported in its cytoplasm. These results are consistent with previous research demonstrating myelin sheath degeneration and splitting [1, 2]. Furthermore, Tamaddonfard et al. [61] suggested that Schwann cells accumulation and the attraction of macrophages to the nerve injury site can assist scavengers of degenerated nerve axons and myelin sheath fragmentation to enhance the initiation of nerve regeneration. Moreover, previous studies have suggested that the regeneration process is influenced by inflammatory changes and oxidative stress at the injury site and the distal nerve [28, 56].

Yuan and Feng [72] demonstrated that Wallerian degeneration can occur after sciatic nerve crush injury, which involves nerve axon degeneration, Schwann cell accumulation, myelin sheath disintegration and macrophage infiltration. Moreover, Schwann cells and macrophages play a major role in the secretion of various cytokines and a variety of inflammatory medi-

ators, such as IL-1 $\beta$ , TNF- $\alpha$  and interferon, all of which regulate Wallerian degeneration [35, 57]. Additionally, damaged tissue proximal to the injured area may inhibit axonal extension and impair the healing process. Wallerian degeneration may assist macrophages and white blood cells accumulation to remove the damaged myelin sheath and injured axons. Furthermore, accelerated Schwann cell division and differentiations plays a major role in axon renewal [41, 66, 75].

L-carnitine is a potent antioxidant with neuroprotective potential and can suppress oxidative damage in neurodegenerative diseases such as Parkinson's and Alzheimer's disease [3, 27]. It is considered as an exogenous neurotrophic factor, decreasing neuronal loss after nerve injury and improving neuronal regeneration [67]. Collectively, we explored the possible ameliorative effects of L-carnitine administration on sciatic nerve crush damage. L-carnitine administration improved the antioxidant status as proved in group III. Administration of L-carnitine after crush nerve injury improved all biochemical parameters as tissue CAT and SOD activities were significantly elevated and MDA level declined significantly ( $p < 0.05$ ) as compared to group II. It also reduces the damage to the axon and myelin sheath, with a near-normal structure observed in the nerve fibres. Our results were in accordance with findings reported by Avsar et al. [6] who studied the alleviating effect of L-carnitine on sciatic nerve crush injury in rats. It was found that L-carnitine had an effect on the recovery of sciatic nerve function as well as enhancing nerve regeneration and suppressing injury-induced degeneration in the nerve axon and its myelin sheath. Wilson et al. [68] and Babicova et al. [7] explained that L-carnitine blocked the cell death pathway at the mitochondrial level by limiting reactive oxygen species synthesis in addition to reducing the nitric oxide and nitric oxide synthase levels.

Sildenafil is a PDE-5 inhibitor with neuroprotective effect, which is initiated by stimulating neurotrophic factors encountered in neuronal regeneration and survival [29]. In this manuscript, SIL administration in group IV led to a mild improvement in the histopathological findings and biochemical parameters as proved by increased CAT and SOD activities and decreased MDA activity as compared to group II but the difference was not statistically significant. These results were in line with those obtained by Vakharia et al. [65] who studied the neuroprotective properties of SIL on facial nerve functional recovery following

nerve crush injury. The study concluded that SIL administration following facial nerve crush injury had only a mild transient effect on the functional recovery of the facial nerve, despite its neuroprotective effect in previous studies. On the other hand, Garcia et al. [24] found that SIL could ameliorate oxidative and inflammatory stress on pelvic ganglion neurons after inducing damage to bilateral cavernosal nerve through compensatory elevated antioxidant enzymes. These findings were proved by an increase in NADPH complex expression such as p22-phox and toxol which represent the main source of ROS formation. It indicates higher ability for superoxide production. It may also induce anti-inflammatory feedback. This was thought to occur by regulating inflammatory cytokine expression by preventing leukocyte accumulation and migration near the neuronal lesion. Moreover, Jeong et al. [31] studied the effect of SIL on the kidneys of streptozotocin-diabetic rats and reported diminished oxidative stress and reduced pro-inflammatory cytokine expression.

Quantitative morphometric study demonstrated a significant increase in the thickness of the myelin sheath, the number of nerve fibres, and the axon cross-sectional area in L-carnitine-treated group. These findings were in agreement with those obtained by Avsar et al. [6] who concluded that L-carnitine had an excellent ability to prevent nerve function loss following nerve injury, accelerate nerve degeneration, and ameliorate axon and myelin sheath degeneration. On contrary to insignificant increase in the previous parameters in the group treated with SIL.

According to the histopathologic, immunohistochemical, and histo-morphometric findings, L-carnitine had an alleviating effect on nerve crush injury lesions, and this effect was greater than that observed by SIL administration. This is suggestive of the more potent antioxidant and anti-inflammatory effect of L-carnitine with respect to nerve injuries.

## CONCLUSIONS

Nerve crush injury can result in serious debilitating effects which can be partially relieved by administering substances such as nutrients and drugs. In this study, by means of histopathology, electron microscopy, and morphometric studies, it was demonstrated that these effects may be alleviated by L-carnitine administration and minimally ameliorated by SIL uptake. It provides a new scope to the neuroregenerative effect of L-carnitine on nerve compression.

## Acknowledgements

Thanks to Elsevier for precise Language Editing Services.

Work was conducted in: Faculty of Medicine, Menoufia University, Egypt; Alexandria Medical Research Institute, Alexandria, Egypt.

**Conflict of interest:** None declared

## REFERENCES

1. Abd-El-Hafez A. Effect of leflunomide on sciatic nerve of Abd-El-Hafez A. Effect of leflunomide on sciatic nerve of adult albino rats. *Egypt J Histol.* 2014; 37(2): 258–268, doi: [10.1097/01.ehx.0000446588.04196.df](https://doi.org/10.1097/01.ehx.0000446588.04196.df).
2. Abd ElS, Raafat M, Shokry Y. ogical study on the role of bone marrow derived mesenchymal stem cells on the sciatic nerve and the gastrocnemius muscle in a model of sciatic nerve crush injury in albino rats. *Egypt J Histol.* 2015; 38(3): 438–451, doi: [10.1097/01.EHX.0000470653.672.31.07](https://doi.org/10.1097/01.EHX.0000470653.672.31.07).
3. Abdul HM, Butterfield DA. Involvement of PI3K/PKG/ERK1/2 signaling pathways in cortical neurons to trigger protection by cotreatment of acetyl-L-carnitine and alpha-lipoic acid against HNE-mediated oxidative stress and neurotoxicity: implications for Alzheimer's disease. *Free Radic Biol Med.* 2007; 42(3): 371–384, doi: [10.1016/j.freeradbiomed.2006.11.006](https://doi.org/10.1016/j.freeradbiomed.2006.11.006), indexed in Pubmed: [17210450](https://pubmed.ncbi.nlm.nih.gov/17210450/).
4. Alqalla M, Tawfik M, Grawish M. The effects of low-level laser treatment on recovery of nerve conduction after sciatic nerve compression injury (experimental study). *J Am Sci.* 2016; 12(9): 5–11, doi: [10.7537/marsjas120916.02](https://doi.org/10.7537/marsjas120916.02).
5. American Heart Association. Viagra Helps Men with Heart Failure. *Science Daily.* [http://www.sciencedaily.com/releases/2002/08/0208070\\_64924.htm](http://www.sciencedaily.com/releases/2002/08/0208070_64924.htm) (2002; 7 August).
6. Avsar UZ, Avsar U, Aydin A, et al. L-carnitine alleviates sciatic nerve crush injury in rats: functional and electron microscopy assessments. *Neural Regen Res.* 2014; 9(10): 1020–1024, doi: [10.4103/1673-5374.133163](https://doi.org/10.4103/1673-5374.133163), indexed in Pubmed: [25206754](https://pubmed.ncbi.nlm.nih.gov/25206754/).
7. Babicová A, Havlínová Z, Hroch M, et al. In vivo study of radioprotective effect of NO-synthase inhibitors and acetyl-L-carnitine. *Physiol Res.* 2013; 62(6): 701–710, doi: [10.33549/physiolres.932541](https://doi.org/10.33549/physiolres.932541), indexed in Pubmed: [23869893](https://pubmed.ncbi.nlm.nih.gov/23869893/).
8. Bagdatoglu C, Saray A, Surucu HS, et al. Effect of trapidil in ischemia/reperfusion injury of peripheral nerves. *Neurosurgery.* 2002; 51(1): 212–9; discussion 219, doi: [10.1097/00006123-200207000-00031](https://doi.org/10.1097/00006123-200207000-00031), indexed in Pubmed: [12182420](https://pubmed.ncbi.nlm.nih.gov/12182420/).
9. Bancroft JD, Gamble M. *Theory and practice of histological techniques*, 6th ed. Churchill Livingstone Elsevier, Philadelphia 2008: 126, 150, 440.
10. Burnett M, Zager E. Pathophysiology of peripheral nerve injury: a brief review. *Neurosurgical Focus.* 2004; 16(5): 1–7, doi: [10.3171/foc.2004.16.5.2](https://doi.org/10.3171/foc.2004.16.5.2).
11. Cavallini G, Caracciolo S, Vitali G, et al. Carnitine versus androgen administration in the treatment of sexual dysfunction, depressed mood, and fatigue associated with male aging. *Urology.* 2004; 63(4): 641–646, doi: [10.1016/j.urology.2003.11.009](https://doi.org/10.1016/j.urology.2003.11.009), indexed in Pubmed: [15072869](https://pubmed.ncbi.nlm.nih.gov/15072869/).
12. Cetinkaya A, Bulbuloglu E, Kantarceken B, et al. Effects of L-carnitine on oxidant/antioxidant status in acetic acid-induced colitis. *Dig Dis Sci.* 2006; 51(3): 488–494, doi: [10.1007/s10620-006-3160-9](https://doi.org/10.1007/s10620-006-3160-9), indexed in Pubmed: [16614957](https://pubmed.ncbi.nlm.nih.gov/16614957/).
13. Chen CJ, Ou YC, Liao SL, et al. Transplantation of bone marrow stromal cells for peripheral nerve repair. *Exp Neurol.* 2007; 204(1): 443–453, doi: [10.1016/j.expneurol.2006.12.004](https://doi.org/10.1016/j.expneurol.2006.12.004), indexed in Pubmed: [17222827](https://pubmed.ncbi.nlm.nih.gov/17222827/).

14. Chiechio S, Copani A, Gereau RW, et al. Acetyl-L-carnitine in neuropathic pain: experimental data. *CNS Drugs*. 2007; 21 Suppl 1: 31–8; discussion 45, doi: [10.2165/00023210-200721001-00005](https://doi.org/10.2165/00023210-200721001-00005), indexed in Pubmed: [17696591](https://pubmed.ncbi.nlm.nih.gov/17696591/).
15. Di Cesare Mannelli L, Ghelardini C, Calvani M, et al. Neuroprotective effects of acetyl-L-carnitine on neuropathic pain and apoptosis: a role for the nicotinic receptor. *J Neurosci Res*. 2009; 87(1): 200–207, doi: [10.1002/jnr.21815](https://doi.org/10.1002/jnr.21815), indexed in Pubmed: [18709658](https://pubmed.ncbi.nlm.nih.gov/18709658/).
16. El-Azab NE, El-Mahalaway A, Mostafa O, et al. Histological and immunohistochemical study of the potential therapeutic impacts of bone marrow mesenchymal stem cells and exosomes for sciatic nerve crush injury model in rats. *J Histotechnol*. 2018; 41(4): 160–176, doi: [10.1080/01478885.2018.1505205](https://doi.org/10.1080/01478885.2018.1505205).
17. El Desoky ES, Fouad IA. Pharmacological evidence for the role of nitric oxide-CGMP in antinociception. *J Appl Res*. 2005; 5: 451–459.
18. Emmez H, Yildirim Z, Kale A, et al. Anti-apoptotic and neuroprotective effects of  $\alpha$ -lipoic acid on spinal cord ischemia-reperfusion injury in rabbits. *Acta Neurochir (Wien)*. 2010; 152(9): 1591–600; discussion 1600, doi: [10.1007/s00701-010-0703-9](https://doi.org/10.1007/s00701-010-0703-9), indexed in Pubmed: [20535507](https://pubmed.ncbi.nlm.nih.gov/20535507/).
19. Emel E, Ergün SS, Kotan D, et al. Effects of insulin-like growth factor-I and platelet-rich plasma on sciatic nerve crush injury in a rat model. *J Neurosurg*. 2011; 114(2): 522–528, doi: [10.3171/2010.9.JNS091928](https://doi.org/10.3171/2010.9.JNS091928), indexed in Pubmed: [21029038](https://pubmed.ncbi.nlm.nih.gov/21029038/).
20. Eto M, Sumi H, Fujimura H, et al. Pioglitazone promotes peripheral nerve remyelination after crush injury through CD36 upregulation. *J Peripher Nerv Syst*. 2008; 13(3): 242–248, doi: [10.1111/j.1529-8027.2008.00183.x](https://doi.org/10.1111/j.1529-8027.2008.00183.x), indexed in Pubmed: [18844791](https://pubmed.ncbi.nlm.nih.gov/18844791/).
21. Feng X, Yuan W. Dexamethasone enhanced functional recovery after sciatic nerve crush injury in rats. *Biomed Res Int*. 2015; 2015: 627923, doi: [10.1155/2015/627923](https://doi.org/10.1155/2015/627923), indexed in Pubmed: [25839037](https://pubmed.ncbi.nlm.nih.gov/25839037/).
22. Galeotti N, Bartolini A, Calvani M, et al. Acetyl-L-carnitine requires phospholipase C-IP3 pathway activation to induce antinociception. *Neuropharmacology*. 2004; 47(2): 286–294, doi: [10.1016/j.neuropharm.2004.03.016](https://doi.org/10.1016/j.neuropharm.2004.03.016), indexed in Pubmed: [15223307](https://pubmed.ncbi.nlm.nih.gov/15223307/).
23. Gao Y, Weng C, Wang X. Changes in nerve microcirculation following peripheral nerve compression. *Neural Regen Res*. 2013; 8(11): 1041–1047, doi: [10.3969/j.issn.1673-5374.2013.11.010](https://doi.org/10.3969/j.issn.1673-5374.2013.11.010), indexed in Pubmed: [25206398](https://pubmed.ncbi.nlm.nih.gov/25206398/).
24. Garcia LA, Hlaing SuM, Gutierrez RA, et al. Sildenafil attenuates inflammation and oxidative stress in pelvic ganglia neurons after bilateral cavernosal nerve damage. *Int J Mol Sci*. 2014; 15(10): 17204–17220, doi: [10.3390/ijms151017204](https://doi.org/10.3390/ijms151017204), indexed in Pubmed: [25264738](https://pubmed.ncbi.nlm.nih.gov/25264738/).
25. Gibson A. Phosphodiesterase 5 inhibitors and nitric transmission — from zaprinast to sildenafil. *Eur J Pharmacol*. 2001; 411(1-2): 1–10, doi: [10.1016/s0014-2999\(00\)00824-4](https://doi.org/10.1016/s0014-2999(00)00824-4).
26. Góth L. A simple method for determination of serum catalase activity and revision of reference range. *Clinica Chimica Acta*. 1991; 196(2-3): 143–151, doi: [10.1016/0009-8981\(91\)90067-m](https://doi.org/10.1016/0009-8981(91)90067-m).
27. Gülçin I. Antioxidant and antiradical activities of L-carnitine. *Life Sci*. 2006; 78(8): 803–811, doi: [10.1016/j.lfs.2005.05.103](https://doi.org/10.1016/j.lfs.2005.05.103), indexed in Pubmed: [16253281](https://pubmed.ncbi.nlm.nih.gov/16253281/).
28. Helvacioğlu F, Kandemir E, Karabacak B, et al. Effect of creatine on rat sciatic nerve injury: a comparative ultrastructural study. *Turk Neurosurg*. 2016; 28(1): 128–136, doi: [10.5137/1019-5149.JTN.18806-16.0](https://doi.org/10.5137/1019-5149.JTN.18806-16.0), indexed in Pubmed: [27858383](https://pubmed.ncbi.nlm.nih.gov/27858383/).
29. Hlaing SuM, Garcia LA, Kovanez I, et al. Sildenafil promotes neuroprotection of the pelvic ganglia neurons after bilateral cavernosal nerve resection in the rat. *BJU Int*. 2013; 111(1): 159–170, doi: [10.1111/j.1464-410X.2012.11278.x](https://doi.org/10.1111/j.1464-410X.2012.11278.x), indexed in Pubmed: [22672418](https://pubmed.ncbi.nlm.nih.gov/22672418/).
30. Duarte I, Lorenzetti BB, Ferreira SH. Peripheral analgesia and activation of the nitric oxide-cyclic GMP pathway. *Eur J Pharmacol*. 1990; 186(2-3): 289–293, doi: [10.1016/0014-2999\(90\)90446-d](https://doi.org/10.1016/0014-2999(90)90446-d).
31. Jeong KH, Lee TW, Ihm CG, et al. Effects of sildenafil on oxidative and inflammatory injuries of the kidney in streptozotocin-induced diabetic rats. *Am J Nephrol*. 2009; 29(3): 274–282, doi: [10.1159/000158635](https://doi.org/10.1159/000158635), indexed in Pubmed: [18812693](https://pubmed.ncbi.nlm.nih.gov/18812693/).
32. Karsidag S, Akcal A, Sahin S, et al. Neurophysiological and morphological responses to treatment with acetyl-L-carnitine in a sciatic nerve injury model: preliminary data. *J Hand Surg Eur Vol*. 2012; 37(6): 529–536, doi: [10.1177/1753193411426969](https://doi.org/10.1177/1753193411426969), indexed in Pubmed: [22080531](https://pubmed.ncbi.nlm.nih.gov/22080531/).
33. Kabiri M, Oraee-Yazdani S, Shafiee A, et al. Neuroregenerative effects of olfactory ensheathing cells transplanted in a multi-layered conductive nanofibrous conduit in peripheral nerve repair in rats. *J Biomed Sci*. 2015; 22(1), doi: [10.1186/s12929-015-0144-0](https://doi.org/10.1186/s12929-015-0144-0).
34. Khan A, Faruqi N, Ansari M. Effects of hydrocortisone on the sciatic nerve crush injury in adult rat: a light microscopic study. *Curr Neurobiol*. 2014; 5(1, 2): 11–16.
35. Khan A, Ajmal M, Faizal M. Effects of vitamin C on regeneration of sciatic nerve crush injury in adult rats: a light microscopic study. *JARM*. 2015; 3(8): 68–77.
36. Kidd PM. Alzheimer's disease, amnesic mild cognitive impairment, and age-associated memory impairment: current understanding and progress toward integrative prevention. *Altern Med Rev*. 2008; 13(2): 85–115, indexed in Pubmed: [18590347](https://pubmed.ncbi.nlm.nih.gov/18590347/).
37. Kim TH, Yoon SJ, Lee WC, et al. Protective effect of GCSB-5, an herbal preparation, against peripheral nerve injury in rats. *J Ethnopharmacol*. 2011; 136(2): 297–304, doi: [10.1016/j.jep.2011.04.037](https://doi.org/10.1016/j.jep.2011.04.037), indexed in Pubmed: [21569830](https://pubmed.ncbi.nlm.nih.gov/21569830/).
38. Kocaoğlu S, Aktaş Ö, Zengi O, et al. Effects of alpha lipoic acid on motor function and antioxidant enzyme activity of nerve tissue after sciatic nerve crush injury in rats. *Turk Neurosurg*. 2017 [Epub ahead of print], doi: [10.5137/1019-5149.JTN.18585-16.1](https://doi.org/10.5137/1019-5149.JTN.18585-16.1), indexed in Pubmed: [29044452](https://pubmed.ncbi.nlm.nih.gov/29044452/).
39. Korkmaz MF, Parlakpınar H, Ceylan MF, et al. The effect of sildenafil on recuperation from sciatic nerve injury in rats. *Balkan Med J*. 2016; 33(2): 204–211, doi: [10.5152/balkan-medj.2016.14701](https://doi.org/10.5152/balkan-medj.2016.14701), indexed in Pubmed: [27403391](https://pubmed.ncbi.nlm.nih.gov/27403391/).
40. Li HF, Wang YR, Huo HP, et al. Neuroprotective effects of ultrasound-guided nerve growth factor injections after sciatic nerve injury. *Neural Regen Res*. 2015; 10(11): 1846–1855, doi: [10.4103/1673-5374.170315](https://doi.org/10.4103/1673-5374.170315), indexed in Pubmed: [26807123](https://pubmed.ncbi.nlm.nih.gov/26807123/).
41. Li R, Wu J, Lin Z, et al. Single injection of a novel nerve growth factor coacervate improves structural and functional regeneration after sciatic nerve injury in adult rats. *Exp Neurol*. 2017; 288: 1–10, doi: [10.1016/j.expneurol.2016.10.015](https://doi.org/10.1016/j.expneurol.2016.10.015), indexed in Pubmed: [27983992](https://pubmed.ncbi.nlm.nih.gov/27983992/).
42. Marconi S, Castiglione G, Turano E, et al. Human adipose-derived mesenchymal stem cells systemically injected promote peripheral nerve regeneration in the mouse model of sciatic crush. *Tissue Eng Part A*. 2012; 18(11-12): 1264–1272, doi: [10.1089/ten.TEA.2011.0491](https://doi.org/10.1089/ten.TEA.2011.0491), indexed in Pubmed: [22332955](https://pubmed.ncbi.nlm.nih.gov/22332955/).
43. Mihara M, Uchiyama M. Determination of malonaldehyde precursor in tissues by thiobarbituric acid test. *Anal Biochem*. 1978; 86(1): 271–278, doi: [10.1016/0003-2697\(78\)90342-1](https://doi.org/10.1016/0003-2697(78)90342-1), indexed in Pubmed: [655387](https://pubmed.ncbi.nlm.nih.gov/655387/).
44. Mixcoatl-Zecuatl T, Aguirre-Bañuelos P, Granados-Soto V. Sildenafil produces antinociception and increases morphine antinociception in the formalin test. *Eur J Pharmacol*. 2000; 400(1): 81–87, doi: [10.1016/s0014-2999\(00\)00361-7](https://doi.org/10.1016/s0014-2999(00)00361-7), indexed in Pubmed: [10913588](https://pubmed.ncbi.nlm.nih.gov/10913588/).
45. Morani A, Bodhankar S. Neuroprotective effect of vitamin E acetate in models of mononeuropathy in rats. *Neuroanatomy*. 2008; 7: 33–37.
46. Namazi H, Emami MJ, Dehghani Nazhvani F, et al. Simvastatin vs. L-Carnitine: An experimental study on optimizing nerve repair.

- Turk Neurosurg. 2019 [Epub ahead of print], doi: [10.5137/1019-5149.JTN.25821-19.2](https://doi.org/10.5137/1019-5149.JTN.25821-19.2), indexed in Pubmed: [31099885](https://pubmed.ncbi.nlm.nih.gov/31099885/).
47. Navarro X, Vivó M, Valero-Cabré A. Neural plasticity after peripheral nerve injury and regeneration. *Prog Neurobiol.* 2007; 82(4): 163–201, doi: [10.1016/j.pneurobio.2007.06.005](https://doi.org/10.1016/j.pneurobio.2007.06.005), indexed in Pubmed: [17643733](https://pubmed.ncbi.nlm.nih.gov/17643733/).
  48. Omura K, Ohbayashi M, Sano M, et al. The recovery of blood-nerve barrier in crush nerve injury--a quantitative analysis utilizing immunohistochemistry. *Brain Res.* 2004; 1001(1-2): 13–21, doi: [10.1016/j.brainres.2003.10.067](https://doi.org/10.1016/j.brainres.2003.10.067), indexed in Pubmed: [14972650](https://pubmed.ncbi.nlm.nih.gov/14972650/).
  49. Pan HC, Yang DY, Ho SP, et al. Escalated regeneration in sciatic nerve crush injury by the combined therapy of human amniotic fluid mesenchymal stem cells and fermented soybean extracts, Natto. *J Biomed Sci.* 2009; 16: 75, doi: [10.1186/1423-0127-16-75](https://doi.org/10.1186/1423-0127-16-75), indexed in Pubmed: [19698158](https://pubmed.ncbi.nlm.nih.gov/19698158/).
  50. Patil CS, Singh VP, Kulkarni SK. Modulatory effect of sildenafil in diabetes and electroconvulsive shock-induced cognitive dysfunction in rats. *Pharmacol Rep.* 2006; 58(3): 373–380, indexed in Pubmed: [16845211](https://pubmed.ncbi.nlm.nih.gov/16845211/).
  51. Pettegrew JW, Levine J, McClure RJ. Acetyl-L-carnitine physical-chemical, metabolic, and therapeutic properties: relevance for its mode of action in Alzheimer's disease and geriatric depression. *Mol Psychiatry.* 2000; 5(6): 616–632, doi: [10.1038/sj.mp.4000805](https://doi.org/10.1038/sj.mp.4000805), indexed in Pubmed: [11126392](https://pubmed.ncbi.nlm.nih.gov/11126392/).
  52. Ragy MM. Effect of exposure and withdrawal of 900-MHz-electromagnetic waves on brain, kidney and liver oxidative stress and some biochemical parameters in male rats. *Electromagn Biol Med.* 2015; 34(4): 279–284, doi: [10.3109/15368378.2014.906446](https://doi.org/10.3109/15368378.2014.906446), indexed in Pubmed: [24712749](https://pubmed.ncbi.nlm.nih.gov/24712749/).
  53. Ramli D, Aziz I, Mohamad M, et al. The changes in rats with sciatic nerve crush injury supplemented with evening primrose oil: behavioural, morphologic, and morphometric analysis. *Evid Based Complement Alternat Med.* 2017; 2017: 3476407, doi: [10.1155/2017/3476407](https://doi.org/10.1155/2017/3476407), indexed in Pubmed: [28620418](https://pubmed.ncbi.nlm.nih.gov/28620418/).
  54. Roglio I, Bianchi R, Gotti S, et al. Neuroprotective effects of dihydroprogesterone in an experimental model of nerve crush injury. *Neuroscience.* 2008; 155: 673–685.
  55. Rump TJ, Abdul Muneer PM, Szlachetka AM, et al. Acetyl-L-carnitine protects neuronal function from alcohol-induced oxidative damage in the brain. *Free Radic Biol Med.* 2010; 49(10): 1494–1504, doi: [10.1016/j.freeradbiomed.2010.08.011](https://doi.org/10.1016/j.freeradbiomed.2010.08.011), indexed in Pubmed: [20708681](https://pubmed.ncbi.nlm.nih.gov/20708681/).
  56. Senoglu M, Nacitarhan V, Kurutas EB, et al. Intraperitoneal Alpha-Lipoic Acid to prevent neural damage after crush injury to the rat sciatic nerve. *J Brachial Plex Peripher Nerve Inj.* 2009; 4: 22, doi: [10.1186/1749-7221-4-22](https://doi.org/10.1186/1749-7221-4-22), indexed in Pubmed: [19939272](https://pubmed.ncbi.nlm.nih.gov/19939272/).
  57. Smith D, Tweed C, Fernyhough P, et al. Nuclear factor-kappaB activation in axons and Schwann cells in experimental sciatic nerve injury and its role in modulating axon regeneration: studies with etanercept. *J Neuropathol Exp Neurol.* 2009; 68(6): 691–700, doi: [10.1097/NEN.0b013e3181a7c14e](https://doi.org/10.1097/NEN.0b013e3181a7c14e), indexed in Pubmed: [19458540](https://pubmed.ncbi.nlm.nih.gov/19458540/).
  58. Song C, Yang Z, Zhong M, et al. Sericin protects against diabetes-induced injuries in sciatic nerve and related nerve cells. *Neural Regen Res.* 2013; 8(6): 506–513, doi: [10.3969/j.issn.1673-5374.2013.06.003](https://doi.org/10.3969/j.issn.1673-5374.2013.06.003), indexed in Pubmed: [25206693](https://pubmed.ncbi.nlm.nih.gov/25206693/).
  59. Stevens A, Wilson IG. The haematoxylin and eosin. In: Bancroft JD, Turner DR. *Theory and practice of histological techniques.* 4th ed. Churchill Livingstone, New York 1996: 99–112.
  60. Sun Y, Oberley LW, Li Y. A simple method for clinical assay of superoxide dismutase. *Clin Chem.* 1988; 34(3): 497–500, indexed in Pubmed: [3349599](https://pubmed.ncbi.nlm.nih.gov/3349599/).
  61. Tamaddonfard E, Farshid AA, Ahmadian E, et al. Crocin enhanced functional recovery after sciatic nerve crush injury in rats. *Iran J Basic Med Sci.* 2013; 16(1): 83–90, indexed in Pubmed: [23638296](https://pubmed.ncbi.nlm.nih.gov/23638296/).
  62. Tkalec M, Stambuk A, Srut M, et al. Oxidative and genotoxic effects of 900 MHz electromagnetic fields in the earthworm *Eisenia fetida*. *Ecotoxicol Environ Saf.* 2013; 90: 7–12, doi: [10.1016/j.ecoenv.2012.12.005](https://doi.org/10.1016/j.ecoenv.2012.12.005), indexed in Pubmed: [23352129](https://pubmed.ncbi.nlm.nih.gov/23352129/).
  63. Tomassoni D, Di Cesare Mannelli L, Bramanti V, et al. Treatment with acetyl-L-carnitine exerts a neuroprotective effect in the sciatic nerve following loose ligation: a functional and micro-anatomical study. *Neural Regen Res.* 2018; 13(4): 692–698, doi: [10.4103/1673-5374.230297](https://doi.org/10.4103/1673-5374.230297), indexed in Pubmed: [29722322](https://pubmed.ncbi.nlm.nih.gov/29722322/).
  64. Uthayathas S, Karuppagounder SS, Thrash BM, et al. Versatile effects of sildenafil: recent pharmacological applications. *Pharmacol Rep.* 2007; 59(2): 150–163, indexed in Pubmed: [17556793](https://pubmed.ncbi.nlm.nih.gov/17556793/).
  65. Vakharia KT, Lindsay RW, Knox C, et al. The effects of potential neuroprotective agents on rat facial function recovery following facial nerve injury. *Otolaryngol Head Neck Surg.* 2011; 144(1): 53–59, doi: [10.1177/0194599810390892](https://doi.org/10.1177/0194599810390892), indexed in Pubmed: [21493387](https://pubmed.ncbi.nlm.nih.gov/21493387/).
  66. Wang Y, Shan Q, Meng Y, et al. Mrpl10 and Tbp are suitable reference genes for peripheral nerve crush injury. *Int J Mol Sci.* 2017; 18(2), doi: [10.3390/ijms18020263](https://doi.org/10.3390/ijms18020263), indexed in Pubmed: [28134789](https://pubmed.ncbi.nlm.nih.gov/28134789/).
  67. Wilson ADH, Hart A, Wiberg M, et al. Acetyl-L-carnitine increases nerve regeneration and target organ reinnervation: a morphological study. *J Plast Reconstr Aesthet Surg.* 2010; 63(7): 1186–1195, doi: [10.1016/j.bjps.2009.05.039](https://doi.org/10.1016/j.bjps.2009.05.039), indexed in Pubmed: [19664977](https://pubmed.ncbi.nlm.nih.gov/19664977/).
  68. Wilson ADH, Hart A, Brannstrom T, et al. Primary sensory neuronal rescue with systemic acetyl-L-carnitine following peripheral axotomy. A dose-response analysis. *Br J Plast Surg.* 2003; 56(8): 732–739, doi: [10.1016/j.bjps.2003.08.005](https://doi.org/10.1016/j.bjps.2003.08.005), indexed in Pubmed: [14615246](https://pubmed.ncbi.nlm.nih.gov/14615246/).
  69. Xia Z, Tian X, Kong W, et al. Effects of L-carnitine on liver injury in rats and its impact on blood lipids. *Int J Clin Exp Med.* 2018; 11(9): 9768–9773.
  70. Yanardag R, Ozsoy-Sacan O, Ozdil S, et al. Combined effects of vitamin C, vitamin E, and sodium selenate supplementation on absolute ethanol-induced injury in various organs of rats. *Int J Toxicol.* 2007; 26(6): 513–523, doi: [10.1080/10915810701707296](https://doi.org/10.1080/10915810701707296), indexed in Pubmed: [18066967](https://pubmed.ncbi.nlm.nih.gov/18066967/).
  71. Yildirim AE, Dalgic A, Divanlioglu D, et al. Biochemical and histopathological effects of catechin on experimental peripheral nerve injuries. *Turk Neurosurg.* 2015; 25(3): 453–460, doi: [10.5137/1019-5149.JTN.12852-14.2](https://doi.org/10.5137/1019-5149.JTN.12852-14.2), indexed in Pubmed: [26037187](https://pubmed.ncbi.nlm.nih.gov/26037187/).
  72. Yuan W, Feng X. Immune cell distribution and immunoglobulin levels change following sciatic nerve injury in a rat model. *Iran J Basic Med Sci.* 2016; 19(7): 794–799, indexed in Pubmed: [27635205](https://pubmed.ncbi.nlm.nih.gov/27635205/).
  73. Yüce S, Cemal Gökçe E, İşkdemir A, et al. An experimental comparison of the effects of propolis, curcumin, and methylprednisolone on crush injuries of the sciatic nerve. *Ann Plast Surg.* 2015; 74(6): 684–692, doi: [10.1097/SAP.000000000000026](https://doi.org/10.1097/SAP.000000000000026), indexed in Pubmed: [24317243](https://pubmed.ncbi.nlm.nih.gov/24317243/).
  74. Zhang Z, Chopp M. Neurorestorative therapies for stroke: underlying mechanisms and translation to the clinic. *Lancet Neurol.* 2009; 8(5): 491–500, doi: [10.1016/s1474-4422\(09\)70061-4](https://doi.org/10.1016/s1474-4422(09)70061-4).
  75. Zhang Q, Nguyen P, Xu Q, et al. Neural progenitor-like cells induced from human gingiva-derived mesenchymal stem cells regulate myelination of schwann cells in rat sciatic nerve regeneration. *Stem Cells Transl Med.* 2017; 6(2): 458–470, doi: [10.5966/sctm.2016-0177](https://doi.org/10.5966/sctm.2016-0177), indexed in Pubmed: [28191764](https://pubmed.ncbi.nlm.nih.gov/28191764/).
  76. Zochodne DW. The challenges and beauty of peripheral nerve regrowth. *J Peripher Nerv Syst.* 2012; 17(1): 1–18, doi: [10.1111/j.1529-8027.2012.00378.x](https://doi.org/10.1111/j.1529-8027.2012.00378.x), indexed in Pubmed: [22462663](https://pubmed.ncbi.nlm.nih.gov/22462663/).

# The morphologic analysis of a not well-known anatomical structure's calcifications (Bochdalek's flower basket calcifications)

E. Doğan, C. Elibol

Department of Radiology, Faculty of Medicine, Mugla Sıtkı Koçman University, Mentese, Mugla, Turkey

[Received: 16 November 2021; Accepted: 8 December 2021; Early publication date: 16 December 2021]

**Background:** The aim of the study was to define the morphology of calcifications belonging to a not very well-known anatomical structure (calcification of foramen of Luschka/Bochdalek's flower basket calcification [Boc FBC]).

**Materials and methods:** Two hundred sixty-four computed tomography (CT) scans obtained from healthy patients were included in the study ( $50.0038 \pm 24.78309$  [0–92 years old] [mean age  $\pm$  standard deviation; range]). The morphology of the calcifications in the fourth ventricle (CFV) and Boc FBC was evaluated and compared with other common intracranial calcifications in each patient.

**Results:** Boc FBC was detected in 22.35% (59/264) of the patients. Out of 101 patients aged above 60 years, 59 presented Boc FBC (the rate increased to 55.45%), thus in our sample 94.91% of the detected Boc FBCs (56/59) were seen after 60 years of age. No Boc FBC was found under the age of 50. Statistically, there was a highly significant correlation between Boc FBC and pineal/habenular ( $p < 0.01$ ) as well as choroid plexus calcifications ( $p < 0.01$ ). The correlation between CFV and Boc FBC was significant ( $p < 0.05$ ). It was found that 37.3% of Boc FBCs had a conical form. This form was not accompanied by any vascular calcifications, either basilar or vertebral. Therefore, seeing the conical form was valuable in the differential diagnosis.

**Conclusions:** In our study, Boc FBCs were seen in advanced age and were not encountered under the age of 50. The conical form was seen in one-third of the cases, but it was a very beneficial finding for distinguishing Boc FBC from other calcifications if any. In the advanced age group, calcifications, especially choroid plexus calcifications and pineal/habenular calcifications, are highly associated with Boc FBC. In the presence of CFV, the probability of encountering Boc FBC is very high. (Folia Morphol 2022; 81, 2: 435–441)

**Key words:** foramen of Luschka, Bochdalek's flower basket, computed tomography, intracranial calcifications

---

Address for correspondence: Ass. Prof. E. Doğan, Mugla Sıtkı Koçman University, Department of Radiology, Mentese, Mugla, Turkey, tel: +90 506 661 97 94, fax: +90 252 212 35 99, e-mail: emrahdogan@mu.edu.tr; Dr. C. Elibol, Specialist MD, Muğla Sıtkı Koçman University Education and Research Hospital, Mentese, Mugla, Turkey, tel: +90 505 397 43 97, e-mail: celibol1068@gmail.com

This article is available in open access under Creative Common Attribution-Non-Commercial-No Derivatives 4.0 International (CC BY-NC-ND 4.0) license, allowing to download articles and share them with others as long as they credit the authors and the publisher, but without permission to change them in any way or use them commercially.

## INTRODUCTION

Outward indentation of the choroid plexus from the foramen of Luschka, also known as Boc FB, was first found by the Czech anatomist Vincent Alexander Bochdalek (1801–1883), who also described the Bochdalek hernia [16]. Although this finding is relatively common, it does not take place in radiological reports and is often overlooked [11]. So far, studies on this subject are based on examination with magnetic resonance imaging (MRI). The morphology of Boc FBC is emphasized in MRI studies. However, Boc FB can also be calcified like the choroid plexus. While MRI shows anatomical structure very well, calcifications are technically the weak point for this method. Therefore, our study was based on non-contrast computed tomography (CT) since it is the gold standard for calcification assessment. To the best of our knowledge, our study is the first CT study on this subject and there is no detailed information in English literature about Boc FB calcifications (Boc FBC). It is important to know the features of calcifications along with the part of the choroid plexus in this region. Since calcifications don't occur in all of the parts of Boc FB, it may be confused with the surrounding non-calcified fragment, haemorrhages and with cerebellopontine angle masses because this entity is not well-known by some radiologists [3, 11, 22]. Although textbooks express that the distinction between haemorrhage and calcifications can be made with coarse morphology and measurements of Hounsfield units (HUs), there are many pitfalls. Based on calcium amount and region of interest cursor, the HU values change [12]. Since vascular calcifications and Boc FBCs are seen in the same age group, when the vessel is tortuous, the Boc FBCs and vascular locations overlap and can be confused. Therefore, calcifications of the vertebral and basilar arteries are part of the differential diagnosis of Boc FBC due not only to the age group but also to the location [3, 11, 12, 18, 22].

When we mention choroid plexus calcifications, usually calcifications of the lateral ventricle or rarely the plexus part of the third ventricle come to mind. However, the choroid plexus extends to the fourth ventricle and can reach variationally cerebellopontine cistern via foramen of Luschka. In other words, calcifications originating from the choroid plexus can be seen not only in the lateral ventricle and the third ventricle but also on the wall of the fourth ventricle as well as out of the ventricles, such as Boc FBC [15, 22].

Some areas such as the basal ganglia, the pineal/habenular glands, other parts of choroid plexus and vascular structures tend to calcify with ageing [25]. As far as we know, the relationship between these calcifications and Boc FBCs has been also compared for the first time in our study.

The study aims to help prevent erroneous reporting by identifying the morphology of a not well-known variational anatomical structure's calcification 'Boc FBC'.

## MATERIALS AND METHODS

This study was approved by Muğla Sıtkı Koçman University Human Research Ethics Committee with the document number: 200027/2020. The design and conduct of the study were in accordance with the general principles set out in the Declaration of Helsinki. The patients who underwent CT scans between January 2016 and June 2021 for various indications were retrospectively evaluated in terms of Boc FBC and accompanying intracranial calcifications. All of the images were obtained from picture archiving communication systems.

Power analysis was performed with a G-power test. An appropriate sample size was calculated at 111 for creating 0.95 (actual power: 0.9503016, critical t: 1.6589535). Power ( $1-\beta$  prob) based on 0.05 alfa error prob. The number of patients in our study was sufficient. Two hundred sixty-four CTs of healthy patients ( $50.0 \pm \pm 24.78/0-92$  years old [mean  $\pm$  standard deviation/range]) as 120 (45.5%) females and 144 (54.5%) males were included in the study. We excluded 34 patients from the study because of the following medical reasons: 23 patients had different major pathologies (mass, infarct, aneurysm, infection, bleeding), 9 had history of operation, 2 had motion artifacts.

Cranial CT scans were performed with a 256-slice multi-detector CT scanner (Somatom, Siemens Healthcare, Erlangen, Germany). The protocol used for cranial CT is as follow: voltage/ampere: 120 kV/35 mA, applied radiation dose: 55–60 mGy, time interval: 1 Sn, slice thickness: 0.6 mm. Evaluation windows are width (W): 80, length (L): 40 for brain, W: 2800, L: 600 for temporal bones, W: 350–400, L: 20–60 for soft tissues.

Double-blind evaluation method was used in the study. Cranial CTs were evaluated separately by 2 radiologists. If a discrepancy was found in the evaluation's result, the cases were re-evaluated by both observers and a common consensus was achieved. The calcifications of fourth ventricle (CFV) were evaluated and classified according to anterior, posterior

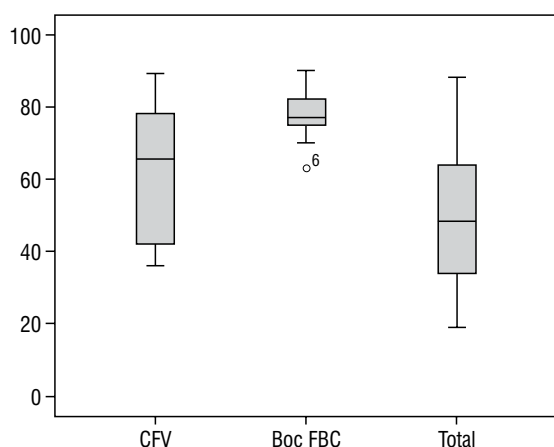


**Figure 1.** Box pilot figure shows age distribution of studied calcifications and study population; CFV — calcification of fourth ventricle; Boc FBC — calcification of foramen of Luschka/Bochdalek's flower basket calcification.

and lateral localisation. Both Boc FBCs were classified as unilateral and bilateral and the measurements were divided into three groups according to size of the calcifications: < 10 mm, between 5 mm and 10 mm, < 5 mm. If there was more than a 10% of difference between the sizes of the calcification, it was considered asymmetric, otherwise it was considered symmetrical. The morphological forms of the calcifications were also taken into account. They were classified into three different groups: linear, oval/nodular and conic. Besides, the presence of four common intracranial calcifications (calcifications of basal ganglion, habenular/pineal gland, choroid plexus, and vascular structures) was assessed. They were cross-matched with Boc FBC and associations were evaluated. The assessed calcifications are shown in Figure 1.

### Statistical analysis

The data were stored on a Microsoft Office Excel file (Excel 2010, Microsoft). Statistical software (SPSS, version 22.0, IBM) was used for analysis. Student's t-test was used for the means of normally distributed data, and Mann-Whitney U test was used for parametric data that did not show normal distribution. Pearson  $\chi^2$  analysis was performed to evaluate the relationship between the categorical variables.  $P \leq 0.05$  was considered significant.

## RESULTS

In 3.78% (10/264) of the patients wall CFV was found. Five of the them were located on the posterior

wall, 3 on the anterior wall and 2 on the lateral wall. Five of these 10 patients had concomitant Boc FBC, and all of them were bilateral. Out of 10 patients with CFV, 9 had also choroid plexus calcifications, 9 had pineal and/or habenular gland calcifications, 3 had basal ganglia calcifications and 2 of them had vertebral artery calcifications. The mean age of the patients with CFV was  $61.6 \pm 19.05$  years old and age range was 36–89 years old. Eight of the patients with CFV were males and 2 were females. There was statistically significant male predominance ( $p = 0.042$ ).

Boc FBC was detected in 22.35% of our sample (59/264) ( $72.6 \pm 12.9$ ; 8–92 years old [age  $\pm$  standard deviation; age range]). Out of 59 patients with Boc FBC, 5 (8.47%) had concomitant CFV. There was no statistically significant gender difference ( $p = 0.76$ ). 69.5% of the Boc FBCs were bilateral. 53.7% of bilateral Boc FBCs were symmetrical while 46.3% of them were asymmetric. 52.6% of unilateral Boc FBCs was located at right while 47.4% were at left. 57.7% of the calcifications were < 5 mm, 25.4% of the calcifications were between 5 mm and 10 mm, 16.9% of the calcifications were > 10 mm.

Shapes of Boc FBC were evaluated. 37.3% of the patients had conic shaped Boc FBCs. Regarding the conical-shaped calcifications, the percentage of calcifications whose size was > 10 mm, 5 mm to 10 mm and < 5 mm was 45.5%, 31.8%, and 22.7%, respectively.

For the Boc FB calcifications whose size was < 5 mm, 41.2% were linear, 44.1% were oval or nodular and 14.7% were conic. For the Boc FB calcifications whose size was > 5 mm, the rates of linear and conic forms were respectively at 32% and 68%. Oval/nodular calcifications were not present in this group. Boc FBCs were accompanied by calcifications of basal ganglia, pineal/habenular, choroid plexus and vascular structures. The rates of these calcifications were respectively 20.3%, 94.9%, 93.2% and 39%. When only the patients with Boc FBCs were taken into account ( $n = 59$ ), there were highly statistically significant correlations between Boc FBC and choroid plexus calcifications as well as pineal/habenular calcifications ( $p < 0.01$ ) but this relationship was not mutual. Out of all patients ( $n = 264$ ), basal ganglia, pineal/habenular, choroid plexus and vascular calcifications were seen respectively at the rate of 8.7% (23/264), 81.1% (214/264), 78.8% (208/264), 14.8% (39/264).

The rates of Boc FB in patients with basal ganglia calcifications and vascular structures calcifications

were respectively 52.2% (12/23) and 59% (23/39). In the comparison to other intracranial calcifications, the correlations between Boc FB and calcifications of the basal ganglia/vascular structures were statistically significant ( $p < 0.05$ ).

The rates of Boc FB in patients with pineal/habenular calcifications and choroid plexus calcifications were respectively 26.2% (56/214) and 26.4% (55/208). However, according to both Pearson  $\chi^2$  test and Whitney-Mann U tests, there was no statistically significant correlation for the latter ( $p > 0.05$ ).

Demographic, morphometric findings and relation with other intracranial calcifications are shown in Table 1.

As for CFV, Boc FBC and total population, age was taken into account. The distribution of age groups from largest to smallest was respectively CFV > Boc FB > study population. The distribution is shown with a box plot graphic in Figure 1.

## DISCUSSION

Boc FB is the overextension of the choroid plexus of the fourth ventricle towards the cerebellopontine angle. Bulbous terminal parts, also known as cornuopiae, are peripheral linear parts of Luschka where the choroid plexus is located and the farthest pieces that include choroid plexus tissue. Body and cornuopiae create an appearance similar to flower basket which gives the name of the anatomical structure [6]. Choroid plexus of the fourth ventricle originates from mesenchymal epithelium [19]. It is constituted by a central portion and lateral parts. The central portion is located on the posterior side of the fourth ventricle while the other parts cover the lateral faces [1, 13].

Anatomical definition is essential because calcifications occur in the same location as the choroid plexus. Foramen of Luschka is therefore a border between the lateral parts and Boc FB, if there is any [14, 24]. Boc FB was considered to be a blind-ending outward extension of the fourth ventricle choroid plexus when this structure was first described by Bochdalek. Later, it was understood that it includes linear structures [11, 19, 24].

In our study, we evaluated Boc FBC besides CFV. There was a significant difference between the frequency of Boc FBCs and CFV. While Boc FBCs were detected in 59 patients, only 10 patients had CFV. Boc FBC accompanied CFV in 50% of patients. But this relationship was not reciprocal. Out of all patients

**Table 1.** The characteristic and prevalence of Boc FBC and the associated calcifications

Parameter (n = 59)	Values	Percentage
Age $\pm$ standard deviation;	72.6 $\pm$ 12.9;	–
age range	8–92	
Gender (male/female)	29/30	49.2%/50.8%
Unilateral/bilateral	18/41	30.5%/69.5%
Symmetrical/asymmetric (bilateral)	22/19	53.7%/46.3%
Left/right (unilateral)	10/9	52.6%/47.4%
Size:		
> 10 mm	10	16.9%
5–10 mm	15	25.4%
< 5 mm	34	57.7%
Conic shape:		
Present	22	37.3%
Absent	37	62.7%
Diameter of conic shaped Boc FBC:		
> 10 mm	10	45.5%
5–10 mm	7	31.8%
< 5 mm	5	22.7%
Morphology of < 5 mm Boc FBC:		
Linear	14	41.2%
Oval or nodular	15	44.1%
Conic	5	14.7%
Morphology of > 5 mm Boc FBC:		
Linear	8	32.0%
Oval or nodular	0	–
Conic	17	68.0%
Basal ganglion calcifications:	12/59	
Present	12	20.3%
Absent	37	79.7%
Pineal habenular calcification:	56/59	
Present	56	94.9%
Absent	3	5.1%
Choroid plexus calcification:	55/59	
Present	55	93.2%
Absent	4	6.8%
Vertebral artery calcification:	23/59	
Present	23	39.0%
Absent	36	61.0%

Boc FBC — calcification of foramen of Luschka/Bochdalek's flower basket calcification

with Boc FBC, only 8.5% of patients had CFV. The samples are demonstrated in Figure 2.

Sharifi et al. [23] divided the Boc FBC into two parts which is similar to the definition of CFV. Ac-

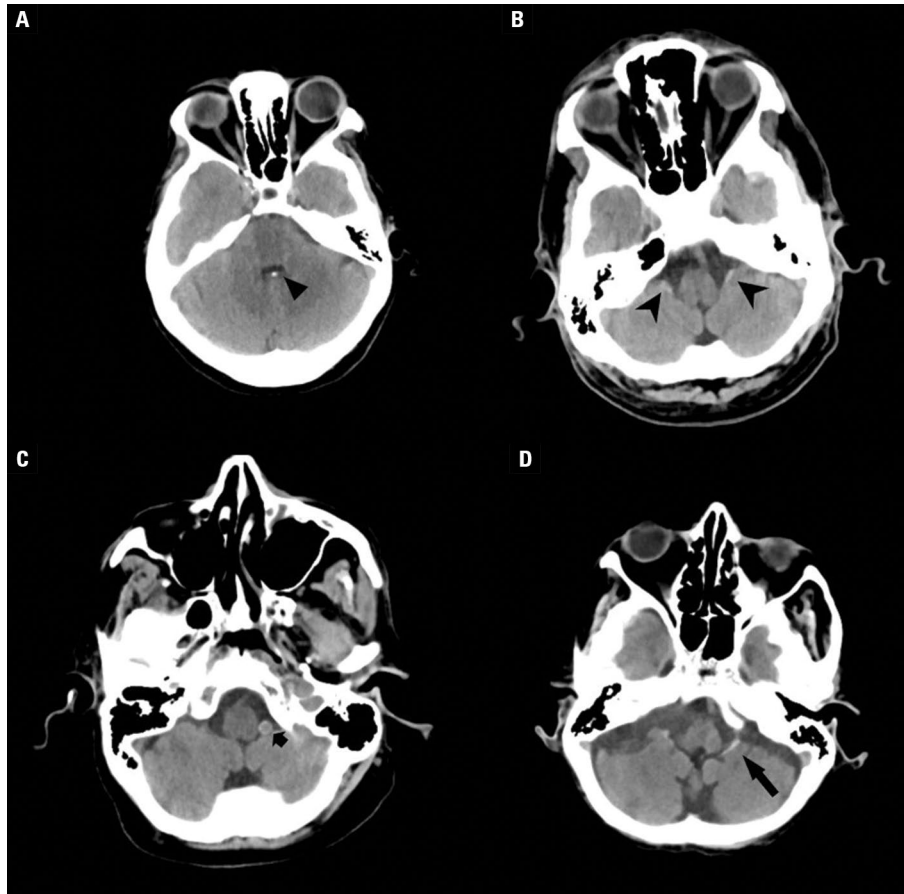


**Figure 2.** **A.** Point calcification (arrowhead) on the posterior wall of the fourth ventricle in 56-year-old female patient; **B.** Bilateral linear calcification of foramen of Luschka/Bochdalek's flower basket calcification (Boc FBC) in a 77-year-old female patient (cut arrowhead); **C.** A 84-year-old male patient with obvious circular left vertebral artery calcification (small arrowhead). Conical Luschka calcification on the left in a 65-year-old female patient (arrowhead).

According to this study, the average choroid plexus extension after the foramen of Luschka was about 5–6 mm. However, according to our study, especially in elderly patients, Boc FBCs extend to 2 cm far from the centre. This different result shows that tortuous basilar and vertebral artery calcifications can overlap with Boc FBCs in the cerebellopontine angle [23]. Bradac et al. [4] found symmetry between two sides of the choroid plexuses of the fourth ventricle in 96.5% of 57 brain dissections. Even though the choroid plexuses are symmetric, their calcification may not be symmetrical. In our study, CFVs were located at different points and asymmetric. Out of all the patients with Boc FBC, 30.5% had unilateral calcifications and only 53.7% of the patients that had bilateral calcifications presented symmetry.

Aneurysms, haemorrhages, cerebellopontine angle masses and tumours take part in the differential diagnosis of Boc FBCs on CT and MRI [11]. In our

study, Boc FBCs were conical shaped with a rate of 37.29%. This shape is not an appearance seen in the pathologies cited above for the differential diagnosis. In the case of the conical-shaped calcifications being over 5 mm, the ratio significantly increased (17/25; 68%). Conical shaped calcifications were never detected among the vertebral artery calcifications seen in the same region. According to our study, conical form is not seen in every patient but it is evidence of Boc FBC if any. As far as we know, it is a new sign and there is no information about this sign in the literature.

It is well known that MRI is better in the demonstration of the choroid plexus. CT cannot show clearly Boc FB. However, CT is superior to MRI in the detection of calcifications. For this reason, we preferred non-contrast CT instead of MRI [11, 24].

Among the patients with Boc FBCs, 94.91% were over 60 years of age. No Boc FBC was found in the

patients under 50; therefore, other diagnoses should be considered in this age group. In elder patients, vascular calcifications included in the differential diagnosis of Boc FBC are vertebral, basilar, anterior inferior cerebellar artery and posterior inferior cerebellar artery calcifications. Venous sinus calcifications may present similar appearances in the initial period. In younger patients, haemorrhages and calcified masses should be primarily considered in the differential diagnosis [5, 8–10, 21].

Intracranial calcifications are caused by calcium and iron deposition with ageing in especially highly vascularised localisations. They are almost always observed during CT examinations. In some cases, these can be linked to pathologies. However, they are often considered physiological when no concomitant disease can be identified [5, 7]. Since intracranial calcifications increase with age [2], they seem associated with the aging process [26].

Modic et al. [17] found that the incidence of lateral ventricular choroid plexus calcifications was 0.5% in the first decade and 86% in the eighth decade. In our study, Boc FBCs were compared with other intracranial calcifications. There is a high rate of association with choroid plexus calcifications and habenular/pineal calcifications. The association rate of Boc FB with choroid plexus calcifications, habenular/pineal calcifications, vertebral calcifications and basal ganglia calcifications was respectively 94.9%, 93.2%, 39.0%, and 20.3%.

Let's point that heterotopic ossification is a different entity that must be differentiated from calcifications. It refers to a large amount of bone and is seen mainly in the extremities. However, heterotopic ossifications may occur because of thermal traumas and surgical procedures of the intracranial region in the head or in soft tissue [20].

The study has some limitations. First, the study was retrospective and a limited number of patients had both MRI and CT; therefore, Boc FBCs were only assessed from CT and the volume of Boc FB omitted. Secondly, since the article length is limited, only the most common four intracranial calcifications were chosen and compared with Boc FBC.

## CONCLUSIONS

There are very limited studies about Boc FB and its calcifications. In other words, Boc FBCs are an underreported finding in the literature. This entity is important because it can be confused with very

important pathologies like haemorrhage or calcified masses. Although, it is reported that Boc FBs are symmetrical, according to our results their calcifications are rarely symmetrical. This condition has increased the margin of error. According to our study's results, Boc FBCs are seen in the advanced age group and not encountered under the age of 50. The conical form is seen in one-third of the cases but it is a very beneficial finding for distinguishing Boc FBC from other calcifications, if any. The advanced age group calcifications especially choroid plexus calcifications and pineal/habenular calcifications are highly associated with Boc FBC. In the case of the presence of CFV, Boc FBCs accompany at a high rate.

**Conflict of interest:** None declared

## REFERENCES

1. Adigun OO, Al-Dhahir MA. Anatomy, Head and Neck, Cerebrospinal Fluid. In: StatPearls [Internet]. Treasure Island (FL): StatPearls Publishing; 2022 Jan. 2021 Jul 26.
2. Al-Ameri L, Al-Zuhairi E, Al-Shirwani H. Prevalence of pineal gland and choroid plexus calcification among iraqi patients attending CT scan units. *Int J Morphol.* 2021; 39(1): 244–251, doi: [10.4067/s0717-95022021000100244](https://doi.org/10.4067/s0717-95022021000100244).
3. Barany L, Baksa G, Patonay L, et al. Morphometry and microsurgical anatomy of Bochdalek's flower basket and the related structures of the cerebellopontine angle. *Acta Neurochir (Wien).* 2017; 159(8): 1539–1545, doi: [10.1007/s00701-017-3234-9](https://doi.org/10.1007/s00701-017-3234-9), indexed in Pubmed: [28584917](https://pubmed.ncbi.nlm.nih.gov/28584917/).
4. Bradac GB, Simon RS, Fiegler W, et al. A radioanatomical study of the choroid plexus of the fourth ventricle. *Neuroradiology.* 1976; 11(2): 87–91, doi: [10.1007/BF00345019](https://doi.org/10.1007/BF00345019), indexed in Pubmed: [948365](https://pubmed.ncbi.nlm.nih.gov/948365/).
5. Daghighi MH, Rezaei V, Zarrintan S, et al. Intracranial physiological calcifications in adults on computed tomography in Tabriz, Iran. *Folia Morphol.* 2007; 66(2): 115–119, indexed in Pubmed: [17594669](https://pubmed.ncbi.nlm.nih.gov/17594669/).
6. Engelhardt E, Moreira DM. Bochdalek's flower basket. *Rev Bras Neurol.* 2019; 55(3).
7. Granger A, Kim S, Kollias T, et al. Ossification of the falx cerebri: A review. *Transl Res Anat.* 2017; 7: 20–22, doi: [10.1016/j.tria.2017.06.004](https://doi.org/10.1016/j.tria.2017.06.004).
8. Guo Z, Li D, Xie Y, et al. Secondary cerebellopontine angle oligodendroglioma after cranial irradiation: A case report and literature review. *Int J Neurosci.* 2021 [Epub ahead of print]: 1–7, doi: [10.1080/00207454.2021.1929209](https://doi.org/10.1080/00207454.2021.1929209), indexed in Pubmed: [33975502](https://pubmed.ncbi.nlm.nih.gov/33975502/).
9. Hirata T, Umekawa M, Sato K, et al. Isolated intracranial mass lesion near the foramen of Luschka: An unusual presentation of granulomatosis with polyangiitis. *Interdisciplinary Neurosurgery.* 2021; 25: 101106, doi: [10.1016/j.inat.2021.101106](https://doi.org/10.1016/j.inat.2021.101106).
10. Hodges TR, Karikari IO, Nimjee SM, et al. Calcifying pseudoneoplasm of the cerebellopontine angle: case report. *Neurosurgery.* 2011; 69(1 Suppl Operative): onsE117–onsE120, doi: [10.1227/NEU.0b013e3182155511](https://doi.org/10.1227/NEU.0b013e3182155511), indexed in Pubmed: [21415795](https://pubmed.ncbi.nlm.nih.gov/21415795/).

11. Horsburgh A, Kirillos RW, Massoud TF. Bochdalek's flower basket: applied neuroimaging morphometry and variants of choroid plexus in the cerebellopontine angles. *Neuroradiology*. 2012; 54(12): 1341–1346, doi: [10.1007/s00234-012-1065-1](https://doi.org/10.1007/s00234-012-1065-1), indexed in Pubmed: [22777194](https://pubmed.ncbi.nlm.nih.gov/22777194/).
12. Hubert V, Chauveau F, Dumot C, et al. Clinical imaging of choroid plexus in health and in brain disorders: a mini-review. *Front Mol Neurosci*. 2019; 12: 34, doi: [10.3389/fnmol.2019.00034](https://doi.org/10.3389/fnmol.2019.00034), indexed in Pubmed: [30809124](https://pubmed.ncbi.nlm.nih.gov/30809124/).
13. Johal J, Paulk PB, Oakes PC, et al. A comprehensive review of the foramina of Luschka: history, anatomy, embryology, and surgery. *Childs Nerv Syst*. 2017; 33(9): 1459–1462, doi: [10.1007/s00381-017-3480-4](https://doi.org/10.1007/s00381-017-3480-4), indexed in Pubmed: [28676975](https://pubmed.ncbi.nlm.nih.gov/28676975/).
14. Johansson PA. The choroid plexuses and their impact on developmental neurogenesis. *Front Neurosci*. 2014; 8: 340, doi: [10.3389/fnins.2014.00340](https://doi.org/10.3389/fnins.2014.00340), indexed in Pubmed: [25386116](https://pubmed.ncbi.nlm.nih.gov/25386116/).
15. Kiroğlu Y, Callı C, Karabulut N, et al. Intracranial calcifications on CT. *Diagn Interv Radiol*. 2010; 16(4): 263–269, doi: [10.4261/1305-3825.DIR.2626-09.1](https://doi.org/10.4261/1305-3825.DIR.2626-09.1), indexed in Pubmed: [20027545](https://pubmed.ncbi.nlm.nih.gov/20027545/).
16. Loukas M, El-Sedfy A, Tubbs RS, et al. Vincent Alexander Bochdalek (1801-1883). *World J Surg*. 2008; 32(10): 2324–2326, doi: [10.1007/s00268-008-9686-6](https://doi.org/10.1007/s00268-008-9686-6), indexed in Pubmed: [18642043](https://pubmed.ncbi.nlm.nih.gov/18642043/).
17. Modic MT, Weinstein MA, Rothner AD, et al. Calcification of the choroid plexus visualized by computed tomography. *Radiology*. 1980; 135(2): 369–372, doi: [10.1148/radiology.135.2.7367628](https://doi.org/10.1148/radiology.135.2.7367628), indexed in Pubmed: [7367628](https://pubmed.ncbi.nlm.nih.gov/7367628/).
18. Nakagawa T, Arita H, Kijima N, et al. Primary central nervous system lymphoma of the bilateral Bochdalek's flower baskets: A case report. *Interdisciplinary Neurosurgery*. 2020; 21: 100756, doi: [10.1016/j.inat.2020.100756](https://doi.org/10.1016/j.inat.2020.100756).
19. Paladini D. The hidden story of the fourth ventricular choroid plexus: the flower basket of an old anatomist.... *Ultrasound Obstet Gynecol*. 2021; 58(4): 505–508, doi: [10.1002/uog.23726](https://doi.org/10.1002/uog.23726), indexed in Pubmed: [34173694](https://pubmed.ncbi.nlm.nih.gov/34173694/).
20. Peters N, Baltin C, Barham M, et al. An unusual finding: Heterotopic ossification located in the subcutis of the iliac region – A case report in the context of current literature. *Transl Res Anat*. 2021; 25: 100137, doi: [10.1016/j.tria.2021.100137](https://doi.org/10.1016/j.tria.2021.100137).
21. Rao P, Thibodeau R, Jafroodifar A, et al. Hypervascular vestibular schwannoma: A case report and review of the literature. *Radiol Case Rep*. 2021; 16(10): 2841–2846, doi: [10.1016/j.radcr.2021.06.082](https://doi.org/10.1016/j.radcr.2021.06.082), indexed in Pubmed: [34401010](https://pubmed.ncbi.nlm.nih.gov/34401010/).
22. Saade C, Najem E, Asmar K, et al. Intracranial calcifications on CT: an updated review. *J Radiol Case Rep*. 2019; 13(8): 1–18, doi: [10.3941/jrcr.v13i8.3633](https://doi.org/10.3941/jrcr.v13i8.3633), indexed in Pubmed: [31558966](https://pubmed.ncbi.nlm.nih.gov/31558966/).
23. Sharifi M, Ungier E, Cizek B, et al. Microsurgical anatomy of the foramen of Luschka in the cerebellopontine angle, and its vascular supply. *Surg Radiol Anat*. 2009; 31(6): 431–437, doi: [10.1007/s00276-009-0464-4](https://doi.org/10.1007/s00276-009-0464-4), indexed in Pubmed: [19190846](https://pubmed.ncbi.nlm.nih.gov/19190846/).
24. Tubbs RS, Shoja MM, Aggarwal A, et al. Choroid plexus of the fourth ventricle: Review and anatomic study highlighting anatomical variations. *J Clin Neurosci*. 2016; 26: 79–83, doi: [10.1016/j.jocn.2015.10.006](https://doi.org/10.1016/j.jocn.2015.10.006), indexed in Pubmed: [26675624](https://pubmed.ncbi.nlm.nih.gov/26675624/).
25. Yalcin A, Ceylan M, Bayraktutan OF, et al. Age and gender related prevalence of intracranial calcifications in CT imaging; data from 12,000 healthy subjects. *J Chem Neuroanat*. 2016; 78: 20–24, doi: [10.1016/j.jchemneu.2016.07.008](https://doi.org/10.1016/j.jchemneu.2016.07.008), indexed in Pubmed: [27475519](https://pubmed.ncbi.nlm.nih.gov/27475519/).
26. Żytkowski A, Skrzat J, Mazurek A, et al. Clinical relevance of the caroticoclinoid foramen: a case report and concise literature review. *Transl Res Anat*. 2021; 25: 100153, doi: [10.1016/j.tria.2021.100153](https://doi.org/10.1016/j.tria.2021.100153).

# Inferior oblique muscle of the eye: its foetal development with special reference to understanding of the frequent variants in adults

Z.W. Jin<sup>1</sup>, S. Umeki<sup>2</sup>, Y. Takeuchi<sup>2</sup>, M. Yamamoto<sup>2</sup>, G. Murakami<sup>2, 3</sup>,  
S. Abe<sup>2</sup>, J.F. Rodríguez-Vázquez<sup>4</sup>

<sup>1</sup>Department of Anatomy, Wuxi School of Medicine, Jiangnan University, Wuxi, China

<sup>2</sup>Department of Anatomy, Tokyo Dental College, Tokyo, Japan

<sup>3</sup>Division of Internal Medicine, Cupid Clinic, Iwamizawa, Japan

<sup>4</sup>Department of Anatomy and Embryology, School of Medicine, Complutense University, Madrid, Spain

[Received: 13 March 2021; Accepted: 9 April 2021; Early publication date: 28 April 2021]

**Background and Materials and methods:** To provide better understanding of frequent variations of the inferior oblique (IO) of adult extraocular muscles, we observed sagittal and horizontal histological sections of the eye and orbits from 32 fetuses (7–34 weeks of gestational age; 24–295 mm of crown-rump length).

**Results:** In early fetuses (7–8 weeks), the IO was restricted at an antero-infero-medial angle of the future orbit. In contrast to extraocular recti, the IO appeared to extend along the mediolateral axis and had no definite tendon. At midterm, the IO tendon became evident. Sometimes, the IO muscle belly attached to the inferior rectus or, the IO tendon divided into two laminae to enclose the lateral rectus. At late-term, a multilayered sheath was evident around the sclera and, via one or some of the fascial layers, the IO was communicated with a fascia enclosing the inferior rectus. At midterm and late-term, the IO originated not only from the maxilla near the orbicularis oculi origin but also from a vein-rich fibrous tissue around the lacrimal sac. Both origins were muscular without intermittent tendon or ligament. Therefore, the fascial connection as well as a direct contact between the IO and the inferior or lateral rectus seemed to provide variant muscular bridges as reported in adults. Moreover, the two attachment sites at the origin seemed to provide double muscle bellies of the adult IO.

**Conclusions:** Consequently, the present specimens contained seeds of any types of adult variations. The muscle fibres from the lacrimal sac might play a role for the lacrimal drainage. (Folia Morphol 2022; 81, 2: 442–450)

**Key words:** inferior oblique muscle of the eye, inferior rectus, lateral rectus, human foetus, muscular bridge, double muscle bellies

## INTRODUCTION

The inferior oblique muscle (IO) shows anatomic variations most frequently in extraocular muscles [8].

The IO is usually or often composed of double or multiple muscle bellies: 8% in DeAngelis and Kraft [1]; 17% in DeAngelis et al. [2]; more than 90% in Yalcin

Address for correspondence: Z.W. Jin, MD, PhD, Department of Anatomy, Wuxi School of Medicine, Jiangnan University, 1800 Lihu Avenue, Wuxi, Jiangsu, 214122, China, tel: +86-510-8519-7079, fax: +86-510-8519-3570, e-mail: zwjin@jiangnan.edu.cn

This article is available in open access under Creative Commons Attribution-Non-Commercial-No Derivatives 4.0 International (CC BY-NC-ND 4.0) license, allowing to download articles and share them with others as long as they credit the authors and the publisher, but without permission to change them in any way or use them commercially.

and Ozan [14]. A muscular bridge was also reported between the IO and inferior rectus: 6.6% in Yalçın et al. [13]. The obliquus accessorius inferior is also known originating from the orbital apex and inserting to a site adjacent to the inferior rectus insertion [8] although it is similar to the inferior rectus rather than the IO. In contrast to the usual close relation with the inferior rectus at the insertion, two case reports demonstrated the IO insertion near or adjacent to the lateral rectus insertion [8]. The first aim of this study was to provide better understanding as to why and how the frequent variants occur in foetal development of the IO.

Another interest of the foetal IO was the muscle belly wrapping around the eyeball: the morphology is quite different from the superior oblique muscle in which a cartilaginous pulley, the trochlea, makes the acute turn of the tendon. Our group hypothesized that the superior oblique tendon is “secondarily” attached to and turned by the trochlea due to rotation of the foetal eyeball [7]. Harayama et al. [6], on the basis of detailed morphometrical data, concluded that medial rotation of the eye ball occurs at 12 weeks and at a stage between 16 and 19 weeks of gestation. De Haan et al. [3] also described the rotation in the prenatal stage. The second aim of this study was to describe a developmental process to form the curved IO belly extending along the eyeball. In contrast to the four recti and levator palpebrae superioris, previous descriptions on the foetal IO were very limited [12].

## MATERIALS AND METHODS

This study was conducted in accordance with the Declaration of Helsinki 1995 (as revised in 2013). We examined paraffin-embedded histological sections from 32 foetuses (7–34 weeks of gestational age [GA]; 24–295 mm of crown-rump length [CRL]). The specimens were categorised into three groups according to age and size: 1) 7 early foetuses at GA 7–8 weeks (CRL 24–35 mm; O’Rahilly’s stage 21–23); 2) 18 midterm foetuses at GA 12–15 weeks (CRL 71–115 mm); 4) 7 late-term foetuses at GA 25–34 weeks (CRL 200–295 mm). All sections were part of the large collection kept at the Department of Anatomy of the Universidad Complutense, Madrid, and were the results of miscarriages and ectopic pregnancies from the Department of Obstetrics of the University. Sections of the embryos, early foetuses and midterm foetuses had been prepared serially, while the late-

stage foetuses had been sectioned 50 or 100 micron interval. The sections were stained with haematoxylin and eosin (HE) or Azan. The sectional plane was often sagittal (26 specimens) and sometimes horizontal (4 of midterm foetuses; 2 of late-term foetuses). This study was approved by the Ethics Committee of Complutense University (B08/374). Most photographs were taken with a Nikon Eclipse 80.

## RESULTS

### Observations of sagittal sections from 7 early foetuses

At GA 7 weeks (Fig. 1), the IO was restricted at a small area near the medial angle of the conjunctiva: this site corresponded to an antero-infero-medial angle of the future orbit. In contrast to the extraocular rectus muscles along the long axis of the developing eyeball, the IO extended along the medio-lateral axis. Thus, in sagittal sections, the IO was cut transversely, while the rectus longitudinally (Fig. 1D, H). The IO was located outside of and inferior to the inferior rectus.

At GA 8 weeks (Fig. 2), the extraocular recti had a distinct tendon to merge with the dense, anterior part of the sclera (Fig. 2C). In contrast, the IO carried no definite tendon and the posterior end dispersed into a loose, posterior part of the sclera (Fig. 2E). The posterior part of the IO was close to the lateral rectus muscle belly (Fig. 2E). The IO muscle belly crossed obliquely in the lateral side of the inferior rectus and extended posterosuperiorly to wrap around the eyeball (Fig. 2B, F). Thus, the IO obtained the final curved course along the eyeball as earlier as the extraocular rect. No cartilage or membranous bone appeared at an antero-infero-medial angle of the future orbit. The orbicularis oculi muscle was separated from the IO origin by a loose mesenchymal tissue (Fig. 2A). Likewise, no hard tissue separated the IO from the infraorbital nerve (Fig. 2G). The IO origin still took a tendon-like appearance at the anterior end (Fig. 2A).

### Observations of sagittal sections from 14 midterm foetuses

At GA 12–15 weeks, the IO originated from the maxilla near the origin of the pars orbitalis of the orbicularis oculi muscle and both muscle origins sandwiched a dense fibrous tissue (Fig. 3). The IO origin was muscular: thus, each muscle fibres appeared to attach to the fibrous tissue. The IO tendon merged with

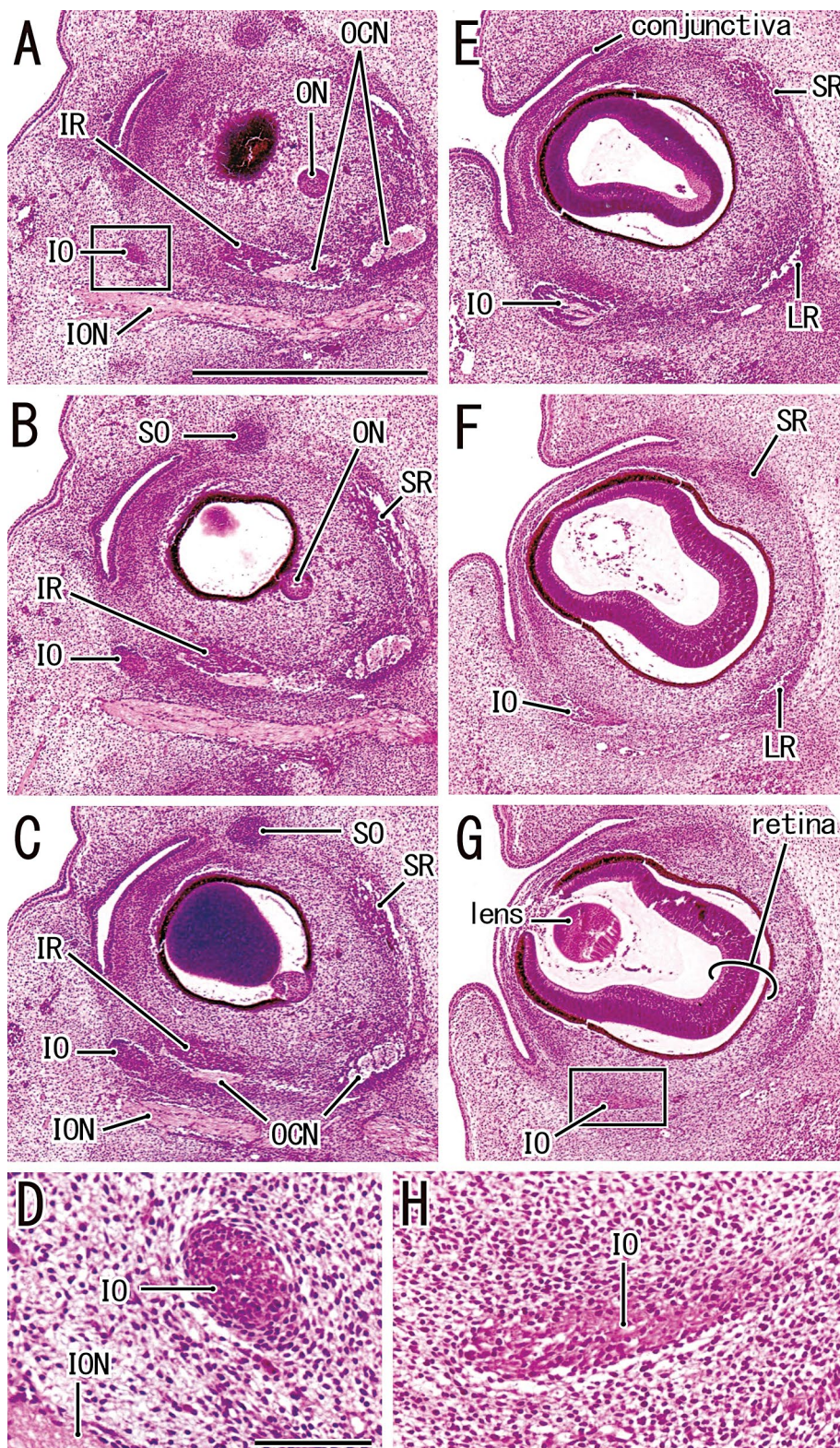


**Figure 1. A–H.** Inferior oblique muscle in an embryo of 24 mm crown-rump length. Sagittal sections. Haematoxylin and eosin staining. Panel A displays the most medial plane in the figure. Panels D and H are higher magnification views of squares in panels A and G, respectively. A future muscle origin of the inferior oblique (IO) is a dense mesenchymal condensation near the infraorbital nerve (ION), but no cartilaginous tissue is developed at the origin (panels A and D). A future insertion of the IO is identified as a primitive tendon-like band in the inferior side of the eyeball (panels G and H). Panels A–C and E–G (or panels D and H) were prepared at the same magnification. Scale bars: 1 mm in panel A and 0.1 mm in panel D; IR — inferior rectus; IO — inferior obliquus; ION — infraorbital nerve; LB — lacrimal bone; LR — lateral rectus; LS — lacrimal sac; MX — maxilla; NLD — nasolacrimal duct; OCN — oculomotor nerve; ON — optic nerve; OO — orbicularis oculi; SO — superior obliquus; SR — superior rectus.

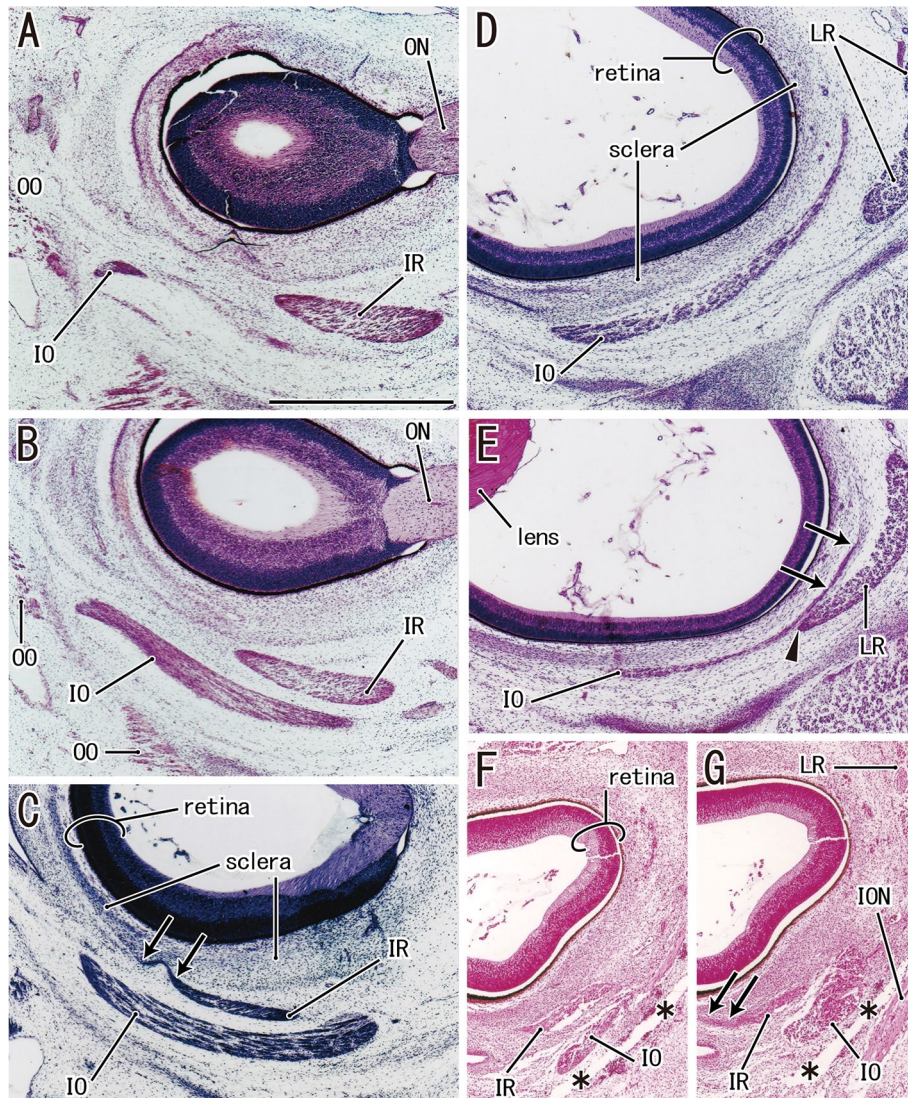


**Figure 2. A–G.** Inferior obliquus muscle in early fetuses of 35 and 38 mm crown-rump length, respectively. Haematoxylin and eosin staining (panels A, B, D–G) or Azan staining (panel C). Panels A–E display sagittal sections from a foetus of 38 mm, while panels F and G a foetus of 35 mm. Panel A displays the most medial plane in the former specimen. Origins of the inferior obliquus (IO) and orbicularis oculi (OO) sandwich a loose mesenchymal tissue (panel A). A tendinous insertion of the inferior rectus (IR) merges with a dense tissue of the sclera anterior part (arrows in panel C), while that of the inferior obliquus disperses in a loose tissue of the sclera posterior part (arrows in panel E). Near the insertion, the inferior obliquus and lateral rectus (LR) are closely located (arrowhead in panel E). Panels F and G exhibit a crossing between the inferior rectus and obliquus muscles. Arrows in panel G indicate an initial tendon of the inferior rectus. Asterisks in panels F and G indicate an artefact space produced during histological procedure. All panels were prepared at the same magnification (scale bar in panel A: 1 mm). Other abbreviation — see Figure 1.

the posterior part of the sclera (Fig. 3D, E), while the inferior rectus inserted to the anterior part (Fig. 3C). The sclera appeared to be dense and homogeneous in the anterior part, while the posterior part was still composed of a relatively loose bundle of irregular fibres. We found two types of the IO variations: 1) the IO muscle belly attached to the inferior rectus in 1 specimen (Fig. 3A) and 2) the IO tendon divided into two laminae to enclose the lateral rectus in two specimens (Fig. 3F).

#### Observations of sagittal sections from 5 late-term fetuses

A multilayered sheath or fascia was much or less evident around the sclera (Figs. 4, 5): a thick fascia from the conjunctiva was particularly thick and it extended posteriorly to disperse into: 1) the orbital fat (Figs. 4B, 5B), 2) a fascia covering the IO (Fig. 4D) and/or 3) a fascia enclosing the inferior rectus (Fig. 5C). The fascia covering the IO was communicated with the other fascia enclosing the inferior rectus

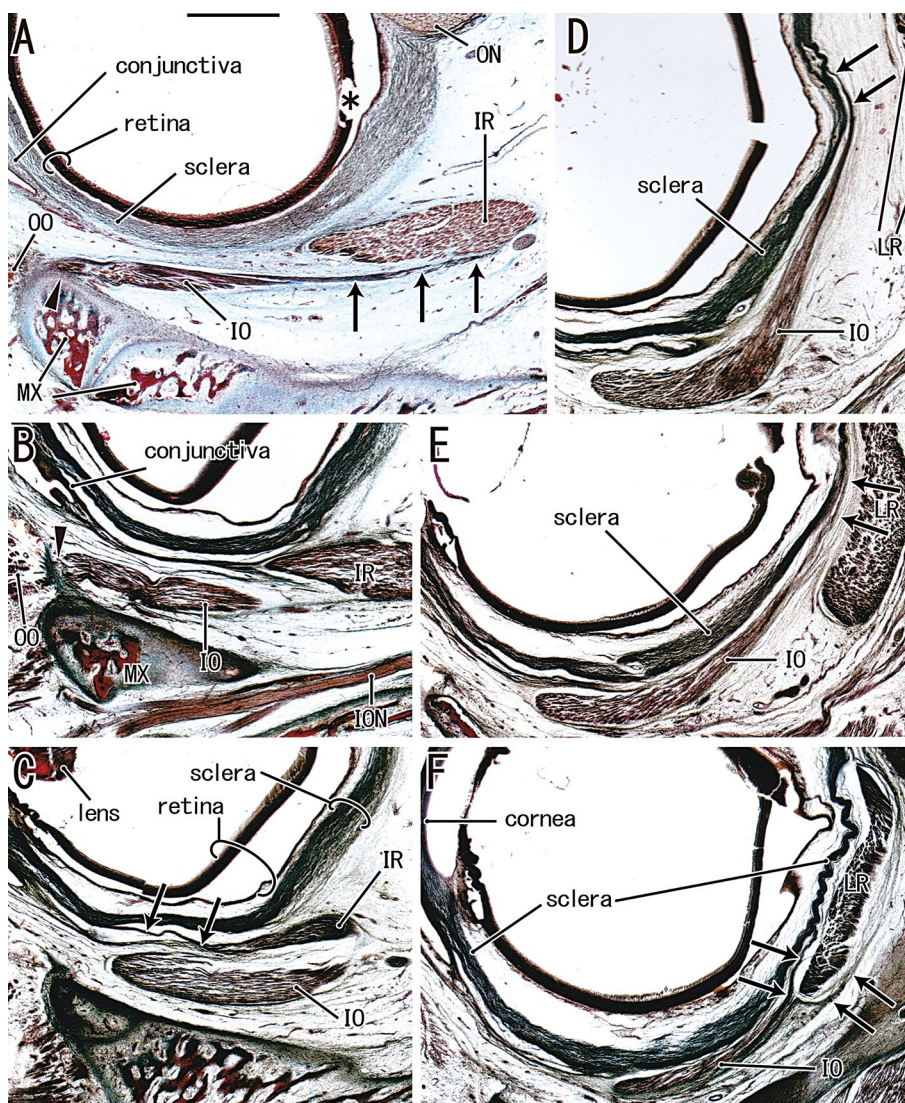


**Figure 3. A–F.** Inferior oblique muscle in two mid-term fetuses of 92 and 97 mm crown-rump length, respectively. Panels A (Azan staining) displays a sagittal section from a foetus of 92 mm, while panels B–F (Azan but long years after staining) a foetus of 97 mm. Panel B displays the most medial plane in the latter specimen. Origins of the inferior oblique (IO; arrowhead) and orbicularis oculi (OO) are muscular and they sandwiched a band-like tissue attaching to the maxilla (MX; panels A and B). In the former foetus, the inferior oblique appears to attach to the inferior rectus (arrows in panel A). In the latter foetus, a tendinous insertion of the inferior oblique not only joins the sclera (arrows in panels D and E) but divides into two laminae to enclose the lateral rectus (LR; arrows in panel F). The inferior rectus (IR) makes a tendinous insertion to the sclera (arrows in panel C). Asterisk in panel A indicates an artifact space produced during histological procedure. All panels were prepared at the same magnification (scale bar in panel A: 1 mm). Other abbreviation — see Figure 1.

(Fig. 4A, 5C). The sclera was composed of regularly-arrayed fibres (Fig. 4F, 5G). The IO tendon merged with the most external layer of the sclera (Figs. 4F, 5G). At the origin from the maxilla, the IO and orbicularis oculi sandwiched a dense fibrous tissue (Fig. 5A). Because of no connection to either the tarsal plate or lacrimal sac, this tissue did not correspond to a part of the medial palpebral ligament. The orbicularis oculi originated not only from the maxilla but from the lacrimal bone (Fig. 5C, D).

#### Observations of horizontal sections from 4 mid-term and 2 late-term fetuses

Horizontal sections well demonstrated an entire area of the IO covering the eyeball as well as an almost anteroposterior direction of the muscle fibres (Fig. 6). However, sagittal sections were better useful than horizontal sections for demonstrations of the curved muscle belly wrapping around the eyeball. Notably, all of the six specimens for horizontal sections carried two muscle attachments at the antero-infero-medial



**Figure 4. A–F.** Inferior obliquus muscle in a late-term foetus of 270 mm crown-rump length. Haematoxylin and eosin staining. Sagittal sections. Panel A displays the most medial plane in the figure. Panels E and F are higher magnification views of squares in panel B. Panel A shows a muscular origin of the inferior obliquus (IO; arrowhead). The inferior rectus (IR) connects with the inferior obliquus by a fascia (arrows in panels B and C). The inferior rectus (IR in panel E) as well as the inferior obliquus tendon (arrows in panel F) inserts to the sclera. A multi-layered sheath covers the sclera (panels E and F) and some of them enclose the inferior obliquus (panel D). Panels A–D (or panels E and F) were prepared at the same magnification (scale bars: 1 mm in panels A and E). Other abbreviation — see Figure 1.

angle of the orbit: 1) a major muscle origin from the maxilla (see the subsection above) and 2) another origin from a fibrous tissue around the lacrimal sac. The latter tissue was still mesenchymal at midterm (Fig. 6C), but at late-term, muscle fibres appeared to intermingle with the vein-rich fibrous tissue around the lacrimal sac (Fig. 6F).

## DISCUSSION

The adult IO frequently shows anatomic variations (see the Introduction). According to the present observation of foetus sections, the fascial connection as well as a direct contact between the IO and the inferior or lateral rectus seemed to provide variant muscular bridges as reported in adults. Moreover, the

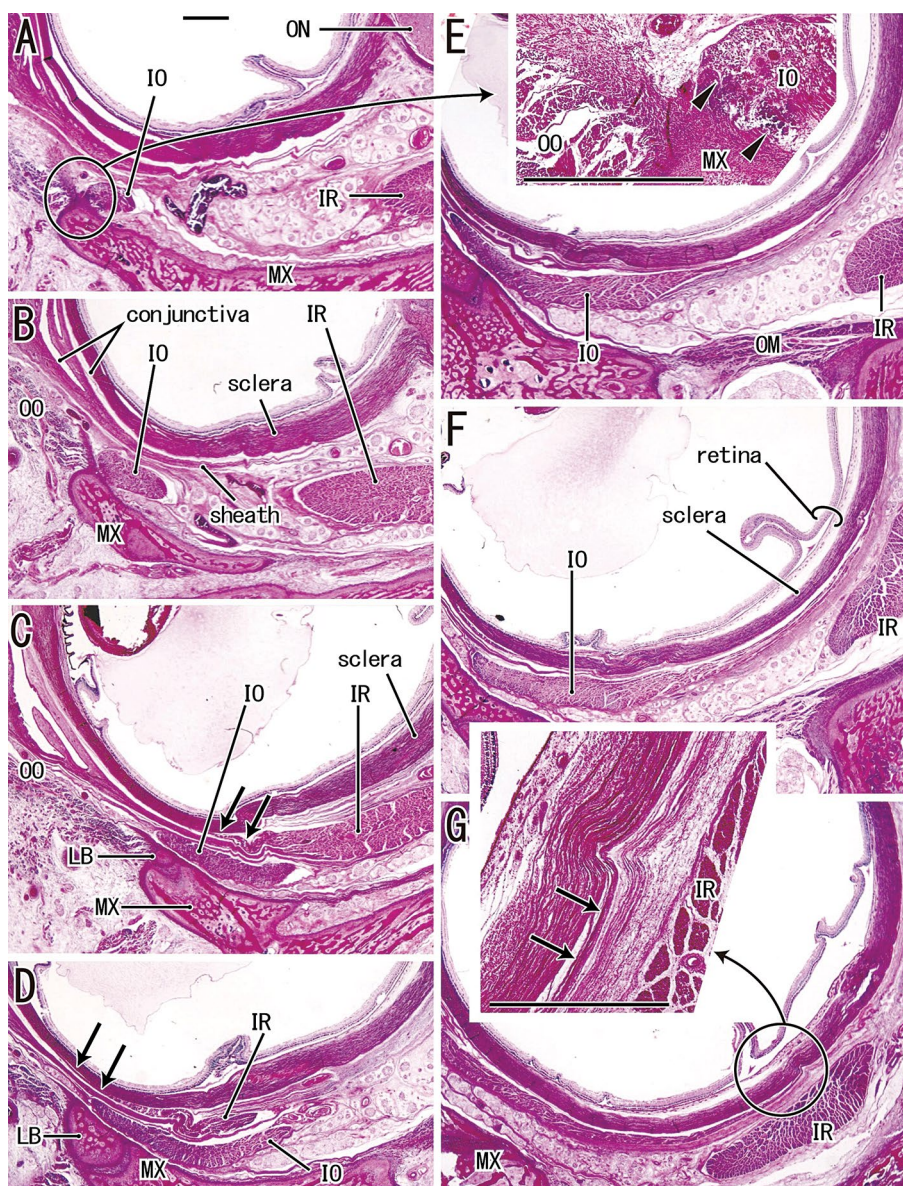


**Figure 5. A–G.** Inferior oblique muscle in a late-term foetus of 276 mm crown-rump length. Haematoxylin and eosin staining. Sagittal sections. Panel A displays the most medial plane in the figure. Inserts in panels E and G are higher magnification views of a circle in panels A and G, respectively. Panel A shows a muscular origin of the inferior oblique (IO; arrowheads in the insert), while panel G exhibits the insertion to the sclera (arrows in the insert). The inferior rectus (IR) inserts to the sclera (arrows in panels C and D). Outside of the sclera, a thick sheath is seen connecting to the conjunctiva (panel B): it covers the inferior rectus in panels C and D. Panels A–G (or two inserts) were prepared at the same magnification (scale bars: 1 mm in panels A and the inserts). Other abbreviation — see Figure 1.

two attachment sites at the origin seemed to cause “tears” of muscle belly to provide double or multiple muscle bundles in adults. Therefore, in spite of the limited number, the present specimens contained seeds of any types of adult variations. In general, numerous variations have been reported in skeletal muscles. Although it is a small striated muscle without contribution to a joint movement, the IO seemed to be the best sample for presentation of a hypothetical

association between the foetal development and the adult variants.

At GA 7 weeks, the IO appeared to extend along the mediolateral axis: this direction was quite different from the extraocular recti extending along the anteroposterior axis. In spite of the early difference, the expanding eyeball made both of the recti and IO take curved courses at GA 8 weeks. A tissue of the sclera was dense in the anterior part near the con-

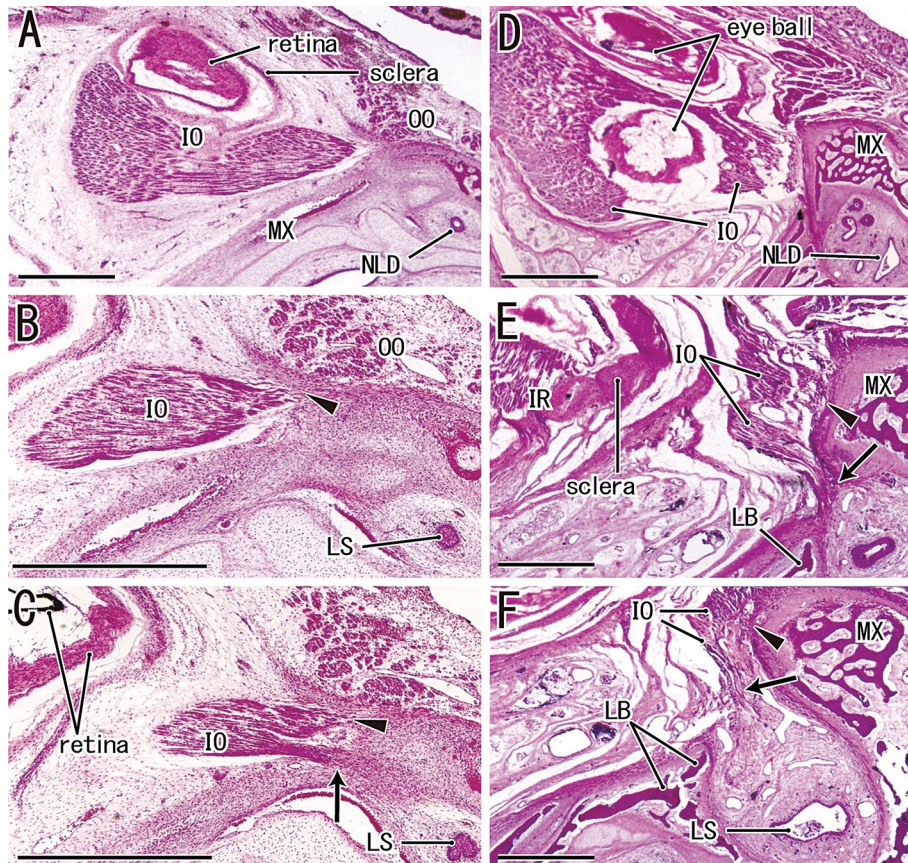


**Figure 6. A–F.** Double attachment sites at the origin of the inferior obliquus muscle at mid-term and late-term. Haematoxylin and eosin staining. Horizontal sections. Panels A–C, a specimen of 118 mm crown-rump length (CRL); panels D–F, a specimen of 262 mm CRL. Panel A or D displays the most inferior site in each specimen. Arrowhead (panels B, C, E, F) indicates the muscle origin from the maxilla (MX), while arrow (panels C, E, F) another origin from a fibrous tissue around the lacrimal sac (LS). In panel D, the eye ball was cut at two sites because of an artefact bending with shrinkage after death. All scale bars, 1 mm. Other abbreviation — see Figure 1.

junctiva and loose in the posterior part still at mid-term. Thus, the muscle insertion established earlier in the recti than the IO. Therefore, a traction by the insertion seemed to play a little role for developing muscles wrapping around the eyeball. The expanding eyeball was most likely to directly push the muscle belly to be curved.

The IO arose from two structures in foetuses: a major muscle bundle from the maxilla and 2) a minor part from a vein-rich fibrous tissue around the lacrimal sac. This dual origin seemed not to be known in adults [5, 11, 15]. Not the IO but the orbicularis oculi lacrimal part originates from the lacrimal sac according to these textbooks. We did not deny a possibility that the minor origin of the IO would be degenerated after birth. However, at least in newborns, the IO muscle fibres from the lacrimal sac might play a role for the lacrimal drainage.

The muscle insertion morphology in late-term foetuses was different from the adult one: not only the IO but the extraocular recti carried definite tendons in contrast to unclear tendons of the adult recti [11, 15]. After birth, the rectus insertion would change to form the so-called extraocular muscle pulley system [4, 9]. We demonstrated a multilayered sheath outside of the sclera at late-term: the thickest fascia to the conjunctiva was similar to the developing check ligament [10]. However, according to the connection to the inferior rectus, it seemed to correspond to the suspensory ligament of the eye [11].

#### Acknowledgements

This work was supported by Six Talent Peaks Project in Jiangsu Province (SZCY-001) and Wuxi Modern Industrial Development Funding (N20202008).

**Conflict of interest:** None declared

## REFERENCES

1. Deangelis DD, Kraft SP. The double-bellied inferior oblique muscle: clinical correlates. *J AAPOS*. 2001; 5(2): 76–81, doi: [10.1067/mpa.2001.111780](https://doi.org/10.1067/mpa.2001.111780), indexed in Pubmed: [11304813](https://pubmed.ncbi.nlm.nih.gov/11304813/).
2. De Angelis D, Makar I, Kraft S. Anatomic variations of the inferior oblique muscle: a potential cause of failed inferior oblique weakening surgery. *Am J Ophthalmol*. 1999; 128(4): 485–488, doi: [10.1016/s0002-9394\(99\)00225-1](https://doi.org/10.1016/s0002-9394(99)00225-1).
3. de Haan AB, Willekens B, Klooster J, et al. The prenatal development of the human orbit. *Strabismus*. 2006; 14(1): 51–56, doi: [10.1080/09273970600579788](https://doi.org/10.1080/09273970600579788), indexed in Pubmed: [16513570](https://pubmed.ncbi.nlm.nih.gov/16513570/).
4. Demer JL, Miller JM, Poukens V, et al. Evidence for fibromuscular pulleys of the recti extraocular muscles. *Invest Ophthalmol Vis Sci*. 1995; 36(6): 1125–1136, indexed in Pubmed: [7730022](https://pubmed.ncbi.nlm.nih.gov/7730022/).
5. Dutton JJ. *Atlas of clinical and surgical orbital anatomy*. WB Saunders, Philadelphia 2011.
6. Harayama K, Amemiya T, Nishimura H. Development of rectus muscles during fetal life: insertion sites and width. *Invest Ophthalmol Vis Sci*. 1980; 19(5): 468–474, indexed in Pubmed: [7372413](https://pubmed.ncbi.nlm.nih.gov/7372413/).
7. Katori Y, Rodríguez-Vázquez JF, Kawase T, et al. Early fetal development of hard tissue pulleys for the human superior oblique and tensor veli palatini muscles. *Ann Anat*. 2011; 193(2): 127–133, doi: [10.1016/j.aanat.2011.01.004](https://doi.org/10.1016/j.aanat.2011.01.004), indexed in Pubmed: [21334866](https://pubmed.ncbi.nlm.nih.gov/21334866/).
8. Kocabiyik N. Orbital muscles. In *Bergman's comprehensive encyclopedia of human anatomic variations*. 1st ed. Wiley & Sons 2016: 207–211.
9. Kono R, Poukens V, Demer JL. Quantitative analysis of the structure of the human extraocular muscle pulley system. *Invest Ophthalmol Vis Sci*. 2002; 43(9): 2923–2932, indexed in Pubmed: [12202511](https://pubmed.ncbi.nlm.nih.gov/12202511/).
10. Osanai H, Rodríguez-Vázquez JF, Abe H, et al. Fetal check ligament connected between the conjunctiva and the medial and lateral recti. *Invest Ophthalmol Vis Sci*. 2011; 52(10): 7175–7179, doi: [10.1167/iovs.11-7426](https://doi.org/10.1167/iovs.11-7426), indexed in Pubmed: [21791584](https://pubmed.ncbi.nlm.nih.gov/21791584/).
11. Standling S. *Gray's Anatomy*, 39th ed. Elsevier Churchill Livingstone, London 2005: 684–694.
12. Tawfik HA, Dutton JJ. Embryologic and Fetal Development of the Human Orbit. *Ophthalmic Plast Reconstr Surg*. 2018; 34(5): 405–421, doi: [10.1097/IOP.0000000000001172](https://doi.org/10.1097/IOP.0000000000001172), indexed in Pubmed: [30134385](https://pubmed.ncbi.nlm.nih.gov/30134385/).
13. Yalçın B, Kocabiyik N, Ozan H, et al. Muscular bridge between the inferior oblique and inferior rectus muscles. *Am J Ophthalmol*. 2004; 137(1): 121–124, doi: [10.1016/s0002-9394\(03\)00787-6](https://doi.org/10.1016/s0002-9394(03)00787-6).
14. Yalçın B, Ozan H. Insertional pattern of the inferior oblique muscle. *Am J Ophthalmol*. 2005; 137: 121–124, doi: [10.1016/j.ajo.2004.10.057](https://doi.org/10.1016/j.ajo.2004.10.057), indexed in Pubmed: [15767061](https://pubmed.ncbi.nlm.nih.gov/15767061/).
15. Warwick R. *Eugene Wolff's anatomy of the eye and orbit*. 7th ed. WB Saunders, Philadelphia 1976.

# Morphological variability of the fibularis tertius tendon in human fetuses

P. Karauda<sup>1</sup>, F. Paulsen<sup>2,3</sup>, M. Polgaj<sup>4</sup>, R. Diogo<sup>5</sup>, Ł. Olewnik<sup>1</sup> 

<sup>1</sup>Department of Anatomical Dissection and Donation, Medical University of Lodz, Poland

<sup>2</sup>Institute of Functional and Clinical Anatomy, Friedrich Alexander University Erlangen-Nürnberg, Erlangen, Germany

<sup>3</sup>Department of Topographic Anatomy and Operative Surgery, Sechenov University, Moscow, Russia

<sup>4</sup>Department of Normal and Clinical Anatomy, Chair of Anatomy and Histology, Medical University of Lodz, Poland

<sup>5</sup>Department of Anatomy, Howard University, Washington, DC, United States

[Received: 25 January 2021; Accepted: 11 March 2021; Early publication date: 13 April 2021]

**Background:** In adults, the fibularis tertius (FT) demonstrates great morphological variation. The present study classifies the types of FT insertion in human fetuses and compares their prevalence to the prevailing classification among adults.

**Materials and methods:** Fifty spontaneously-aborted human fetuses (19 male, 31 female, 100 upper limbs in total) aged 18–38 weeks of gestation at death were examined. The fetuses were obtained from spontaneous abortion after parental consent. The study was performed in accordance with the legal procedures in force in Poland and with the Body Donation Programme for both adults and fetuses.

**Results:** The most common type of FT found was type VI (32%), characterised by a bifurcated distal attachment: a main tendon inserting onto the base of the fourth metatarsal bone, and accessory bands inserting onto the fourth interosseous space. Five other types were observed: type IV (20%), with a single tendon inserting distally to the fascia covering the fourth interosseous space; type I (18%), with a single tendon inserting distally onto the shaft of the fifth metatarsal bone; type V (14%), with a bifurcated arrangement comprising a main tendon characterised by a very wide insertion onto the base of the fifth metatarsal bone and an accessory band inserting onto the base of the fourth metatarsal bone; and type III (12%) with a single tendon inserting distally onto the shaft of the fourth metatarsal bone and fascia covering the fourth interosseous space. Finally, type II (4%) was characterised by a single tendon inserting onto the base of the fifth metatarsal bone via a very wide distal insertion.

**Conclusions:** The FT demonstrates high morphological variability, with the most common configuration found in adults — a single insertion onto metatarsal 5 — being actually uncommonly found in fetuses. (Folia Morphol 2022; 81, 2: 451–457)

**Key words:** fibularis tertius, fibularis tertius tendon, anatomical variations, new classification, fetuses, variations, development

## INTRODUCTION

The anterior compartment of the leg contains four muscles: the tibialis anterior, the extensor hallucis

longus, extensor digitorum longus and the fibularis tertius muscle (FTM). Of this group of muscles, the FTM is the most superficial; it usually originates from

Address for correspondence: Dr. P. Karauda, Department of Normal and Clinical Anatomy, Interfaculty Chair of Anatomy and Histology, Medical University of Lodz, ul. Kościuszki 4, 90–419 Łódź, Poland, e-mail: piotr.karauda@umed.lodz.pl

This article is available in open access under Creative Commons Attribution-Non-Commercial-No Derivatives 4.0 International (CC BY-NC-ND 4.0) license, allowing to download articles and share them with others as long as they credit the authors and the publisher, but without permission to change them in any way or use them commercially.

the distal third or half of the fibula and of the intermuscular septum. The fibres of the muscle belly pass vertically downward until the muscle belly becomes the fibularis tertius tendon (FTT). After passing under the superior extensor retinaculum and inferior extensor retinaculum of the foot in the same canal as the extensor digitorum longus, the FTT inserts into the dorsal surface of the base of the fifth metatarsal bone [19]

In adults, the fibular muscle is characterised by frequent morphological variations, which mainly involve the presence of additional bands or muscles such as the fibularis digiti quinti and fibularis quartus [5, 6, 24, 25, 27–29, 33, 37]. The fibularis longus, fibularis brevis and fibularis tertius often demonstrate additional bands; this criterion also forms the basis of the adult classification by Olewnik et al. [24, 25, 27]. Earlier studies on foetal volatility of morphological variation in FTM are based on proximal attachment [11].

The FTM is used as a reference for the anterolateral aspect/portal during ankle arthroscopy [37]. The fibularis brevis and FTT insert at the fifth metatarsal; this implies that they can place torsional stress on areas where Jones fractures and stress fractures occur [35]. The FTM can be used in tendoplasty, tendon transfer, or resection surgeries on the foot.

The goal of our present work was to classify the types of fibularis tertius (FT) insertion in human foetuses and compare the results with those observed in the prevailing classification among adults. It will establish the first such classification for human foetuses.

## MATERIALS AND METHODS

Permission for the study was granted by the Local Bioethics Committee (agreement no RNN/130/20/KE). Fifty spontaneously-aborted human foetuses (19 male, 31 female, 100 lower limbs) aged 18–38 weeks of gestation at death were examined. The foetuses were obtained from spontaneous abortion after parental consent. The study was performed in accordance with the legal procedures in force in Poland and in accordance with the Body Donation Programme for both adults and foetuses. Their ages were determined on the basis of cranio-sacral and head measurements [26].

The leg and foot area was dissected as described previously [21–23, 25]. The procedure began with the removal of the skin and superficial fascia of the leg up to the crural fascia. The skin and subcutaneous

tissue of the foot were then removed, and then as much of the crural fascia as possible was removed without tearing the muscle bellies (starting proximal to the retinaculum). The bellies and muscle tendons were then cleaned from the medial to the lateral side. The tendon was carefully dissected to the bone attachment itself. The course of each tendon was recorded.

Upon dissection, the following features of the FT were recorded: 1) the type of FT insertion; 2) FT morphometric measurements.

Measurements were taken using an electronic digital calliper (Mitutoyo Corporation, Kawasaki-shi, Kanagawa, Japan) with an accuracy of up to 0.1 mm. Two measurements were taken in each case and the mean values were recorded.

## Ethical approval and consent to participate

The cadavers belonged to the Department of Anatomical Dissection and Donation, Medical University of Lodz.

## Statistical analysis

Differences in tendon types between genders and body sides were tested using the  $\chi^2$  test. The normality of the continuous data was tested using the Shapiro-Wilk test. As the data was not normally distributed, non-parametrical tests were used. Morphological measurements between two groups were compared using the Mann-Whitney test, and measurements between EHL types were compared using the Kruskal-Wallis test by ranks with dedicated *post hoc* test.

All statistical analyses were performed using Statistica 13 software (StatSoft Polska, Cracow, Poland). A p-value lower than 0.05 was considered significant, with Bonferroni correction for multiple testing. The results are presented as mean and standard deviation unless otherwise stated.

## RESULTS

The fibularis tertius muscle was present in 50 cases (31 females and 19 males,  $p = 0.0278$ ; 26 right and 24 left limbs,  $p = 0.8415$ ). It occurred significantly more often in specimens with shorter lower legs ( $56.2 \pm 7.2$  mm vs.  $88.0 \pm 18.9$  mm,  $p < 0.0001$ ) but with greater cranio-sacral length ( $247.2 \pm 33.05$  mm vs.  $226.76 \pm 39.90$  mm,  $p < 0.0172$ ).

It was classified according to the following types, based on type of distal insertion:

- type I — single distal attachment. The tendon inserts into the shaft of the fifth metatarsal bone (Fig. 1). This type was found in 9 cases;
- type II — single distal attachment. The tendon is characterised by a very wide insertion into the base of the fifth metatarsal bone. This type was observed in 2 cases (Fig. 1);
- type III — single distal attachment. The tendon inserts into the shaft of the fourth metatarsal bone and fascia covering the fourth interosseous space. This type was found in 6 cases (Fig. 1);
- type IV — single distal attachment. The tendon inserts to the fascia covering the fourth interosseous space. This type was found in 10 limbs (Fig. 1);
- type V — bifurcated distal attachment. The main tendon is characterised by a very wide insertion into the base of the fifth metatarsal bone, and the accessory band inserts into the base of the four metatarsal bone. This type was observed in 7 lower limbs (Fig. 1);
- type VI — bifurcated distal attachment. The main tendon inserts into the base of the fourth metatarsal bone, and the accessory bands inserts into the fourth interosseous space. This type was found in 16 cases (Fig. 1).

All types are also shown in the scheme (Fig. 2).

Table 1 presents the morphological parameters for the whole group and according to the above types.

Where possible, the type of insertion morphology was classified as band-shaped (18 cases in general) or fan-shaped (27 cases in general). The distribution of these types is presented in Table 2.

## DISCUSSION

The present study has two key values. It presents the first systematic classification of FT insertion, and highlights its variability, classifying it as band-shaped or fan-shaped in human foetuses. Earlier studies did not describe such a large morphological variability of FT insertion in human foetuses.

To understand the potential morphological variation of the FTM, it is important to explain embryological basis. The common extensor mass of the foot is connected with the peroneal mass in the early stages of development, but these diverge in a 14-mm embryo: the extensor mass has differentiated into the tibialis anterior muscle, extensor digitorum longus, and extensor hallucis longus. The tibialis anterior muscle demonstrates a broad tendon reaching the cuneiform

primum bone. It demonstrates adult attachments in a 20-mm. embryo. The extensor digitorum longus is differentiated from the central portion of the muscle mass and is relatively more on the fibular side than in the adult. At first it ends distally in a broad flat plate which later, in a 20-mm. embryo, gives off the broad tendons to the digits. The FTM is early distinct from the extensor digitorum longus.

The FTM varies in its development and the nature of its origin and insertion. The FTM is topographically very closely related to the extensor digitorum longus, and there is every evidence that it is formed as a secondary attachment of the deep extensor stratum, which has migrated in an upward direction and has separated from the extensor digitorum brevis. In this sense, it may represent a missing tendon for the fifth toe, which became an independent muscle following migration in response to the specialised functional requirements of the human foot [14]. Therefore, like the foot to which it belongs, the FTM must be idiosyncratic feature that evolved early in human phylogenetic development [11]: it is very rare in the great apes but is found in about 29.6% of gorillas (terrestrial apes). Its overwhelming presence in both humans and gorillas, and its lack or rarity in the great apes, would indicate an evolutionary acquisition related to *bipedalism* [4, 7–10, 37]. Hence, from an evolutionary point of view, FTM most likely serves a very important function when walking. Therefore, any morphological changes in insertion may indicate that they have not yet reached the final evolutionary stage; the FTM has been found to have a range of insertion types, and to display accessory bands [24].

Among adults, the presence or absence of the FTM depends on the population studied. The widest range in its prevalence has so far been observed in Asian populations, ranging from 38.5% to 95.5% [1, 13, 14, 20, 32]. In North Africa, it was present in 52.8% of an Egyptian population and 67.7% of a Tunisian population [32]. In South America, it was present in 49.1%, 100% [30] and 93.8% of Brazilian populations [18], and interestingly, in 100% of a studied Bolivian population [16, 18, 30]. European population ranked between 38.2% and 92.9% [3, 15, 17, 24, 31, 36].

In the foetus, the FTM was found to be present in only 83.16% of cases in a Polish population [11]. Interestingly, our present findings, also obtained from Polish foetuses, found it to be present in only 50%.

Many FT classifications have been described [12, 14, 31, 34]. However, the most recent classifica-

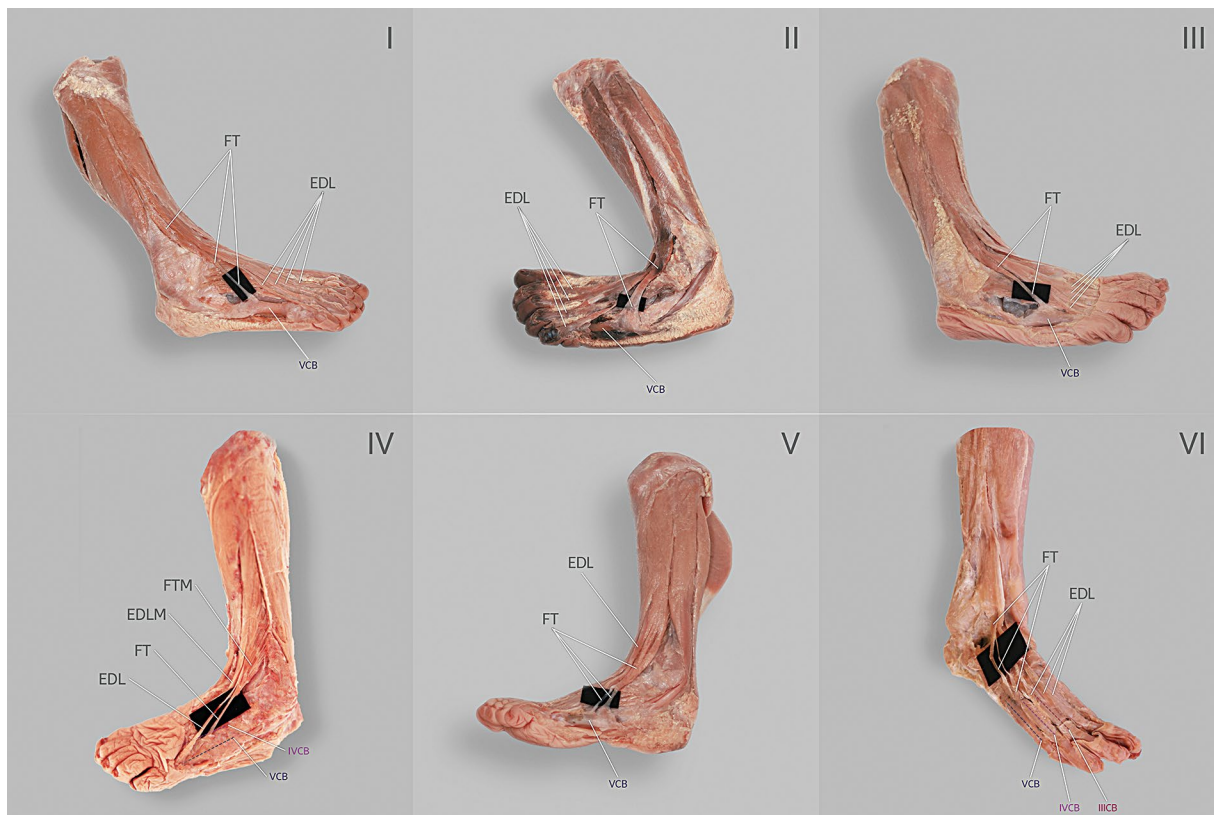


**Figure 1.** Types of the fibularis tertius tendon: Type I of the fibularis tertius tendon. Right leg; Type II of the fibularis tertius tendon. Left leg; Type III of the fibularis tertius tendon. Right leg; Type IV of the fibularis tertius tendon. Left leg; Type V of the fibularis tertius tendon. Left leg; Type VI of the fibularis tertius tendon. Right leg; EDL — extensor digitorum longus; EDLM — extensor digitorum longus muscle; FT — fibularis tertius; FTM — fibularis tertius muscle; IIICB — third metatarsal bone; IVCB — fourth metatarsal bone; VCB — fifth metatarsal bone.

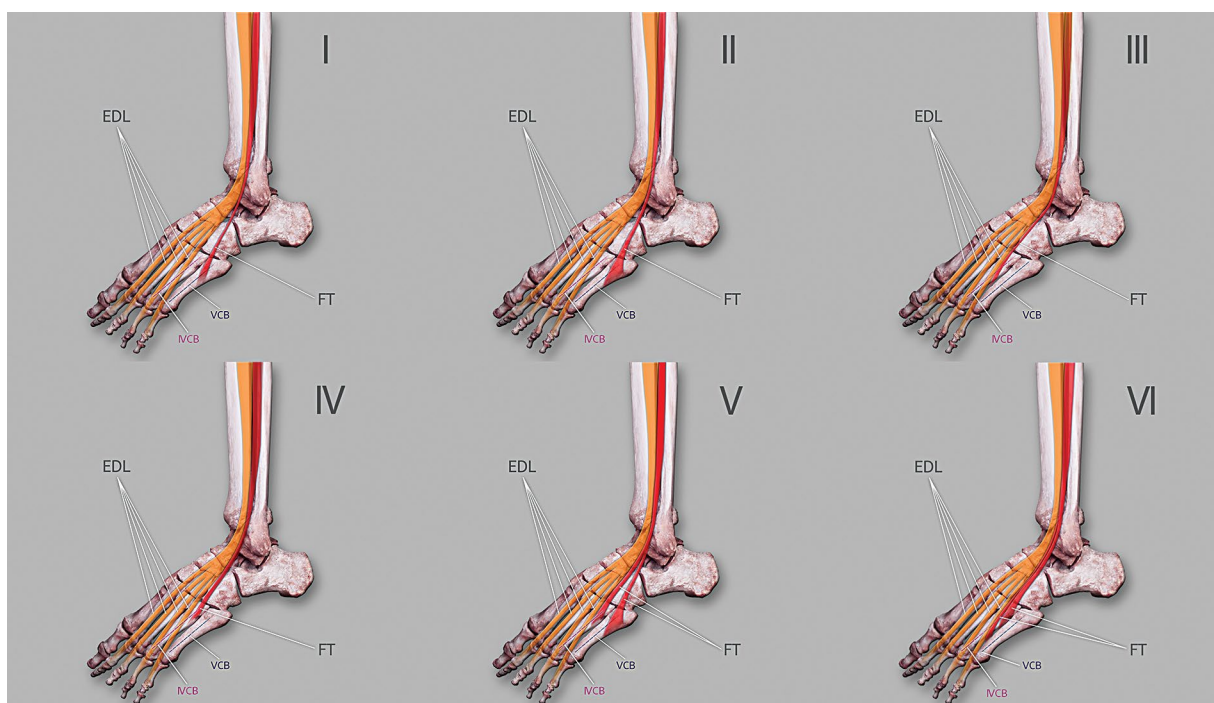


**Figure 2.** Scheme of all types. Left leg; EDL — extensor digitorum longus; FT — fibularis tertius; IVCB — fourth metatarsal bone; VCB — fifth metatarsal bone.

**Table 1.** Morphological parameters according to type of insertion

Parameter	General	Insertion type						P
		I	II	III	IV	V	VI	
Muscle length	12.99 (4.29)	13.63 (2.44)	11.32 (1.01)	10.78 (0.93)	11.65 (0.96)	15.35 (4.71)	14.02 (6.39)	0.2080
Tendon width MTJ	0.85 (1.51)	0.61 (0.33)	0.62 (0.08)	0.21* (0.03)	0.26* (0.07)	1.01* (0.22)	1.56* (2.52)	0.0002*
Tendon thickness MTJ	0.18 (0.16)	0.13 (0.08)	0.22 (0.01)	0.19 (0.24)	0.09 (0.05)	0.18 (0.08)	0.26 (0.21)	0.0163
Tendon length	11.40 (3.12)	11.14 (2.01)	12.09 (1.36)	11.60 (0.58)	13.58* (1.85)	9.64* (3.84)	10.79 (4.04)	0.0050*
Accessory tendon length	9.30 (2.95)					5.61 (0.23)	11.15 (0.92)	0.1051
Distance from ExP	3.57 (1.12)	2.54 (0.62)	3.31 (1.00)	4.63 (0.28)		3.38 (1.45)	3.75 (0.95)	0.0179
ExP width	1.05 (0.39)	0.77 (0.15)	1.09 (0.01)	1.35 (0.15)		1.03 (0.56)	1.06 (0.39)	0.0537
ExP thickness	0.28 (0.84)	0.12 (0.05)	0.10 (0.01)	0.13 (0.08)		0.83 (1.74)	0.11 (0.06)	0.2262
ExP width	2.12 (0.64)	1.69 (0.68)	1.94 (1.05)	2.51 (0.16)		2.54 (0.57)	1.90 (0.58)	0.0718
ExP thickness	0.22 (0.21)	0.14 (0.06)	0.61 (0.73)	0.14 (0.06)		0.28 (0.21)	0.18 (0.07)	0.5020

\*Significant P according to Bonferroni correction was 0.005; MTJ — musculo-tendinous junction; ExP — extension point

**Table 2.** Shape of distal tendon insertion according to insertion type

Insertion type	Insertion shape	
	Fan	Band
I	5 (18.5%)	3 (16.7%)
II	1 (3.7%)	0 (0.0%)
III	6 (22.2%)	0 (0.0%)
IV	0 (0.0%)	10 (55.6%)
V	7 (25.9%)	0 (0.0%)
VI	8 (29.6%)	5 (27.8%)

tion was the 6-fold classification (I–VI) proposed by Olewnik [24]. Briefly, type I (45%), i.e. a single distal attachment inserting into the shaft of the V metatarsal bone [24], was observed in 18% of cases in the present study; type II (22%), with a single, broad distal attachment insertion to the base of the V metatarsal bone [24], was present in 4%. Type III (16.5%), characterised by a single, very wide distal attachment to the base of the V metatarsal bone, and to the base and shaft of the IV metatarsal bone, and to the fascia covering the fourth interosseous space [24], was not observed in the current study. It is possible that it appears at a later date — tendon dehiscence can occur postnatally. In addition, type IV (8.8%), characterised by a bifurcated distal attachment into the base of the fifth metatarsal bone, and the accessory band inserts to the shaft of the V metatarsal bone, was not observed. Type V (5.5%), characterised by a bifurcated distal attachment, the main tendon having a very wide insertion to the base of the V meta-

tarsal bone, and the accessory band inserting to the base of the IV metatarsal bone [24]. In addition, type VI, characterised by fusion with fibularis brevis tendon, was not observed by us either.

Interestingly, of the tendon types proposed in the present study, type III, with a single distal attachment into the shaft of the fourth metatarsal bone and fascia covering the fourth interosseous space, was not observed in studies on adults, or in foetal studies [11]. Similarly, type IV, characterised by single distal attachment and tendon inserts to the fascia covering the fourth interosseous space, was not recorded by either Olewnik [24] in adults or Domagała et al. [11] in foetuses. Type V, with a bifurcated distal attachment where the main tendon has a very wide insertion into the base of the fifth metatarsal bone, and the accessory band inserts into the base of the four-metatarsal bone, was not found previously. Interestingly, type VI has not been observed in other studies, despite being the most frequent type (32%); this was characterised by a bifurcated distal attachment where the main tendon inserts into the base of the fourth metatarsal bone, and the accessory bands inserts into the fourth interosseous space. Albay and Candan [2] also did not describe the morphological variability of fibularis tertius tendon, focusing only on the assessment of the incidence of additional fibular muscles.

Albay and Candan [2] performed morphometric measurements of FT depending on trimesters. In the second trimester, the average muscle belly length was 19.18 mm, and the tendons were 12.13 mm. In the third trimester, the muscle belly was 30.26 mm, and the tendon was 15.68 mm. Our research focused on

morphometric measurements depending on the type of insertion. And the longest muscle belly was type V (15.35 mm) and the shortest was type III (10.78 mm). The tendon length was the longest in type IV (13.59 mm), and the smallest in type V (9.64 mm).

A second feature in our proposed classification is insertion type. Both band-shaped and fan-shaped types were observed. Interestingly, although the presence of a band-shaped or fan-shaped type was closely correlated with the corresponding type of insertion in adults [24], no such a correlation was observed in the present study. This might be an important consideration when stripping tendons during surgery.

## CONCLUSIONS

We propose a six-fold classification that can be used to elucidate the appearance of accessory tendon bands. The fibularis tertius demonstrates high morphological variability, with the most common configuration found in adults — a single insertion onto metatarsal 5 — being actually uncommonly found in foetuses.

**Conflict of interest:** None declared

## REFERENCES

- Adachi B. Beitrage zur anatomie der Japaner. XII. Die statistic der muskelvarietten. *Z Morphol Anthr.* 1909; 12: 261–312.
- Albay S, Candan B. Evaluation of fibular muscles and prevalence of accessory fibular muscles on fetal cadavers. *Surg Radiol Anat.* 2017; 39(12): 1337–1341, doi: [10.1007/s00276-017-1887-y](https://doi.org/10.1007/s00276-017-1887-y), indexed in Pubmed: [28608130](https://pubmed.ncbi.nlm.nih.gov/28608130/).
- Bertelli J, Khoury Z. The peroneus tertius island muscle. *Flap Surg Radiol Anat.* 1991; 13(3): 243–244.
- Boyle EK, Mahon V, Diogo R. Muscles Lost in Our Adult Primate Ancestors Still Imprint in Us: on Muscle Evolution, Development, Variations, and Pathologies. *Current Molecular Biology Reports.* 2020; 6(2): 32–50, doi: [10.1007/s40610-020-00128-x](https://doi.org/10.1007/s40610-020-00128-x).
- Chaney ME, Dao TV, Brechtel BS, et al. The fibularis digiti quinti tendon: a cadaveric study with anthropological and clinical considerations. *Foot (Edinb).* 2018; 34: 45–47, doi: [10.1016/j.foot.2017.11.012](https://doi.org/10.1016/j.foot.2017.11.012), indexed in Pubmed: [29278836](https://pubmed.ncbi.nlm.nih.gov/29278836/).
- Demir BT, Gümüşalan Y, Üzel M, et al. The variations of peroneus digiti quinti muscle and its contribution to the extension of the fifth toe. A cadaveric study. *Saudi Med J.* 2015; 36(11): 1285–1289, doi: [10.15537/smj.2015.11.12657](https://doi.org/10.15537/smj.2015.11.12657), indexed in Pubmed: [26593160](https://pubmed.ncbi.nlm.nih.gov/26593160/).
- Diogo R. Introduction to evolutionary developmental pathology, or evo-devo-path: on neodarwinism, natural mutants, hopeful monsters, syndromes, genomics, variations, humans, apes, chameleons, and dinosaurs. *Curr Mol Biol Rep.* 2020; 6(2): 11–15, doi: [10.1007/s40610-020-00133-0](https://doi.org/10.1007/s40610-020-00133-0).
- Diogo R, Molnar J. Comparative anatomy, evolution, and homologies of tetrapod hindlimb muscles, comparison with forelimb muscles, and deconstruction of the forelimb-hindlimb serial homology hypothesis. *Anat Rec (Hoboken).* 2014; 297(6): 1047–1075, doi: [10.1002/ar.22919](https://doi.org/10.1002/ar.22919), indexed in Pubmed: [24729440](https://pubmed.ncbi.nlm.nih.gov/24729440/).
- Diogo R, Molnar JL, Wood B. Bonobo anatomy reveals stasis and mosaicism in chimpanzee evolution, and supports bonobos as the most appropriate extant model for the common ancestor of chimpanzees and humans. *Sci Rep.* 2017; 7(1): 608, doi: [10.1038/s41598-017-00548-3](https://doi.org/10.1038/s41598-017-00548-3), indexed in Pubmed: [28377592](https://pubmed.ncbi.nlm.nih.gov/28377592/).
- Diogo R, Siomava N, Gitton Y. Development of human limb muscles based on whole-mount immunostaining and the links between ontogeny and evolution. *Development.* 2019; 146(20), doi: [10.1242/dev.180349](https://doi.org/10.1242/dev.180349), indexed in Pubmed: [31575609](https://pubmed.ncbi.nlm.nih.gov/31575609/).
- Domagała Z, Gworys B, Kreczyńska B, et al. A contribution to the discussion concerning the variability of the third peroneal muscle: An anatomical analysis on the basis of foetal material. *Folia Morphol.* 2006; 65(4): 329–336, indexed in Pubmed: [17171612](https://pubmed.ncbi.nlm.nih.gov/17171612/).
- Ercikti N, Apaydin N, Kocabiyik N, et al. Insertional characteristics of the peroneus tertius tendon: revisiting the anatomy of an underestimated muscle. *J Foot Ankle Surg.* 2016; 55(4): 709–713, doi: [10.1053/j.jfas.2016.01.018](https://doi.org/10.1053/j.jfas.2016.01.018), indexed in Pubmed: [26860045](https://pubmed.ncbi.nlm.nih.gov/26860045/).
- Jadhav Surekha D, et al. Fibularis tertius muscle: Cadaveric study in Indians. *J Krishna Inst Med Sci Univ.* 2015; 4(1): 64–69.
- Joshi SD, Joshi SS, Athavale SA. Morphology of peroneus tertius muscle. *Clin Anat.* 2006; 19(7): 611–614, doi: [10.1002/ca.20243](https://doi.org/10.1002/ca.20243), indexed in Pubmed: [16317742](https://pubmed.ncbi.nlm.nih.gov/16317742/).
- Krammer EB, Lischka MF, Gruber H. Gross anatomy and evolutionary significance of the human peroneus III. *Anat Embryol (Berl).* 1979; 155(3): 291–302, doi: [10.1007/BF00317642](https://doi.org/10.1007/BF00317642), indexed in Pubmed: [572152](https://pubmed.ncbi.nlm.nih.gov/572152/).
- Larico I, Jorda L. Frecuencia del mu ´sculo peroneo tertius. *Rev Inv e Info Salud.* 2005; 29–32.
- Losa-Iglesias ME, Calvo-Lobo C, Rodríguez-Sanz D, et al. Fibularis tertius muscle in women and men: A surface anatomy cross-sectional study across countries. *PLoS One.* 2019; 14(4): e0215118, doi: [10.1371/journal.pone.0215118](https://doi.org/10.1371/journal.pone.0215118), indexed in Pubmed: [30964928](https://pubmed.ncbi.nlm.nih.gov/30964928/).
- Marin L, et al. Estudo anatomico do musculo fibular terceiro em humanos. *Arq Méd ABC.* 2006; 31: 23–26.
- Moore K, Dalley A. Lower Limb. *Clinically Oriented Anatomy.* Lippincott Williams and Wilkins, Philadelphia 2006.
- Nakano T. Beitrage zur Anatomie der Chinesen: Die Statistik der Muskelvarietaten. *Folia Anat Jpn.* 1923; 1(5): 273–282, doi: [10.2535/ofaj1922.1.5\\_273](https://doi.org/10.2535/ofaj1922.1.5_273).
- Olewnik Ł, Podgórski M, Polguj M, et al. A cadaveric and sonographic study of the morphology of the tibialis anterior tendon: a proposal for a new classification. *J Foot Ankle Res.* 2019; 12: 9, doi: [10.1186/s13047-019-0319-0](https://doi.org/10.1186/s13047-019-0319-0), indexed in Pubmed: [30733832](https://pubmed.ncbi.nlm.nih.gov/30733832/).
- Olewnik Ł, Podgórski M, Polguj M, et al. A cadaveric study of the morphology of the extensor hallucis longus — a proposal for a new classification. *BMC Musculoskelet Disord.* 2019; 20(1): 310, doi: [10.1186/s12891-019-2688-8](https://doi.org/10.1186/s12891-019-2688-8), indexed in Pubmed: [31266496](https://pubmed.ncbi.nlm.nih.gov/31266496/).

23. Olewnik Ł. A proposal for a new classification for the tendon of insertion of tibialis posterior. *Clin Anat.* 2019; 32(4): 557–565, doi: [10.1002/ca.23350](https://doi.org/10.1002/ca.23350), indexed in Pubmed: [30758860](https://pubmed.ncbi.nlm.nih.gov/30758860/).
24. Olewnik Ł. Fibularis tertius: anatomical study and review of the literature. *Clin Anat.* 2019; 32(8): 1082–1093, doi: [10.1002/ca.23449](https://doi.org/10.1002/ca.23449), indexed in Pubmed: [31408221](https://pubmed.ncbi.nlm.nih.gov/31408221/).
25. Olewnik Ł. Is there a relationship between the occurrence of frenular ligaments and the type of fibularis longus tendon insertion? *Ann Anat.* 2019; 224: 47–53, doi: [10.1016/j.aanat.2019.03.002](https://doi.org/10.1016/j.aanat.2019.03.002), indexed in Pubmed: [30930196](https://pubmed.ncbi.nlm.nih.gov/30930196/).
26. Olewnik Ł, Waśniewska A, Polguy M, et al. Morphological variability of the palmaris longus muscle in human fetuses. *Surg Radiol Anat.* 2018; 40(11): 1283–1291, doi: [10.1007/s00276-018-2069-2](https://doi.org/10.1007/s00276-018-2069-2), indexed in Pubmed: [30022223](https://pubmed.ncbi.nlm.nih.gov/30022223/).
27. Olewnik Ł, Podgórski M, Ruzik K, et al. New classification of the distal attachment of the fibularis brevis: anatomical variations and potential clinical implications. *Foot Ankle Surg.* 2020; 26(3): 308–313, doi: [10.1016/j.fas.2019.04.002](https://doi.org/10.1016/j.fas.2019.04.002), indexed in Pubmed: [31031151](https://pubmed.ncbi.nlm.nih.gov/31031151/).
28. Ashaolu JO, Olorunyomi OI, Opabunmi OA, et al. Surface anatomy and prevalence of fibularis tertius muscle in a south-western Nigerian population. *Forensic Med Anat Res.* 2013; 01(02): 25–29, doi: [10.4236/fmar.2013.12005](https://doi.org/10.4236/fmar.2013.12005).
29. Prakash, Narayanswamy C, Singh DK, et al. Anatomical variations of peroneal muscles: a cadaver study in an Indian population and a review of the literature. *J Am Podiatr Med Assoc.* 2011; 101(6): 505–508, doi: [10.7547/1010505](https://doi.org/10.7547/1010505), indexed in Pubmed: [22106198](https://pubmed.ncbi.nlm.nih.gov/22106198/).
30. Ramirez D, Gajardo C, Caballero P, et al. Clinical evaluation of fibularis tertius muscle prevalence. *Int J Morphol.* 2010; 28(3), doi: [10.4067/s0717-95022010000300016](https://doi.org/10.4067/s0717-95022010000300016).
31. Rourke K, Dafydd H, Parkin IG. Fibularis tertius: revisiting the anatomy. *Clin Anat.* 2007; 20(8): 946–949, doi: [10.1002/ca.20500](https://doi.org/10.1002/ca.20500), indexed in Pubmed: [17584875](https://pubmed.ncbi.nlm.nih.gov/17584875/).
32. Salem A, Kader GA, Almallah A, et al. Variations of peroneus tertius muscle in five Arab populations: a clinical study. *Trans Res Anat.* 2018; 13: 1–6, doi: [10.1016/j.tria.2018.11.001](https://doi.org/10.1016/j.tria.2018.11.001).
33. Sookur PA, Naraghi AM, Bleakney RR, et al. Accessory muscles: anatomy, symptoms, and radiologic evaluation. *Radiographics.* 2008; 28(2): 481–499, doi: [10.1148/rg.282075064](https://doi.org/10.1148/rg.282075064), indexed in Pubmed: [18349452](https://pubmed.ncbi.nlm.nih.gov/18349452/).
34. Stevens K, Platt A, Ellis H. A cadaveric study of the peroneus tertius muscle. *Clin Anat.* 1993; 6(2): 106–110, doi: [10.1002/ca.980060206](https://doi.org/10.1002/ca.980060206).
35. Vertullo CJ, Glisson RR, Nunley JA. Torsional strains in the proximal fifth metatarsal: implications for Jones and stress fracture management. *Foot Ankle Int.* 2004; 25(9): 650–656, doi: [10.1177/107110070402500910](https://doi.org/10.1177/107110070402500910), indexed in Pubmed: [15563388](https://pubmed.ncbi.nlm.nih.gov/15563388/).
36. Witvrouw E, Borre KV, Willems TM, et al. The significance of peroneus tertius muscle in ankle injuries: a prospective study. *Am J Sports Med.* 2006; 34(7): 1159–1163, doi: [10.1177/0363546505286021](https://doi.org/10.1177/0363546505286021), indexed in Pubmed: [16493171](https://pubmed.ncbi.nlm.nih.gov/16493171/).
37. Yammine K, Erić M. The fibularis (peroneus) tertius muscle in humans: a meta-analysis of anatomical studies with clinical and evolutionary implications. *Biomed Res Int.* 2017; 2017: 6021707, doi: [10.1155/2017/6021707](https://doi.org/10.1155/2017/6021707), indexed in Pubmed: [28596965](https://pubmed.ncbi.nlm.nih.gov/28596965/).

# Relationship between maxillary central incisors and incisive canal: a cone-beam computed tomography study

A.I. Linjawi<sup>1</sup>, H.Y.A. Marghalani<sup>1</sup>

Orthodontic Department, Faculty of Dentistry King Abdulaziz University, Jeddah, Saudi Arabia

[Received: 9 April 2021; Accepted: 22 April 2021; Early publication date: 29 April 2021]

**Background:** This study aimed to assess the relationship between the maxillary incisors and the incisive canal (IC) using cone-beam computed tomography (CBCT).

**Materials and methods:** Archived CBCT scan from 120 subjects (60 males and 60 females, mean age  $34.2 \pm 13.1$  years) were analysed in this cross-sectional study. The following variables were measured: incisor/palatal plane (PP), IC/PP angles, palatal alveolar bone width (PABW) at apex, IC width, inter-root width at apex and IC level to incisor apex. The relationship between the incisors and IC with respect to sex and age was calculated using one-way analysis of variance, independent samples *t*-test, and regression analysis.

**Results:** The confidence level was set at 95%. Results showed that half of the study population exhibited IC palatal opening at the level of the maxillary incisor apices. Significant associations were observed between IC/PP and incisor/PP angles and between IC width and PABW at the apical level ( $p < 0.05$ ), and between age and IC width in the sagittal and axial perspectives and age and IC level relative to the incisor apices. A significant association was observed between sex and IC/PP angle, IC width in the sagittal perspective, and PABW at the apical level. The association was found between IC and maxillary incisors angulations but not between IC width and inter-root distance.

**Conclusions:** Age showed varied associations while sex was significantly associated with most variables assessed. (Folia Morphol 2022; 81, 2: 458–463)

**Key words:** alveolar bone thickness, cone-beam computed tomography, incisive canal, incisors' characteristics, inter-root distance

## INTRODUCTION

Orthodontics focuses on the improvement of facial aesthetics via retraction of the maxillary anterior teeth to provide maximum anchorage [19, 22]. However, complications such as fenestrations, loss of alveolar bone, root resorption, or dehiscence can occur when the teeth are moved out of the cortical bone, which leads us to scrutinize the confines of orthodontic treatment [1, 12, 18, 21, 24].

Recently, research focused on craniofacial anatomy has demonstrated the close proximity between the incisive canal (IC) and the maxillary central incisors, which is closer than that of the cortical plate in the palate [2]. The IC is located behind the maxillary central incisor roots at the middle level of the maxillary palatine process. Therefore, it is considered the most significant anatomical structure in the premaxilla [7]. It links the nasal and the oral cavities by connecting

Address for correspondence: A.I. Linjawi, BDS, MSc, PhD, Ass. Prof., Orthodontic Department, Faculty of Dentistry, King Abdulaziz University, P.O. Box 80209, Jeddah 21589, Saudi Arabia, tel: +966504155573, e-mail: ailinjawi@kau.edu.sa

This article is available in open access under Creative Common Attribution-Non-Commercial-No Derivatives 4.0 International (CC BY-NC-ND 4.0) license, allowing to download articles and share them with others as long as they credit the authors and the publisher, but without permission to change them in any way or use them commercially.

the incisive foramen and the nasal foramen. It is surrounded by dense cortical bone and the nasopalatine vessels pass through it [7]. These vessels include the incisive nerve and the sphenopalatine artery. The latter is the end branch of the nasopalatine artery [11, 16].

Disparities in incisor angulations, alveolar bone thickness and IC morphology are challenging variables that can affect the movement of the maxillary incisors [12, 13, 20, 26, 28]. The proximity of the maxillary central incisor roots to the walls of the IC cortex might lead to incisor root resorption during maximum orthodontic retraction of incisors [5, 17]. The research conducted by Pan and Chen [19] revealed the risk posed by IC contact with the maxillary central incisors during incisors retraction, leading to external resorption of the root apex [19]. Similarly, Chatriyanuyoke et al. [4] suggested that more caution should be exercised during immediate placement of implants at the mid-root level of the maxillary central incisors in younger and female patients to prevent IC penetration. To prevent this complication, analysis of IC dimensions and morphology should be accurately implemented before any dental procedures within the vicinity of this anatomical structure [5, 17].

Accurate radiographic imaging is essential to obtain the best diagnosis and ideal management as well as to monitor the development and the results of treatment [10, 23]. Cone-beam computed tomography (CBCT) has been considered more accurate in assessing incisor inclinations and the morphology of the alveolar bone [6, 15, 25, 27, 29]. It can be utilised as an adjunct in case analysis and treatment planning as it minimises difficulties in dental procedures [3, 13, 14]. However, the widely used diagnostic radiographs by most orthodontists are cephalometric and panoramic radiographs. Incisors' angulation and inter-root distances can be easily measured using those conventional radiographs. Thus, finding some predictive measures and correlations between the maxillary incisors' roots and the IC that can be assessed by both conventional and three-dimensional radiographs might help the orthodontists to predict the risk of maxillary incisors' root resorption during orthodontic tooth movement using the available radiographs.

The aim of the present study is to assess the association between the IC and the maxillary incisors using different linear and angular CBCT measurements.

## MATERIALS AND METHODS

### Study design

This cross-sectional study utilized archived CBCT records of adult Saudi patients with middle-eastern ethnic background who were treated at Orthodontic Department, Faculty of Dentistry King Abdulaziz University, Jeddah, Saudi Arabia. This research was approved by the institutional ethical committee (ethical approval no. 100-06-19), and the study procedures were performed in accordance with the principles of the Declaration of Helsinki, 1975 (as revised in 2008).

### Sample characteristics

The inclusion criteria were as follows: 1) CBCT images showing the maxilla clearly, 2) no history of orthodontic treatment, 3) presence of the maxillary incisors, 4) no history of dental treatment related to the maxillary incisors, 5) no history of trauma to the incisors, and 6) no congenital or developmental abnormalities such as cleft palate and cleft lip. The sample groups were organized according to age and sex. Patients were divided into four age groups:  $\leq 20$  years, 21–40 years, 41–60 years, and  $> 60$  years.

### CBCT images

The following specifications were used for the CBCT images: field of view:  $81 \times 74$  mm, voxel size: 0.146 mm, slice thickness: 0.147 mm, normal mode: 90 kV, 4 mA, 4.10 mGy, and 16.8 s. Image acquisition was performed by positioning the head such that the Frankfort horizontal plane was parallel to the floor. Images were stored in the digital format as DICOM files. Both sagittal and coronal perspectives were obtained and assessed using OnDemand 3D Imaging software (Seoul, Korea).

### Measurements

The following linear and angular measurements on sagittal reconstruction were evaluated in relation to the maxillary central incisors (Fig. 1):

- incisor/palatal plane (PP) angle: the angle between the long axis of each central incisor and the palatal plane;
- palatal alveolar bone width (PABW) at the apical level: the palatal bone width at the level of the central incisor apices.

For IC, the following linear and angular dimensions were determined using sagittal reconstruction (Fig. 1):

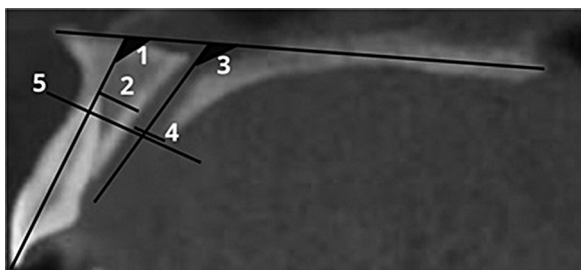


**Figure 1.** Linear and angular measurements on the sagittal reconstruction; 1 — incisor/palatal plane angle: the angle between the long axis of each central incisor and the palatal plane; 2 — palatal alveolar bone width at apex level: the palatal bone width at apical level of central incisor; 3 — the IC/PP angle: the angle between the long axis of the IC and the palatal plane; 4 — IC width at palatal opening: width of the incisive canal at palatal opening; 5 — the IC palatal opening level relative to the apex of the central incisors: the level was characterised into three types: below apex, at apex and above apex.

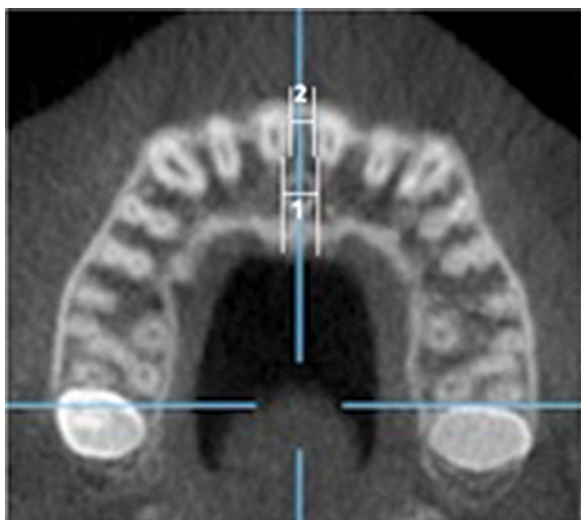


**Figure 2.** Linear measurements on the axial reconstruction; 1 — incisive canal width at incisor's apical level; 2 — inter-root distance at apex level of incisors: the distance between the two central incisor roots at the apical level.

- IC/PP angle: the angle between the long axis of the IC and the palatal plane;
- level of IC palatal opening relative to the apices of the central incisors; the level was classified into three types: below the apex, at the apex, and above the apex;
- IC width at palatal opening.

On axial reconstruction, the following linear dimensions were assessed (Fig. 2):

- IC width at the level of incisor apices;

- inter-root distance at the level of incisor apices: the distance between the two central incisor roots at the apical level.

#### Measurement error

A single examiner performed all measurements and repeated the measurements after a 2-week interval. The independent t-test showed no substantial deviation between the two sets of measurements ( $p < 0.05$ ). Similarly, an intraclass correlation coefficient of 0.78 indicated good reliability.

#### Statistical analysis

The evaluated variables are presented as mean values with standard deviations, numbers, and percentages. Comparative data for variables involving the maxillary incisors and the IC were compared using independent samples t-test. Bonferroni correction for multiple comparisons and one-way analysis of variance were used for data related to sex and age, respectively. Regression analysis was used to examine the correlation between the variables. All statistical analyses were performed using IBM SPSS Statistics 22.0 (IBM Corp., Armonk, NY, USA). The confidence level was 95% for all analyses.

## RESULTS

Archived CBCT data from 120 subjects (60 males and 60 females, mean age  $34.2 \pm 13.1$  years) were analysed in this study. The mean IC/PP angle was  $111.17 \pm 8.06^\circ$ . The mean IC width was 3.82 mm in both sagittal and axial perspectives. The mean incisor/PP angle was  $116.88 \pm 9.50^\circ$ , which was higher than the IC/PP angle. The mean PABW and inter-root distance at the apical level were 4.28 mm and 3.66 mm, respectively (Table 1).

Half of the study population exhibited an IC palatal opening at the level of the maxillary incisor apices. In 43.3% of the subjects, the IC palatal opening was below the level of the maxillary incisor apices, and in 6.7% of the participants, it was above the level of the maxillary incisor apices (Table 2).

A significant positive association was observed between IC/PP and incisor/PP angles ( $p < 0.01$ ). Similarly, a significant positive association was observed between IC width in the sagittal perspective and PABW at the apical level ( $p < 0.01$ ). By contrast, there was no significant association between IC width in the axial perspective and the maxillary incisor inter-root distance at the apical level ( $p > 0.05$ ) (Table 3).

**Table 1.** Mean and standard deviations for the incisive canal (IC) and the maxillary central incisors measurements

	Mean	SD
<b>IC measurements</b>		
IC/PP [°]	111.17	8.06
IC width in sagittal view [mm]	3.82	1.07
IC width in axial view [mm]	3.82	0.91
<b>Maxillary incisors measurements</b>		
Incisor/PP [°]	116.88	9.50
PABW at apex level [mm]	4.28	1.69
Inter-root distance at apex [mm]	3.66	1.53

PP — palatal plane; PABW — palatal alveolar bone width; SD — standard deviation

**Table 2.** Number and percentages of incisive canal (IC) level to maxillary incisors apex level

IC level to incisors' apex	N (%)
Below apex	52 (43.3%)
At apex	60 (50.0%)
Above apex	8 (6.7%)
Total	120 (100%)

No significant association was observed between age and all measurements used to assess the maxillary incisors ( $p > 0.05$ ) (Table 4). However, a significant negative association was observed between sex and

**Table 3.** Association between incisive canal (IC) and the maxillary central incisors

	R-squared	CC	P-value
IC/PP	0.084	0.289	0.001*
Incisor/PP			
IC width at sagittal view	0.083	0.288	0.001*
PABW at apex level			
IC width at axial view	0.028	0.166	0.07
Inter-root distance at apex			

Significance level: \* $p < 0.01$ , CC — correlation coefficient; PP — palatal plane, PABW — palatal alveolar bone width

PABW at the apical level ( $p < 0.001$ ), and males exhibited a stronger association than females (Table 4).

By contrast, age showed a significant positive association with IC width in the sagittal ( $p < 0.05$ ) and axial perspectives ( $p < 0.01$ ) and a negative association with IC level relative to the incisor apices ( $p < 0.05$ ). Sex was significantly associated with the IC/PP angle and IC width in the sagittal perspective ( $p < 0.01$ ), and males exhibited a stronger association than females (Table 5).

## DISCUSSION

The present study assessed the relationship between the maxillary incisors and the IC using CBCT. The results revealed a substantial association between the IC/PP and the incisors/PP angles and between IC width in the sagittal perspective and PABW at the

**Table 4.** Association between the assessed variables for the incisors according to gender and age

	P-value — according to gender			P-value — according to age		
	R-squared	CC	P-value	R-squared	CC	P-value
Incisor/PP	0.010	-0.101	0.136	0.022	0.147	0.054
PABW at apex level	0.115	-0.339	0.000*	0.000	-0.008	0.465
Inter-root distance at apex	0.000	-0.018	0.422	0.015	-0.121	0.094

Significance level: \* $p < 0.001$ , CC — correlation coefficient; PP — palatal plane, PABW — palatal alveolar bone width

**Table 5.** Association between the assessed variables for the incisive canal (IC) according to gender and age

	P-value — according to gender			P-value — according to age		
	R-squared	CC	P-value	R-squared	CC	P-value
IC/PP	0.076	-0.276	0.001**	0.001	-0.037	0.343
IC width sagittal view	0.087	-0.295	0.001**	0.027	0.165	0.036*
IC width axial view	0.001	-0.034	0.357	0.086	0.293	0.001**
IC level to incisors' apex	0.003	0.055	0.275	0.023	-0.153	0.047

Significance level: \* $p < 0.05$ , \*\* $p < 0.01$ , CC — correlation coefficient; PP — palatal plane, PABW — palatal alveolar bone width

apical level. Age was an influencing factor for the IC dimensions including IC width in the sagittal and axial perspectives and IC level relative to the incisor apices. By contrast, sex was an influencing factor for changes in the IC/PP angle, IC width in the sagittal perspective, and PABW at the apical level.

The morphologic aspects of the maxillary central incisors and their proximity with the IC have been evaluated using CBCT in many studies [4, 8]. Chatriyanuyoke et al. [4] examined the proximity of the IC to the roots of the maxillary central incisors (MCIR) in 120 subjects. They observed that the mean IC-to-MCIR distances were greater at the apex than at the mid-root level and greater in male subjects than in female subjects. They also observed that the IC length was significantly affected by age. Thus, dental procedures at the maxillary central incisor mid-root region require more precautionary measures, especially in younger and female patients, to avoid IC penetration [4].

By contrast, Gull et al. [8] found a significant association between inter-root distance and palatal IC opening. However, the present study did not show any association between the inter-root distance at the apex and IC width, age, or sex. Such variability in the results might indicate that it is important to assess the maxillary incisor roots and their relationship with the surrounding structures using three-dimensional evaluation to avoid probable complications in each case wherein retraction of incisors is considered.

Panda et al. [20] used CBCT to determine the influence of different sociodemographic characteristics such as age, ethnicity, edentulism, and sex on the IC dimensions and anterior maxillary bone width among 300 Indian patients. They reported that age had a significant influence on the mean frontal maxillary bone thickness. Subjects aged 16 to 25 years had greater bone width than those aged above 45 years [20]. By contrast, the present study did not show any association between age and bone thickness. Panda et al. [20] also reported that sex had a pivotal influence on the diameter of the IC foramen. Male subjects exhibited greater foramen diameter than female subjects. Similar findings were observed in the present study.

In a previous study, the association between the frontal IC ridge conformation and incisor implant placement was determined for both dentulous and partially edentulous individuals. Edentulous subjects exhibited lower bone thickness at the level of the IC compared to dentulous subjects [9]. This indicates

that the probability of IC damage in elderly patients is greater during implant placement in patients with missing incisors. Although this variable was not assessed in the present study, IC width and length relative to the roots of the maxillary incisors seem to change with age, as confirmed in the present study. Thus, a more cautious and in-depth assessment is important in elderly patients before dental procedures.

## CONCLUSIONS

A significant positive association was observed between IC/PP and incisor/PP angles.

A significant positive association was observed between IC width and PABW at the apical level.

No significant association between IC width and the maxillary incisor inter-root distance at the apical level.

No significant association was observed between age and all measurements used to assess the maxillary incisors. By contrast, age showed a significant positive association with IC width and axial perspectives, and a negative association with IC level relative to the incisor apices.

Sex was significantly associated with PABW at the apical level, the IC/PP angle and the IC width.

## Acknowledgements

The author would like to thank Dr. Mashael Othman and Dr. Areej Dirham for their contribution to data collection.

**Conflict of interest:** None declared

## REFERENCES

1. Akin M, Baka ZM, Ileri Z, et al. Alveolar bone changes after asymmetric rapid maxillary expansion. *Angle Orthod.* 2015; 85(5): 799–805, doi: [10.2319/090214.1](https://doi.org/10.2319/090214.1), indexed in Pubmed: [25478739](https://pubmed.ncbi.nlm.nih.gov/25478739/).
2. Al-Amery SM, Nambiar P, Jamaludin M, et al. Cone beam computed tomography assessment of the maxillary incisive canal and foramen: considerations of anatomical variations when placing immediate implants. *PLoS One.* 2015; 10(2): e0117251, doi: [10.1371/journal.pone.0117251](https://doi.org/10.1371/journal.pone.0117251), indexed in Pubmed: [25679505](https://pubmed.ncbi.nlm.nih.gov/25679505/).
3. Braut V, Bornstein MM, Belsler U, et al. Thickness of the anterior maxillary facial bone wall—a retrospective radiographic study using cone beam computed tomography. *Int J Periodontics Restorative Dent.* 2011; 31(2): 125–131, indexed in Pubmed: [21491011](https://pubmed.ncbi.nlm.nih.gov/21491011/).
4. Chatriyanuyoke P, Lu CI, Suzuki Y, et al. Nasopalatine canal position relative to the maxillary central incisors: a cone beam computed tomography assessment. *J Oral Implantol.* 2012; 38(6): 713–717, doi: [10.1563/AAID-JOI-D-10-00106](https://doi.org/10.1563/AAID-JOI-D-10-00106), indexed in Pubmed: [20932126](https://pubmed.ncbi.nlm.nih.gov/20932126/).

5. Etoz M, Sisman Y. Evaluation of the nasopalatine canal and variations with cone-beam computed tomography. *Surg Radiol Anat.* 2014; 36(8): 805–812, doi: [10.1007/s00276-014-1259-9](https://doi.org/10.1007/s00276-014-1259-9), indexed in Pubmed: [24488202](https://pubmed.ncbi.nlm.nih.gov/24488202/).
6. Fu JH, Wang HL. Reliability of volumetric imaging software for cone-beam computed tomography – influence of medical education. *Dentomaxillofac Radiol.* 2013; 22: 182–186.
7. Gönül Y, Bucak A, Atalay Y, et al. MDCT evaluation of nasopalatine canal morphometry and variations: An analysis of 100 patients. *Diagn Interv Imaging.* 2016; 97(11): 1165–1172, doi: [10.1016/j.diii.2015.11.012](https://doi.org/10.1016/j.diii.2015.11.012), indexed in Pubmed: [26797526](https://pubmed.ncbi.nlm.nih.gov/26797526/).
8. Gull MAB, Maqbool S, Mushtaq M, et al. Evaluation of morphologic features and proximity of incisive canal to the maxillary central incisors using cone beam computed tomography. *IOSR J Dent Med Sci.* 2018; 17(01): 46–50.
9. Jia X, Hu W, Meng H. Relationship of central incisor implant placement to the ridge configuration anterior to the nasopalatine canal in dentate and partially edentulous individuals: a comparative study. *PeerJ.* 2015; 3: e1315, doi: [10.7717/peerj.1315](https://doi.org/10.7717/peerj.1315), indexed in Pubmed: [26557434](https://pubmed.ncbi.nlm.nih.gov/26557434/).
10. Kapila S, Conley RS, Harrell WE. The current status of cone beam computed tomography imaging in orthodontics. *Dentomaxillofac Radiol.* 2011; 40(1): 24–34, doi: [10.1259/dmfr/12615645](https://doi.org/10.1259/dmfr/12615645), indexed in Pubmed: [21159912](https://pubmed.ncbi.nlm.nih.gov/21159912/).
11. Keith DA. Phenomenon of mucous retention in the incisive canal. *J Oral Surg.* 1979; 37(11): 832–834, indexed in Pubmed: [290778](https://pubmed.ncbi.nlm.nih.gov/290778/).
12. Kook YA, Kim G, Kim Y. Comparison of alveolar bone loss around incisors in normal occlusion samples and surgical skeletal class III patients. *Angle Orthod.* 2012; 82(4): 645–652, doi: [10.2319/070111-424.1](https://doi.org/10.2319/070111-424.1), indexed in Pubmed: [22129151](https://pubmed.ncbi.nlm.nih.gov/22129151/).
13. Lee JE, Jung CY, Kim Y, et al. Analysis of alveolar bone morphology of the maxillary central and lateral incisors with normal occlusion. *Medicina (Kaunas).* 2019; 55(9): 565, doi: [10.3390/medicina55090565](https://doi.org/10.3390/medicina55090565), indexed in Pubmed: [31484416](https://pubmed.ncbi.nlm.nih.gov/31484416/).
14. Lee JE, Lee YJ, Jin SH, et al. Topographic analysis of the mandibular symphysis in a normal occlusion population using cone-beam computed tomography. *Exp Ther Med.* 2015; 10(6): 2150–2156, doi: [10.3892/etm.2015.2842](https://doi.org/10.3892/etm.2015.2842), indexed in Pubmed: [26668608](https://pubmed.ncbi.nlm.nih.gov/26668608/).
15. Leung CC, Palomo L, Griffith R, et al. Accuracy and reliability of cone-beam computed tomography for measuring alveolar bone height and detecting bony dehiscences and fenestrations. *Am J Orthod Dentofacial Orthop.* 2010; 137(4 Suppl): S109–S119, doi: [10.1016/j.ajodo.2009.07.013](https://doi.org/10.1016/j.ajodo.2009.07.013), indexed in Pubmed: [20381751](https://pubmed.ncbi.nlm.nih.gov/20381751/).
16. Liang X, Jacobs R, Martens W, et al. Macro- and micro-anatomical, histological and computed tomography scan characterization of the nasopalatine canal. *J Clin Periodontol.* 2009; 36(7): 598–603, doi: [10.1111/j.1600-051X.2009.01429.x](https://doi.org/10.1111/j.1600-051X.2009.01429.x), indexed in Pubmed: [19538333](https://pubmed.ncbi.nlm.nih.gov/19538333/).
17. López Jornet P, Boix P, Sanchez Perez A, et al. Morphological characterization of the anterior palatine region using cone beam computed tomography. *Clin Implant Dent Relat Res.* 2015; 17 Suppl 2: e459–e464, doi: [10.1111/cid.12271](https://doi.org/10.1111/cid.12271), indexed in Pubmed: [25263847](https://pubmed.ncbi.nlm.nih.gov/25263847/).
18. Nahm KY, Kang JH, Moon SC, et al. Alveolar bone loss around incisors in class I bidentoalveolar protrusion patients: a retrospective three-dimensional cone beam CT study. *Dentomaxillofac Radiol.* 2012; 41(6): 481–488, doi: [10.1259/dmfr/30845402](https://doi.org/10.1259/dmfr/30845402), indexed in Pubmed: [22184474](https://pubmed.ncbi.nlm.nih.gov/22184474/).
19. Pan Y, Chen S. Contact of the incisive canal and upper central incisors causing root resorption after retraction with orthodontic mini-implants: A CBCT study. *Angle Orthod.* 2019; 89(2): 200–205, doi: [10.2319/042318-311.1](https://doi.org/10.2319/042318-311.1), indexed in Pubmed: [30484326](https://pubmed.ncbi.nlm.nih.gov/30484326/).
20. Panda M, Shankar T, Raut A, et al. Cone beam computerized tomography evaluation of incisive canal and anterior maxillary bone thickness for placement of immediate implants. *J Indian Prosthodont Soc.* 2018; 18(4): 356–363, doi: [10.4103/jips.jips\\_167\\_18](https://doi.org/10.4103/jips.jips_167_18), indexed in Pubmed: [30449964](https://pubmed.ncbi.nlm.nih.gov/30449964/).
21. Sarikaya S, Haydar B, Cığır S, et al. Changes in alveolar bone thickness due to retraction of anterior teeth. *Am J Orthod Dentofacial Orthop.* 2002; 122(1): 15–26, doi: [10.1067/mod.2002.119804](https://doi.org/10.1067/mod.2002.119804), indexed in Pubmed: [12142888](https://pubmed.ncbi.nlm.nih.gov/12142888/).
22. Sebastian B. Mini-implants: new possibilities in interdisciplinary treatment approaches. *Case Rep Dent.* 2014; 2014: 140760, doi: [10.1155/2014/140760](https://doi.org/10.1155/2014/140760), indexed in Pubmed: [25580307](https://pubmed.ncbi.nlm.nih.gov/25580307/).
23. Shortliffe E, Perreault LE, Wiederhold G. *Medical informatics: computer applications in health care and biomedicine.* 2nd ed. Springer, New York 2001.
24. Tian YL, Liu F, Sun HJ, et al. Alveolar bone thickness around maxillary central incisors of different inclination assessed with cone-beam computed tomography. *Korean J Orthod.* 2015; 45(5): 245–252, doi: [10.4041/kjod.2015.45.5.245](https://doi.org/10.4041/kjod.2015.45.5.245), indexed in Pubmed: [26445719](https://pubmed.ncbi.nlm.nih.gov/26445719/).
25. Timock AM, Cook V, McDonald T, et al. Accuracy and reliability of buccal bone height and thickness measurements from cone-beam computed tomography imaging. *Am J Orthod Dentofacial Orthop.* 2011; 140(5): 734–744, doi: [10.1016/j.ajodo.2011.06.021](https://doi.org/10.1016/j.ajodo.2011.06.021), indexed in Pubmed: [22051495](https://pubmed.ncbi.nlm.nih.gov/22051495/).
26. Yu Q, Pan XG, Ji GP, et al. The association between lower incisal inclination and morphology of the supporting alveolar bone--a cone-beam CT study. *Int J Oral Sci.* 2009; 1(4): 217–223, doi: [10.4248/IJOS09047](https://doi.org/10.4248/IJOS09047), indexed in Pubmed: [20690425](https://pubmed.ncbi.nlm.nih.gov/20690425/).
27. Zamora N, Llamas JM, Cibrián R, et al. Cephalometric measurements from 3D reconstructed images compared with conventional 2D images. *Angle Orthod.* 2011; 81(5): 856–864, doi: [10.2319/121210-717.1](https://doi.org/10.2319/121210-717.1), indexed in Pubmed: [21469969](https://pubmed.ncbi.nlm.nih.gov/21469969/).
28. Zhang W, Skrypczak A, Weltman R. Anterior maxilla alveolar ridge dimension and morphology measurement by cone beam computerized tomography (CBCT) for immediate implant treatment planning. *BMC Oral Health.* 2015; 15: 65, doi: [10.1186/s12903-015-0055-1](https://doi.org/10.1186/s12903-015-0055-1), indexed in Pubmed: [26059796](https://pubmed.ncbi.nlm.nih.gov/26059796/).
29. Zhou Z, Chen Wu, Shen M, et al. Cone beam computed tomographic analyses of alveolar bone anatomy at the maxillary anterior region in Chinese adults. *J Biomed Res.* 2014; 28(6): 498–505, doi: [10.7555/JBR.27.20130002](https://doi.org/10.7555/JBR.27.20130002), indexed in Pubmed: [25469120](https://pubmed.ncbi.nlm.nih.gov/25469120/).

# Relationship between mandibular symphysis dimensions and skeletal pattern in adults

H.Y.A. Marghalani<sup>1</sup> , G. Guan<sup>2</sup>, P. Hyun<sup>3</sup>, S. Tabbaa<sup>4</sup>, A.I. Linjawi<sup>1</sup> , T. Al-Jewair<sup>5</sup>

<sup>1</sup>Orthodontic Department, Faculty of Dentistry King Abdulaziz University, Jeddah, Saudi Arabia

<sup>2</sup>Department of Orthodontics, University of Pennsylvania, Philadelphia, United States

<sup>3</sup>Private Practice, Albany, NY, United States

<sup>4</sup>School of Orthodontics, Jacksonville University, United States

<sup>5</sup>Department of Orthodontics, School of Dental Medicine, University of Buffalo, NY, United States

[Received: 12 March 2021; Accepted: 19 April 2021; Early publication date: 29 April 2021]

**Background:** The knowledge of dimensions of the symphysis is important for morphological and orthodontic studies. This research evaluates the association between mandibular symphysis dimensions and anteroposterior and vertical skeletal patterns in adults.

**Materials and methods:** This cross-sectional cephalometric study included 90 lateral cephalograms of untreated subjects presenting for orthodontic treatment. The inclusion criteria were adults with lateral cephalograms showing the symphyseal region and anterior cranial base. One investigator traced and analysed all cephalograms. Symphyseal height, thickness, and ratio between height and thickness were measured in relation to seven anteroposterior and vertical skeletal measurements in females and males.

**Results:** Symphyseal measurements were associated with SNA° (anteroposterior) in females and Gonial angle (vertical) in males. When analysed by anteroposterior skeletal classification (ANB°), no significant differences in symphyseal dimensions were found. Multiple linear regression analyses showed that Gonion-Nerve (mm) and Gonial angle were significantly associated with symphyseal height. Gonion-Nerve (mm), basal bone width (mm), and alveolar bone height (mm) were associated with symphyseal thickness. Basal bone width (mm) and alveolar bone height (mm) were associated with symphyseal ratio.

**Conclusions:** Symphyseal dimensions were significantly associated with vertical but not anteroposterior skeletal patterns. Future studies are warranted to evaluate the Gonion-Nerve measurements concerning the symphysis in relation to vertical and anteroposterior skeletal patterns. (Folia Morphol 2022; 81, 2: 464–471)

**Key words:** mandible, skeletal patterns, dimensions, symphysis

## INTRODUCTION

The mandibular symphysis plays an essential role in determining the profile of patients and is important part of the mandible anatomy. The boundaries of the den-toalveolar symphysis can define the limits of orthodontic

tooth movement since larger symphysis may allow for the proclination of the lower incisors [2]. Hence, the dimensions of the mandibular symphysis can serve as important diagnostic tool in the orthodontic treatment planning because of its anatomical importance.

Address for correspondence: Dr. H.Y.A. Marghalani, Faculty of Dentistry King Abdulaziz University, P.O. Box 80209, 21589 Jeddah, Saudi Arabia, e-mail: hymarghalani@kau.edu.sa

This article is available in open access under Creative Common Attribution-Non-Commercial-No Derivatives 4.0 International (CC BY-NC-ND 4.0) license, allowing to download articles and share them with others as long as they credit the authors and the publisher, but without permission to change them in any way or use them commercially.

The growth of the symphysis shows changes from childhood to adulthood in both sexes. Males demonstrate larger and later changes in symphyseal dimensions as compared to females [2]. With age, the symphyseal angle (measured between the mandibular plane and a line between the lowest point on the symphysis, or Menton and the deepest point on the anterior concavity of the symphysis, or B-point) decreases and the reduction is more significant in males than in females [2]. Also as age increases, the ratio between symphysis height and thickness also increases [2]. Symphysis ratio is important for the assessment of chin morphology. A smaller symphysis ratio, more common in males, indicates a prominent chin while a larger ratio denotes a receding chin [2].

Studies have found that symphysis ratio and morphology are strongly associated with mandibular growth direction, especially in males [2, 12]. Dolico-facial subjects (with long face) have thinner and longer dentoalveolar and basal symphyses and greater lingual dentoalveolar inclination than brachyfacial subjects (with short face) [4]. The average thickness of the symphysis at the mandibular incisor apex region is 7.32 mm, 8.72 mm, and 9.94 mm in dolico-facial, mesofacial and brachyfacial groups, respectively [4].

Moreover, vertical skeletal pattern may also influence symphysis height. A study by Ceylan et al. [7] found that mandibular dentoalveolar heights and symphyseal height and area were greater in individuals with open bites and shorter and wider in subjects with deep bites. Overall, males showed greater vertical growth rate than females in the upper 20% of the symphysis. The average height of the symphysis in adults with normal occlusion and well-balanced faces is 47 mm in males and 42.5 mm in females [4].

The symphysis may be affected by anteroposterior skeletal classification. Class I skeletal pattern has normal relationship of the maxilla (SNA) to the mandible position (SNB) measured by ANB angle. Class II skeletal pattern has backward position of mandible (large ANB value) and class III has advanced position of the mandible (less ANB value). Previous literature found that class III skeletal pattern is associated with smaller angle of the anterior concavity of the symphysis compared to class I and II. Also, the alveolus of the mandibular incisor is closer to the mandibular plane. Class III subjects also have larger symphyseal area than class I or II [5].

Evaluating the symphyseal height, thickness, and ratio is essential knowledge to the anatomy and morphology of the mandible. The aim of this study was

to evaluate the symphyseal morphology in adults presenting with different anteroposterior and vertical skeletal patterns. We hypothesized that there will be no significant association between symphyseal and skeletal features.

## MATERIALS AND METHODS

This cross-sectional cephalometric study was conducted between 2016 and 2017 using lateral cephalograms selected from Caucasian subjects presenting for orthodontic treatment at one orthodontic clinic. Ethical approval was obtained from the University at Buffalo Institutional Review Board (#419644-4). The inclusion criteria were adults 18 years old or above with pre-treatment lateral cephalograms that clearly displayed the symphyseal region and anterior cranial base. Exclusion criteria were history of orthodontic treatment or orthognathic surgery, missing teeth other than third molars, craniofacial anomalies or syndromes, musculoskeletal disorders, and history of trauma. Sample size estimation showed that a minimum of 85 records were needed to detect a correlation of  $r = 0.3$  or above between variables with a significance level of 5% and power of 80%.

A total of 90 lateral cephalograms met the inclusion criteria for this study from a pool of 5299 pre-treatment records organised by year. The sample included 44 females and 46 males with age range of 18–44 years old. Lateral cephalograms then were traced and analysed by one author (H.M.) using Dolphin imaging software (Version 11.7.05.66 Premium; Dolphin Imaging and Management Solutions, Chatsworth, California). The study used modified landmarks from those presented by Chung et al. [8] and Suri et al. [17] (Fig. 1). The posterior alveolar point (PAP), the most inferior and posterior point on the anterior border of the ramus, as defined by Suri et al. [17] was hard to locate on the cephalograms. Therefore, a modification to this analysis was made. The analysis utilised the bisecting line of the Gonial angle (formed by lines tangent to the lower and posterior parts of the mandible) to locate the 'nerve' point. This point is the intersection of that line with inferior alveolar nerve. Ten linear and angular measurements were used for this study. Symphyseal measurements included the height, thickness, and ratio of height to thickness. Anteroposterior and vertical skeletal measurements included the  $SNA^\circ$ ,  $SNB^\circ$ ,  $ANB^\circ$ , alveolar bone height (mm), basal bone width (mm), Ar-Go-Me $^\circ$  (Gonial angle), and Gonion-Nerve distance (mm).

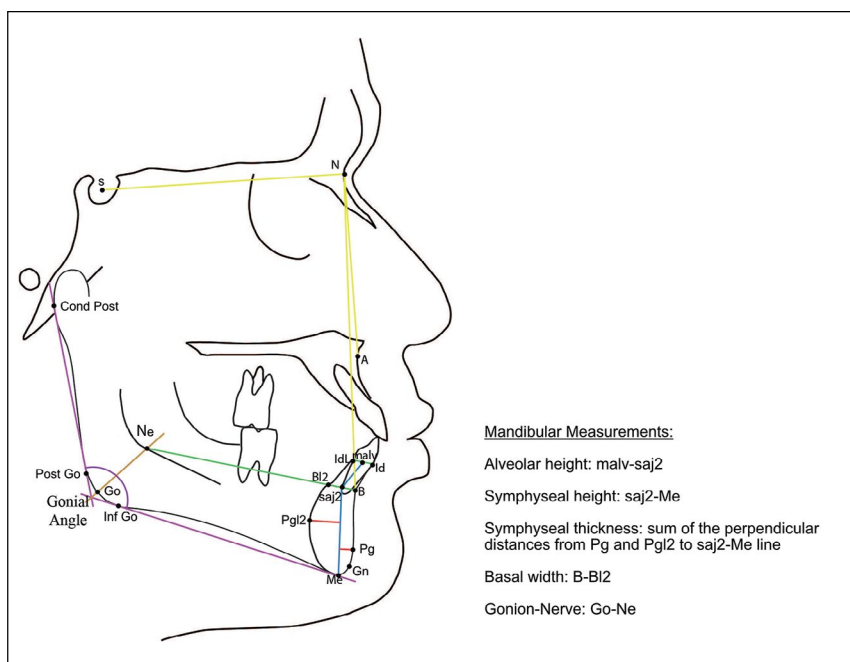


**Figure 1.** Landmarks and measurements used in this study. N — nasion; S — sella; Point A — subspinale; Point B — supramentale; Id — infradentale; Pg — pogonion; Gn — gnathion; Me — menton; Go — Gonion. Other Landmarks: Gonial Angle — formed by the intersection of 2 lines; one from Menton (Me) to Inferior Gonion (Inf Go) and the other from Condyle Posterior (Cond Post) to Posterior Gonion (Post Go); Nerve (Ne) — formed by a line that bisects Gonial angle (formed by the intersection of the previous two lines which intersects with inferior alveolar nerve at Ne); B12 — the point of intersection of a line drawn from Ne to B, with the lingual surface of symphysis; saj2 — the mid-point of a line drawn from B12 to B; Pgl2 — the furthest point on the lingual contour of the symphysis, located by the largest perpendicular distance from a line drawn from the saj2 to Me; malv — middle point of a line drawn from Idl to Id. Mandibular measurements: alveolar height — distance of a line drawn from malv to saj2; symphyseal height — the line drawn from saj2 to Me; symphyseal thickness — the sum of the distances of the perpendiculars from Pg and Pgl2 to a line drawn from saj2 to Me; basal width — distance of a line drawn from B12 to B; Gonial angle: angle formed by the intersection of two lines (Post Go-Condyle Posterior and Me-Inf Go); Gonion-Nerve (mm): distance from the intersection of two lines (Post Go-Condyle Posterior and Me-Inf Go) and Ne point in mm.

### Statistical analysis

Ten cephalograms were randomly chosen and re-measured by one author (H.M.) to assess the intra-examiner reliability using intraclass correlation coefficient (ICC). Data were analysed using SPSS software (PASW statistics version 19). Pearson correlation coefficients between each of the independent variables ( $ANB^\circ$ ,  $SNA^\circ$ ,  $SNB^\circ$ , alveolar height, basal width, Gonial angle, and Gonion-Nerve distance) with the dependent variables (symphysis height, thickness, and ratio) were assessed. Correlations between anteroposterior skeletal classification and symphyseal variables were calculated according to  $ANB^\circ$  values ( $1-4^\circ =$  class I; more than  $4^\circ =$  class II; and less than  $1^\circ =$  class III). Correlation strengths were analysed according to Evans [9]. Multiple linear regression analyses were conducted to determine strength of association between symphyseal height, thickness, and ratio with multiple independent variables. Significance was set at 5%.

## RESULTS

### Intra-examiner reliability

There was significant correlation between the repeated measurements for all variables with the ICC ranging from 0.97 to 0.82 (Table 1).

### Descriptive statistics

Table 1 presents the mean skeletal measurements according to sex. Overall, the mean  $ANB^\circ$  was  $2.3^\circ$  (standard deviation [SD] of 3.1). The mean  $SNA^\circ$  and  $SNB^\circ$  were  $82.5^\circ$  (SD of 3.8 $^\circ$ ) and  $80.2^\circ$  (SD of 3.95 $^\circ$ ), respectively. Significant differences between males and females were noted for  $ANB^\circ$  ( $p = 0.003$ ) and Gonion-Nerve distance ( $p < 0.01$ ).

Table 2 presents the means for the outcomes of interest: symphysis height, thickness, and ratio according to sex. They were significantly different between females and males with a general trend of being smaller in females compared to males. For example, the symphyseal thickness in females was

**Table 1.** Mean anteroposterior and vertical skeletal measurements in females (n = 44) and males (n = 46)

Variable	Sex	Mean	SD	Median	Significance*
ANB°	Female	3.29	2.85	3.55	0.003
	Male	1.37	3.15	.8	
SNA°	Female	83.12	3.8	82.9	0.103
	Male	81.82	3.65	81.65	
SNB°	Female	79.84	4.23	80.15	0.448
	Male	80.47	3.69	80.15	
Ar-Go-Me°	Female	123.35	6.98	122.35	0.277
	Male	121.44	9.35	123.3	
Alveolar bone height [mm]	Female	12.71	2.82	12.45	0.226
	Male	13.4	2.57	13.15	
Basal bone width [mm]	Female	7.11	1.47	7.2	0.536
	Male	7.32	1.76	7.5	
Gonion-Nerve [mm]	Female	16.68	3.03	16.95	< 0.001
	Male	19.28	3.06	19.15	

\*Independent t-test,  $p < 0.05$ ; SD — standard deviation

**Table 2.** Mean symphyseal measurements in females and males

Variable	Sex	Mean	Standard deviation	Median	Significance
Symphyseal height [mm]	Female	18.25	2.2	18.1	< 0.001
	Male	21.22	2.04	21.5	
Symphyseal thickness [mm]	Female	11.92	1.68	12.15	0.005
	Male	12.95	1.75	13.15	
Height to thick ratio [%]	Female	1.55	0.22	1.53	0.029
	Male	1.67	0.28	1.63	

less than males by about 1 mm ( $p = 0.005$ ). Table 3 presents the measured values in each skeletal class.

#### Association between symphysis measurements and skeletal morphology

Table 4 shows the correlations between symphysis dimensions and multiple skeletal measurements. In females, there was a statistically significant but weak correlation between SNA° and symphyseal height ( $r = 0.35$ ,  $p = 0.021$ ) and symphyseal thickness ( $r = 0.4$ ,  $p = 0.021$ ). There was also a strong inverse relationship between symphyseal ratio and basal width ( $r = -0.71$ ,  $p < 0.001$ ). In males, significant correlations were noted between the three symphyseal measurements and Gonial angle. Table 5 presents the correlation between anteroposterior skeletal classification by ANB° and the three symphyseal dimensions. None of the correlations was statistically significant.

Three multivariate models were produced using stepwise multiple regression analysis for symphyseal height, thickness, and ratio. The first model (Table 5) used the symphyseal height as the dependent var-

iable, Gonion-Nerve ( $p < 0.001$ ), and Gonial angle ( $p = 0.005$ ) were the only significant variables. For every 1 mm increase in Gonion-Nerve, the symphysis height increases by 0.37 mm and for every 1 degree increase in the Gonial angle, the symphysis height increases by 0.11 mm. For symphyseal thickness, basal width ( $p < 0.001$ ), Gonion-Nerve ( $p = 0.01$ ), and alveolar height ( $p = 0.18$ ) showed statistical significance. The symphyseal thickness relationship was proportional to basal width and inverse to alveolar height. Basal bone width ( $p < 0.001$ ) and alveolar bone height ( $p = 0.015$ ) showed significant association with symphysis ratio (Table 6).

## DISCUSSION

This study was conducted to determine associations between symphysis height, thickness, and ratio and multiple skeletal variables and using a modified analysis from two previous studies [8, 17]. The modified analysis utilised the bisecting line of the Gonial angle to locate the landmark 'nerve' point. This land-

**Table 3.** Mean symphyseal measurements in each skeletal classification

Variable	Class	N	Mean	Standard deviation	Median
Symphyseal height [mm]	Class III	33	20.4	2.5	20.2
	Class I	29	19.32	2.34	19.5
	Class II	28	19.48	2.85	19.1
	Total	90	19.77	2.59	19.5
Symphyseal thickness [mm]	Class III	33	12.43	1.99	12.7
	Class I	29	12.27	1.68	12.2
	Class II	28	12.65	1.66	12.7
	Total	90	12.45	1.78	12.5
Height/thick ratio [%]	Class III	33	1.68	0.3	1.63
	Class I	29	1.59	0.21	1.62
	Class II	28	1.55	0.23	1.55
	Total	90	1.61	0.26	1.6

**Table 4.** Correlations between symphyseal measurements and skeletal pattern in females and males

Symphyseal measurement	Correlation	ANB°	SNA°	SNB°	Ar-Go-Me°	Alveolar height [mm]	Basal width [mm]	Gonion-Nerve [mm]
<b>Females (n = 44)</b>								
Symphyseal height	r	0.18	0.35	0.19	-0.05	-0.02	-0.12	0.21
	Sig.	0.252	0.021	0.206	0.751	0.881	0.435	0.175
Symphyseal thickness	r	0.22	0.4	0.21	-0.1	-0.16	0.57	0.15
	Sig.	0.252	0.021	0.206	0.751	0.881	0.435	0.175
Height/thickness ratio	r	-0.09	-0.14	-0.07	0.06	0.15	-0.71	0.01
	Sig.	0.566	0.367	0.669	0.721	0.343	< 0.001	0.969
<b>Males (n = 46)</b>								
Symphyseal height	r	0.1	0.13	0.05	0.37	-0.14	-0.22	-0.08
	Sig.	0.518	0.374	0.754	0.012	0.355	0.134	0.598
Symphyseal thickness	r	0.2	0.14	-0.03	-0.49	-0.23	0.68	0.36
	Sig.	0.190	0.345	0.870	0.001	0.124	< 0.001	0.033
Height/thickness ratio	r	-0.18	-0.07	0.08	0.66	0.15	-0.75	-0.3
	Sig.	0.230	0.652	0.584	< 0.001	0.311	< 0.001	0.040

**Table 5.** Correlations between symphyseal measurements and sagittal skeletal classification

Anteroposterior skeletal pattern	Correlation	Symphyseal height	Symphyseal thickness	Height/thick ratio
Class I (n = 29)	r	0.04	0.06	0.003
	Sig.	0.831	0.751	0.990
Class II (n = 28)	r	0.06	0.12	-0.04
	Sig.	0.765	0.548	0.850
Class III (n = 33)	r	0.29	0.18	-0.08
	Sig.	0.108	0.311	0.662

mark was more reproducible than the ramus body syncline 'RBS' point, which is formed by the intersection of the line from Gonion to posterior alveolar 'PAP' point. PAP point is the most posterior inferior point on the anterior border of the ramus. Replacing PAP and RBS with the new landmarks increased the accuracy of data identification in this study.

Gonion-Nerve measurement represents the intersection of the ramus with the body of the mandible. Its correlation with the symphyseal height demonstrates that when the Gonion-Nerve distance in the posterior mandible is increased, the height will increase in the anterior of the mandible. Also, as the Gonion-Nerve distance increased, the thickness of the

**Table 6.** Multiple linear regression models for association between symphyseal measurements and skeletal pattern

Model	Unstandardised coefficients		Standardised coefficients	t	Significance	Adjusted R <sup>2</sup>
	B	Standard error	Beta			
<b>Symphyseal height [mm]</b>						
(Constant)	0.16	5.61		0.03	0.977	0.14
Gonion-Nerve	0.37	0.09	0.47	3.96	< 0.001	
Ar-Go-Me (Gonial angle)	0.11	0.04	0.34	2.88	0.005	
<b>Symphyseal thickness [mm]</b>						
(Constant)	7.45	1.07		6.96	< 0.001	0.44
Basal bone width	0.63	0.09	0.57	6.96	< 0.001	
Gonion-Nerve	0.12	0.05	0.22	2.64	0.010	
Alveolar bone height	-0.13	0.05	-0.2	-2.42	0.018	
<b>Height to thickness ratio [%]</b>						
(Constant)	2.19	0.13		17.3	< 0.001	0.51
Basal bone width	-0.11	0.01	-0.7	-9.44	< 0.001	
Alveolar bone height	0.018	0.01	0.18	2.48	0.015	

symphysis also increased ( $p = 0.002$ ). So, measuring the Gonion-Nerve can give an estimate of both the height and thickness of the symphysis. Future studies are warranted to fully investigate this measurement in its correlation with symphyseal dimensions.

This study found sexual dimorphism in regard to mean symphyseal heights. The mean symphyseal height was greater in males (21.22 mm) compared to females (18.25 mm). This result is supported by another study which found that the symphyseal vertical dimension is larger in males than females [11]. Moreover, the height to thickness ratio was close to 1.5 in both males and females suggesting that overall, normal height is 1.5 times larger than the thickness. This is different from a previous study that reported that symphysis ratio is smaller in males compared to females [2]. This could be attributed to the differences in sample ethnicity and methodology applied in the two studies.

This study assessed the correlation between anteroposterior skeletal pattern and symphysis dimensions. There was no significant relationship between symphysis height, thickness or ratio and ANB°, SNA°, or SNB° in both males and females except for SNA°. This variable had a weak to moderate correlation with symphyseal height and thickness but not ratio in females.

When ANB° was analysed categorically, no significant associations were noted between ANB° values in each skeletal class and symphysis height, thickness,

or ratio. This disagrees with Torgut and Akan [19] who found that symphyseal vertical development is negatively related to ANB°. It also contradicts with Al-Khateeb et al. [3] results who found a significant relationship between skeletal class III and the vertical dimension of the mandibular symphysis. Al-Khateeb et al. [3] used a different line extending between point infradentale, which is the most anterior superior point on the buccal alveolar crest of the mandible, and Menton to measure the total length of the mandibular symphysis. Thus, combining both the symphysis and alveolus in the total length of the mandibular symphysis. Meanwhile, in this study, the alveolus and the symphysis were separated by line B to BI2. The symphysis length is the distance from the midpoint of a line connecting B to BI2, or saj2, to Menton.

A recent study evaluated symphyseal dimensions according to sagittal and vertical skeletal relationships in both genders. It found that males had increased mandibular symphysis surface area and linear dimensions compared to females. Also, subjects with skeletal class II relationship had greater dentoalveolar length compared to those with class I and III. Chin length was also greater in subjects with average mandibular plane angle [14].

Our study found a strong positive correlation ( $p < 0.001$ ) between Gonial angle and symphysis ratio in males as compared to females ( $p = 0.721$ ). This is expected since symphysis ratio is the height divided by thickness and thus the ratio would be greater in

hyperdivergent subjects. Similar to our study, Aki et al. [2] divided the chin into symphyseal and alveolar components utilizing B-point, and showed that in individuals with receding chins, the symphysis ratio, Gonial angle, and both the lower and anterior facial height would be large. In high angle patients, dentoalveolar compensation of the alveolar bone occurs by vertical lengthening [16]. This compensation is further explained in previous studies [3, 5] which have attributed vertical growth of the symphysis to the supraeruption of dentition due to the absence of antagonist teeth in open bite cases.

The Gonial angle showed a significant negative correlation to symphysis thickness ( $p = 0.001$ ). This relationship can be demonstrated in deep bite cases that have smaller values for Gonial angle [7] where the increase in thickness could be attributed to the masseter muscle hyperfunction [18]. This also explains the larger ratio in open bite cases that have no incisor contact [2].

This study found no correlation between alveolar bone height and symphyseal height, thickness, or ratio in both genders. This might be due to the fact that alveolar bone height is mainly affected by lower incisor position and root length (measured from midpoint of the CEJ line to the midpoint of B-BI2 line) [20], independent of symphyseal height. This study however, only assessed height and not thickness of the alveolar bone. Foosiri et al. [10] evaluated alveolar thickness in relation symphyseal ratio and found that the ratio is negatively correlated with buccal and lingual alveolar bone thickness. Future studies may consider evaluating both dimensions of the alveolar bone.

The multiple linear regression model for symphysis height showed a statistically significant association with Gonial angle and Gonion-Nerve measurements, rejecting the hypothesis of this study. This finding was confirmed in previous studies [6, 15] and is also consistent with Kasai et al. [13] who showed a positive relationship between Gonial angle and symphyseal height. Moreover, Ahn et al. [1] found that vertical skeletal dimension was related to the symphyseal morphology more than transverse or anteroposterior dimensions. Therefore, it can be concluded that individuals long anterior face height had elongated symphysis, and those with short face height have wide symphysis. Regarding the multiple regression model for symphyseal thickness, basal bone width and alveolar bone height were entered in addition to Gonion-Nerve. Basal bone width is more related to

symphysis thickness, as it is measured more superior and parallel to symphysis thickness on the cephalograms. In terms of the model for symphysis ratio, basal width and alveolar height were significantly associated with the ratio of height to thickness.

### Limitations of the study

This study had several limitations. The study used two-dimensional lateral cephalograms and did not assess the structures in all three-dimensions. Also, due to the stringent inclusion criteria applied in this study, the sample size included was small. Large future three-dimensional studies are warranted to confirm the results and to evaluate additional variables in relation to symphyseal dimensions. Further studying of Gonion-Nerve in individuals with different anteroposterior skeletal patterns is recommended to fully understand the association between this variable and symphysis dimensions. This study shed light on the morphological features of the mandibular symphysis. These features can be assessed clinically to ensure proper orthodontic diagnosis and planning and to prevent movement of teeth out of the symphyseal envelope during treatment.

### CONCLUSIONS

The mean symphyseal height, thickness, and ratio of height to thickness were significantly greater in males than in females.

Symphyseal height, thickness, and ratio were not significantly associated with anteroposterior skeletal classification (ANB°).

Symphyseal height, thickness, and ratio were significantly associated with Gonial angle (vertical skeletal pattern), Gonion-Nerve, basal bone width, and alveolar bone height.

Future studies are warranted to evaluate Gonion-Nerve measurements concerning the symphysis in relation to different skeletal pattern.

**Conflict of interest:** None declared

### REFERENCES

1. Ahn MS, Shin SM, Yamaguchi T, et al. Relationship between the maxillofacial skeletal pattern and the morphology of the mandibular symphysis: Structural equation modeling. *Korean J Orthod.* 2019; 49(3): 170–180, doi: [10.4041/kjod.2019.49.3.170](https://doi.org/10.4041/kjod.2019.49.3.170), indexed in Pubmed: [31149607](https://pubmed.ncbi.nlm.nih.gov/31149607/).
2. Aki T, Nanda RS, Currier GF, et al. Assessment of symphysis morphology as a predictor of the direction of mandibular growth. *Am J Orthod Dentofacial Orthop.* 1994; 106(1): 60–69, doi: [10.1016/S0889-5406\(94\)70022-2](https://doi.org/10.1016/S0889-5406(94)70022-2), indexed in Pubmed: [8017351](https://pubmed.ncbi.nlm.nih.gov/8017351/).

3. Al-Khateeb SN, Al Maaitah EF, Abu Alhaja ES, et al. Mandibular symphysis morphology and dimensions in different anteroposterior jaw relationships. *Angle Orthod.* 2014; 84(2): 304–309, doi: [10.2319/030513-185.1](https://doi.org/10.2319/030513-185.1), indexed in Pubmed: [23914822](https://pubmed.ncbi.nlm.nih.gov/23914822/).
4. Arruda K, Neto JV, Almeida G. Assessment of the mandibular symphysis of Caucasian Brazilian adults with well-balanced faces and normal occlusion: the influence of gender and facial type. *Dental Press J Orthod.* 2012; 17(3): 40–50, doi: [10.1590/s2176-94512012000300012](https://doi.org/10.1590/s2176-94512012000300012).
5. Buschang PH, Julien K, Sachdeva R, et al. Childhood and pubertal growth changes of the human symphysis. *Angle Orthod.* 1992; 62(3): 203–210, doi: [10.1043/0003-3219\(1992\)062<0203:CAPGCO>2.0.CO;2](https://doi.org/10.1043/0003-3219(1992)062<0203:CAPGCO>2.0.CO;2), indexed in Pubmed: [1416240](https://pubmed.ncbi.nlm.nih.gov/1416240/).
6. Buschang PH, Jacob H, Carrillo R. The morphological characteristics, growth, and etiology of the hyperdivergent phenotype. *Seminars in Orthodontics.* 2013; 19(4): 212–226, doi: [10.1053/j.sodo.2013.07.002](https://doi.org/10.1053/j.sodo.2013.07.002).
7. Ceylan I, Eröz UB. The effects of overbite on the maxillary and mandibular morphology. *Angle Orthod.* 2001; 71(2): 110–115, doi: [10.1043/0003-3219\(2001\)071<0110:TEOOOT>2.0.CO;2](https://doi.org/10.1043/0003-3219(2001)071<0110:TEOOOT>2.0.CO;2), indexed in Pubmed: [11302586](https://pubmed.ncbi.nlm.nih.gov/11302586/).
8. Chung CJ, Jung S, Baik HS. Morphological characteristics of the symphyseal region in adult skeletal Class III crossbite and openbite malocclusions. *Angle Orthod.* 2008; 78(1): 38–43, doi: [10.2319/101606-427.1](https://doi.org/10.2319/101606-427.1), indexed in Pubmed: [18193946](https://pubmed.ncbi.nlm.nih.gov/18193946/).
9. Evans JD. *Straightforward statistics for the behavioral sciences.* Brooks/Cole Publishing, Pacific Grove, CA 1996.
10. Foosiri P, Mahatumarat K, Panmekiate S. Relationship between mandibular symphysis dimensions and mandibular anterior alveolar bone thickness as assessed with cone-beam computed tomography. *Dental Press J Orthod.* 2018; 23(1): 54–62, doi: [10.1590/2177-6709.23.1.054-062.oar](https://doi.org/10.1590/2177-6709.23.1.054-062.oar), indexed in Pubmed: [29791685](https://pubmed.ncbi.nlm.nih.gov/29791685/).
11. Gómez Y, García-Sanz V, Zamora N, et al. Associations between mandibular symphysis form and craniofacial structures. *Oral Radiol.* 2018; 34(2): 161–171, doi: [10.1007/s11282-017-0292-x](https://doi.org/10.1007/s11282-017-0292-x), indexed in Pubmed: [30484128](https://pubmed.ncbi.nlm.nih.gov/30484128/).
12. Haskell BS. The human chin and its relationship to mandibular morphology. *Angle Orthod.* 1979; 49(3): 153–166, doi: [10.1043/0003-3219\(1979\)049<0153:THCAIR>2.0.CO;2](https://doi.org/10.1043/0003-3219(1979)049<0153:THCAIR>2.0.CO;2), indexed in Pubmed: [290281](https://pubmed.ncbi.nlm.nih.gov/290281/).
13. Kasai K, Enomoto Y, Ogawa T, et al. Morphological characteristics of vertical sections of the mandible obtained by CT scanning. *Anthropol Sci.* 1996; 104(3): 187–198, doi: [10.1537/ase.104.187](https://doi.org/10.1537/ase.104.187).
14. Linjawi AI, Afify AR, Baeshen HA, et al. Mandibular symphysis dimensions in different sagittal and vertical skeletal relationships. *Saudi J Biol Sci.* 2021; 28(1): 280–285, doi: [10.1016/j.sjbs.2020.09.062](https://doi.org/10.1016/j.sjbs.2020.09.062), indexed in Pubmed: [33424307](https://pubmed.ncbi.nlm.nih.gov/33424307/).
15. Puigdollers A, Molina-Berlanga N, Llopis-Perez J, et al. Lower incisor dentoalveolar compensation and symphysis dimensions among Class I and III malocclusion patients with different facial vertical skeletal patterns. *Angle Orthod.* 2013; 83(6): 948–955, doi: [10.2319/011913-48.1](https://doi.org/10.2319/011913-48.1), indexed in Pubmed: [23758599](https://pubmed.ncbi.nlm.nih.gov/23758599/).
16. Sadek MM, Sabet NE, Hassan IT, et al. Alveolar bone mapping in subjects with different vertical facial dimensions. *Eur J Orthod.* 2015; 37(2): 194–201, doi: [10.1093/ejo/cju034](https://doi.org/10.1093/ejo/cju034), indexed in Pubmed: [25114124](https://pubmed.ncbi.nlm.nih.gov/25114124/).
17. Suri S, Ross RB, Tompson BD. Mandibular morphology and growth with and without hypodontia in subjects with Pierre Robin sequence. *Am J Orthod Dentofacial Orthop.* 2006; 130(1): 37–46, doi: [10.1016/j.ajodo.2005.09.026](https://doi.org/10.1016/j.ajodo.2005.09.026), indexed in Pubmed: [16849070](https://pubmed.ncbi.nlm.nih.gov/16849070/).
18. Swasty D, Lee JS, Huang JC, et al. Anthropometric analysis of the human mandibular cortical bone as assessed by cone-beam computed tomography. *J Oral Maxillofac Surg.* 2009; 67(3): 491–500, doi: [10.1016/j.joms.2008.06.089](https://doi.org/10.1016/j.joms.2008.06.089), indexed in Pubmed: [19231771](https://pubmed.ncbi.nlm.nih.gov/19231771/).
19. Torgut AG, Akan S. Mandibular symphysis morphology in different skeletal malocclusions and its correlation with uvulo-glossopharyngeal structures. *Cranio.* 2021; 39(6): 533–540, doi: [10.1080/08869634.2019.1677311](https://doi.org/10.1080/08869634.2019.1677311), indexed in Pubmed: [31601164](https://pubmed.ncbi.nlm.nih.gov/31601164/).
20. Wehrbein H, Bauer W, Diedrich P. Mandibular incisors, alveolar bone, and symphysis after orthodontic treatment. A retrospective study. *Am J Orthod Dentofacial Orthop.* 1996; 110(3): 239–246, doi: [10.1016/s0889-5406\(96\)80006-0](https://doi.org/10.1016/s0889-5406(96)80006-0), indexed in Pubmed: [8814023](https://pubmed.ncbi.nlm.nih.gov/8814023/).

# The influence of mandibular divergence on facial soft tissue thickness in class I patients: a cephalometric study

T.M. Perović<sup>1,2</sup> , M. Blažej<sup>3</sup>, I. Jovanović<sup>1</sup>

<sup>1</sup>Faculty of Medicine, University of Niš, Niš, Serbia

<sup>2</sup>Dental Clinic, Department for Orthodontics, Niš, Serbia

<sup>3</sup>Private Dental Clinic, Smiledent, Niš, Serbia

[Received: 12 January 2021; Accepted: 3 March 2021; Early publication date: 22 March 2021]

**Background:** The aims of this study were to evaluate the association between mandibular divergence and facial soft tissue thickness (FSTT) measured at different profile levels, and the gender difference in FSTT.

**Materials and methods:** Lateral cephalograms were used to examine nine linear distances: the glabella area (G-G1), nasal (N-N1) and subnasal area (A-Sn), upper (Sd-Ls) and lower lip thickness (Id-Li), mentolabial sulcus (B-Sm), chin area (Pg-Pg1), gnathion area (Gn-Gn1) and menton area (Me-Me1) in 155 adult Caucasian subjects (79 males, 76 females) from the central Balkan area. Subjects were divided into three groups according to the ANB angle, Wit's appraisal and SN/GoGn angle into normodivergent (28 male, 27 female subjects), hypodivergent (26 males, 25 females) and hyperdivergent (25 males, 24 females).

**Results:** Progressive decreasing in the soft tissue thickness from hypo- towards hyperdivergent group was established in N-N1, A-Sn, Gn-Gn1, Me-Me1. There are significant differences in Gn-Gn1 and Me-Me1 ( $p < 0.02$ ). Progressive increasing of FSTT happens only at the level of mentolabial sulcus and these differences are significant. Significant gender differences were established for the following distances: N-N1 in hyperdivergent, A-Sn in all three examined groups, the upper lip thickness in normo- and hyperdivergent, the lower lip thickness in hypodivergent, the thickness of mentolabial sulcus in hypo- and normodivergent, Pg-Pg1 in hyperdivergent and Me-Me1 in normodivergent subjects ( $p < 0.05$ ).

**Conclusions:** Facial soft tissue thickness showed a various degree of dependence on vertical developmental pattern at different levels of measurement. The areas whose thickness is significantly conditioned by this pattern were established: the chin area at level Gn-Gn1, Me-Me1 and the region of the mentolabial sulcus (B-Sm). At most levels, male subjects have thicker soft tissues and these differences are significant for all three groups in the subnasal area. (Folia Morphol 2022; 81, 2: 472–480)

**Key words:** mandibular divergence, soft tissue thickness, face

Address for correspondence: Dr. T. Perović, Sestre Baković 16/22, 18000 Niš, Serbia, tel: +381 18 520 763, fax: +381 18 453 67 36, e-mail: tatjana.tanic@gmail.com

This article is available in open access under Creative Common Attribution-Non-Commercial-No Derivatives 4.0 International (CC BY-NC-ND 4.0) license, allowing to download articles and share them with others as long as they credit the authors and the publisher, but without permission to change them in any way or use them commercially.

## INTRODUCTION

Facial contours are traditionally considered to be a result of the position of basic dentoskeletal tissue followed by soft tissue [19]. However, a contemporary approach shows a change in this attitude in terms of variability of the thickness of the covering soft tissue, which does not only passively follow the bone tissue. The covering soft tissues of the face (skin, fat and muscles) can develop proportionately or disproportionately relative to the corresponding skeletal structures. Variations can include thickness, length and the tone of soft tissue and they are conditioned by the sex, age, race and ethnicity, as well as the growth pattern [17, 22–24].

The influence of sagittal developmental pattern on the facial soft tissue thickness (FSTT) was proven in multiple contemporary studies. Increased soft tissue thickness was reported where there is anteroposterior skeletal jaw deficiency [2, 18]. Where there is not a jawbone deficiency, there are the greatest gender differences in the soft tissue thickness [16].

However, according to the latest knowledge, vertical pattern of growth also affects the relationship between the bone tissue and covering soft tissue. According to the type of mandibular divergence, faces can be hyperdivergent (high angle-mandibular clockwise rotation) (Fig. 1), hypodivergent (low angle-mandibular counterclockwise rotation) (Fig. 2) and average, normodivergent faces (normal angle) (Fig. 3).

Developmental changes of cranial base and mandibular ramus with condyle and gonial angle determine the direction in which vertical face development will dominate. The characteristics of hyperdivergent growth are increased gonial angle, retroflexion of condyles in relation to mandibular ramus, decreasing in the length of the back part of cranial plane and the decreasing of the angle of cranial base. This excessive vertical growth may result in a gummy smile, lip incompetence and elongated face. In hypodivergent growth, these changes are reverse. There is a lack of vertical growth which can lead to the excessive exposure of incisors, deep bite and the reduced lower third of the face [1, 5, 25]. In normal divergence growth, vertical face growth is harmonious in relation to the growth in other directions.

The behaviour of soft tissue in relation to mandibular divergence pattern was mostly researched in the chin area. Therefore, decreased chin prominence in vertical growth pattern was established; in horizontal growth pattern there is a normal or increased chin

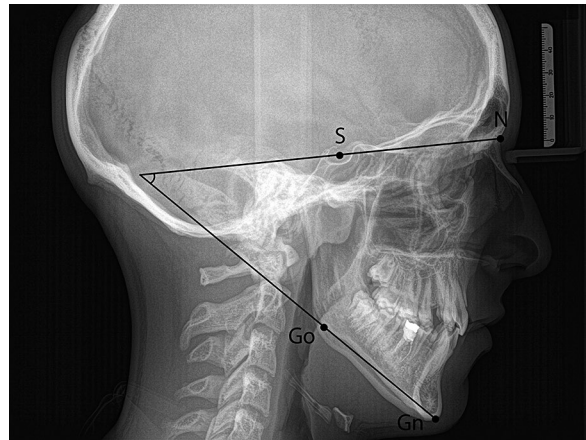


Figure 1. Lateral cephalogram of hyperdivergent pattern.

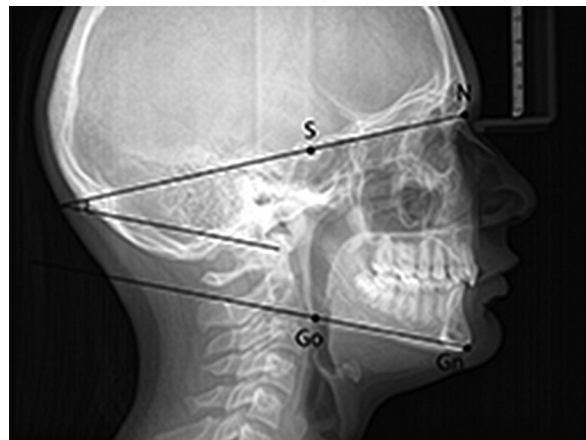


Figure 2. Lateral cephalogram of hypodivergent pattern.

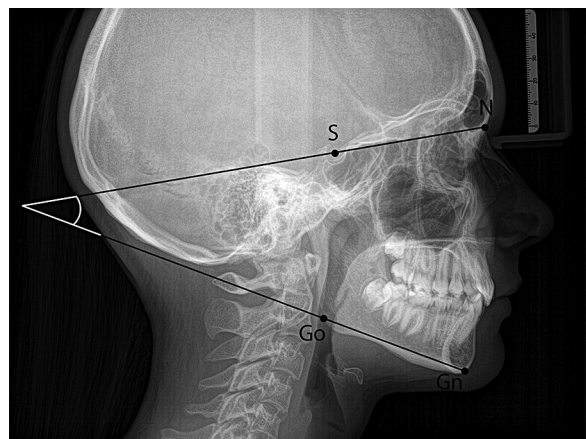


Figure 3. Lateral cephalogram of normodivergent pattern.

prominence by virtue of the mandibular counterclockwise rotation [6]. According to Shinde et al. [21], soft

tissue chin thickness adjusts to the position of skeletal chin and it is different at various levels of the chin. Divergent patterns of the mandible not only affect the soft tissue chin thickness, but they can cause changes in the length and thickness of the upper lip [6].

The aims of this study were to evaluate the following in adult patients: 1) the association between mandibular divergence and FSTT measured at different profile levels and 2) the difference in FSTT between males and females.

## MATERIALS AND METHODS

A cross-sectional, comparative, descriptive clinical study was undertaken, which was approved by the Faculty of Medicine in Niš under the general project title of Clinical and Experimental Examination of the Stomatognathic System and Modern Therapeutic Procedures, Project Number 11, from March 8, 2017, Niš, Republic of Serbia. All patients provided written informed consent to participate in the study.

This study included the examination and the analysis of cephalometric radiography-derived lateral cephalograms to evaluate FSTT for 155 adult Caucasian orthodontic patients (79 males, 76 females) from the mid-Balkan region, which were taken from the patient archives. Cephalometric radiography-derived lateral cephalograms were recorded during routine diagnostic procedures for patients who were examined in the Department of Jaw Orthopaedics at the Clinic of Dentistry in Niš, who were aged between 18 and 22 years, and who underwent orthodontic therapy for the first time. Patients were excluded from the study if they had a history of trauma, craniofacial anomalies, cleft lip and palate, forced bite and previous orthodontic, prosthetic or orthognathic surgical treatment.

All patients included in the study underwent a detailed clinical assessment and analysis of their dental and skeletal profiles, as well as soft tissue profiles on cephalometric radiography. The equipment used for the imaging analysis was the Rotograf Plus (20090 Buccinasco MI Italy) (number and series: 00036045), and the CEI-OPX/105 X-ray tube (CEI, Bologna) in March 2000, which had a protective filter (2.5 mm aluminum-equivalent). Lateral cephalometric films were taken from a distance of 165 cm from the tube, using a cephalostat to ensure rigid head fixation (head-holding device).

The patients were placed in the cephalostat in such a way that the sagittal plane of the head was

at a 90° angle to the path of the X-rays. The Frankfort horizontal plane (it connects the upper edge of the external auditory orifice and the lowest point of the infraorbital edge) was parallel to the ground, the teeth were in a central occlusion position, and the lips were in a relaxed position. Each cephalogram was fixed on the viewing box with the profile to the right, and the acetate tracing paper was fixed by tape at the top. The soft tissue and skeletal features were traced manually in a darkened room, using a 0.5 mm lead pencil. All the image tracing was done by the main investigator.

Based on the values of ANB angle, Wit's appraisal, SN/GoGn angle, 155 cephalograms were finally chosen for the study and three study groups were formed. The cephalometric ANB angle (the points that determined the ANB angle included point 'N', the nasion, located on the suture between the frontal and nasal bones; point 'A', the lowest point on the line between the anterior nasal spine and the prosthion [alveolar point]; and point 'B', the lowest point from the line between the infradentale and the pogonion [midline of the chin]) was the parameter that defined the mutual sagittal relationship between the upper and lower jaw as orthognathic ( $1^\circ \leq \text{ANB} \leq 3^\circ$ ) and a Wit's appraisal  $\pm 1$  mm were categorised as skeletal class I. Wit's appraisal was used to overcome the limitations of the ANB angle and entails drawing perpendiculars from points A and B onto the occlusal plane. The results of the Wit's appraisal were evaluated in order to eliminate the possibility of the mandibular posterior rotation obscuring any skeletal anomalies in the patients with increased vertical direction values. For this purpose, the radiographs were excluded if the results from the ANB angle measurements and Wit's appraisal did not coincide (Fig. 4).

S-N/Go-Gn — angle formed by lines S-N and Go-Gn and allows for the identification of relationship between the mandibular plane and the cranial base. It indicates the mandibular vertical developmental trend as it identifies the direction of mandibular growth rotation (Fig. 5).

According to this angle, the types are divided into hypodivergent group (angle value less than 26° in 26 male, 25 female subjects), normodivergent group (angle value between 26° and 38° in 28 males, 27 females) and hyperdivergent group (angle value greater than 38° in 25 males, 24 females).

Each cephalogram was checked for its magnification and dealt with accordingly. Then, the soft tissue thick-

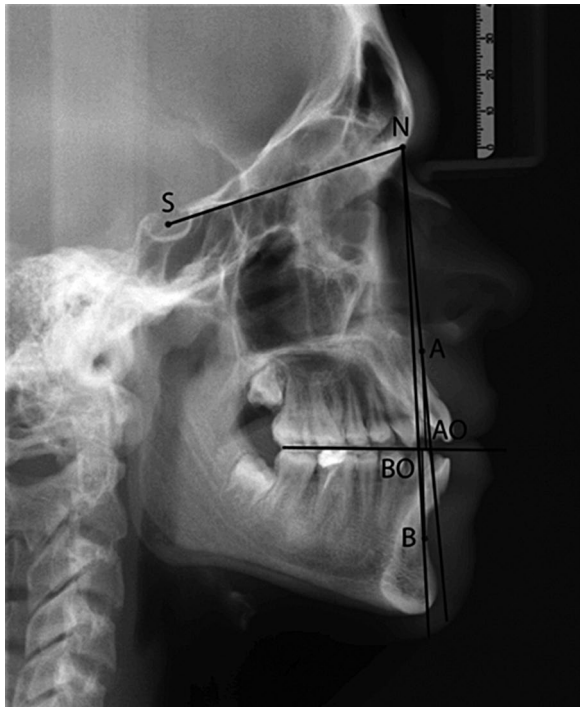


**Figure 4.** Cephalometric planes and angles: ANB angle and Wit's appraisal for the identification of mutual sagittal jaw relationship.

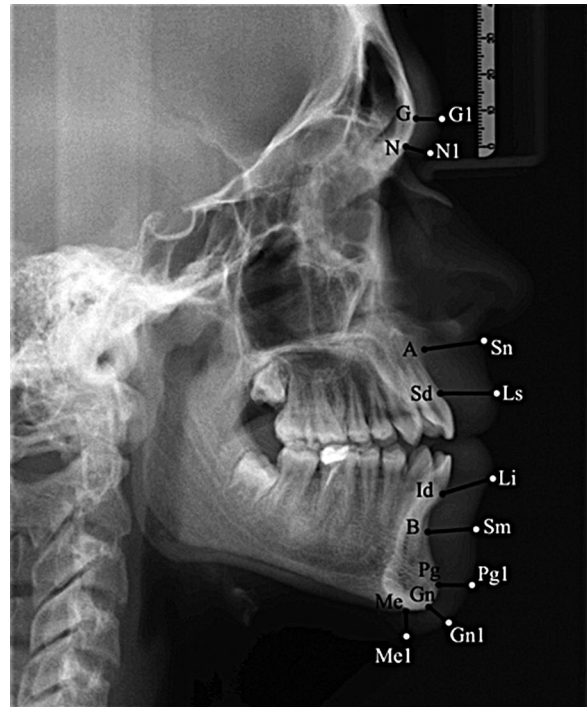


**Figure 6.** Nine soft tissue cephalometric landmarks (from top to bottom): G-G1, N-N1, A-Sn, Sd-Ls, Id-Li, B-Sm, Pg-Pg1, Gn-Gn1, Me-Me1.

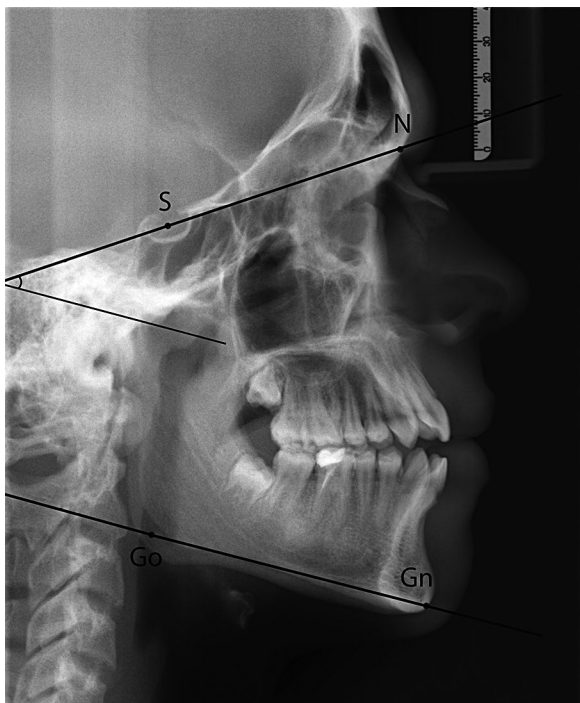


**Figure 5.** Cephalometric S-N/Go-Gn angle for the identification of mandibular divergence pattern.

ness was measured for each cephalogram at nine selected distances (Fig. 6). The following areas were used:

- the glabella area (G-G1) — the linear distance between the G point (the most prominent point on the frontal bone) and the soft tissue, or analogue point (G1);
- the nasal area (N-N1) — the linear distance between the N point and on the soft tissue, the deepest point of the root of the nose (N1);
- the subnasal area (A-Sn) — the distance between point A (the most concave point of the anterior maxilla) and subnasale (the point at which the nasal septum merges with the upper lip);
- upper lip thickness (Sd-Ls) — the distance between the Sd point (supradentale, prosthion — the most inferior anterior point on the maxillary alveolar process between the central incisors) and the Ls (labrale superius — the most anterior point on the upper lip);
- lower lip thickness (Id-Li) — the distance between the Id point (infradentale — the highest point of the mandibular alveolar process between the two central incisors) and Li point (labrale inferius — the most anterior point on the lower lip);
- the sulcus mentolabialis (B-Sm), the distance between the B point (the most concave point on mandibular symphysis) and Sm (mentolabial sulcus — the point on greatest concavity in the midline between the labrale inferius and soft tissue pogonion);

**Table 1.** Median value of facial soft tissue thickness in subjects with different mandibular divergence pattern and group differences

	Hypodivergent				Normodivergent				Hyperdivergent			
	N	Median	25%	75%	N	Median	25%	75%	N	Median	25%	75%
G-G1	51	6.00	5.68	6.15	55	6.20	5.69	6.63	49	5.85	5.47	6.85
N-N1	51	6.78	6.15	6.97	55	6.53	5.72	7.15	49	5.88	5.34	7.24
A-Sn	51	15.99	13.30	16.35	55	14.91	13.70	16.69	49	14.58	13.16	16.35
Sd-Ls	51	14.82	13.86	15.63	54	15.14	13.44	16.70	49	14.59	12.60	16.93
Id-Li	51	15.25	14.44	16.68	55	15.91	14.34	17.08	49	15.60	14.28	17.21
B-Sm	51	10.44	9.84	10.99	55	<b>11.03<sup>b</sup></b>	10.10	12.10	49	<b>11.61<sup>d</sup></b>	10.18	12.63
Pg-Pg1	51	11.08	10.00	13.97	55	12.14	10.73	13.68	49	11.27	9.76	13.18
Gn-Gn1	51	<b>9.80<sup>d</sup></b>	8.09	11.12	55	9.22	7.76	10.72	49	7.31	6.26	9.65
Me-Me1	51	8.29 <sup>d</sup>	6.46	9.62	55	7.91 <sup>c</sup>	6.75	8.81	49	7.10	5.49	8.67

<sup>b</sup>Normal vs. hypodivergent,  $p < 0.02$ ; <sup>c</sup>normal vs. hyperdivergent,  $p < 0.02$ ; <sup>d</sup>hypo vs. hyperdivergent,  $p < 0.02$

**Table 2.** Results of Kruskal-Wallis ANOVA test of the facial soft tissue thickness of groups with different mandibular divergence pattern

	G-G1	N-N1	A-Sn	Sd-Ls	Id-Li	B-Sm	Pg-Pg1	Gn-Gn1	Me-Me1
Kruskal-Wallis H	2.838	3.407	0.429	1.243	1.576	13.768	2.635	15.412	8.236
df	2	2	2	2	2	2	2	2	2
Asymp. Sig.	0.242	0.182	0.807	0.537	0.455	0.001	0.268	< 0.001	0.016

- the chin area (Pg-Pg1) — the distance between the Pg point (the pogonion — the most prominent point of the chin), and soft tissue pogonion Pg1 (the most anterior point on the soft tissue chin);
- the gnathion area (Gn-Gn1) — the distance between bony Gn (gnathion — the lowest point on the anterior margin of the lower jaw in the midsagittal plane) and soft tissue Gn1 (the constructed midpoint between soft tissue pogonion and soft tissue menton);
- the menton area (Me-Me1) — the distance between the Me (menton — at the junction between the mandibular symphyseal outline and the inferior border of the mandibular body) and Me1 point (soft tissue menton — lowest point on the contour of the soft tissue chin).

The values of the soft tissue thickness were measured with a digital calliper (in millimetres). All the measurements were randomly done once by an experienced orthodontist (principal investigator). Nine linear distances analysed statistically in the three groups of subjects and categorised according to gender. The median values in males and females were compared in each group of subjects with different types of divergence.

### Statistical method

Statistical analysis was performed by IBM SPSS statistical package (version 23). Significance of differences between analysed groups was analysed by Kruskal-Wallis H test. Detected significant differences were additionally analysed by Mann-Whitney U test with  $p$  values modified according to Bonferroni correction ( $p < 0.02$ ). Significance of gender differences in analysed groups were evaluated by Mann-Whitney U test.

## RESULTS

The values of the examined parameters, compared to vertical pattern and gender, are presented in Tables 1, 2, and 3.

**Group differences.** Progressive decreasing of the soft tissue thickness from hypo- towards hyperdivergent group was established in N-N1, A-Sn, Gn-Gn1, Me-Me1. There are significant differences in Gn-Gn1 and Me-Me1 ( $p < 0.02$ ). Progressive increasing of the soft tissue thickness happens only at the level of mentolabial sulcus and these differences are significant (Tables 2, 3).

**Gender differences.** For the greatest number of the examined distances, there is a rule that the

**Table 3.** Descriptive statistics of the facial soft tissue thickness linear parameters in male and female subjects with different mandibular divergence pattern

Gender	Hypodivergent				Normodivergent				Hyperdivergent			
	N	Median	25%	75%	N	Median	25%	75%	N	Median	25%	75%
<b>Male</b>												
G-G1	26	5.98	5.85	6.19	28	6.08	5.65	6.47	25	5.94	5.51	7.08
N-N1	26	6.73	6.15	8.11	28	6.73	5.90	7.21	25	<b>6.39<sup>a</sup></b>	5.70	7.54
A-Sn	26	<b>16.34<sup>a</sup></b>	16.23	16.41	28	<b>16.02<sup>a</sup></b>	14.91	17.29	25	<b>16.00<sup>a</sup></b>	14.73	16.82
Sd-Ls	26	15.36	14.51	15.63	28	<b>16.13<sup>a</sup></b>	15.05	17.45	25	<b>16.15<sup>a</sup></b>	14.71	18.29
ld-Li	26	<b>16.24<sup>a</sup></b>	15.46	17.89	28	16.22	14.81	17.17	25	16.46	14.82	18.12
B-Sm	26	<b>10.68<sup>a</sup></b>	10.15	11.45	28	<b>11.33<sup>a</sup></b>	10.84	12.77	25	11.62	11.08	13.14
Pg-Pg1	26	12.62	9.41	14.40	28	12.25	10.84	13.71	25	<b>11.90<sup>a</sup></b>	10.49	13.30
Gn-Gn1	26	9.06	7.93	12.39	28	9.65	8.25	10.89	25	7.76	6.76	10.24
Me-Me1	26	8.47	6.22	9.62	28	<b>8.15<sup>a</sup></b>	7.40	9.75	25	7.13	5.88	9.82
<b>Female</b>												
G-G1	25	6.00	5.49	6.15	27	6.23	5.86	6.78	24	5.71	5.36	6.67
N-N1	25	6.78	5.38	6.97	27	6.43	5.71	6.98	24	5.59	5.13	6.50
A-Sn	25	14.30	11.45	15.64	27	14.17	12.61	14.62	24	13.36	11.81	14.54
Sd-Ls	25	13.91	10.59	15.20	27	13.85	12.45	15.22	24	13.16	11.93	14.49
ld-Li	25	14.64	13.49	14.99	27	15.17	14.12	16.81	24	15.15	13.69	16.15
B-Sm	25	10.27	9.47	10.72	27	10.58	9.90	11.49	24	10.90	9.92	12.20
Pg-Pg1	25	10.87	10.16	11.27	27	11.59	9.95	13.51	24	10.63	9.03	12.88
Gn-Gn1	25	9.80	8.45	11.12	27	8.64	6.81	10.30	24	6.90	5.75	8.38

<sup>a</sup>Males vs. females,  $p < 0.05$ 

larger values of the soft tissue thickness were recorded in males. The exception is G-G1 in normal and hypodivergent subjects; N-N1 and Gn-Gn1 in hypodivergent subjects, where the larger values were established in females. Significant gender differences were established for the following distances: N-N1 in hyperdivergent, A-Sn in all three examined groups, the upper lip thickness in normal and hyperdivergent, the lower lip thickness in hypodivergent, the thickness of mentolabial sulcus in hypo- and normodivergent, Pg-Pg1 in hyperdivergent and Me-Me1 in normodivergent subjects ( $p < 0.05$ ; Table 1).

## DISCUSSION

The basic issue in this research was, how do the covering soft tissues adjust to the mandibular divergence? Do they passively follow the bone base, so that by 'elongating' the facial skeleton soft tissues become thinner? Or, similar to sagittal developmental pattern, soft tissues compensate for the vertical disharmony with their thickness? Ajwa et al. [2] and Jazmati et al. [10] think that variations in the soft tissue thickness are not correlated with craniofacial

morphology. Kamak and Celikoglu [12] established that there are only differences in the lip area.

In general, the majority of studies reported that male subjects had thicker soft tissue than female subjects with the variable degree of significance. In the present study, there are levels at which female subjects have thicker soft tissues such is the level G-G1, for example, but these differences are not significant. Furthermore, the differences between various groups of divergence at G-G1 level do not show significance or a clear tendency of changes in thickness, going from hypo- towards hyperdivergent group. At level N-N1, there is already a slightly pronounced tendency of decreasing of soft tissue thickness. This phenomenon is more conspicuous in females, but without statistical relevance among groups. Significant gender differences were established only in hyperdivergent group. According to Al Mashadany et al. [4], the soft tissues thickness in glabella in males is insignificantly larger in hypodivergent group. The majority of group differences were established between hypo- and hyperdivergent groups, which was confirmed by our study as well. On the other hand, the same

author recorded significant difference at level N-N1, especially between hypo- and hyperdivergent group.

At level A-Sn, progressive decreasing in soft tissue thickness happens, from hypo- towards hyperdivergent pattern. This phenomenon is established in both gender, but group differences are not significant. However, Khare and Niwlikar [13] reported that subjects with hyperdivergent growth will develop thicker soft tissue at this level, which is opposite to the current study. Males at this level had larger soft tissue thickness than females and these differences are significant for all three groups of divergence.

In the present study, the thickness of the upper and lower lip differs slightly among the groups of various divergences, and there are significant gender differences for the upper lip in normal and hyperdivergent group, and for the lower lip in hypodivergent group in favour of males. According to Al Sajagh et al. [3], hyperdivergent females exhibited significantly larger lower lip thickness compared to the other two types of face, which was not the case in the present study — the average values in normal and hyperdivergent females differ insignificantly. In normodivergent males there is significantly larger upper lip thickness at level A-Sn and Sd-Ls, as well as for lower lip thickness Id-Li, compared to female subjects. The upper lip thickness at point A-Sn and Sd-Ls, and lower lip thickness in Li were significantly larger in males than in females [3], which is also similar to our results. Celikoglu et al. [7] established only in females smaller values of the thickness of the upper and lower lip of statistical relevance in hyperdivergent group compared to the values in normodivergent group. Furthermore, hypo- and normodivergent groups showed similar values of thickness. In males, there were not any statistically significant differences among various mandibular divergence patterns [7], which is similar to our results. Khatri and Sanap [14] established larger lower lip thickness in hyperdivergent subjects in comparison to the hypodivergent, except from the fact that he examined subjects with skeletal class II. Feres et al. [9] established that soft tissue thickness of the upper and lower lip shows no differences in all morphological groups, whereas Ashraf et al. [6] established significant difference in the upper lip thickness only between hypo- and hyperdivergent group. The larger values for the lip thickness were noticed in the hypodivergent group. It was determined that the difference in the upper lip thickness is statistically significant among the three examined groups.



**Figure 7.** The increased soft tissue thickness in mentolabial sulcus area in subject with hyperdivergent pattern.

The discrepancy between our and other findings may be the result of racial differences, age group taken for the study and the size of the sample [6, 11].

The mentolabial sulcus area shows the opposite tendency compared to the other levels of measurement. This area increases the thickness going from hypo- towards hyperdivergent groups. According to Al Sajagh et al. [3], male hyperdivergent subjects have significantly larger soft tissue thickness at level B-Sm compared to normal and hypodivergent, which is similar to our results. This phenomenon of the increasing of the soft tissue thickness of mentolabial sulcus in hyperdivergent growth pattern, in which the majority of average thicknesses showed the smallest values, can be explained by the hypertrophy of the perioral musculature that tends to overcome vertical discrepancy and maintain lip competence (Fig. 7).

The results obtained by measuring the soft tissue chin thickness can be categorised into two groups. According to the first group, soft tissue chin thickness in all three levels (Pg-Pg1, Gn-Gn1 and Me-Me1) decreases by going from hypo- towards hyperdivergent group, and it is statistically significant only between these two groups [5–8, 22, 24], which is only partly similar to our results. Namely, in the present study there is a significant difference between hypo- and hyperdivergent group at level Gn-Gn1, whereas at level Me-Me1 significant differences exist between normal and hyperdivergent group. At level Pg-Pg1, significant differences were not established, which was confirmed by another group of researchers [9, 15, 20, 21, 23]. They determined that hyperdivergent subjects have thinner soft tissues at level Gn-Gn1

and Me-Me1, but not at level Pg-Pg1, the fact that they explained through the existence of differential extension between hard and soft tissues during growth. Shinde et al. [21] think that the area of pogonion is the least affected by (hyper) divergence. This is perhaps a natural manner to camouflage the existing state and give a more normal facial appearance. The reason that could account for the difference on menton between hyper- and normodivergent pattern may be the one that the soft tissue on menton apparently adjusts to the severe hyperdivergence, probably with the increased stretching of the soft tissue due to the increased divergence of the face. The finding that statistically significant difference happened between hyper- and hypodivergent patients emphasizes the fact that soft tissue thickness at menton is actually the thinnest of all distances in all groups. Our finding that soft tissue thickness at menton is minimal in hyperdivergent types of the face correlates with the research of Macari et al. [15] and Ashraf et al. [6]. Sodawala et al. [22] also did not report gender dimorphism for FSTT at all three levels of chin area, as opposed to the present study, where significant differences were established at level Me-Me1 in normodivergent group and at level Pg-Pg1 in hyperdivergent group. Somaiah et al. [23] were the only to publish the original result according to which females in hyperdivergent group had thicker FSTT than males at all tree levels, that is Pg-Pg1, Gn-Gn1 and Me-Me1.

The contrasting results of various studies suggest that the growth of soft tissue is different in individuals, different races and gender. The mechanism of compensational growth of soft tissue that happens only in one race may not happen in the other one [22]. The obtained results can be applied in forensic reconstruction of the face, orthognatic surgery and anthropology.

## CONCLUSIONS

Facial soft tissue thickness showed a various degree of dependence on mandibular divergence pattern at different levels of measurement. The areas whose thickness is significantly conditioned by this pattern were established: the chin area at level Gn-Gn1, Me-Me1 and the region of the mentolabial sulcus (B-Sm). There are levels at which soft tissues get thinner from hypo- towards hyperdivergent group, but without statistical relevance, such as A-Sn and N-N1, and there are levels on which vertical pattern has no influence, and that is the region of glabella

and upper and lower lip thickness. At most levels, male subjects have thicker soft tissues and these differences are significant for all three groups in the subnasal area, whereas for some groups of divergence differences are significant in the area of lips, mentolabial sulcus and chin.

**Conflict of interest:** None declared

## REFERENCES

1. Ahmed M, Shaikh A, Fida M. Diagnostic performance of various cephalometric parameters for the assessment of vertical growth pattern. *Dental Press J Orthod.* 2016; 21(4): 41–49, doi: [10.1590/2177-6709.21.4.041-049.oar](https://doi.org/10.1590/2177-6709.21.4.041-049.oar), indexed in Pubmed: [27653263](https://pubmed.ncbi.nlm.nih.gov/27653263/).
2. Ajwa N, Alkhars FA, AlMubarak FH, et al. Correlation between sex and facial soft tissue characteristics among young Saudi patients with various orthodontic skeletal malocclusions. *Med Sci Monit.* 2020; 26: e919771, doi: [10.12659/MSM.919771](https://doi.org/10.12659/MSM.919771), indexed in Pubmed: [32101535](https://pubmed.ncbi.nlm.nih.gov/32101535/).
3. Al-Sayagh NM, Saleem NR, Abdul-Qadir MY. Analysis of soft tissue facial profile in different vertical growth patterns. *Al-Rafidain Dent J.* 2011; 11(2): 346–356.
4. Al-Mashhadany S, Al-Chalabi H, Nadih M. Evaluation of facial soft tissue thickness in normal adults with different vertical discrepancies. *Int J Sci Res.* 2017; 6(2): 938–942, doi: [10.21275/ART2017603](https://doi.org/10.21275/ART2017603).
5. Anam S, Imtiaz A, Taskeen K. Assessment of the soft tissue chins thickness with different skeletal vertical patterns in Pakistani adults. *J Dentistry Oral Hygiene.* 2018; 10(1): 1–6, doi: [10.5897/jdoh2016.0192](https://doi.org/10.5897/jdoh2016.0192).
6. Ashraf K, Kulshrestha R, Azam A, et al. Soft tissue analysis of chin, upper lip length and thickness in patients with different mandibular divergent patterns: a cephalometric study. *Indian J Orthodontics Dentofacial Res.* 2020; 4(2): 88–93, doi: [10.18231/2455-6785.2018.0018](https://doi.org/10.18231/2455-6785.2018.0018).
7. Celikoglu M, Buyuk SK, Ekizer A, et al. Assessment of the soft tissue thickness at the lower anterior face in adult patients with different skeletal vertical patterns using cone-beam computed tomography. *Angle Orthod.* 2015; 85(2): 211–217, doi: [10.2319/040114-237.1](https://doi.org/10.2319/040114-237.1), indexed in Pubmed: [24998911](https://pubmed.ncbi.nlm.nih.gov/24998911/).
8. Cezairli N. Comparisons of soft tissue thickness measurements in adult patients with various vertical patterns. *Meandros Med Dental J.* 2017; 18(2): 120–129, doi: [10.4274/meandros.76376](https://doi.org/10.4274/meandros.76376).
9. Feres M, Hitos S, Sousa H, et al. Comparação das dimensões de tecido mole entre padrões faciais distintos. *Dental Press J Orthodontics.* 2010; 15(4): 84–93, doi: [10.1590/s2176-94512010000400013](https://doi.org/10.1590/s2176-94512010000400013).
10. Jazmati HM, Ajaj MA, Hajeer MY. Assessment of facial soft tissue dimensions in adult patients with different sagittal skeletal classes using cone beam computed tomography. *J Contemp Dent Pract.* 2016; 17(7): 542–548, indexed in Pubmed: [27595719](https://pubmed.ncbi.nlm.nih.gov/27595719/).
11. Jeelani W, Fida M, Shaikh A, et al. Facial soft tissue thickness among various vertical facial patterns in adult Pakistani subjects. *Forensic Sci Int.* 2015; 257(1): 517.e1–517.e6, doi: [10.1016/j.forsciint.2015.09.006](https://doi.org/10.1016/j.forsciint.2015.09.006), indexed in Pubmed: [26476716](https://pubmed.ncbi.nlm.nih.gov/26476716/).

12. Kamak H, Celikoglu M. Facial soft tissue thickness among skeletal malocclusions: is there a difference? *Korean J Orthod.* 2012; 42(1): 23–31, doi: [10.4041/kjod.2012.42.1.23](https://doi.org/10.4041/kjod.2012.42.1.23), indexed in Pubmed: [23112928](https://pubmed.ncbi.nlm.nih.gov/23112928/).
13. Khare V, Niwlikar KB. Effect of vertical maxillary skeletal pattern on nasal morphology in high and low angle cases. *Int J Oral Health Med Res.* 2017; 3(6): 75–79.
14. Khatri JM, Sanap NB. Comparative evaluation of perioral soft tissue of skeletal normal Class I and Class II Division 1 subjects: A lateral cephalometric study. *Int J Orthod Rehabil.* 2020; 11(1): 1, doi: [10.4103/ijor.ijor\\_43\\_19](https://doi.org/10.4103/ijor.ijor_43_19).
15. Macari AT, Hanna AE. Comparisons of soft tissue chin thickness in adult patients with various mandibular divergence patterns. *Angle Orthod.* 2014; 84(4): 708–714, doi: [10.2319/062613-474.1](https://doi.org/10.2319/062613-474.1), indexed in Pubmed: [24188123](https://pubmed.ncbi.nlm.nih.gov/24188123/).
16. Meundi M, David C. Facial soft tissue thickness in South Indian adults with varied occlusions: a cone beam computed tomography study. *J Indian Acad Oral Med Radiol.* 2019; 31(3): 194, doi: [10.4103/jiaomr.jiaomr\\_83\\_19](https://doi.org/10.4103/jiaomr.jiaomr_83_19).
17. Oyonarte R, Hurtado M, Castro MV. Evolution of ANB and SN-GoGn angles during craniofacial growth: A retrospective longitudinal study. *APOS Trends Orthod.* 2016; 6: 295–301, doi: [10.4274/meandros.76376](https://doi.org/10.4274/meandros.76376).
18. Perović T, Blažej Z. Male and female characteristics of facial soft tissue thickness in different orthodontic malocclusions evaluated by cephalometric radiography. *Med Sci Monit.* 2018; 24: 3415–3424, doi: [10.12659/MSM.907485](https://doi.org/10.12659/MSM.907485), indexed in Pubmed: [29791323](https://pubmed.ncbi.nlm.nih.gov/29791323/).
19. Ramesh G, Sreedhar NG, Narayanappa M. Facial soft tissue thickness in forensic facial reconstruction: is it enough if norms set? *J Forensic Res.* 2015; 06(05), doi: [10.4172/2157-7145.1000299](https://doi.org/10.4172/2157-7145.1000299).
20. Rasool G, Hussain T, Hussain U, et al. Comparisons of soft tissue chin thickness in adult patients with various mandibular divergence patterns. *Pakistan Orthodontic J.* 2016; 8(1): 53–57.
21. Shinde N, Jethe S, Agarkar S, et al. Comparative evaluation of soft tissue chin thickness in skeletal class I and class II adults with three mandibular divergence: a cephalometric study. *J Adv Med Dent Scie Res.* 2019; 7(2): 33–40, doi: [10.21276/jamdsr](https://doi.org/10.21276/jamdsr).
22. Sodawala J, Akolkar A, Sodawala F, et al. Comparison of soft tissue chin thickness at different levels of chin in subjects with various growth patterns. *Indian J Dent Res.* 2020; 31(2): 224–228, doi: [10.4103/ijdr.IJDR\\_389\\_17](https://doi.org/10.4103/ijdr.IJDR_389_17), indexed in Pubmed: [32436901](https://pubmed.ncbi.nlm.nih.gov/32436901/).
23. Khan MU, Somaiah S, Muddaiah S, et al. Comparison of soft tissue chin thickness in adult patients with various mandibular divergence patterns in Kodava population. *Int J Orthod Rehabil.* 2017; 8(2): 51, doi: [10.4103/ijor.ijor\\_38\\_16](https://doi.org/10.4103/ijor.ijor_38_16).
24. Subramaniam S, Karthi M, Kumar K, et al. Comparison of soft tissue chin prominence in various mandibular divergence patterns of Tamil Nadu population. *J Indian Acad Dent Spec Res.* 2016; 3(2): 39, doi: [10.4103/jiadsr.jiadsr\\_3\\_17](https://doi.org/10.4103/jiadsr.jiadsr_3_17).
25. Yemitan TA, Oludare YS, Ogunbanjo BO, et al. Vertical facial height and its correlation with skeletal pattern among young nigerian orthodontic patients. *Int J Dentistry Oral Sci.* 2018; 661–666, doi: [10.19070/2377-8075-18000130](https://doi.org/10.19070/2377-8075-18000130).

# Assessment of radiographic morphology of mandibular condyles: a radiographic study

A.H. Shaikh<sup>1</sup>, S. Ahmed<sup>1</sup>, A.R. Ahmed<sup>2</sup> , G. Das<sup>2</sup> , M. Taqi<sup>3</sup>, S. Nisar<sup>4</sup>, O. Khan<sup>4</sup>

<sup>1</sup>Dow International Dental College, Dow University of Health Sciences, Karachi, Pakistan

<sup>2</sup>College of Dentistry, King Khalid University, Abha, Saudi Arabia

<sup>3</sup>Dow Dental College, Dow University of Health Sciences, Karachi, Pakistan

<sup>4</sup>Drlshratulebad Khan Institute of Oral and Health Sciences, Dow University of Health Sciences, Karachi, Pakistan

[Received: 16 April 2021; Accepted: 4 May 2021; Early publication date: 17 May 2021]

**Background:** Panoramic radiographs are the most common radiographic tool used by the dental clinicians to evaluate teeth, mandible and other related structures of the jaws. Mandibular condyle is an important anatomical landmark for facial growth, expressed in an upward and backward direction. The presentation of mandibular condyle differs widely among different group of ages and individuals.

**Materials and methods:** The retrospective cross-sectional study was conducted from November 2018 to March 2019 at Dow International Dental College Karachi that includes radiographic evaluation of 500 mandibular condyles. All retrievable orthopantomograms were obtained and data were extracted regarding age, gender and condylar morphology.

**Results:** The morphological appearances of mandibular condyle have great variation among different age groups and subjects. Normally, we recognise five basic shapes i.e. oval, bird beak, crooked finger, diamond and mixed. Out of 250 pair of condylar heads that were evaluated, 50% were oval, 40% bird beak, 4.8% crooked finger and diamond 4.8%.

**Conclusions:** All four morphological types of mandibular condyles were observed and the oval shape condyles were most prevalent among both genders and all age groups. In future studies, the inclusion of other parameters and large sample size may provide unique information. (Folia Morphol 2022; 81, 2: 481–486)

**Key words:** mandibular condyle, orthopantomogram, temporomandibular joint morphology

## INTRODUCTION

Panoramic radiographs (orthopantomograms [OPG]) are the most routinely and widely used diagnostic tool used by the dental clinicians to get valuable information about teeth, mandible and other related structures of the jaw [13]. It gives us valuable knowledge about the anatomical variation of maxilla and mandible and also osseous changes or flattening happening with time [9]. Routine panoramic view has

also been recommended by the American Academy of Oral and Maxillofacial Radiology for assessing the structural components of the temporomandibular joint (TMJ) because of the cost and risk of the relatively low radiation exposure associated with computed tomography [7].

Mandibular condyle is an important anatomical landmark for facial growth, expressed in an upward and backward direction [17]. The presentation of

Address for correspondence: Dr. G. Das, Assistant Professor Prosthodontics, College of Dentistry, King Khalid University, King Fahad Road, 61421 Abha, Saudi Arabia, e-mail: a\_razzaq1@hotmail.com; drgotam2000@gmail.com

This article is available in open access under Creative Common Attribution-Non-Commercial-No Derivatives 4.0 International (CC BY-NC-ND 4.0) license, allowing to download articles and share them with others as long as they credit the authors and the publisher, but without permission to change them in any way or use them commercially.

mandibular condyle differs widely among different age groups and individuals. Morphological variations depend upon developmental variation along with condylar remodelling to accommodate malocclusion, trauma and other pathological and developmental abnormalities [2]. Variability in the shapes and sizes of condyles helps to diagnose the TMJ disorders associated with malocclusions such as crossbite, deep bite, and open bite [3].

The mandibular condyle varies considerably both in size and shape. The typical condylar head has a convex arrangement throughout, and symmetry should exist between contralateral sides within the same individual [12, 17]. Several studies have endeavoured to assess the morphology of human condyle. Past researchers evaluated a variety within the mandibular condyle shapes [12, 14]. Yale et al. [19] first classifies the shapes of the mandibular condyle as convex, flat and concave when having a superior view by examining the skulls of Terry collection. However, later Yale simplified classification into four categories flattened, convex, angled, rounded [19].

Upon surgical exposure, four different types of condyles shapes were noted, which include excavated form, oblique form, and the small round shape and flattened [11]. On the other hand, flat, convex, concave, round and angled types of condylar morphology were noted when computed tomography images were observed [8].

In Pakistan, limited data is available regarding the morphological appearance of the condyle. The thorough understanding of the morphological variations in the shape of the mandibular condyle is essential so that a standard variant can be distinguished from the abnormal condition. Therefore, this study aims to record different types of normal morphological variations of the condyle through an OPG. The objective of this study is to assess the frequency of different condylar morphological variations in both genders and age groups.

## MATERIALS AND METHODS

### Study design and patients

The retrospective cross-sectional study was conducted from November 2018 to March 2019 at Dow International Dental College Karachi; it included radiographic evaluation of 500 mandibular condyles. All retrievable OPGs were obtained, and necessary data was extracted regarding age, gender and condylar morphology. Ethical approval for this study was

obtained from the Institutional Review Board, Dow University of Health Sciences.

Digital orthopantomograms (OPG) taken on Villa Rotograph EVO 3D, (exposure parameters being: 10 mA, 82 Kv) free of any projection errors, that showed a complete view of condyle on either side with optimum density and contrast were selected. The radiographs of the individuals with a history of TMJ dysfunction, occlusal discrepancy, pathological and developmental abnormalities were excluded.

Sum of 250 OPGs was visualized for a routine investigation. The OPGs were evaluated by two maxillofacial surgeons to determine the morphology of condyle. The statistical analysis was conducted using SPSS version 17. The participants were divided into three groups according to the age: (i) young adults (18–35 years), (ii) middle age (36–55 years), (iii) older adults (56 or above). Descriptive statistics were conducted to estimate the frequency of normal morphological variations of condyles. Chi-square test was conducted to assess the difference in frequency of normal condylar morphological variations about age and gender.

### Ethical approval

All procedures performed in studies followed the ethical standards of the institutional research committee and the 1964 Helsinki declaration and its later amendments.

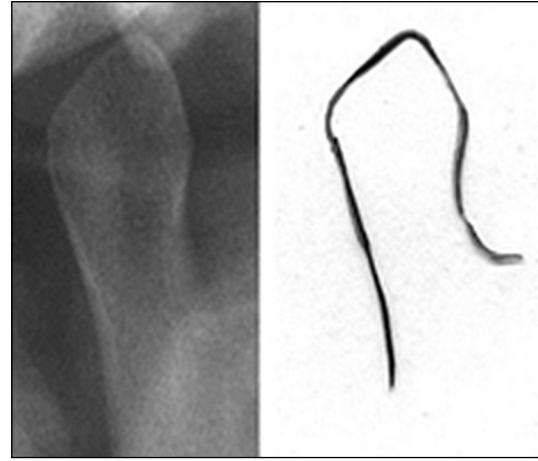
## RESULTS

Total of 500 condyles from 250 OPGs was examined. Out of 250 radiographs, half of them belong to females, and half belong to males, as shown in Table 1. In terms of age, the majority of radiographs were of participants belonging to middle age groups, as shown in Table 1.

The shapes of the condyles that have been identified in this study are: bird beak, oval, diamond, and crooked finger, as shown in Figures 1, 2, 3, and 4. The commonest form of condylar morphology was oval (50%), followed by the bird beak (40%), diamond (4.8%) and crooked finger (4.8%). The frequency of oval condylar morphology was 57.6% among males and 42.4% among female participant, as shown in Table 2. In all age groups, the most dominant form of condylar morphology was oval, followed by the bird beak diamond and crooked finger. The frequency of oval condylar morphology was 36% in age group 1, 44% in age group 2 and 20% in age group 3, as shown in Table 2.

**Table 1.** Demographic distribution of the participants according to gender and age

Gender	Age			Total
	Young adults (18–35 years)	Middle age (36–55 years)	Older adults (56 or above)	
Male	50 (40%)	54 (43.2%)	21 (16.8%)	125 (100%)
Female	38 (30.4%)	69 (55.2%)	18 (14.4%)	125 (100%)

**Figure 1.** Type I — bird beak**Figure 3.** Type III — diamond.**Figure 2.** Type II — oval.**Figure 4.** Type IV — crooked finger.

When the frequency of condylar morphological types was compared with the gender, it was observed that among male study participants, the oval condylar morphology was significantly higher ( $p = 0.016$ ). On the other hand, among females study participants, the diamond condylar morphology was significantly higher ( $p = 0.018$ ), as shown in Table 3.

The frequency of condylar morphological types was compared with the age groups in Table 3. Among participants of age group 1, the frequen-

cy of diamond condyles was significantly lower as compared to other age groups. In the case of age group 2, the frequency of crooked finger condyles was significantly higher ( $p = 0.002$ ) as compared to other age groups. Among participants of age group 3 the frequency of bird beak condyles were significantly lower ( $p = 0.001$ ) as compared to other age groups and diamond condylar morphology was significantly higher ( $p = 0.0001$ ) as compared to other age groups.

**Table 2.** Distribution of the condylar morphology according to gender and age

	Bird beak	Diamond	Crooked finger	Oval
<b>Gender</b>				
Male	48 (47.5%)	2 (16.7%)	3 (25%)	72 (57.6%)
Female	53 (52.5%)	10 (83.3%)	9 (75%)	53 (42.4%)
Total	101 (100%)	12 (100%)	12 (100%)	125 (100%)
<b>Age groups</b>				
Group 1	42 (41.6%)	0 (0%)	1 (8.3%)	45 (36%)
Group 2	53 (52.5%)	4 (33.3%)	11 (91.7%)	55 (44%)
Group 3	6 (5.9%)	8 (66.7%)	0 (0%)	25 (20%)
Total	101 (100%)	12 (100%)	12 (100%)	125 (100%)

Group 1: 18–35 years old, Group 2: 36–55 years old, Group 3: 56 or above

**Table 3.** Comparing the frequency of condylar morphology between both genders

Gender	Bird beak			Diamond			Crooked finger			Oval		
	Yes	No	P	Yes	No	P	Yes	No	P	Yes	No	P
Male	48 (38.4%)	77 (61.6%)	0.51	2 (1.6%)	123 (98.4%)	0.018	3 (2.4%)	122 (97.6%)	0.076	72 (57.6%)	53 (42.4%)	0.016
Female	53 (57.6%)	72 (42.4%)		10 (8%)	115 (92%)		9 (7.2%)	116 (92.8%)		53 (42.4%)	72 (57.6%)	

Chi-square test

## DISCUSSION

The morphological appearances of mandibular condyle have great variation among different age groups and subjects [15, 18]. Normally, we recognize five basic shapes, i.e. oval, bird beak, crooked finger, diamond and mixed. In Pakistan, limited data is available regarding the morphological appearance of the condyle. Therefore the present study highlights the prevalent radiographic shapes of the condylar head-on OPG. Out of 250 pair of condylar heads that were evaluated, 50% were oval, 40% bird beak, 4.8% crooked finger and diamond 4.8%. In our study, the oval condylar morphology was most common and significantly higher among male individuals (Table 3). The studies reported by Choudhary et al. [6] and Ribeiro et al. [14] pertaining to the Brazilian and East Indian population respectively showed round/oval shape to be common in both sexes which goes in accordance with our study.

The morphological knowledge of the TMJ is an important tool for evaluation of normal growth and development. This may also be helpful in the near future for the development of forensic odontology [6, 8, 17]. The growth of mandibular condyle is indicated in an upward and backward direction. It is considered as major areas of facial growth. The

appearance and the shape of mandibular condyle vary enormously among individuals and different age groups, which is in accordance with the present study [11–13].

The present study on the radiological examination using OPG revealed flat, pointed, angled and round condylar morphology. Similarly, several other studies also showed the bird beak, oval, diamond, and crooked finger type condylar morphology [1, 10, 18]. In our study the second most common condylar morphology observed was bird beak. The frequency of bird beak condylar morphology was higher among females as compared to males. However, no statistically significant difference was observed when both genders were compared (Table 3). Similarly, Sonal et al. (2016) [16] also reported the bird beak as a second most common condylar morphology among females. On the other hand, the diamond and crooked finger morphology were a rarity [4, 18].

We compared the participant age with the condylar morphology. However, to our knowledge, no such data is reported in previous studies; thus, a comparison is not possible. The diamond shape condyles were significantly higher among participants of age group 3 as compared to other age groups (Table 4). The frequency of crooked finger condyles was significantly

**Table 4.** Comparing the frequency of condylar morphology between age groups

Age group	Bird beak			Diamond			Crooked finger			Oval		
	Yes	No	P	Yes	No	P	Yes	No	P	Yes	No	P
Group 1	42 (47.7%)	46 (52.3%)	0.105	0 (0%)	88 (100%)	0.010	1 (1.1%)	87 (98.9%)	0.061	45 (51.1%)	43 (48.9%)	0.895
Groups 2, 3	59 (36.4%)	103 (63.6%)		12 (7.4%)	150 (92.6%)		11 (6.8%)	151 (93.2%)		80 (49.4%)	82 (50.6%)	
Group 2	53 (43.1%)	70 (56.9%)	0.440	4 (3.3%)	119 (96.7%)	0.377	11 (8.9%)	112 (91.1%)	0.002	55 (44.7%)	68 (55.3%)	0.129
Groups 1, 3	48 (37.8%)	79 (62.2%)		8 (6.3%)	119 (93.7%)		1 (0.8%)	126 (99.2%)		70 (55.1%)	57 (44.9%)	
Group 3	6 (15.4%)	33 (84.6%)	0.001	8 (20.5%)	31 (79.5%)	0.001	0 (0%)	39 (100%)	0.223	25 (64.1%)	14 (35.9%)	0.080
Groups 1, 2	95 (45%)	116 (55%)		4 (1.9%)	207 (98.1%)		12 (5.7%)	199 (94.3%)		100 (47.4%)	111 (52.6%)	

Group 1: 18–35 years old, Group 2: 36–55 years old, Group 3: 56 or above; Chi-square test

higher among participants of age group 2 (Table 4). The frequency of bird beak condyles was significantly higher among group 1 and 2 as compared to group 3 (Table 4).

In comparison of our results, several other studies investigated that it is very important to evaluate condyle morphology with changes in condyle surface shapes, radiological dimensional measurements with malocclusion. A study reported that there was a significant relation between open bite and erosion of the head of the condyle. Ari-Demirkaya et al. [5] found that there was no difference between open, deep or normal bite groups in subjects with different condylar morphology.

Currently, various advanced radiographic modalities are available, such as computed tomography scan, cone beam volumetric imaging, which can give detailed information of the condyle. However, oral health practitioners usually prefer OPG to screen TMJ. The possible explanation due to which oral health practitioners still prefers OPG include favourable cost-benefit relationship, low doses of radiation exposure, ease of prescription and lack of image superimposition [4, 14, 15]. The use of OPG has its limitations such as a two-dimensional view. In addition to that, the limitations of this study include small sample size and lack of examiner reliability.

## CONCLUSIONS

In conclusion, all four morphological types of mandibular condyles were observed and the oval shape condyles were most prevalent among both genders and all age groups. In future studies, the inclusion of other parameters and large sample size may provide unique information.

## Acknowledgements and funding

The authors extend their appreciation to the Deanship of Scientific Research at King Khalid University, KSA for funding this work through research groups programme under Grant No. RGP.1/343/42.

**Conflict of interest:** None declared

## REFERENCES

- Ahmed MA, Subramaniam N. Prevalence of morphological variation of condyle in patients undergoing routine dental treatment-A retrospective orthopantomographic study. *Drug Invention Today*. 2019; 12(9).
- Ahn SJ, Kim TW, Lee DY, et al. Evaluation of internal derangement of the temporomandibular joint by panoramic radiographs compared with magnetic resonance imaging. *Am J Orthod Dentofacial Orthop*. 2006; 129(4): 479–485, doi: [10.1016/j.ajodo.2005.12.009](https://doi.org/10.1016/j.ajodo.2005.12.009), indexed in Pubmed: [16627173](https://pubmed.ncbi.nlm.nih.gov/16627173/).
- Al-Saedi AI, Riad AT, AL-Jasim N, et al. A panoramic study of the morphology of mandibular condyle in a sample of population from basrah city. *Int J Morphol*. 2020; 38(6): 1707–1712, doi: [10.4067/s0717-95022020000601707](https://doi.org/10.4067/s0717-95022020000601707).
- Anisuzzaman MM, Khan S, Khan M, et al. Evaluation of mandibular condylar morphology by orthopantomogram in bangladeshi population. *Update Dental Coll J*. 2019; 9(1): 29–31, doi: [10.3329/updcj.v9i1.41203](https://doi.org/10.3329/updcj.v9i1.41203).
- Ari-Demirkaya A, Biren S, Ozkan H, et al. Comparison of deep bite and open bite cases: normative data for condylar positions, paths and radiographic appearances. *J Oral Rehabil*. 2004; 31(3): 213–224, doi: [10.1046/j.0305-182X.2003.01236.x](https://doi.org/10.1046/j.0305-182X.2003.01236.x), indexed in Pubmed: [15025653](https://pubmed.ncbi.nlm.nih.gov/15025653/).
- Choudhary A, Ahuja US, Rathore A, et al. Association of temporomandibular joint morphology in patients with and without temporomandibular joint dysfunction: A cone-beam computed tomography based study. *Dent Res J (Isfahan)*. 2020; 17(5): 338–346, indexed in Pubmed: [33343841](https://pubmed.ncbi.nlm.nih.gov/33343841/).
- Epstein JB, Caldwell J, Black G. The utility of panoramic imaging of the temporomandibular joint in patients with temporomandibular disorders. *Oral Surg Oral Med Oral Pathol Oral Radiol Endod*. 2001; 92(2): 236–239,

- doi: [10.1067/moe.2001.114158](https://doi.org/10.1067/moe.2001.114158), indexed in Pubmed: [11505273](https://pubmed.ncbi.nlm.nih.gov/11505273/).
8. Hegde S, Praveen BN, Shetty SR. Morphological and radiological variations of mandibular condyles in health and diseases: a systematic review. *Dentistry*. 2013; 03(01), doi: [10.4172/2161-1122.1000154](https://doi.org/10.4172/2161-1122.1000154).
  9. Honda E, Yoshino N, Sasaki T. Condylar appearance in panoramic radiograms of asymptomatic subjects and patients with temporomandibular disorders. *Oral Radiol*. 1994; 10(2): 43–53, doi: [10.1007/bf02390715](https://doi.org/10.1007/bf02390715).
  10. Jawahar A, Maragathavalli G. Analysis of condylar morphological variations using digital panoramic radiographs-a retrospective study. *Indian J Public Health Res Develop*. 2019; 10(11): 3450, doi: [10.5958/0976-5506.2019.04116.0](https://doi.org/10.5958/0976-5506.2019.04116.0).
  11. Juniper RP. The shape of the condyle and position of the meniscus in temporomandibular joint dysfunction. *Br J Oral Maxillofac Surg*. 1994; 32(2): 71–76, doi: [10.1016/0266-4356\(94\)90130-9](https://doi.org/10.1016/0266-4356(94)90130-9), indexed in Pubmed: [8199150](https://pubmed.ncbi.nlm.nih.gov/8199150/).
  12. Katsavrias EG, Halazonetis DJ. Condyle and fossa shape in Class II and Class III skeletal patterns: a morphometric tomographic study. *Am J Orthod Dentofacial Orthop*. 2005; 128(3): 337–346, doi: [10.1016/j.ajodo.2004.05.024](https://doi.org/10.1016/j.ajodo.2004.05.024), indexed in Pubmed: [16168330](https://pubmed.ncbi.nlm.nih.gov/16168330/).
  13. Momjian A, Courvoisier D, Kiliaridis S, et al. Reliability of computational measurement of the condyles on digital panoramic radiographs. *Dentomaxillofac Radiol*. 2011; 40(7): 444–450, doi: [10.1259/dmfr/83507370](https://doi.org/10.1259/dmfr/83507370), indexed in Pubmed: [21960403](https://pubmed.ncbi.nlm.nih.gov/21960403/).
  14. Ribeiro E, Sanches M, Alonso L, et al. Shape and symmetry of human condyle and mandibular fossa. *Int J Odontostomatol*. 2015; 9(1): 65–72, doi: [10.4067/s0718-381x2015000100010](https://doi.org/10.4067/s0718-381x2015000100010).
  15. Singh B, Kumar NR, Balan A, et al. Evaluation of normal morphology of mandibular condyle: a radiographic survey. *J Clin Imaging Sci*. 2020; 10: 51, doi: [10.25259/JCIS\\_84\\_2020](https://doi.org/10.25259/JCIS_84_2020), indexed in Pubmed: [32874756](https://pubmed.ncbi.nlm.nih.gov/32874756/).
  16. Sonal V, Sandeep P, Kapil G, et al. Evaluation of condylar morphology using panoramic radiography. *J Adv Clin Res Ins*. 2016; 3: 5–8, doi: [10.15713/ins.jcri.94](https://doi.org/10.15713/ins.jcri.94).
  17. Valladares Neto J, Estrela C, Bueno MR, et al. Mandibular condyle dimensional changes in subjects from 3 to 20 years of age using cone-beam computed tomography: a preliminary study. *Dental Press J Orthodontics*. 2010; 15(5): 172–81.
  18. Yalcin ED, Ararat E. Cone-Beam computed tomography study of mandibular condylar morphology. *J Craniofac Surg*. 2019; 30(8): 2621–2624, doi: [10.1097/SCS.0000000000005699](https://doi.org/10.1097/SCS.0000000000005699), indexed in Pubmed: [31261335](https://pubmed.ncbi.nlm.nih.gov/31261335/).
  19. Yale SH, Allison BD, Hauptfuehrer JD. An epidemiological assessment of mandibular condyle morphology. *Oral Surg Oral Med Oral Pathol*. 1966; 21(2): 169–177, doi: [10.1016/0030-4220\(66\)90238-6](https://doi.org/10.1016/0030-4220(66)90238-6), indexed in Pubmed: [5215976](https://pubmed.ncbi.nlm.nih.gov/5215976/).

# Assessment of morphological changes degree on the articular surfaces of the temporomandibular joints on the historical skeleton material

A. Stangret<sup>ID</sup>, I. Teul<sup>ID</sup>

Chair and Department of Normal Anatomy, Pomeranian Medical University, Szczecin, Poland

[Received: 10 January 2022; Accepted: 7 February 2022; Early publication date: 22 March 2022]

**Background:** The aging process in the temporomandibular joints (TMJs) is related, more or less, with degenerative processes. Despite the rich literature on morphology and anatomy and the functioning of the components of the TMJs, there is much less research studies on the anatomy and diseases of these joints on historical populations. The aim of the study was to analyse the frequency and intensity of morphological and dysfunctional changes within the TMJ.

**Materials and methods:** The research material included skeleton material from three chronologically and geographically diverse archaeological series located in Poland in the cities: Strzelce Krajskie ( $n = 86$ ), Santok ( $n = 86$ ) and Wrocław ('Kuronia' collection) ( $n = 70$ ). The examination of the skeletal material was based on the macroscopic analysis of the articular surfaces of the TMJ.

**Results and Conclusions:** The difference in the frequency of degenerative changes observed on the articular surfaces of the TMJs between the examined skeletal series from selected cities was insignificant (Santok: 81.4%, Strzelce Krajskie: 72.1%, 'Kuronia': 68.6%). However, the obtained results showed a difference in the intensity of changes in the TMJ between individuals representing the early medieval population from Santok and individuals from the beginning of the 20<sup>th</sup> century collection 'Kuronia'. (Folia Morphol 2022; 81, 2: 487–492)

**Key words:** temporomandibular joints, degenerative changes in joints, temporomandibular disorders, determinant of physiological stress

## INTRODUCTION

Temporomandibular joints (TMJs), *Articulatio temporomandibularis*, due to their morphological structures, are the bicondylar joints, coupled in every movement. Their anatomical and functional structure is more complex than in other joints of the human body [1, 30].

The articular surface on the temporal bone is the acetabulum. It consists of glenoid fossa (the front part of the mandibular fossa) and the articular eminence

of the temporal bone. The articular head is the surface of the mandible (ovoid condylar process seated atop a narrow mandibular neck) [1, 38].

Temporomandibular joints in apes are characterised by a much shallower acetabular fossa and slightly marked articular eminence, while in humans TMJs have a deep fossa and well-marked eminence [2, 3, 14].

Distinguishing feature of the TMJ is its articular surface, covered with avascular fibrocartilage. There-

Address for correspondence: Dr. A. Stangret, Chair and Department of Normal Anatomy, Pomeranian Medical University, al. Powstańców Wielkopolskich 72, 70–111 Szczecin, Poland, tel: +48 91 466 1543, e-mail: anatomia@pum.edu.pl

This article is available in open access under Creative Common Attribution-Non-Commercial-No Derivatives 4.0 International (CC BY-NC-ND 4.0) license, allowing to download articles and share them with others as long as they credit the authors and the publisher, but without permission to change them in any way or use them commercially.

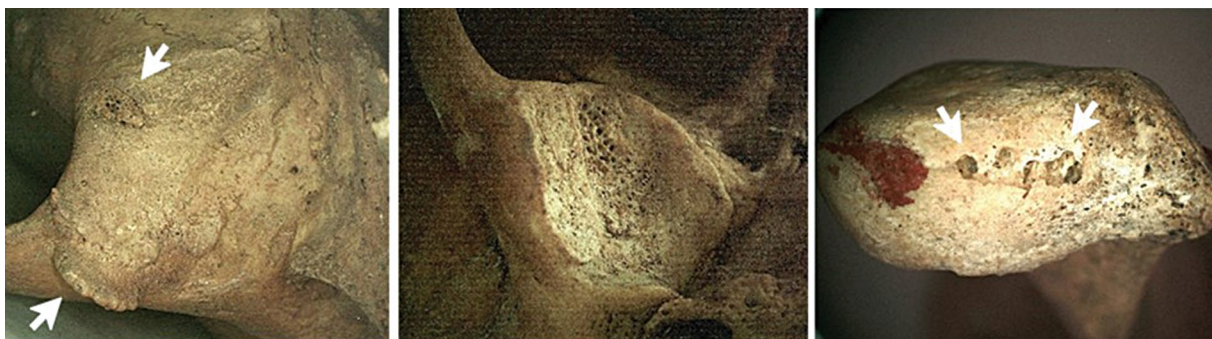


**Figure 1.** Examples of changes observed on the articular surfaces of the temporomandibular joints.

fore, cartilage is abrading relatively quickly, which makes TMJ prone to various factors (e.g. masticatory system load level), exposing it to dysfunctional changes. What is more it works all the time, also at night [1].

Temporomandibular disorder is a condition characterised by dysfunctional or/and painful changes that affect masticatory muscles, TMJ and associated structures [5, 7]. The disorders within the TMJs constitute a large percentage among viscerocranium diseases [1, 10].

The ageing process in the TMJ is related inter alia to degenerative processes [18]. Despite the rich literature on morphology of the components of the TMJ [13, 15–17, 19, 23, 25, 26, 33], there is much less research studies (especially from last two decades) in this subject on historical populations [20, 27, 34].

The morphology of the viscerocranium adapts to the environment; therefore, extinct prehistoric and historical populations may be valuable for testing hypotheses [6]. In addition, the analysis of TMJs degenerations can enrich the research on factors that are responsible for the functional structure of the viscerocranium [24, 27].

Bone changes, as marks of a past infection process or a reaction to biomechanical overload on bone surfaces, do not manifest equally. They differ in intensity, take different forms and shapes. From very delicate individual spikes and stripes, through characteristic patterns, to strong protuberances and massive ridges of irregular bone.

Changes in the morphology of the articular surfaces of the TMJs are the basis for the classification of the periosteum and bone tissue reactions as a result of the reaction of osteoclasts and osteoblasts to the pathogen. Among bone reactions, there are repair processes that cause bone thickening, and osteolytic

(degenerative, erosive) processes, resulting in a lack of bone tissue (Fig. 1) [27–29].

## MATERIALS AND METHODS

The selection of osteological material in this study depended on the state of bone preservation. The decisive factor qualifying the suitability for the study was the state of preservation of the articular surfaces of the TMJs of the temporal bone and the head of the mandible. The material differed in terms of sex and age-at-death. Individuals from Infants I and II groups were excluded from the study due to the lack of complete development of articular surfaces of the TMJs.

As the abnormal articular surface of the TMJs we considered the one in which at least one of its surfaces has been diagnosed with single or collective combinations of pathological changes as signs of erosive and proliferative reactions, as a result of the activity of a pathogenic factor.

The research material includes skeleton material from the three chronologically and geographically diverse archaeological series located in Poland in the cities: Strzelce Krajeńskie (XIII–XV c.), Santok (XIII c.), Wrocław ('Kurononia' collection) (XIX/XX c.).

Eighty six individuals (43 males and 36 females, and 7 individuals of undefined sex) were analysed from the Santok skeleton series, representing the population of the early middle ages; also 86 individuals (42 males, 29 females and 15 adults of undefined sex) were analysed from the Strzelce Krajeńskie skeleton series and 70 individuals (34 men and 36 women) from the 'Kurononia' collection.

The examination and classification of the bone changes resulting from disease processes in TMJs of individuals from historical populations was performed

based on the methods used in previous anthropological, paleopathological and bioarchaeological studies [27, 28].

During the research, each of the preserved surfaces of the TMJs was carefully examined and analysed macroscopically. Additionally, an electronic microscope DigiMicro 2.0 was used for the observation.

Changes in the TMJs were classified based on the Richards and Brown scale modified for the purposes of this work (taking into account the comments of Rando and Waldron [2012]) [27]. According to the criteria proposed by Richards and Brown (1981) [28], the degree of degeneration of the condylar process of the mandible and the fossa and articular eminence of the temporal bone was assessed. Each TMJ articular surface was examined and divided into areas for evaluation purposes. In the case of the condyle, the divisions proposed by Mongini (1972) [22] were used. Three 60° areas were designated, and each of them was further divided into posterior, top, and anterior areas. In the case of the articular surface on the temporal bone, the articular eminence and the fossa were distinguished, and then the medial, central and lateral areas were separated.

First, the entire material was divided according to the frequency of degenerative changes according to the following scale (scale 1):

- 0: no degenerative changes;
- 1: any degenerative changes present.

The intensity of changes on the articular surfaces of the condylar process of the mandible and the fossa as well as the articular eminence of the temporal bone was assessed according to the criteria for assessing changes and degenerations (scale 2):

- 0: norm;
- 1: remodelling;
- 2: local erosion;
- 3: local proliferation/osteophytes and/or erosion (in less than 5 areas);
- 4: general proliferation and/or erosion (in 5 and more areas);
- 5: eburnation and/or complete destruction of articular surfaces.

Erosion was defined as the area of pitting or porosity on the joint surface (macroporosity or microporosity, localised or spread). Proliferation is new bone growth on the surface of a joint. It can appear as bumps or flat growths. The presence of new bone on the surface of the joint indicates an attempt to “stabilise” the joint. Additionally, marginal osteo-

phytes were noted as bone growths forming along the edges of the joint.

In addition, the presence of reconstruction of the articular surface was noted, being an adaptation to occlusive stress preceding erosion and degeneration of the cortex. Moffett (1974) [21] suggested that the TMJs are in a state of constant equilibrium between structure and function [4]. Under normal conditions, equilibrium is maintained by the processes of adaptive remodelling. This can be disrupted by functional requirements that are too high, leading to the next degeneration of the joints.

For each series basic statistics in the form of frequency tables were performed. Differences in frequency and intensity of changes on the articular surfaces of the TMJs were tested using Kruskal-Wallis test and post-hoc tests to check between which groups the differences were statistically significant.

## RESULTS

In the examined skeleton series from Santok, the percentage of bone changes (according to scale 1) on the articular surfaces of the TMJ was 81%. The analysis of the results showed that the local proliferative and erosive changes were the most common in the Santok individuals ('2' and '3' — scale 2). The strongest degenerative change observed on all examined articular surfaces of the TMJs was the general proliferation of the articular surface or erosion in more than five areas. No changes of the '5' level were observed in any individual from this skeleton series

In series from Strzelce Krajenckie, the percentage of bone changes (according to scale 1) on the articular surfaces of the TMJ was 72%. The analysis of the results showed that in individuals from this series, local proliferative and erosive changes were the most common on the TMJ articular surfaces ('2' and '3' — scale 2). The strongest degenerative change observed on all examined articular surfaces of the TMJs was the general proliferation of the articular surface or erosion in more than five areas. In this skeleton series, no changes at the '5' level were observed in any individual.

In the examined skeletal series from Wroclaw, the percentage of bone changes (according to scale 1) on the articular surfaces of the TMJ was 68.5%. The analysis of the results showed that in individuals from the 'Kurononia' collection, local erosive lesions ('2' — scale 2) were the most common — 41%. The most severe degenerative change observed on all

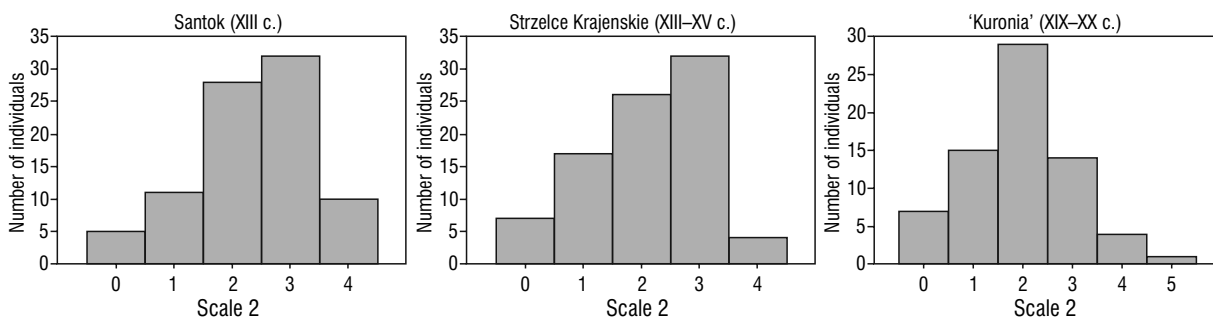


**Figure 2.** Distribution of degenerative changes in the temporomandibular joints of the studied individuals, based on the scale 2.

**Table 1.** Differences between the studied skeleton series

Series	Time period	N	TMJ	TMJ (%)
Santok	XIII c.	86	70	81%
Strzelce Krajenkie	XIII–XV c.	86	62	72%
'Kurononia'	XIX/XX c.	70	48	68.5%

N — number of examined individuals; TMJ — the total number of all individuals with bone changes in the temporomandibular joint (one or both); TMJ (%) — the percentage of all individuals with bone changes in the temporomandibular joint

**Table 2.** P-value for multiple comparisons (bilateral) (Scale 1)

	Santok R: 129,99	Strzelce Krajenkie R: 118,73	'Kurononia' R: 114,47
Santok (XIII c.)		0.87	0.51
Strzelce Krajenkie (XIII–XV c.)	0.87		1.00
'Kurononia' (XIX/XX c.)	0.51	1.00	

Independent variable (grouping): Series. Kruskal-Wallis test:  $H(2, N = 242) = 3.68$ ,  $p = 0.16$ .

**Table 3.** P-value for multiple comparisons (bilateral) (Scale 2)

	Santok R: 135,37	Strzelce Krajenkie R: 119,83	'Kurononia' R: 106,51
Santok (XIII c.)		0.8744	0.03
Strzelce Krajenkie (XIII–XV c.)	0.44		0.71
'Kurononia' (XIX/XX c.)	0.03	0.71	

Independent variable (grouping): Series. Kruskal-Wallis test:  $H(2, n = 242) = 7.21$ ,  $p = 0.03$ .

examined articular surfaces of the TMJs was complete destruction of the articular surfaces present in only one individual (Fig. 2).

Table 1 presents the most important differences between the studied historical series.

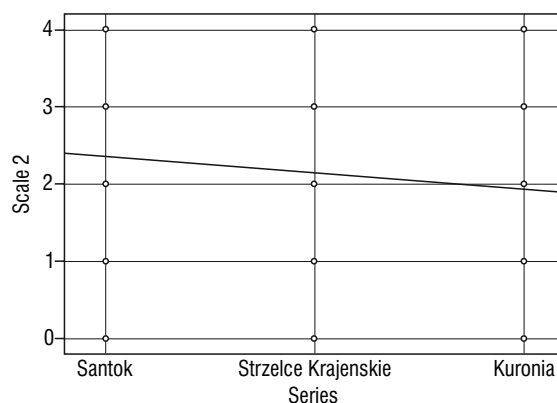


**Figure 3.** Comparison of skeletal series in relation to the intensity of bone changes in the temporomandibular joints (scale 2).

A statistical analysis was performed to check whether there were differences between the skeletal series in frequency and intensity of bone changes in the TMJs (Tables 2, 3). The analysis with the Kruskal-Wallis test showed statistically significant differences between the series from Santok and the 'Kurononia' collection. In individuals from Santok there were more intense bone changes (scale 2) in the area of TMJs (Fig. 3).

## DISCUSSION

In the studied skeleton material, statistical analysis did not show any significance in the differences in the frequency of bone changes in TMJ between individuals from the examined series. However, the obtained results showed a difference in the intensity of changes observed on the articular surfaces of the TMJs between individuals from the Santok series and from the 'Kurononia' collection. Adaptive reconstruction also occurred more frequently among individuals from the 'Kurononia' collection, suggesting a large

predisposition of these joints to adapt to occlusive conditions or the harmful influence of factors. More intense degenerative changes of the TMJ, manifested by bone changes on the articular surfaces, occurred more frequently in individuals from the skeleton series from an early medieval site, i.e. exposed to more severe living conditions, especially related to diet, which directly and indirectly affects the occlusion, and the latter affects the TMJs.

The formation of the elements of the TMJs depends on many factors; therefore, the analysis of their changes can provide a number of important information about the life of historic populations. The analysis of bone changes in TMJ, which is one of the most important elements of our masticatory system, may not be such a good indicator of living conditions and their sensitive measure, such as body height. However, included in the methods used as determinants of pressure level from environmental factors, it will enrich the research and analysis of changes in the biocultural system and biological condition of historical populations, as a source of information about lifestyle and nutrition.

The results of analyses of the differentiation of bone changes in the TMJ over time in the skeleton material representing the populations from the early and late middle ages, the 19<sup>th</sup> and 20<sup>th</sup> centuries, presented in this work, prove that changes in the biological condition of these communities may have occurred in the aspect of the presence of TMJ dysfunction.

Research on the skeleton material concerning the issue discussed in this article has been ignored in the last two decades. Despite the enormous amount of information that the TMJ may carry, on the environment, diet, and the general condition of the studied population, most of them date back to the 1990s [8, 9, 11, 12, 28, 31, 32, 35–37]. It is suggested to continue and expand research in this area in order to clarify the relationship between the environment, and the occurrence of changes in the TMJ. This joint, like all joints in the human body, reacts to the external environment and the information obtained from them is scientifically significant.

## CONCLUSIONS

More intense degenerative changes of the TMJs, manifested as bone changes on the articular surfaces, occurred more often in individuals from the early

medieval skeleton series, i.e. exposed to more severe living conditions.

The study of the frequency and intensity of changes in the TMJ can be used as a determinant of physiological stress affecting biological condition in the examined skeletal series.

**Conflict of interest:** None declared

## REFERENCES

1. Alomar X, Medrano J, Cabratosa J, et al. Anatomy of the temporomandibular joint. *Semin Ultrasound CT MR*. 2007; 28(3): 170–183, doi: [10.1053/j.sult.2007.02.002](https://doi.org/10.1053/j.sult.2007.02.002), indexed in Pubmed: [17571700](https://pubmed.ncbi.nlm.nih.gov/17571700/).
2. Aiello L, Dean C. *An Introduction to Human Evolutionary Anthropology*. Academic Press, London 1990.
3. Alt KW, Turp JC. Morphology of the temporomandibular joint of higher primates. In: Koppe T, Nagai H. *The Paranasal Sinuses of Higher Primates: Development, Function, and Evolution*. Quintessence, Chicago 1999: 235–250.
4. Blackwood HJJ. *Adaptive Changes in the Mandibular Joint with Function*. The Dental Clinics of North America. Saunders Co, Philadelphia 1966.
5. Bonato LL, Quinelato V, De Felipe Cordeiro PC, et al. Association between temporomandibular disorders and pain in other regions of the body. *J Oral Rehabil*. 2017; 44(1): 9–15, doi: [10.1111/joor.12457](https://doi.org/10.1111/joor.12457), indexed in Pubmed: [27862166](https://pubmed.ncbi.nlm.nih.gov/27862166/).
6. Brothwell DR. The macroscopic dental pathology of some earlier human populations. *Dental Anthropology*. Pergamon Press, London 1963: 272–287.
7. Câmara-Souza MB, Figueredo OM, Maia PR, et al. Cervical posture analysis in dental students and its correlation with temporomandibular disorder. *Cranio*. 2018; 36(2): 85–90, doi: [10.1080/08869634.2017.1298226](https://doi.org/10.1080/08869634.2017.1298226), indexed in Pubmed: [28274183](https://pubmed.ncbi.nlm.nih.gov/28274183/).
8. Eversole LR, Pappas JR, Graham R. Dental occlusal wear and degenerative disease of the temporomandibular joint: a correlational study utilizing skeletal material from a contemporary population. *J Oral Rehabil*. 1985; 12(5): 401–406, doi: [10.1111/j.1365-2842.1985.tb01545.x](https://doi.org/10.1111/j.1365-2842.1985.tb01545.x), indexed in Pubmed: [3862799](https://pubmed.ncbi.nlm.nih.gov/3862799/).
9. Filce Leek F. Bite, attrition and associated oral conditions as seen in ancient Egyptian skulls. *J Hum Evol*. 1972; 1(3): 289–295, doi: [10.1016/0047-2484\(72\)90064-4](https://doi.org/10.1016/0047-2484(72)90064-4).
10. Gonçalves DAG, Fabbro ALD, Campos ADB, et al. Symptoms of temporomandibular disorders in the population: an epidemiological study. *J Orofac Pain*. 2010; 24(3): 270–278.
11. Griffin CJ, Powers R, Kruszynski R. The incidence of osteo-arthritis of the temporomandibular joint in various cultures. *Aust Dent J*. 1979; 24(2): 94–106, doi: [10.1111/j.1834-7819.1979.tb03615.x](https://doi.org/10.1111/j.1834-7819.1979.tb03615.x), indexed in Pubmed: [380538](https://pubmed.ncbi.nlm.nih.gov/380538/).
12. Hodges DC. Temporomandibular joint osteoarthritis in a British skeletal population. *Am J Phys Anthropol*. 1991; 85(4): 367–377, doi: [10.1002/ajpa.1330850402](https://doi.org/10.1002/ajpa.1330850402), indexed in Pubmed: [1928311](https://pubmed.ncbi.nlm.nih.gov/1928311/).

13. Ingawalé S, Goswami T. Temporomandibular joint: disorders, treatments, and biomechanics. *Ann Biomed Eng.* 2009; 37(5): 976–996, doi: [10.1007/s10439-009-9659-4](https://doi.org/10.1007/s10439-009-9659-4), indexed in Pubmed: [19252985](https://pubmed.ncbi.nlm.nih.gov/19252985/).
14. Koppe T, Schöbel SL, Bärenklau M, et al. Factors affecting the variation in the adult temporomandibular joint of archaeological human populations. *Ann Anat.* 2007; 189(4): 320–325, doi: [10.1016/j.aanat.2007.02.018](https://doi.org/10.1016/j.aanat.2007.02.018), indexed in Pubmed: [17695984](https://pubmed.ncbi.nlm.nih.gov/17695984/).
15. Lobbezoo F, Drangsholt M, Peck C, et al. Topical review: new insights into the pathology and diagnosis of disorders of the temporomandibular joint. *J Orofac Pain.* 2004; 18(3): 181–191, indexed in Pubmed: [15508997](https://pubmed.ncbi.nlm.nih.gov/15508997/).
16. Luther F. TMD and occlusion part I. Damned if we do? Occlusion: the interface of dentistry and orthodontics. *Br Dent J.* 2007; 202(1): E2; discussion 38–E2; discussion 39, doi: [10.1038/bdj.2006.122](https://doi.org/10.1038/bdj.2006.122), indexed in Pubmed: [17220827](https://pubmed.ncbi.nlm.nih.gov/17220827/).
17. Luther F. TMD and occlusion part II. Damned if we don't? Functional occlusal problems: TMD epidemiology in a wider context. *Br Dent J.* 2007; 202(1): E3; discussion 38–E3; discussion 39, doi: [10.1038/bdj.2006.123](https://doi.org/10.1038/bdj.2006.123), indexed in Pubmed: [17220828](https://pubmed.ncbi.nlm.nih.gov/17220828/).
18. McNeill C. History and evolution of TMD concepts. *Oral Surg Oral Med Oral Pathol Oral Radiol Endod.* 1997; 83(1): 51–60, doi: [10.1016/s1079-2104\(97\)90091-3](https://doi.org/10.1016/s1079-2104(97)90091-3), indexed in Pubmed: [9007924](https://pubmed.ncbi.nlm.nih.gov/9007924/).
19. Milam SB, Schmitz JP. Molecular biology of temporomandibular joint disorders: proposed mechanisms of disease. *J Oral Maxillofac Surg.* 1995; 53(12): 1448–1454, doi: [10.1016/0278-2391\(95\)90675-4](https://doi.org/10.1016/0278-2391(95)90675-4), indexed in Pubmed: [7490656](https://pubmed.ncbi.nlm.nih.gov/7490656/).
20. Miller J. An appraisal of the skulls and dentition of ancient Egyptians, highlighting the pathology and speculating on the influence of diet and environment. 2008, doi: [10.30861/9781407302829](https://doi.org/10.30861/9781407302829).
21. Moffett BC. The temporomandibular joint. In: *Complete Denture Prosthodontics* 3. Edition 56, 1974 .
22. Mongini F. Remodelling of the mandibular condyle in the adult and its relationship to the condition of the dental arches. *Acta Anat (Basel).* 1972; 82(3): 437–453, doi: [10.1159/000143825](https://doi.org/10.1159/000143825), indexed in Pubmed: [5048605](https://pubmed.ncbi.nlm.nih.gov/5048605/).
23. Oberg T, Carlsson GE, Fajers CM. The temporomandibular joint. A morphologic study on a human autopsy material. *Acta Odontol Scand.* 1971; 29(3): 349–384, doi: [10.3109/00016357109026526](https://doi.org/10.3109/00016357109026526), indexed in Pubmed: [5286674](https://pubmed.ncbi.nlm.nih.gov/5286674/).
24. Palubeckaite Z, Jankauskas R. Dental enamel hypoplasia in Lithuanian paleopopulations. *Acta Med Litu.* 2001; 8(Suppl. ): 12–17.
25. Pullinger A, Seligman D, Solberg W. Temporomandibular disorders. Part I: Functional status, dentomorphologic features, and sex differences in a nonpatient population. *J Prosthet Dent.* 1988; 59(2): 228–235, doi: [10.1016/0022-3913\(88\)90019-4](https://doi.org/10.1016/0022-3913(88)90019-4).
26. Pullinger AG, Solberg WK, Pullinger AG, et al. Temporomandibular disorders. Part II: occlusal factors associated with temporomandibular joint tenderness and dysfunction. *J Prosthet Dent.* 1988; 59(3): 363–367, doi: [10.1016/0022-3913\(88\)90191-6](https://doi.org/10.1016/0022-3913(88)90191-6), indexed in Pubmed: [3162277](https://pubmed.ncbi.nlm.nih.gov/3162277/).
27. Rando C, Waldron T. TMJ osteoarthritis: a new approach to diagnosis. *Am J Phys Anthropol.* 2012; 148(1): 45–53, doi: [10.1002/ajpa.22039](https://doi.org/10.1002/ajpa.22039), indexed in Pubmed: [22371124](https://pubmed.ncbi.nlm.nih.gov/22371124/).
28. Richards LC, Brown T. Dental attrition and degenerative arthritis of the temporomandibular joint. *J Oral Rehabil.* 1981; 8(4): 293–307, doi: [10.1111/j.1365-2842.1981.tb00504.x](https://doi.org/10.1111/j.1365-2842.1981.tb00504.x), indexed in Pubmed: [7024487](https://pubmed.ncbi.nlm.nih.gov/7024487/).
29. Richards LC. Tooth wear and temporomandibular joint change in Australian aboriginal populations. *Am J Phys Anthropol.* 1990; 82(3): 377–384, doi: [10.1002/ajpa.1330820313](https://doi.org/10.1002/ajpa.1330820313), indexed in Pubmed: [2375385](https://pubmed.ncbi.nlm.nih.gov/2375385/).
30. Rutkiewicz T, Könönen M, Suominen-Taipale L, et al. Occurrence of clinical signs of temporomandibular disorders in adult Finns. *J Orofac Pain.* 2006; 20(3): 208–217, indexed in Pubmed: [16913430](https://pubmed.ncbi.nlm.nih.gov/16913430/).
31. Seward FS. Tooth attrition and the temporomandibular joint. *Angle Orthod.* 1976; 46(2): 162–170, doi: [10.1043/0003-3219\(1976\)046<0162:TAATTJ>2.0.CO;2](https://doi.org/10.1043/0003-3219(1976)046<0162:TAATTJ>2.0.CO;2), indexed in Pubmed: [776043](https://pubmed.ncbi.nlm.nih.gov/776043/).
32. Sheridan SG, Mittler DM, Van Gerven DP, et al. Biomechanical association of dental and temporomandibular pathology in a medieval Nubian population. *Am J Phys Anthropol.* 1991; 85(2): 201–205, doi: [10.1002/ajpa.1330850208](https://doi.org/10.1002/ajpa.1330850208), indexed in Pubmed: [1882982](https://pubmed.ncbi.nlm.nih.gov/1882982/).
33. Tanaka E, Koolstra JH. Biomechanics of the temporomandibular joint. *J Dent Res.* 2008; 87(11): 989–991, doi: [10.1177/154405910808701101](https://doi.org/10.1177/154405910808701101), indexed in Pubmed: [18946004](https://pubmed.ncbi.nlm.nih.gov/18946004/).
34. Tanaka T, Morimoto Y, Tanaka Y, et al. Radiographic examination of the mandibular (glenoid) fossa in ancient and modern man. *Oral Dis.* 2004; 10(6): 369–377, doi: [10.1111/j.1601-0825.2004.01022.x](https://doi.org/10.1111/j.1601-0825.2004.01022.x), indexed in Pubmed: [15533214](https://pubmed.ncbi.nlm.nih.gov/15533214/).
35. Webb S. *Palaeopathology of Aboriginal Australians: health and disease across a hunter-gatherer continent.* Cambridge University Press, Cambridge 1995.
36. Wedel A, Carlsson GE, Sagne S. Temporomandibular joint morphology in a medieval skull material. *Swed Dent J.* 1978; 2: 177–187.
37. Whittaker DK, Davies G, Brown M. Tooth loss, attrition and temporomandibular joint changes in a Romano-British population. *J Oral Rehabil.* 1985; 12(5): 407–419, doi: [10.1111/j.1365-2842.1985.tb01546.x](https://doi.org/10.1111/j.1365-2842.1985.tb01546.x), indexed in Pubmed: [3862800](https://pubmed.ncbi.nlm.nih.gov/3862800/).
38. Williams PL. *Gray's anatomy, in Skeletal System (ed 38).* Churchill Livingstone, London 1999: 578–582.

# A gross anatomical study of the styloid process of the temporal bone in Japanese cadavers

S. Tanaka<sup>1\*</sup>, H. Terayama<sup>1\*</sup>, Y. Miyaki<sup>1</sup>, D. Kiyoshima<sup>1</sup>, N. Qu<sup>1</sup>, K. Umemoto<sup>1</sup>,  
O. Tanaka<sup>1</sup>, M. Naito<sup>2</sup>, K. Sakabe<sup>1</sup>

<sup>1</sup>Department of Anatomy, Division of Basic Medical Science, Tokai University School of Medicine, Kanagawa, Japan

<sup>2</sup>Department of Anatomy, Aichi Medical University, Aichi, Japan

[Received: 8 December 2020; Accepted: 17 January 2021; Early publication date: 23 February 2021]

**Background:** The incidence of an elongated styloid process (SP) and average length and diameter of SP have not been reported using Japanese cadavers. Data on the female-to-male ratio of an elongated SP vary. We calculated the average length and diameter of SP in Japanese cadavers and compared SP lengths between sexes.

**Materials and methods:** Twenty-seven sides (right and left of bodies) in males and 51 sides in females were analysed. Measurements were obtained from the inferior external acoustic meatus to the distal tip of the SP. SP diameters at the proximal base, midpoint, and distal tip were measured. SP > 30 mm was considered elongated. We used Welch's t-test for the statistical analysis. Fisher's exact two-tailed test was also performed to analyse the female-to-male elongation ratio. A p-value < 0.05 was considered statistically significant.

**Results:** Styloid process elongation prevalence was 29.5% in our sample. The average full length was 27.04 ± 7.88 mm overall; the average diameters were 5.41 ± 1.77 mm at the proximal base and 2.21 ± 1.22 mm at the distal tip. The average SP measurement was 26.81 ± 5.92 mm in males and 27.16 ± 8.79 mm in females (p = 0.74). The female-to-male ratio of SP elongation was 1:2 (p = 0.041). Females had longer full lengths of non-elongated SPs than males (p = 0.004). Males had wider diameters at the proximal base of elongated SPs than females (p = 0.017).

**Conclusions:** The average length of SP was 27.04 mm in the Japanese population and about 30% of the Japanese presented SP ≥ 30 mm. Male had significantly higher rate than female among the SP ≥ 30 mm, and female had significantly longer SPs than male among the SP < 30 mm. Anatomically, the SP gets narrow as distally goes. Our anatomical findings would be beneficial to creating treatment plans, diagnosis, and surgery. (Folia Morphol 2022; 81, 2: 493–502)

**Key words:** Eagle syndrome, elongation, styloid process, cadaver, second branchial arch

---

Address for correspondence: Dr. H. Terayama, Department of Anatomy, Division of Basic Medical Science, Tokai University School of Medicine, 143 Shimokasuya, Isehara-shi, Kanagawa 259-1193, Japan, tel: +81-463-931121 (ext: 2513), e-mail: terahaya@tokai-u.jp

\*S. Tanaka and H. Terayama contributed equally to this work.

This article is available in open access under Creative Common Attribution-Non-Commercial-No Derivatives 4.0 International (CC BY-NC-ND 4.0) license, allowing to download articles and share them with others as long as they credit the authors and the publisher, but without permission to change them in any way or use them commercially.

## INTRODUCTION

The styloid process (SP) is a slender bony structure projecting out downwardly from the temporal bone and lying anterior to the stylomastoid foramen [3, 25]. The average normal length of the SP ranges from 20 mm to 30 mm [18, 25, 45]; the SP of > 30 mm is considered elongated [26, 28, 42]. The distal tip of the SP is usually located posterior to the tonsil fossa [3]. Because external and internal carotid arteries run at the distal aspect of the SP, the SP is clinically significant [7, 38]. The internal jugular vein also runs posteriorly to the carotid arteries [35]. In addition to these blood vessels, the accessory, vagus, facial, and glossopharyngeal nerves run close to the styloid process [35]. The accessory and vagus nerves pass medially to the SP, and the facial nerve lies anteromedially to it [36]. The glossopharyngeal nerve is the most proximal to the SP and runs from the jugular foramen [25, 35].

The symptoms of Eagle's syndrome are associated with styloid process elongation and mineralisation of a part of the stylohyoid ligament [35]. An elongated styloid process results in irritation of cranial nerves and impingement of the circulation at the distal tip [18, 35]. Vague neck pain is often reported as a primary symptom [37]. Tongue pain, dysphonia, ear pain, dysphagia, odynophagia, vertigo and tinnitus, facial paraesthesia, vocal change, and sore throat (pharyngolaryngeal paraesthesia) could also occur [35]. Clinically, patients who have elongated SP are often asymptomatic [32], and only 4% of the patients with elongated SP present symptoms [7]. Symptomatic patients were usually over 40 years old [3], and females are twice likely to present symptoms [2]. Another study indicated that 12 females and 9 males with Eagle syndrome had elongated SPs and clinical presentation [46]. Association between SP and sex is important. Patients with SP elongation had headaches (18.7%) and hypertension (17.1%) [1]. Clinical signs and symptoms are influenced by not only length but also the location and size of the SP. Nevertheless, studies investigating the average of SP diameter are scarce. While the proximal base thickness was reported to be approximately 4.4 mm [24, 49], the average diameter in the Japanese population has not been investigated.

Most previous studies investigated the length of the SP and incidence of SP elongation [1–8, 10, 12–14, 16, 18, 19, 21, 22, 25–27, 29–31, 33, 34, 39, 40, 43]. Eagle (1958) [7] reported that only 4% of the general

population experience Eagle's syndrome. Rogers and Chang (2007) [41] noted that the frequency is "very controversial." Another study found that the prevalence of enlarged SP was higher in females than in males [37].

A few studies on the prevalence of SP elongation in the Japanese population have been conducted, showing that the average SP lengths were 17.4 mm and  $18.8 \pm 5.26$  mm, respectively [29, 30]. These studies evaluated the SP using posteroanterior X-ray and panoramic radiographs; however, none of the studies performed measurements in a Japanese population. Only two cadaver studies [3, 25] and three skulls studies [3, 31, 39] were done to determine the prevalence of elongated SP. In cadaver studies, 80 SPs were measured and 22 cadavers were examined by Moffat et al. [25] and Balcioglu et al. [3], respectively. In skull studies, 232 skulls, 41 SPs, and 262 SPs were evaluated [3, 31, 39]. Few studies on cadavers have been reported.

Therefore, this study aimed: 1) to examine the average length and diameter of the SP, 2) to determine the prevalence of elongated SP in a Japanese population, and 3) to compare the SP lengths between sexes.

## MATERIALS AND METHODS

Of the 92 sides of the cadavers included in this study, only 78 (27 sides in males and 51 sides in females) were analysed. The cadavers were fixated using formaldehyde. Broken SPs were excluded and all other SPs were included. Gross dissections were performed in the dissection room. This study was approved by the Institutional Review Board for Clinical Research, Tokai University (No. 17R-310).

We dissected the epidermis to remove the subcutaneous tissues. The sternocleidomastoids, parotid salivary gland, and masticatory muscles were removed. Subsequently, we broke the mandible, and the medial and lateral pterygoid muscles were removed to expose the SP and the styloglossus, stylohyoid, and stylopharyngeus muscles.

Measurements were performed from the inferior part of the external acoustic meatus to the distal tip of the SP, according to a previous study [31]. Figure 1 shows the SP dissection. In our study, a string and a pair of tweezers were directly used for the measurement of SP length. Thereafter, a ruler and a calliper were used to measure diameter. Diameters of the proximal base (Fig. 1 /1/), mid-point (Fig. 1 /2/), and distal tip (Fig. 1 /3/) were measured. The mid-point

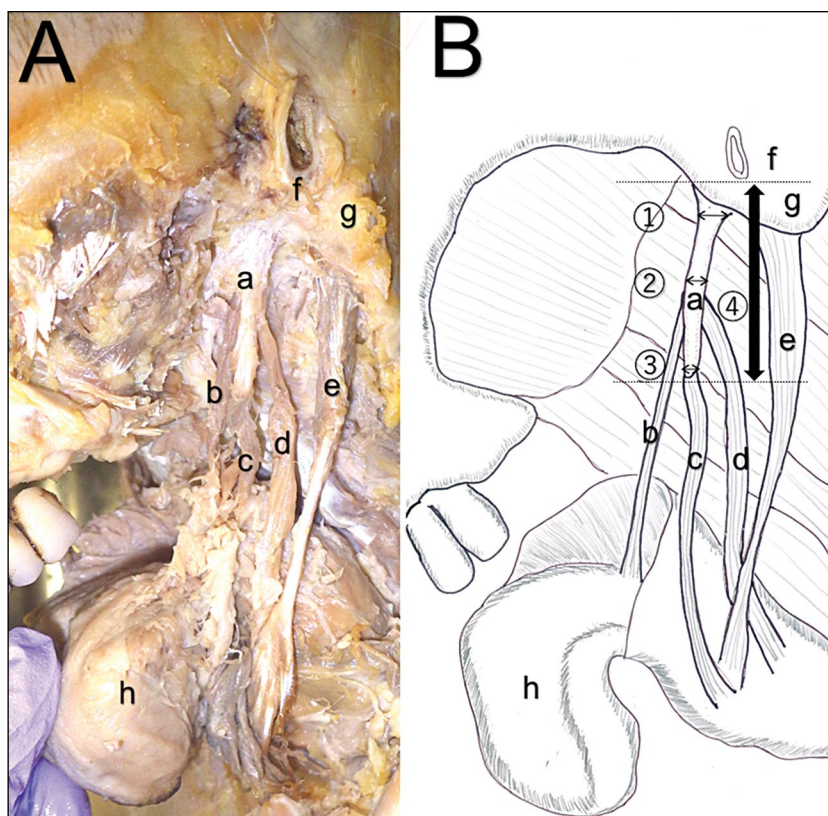


**Figure 1.** Styloid process from dissection (A) and a schema of the left inferolateral view (B); a — styloid process; b — styloglossus muscle; c — stylohyoid muscle; d — stylopharyngeus muscle; e — digastric muscle; f — external acoustic meatus; g — mastoid process; h — tongue. The length and width were measured (B); 1 — the proximal base; 2 — the mid-point; 3 — the distal tip (the horizontal double-headed arrows); 4 — length (the vertical double-headed arrow) from the external acoustic meatus (the upper dotted line) to the styloid process (the lower dotted line).

diameter was measured at the middle of the full length of the SP. Moreover, length was measured from the inferior part of the external acoustic meatus to the distal tip of the styloid process (Fig. 1 /4/). Based on previous studies [6, 19, 23], an SP  $\geq 30$  mm is considered elongated. Previous reports on the SP are shown in Table 1. This study had a limitation, i.e. the medical history prior to death was not identified; therefore, any pre-existing symptoms were unknown.

As shown in Table 2, the SP measurements were divided into three categories: all,  $> 30$  mm, and  $< 30$  mm. Length and diameter according to sex (male and female) and side (right and left) were compared among the three categories. We compared the differences in the average values. Because the sample sizes differed among the categories, we used Welch's t-test for the statistical analysis. Fisher's exact two-tailed test was also performed to analyse the female-to-male elongation ratio. A p-value  $< 0.05$  was considered statistically significant. The analyses were performed using Excel (Microsoft, USA).

## RESULTS

A comparison of the prevalence of elongated SP and the average length of the SP according to previous studies is shown in Table 1. Only two cadaver studies of the SP have been conducted, which were not in Japan (Table 1). In our cadaver study, which included Japanese individuals, the prevalence of SP elongation was 29.5% (Table 1). Of the 78 SPs, 23 measured  $\geq 30$  mm. Three cadavers presented bilateral elongation and 17 had unilateral elongation. The longest SP was from an 89-year-old female (47.0 mm on the right and 55.0 mm on the left). In Table 2, a comparison of the characteristics of the SP is shown. The differences in the length of the SP (i.e.,  $> 30$  mm or not) were evaluated according to sex and side of the SP. The average length was  $27.04 \pm 7.88$  mm (Tables 1, 2), and the average diameter was  $5.41 \pm 1.77$  mm at the proximal base,  $3.68 \pm 1.77$  mm at the mid-point, and  $2.21 \pm 1.22$  mm at the distal tip (Table 2). Eleven and 12 SPs  $> 30$  mm were found in females and males, respectively. In females,

**Table 1.** Comparison of the prevalence of elongated styloid process (SP) and mean SP length from previous studies

Article	Prevalence of elongated SP	Population	Measurement method	N	Average length of SP [mm]			Average length of elongated SP [mm]		
					Total	Right	Left	Total	Right	Left
Eagle (1958)	4.0%	American	Clinical	-	-	-	-	-	-	-
Nara (1958)	3.40%	Japanese	Posteroanterior X-ray	2350	17.4	-	-	-	-	-
	5.20%		Bitemporal X-ray	500	-	-	-	-	-	-
Kaufman et al. (1970)	28.0%	American	Panoramic radiographs	484 (M: 478, F: 6)	29.67*	29.92	29.49	32.85*	33.2	32.5
Gossman and Tarsitano (1977)	1.4% (elongation: > 25 mm)**	American	Panoramic radiographs	4200	-	-	-	-	-	-
Moffat et al. (1977)	-	British	Cadavers	80	32.70 ± 7.50	-	-	-	-	-
Correll et al. (1979)	18.2% (M: 17.9%, F: 30.8%)	American	Panoramic radiographs	1771 (M: 1719, F: 52)	-	-	-	43.6	-	-
O'Carroll (1984)	78.5% (M: 74.91%, F: 81.99%)	American	Panoramic radiographs	479	-	-	-	-	-	-
Keur et al. (1986)	30% (M: 28.5%, F: 32.9%)	Australian	Panoramic radiographs	1135 (M: 396, F: 739)	-	-	-	45.63 ± 10.93*	45.60 ± 10.38* (M: 47.95 ± 12.85, F: 44.53 ± 9.04)	45.67 ± 11.49* (M: 47.95 ± 13.28, F: 44.59 ± 10.54)
Monsour and Young (1986)	21.1% (elongation: > 40 mm)**	Australian	Panoramic radiographs	670	29.20 ± 4.85	-	-	-	-	-
Nakata et al. (1987)	15.5% (M: 16.8%, F: 14.2%)	Japanese	Panoramic radiographs	633	18.8 ± 5.26	-	-	-	-	-
Ferrario et al. (1990)	84.4% (elongation: original method)**	Italian	Orthopantomographs	286	-	-	-	-	-	-
Rath and Anand (1991)	0.4%	Indian	Skulls	232	2.53*	2.55	2.50	6.75*	7.00	6.50
Erol (1996)	1.1%	Turkish	Panoramic radiographs	900	-	-	-	48.15	-	-
Bozkir et al. (1997)	4.0%	Turkish	Panoramic radiographs	200 (M: 100, F: 100)	-	-	-	53.0	-	-
Gozli et al. (2001)	13.3% (M: 11.8%, F: 3.4%) (elongation: > 40 mm)**	Turkish	CT images	105 (M: 47, F: 58)	28.42 ± 12.49	28.58 ± 12.43	28.25 ± 12.62	42.55*	42.64 ± 1.94	42.46 ± 2.77
Igüy et al. (2005)	3.7%	Turkish	Panoramic radiographs	860	34.5*	35 ± 15	34 ± 8	-	-	-
Rizzatti-Barbosa et al. (2005)	20% (n = 451)	Brazilian	Panoramic radiographs	2252	-	M: 26.5, F: 27.0	M: 27.2, F: 29.5	-	-	-
Kursoglu et al. (2005)	83.6% (M: 79.3%, F: 88.5%)	Turkish	Panoramic radiographs	55 (M: 29, F: 26)	-	-	-	-	-	-
Basekim et al. (2005)	-	Turkish	3D CT	138 (M: 87, F: 51)	2.84 ± 0.76	-	-	-	-	-
Gokce et al. (2008)	7.7%	Turkish	Panoramic radiographs	698	-	-	-	38.7 ± 13.1 (M: 39.1 ± 14.0, F: 37.5 ± 10.7)	-	-



**Table 1 (cont.).** Comparison of the prevalence of elongated styloid process (SP) and mean SP length from previous studies

Article	Prevalence of elongated SP	Population	Measurement method	N	Average length of SP [mm]			Average length of elongated SP [mm]		
					Total	Right	Left	Total	Right	Left
Baicioglu et al. (2009)	3.3%	Turkish	Panoramic radiographs	227 (M: 103, F: 124)	24.11 ± 4.71*	24.09 ± 4.69* (M: 25.78 ± 5.68, F: 22.69 ± 3.68)	24.13 ± 4.72* (M: 25.80 ± 5.75, F: 22.75 ± 3.65)	—	—	—
Sisman et al. (2009)	15.0%	Turkish	Cadavers Dry skulls and isolated temporal bone	22 (M: 19, F: 3) 41	22.54 ± 4.24	—	—	36.06 ± 6.12	—	—
More and Astrani (2010)	19.4%	Indian	Panoramic radiographs	133 (M: 28, F: 105)	—	—	—	33.2 ± 1.9	—	—
Phulambrikar et al. (2011)	24.8% (M: 22.6%, F: 27.0%)	Indian	Panoramic radiographs	500 (M: 242, F: 258)	25.47 ± 6.45*	25.53 ± 6.62 (M: 25.90 ± 6.68, F: 25.17 ± 6.55)	25.41 ± 6.32 (M: 26.18 ± 6.59, F: 24.69 ± 5.97)	—	—	—
Bagga et al. (2012)	52.1%	Indian	Panoramic radiographs	2706	23.2 ± 10.70 (M: 22.6 ± 8.98, F: 23.7 ± 11.08)	—	—	—	—	—
Natsis et al. (2015)	26.7% (R 28.3%, L 25.2%) (elongation: > 33 mm)**	Greek	Skulls	149 (R: 127, L: 135)	26.08*	26.8 ± 10.6	25.4 ± 10.0	43.33*	44.0 ± 8.7	42.7 ± 9.6
Kumar and Kumar (2016)	2.7%	Indian	Skulls	73	—	18.2	16.8	—	—	—
This study	29.5%	Japanese	Cadavers	78 (R: 41, L: 37)	27.04 ± 7.88	25.93 ± 7.29	28.27 ± 8.41	36.30 ± 7.74	35.60 ± 6.88	36.85 ± 8.58

\*Modified; calculated by authors; \*\*Definition of elongation was different in some studies (as indicated in the Table); when not indicated, elongation was defined as > 30 mm; M — male; F — female; R — right side; L — left side; 3D CT — three-dimensional computed tomography

**Table 2.** Comparison of the length and diameter of the styloid process (SP) among three categories (all, < 30 mm, and > 30 mm)

	All			Side			Sex				
	n	Mean ± SD	P	Right		Left		Male		Female	
				n	Mean ± SD	n	Mean ± SD	n	Mean ± SD	n	Mean ± SD
<b>All</b>	78			41	37	27	51				
Length: Full [mm]		27.04 ± 7.88	0.09	25.59 ± 7.29	28.27 ± 8.41	26.81 ± 5.92	27.16 ± 8.79	0.74			
Diameter: Proximal base [mm]		5.41 ± 1.77	0.96	5.41 ± 1.91	5.41 ± 1.63	5.16 ± 1.69	5.55 ± 1.81	0.20			
Diameter: Mid-point [mm]		3.68 ± 1.18	0.53	3.74 ± 1.23	3.61 ± 1.14	3.61 ± 1.27	3.72 ± 1.14	0.66			
Diameter: Distal tip [mm]		2.21 ± 1.22	0.18	2.33 ± 1.27	2.07 ± 1.17	2.35 ± 1.28	2.13 ± 1.20	0.29			
<b>Non-elongated SP (&lt; 30 mm)</b>	55			31	24	15	40				
Length: Full [mm]		23.16 ± 3.49	0.21	22.81 ± 3.92	23.63 ± 2.87	22.27 ± 3.41	23.50 ± 3.51	0.004*			
Diameter: Proximal base [mm]		5.20 ± 1.84	0.34	5.23 ± 1.98	5.18 ± 1.57	4.55 ± 1.58	5.45 ± 1.88	0.60			
Diameter: Mid-point [mm]		3.71 ± 1.23	0.10	3.76 ± 1.24	3.65 ± 1.24	3.43 ± 1.59	3.81 ± 1.07	0.48			
Diameter: Distal tip [mm]		2.25 ± 1.28	0.10	2.31 ± 1.30	2.19 ± 1.29	2.37 ± 1.37	2.21 ± 1.27	0.18			
<b>Elongated SP (≥ 30 mm)</b>	23			10	13	12	11				
Length: Full [mm]		36.04 ± 7.74	0.20	35.60 ± 6.88	36.85 ± 8.58	32.50 ± 2.15	40.45 ± 9.51	0.25			
Diameter: Proximal base [mm]		5.91 ± 1.53	0.98	6.00 ± 1.63	5.85 ± 1.52	5.92 ± 1.56	5.91 ± 1.58	0.017*			
Diameter: Mid-point [mm]		3.61 ± 1.08	0.98	3.70 ± 1.25	3.54 ± 0.97	3.83 ± 0.72	3.36 ± 1.36	0.35			
Diameter: Distal tip [mm]		2.09 ± 1.08	0.77	2.40 ± 1.26	1.85 ± 0.90	2.33 ± 1.23	1.82 ± 0.87	0.51			

\*p < 0.05; SD — standard deviation

11 elongations were found in 51 SPs (22%). In males, 12 elongations were found in 27 SPs (44%). Males had a greater tendency to develop SP elongation, and the female-to-male ratio of SP elongation was 1:2 ( $p = 0.041$ ). Elongation rates were not significantly different between the left and right side ( $p = 0.33$ ). No statistically significant difference in the diameter or length in all cases (left and right) was found (Table 2). Males had a full SP length of  $26.81 \pm 5.92$  mm, while females had a length of  $27.16 \pm 8.79$  mm. Significant differences in full length on the non-elongated SP ( $p = 0.004$ ) and in diameter at the proximal base of the elongated SP ( $p = 0.017$ ) were noted between sexes. The diameter and length were not significantly different between sexes in other cases (Table 2).

## DISCUSSION

The prevalence of SP elongation was 29.5% from the 78 sides in our study. The average SP length was  $27.04 \pm 7.88$  mm ( $27.16 \pm 8.79$  mm in females and  $26.81 \pm 5.92$  mm in males). The average diameter at the proximal base on the elongated SP was  $5.91 \pm 1.53$  mm ( $5.92 \pm 1.56$  mm in males and  $5.91 \pm 1.58$  mm in females); a significant difference was noted between sexes. The female-to-male SP elongation ratio was 1:2. Thus, sex may influence SP elongation.

The prevalence of SP elongation varied from 0.4% to 84.4% in previous studies (Table 1). Rath and Anand (1991) [39] reported that the prevalence of enlarged styloid in their skull study ( $n = 232$ ) was 0.4%, whereas X-ray based studies showed prevalences of 4% [7], 18.2% [6], and 84.4% [10]. In our study, we evaluated 78 SPs and found that 23 SPs measured  $> 30$  mm. The prevalence of SP elongation in our study was 29.5%, consistent with the finding of Keur et al. (1986) [19], i.e. 30.0%. Nara (1958) [30] reported a 3.4% and 5.2% rates, and Nakata et al. (1987) [29] reported 15.5%. However, these studies were performed using X-ray, whereas our study was the first to measure the prevalence in Japanese cadavers.

Balcioglu et al. (2009) [3] showed that the average SP length ranged from 20 and 30 mm; thus, in most studies,  $\geq 30$  mm is considered elongation [3, 6, 15, 19], a value we adopted in this study. The method of dry skulls and panoramic radiographs measurement was conducted in several ways. According to Eagle (1958) [7], only 4% of patients who had elongated SP complained of pain and presented sign and symptoms. The average SP length has been highlighted in

previous studies; however, only few studies focused on the diameter. Anatomically, nerves and blood vessels are located closely around the SP; hence, the diameter of the SP is a factor that could influence clinical symptoms. A small diameter may impinge glossopharyngeal, accessory, and vagus nerves and internal/external carotid arteries, and various symptoms and signs could be attributed to the anatomy and location of these vessels and nerves.

Styloid process thickness is also important. A skull study showed that thickness at the proximal base varied from 4.34 to  $4.4 \pm 1.2$  mm on the right side and from 4.47 to  $4.4 \pm 0.9$  mm on the left side [21, 49]. Margam and Jadhav (2015) [24] demonstrated that at the proximal base males had 4.53-mm thickness on the right and 4.83-mm thickness on left; for females, it was 4.33 mm and 5.00 mm, respectively. Average thickness at the distal tip for both sexes was  $1.5 \pm 0.6$  mm on the right and  $1.4 \pm 0.5$  mm on the left [49]. To the best of our knowledge, our study is the first to examine the diameter of the SP in the Japanese population. We found that thickness at the proximal base was  $5.41 \pm 1.91$  mm on the right and  $5.41 \pm 1.63$  mm on the left, and thickness at the distal tip was  $2.33 \pm 1.27$  mm on the right and  $2.07 \pm 1.17$  mm on the left (Table 2). Regardless of the presence of elongation, SPs tended to narrow distally in most of the cases. Previous studies in the Indian population indicated that increased thickness at the proximal base would compress facial nerves [21, 24]. Therefore, SP thickness is a factor influencing the signs and symptoms. Presenting symptoms depend on the location of the anatomical structure instead of the SP length. Katayama et al. (1989) [17] reported a patient with 71-mm SP on X-ray who showed no symptoms. Nevertheless, it is highly possible that a long and wide SP could compress the carotid artery or nerves. Tsuruta et al. (1985) [48] suggested other possible mechanisms of the symptoms: 1) sympathetic nerves could be stimulated, resulting in dull pain on the area of vascular distribution, 2) glossopharyngeal nerve stimulation results in tinnitus and earache, and 3) a long SP could limit the movement of the hyoid bone, which in turn affects swallowing and speaking. These findings suggest that a combination of length and thickness of the SP and location of the anatomical structure could lead to clinical symptoms and signs.

In our study, the longest SP was found in a female patient who presented bilateral enlarged SPs (47.00 mm on the right and 55.00 mm on the left). The

average length was  $27.16 \pm 8.79$  mm in females and  $26.81 \pm 5.92$  mm in males; no significant difference was observed. In a previous panoramic radiogram-based Japanese study, the average was  $23.1 \pm 7.0$  mm in females and  $22.5 \pm 8.1$  mm in males; no significant difference was noted [47]. Takeuchi et al. (1987) [47] reported no significant difference in the average length between sexes in Japan, similar to our study's finding. Although in the Japanese population, females have a longer average length; no statistical significance was noted. However, Balcioglu et al. (2009) [3] showed that males had a longer average SP length than females in the Turkish population, although no statistical significance was found. In our study, females had 11 and males had 12 elongated SPs, and the female-to-male elongation ratio was 1:2, a significant difference. Swain et al. (2017) [46] showed a 0.75:1 ratio in the Indian population; however, a significant difference was not reported. On the other hand, its rate was reported differently depending on population as the ratio of 3:1 in the Indian population [37] and 9:1 in Turkish population [3]. These findings suggest that the differences in prevalence of elongation and average SP length between sexes vary by race. Sex is a critical factor for the facial dimension differences as females have smaller bigonial breadth, face length, and face width than males [52]. Based on previous studies, females have shorter facial anthropometric dimensions. In our study, males had a significantly higher rate of elongation than females; this suggests that the size of the face is possibly an influencing factor. According to a study on facial morphological characteristics across various races, both sexes in India are known to have smaller nose height and identical intercanthal width, whereas Japanese males have greater intercanthal width [9]. The average distance between the sides of the SP at the distal tip was 64.4 mm in the Indian population [21]. Therefore, not only gender but also race or ethnicity contributes to the incidence of Eagle's syndrome. When comparing average lengths, attention must be paid to the anthropometric measurement, which should be investigated in future research on the SP. Moreover, statistical differences in full length on the non-elongated SP and in diameter at the proximal base on the elongated SP were noted between sexes in this study. Such a difference in morphology between sexes can contribute to the field of forensic medicine. In the future, autopsy cases will need to be increased.

The SP originates from Reichert's cartilage, which is from the second brachial arch. Reichert's cartilage consisted of four segments: tympanohyal, stylohyal, ceratohyal, and hypohyal. The tympanohyal is responsible for the formation of the proximal part and stylohyal for the formation of the distal part of the SP. The ceratohyal is responsible for the formation of the stylohyoid ligament and hypohyal for the formation of the lesser horn of the hyoid bone. The ceratohyal of Reichert's cartilage becomes the stylohyoid ligament; however, ossification occurs due to unknown causes [25]. One case report found that extensive bilateral ossification of stylohyoid complex, which lengthen 65 mm on the right and 62 mm on left [44]. The cause of ossification could be trauma, bone malformation, or abnormal bone metabolism; the exact details remain unknown [11].

Kaufman et al. (1970) [18] showed that in most cases, patients aged  $\geq 40$  years commonly present symptoms. In a Japanese study that considered  $> 20$  mm as elongation, age between 30 and 50 years accounted for 70% of the 55 cases with pharyngolaryngeal paraesthesia, and elongation was considered a factor for pharyngolaryngeal paraesthesia; 43.0% of elongations were found in patients without any symptoms, whereas 74.5% of elongations were found in those with pharyngolaryngeal paraesthesia [17]. To confirm the diagnosis of pharyngolaryngeal paraesthesia, the following three factors must be observed: SP length  $> 30$  mm based on imaging test, clinical symptoms, and Eagle's syndrome symptoms that are aggravated by tonsillar pillar palpation exam [11, 15].

Natsis et al. (2015) [31] claimed that no gold standard for measuring the length of the SP exists; however, recently, panoramic radiograph has been used to confirm elongation [2, 50], as well as three-dimensional computed tomography [20]. Treatment options for enlarged SP include conservative therapy and surgery. Surgery is usually performed after conservative therapy, including steroid injection and non-steroidal anti-inflammatory drugs. Surgical treatment includes extraoral and intraoral approaches. Prior to the SP cut, the fascia and periosteum are dissected to reveal the SP [15, 20, 35]. Thereafter, the styloglossus, stylohyoid, and stylopharyngeus muscles and the SP are removed. The three muscles are removed to prevent the occurrence of dysfunction [51]. Thus, understanding muscle attachments and the anatomical structure surrounding the SP is vital.

### Limitations of the study

This study has four limitations. First, we were unable to access past medical records; therefore, no information on any symptoms and signs related to elongated SP was obtained. Second, the sample size was limited. Third, clinical symptoms and the nerve pathways around SP were not observed in this study. As a nature of the study, this study was not able to assess any clinical presentation during examined people's lifetime. When patients present any symptoms, it is necessary for clinicians to search nerve anatomical location. Fourth, muscle origins and the characteristics of the styloglossus, stylohyoid, stylopharyngeus muscles were not identified in all cases. During dissection, we found that the three muscles and the stylohyoid ligament arose from different locations. The run of the muscle structure is vague. Therefore, determining the muscle attachments is necessary in the surgical treatment for Eagle syndrome. Muscles need to be cut, and understanding the structure is crucial for surgery. Future studies should examine the variations in the origin of the muscles attached to the SP.

### CONCLUSIONS

This study is the first cadaver study measuring the average SP lengths and diameters in the Japanese population. The prevalence of SP elongation was 29.5% in the Japanese population. The average length was 27.04 mm with no difference between sexes among all SPs, but female had significantly longer SPs among the SP < 30 mm. Elongation is twice as common in males (12 out of 27 sides) as in females (11 out of 51 sides) in the Japanese population. Anatomically, the SP gets narrow as distally goes; the average diameter was 5.41 mm at the proximal base and 2.21 mm at the distal tip. Our anatomical findings would be beneficial to creating treatment plans, diagnosis, and surgery.

### Acknowledgements

The authors thank Prof. Tsutomu Sato, Dr. Kaori Suyama, Mr. Noriyuki Kosemura, Ms. Kyoko Endo, and Ms. Yuko Furuya for their excellent secretarial support. We also thank Mr. Taiju Nagai, Mr. Hayata Fukushima, Mr. Kohei Nakanishi, and Mr. Runo Tomita for their assistance in data collection. We would like to thank Editage ([www.editage.jp](http://www.editage.jp)) for the English language editing.

**Conflict of interest:** None declared

### REFERENCES

1. Asutay F, Erdem N, Atalay Y, et al. Prevalence of elongated styloid process and Eagle syndrome in East Egean population. *Bezmialem Sci.* 2019; 7(1): 28–32, doi: [10.14235/bas.galenos.2018.991](https://doi.org/10.14235/bas.galenos.2018.991).
2. Bagga MB, Kumar CA, Yeluri G. Clinoradiologic evaluation of styloid process calcification. *Imaging Sci Dent.* 2012; 42(3): 155–161, doi: [10.5624/isd.2012.42.3.155](https://doi.org/10.5624/isd.2012.42.3.155), indexed in Pubmed: [23071965](https://pubmed.ncbi.nlm.nih.gov/23071965/).
3. Balcioglu HA, Kilic C, Akyol M, et al. Length of the styloid process and anatomical implications for Eagle's syndrome. *Folia Morphol.* 2009; 68(4): 265–270, indexed in Pubmed: [19950078](https://pubmed.ncbi.nlm.nih.gov/19950078/).
4. Başekim CC, Mutlu H, Güngör A, et al. Evaluation of styloid process by three-dimensional computed tomography. *Eur Radiol.* 2005; 15(1): 134–139, doi: [10.1007/s00330-004-2354-9](https://doi.org/10.1007/s00330-004-2354-9), indexed in Pubmed: [15221266](https://pubmed.ncbi.nlm.nih.gov/15221266/).
5. Bozkir MG, Boğa H, Dere F. The evaluation of elongated styloid process in panoramic radiographs in edentulous patients. *Turk J Med Sci.* 1999; 29(4): 481–486.
6. Correll RW, Jensen JL, Taylor JB, et al. Mineralization of the stylohyoid-stylomandibular ligament complex. A radiographic incidence study. *Oral Surg Oral Med Oral Pathol.* 1979; 48(4): 286–291, doi: [10.1016/0030-4220\(79\)90025-2](https://doi.org/10.1016/0030-4220(79)90025-2), indexed in Pubmed: [116179](https://pubmed.ncbi.nlm.nih.gov/116179/).
7. Eagle WW. Elongated Styloid Process: Symptoms and Treatment. *Arch Otolaryngol Head Neck Surg.* 1958; 67(2): 172–176, doi: [10.1001/archotol.1958.00730010178007](https://doi.org/10.1001/archotol.1958.00730010178007).
8. Erol B. Radiological assessment of elongated styloid process and ossified stylohyoid ligament. *J Marmara Univ Dent Fac.* 1996; 2(2-3): 554–556, indexed in Pubmed: [9569816](https://pubmed.ncbi.nlm.nih.gov/9569816/).
9. Farkas LG, Katic MJ, Forrest CR, et al. International anthropometric study of facial morphology in various ethnic groups/races. *J Craniofac Surg.* 2005; 16(4): 615–646, doi: [10.1097/01.scs.0000171847.58031.9e](https://doi.org/10.1097/01.scs.0000171847.58031.9e), indexed in Pubmed: [16077306](https://pubmed.ncbi.nlm.nih.gov/16077306/).
10. Ferrario VF, Sigurtá D, Daddona A, et al. Calcification of the stylohyoid ligament: incidence and morphoquantitative evaluations. *Oral Surg Oral Med Oral Pathol.* 1990; 69(4): 524–529, doi: [10.1016/0030-4220\(90\)90390-e](https://doi.org/10.1016/0030-4220(90)90390-e), indexed in Pubmed: [2326043](https://pubmed.ncbi.nlm.nih.gov/2326043/).
11. Fusco DJ, Asteraki S, Spetzler RF. Eagle's syndrome: embryology, anatomy, and clinical management. *Acta Neurochir (Wien).* 2012; 154(7): 1119–1126, doi: [10.1007/s00701-012-1385-2](https://doi.org/10.1007/s00701-012-1385-2), indexed in Pubmed: [22638594](https://pubmed.ncbi.nlm.nih.gov/22638594/).
12. Gokce C, Sisman Y, Ertas ET, et al. Prevalence of styloid process elongation on panoramic radiography in the Turkey population from cappadocia region. *Eur J Dent.* 2008; 2(1): 18–22, indexed in Pubmed: [19212504](https://pubmed.ncbi.nlm.nih.gov/19212504/).
13. Gossman JR, Tarsitano JJ. The styloid-stylohyoid syndrome. *J Oral Surg.* 1977; 35(7): 555–560, indexed in Pubmed: [406372](https://pubmed.ncbi.nlm.nih.gov/406372/).
14. Gözül R, Yener N, Calgüner E, et al. Morphological characteristics of styloid process evaluated by computerized axial tomography. *Ann Anat.* 2001; 183(6): 527–535, doi: [10.1016/S0940-9602\(01\)80060-1](https://doi.org/10.1016/S0940-9602(01)80060-1), indexed in Pubmed: [11766524](https://pubmed.ncbi.nlm.nih.gov/11766524/).
15. Hosokawa K, Shigematsu H, Oku Y, et al. Extraoral surgical treatment for styloid process syndrome: a case report. *Jpn J Oral Maxillofac Surg.* 2011; 57(5): 299–303, doi: [10.5794/jjoms.57.299](https://doi.org/10.5794/jjoms.57.299).
16. Ilgüy M, Ilgüy D, Güler N, et al. Incidence of the type and calcification patterns in patients with elongated styloid process. *J Int Med Res.* 2005; 33(1): 96–102, doi: [10.1177/147323000503300110](https://doi.org/10.1177/147323000503300110), indexed in Pubmed: [15651721](https://pubmed.ncbi.nlm.nih.gov/15651721/).
17. Katayama N, Egawa K, Kashiwagi H, et al. The elongated styloid process. *Oto-Rhino-Laryngology.* 1989; 32(1): 51–58.

18. Kaufman SM, Elzay RP, Irish EF. Styloid process variation. Radiologic and clinical study. *Arch Otolaryngol*. 1970; 91(5): 460–463, doi: [10.1001/archotol.1970.00770040654013](https://doi.org/10.1001/archotol.1970.00770040654013), indexed in Pubmed: [5442737](https://pubmed.ncbi.nlm.nih.gov/5442737/).
19. Keur JJ, Campbell JP, McCarthy JF, et al. The clinical significance of the elongated styloid process. *Oral Surg Oral Med Oral Pathol*. 1986; 61(4): 399–404, doi: [10.1016/0030-4220\(86\)90426-3](https://doi.org/10.1016/0030-4220(86)90426-3), indexed in Pubmed: [3458151](https://pubmed.ncbi.nlm.nih.gov/3458151/).
20. Kitoh R, Takumi Y, Usami S. One case with a giant elongated styloid process surgically resected using the trans-cervical approach. *Stomato-Pharyngology*. 2013; 26(1): 105–109.
21. Kumar SS, Kumar TS, et al. Morphometric study of styloid process of the temporal bone and its clinical importance. *Int J Anat Res*. 2016; 4(1): 2134–2138, doi: [10.16965/ijar.2016.163](https://doi.org/10.16965/ijar.2016.163).
22. Kursoglu P, Unalan F, Erdem T. Radiological evaluation of the styloid process in young adults resident in Turkey's Yeditepe University faculty of dentistry. *Oral Surg Oral Med Oral Pathol Oral Radiol Endod*. 2005; 100(4): 491–494, doi: [10.1016/j.tripleo.2005.05.061](https://doi.org/10.1016/j.tripleo.2005.05.061), indexed in Pubmed: [16182171](https://pubmed.ncbi.nlm.nih.gov/16182171/).
23. Langlais R, Miles D, Van Dis ML. Elongated and mineralized stylohyoid ligament complex: a proposed classification and report of a case of Eagle's syndrome. *Oral Surgery, Oral Medicine, Oral Pathology*. 1986; 61(5): 527–532, doi: [10.1016/0030-4220\(86\)90400-7](https://doi.org/10.1016/0030-4220(86)90400-7).
24. Margam S, Jadhav S. Morphometric study of styloid process of temporal bone in Indian adult dry skull. *Int J Res Med Sci*. 2015: 1348–1352, doi: [10.18203/2320-6012.ijrms20150145](https://doi.org/10.18203/2320-6012.ijrms20150145).
25. Moffat DA, Ramsden RT, Shaw HJ. The styloid process syndrome: aetiological factors and surgical management. *J Laryngol Otol*. 1977; 91(4): 279–294, doi: [10.1017/s0022215100083699](https://doi.org/10.1017/s0022215100083699), indexed in Pubmed: [856922](https://pubmed.ncbi.nlm.nih.gov/856922/).
26. Monsour PA, Young WG. Variability of the styloid process and stylohyoid ligament in panoramic radiographs. *Oral Surg Oral Med Oral Pathol*. 1986; 61(5): 522–526, doi: [10.1016/0030-4220\(86\)90399-3](https://doi.org/10.1016/0030-4220(86)90399-3), indexed in Pubmed: [3086788](https://pubmed.ncbi.nlm.nih.gov/3086788/).
27. More CB, Asrani MK. Evaluation of the styloid process on digital panoramic radiographs. *Indian J Radiol Imaging*. 2010; 20(4): 261–265, doi: [10.4103/0971-3026.73537](https://doi.org/10.4103/0971-3026.73537), indexed in Pubmed: [21423900](https://pubmed.ncbi.nlm.nih.gov/21423900/).
28. Murtagh RD, Caracciolo T, Fernandez GCT. Findings associated with Eagle syndrome. *AJNR Am J Neuroradiol*. 2001; 22(7): 1401–1412.
29. Nakata M, Nishio J, Watatani K, et al. A radiographic analysis of styloid process. *Jpn J Oral Maxillofac Surg*. 1987; 33(11): 2224–2229, doi: [10.5794/jjoms.33.2224](https://doi.org/10.5794/jjoms.33.2224).
30. Nara S. Clinical and roentgenological study of abnormal styloid process. *J Otolaryngol Jpn*. 1958; 61(8): 1295–1301, doi: [10.3950/jibiinkoka.61.1295](https://doi.org/10.3950/jibiinkoka.61.1295).
31. Natsis K, Repousi E, Nouisios G, et al. The styloid process in a Greek population: an anatomical study with clinical implications. *Anat Sci Int*. 2015; 90(2): 67–74, doi: [10.1007/s12565-014-0232-3](https://doi.org/10.1007/s12565-014-0232-3), indexed in Pubmed: [24664363](https://pubmed.ncbi.nlm.nih.gov/24664363/).
32. Nedunchezian K. Eagle syndrome: an overview. *S Afr J Rad*. 2017; 21(1), doi: [10.4102/sajr.v21i1.1247](https://doi.org/10.4102/sajr.v21i1.1247).
33. O'Carroll MK. Calcification in the stylohyoid ligament. *Oral Surg Oral Med Oral Pathol*. 1984; 58(5): 617–621, doi: [10.1016/0030-4220\(84\)90089-6](https://doi.org/10.1016/0030-4220(84)90089-6).
34. Phulambrikar T, Rajeshwari A, Rao B, et al. Incidence of elongated styloid process: a radiographic study. *J Indian Acad Oral Med Radiol*. 2011; 23: S344–S346, doi: [10.5005/jp-journals-10011-1165](https://doi.org/10.5005/jp-journals-10011-1165).
35. Piagkou M, Anagnostopoulou S, Kouladouros K, et al. Eagle's syndrome: a review of the literature. *Clin Anat*. 2009; 22(5): 545–558, doi: [10.1002/ca.20804](https://doi.org/10.1002/ca.20804), indexed in Pubmed: [19418452](https://pubmed.ncbi.nlm.nih.gov/19418452/).
36. Prabhu LV, Nayak SR, Pai MM, et al. An unusually lengthy styloid process. *Singapore Med J*. 2007; 48(2): e34–e36, indexed in Pubmed: [17304374](https://pubmed.ncbi.nlm.nih.gov/17304374/).
37. Prasad KC, Kamath MP, Reddy KJ, et al. Elongated styloid process (Eagle's syndrome): a clinical study. *J Oral Maxillofac Surg*. 2002; 60(2): 171–175, doi: [10.1053/joms.2002.29814](https://doi.org/10.1053/joms.2002.29814), indexed in Pubmed: [11815916](https://pubmed.ncbi.nlm.nih.gov/11815916/).
38. Pushpalatha K, Bhat D. Bilaterally elongated styloid process: a case report. *Int J Sci Stud*. 2014; 2(4): 100–102.
39. Rath G, Anand C. Abnormal styloid process in a human skull. *Surg Radiol Anat*. 1991; 13(3): 227–229, doi: [10.1007/BF01627991](https://doi.org/10.1007/BF01627991), indexed in Pubmed: [1754958](https://pubmed.ncbi.nlm.nih.gov/1754958/).
40. Rizzatti-Barbosa CM, Ribeiro MC, Silva-Concilio LR, et al. Is an elongated stylohyoid process prevalent in the elderly? A radiographic study in a Brazilian population. *Gerodontology*. 2005; 22(2): 112–115, doi: [10.1111/j.1741-2358.2005.00046.x](https://doi.org/10.1111/j.1741-2358.2005.00046.x), indexed in Pubmed: [15934355](https://pubmed.ncbi.nlm.nih.gov/15934355/).
41. Rogers K, Chang H. Eagle's syndrome: a case report. *Columbia Dent Rev*. 2007; 11: 12–14.
42. Russell TE. Eagle's syndrome: diagnostic considerations and report of case. *J Am Dent Assoc*. 1977; 94(3): 548–550, doi: [10.14219/jada.archive.1977.0003](https://doi.org/10.14219/jada.archive.1977.0003), indexed in Pubmed: [264925](https://pubmed.ncbi.nlm.nih.gov/264925/).
43. Sisman Y, Gokce C, Ertas ET, et al. Investigation of elongated styloid process prevalence in patients with torus palatinus. *Clinical Oral Investigations*. 2008; 13(3): 269–272, doi: [10.1007/s00784-008-0232-6](https://doi.org/10.1007/s00784-008-0232-6).
44. Skrzat J, Mróz I, Walocha J, et al. Bilateral ossification of the stylohyoid ligament. *Folia Morphol*. 2007; 66(3): 203–206, indexed in Pubmed: [17985321](https://pubmed.ncbi.nlm.nih.gov/17985321/).
45. Strauss M, Zohar Y, Laurian N. Elongated styloid process syndrome: intraoral versus external approach for styloid surgery. *Laryngoscope*. 1985; 95(8): 976–979, indexed in Pubmed: [4021692](https://pubmed.ncbi.nlm.nih.gov/4021692/).
46. Swain S, Jena A, Sahu M, et al. Eagle's syndrome: our experiences in a tertiary care teaching hospital of eastern India. *J Head Neck Physicians Surg*. 2017; 5(2): 66, doi: [10.4103/jhnps.jhnps\\_29\\_17](https://doi.org/10.4103/jhnps.jhnps_29_17).
47. Takeuchi S, Kishimoto S, Miyashita H. The length of the styloid process on the oral panoramic radiograms. Its relationship to the abnormal sensation in the throat. *Practica Oto-Rhino-Laryngologica*. 1987; 80(1): 133–138, doi: [10.5631/jibirin.80.133](https://doi.org/10.5631/jibirin.80.133).
48. Tsuruta Y, Sato T, Miyahara H, et al. Four cases of elongated styloid process: Patients with abnormal feeling in the throat. *Practica Oto-Rhino-Laryngologica*. 1985; 78(12): 2783–2791, doi: [10.5631/jibirin.78.2783](https://doi.org/10.5631/jibirin.78.2783).
49. Vadgaonkar R, Murlimanju BV, Prabhu LV, et al. Morphological study of styloid process of the temporal bone and its clinical implications. *Anat Cell Biol*. 2015; 48(3): 195–200, doi: [10.5115/acb.2015.48.3.195](https://doi.org/10.5115/acb.2015.48.3.195), indexed in Pubmed: [26417479](https://pubmed.ncbi.nlm.nih.gov/26417479/).
50. Vieira EM, Guedes OA, Morais SD, et al. Prevalence of elongated styloid process in a Central Brazilian population. *J Clin Diagn Res*. 2015; 9(9): ZC90–ZC92, doi: [10.7860/JCDR/2015/14599.6567](https://doi.org/10.7860/JCDR/2015/14599.6567), indexed in Pubmed: [26501021](https://pubmed.ncbi.nlm.nih.gov/26501021/).
51. Yoshihama K, Mikoshiba T, Takei S. Transcervical operative approach of elongated styloid process. *J Jpn Soc Head Neck Surg*. 2016; 25(3): 385–388, doi: [10.5106/jjshns.25.385](https://doi.org/10.5106/jjshns.25.385).
52. Zhuang Z, Landsittel D, Benson S, et al. Facial anthropometric differences among gender, ethnicity, and age groups. *Ann Occup Hyg*. 2010; 54(4): 391–402, doi: [10.1093/annhyg/meq007](https://doi.org/10.1093/annhyg/meq007), indexed in Pubmed: [20219836](https://pubmed.ncbi.nlm.nih.gov/20219836/).

# Correlation of morphological and radiological characteristics of degenerative disc disease in lumbar spine: a cadaveric study

P.A. Pękala<sup>1, 2, 3\*</sup>, D. Tattera<sup>1, 2\*</sup>, K. Krupa<sup>1, 2</sup>, M. Paziowski<sup>1, 2</sup>, W. Wojciechowski<sup>4</sup>, T. Konopka<sup>5</sup>, J.A. Walocha<sup>1, 2</sup>, K.A. Tomaszewski<sup>1, 3, 6</sup>

<sup>1</sup>International Evidence-Based Anatomy Working Group, Krakow, Poland

<sup>2</sup>Department of Anatomy, Jagiellonian University Medical College, Krakow, Poland

<sup>3</sup>Faculty of Medicine and Health Sciences, Andrzej Frycz Modrzewski Krakow University, Krakow, Poland

<sup>4</sup>Department of Radiology, Jagiellonian University Medical College, Krakow, Poland

<sup>5</sup>Department of Forensic Medicine, Jagiellonian University Medical College, Krakow, Poland

<sup>6</sup>Scanmed St. Raphael Hospital, Krakow, Poland

[Received: 12 January 2021; Accepted: 15 March 2021; Early publication date: 13 April 2021]

**Background:** Intervertebral disc (IVD) degeneration plays a crucial role in the pathophysiology of low back pain. Several grading systems have been developed for both morphological and radiological assessment. The aim of this study was to assess the morphological and radiological characteristics of IVD degeneration and validate popular radiological Pfirrmann scale against morphological Thompson grading system.

**Materials and methods:** Full spinal columns (vertebrae L1–S1 and IVD between them) were harvested from cadavers through an anterior dissection. Magnetic resonance imaging scans of all samples were conducted. Then, all vertebral columns were cut in the midsagittal plane and assessed morphologically.

**Results:** A total of 100 lumbar spine columns (446 IVDs) were included in the analysis of the degeneration grade. Morphologic Thompson scale graded the majority of discs as grade 2 and 3 (44.2% and 32.1%, respectively), followed by grade 4 (16.8%), grade 1 (5.8%) and grade 5 (1.1%). The radiologic Pfirrmann grading system classified 44.2% of discs as grade 2, 32.1% as grade 3, 16.8% as grade 4, 5.8% as grade 1, and 1.1% as grade 5. The analysis on the effect of age on degeneration revealed significant, although moderate, positive correlation with both scales. Analysis of the agreement between scales showed weighted Cohen's kappa equal to 0.61 ( $p < 0.001$ ). Most of the disagreement occurred due to a 1 grade difference (91.5%), whereas only 8.5% due to a 2 grade difference.

**Conclusions:** With the increase of the prevalence of IVD disease in the population, reliable grading systems of IVD degeneration are crucial for spine surgeons in their clinical assessment. While overall there is agreement between both grading systems, clinicians should remain careful when using Pfirrmann scale as the grades tend to deviate from the morphological assessment. (Folia Morphol 2022; 81, 2: 503–509)

**Key words:** low back pain, discopathy, Thompson scale, Pfirrmann scale

Address for correspondence: P.A. Pękala, MD, PhD, Department of Anatomy, Jagiellonian University Medical College, ul. Kopernika 12, 31–034 Kraków, Poland, tel/fax: +48 12 422 95 11, e-mail: pekala.pa@gmail.com

\*Equal contributors

This article is available in open access under Creative Common Attribution-Non-Commercial-No Derivatives 4.0 International (CC BY-NC-ND 4.0) license, allowing to download articles and share them with others as long as they credit the authors and the publisher, but without permission to change them in any way or use them commercially.

## INTRODUCTION

Lower back pain (LBP) remains a leading cause of disability and morbidity in today's society. Even up to 70% of the population experiences LBP throughout their lives [5]. With an estimated societal cost of LBP at 85 billion dollars annually, only in the United States in 2008, and expected several-fold increase in the next decades, it constitutes an enormous burden to the healthcare system [7].

The aetiology of LBP is multifactorial with both genetic and environmental factors contributing to its development. Intervertebral disc (IVD) degeneration is considered to be a crucial component in the aetiology of this condition. The IVD is formed by gelatinous, centrally located nucleus pulposus (NP), which is surrounded by annulus fibrosus (AF). Morphologically, the NP consists of collagen II fibres and elastin randomly arranged in highly hydrated, aggregate-based gel, which also contains low concentration of chondrocyte-like cells [15]. The AF can be divided into an inner AF, which can be viewed as a transition zone and the outer AF, which in turn is formed by distinct, highly organized lamellae consisting of collagen I fibres, intertwined with elastin, lubricin and collagen VI fibres [15]. Moreover, the IVD is bound caudally and rostrally by IVD endplates, which separate intervertebral bodies from the IVD. The highly hydrated NP, which is constrained both by the AF and the endplates, distributes mechanical loads evenly, dissipates energy and allows for the movement of the vertebral column [15]. Deterioration in the function of IVD is associated with the changes in the content of extracellular matrix of the NP, which occur with age and degeneration [10]. These include loss of water content, degradation of proteoglycans and collagen as well as upregulation of inflammatory cytokines [10]. The deterioration of the NP leads to irreversible structural changes of the IVD and its surrounding. A common macroscopic characteristic of degeneration is the presence of clefts and tears within the IVD and the loss of demarcation between the NP and the AF [11]. As such, the IVD loses its mechanical bearing properties [17] with a transfer of pressure exertion point from NP to AF [1]. This can result in NP bulging, herniation, compression syndrome and effectively low back pain.

There are several grading systems used to assess the degree of degeneration based on the modality used. A grading system to assess morphologic changes due to IVD degeneration was proposed by Thomp-

son et al. [14] in 1990. Moreover, the magnetic resonance imaging (MRI) has been widely used to study and assess IVD degeneration. The signal intensity loss in T2-weighted images correlates with the degree of degeneration [4]. Pfirrmann et al. [9] classification is a popular grading system for the degenerative changes of the lumbar spine observed in MRI. It is broadly used to study lumbar degeneration, but has also been adopted by neurosurgeons and orthopaedic surgeons in the perioperative setting. It has been validated in multiple studies [12, 16]; however, the assessment of the correlation between macroscopic Thompson's and radiologic Pfirrmann's grading systems has not been studied comprehensively.

Therefore, the aim of this study was to compare the macroscopic appearance of the lumbar spine specimens with their MRI appearance and check the reliability of the popular Pfirrmann classification of the degenerative changes in the lumbar spine.

## MATERIALS AND METHODS

### Specimen collection

The study protocol was approved by our institutional Bioethics Committee. Moreover, study strictly adhered to ethical principles for medical research involving human subjects set by the Declaration of Helsinki.

Full spinal columns (vertebrae L1–S1 and IVD between them) were harvested from fresh cadavers through an anterior dissection. Inclusion criteria were as follows: 1) age 18–80, 2) possibility to dissect specific lumbar column. Any donors that were deceased due to trauma or had a visible spinal trauma, spinal surgery, spinal tumours, ankylosing spondylitis were excluded from this study.

Intervertebral discs that became damaged during dissection or had artefacts in MRI scans that did not allow for full and reliable assessment were excluded from further analyses.

### Magnetic resonance imaging

Magnetic resonance imaging scans of the harvested spinal columns were conducted with the use of Philips Achieva 3.0T TX apparatus. Two independent reviewers assessed the IVD degeneration according to Pfirrmann et al. [9] scale. In summary, Pfirrmann grading system assesses changes in T2 spin-echo weighted images on a scale from 1 to 5, with grade 1 describing healthy disc (homogeneous with bright hyperintense white signal intensity and normal disc

height), while grade 5 describing heavily degenerated disc (disc space is collapsed, inhomogeneous with a hypointense black signal intensity) (Fig. 1) [9].

Moreover, the MRI scans were assessed for Modic type endplate changes [8]. Type 1 changes were defined as decreased signal intensity on T1-weighted images and increased signal intensity on T2-weighted images. Type 2 changes were defined as increased signal intensity on T1-weighted images and isointense or slightly increased signal intensity on T2-weighted images [8]. Modic type III changes showed decreased signal intensity on both T1- and T2-weighted images. Any radiologic findings, such as Schmorl's nodes, disc bulging or herniation were also noted.

### Morphologic assessment

All vertebral columns were cut in the midsagittal plane. High resolution images of each column were taken and used for later assessment. The IVD degeneration was graded on a scale from 1 to 5 based on criteria developed by Thompson et al. [14] by two independent reviewers. In summary, each grade is determined through assessing specific morphologic changes of nucleus pulposus, annulus fibrosus, IVD end-plates and adjacent vertebral bodies with grade 1 being healthy IVD, while grade 5 being heavily degenerated disc (Fig. 1) [14].

Moreover, any macroscopic alterations in the structure of lumbar columns were noted and included the following: osteophytes, Schmorl's nodes, IVD clefts, tears, bulging and herniation.

### Statistical analysis

All statistical analyses were conducted using STATISTICA (v.13.3) and PQStat (v.1.8.0). Frequency distribution, mean and standard deviation were used to characterise study group and degeneration grades. Spearman's rank correlation coefficient statistic was conducted to assess the relation between the age and degeneration. Moreover, in order to determine agreement between specific Pfirrmann and Thompson grades, weighted Cohen's kappa coefficient was utilised. This statistic assigns weights to disagreement values, with the higher the degree of disagreement the higher the weight. A kappa value of 1 indicates perfect agreement, while value of 0 indicates agreement equivalent to chance. A p-value of  $< 0.05$  determines statistically significant agreement between the two scores. Subgroup analysis on the agreement

between degeneration grades for specific IVD levels was also conducted.

## RESULTS

### Study group

One hundred lumbar spine columns (L1–S1) were harvested from male cadavers. Mean age of the donor was  $42.2 \pm 12.3$  years. There were 54 IVDs which visualisation did not allow for full and reliable assessment, therefore authors decided to exclude them from the analysis.

### Degeneration assessment

A total of 446 IVDs were included in the analysis of the degeneration grade. Radiologic assessment using the Pfirrmann grading system classified 44.2% of discs as grade 2, 32.1% as grade 3, 16.8% as grade 4, 5.8% as grade 1 and 1.1% as grade 5. Morphologic Thompson scale graded the majority of discs as grade 2 and 3 (44.2% and 32.1%, respectively), followed by grade 4 (16.8%), grade 1 (5.8%) and grade 5 (1.1%).

There were 42 discs (9.4% of all discs) that showed Modic type endplate changes, with 8.7% of all discs grades as Modic type 2 and 0.7% as Modic type 1.

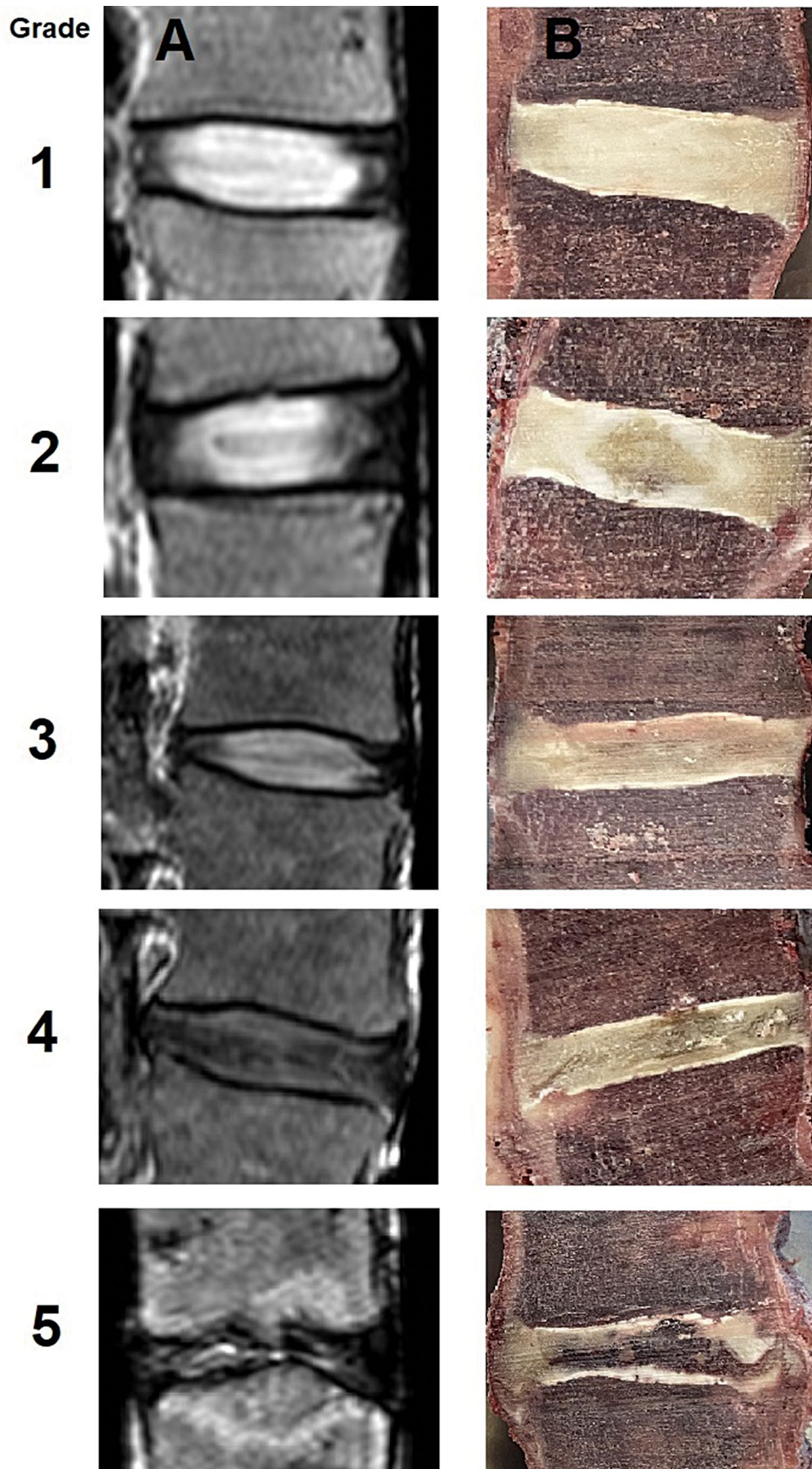
The analysis on the effect of age on degeneration revealed significant, although moderate, positive correlation with both Thompson ( $\rho = 0.38$ ,  $p < 0.001$ ) and Pfirrmann ( $\rho = 0.36$ ,  $p < 0.001$ ) average grade.

Table 1 summarises subgroup analyses of the Thompson and Pfirrmann grades based on the spinal level.

### Inter-grading system agreement

A total of 446 pairs of Thompson and Pfirrmann grades for specific IVDs were compared. Analysis showed weighted Cohen's kappa equal to 0.61 ( $p < 0.001$ ), which suggests significant and substantial agreement between the two grading systems. The highest percentage agreement was achieved for grade 2 (67.2% of discs). All other grades showed an agreement in less than half of the cases. The highest percentage disagreement was observed for Thompson grade 1 with 70.0% of discs graded as Pfirrmann grade 2. Most of the disagreement occurred due to a 1 grade difference (91.5%), whereas only 8.5% due to a 2 grade difference.

In summary, Pfirrmann scale tended to under-score degeneration when compared to Thompson grades. Majority of Thompson grades 5 were scored as Pfirrmann grades 4–5 (83.3%). Thompson grades 4



**Figure 1.** Representative micrographs of radiologic Pfirrmann (A) and morphologic Thompson (B) grading scores.

**Table 1.** Subgroup analyses of the Thompson and Pfirrmann grades based on the spinal level

Intervertebral disc level	Thompson grades	Pfirrmann grades
L1/L2	Grade 1 — 7%	Grade 1 — 4%
	Grade 2 — 39%	Grade 2 — 63%
	Grade 3 — 50%	Grade 3 — 24%
	Grade 4 — 4%	Grade 4 — 9%
	Grade 5 — 0%	Grade 5 — 0%
L2/L3	Grade 1 — 7%	Grade 1 — 3%
	Grade 2 — 32%	Grade 2 — 59%
	Grade 3 — 50%	Grade 3 — 31%
	Grade 4 — 10%	Grade 4 — 7%
	Grade 5 — 1%	Grade 5 — 0%
L3/L4	Grade 1 — 5%	Grade 1 — 3%
	Grade 2 — 25%	Grade 2 — 57%
	Grade 3 — 45%	Grade 3 — 23%
	Grade 4 — 21%	Grade 4 — 16%
	Grade 5 — 4%	Grade 5 — 1%
L4/L5	Grade 1 — 9%	Grade 1 — 5%
	Grade 2 — 21%	Grade 2 — 31%
	Grade 3 — 37%	Grade 3 — 43%
	Grade 4 — 27%	Grade 4 — 21%
	Grade 5 — 6%	Grade 5 — 0%
L5/S1	Grade 1 — 6%	Grade 1 — 13%
	Grade 2 — 23%	Grade 2 — 22%
	Grade 3 — 36%	Grade 3 — 34%
	Grade 4 — 22%	Grade 4 — 27%
	Grade 5 — 13%	Grade 5 — 4%

were scored as Pfirrmann grades 3–4 in 86.6% of cases, Thompson grades 3 as Pfirrmann grades 2–3 in 87.9% of cases, Thompson grades 2 as Pfirrmann grades 1–2 in 79.8% of cases.

A subgroup analysis based on the spinal level revealed weighted Cohen's kappa ranging from 0.40 to 0.70, with the highest value for L5/S1 discs (Table 2).

Percentage agreement ranged from 41% to 56%, however majority of disagreement occurred due to a one grade difference.

## DISCUSSION

The IVD degeneration is commonly classified using the Pfirrmann grading system when assessed with MRI. There is a scarcity of studies [3] correlating morphological appearance of degeneration with MRI appearance in cadaveric samples. The reliability of the popular Pfirrmann scale has not been comprehensively validated on a large sample using 3 T MRI against the morphological Thompson scale so far. Therefore, the aim of our study was to assess morphological and radiological characteristics of the IVD degeneration and assess the correlation between the Pfirrmann and the Thompson grading systems.

The results of this study showed that overall there is a significant and substantial agreement between morphological and radiological degeneration scales. However, when analysed by IVD levels considerable variability was observed in terms of kappa coefficients, with values as low as 0.4. Moreover, there was more disagreement in lower grades of degeneration as compared to higher grades, which tended to show more agreement. This suggests better reflection of the stage of degenerative disc disease and as such the clinical applicability of Pfirrmann scale for patients with more degenerated discs. While in vast majority the disagreement between the scales occurred due to a one grade difference, the fact that Pfirrmann scale underscores majority of grades when compared to morphological scale warrants its thoughtful use in a clinical setting. Clinicians should remain careful when following up the patients and relying solely on the descriptions of the MRI exams in the assessment of the progression from lower to higher grades. In such cases, MRI scans should always be evaluated.

The original Pfirrmann grading system was applied to 1 T MRI [9] and further analysed with 1.5 T MRI

**Table 2.** Agreement assessment between morphologic Thompson and radiologic Pfirrmann grading systems for degenerative disc disease based on intervertebral disc level

Intervertebral disc level	Weighted Cohen's kappa coefficient	P value	Percentage agreement
L1/L2	0.40	< 0.05	48.0%
L2/L3	0.53	< 0.001	56.0%
L3/L4	0.54	< 0.001	41.0%
L4/L5	0.59	< 0.001	44.0%
L5/S1	0.70	< 0.001	48.0%

[6, 16] as well as with 3 T and high-resolution 9.4 T MRI in a pre-clinical research [12]. Our study incorporated 3 T MRI, which allowed for detailed visualisation of spinal columns. Previous studies have repeatedly shown that T2-signal intensity loss, as one of the few radiological characteristics, is associated with morphologically observed degeneration in cadaveric samples [3, 13]. Moreover, T2-signal intensity correlates strongly with water and proteoglycan content of the disc [2, 18], thus its loss should represent the chemical changes that occur within the disc during the degeneration. The T2-signal intensity loss is the main criterion employed in the Pfirrmann scale. Similarly to previous research, the results of this study showed indirectly that the T2-signal intensity loss reflects the process of degeneration, especially for patients with late stages of IVD degeneration.

The use of Thompson grading system in the assessment of the morphology of IVD degeneration has an inherent limitation. The use of only one sagittal section allows only for a limited evaluation of the IVD and might not represent full degree of degeneration throughout the whole IVD. Nonetheless, the midsagittal section provides visualisation of all tissues of the disc structure (NP, AF, endplates, adjacent vertebral bodies) as well as degenerative changes that occur both in coronal and horizontal planes and as such is the most likely to establish the most authentic grade of the degeneration [14]. Moreover, this plane was utilised in the assessment of degeneration using Pfirrmann scale and thus allowed us to directly compare the two grading systems.

The limitation of this study was the use of only male specimens. However, along with the large sample size, this study provides a focused and more representative image of IVD disease for this sex. Further studies should be performed with female patients in order to evaluate any possible sexual dimorphism.

Moreover, the MRI has been performed post-mortem, with absent normal metabolism of tissues. However, only such methodology allows to compare MRI data with full direct macroscopic assessment, and therefore provide reliable and comparable view.

## CONCLUSIONS

With the aging population and with the increase of the prevalence of IVD disease, reliable grading systems of IVD degeneration are crucial for spine surgeons in their clinical assessment. The results of

this study showed that overall there was a significant and substantial agreement between radiological Pfirrmann and morphological Thompson grading systems. Nonetheless, clinicians should remain careful when using Pfirrmann scale as the grades tend to deviate from the morphological assessment. Thus, the knowledge of the proper assessment of MRI scans is crucial for spine surgeons.

## Acknowledgements

This research was supported by governmental funds for research in 2016–2019 (Polish Ministry of Science and Higher Education, Diamond Grant, 0182/DIA/2016/45). We would like to acknowledge all the donors and their families, whose contribution allowed us to conduct this research.

**Conflict of interest:** None declared

## REFERENCES

1. Adams MA, McNally DS, Dolan P. 'Stress' distributions inside intervertebral discs. The effects of age and degeneration. *J Bone Joint Surg Br.* 1996; 78(6): 965–972, doi: [10.1302/0301-620x78b6.1287](https://doi.org/10.1302/0301-620x78b6.1287), indexed in Pubmed: [8951017](https://pubmed.ncbi.nlm.nih.gov/8951017/).
2. Antoniou J, Steffen T, Nelson F, et al. The human lumbar intervertebral disc: evidence for changes in the biosynthesis and denaturation of the extracellular matrix with growth, maturation, ageing, and degeneration. *J Clin Invest.* 1996; 98(4): 996–1003, doi: [10.1172/JCI118884](https://doi.org/10.1172/JCI118884), indexed in Pubmed: [8770872](https://pubmed.ncbi.nlm.nih.gov/8770872/).
3. Benneker LM, Heini PF, Anderson SE, et al. Correlation of radiographic and MRI parameters to morphological and biochemical assessment of intervertebral disc degeneration. *Eur Spine J.* 2005; 14(1): 27–35, doi: [10.1007/s00586-004-0759-4](https://doi.org/10.1007/s00586-004-0759-4), indexed in Pubmed: [15723249](https://pubmed.ncbi.nlm.nih.gov/15723249/).
4. Brinjikji W, Diehn FE, Jarvik JG, et al. MRI findings of disc degeneration are more prevalent in adults with low back pain than in asymptomatic controls: a systematic review and meta-analysis. *AJNR Am J Neuroradiol.* 2015; 36(12): 2394–2399, doi: [10.3174/ajnr.A4498](https://doi.org/10.3174/ajnr.A4498), indexed in Pubmed: [26359154](https://pubmed.ncbi.nlm.nih.gov/26359154/).
5. GBD 2016 Disease and Injury Incidence and Prevalence Collaborators. Global, regional, and national incidence, prevalence, and years lived with disability for 328 diseases and injuries for 195 countries, 1990–2016: a systematic analysis for the Global Burden of Disease Study 2016. *Lancet.* 2017; 390(10100): 1211–1259, doi: [10.1016/S0140-6736\(17\)32154-2](https://doi.org/10.1016/S0140-6736(17)32154-2), indexed in Pubmed: [28919117](https://pubmed.ncbi.nlm.nih.gov/28919117/).
6. Griffith JF, Wang YXJ, Antonio GE, et al. Modified Pfirrmann grading system for lumbar intervertebral disc degeneration. *Spine (Phila Pa 1976).* 2007; 32(24): E708–E712, doi: [10.1097/BRS.0b013e31815a59a0](https://doi.org/10.1097/BRS.0b013e31815a59a0), indexed in Pubmed: [18007231](https://pubmed.ncbi.nlm.nih.gov/18007231/).
7. Martin BI, Gerkovich MM, Deyo RA, et al. Expenditures and health status among adults with back and neck problems. *JAMA.* 2008; 299(6): 656–664, doi: [10.1001/jama.299.6.656](https://doi.org/10.1001/jama.299.6.656), indexed in Pubmed: [18270354](https://pubmed.ncbi.nlm.nih.gov/18270354/).

8. Modic MT, Steinberg PM, Ross JS, et al. Degenerative disk disease: assessment of changes in vertebral body marrow with MR imaging. *Radiology*. 1988; 166(1 Pt 1): 193–199, doi: [10.1148/radiology.166.1.3336678](https://doi.org/10.1148/radiology.166.1.3336678), indexed in Pubmed: [3336678](https://pubmed.ncbi.nlm.nih.gov/3336678/).
9. Pfirrmann CW, Metzdorf A, Zanetti M, et al. Magnetic resonance classification of lumbar intervertebral disc degeneration. *Spine (Phila Pa 1976)*. 2001; 26(17): 1873–1878, doi: [10.1097/00007632-200109010-00011](https://doi.org/10.1097/00007632-200109010-00011), indexed in Pubmed: [11568697](https://pubmed.ncbi.nlm.nih.gov/11568697/).
10. Risbud MV, Shapiro IM. Role of cytokines in intervertebral disc degeneration: pain and disc content. *Nat Rev Rheumatol*. 2014; 10(1): 44–56, doi: [10.1038/nrrheum.2013.160](https://doi.org/10.1038/nrrheum.2013.160), indexed in Pubmed: [24166242](https://pubmed.ncbi.nlm.nih.gov/24166242/).
11. Roberts S. Histology and pathology of the human intervertebral disc. *J Bone Jt Surg*. 2006; 88(2 suppl.): 10.
12. Sher I, Daly C, Oehme D, et al. Novel application of the pfirrmann disc degeneration grading system to 9.4T MRI: higher reliability compared to 3T MRI. *Spine (Phila Pa 1976)*. 2019; 44(13): E766–E773, doi: [10.1097/BRS.0000000000002967](https://doi.org/10.1097/BRS.0000000000002967), indexed in Pubmed: [31205169](https://pubmed.ncbi.nlm.nih.gov/31205169/).
13. Tertti M, Paajanen H, Laato M, et al. Disc degeneration in magnetic resonance imaging. A comparative biochemical, histologic, and radiologic study in cadaver spines. *Spine (Phila Pa 1976)*. 1991; 16(6): 629–634, doi: [10.1097/00007632-199106000-00006](https://doi.org/10.1097/00007632-199106000-00006), indexed in Pubmed: [1862401](https://pubmed.ncbi.nlm.nih.gov/1862401/).
14. Thompson JP, Schechter MT, Adams ME, et al. Preliminary evaluation of a scheme for grading the gross morphology of the human intervertebral disc. *Spine (Phila Pa 1976)*. 1990; 15(5): 411–415, doi: [10.1097/00007632-199005000-00012](https://doi.org/10.1097/00007632-199005000-00012), indexed in Pubmed: [2363069](https://pubmed.ncbi.nlm.nih.gov/2363069/).
15. Tomaszewski KA, Saganiak K, Gładysz T, et al. The biology behind the human intervertebral disc and its endplates. *Folia Morphol*. 2015; 74(2): 157–168, doi: [10.5603/FM.2015.0026](https://doi.org/10.5603/FM.2015.0026), indexed in Pubmed: [26050801](https://pubmed.ncbi.nlm.nih.gov/26050801/).
16. Urrutia J, Besa P, Campos M, et al. The Pfirrmann classification of lumbar intervertebral disc degeneration: an independent inter- and intra-observer agreement assessment. *Eur Spine J*. 2016; 25(9): 2728–2733, doi: [10.1007/s00586-016-4438-z](https://doi.org/10.1007/s00586-016-4438-z), indexed in Pubmed: [26879918](https://pubmed.ncbi.nlm.nih.gov/26879918/).
17. Vergroesen PPA, Kingma I, Emanuel KS, et al. Mechanics and biology in intervertebral disc degeneration: a vicious circle. *Osteoarthritis Cartilage*. 2015; 23(7): 1057–1070, doi: [10.1016/j.joca.2015.03.028](https://doi.org/10.1016/j.joca.2015.03.028), indexed in Pubmed: [25827971](https://pubmed.ncbi.nlm.nih.gov/25827971/).
18. Weidenbaum M, Foster RJ, Best BA, et al. Correlating magnetic resonance imaging with the biochemical content of the normal human intervertebral disc. *J Orthop Res*. 1992; 10(4): 552–561, doi: [10.1002/jor.1100100410](https://doi.org/10.1002/jor.1100100410), indexed in Pubmed: [1613629](https://pubmed.ncbi.nlm.nih.gov/1613629/).

# Fenestration of the vertebrobasilar junction detected with multidetector computed tomography angiography

B.R. Omotoso<sup>1</sup>, R. Harrichandparsad<sup>2</sup>, I.G. Moodley<sup>3</sup>, K.S. Satyapal<sup>1</sup>, L. Lazarus<sup>1</sup>

<sup>1</sup>Discipline of Clinical Anatomy, School of Laboratory Medicine and Medical Sciences, College of Health Sciences, University of KwaZulu-Natal, Westville Campus, Durban, South Africa

<sup>2</sup>Department of Neurosurgery, School of Clinical Medicine, College of Health Sciences, Nelson R Mandela School of Medicine, University of KwaZulu-Natal, Durban, South Africa

<sup>3</sup>Department of Radiology, Jackpersad and Partners Inc., Specialist Diagnostic Radiologists, Lenmed Ethekwini Hospital and Heart Centre, South Africa

[Received: 5 June 2020; Accepted: 20 July 2020; Early publication date: 2 March 2021]

*The complex embryonic origin of the vertebrobasilar system may result in a wide range of anatomical variations. It has been hypothesized that the formation of fenestrations are likely to occur due to the failure of regression of the bridging arteries that connect the longitudinal neural arteries during embryogenesis. Fenestration of the vertebrobasilar system is a rare anatomical variation that involves a luminal division of the artery, that has a single origin into two separate and parallel channels which are rejoined distally. Fenestrations are important anatomical variants in patients undergoing endovascular and invasive intracranial interventions. Vascular fenestration has been associated with aneurysms, arteriovenous malformations, neuralgia, and vertebrobasilar ischaemia. We report on 3 cases of fenestration at the vertebrobasilar junction in 1 female and 2 male patients, respectively, using multidetector computed tomography angiography. The length of the fenestrated segment of the artery measured 4.41 mm, 3.90 mm, and 5.90 mm, respectively in the patients. Our report is clinically important as the presence of this anatomical variation may influence the management of cervical and intracranial pathologies. Increased awareness of the prevalence of anatomic variations contributes to the advancement of noninvasive imaging capabilities. (Folia Morphol 2022; 81, 2: 510–514)*

**Key words:** morphological variation, vertebral artery, basilar artery

## INTRODUCTION

The vertebrobasilar system is the combination of the two vertebral arteries (VAs) together with the basilar artery. The vertebrobasilar junction (VBJ) is the point of union of the bilateral VAs, mostly at the lower border of the pons [19] to form the basilar artery. The vertebrobasilar system provides the blood supply to

vital structures like the cervical spinal cord, brainstem, thalamus, cerebellum, and occipital lobes [18]. Therefore, a morphological variation of either of the VA or basilar trunk can influence vascular supply to the aforementioned structures. Anatomically, VAs are divided into four segments: prevertebral (V1), vertebral (V2), atlantoaxial (V3), and intracranial (V4) segments [1]. Pre-

Address for correspondence: Prof. L. Lazarus, Department of Clinical Anatomy, School of Laboratory Medicine and Medical Sciences, College of Health Sciences, University of KwaZulu-Natal, Private Bag X54001, Durban, 4000, South Africa, tel: +27 31 260 7899, e-mail: ramsaroopl@ukzn.ac.za

This article is available in open access under Creative Common Attribution-Non-Commercial-No Derivatives 4.0 International (CC BY-NC-ND 4.0) license, allowing to download articles and share them with others as long as they credit the authors and the publisher, but without permission to change them in any way or use them commercially.

**Table 1.** Incidence of vertebrobasilar junction (VBJ) fenestration in different population groups

Author (year)	Country	Type of study	Number of cases	Sex: male/female	Segment of vertebral arteries
Campos et al. (1987) [2]	Canada	DSA	21	7/14	VBJ
Yoon et al. (2004) [24]	South Korea	CTA	4	2/2	VBJ
Consoli et al. (2013) [3]	Italy	DSA	2	Female	VBJ
Kan et al. (2013) [9]	United States	DSA	1	Female	VBJ
Gupta et al. (2013) [7]	India	CTA, DSA	4	3/1	VBJ
Trivelato et al. (2016) [22]	Brazil	DSA	5	1/4	VBJ
Zhu et al. (2016) [25]	China	DSA	10	6/4	VBJ
Present study	South Africa	CTA	3	1/2	VBJ

CTA — computed tomography angiography; DSA — digital subtraction angiography

vious studies regarding the morphology of the VA have shown the existence of variation in its course [5, 6, 11].

Fenestration is an uncommon anatomical variation that involves a luminal division of an artery that has a common origin into two separate and parallel channels anywhere along its course to rejoin distally. Fenestration is sometimes mistaken for duplication, but should, however, be differentiated. Duplication normally involves double vascular origin which later fuse during the course of the artery [8].

Fenestration of the VBJ has been reported to be a predisposing factor to other vascular malformations like aneurysms [24], arteriovenous malformations [12], and neuralgia [10]. Furthermore, fenestration has been associated with epidermoid cysts and vertebrobasilar ischaemia [13, 23]. A thorough understanding of the anatomy and knowledge of anatomical variations of the vertebrobasilar artery is essential for assessing neurologic syndromes and preoperative neurosurgical planning. In this report, we describe three cases of VBJ fenestration using multidetector computed tomography angiography.

Fenestration of the VBJ is a morphological variation that has been previously reported in the international population, for example in China, United States, Canada and Brazil (Table 1). In this report, we present 3 cases of fenestration of the VBJ in 2 White and 1 Indian South Africans.

## CASE REPORT

Our study is retrospective in nature, therefore, written informed consent was not obtained. However, the design of this study was approved by our Institutional Review Board/Ethics Committee (Biomedical Research Ethics Committee of the University of Kwa-

Zulu-Natal with ethical No: BE 148/19). No identifying patient information is present in this paper.

### Case 1

Computed tomography angiography (CTA) scan of intracranial vessels of a 34-year-old Indian South African female at Lenmed Ethekwini Hospital and Heart Centre illustrated fenestration at the VBJ (Fig. 1A). The length of the fenestrated segment at the VBJ was 4.41 mm with the two limbs having a similar diameter. Clinical examination showed extensive aneurysmal subarachnoid haemorrhage in the right Sylvian fissure with intracerebral extension into the adjacent peri-lenticular parenchyma. Ruptured right middle cerebral artery saccular aneurysm, and further multilobulated anterior cerebral artery aneurysm was noted with the incorporation of large left A3 segment.

### Case 2

A 79-year-old male White South African presented to Lenmed Ethekwini Hospital and Heart Centre for the history of vertebrobasilar transient ischaemic attack (TIA) and acute unsteadiness. CTA scan revealed fenestration at the VBJ (Fig. 1B). The length of the fenestrated segment at the VBJ was 3.90 mm with the two limbs having a similar diameter. The posterior communicating artery was hypoplastic on the right when compared to the left and no intracranial aneurysm was demonstrated.

### Case 3

An 83-year-old male White South African presented to Lenmed Ethekwini Hospital and Heart Centre for a clinical history of collapse, recurrent TIA, ataxia, and diplopia. CTA showed fenestration at the VBJ

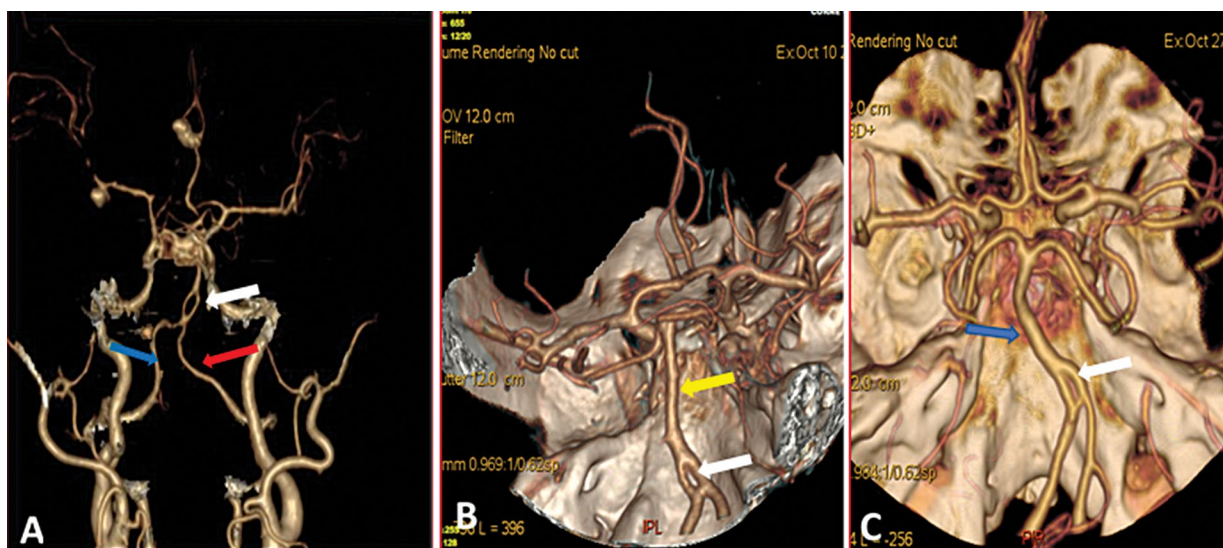


**Figure 1.** Computed tomography angiography images of case 1 (A), case 2 (B) and case 3 (C); A. Three-dimensional reconstructed image shows vessels of anterior and posterior circulation. Blue arrow shows intracranial segment of right vertebral artery (VA) while the red arrow shows intracranial segment of the left VA. The white arrow shows fenestration at the vertebrobasilar junction (VBJ) between the confluence of bilateral VAs and proximal part of the basilar artery; B. Three-dimensional reconstructed image shows the intracranial VA, bending basilar artery and the circle of Willis. The white arrow shows fenestration at the VBJ while the yellow arrow shows the basilar artery; C. Three-dimensional reconstructed image shows the intracranial VA, bending basilar artery and the circle of Willis. The white arrow shows fenestration at the VBJ while the blue arrow shows the basilar artery.

(Fig. 1C). The length of the fenestrated segment at the VBJ was 5.90 mm with the two limbs having a similar diameter. The basilar artery was minimally ectatic involving the medial and lateral margin at its bifurcation.

## DISCUSSION

Anatomical variation in the origin of the VA is the most reported morphological variation. This has also been reported in the South African population [4, 15]. However, reports on fenestration at the VBJ are scarce and are mostly reported internationally (Table 1). Previous studies regarding the morphology of the VA have shown the existence of variation with demographic and ethnic/racial differences [5, 6, 11]. Complex embryogenesis of the vertebrobasilar system results in vascular fenestration and it is frequently reported at the extracranial portion of the VA [12]. In contrast, the three cases we report showed fenestration at the VBJ.

Embryologically, the VA is formed during the 32<sup>nd</sup> to 40<sup>th</sup> days by the development of longitudinal anastomosis between the seven adjacent cervical intersegmental arteries that are formed from the primitive dorsal aorta [17]. Later, however, the first six cervical intersegmental arteries regress, while the seventh persists to form the proximal part of the subclavian artery

and the point of origin of the adult VA. The basilar trunk is formed from the fusion of primitive embryonic longitudinal neural arteries by approximately the fifth foetal week [14]. Generally, fenestration at any of the segments of the VA (V1–V4) is due to the absence of obliterations of two intersegmental vessels which fuse, or by segmental arteries which become short or disappear while a portion of the dorsal aorta remains against the VA [1]. Basilar artery fenestration occurs as a result of partial failure or incomplete fusion of the longitudinal neural arteries and regression of the bridging arteries connecting the longitudinal arteries [25]. Although fenestration at the VBJ is formed between the confluence of the bilateral distal VA and proximal part of the basilar artery, researchers agree that the best explanation for this morphological variation is the persistence or incomplete fusion of one of the temporary bridging arteries between the embryologic bilateral longitudinal neural arteries that form the basilar artery [7, 25]. This could occur as a result of some genetic or environmental factors [25]. In the cases we observed, fenestration was found at the VBJ in 3 patients (Figs. 1A–C).

The macroscopic examination of the fenestrated segment revealed a unique fusiform thickened vessel [1]. Furthermore, microscopic and histopathological examination of the limbs has shown irregularities in the lateral and medial wall structure [1, 13]. These

irregularities may alter the haemodynamics of blood flow at the proximal and distal end of the fenestrated segment causing TIA as reported in two of our patients (cases 2 and 3).

Vertebral artery dominance and bending of the basilar artery have also been reported as risk factors for brainstem infarction and TIA [16]. Morphologically, the VBJ is subjected to the greatest stresses of flow and turbulence from the bilateral VA below. This complex geometry of the VBJ, in addition to fenestration and basilar bends (Fig. 1A–C), may also contribute to the clinical history of TIA in cases 2 and 3.

Some authors suggest that fenestration of the VA is an incidental finding and has no pathological and clinical importance [20], while others hypothesized that its occurrence increases the prevalence of aneurysms (most especially at the VBJ) [2, 24]. Fenestration has also been associated with the brain, spinal cord, and spinal column abnormalities in addition to other vascular disorders [21]. In case 1, there is a middle cerebral artery and anterior cerebral artery aneurysm, which is not associated with the fenestration. According to the report by Campos et al. [2] and review of literature (Table 1), fenestration at the VBJ is more common in female subjects while VA fenestration is considered to be more frequent in male subject [12]. This may not be comparable due to different embryological processes in the formation of the basilar artery as opposed to the vertebral arteries. Also, our report is a small series with only 3 subjects comprising 2 males and 1 female.

## CONCLUSIONS

The authors presented 3 cases of fenestration at the VBJ in 2 White males and 1 female Indian South African patients. The presence of this morphological variation can increase the incidence of an aneurysm. Since most intracranial vascular disorders such as aneurysm are treated using endovascular procedures, a knowledge of the presence of fenestrations may influence the endovascular strategy. Therefore, knowledge of this anatomical variation will help in the preoperative workup and contribute to the correct interpretation of preoperative images. This report will also contribute to the demography of the South African population.

**Conflict of interest:** None declared

## REFERENCES

1. Bruneau M, De Witte O, Regli L. Anatomical variations, in Pathology and surgery around the vertebral artery. Springer Paris, Paris 2011: 53–74.
2. Campos J, Fox A, Vinuela F. Saccular aneurysms in basilar artery fenestration. *AJNR Am J Neuroradiol.* 1987; 8(2): 233–236.
3. Consoli A, Renieri L, Nappini S, et al. Endovascular treatment with ‘kissing’ flow diverter stents of two unruptured aneurysms at a fenestrated vertebrobasilar junction. *J Neurointerv Surg.* 2013; 5(2): e9, doi: [10.1136/neurintsurg-2011-010188](https://doi.org/10.1136/neurintsurg-2011-010188), indexed in Pubmed: [22315285](https://pubmed.ncbi.nlm.nih.gov/22315285/).
4. Da Silva R. Anatomical study of the variation in the branching patterns and histology of the aorta in a South African population. University of Cape Town 2013.
5. Deng D, Cheng FuBo, Zhang Y, et al. Morphological analysis of the vertebral and basilar arteries in the Chinese population provides greater diagnostic accuracy of vertebrobasilar dolichoectasia and reveals gender differences. *Surg Radiol Anat.* 2012; 34(7): 645–650, doi: [10.1007/s00276-012-0960-9](https://doi.org/10.1007/s00276-012-0960-9), indexed in Pubmed: [22427028](https://pubmed.ncbi.nlm.nih.gov/22427028/).
6. Gaigalaite V, Vilimas A, Ozeraitiene V, et al. Association between vertebral artery hypoplasia and posterior circulation stroke. *BMC Neurol.* 2016; 16: 118, doi: [10.1186/s12883-016-0644-x](https://doi.org/10.1186/s12883-016-0644-x), indexed in Pubmed: [27461465](https://pubmed.ncbi.nlm.nih.gov/27461465/).
7. Gupta V, Ahuja CK, Khandelwal N, et al. Treatment of ruptured saccular aneurysms of the fenestrated vertebrobasilar junction with balloon remodeling technique. A short case series and review of the literature. *Interv Neuroradiol.* 2013; 19(3): 289–298, doi: [10.1177/159101991301900305](https://doi.org/10.1177/159101991301900305), indexed in Pubmed: [24070077](https://pubmed.ncbi.nlm.nih.gov/24070077/).
8. Ionete C, Omojola MF. MR angiographic demonstration of bilateral duplication of the extracranial vertebral artery unusual course and review of the literature. *AJNR Am J Neuroradiol.* 2006; 27(6): 1304–1306.
9. Kan P, Abla AA, Dumont TM, et al. Double-barrel stent-assisted coiling of a basilar artery fenestration aneurysm. *J Neuroimaging.* 2013; 23(3): 496–499, doi: [10.1111/j.1552-6569.2012.00720.x](https://doi.org/10.1111/j.1552-6569.2012.00720.x), indexed in Pubmed: [22607550](https://pubmed.ncbi.nlm.nih.gov/22607550/).
10. Kim K, Mizunari T, Kobayashi S, et al. [Occipital neuralgia caused by the compression of the fenestrated vertebral artery: a case report]. *J Neurosurg.* 1999; 27(7): 645–650, indexed in Pubmed: [10440039](https://pubmed.ncbi.nlm.nih.gov/10440039/).
11. Kornieieva M, Al-Hadidi A. Morphology of the vertebral artery in Asian population. *Asian J Med Sci.* 2014; 5(4): 84–88, doi: [10.3126/ajms.v5i4.6150](https://doi.org/10.3126/ajms.v5i4.6150).
12. Kowada M, Yamaguchi K, Takahashi H. Fenestration of the vertebral artery with a review of 23 cases in Japan. *Radiology.* 1972; 103(2): 343–346, doi: [10.1148/103.2.343](https://doi.org/10.1148/103.2.343), indexed in Pubmed: [5024559](https://pubmed.ncbi.nlm.nih.gov/5024559/).
13. Kubo M, Hacein-Bey L, Varelas PN, et al. Ruptured saccular aneurysm of distal vertebral artery fenestration managed with Guglielmi detachable coils and intraventricular tissue plasminogen activator. *Surg Neurol.* 2005; 63(3): 244–248, doi: [10.1016/j.surneu.2004.02.038](https://doi.org/10.1016/j.surneu.2004.02.038), indexed in Pubmed: [15734513](https://pubmed.ncbi.nlm.nih.gov/15734513/).

14. Luh GY, Dean BL, Tomsick TA, et al. The persistent fetal carotid-vertebrobasilar anastomoses. *AJR Am J Roentgenol.* 1999; 172(5): 1427–1432, doi: [10.2214/ajr.172.5.10227532](https://doi.org/10.2214/ajr.172.5.10227532), indexed in Pubmed: [10227532](https://pubmed.ncbi.nlm.nih.gov/10227532/).
15. Makhanya NZ, Mamogale RT, Khan N. Variants of the left aortic arch branches. *SA J Radiol.* 2004; 8(4): 10, doi: [10.4102/sajr.v8i4.102](https://doi.org/10.4102/sajr.v8i4.102).
16. Meng X, Ding W, Wu X, et al. Clinical investigation and characterization of vertebrobasilar dolichoectasia and vertebral artery dominance. *Discov Med.* 2018; 25(138): 151–158, indexed in Pubmed: [29723487](https://pubmed.ncbi.nlm.nih.gov/29723487/).
17. Padgett DH. The development of the cranial arteries in the human embryo. *J Contrib Embryol.* 1948; 32: 205–261.
18. Piccinin MA, Munakomi S, Neuroanatomy, Vertebrobasilar System, in StatPearls [Internet]. StatPearls Publishing, 2019.
19. Standring S. *Gray's anatomy e-book: the anatomical basis of clinical practice.* Elsevier Health Sciences 2015.
20. Tetiker H, Cimen M, Koşar Mİ. Fenestration of the vertebral artery: case presentation. *Folia Morphol.* 2014; 73(1): 84–86, doi: [10.5603/FM.2014.0012](https://doi.org/10.5603/FM.2014.0012), indexed in Pubmed: [24590528](https://pubmed.ncbi.nlm.nih.gov/24590528/).
21. Tran-Dinh HD, Soo YS, Jayasinghe LS. Duplication of the vertebro-basilar system. *Australas Radiol.* 1991; 35(3): 220–224, doi: [10.1111/j.1440-1673.1991.tb03012.x](https://doi.org/10.1111/j.1440-1673.1991.tb03012.x), indexed in Pubmed: [1763984](https://pubmed.ncbi.nlm.nih.gov/1763984/).
22. Trivelato FP, Abud DG, Nakiri GS, et al. Basilar artery fenestration aneurysms: endovascular treatment strategies based on 3D morphology. *Clin Neuroradiol.* 2016; 26(1): 73–79, doi: [10.1007/s00062-014-0336-0](https://doi.org/10.1007/s00062-014-0336-0), indexed in Pubmed: [25164692](https://pubmed.ncbi.nlm.nih.gov/25164692/).
23. Weis J, Reul J, Mayfrank L, et al. Duplication of a vertebral artery associated with epidermoid cyst of the posterior fossa. *Eur Radiol.* 1997; 7(3): 412–414, doi: [10.1007/s003300050177](https://doi.org/10.1007/s003300050177), indexed in Pubmed: [9087368](https://pubmed.ncbi.nlm.nih.gov/9087368/).
24. Yoon S, Chun Y, Kwon Y, et al. Vertebrobasilar junction aneurysms associated with fenestration: experience of five cases treated with Guglielmi detachable coils. *Surgical Neurology.* 2004; 61(3): 248–254, doi: [10.1016/s0090-3019\(03\)00485-3](https://doi.org/10.1016/s0090-3019(03)00485-3).
25. Zhu DY, Fang YB, Wu YN, et al. Treatment of fenestrated vertebrobasilar junction-related aneurysms with endovascular techniques. *J Clin Neurosci.* 2016; 28: 112–116, doi: [10.1016/j.jocn.2015.09.018](https://doi.org/10.1016/j.jocn.2015.09.018), indexed in Pubmed: [26778513](https://pubmed.ncbi.nlm.nih.gov/26778513/).

# A novel accessory muscle in the flexor compartment of anterior forearm inserting into the tenosynovium of the flexor pollicis longus

A. Gurvich<sup>1</sup>, N. Shridhar<sup>1</sup>, A. Felman<sup>1</sup>, M. Shi<sup>1</sup>, A. Pinkas<sup>1</sup>, S.A. Downie<sup>1,2</sup>, P.L. Mishall<sup>1,3</sup> 

<sup>1</sup>Department of Anatomy and Structural Biology, Albert Einstein College of Medicine, Bronx, NY, United States

<sup>2</sup>Department of Physical Medicine and Rehabilitation, Albert Einstein College of Medicine, Bronx, NY, United States

<sup>3</sup>Department of Ophthalmology and Visual Sciences, Albert Einstein College of Medicine, Bronx, NY, United States

[Received: 5 March 2021; Accepted: 18 March 2021; Early publication date: 9 April 2021]

*A common variant of accessory muscles in the anterior forearm is the Gantzer's muscle (GM). GM arises as a muscle belly from flexor digitorum superficialis (FDS) or ulnar coronoid process to merge distally with the flexor pollicis longus (FPL) muscle. In the present case report, we describe a novel accessory muscle in the flexor compartment of the forearm. The proximal attachment was tendinous and came from three sources: FDS muscle, ulnar coronoid process, and the medial aspect of the proximal radius. The distal tendon of the novel accessory muscle ran parallel to FPL, passed through the carpal tunnel, and entered the palmar aspect of the hand. In the hand, the tendon thinned out and blended with the tenosynovium of the FPL, contributing to the sheath around the FPL tendon. This accessory muscle of the FPL is comparable to the frequently documented GM; however, the present case exhibited fundamental nuances that distinguish it from the previously described iterations of the GM in the following ways: 1) The novel accessory muscle is tendinous from its proximal origin and throughout the upper one-third of the forearm, and one component of its origin arose from the medial aspect of the radius. GMs with an origin on the radius have not been previously reported. 2) In the middle one-third, the tendinous proximal attachment transitioned to a muscle belly that passed through the carpal tunnel and entered the hand. 3) In the hand, the novel tendon widened, thinned, and merged with the tenosynovium of the FPL. Accessory muscles are a common finding in the anterior forearm during cadaveric dissection. In patients, they can be the cause of neuropathies due to compression of the anterior interosseous nerve. Awareness of variations is also important for clinicians who examine the forearm and hand, as well as hand surgeons. (Folia Morphol 2022; 81, 2: 515–519)*

**Key words:** Gantzer, forearm, flexor pollicis longus, carpal tunnel

## INTRODUCTION

Anatomical variations of the flexor muscles of the anterior forearm are commonly found in cadaveric dissections. The Gantzer muscle (GM), accessory head

of the flexor pollicis longus (FPL), is a well-documented and highly prevalent anterior compartment variation. One meta-analysis reported a prevalence rate of 44.2% from 24 cadaveric studies [11]. Typically, the

Address for correspondence: P.L. Mishall, Ass. Prof., Departments of Anatomy and Structural Biology and Ophthalmology and Visual Sciences, Albert Einstein College of Medicine, 1300 Morris Park Ave, F620SD, Bronx, NY 10461, United States, tel: +1 (718) 430-3423, fax: +1 (718) 430-8996, e-mail: priti.mishall@einsteinmed.org

This article is available in open access under Creative Commons Attribution-Non-Commercial-No Derivatives 4.0 International (CC BY-NC-ND 4.0) license, allowing to download articles and share them with others as long as they credit the authors and the publisher, but without permission to change them in any way or use them commercially.

GM originates in the proximal forearm as fibres from the deep aspect of the flexor digitorum superficialis (FDS) alone, or from the FDS together with the medial epicondyle of the humerus and/or with the ulnar coronoid process [10]. Distally, GMs blend in with the proximal tendon of the FPL at the midpoint of the radius. At that insertion, they exert a flexion force on the FPL. Also reported are accessory flexor digitorum profundus (FDP) muscles which have the same origin as the GM but insert into the FDP [15]. Some variants insert into both the FPL and the FDP [15].

Accessory muscles in the anterior forearm become clinically relevant when they compress local neurovasculature. An accessory head of the FPL has been the aetiology of compressive neuropathies of either the median nerve (MN) or the anterior interosseous nerve [13, 15]. Here, we present a muscle that would raise similar concerns in the clinical setting.

### CASE REPORT

An 84-year-old female donor was dissected by undergraduate medical students at the Albert Einstein College of Medicine, Bronx, NY, as part of the first-year Clinical and Developmental Anatomy course. They identified a novel accessory muscle in the anterior flexor compartment of the right forearm. It originated via tendinous bands from the deep side of the FDS, the ulnar coronoid process, and the medial aspect of the proximal radius. These two tendinous bands united at the upper one-third of the forearm to form a single tendon (Fig. 1). These proximal tendons were positioned anterior to the anterior interosseous nerve (AIN). In the distal half of the forearm, the single tendon transitioned into a muscle belly located deep to the FDS and between the FDS and the MN. The muscle again became tendinous at the level of the radial styloid process. This distal tendon was situated between the FDS and the MN, and ran parallel to the FPL (Figs. 2, 3). It passed through the carpal tunnel and entered the hand, where it widened out and blended with the tenosynovium of the FPL (Figs. 4, 5).

The dissection of the left anterior forearm revealed an accessory head of FPL that originated from the deep side of the FDS and inserted into the FPL tendon as has been described previously [2].

### DISCUSSION

The accessory muscle reported here is atypical of GMs and other accessory muscles of the forearm. This novel muscle's proximal origins — contributions from



**Figure 1.** Dissection of the anterior proximal forearm. The novel muscle (white arrow) seen with its origins in the medial aspect of the radius (\*) and the ulnar coronoid process (\*\*), with contributory fibres from the flexor digitorum superficialis (FDS), converging in the form of a “Y”. The position of the muscle is shown relative to the median nerve (MN).

the undersurface of the FDS, the ulnar coronoid, and the proximal medial radius — have not been previously reported. Pai et al. [10] surveyed 126 upper limbs and found that 76 had a GM, either as an accessory head of FDP (FDPah) or of FPL (FPLah). In all cases, the origin was from the deep surface of the FDS alone, or in combination with fibres originating on the medial epicondyle and/or the coronoid process. In no cases did the GM originate on the coronoid process or medial epicondyle without the FDS contribution. Pai et al. [10] also writes they found no muscle arising from other structures such as the pronator teres or the brachialis. The novel muscle is most similar to one case Pai et al. [10] found, involving a single muscle belly of a GM that originated from the FDS, and then divided into an FPLah and an FDPah to insert into the FPL and FDP, respectively.

Caetano et al. [2] conducted a survey of 80 upper limbs and found GM in 54 (68%). In 42 of these cases the GM originated from the undersurface of the FDS, in 8 cases it originated from the coronoid process,

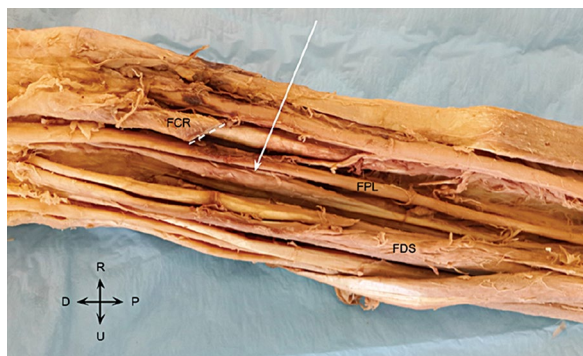


**Figure 2.** Dissection of the distal forearm. The flexor carpi radialis (FCR) was cut (at dashed line) from its distal attachment and reflected to better visualise the flexor pollicis longus (FPL). The novel muscle is denoted by the white arrow, medial to the FPL. The flexor digitorum superficialis (FDS) remains *in situ*.



**Figure 3.** Dissection of anterior compartment of right distal forearm and hand. The palmaris longus, with the palmar aponeurosis (PA), was reflected. The flexor digitorum superficialis (FDS), flexor pollicis longus (FPL), and flexor carpi radialis (FCR) are shown *in situ*. White arrow denotes the novel muscle, medial to FPL; \* (asterisk) — the fourth digit was surgically amputated in life.

and in 7 cases from the medial epicondyle (3 of the cases were a GM with 2 origins, both the FDS and the coronoid process). In all of the cases Caetano et al. [2] examined, the GM always lay posterior to both the median and anterior interosseous nerve.

Regarding the distal insertion of the GM, Pai et al. [10] conducted a cadaveric survey of 126 upper limbs and found that GMs inserted into the FPL at a prevalence of 46.03%, and into the FDP at that of 14.28%. Among those GMs positioned as FPLah, 80% inserted into the proximal third of the FPL, and the rest mostly inserted into the middle third, except for 2 cases in which the FPLah inserted into the distal

third of the FPL. No cases were found in which FPLah inserted into the tendon of the FPL distal to the carpal tunnel. Similarly, Zdilla et al. [15] reported a belly of a GM which became tendinous at 52 mm from its most distal origin in the FDS; this tendon travelled 6 mm before joining the proximal one third of the FPL.

In the study conducted by Caetano et al. [2], the GM inserted into the FPL in 36 of the 54 limbs. It inserted into the FDP in 21 of the upper limbs, totalling 57 insertions in 54 limbs (in 3 cases of GM that inserted into the FDP, the GM had 2 origins, and therefore was counted twice).

There have been various descriptions in the literature of the location of the GM relative to the MN and AIN. Mangini [8] found that the FPLah lies posterior to the MN and anterior to the AIN in 100% of his cases, and this finding was confirmed by Pai et al. [10]. However, Al-Qattan [1] found in 13 cadavers that the FPLah lies posterior to the AIN, as was described by Dellon and Mackinnon [4] in all 14 cadavers with a GM present. In this case report, the novel muscle was found to lie posterior to the MN, and anterior and parallel to the AIN, in line with the findings of Mangini [8] and Pai et al. [10].

The accessory head of FPL has been implicated in the compression of the AIN [4, 14]. This has been termed Kiloh-Nevin syndrome or AIN syndrome. Spinner [14] describes this compression as causing AIN paralysis, thus affecting the FPL, the lateral two fascicles of FDP, and pronator quadratus muscles. Clinically, this syndrome presents with increased extension of the distal interphalangeal joint and increased flexion of the proximal interphalangeal joint on the index finger during the pinch motion. This has been dubbed “Spinner’s sign” [3], and the accessory head of the FPL has been implicated in this syndrome. However, per the literature review of Orellana-Donoso et al. [9], a compressive neuropathy of the AIN by an accessory head of the FPL mainly presents clinically as carpal tunnel syndrome. Alternatively, the presence of an anomalous muscle or tendon in the forearm has been implicated in symptomatic supernumerary muscle belly syndrome [12]. This presents as pain in the distal forearm due to shearing between adjacent muscle fibres as a result of the extra muscle or tendon in the forearm [12].

The musculature of the human anterior forearm has its embryological origins in somatic mesoderm which invades the limb anlage at 4 weeks of gestation. The flexor mass subsequently divides into



**Figure 4.** Dissection of palm of hand. The novel muscle (single arrow) separated from the flexor pollicis longus (FPL). The transverse carpal ligament was dissected to visualise the distal continuity of these two muscles. The tendon of the novel muscle distally feeds into the tenosynovium of the FPL (double arrows) immediately distal to the carpal tunnel, forming a sheath (double asterisk); \* (asterisk) — the fourth digit was surgically amputated in life.



**Figure 5.** Deep dissection of palm of hand. Sheath formed by tendon of novel muscle (arrow) further dissected from the tendon of the flexor pollicis longus (FPL); \* (asterisk) — the fourth digit was surgically amputated in life.

two layers that condense: one more superficial, and another deeper. The former splits into flexor carpi radialis, pronator teres, and the palmaris longus. The deep muscle mass originates on the medial epicondyle and inserts into the developing digits. It initially gives rise to the flexor carpi ulnaris and then cleaves into two layers: the FDS and the FDP. The FPL splits from the FDP [7]. Accessory muscles that connect the FDS, FDP, and FPL are thought to be the result of incomplete cleavage of the deeper embryological mass in the anterior forearm [6]. According to Eid

and Otsuki [5], an accessory head of the flexor compartment, in other mammals, is a belly connecting the part of FDS originating in the medial epicondyle to the deep flexor muscles. These observations of FPL splitting from FDP are consistent with our findings of the novel muscle originating from deep side of FDS, although they do not address the unique origin of the novel muscle fibres from medial aspect of radius.

The accessory muscle in the right forearm identified by the authors differs from previously described GMs in three ways:

- this accessory muscle had one origin from the medial aspect of the radius. GMs with an origin on the radius have not been previously reported;
- this accessory muscle presented as a muscle belly in the middle of the forearm. The tendon of the belly passed through the carpal tunnel and travelled further into the hand. Even the most distally inserted GMs found by Pai et al. [10] inserted into the FPL proximal to the carpal tunnel;
- in the hand, the distal tendon of the accessory muscle formed a synovial sheath around the tendon of the FPL medial to the thenar eminence. This is a previously unreported finding.

## CONCLUSIONS

To our knowledge, this is the first report of an accessory muscle in the anterior forearm with a proximal origin that included the radius. The belly of this muscle transitioned into a tendon at the radial styloid process, entered the hand through the carpal tunnel, and fused with the tenosynovial sheath of the FPL. GM usually inserts into the FPL tendon in the middle third of the forearm. More generally, the presence of accessory muscles such as the one described here has clinical implications for the diagnosis and treatment of compression injuries of the median and anterior interosseous nerves.

## Acknowledgements

The authors acknowledge and gratefully thank the individual whose body and tissues were used in this study for the advancement of physician education and patient care.

**Conflict of interest:** None declared

## REFERENCES

1. Al-Qattan MM. Gantzer's muscle. An anatomical study of the accessory head of the flexor pollicis longus muscle. *J Hand Surg (Br)*. 1996; 21: 269–270, doi: [10.1016/s0266-7681\(96\)80114-8](https://doi.org/10.1016/s0266-7681(96)80114-8), indexed in Pubmed: [8732417](https://pubmed.ncbi.nlm.nih.gov/8732417/).
2. Caetano EB, Sabongi JJ, Vieira LÂ, et al. Gantzer muscle. An anatomical study. *Acta Ortop Bras*. 2015; 23(2): 72–75, doi: [10.1590/1413-78522015230200955](https://doi.org/10.1590/1413-78522015230200955), indexed in Pubmed: [27069404](https://pubmed.ncbi.nlm.nih.gov/27069404/).
3. Degreeef I, De Smet L. Anterior interosseous nerve paralysis due to Gantzer's muscle. *Acta Orthop Belg*. 2004; 70(5): 482–484, indexed in Pubmed: [15587039](https://pubmed.ncbi.nlm.nih.gov/15587039/).
4. Dellon AL, Mackinnon SE. Musculoaponeurotic variations along the course of the median nerve in the proximal forearm. *J Hand Surg (Br)*. 1987; 12: 359–363, doi: [10.1016/0266-7681\(87\)90189-6](https://doi.org/10.1016/0266-7681(87)90189-6), indexed in Pubmed: [3437205](https://pubmed.ncbi.nlm.nih.gov/3437205/).
5. Eid N, Otsuki Y. A case of double Gantzer's muscle and its possible role in nerve entrapment. *Clin Anat*. 2009; 22(8): 881–882, doi: [10.1002/ca.20862](https://doi.org/10.1002/ca.20862), indexed in Pubmed: [19806672](https://pubmed.ncbi.nlm.nih.gov/19806672/).
6. Jones M, Abrahams PH, Sañudo JR, et al. Incidence and morphology of accessory heads of flexor pollicis longus and flexor digitorum profundus (Gantzer's muscles). *J Anat*. 1997; 191 ( Pt 3): 451–455, doi: [10.1046/j.1469-7580.1997.19130451.x](https://doi.org/10.1046/j.1469-7580.1997.19130451.x), indexed in Pubmed: [9419002](https://pubmed.ncbi.nlm.nih.gov/9419002/).
7. Lewis WH. The development of the muscular system. *Manual of Embryology*. 1910; 2: 455–522.
8. Mangini U. Flexor pollicis longus muscle. Its morphology and clinical significance. *J Bone Joint Surg Am*. 1960; 42(A): 467–470, indexed in Pubmed: [13853793](https://pubmed.ncbi.nlm.nih.gov/13853793/).
9. Orellana-Donoso M, Valenzuela-Fuenzalida J, Gold-Semmler M, et al. Neural entrapments associated with musculoskeletal anatomical variations of the upper limb: Literature review. *Transl Rev Anat*. 2021; 22: 100094, doi: [10.1016/j.tria.2020.100094](https://doi.org/10.1016/j.tria.2020.100094).
10. Pai MM, Nayak SR, Krishnamurthy A, et al. The accessory heads of flexor pollicis longus and flexor digitorum profundus: Incidence and morphology. *Clin Anat*. 2008; 21(3): 252–258, doi: [10.1002/ca.20612](https://doi.org/10.1002/ca.20612), indexed in Pubmed: [18351652](https://pubmed.ncbi.nlm.nih.gov/18351652/).
11. Roy J, Henry BM, Pękala PA, et al. The prevalence and anatomical characteristics of the accessory head of the flexor pollicis longus muscle: a meta-analysis. *Peer J*. 2015; 3: e1255, doi: [10.7717/peerj.1255](https://doi.org/10.7717/peerj.1255), indexed in Pubmed: [26557419](https://pubmed.ncbi.nlm.nih.gov/26557419/).
12. Ryu JY, Watson HK. SSMB syndrome. Symptomatic supernumerary muscle belly syndrome. *Clin Orthop Relat Res*. 1987(216): 195–202, indexed in Pubmed: [3815948](https://pubmed.ncbi.nlm.nih.gov/3815948/).
13. Sookur PA, Naraghi AM, Bleakney RR, et al. Accessory muscles: anatomy, symptoms, and radiologic evaluation. *Radiographics*. 2008; 28(2): 481–499, doi: [10.1148/rq.282075064](https://doi.org/10.1148/rq.282075064), indexed in Pubmed: [18349452](https://pubmed.ncbi.nlm.nih.gov/18349452/).
14. Spinner M. The anterior interosseous-nerve syndrome, with special attention to its variations. *J Bone Joint Surg Am*. 1970; 52(1): 84–94, doi: [10.1007/s12565-018-0466-6](https://doi.org/10.1007/s12565-018-0466-6), indexed in Pubmed: [5411776](https://pubmed.ncbi.nlm.nih.gov/5411776/).
15. Zdilla MJ, Pacurari P, Celuck TJ, et al. A Gantzer muscle arising from the brachialis and flexor digitorum superficialis: embryological considerations and implications for median nerve entrapment. *Anat Sci Int*. 2019; 94(1): 150–153, doi: [10.1007/s12565-018-0466-6](https://doi.org/10.1007/s12565-018-0466-6), indexed in Pubmed: [30382571](https://pubmed.ncbi.nlm.nih.gov/30382571/).

# Pointing in a different direction: a case of bilateral absence of extensor indicis

A. Ma<sup>1</sup>, J. Kim<sup>1</sup>, C.E. Miller<sup>1</sup>, T.L. Mustapich<sup>1</sup>, J.P. Abraham<sup>1</sup>, S.A. Downie<sup>1,2</sup>, P.L. Mishall<sup>1,3</sup> 

<sup>1</sup>Department of Anatomy and Structural Biology, Albert Einstein College of Medicine, Bronx, NY, United States

<sup>2</sup>Department of Physical Medicine and Rehabilitation, Albert Einstein College of Medicine, Bronx, NY, United States

<sup>3</sup>Department of Ophthalmology and Visual Sciences, Albert Einstein College of Medicine, Bronx, NY, United States

[Received: 5 November 2020; Accepted: 5 March 2021; Early publication date: 22 March 2021]

*Understanding anatomical variations as well as normal anatomy of the muscles and tendons of the hand is vital for successful clinical evaluation and surgery. A number of extensor muscle and tendon variations have been reported in the literature, including duplication, triplication, and absence. We report a rare anatomical variation that includes bilateral absence of the extensor indicis (EI) muscles and bilateral duplication of the extensor digitorum (ED) tendon to the second digit in the forearm of an 83-year-old male cadaver during routine upper limbs dissection. In the present case, only three muscles were present in the deep compartment: extensor pollicis longus (EPL), extensor pollicis brevis (EPB), and abductor pollicis longus (APL) with bilateral absence of EI. The reported prevalence of bilateral absence of EI muscle and tendon ranges from 0.5% to 3.5%. The prevalence of an additional index tendon arising bilaterally from the ED muscle belly is 3.2% of the population. Extension of the index finger is governed by the actions of EI and ED. However, the four tendons of ED are linked to each other by juncturae tendinum, restricting independent extension of the digits in certain postures, e.g. when the hand is fistled. With fistled hand, EI controls extension of the index finger. Clinically, EI tendons are used for tendon reconstruction procedures to restore function to the hand and thumb after trauma or tendon rupture. This report highlights the importance of anticipating anatomical variations and conducting pre-operative evaluations to confirm the presence of EI when planning tendon transfer procedures. (Folia Morphol 2022; 81, 2: 520–525)*

**Key words:** extensor indicis, forearm, congenital, index finger, hand

## INTRODUCTION

Thorough knowledge of the arrangement of tendons on the dorsum of the hand is essential when performing surgical procedures for tendon repair or tendon transfer within the hand. The extensor muscle-tendon units serving the second digit include

extensor indicis (EI) and extensor digitorum (ED). EI attaches proximally to the posterior surface of the distal third of the ulna and interosseous membrane and passes distally through the fourth dorsal compartment of the wrist together with ED tendons. The EI tendon travels on the ulnar side of the ED index

---

Address for correspondence: P.L. Mishall, Ass. Prof., Departments of Anatomy and Structural Biology and Ophthalmology and Visual Sciences, Albert Einstein College of Medicine, 1300 Morris Park Ave, F620SD, Bronx, NY 10461, USA, tel: +1 (718) 430-3423, fax: +1 (718) 430-8996, e-mail: priti.mishall@einsteinmed.org

This article is available in open access under Creative Common Attribution-Non-Commercial-No Derivatives 4.0 International (CC BY-NC-ND 4.0) license, allowing to download articles and share them with others as long as they credit the authors and the publisher, but without permission to change them in any way or use them commercially.

tendon to insert into the extensor expansion of the second digit [4]. Typically, EI produces extension of the second digit at the metacarpophalangeal, proximal and distal interphalangeal joints independent of the ED index tendon [9, 12]. It serves this function regardless of hand posture.

The four tendons of ED arise proximally from a common muscle belly attached to the lateral epicondyle of the humerus, and insert distally into the extensor hoods on the dorsum of the second through fifth metacarpal heads [8]. Just proximal to the metacarpophalangeal (MCP) joints, the ED tendons are joined to each other by oblique connective tissue bands, juncturae tendinum (JT) [6]. ED produces extension of the digits primarily at the MCP joints and secondarily at the interphalangeal joints. However, due to the JT, digital extension is restricted in certain postures such as fistled hand.

Instances of EI variants, including multiple tendon slips [9, 14, 15] or absence of the tendon [8, 10, 18], have been noted in the literature. Absence of the EI muscle-tendon unit is very uncommon with a reported prevalence of 0.5–3.5% in previous meta-analyses [8, 25]. Only 2 case reports describe the absence of EI bilaterally [22, 26]. Variations of the ED attachment to the second digit are also uncommon, with double slip tendon variants observed at a prevalence of 3.2% [1].

Extensor indicis tendons are commonly used in tendon transfer procedures to reconstruct the abductor pollicis longus (APL) or extensor pollicis longus (EPL) tendons. Because the index finger receives the ED tendon as well as the EI tendon, it should maintain the ability to extend if the EI tendon is removed [11, 13]. It is critical, therefore, to be aware of variations of the EI muscle, especially those that involve absence of its tendon, to evaluate patients prior to tendon transfer surgery [16, 21]. We report a case of bilateral absence of the EI muscle-tendon unit and bilateral presence of an additional tendon slip arising from ED to the second digit.

### CASE REPORT

During routine dissection of an 83-year-old male cadaver at the Albert Einstein College of Medicine, Bronx, NY, the extensor compartments of the forearms and dorsum of the hands were dissected by removing the skin and fascia to visualise the underlying muscles. The extensor muscles were identified and their tendons cleaned and followed to their distal attachments. Both the muscle belly and tendon of

the EI were absent bilaterally. And, bilaterally, an additional tendon slip arose from the ED muscle belly and inserted at the second digit (Figs. 1B, C). The presumptive normal tendon of ED to the second digit was connected with the other ED tendons via JT. On close observation, the JT were thin fascia-like tissues, as opposed to dense fibrous tissues. This quality confers a wider range of mobility for independent digital extension. No surgical incisions were found on either hand or forearm, suggesting that no surgical procedures had been performed. Further inspection of the extensor compartment showed only three muscles arising from the posterior surface of the radius, ulna, and interosseous membrane (Figs. 2B, C). These three muscles were the EPL, extensor pollicis brevis (EPB), and APL. Also, normal right hand with EI is shown (Figs. 1A, 2A).

### DISCUSSION

The normal presentation of EI is one muscle belly attached to the posterior surface of the ulna and interosseous membrane with one tendon descending to the extensor aponeurosis of the second digit. The EI tendon typically runs deep, ulnar and parallel to the ED index tendon. Studies of the dorsum of the hand indicate that variations in tendons to the second digit are rare [1, 6]. An extensive literature review revealed only 2 case reports of bilateral absence of the EI similar to our case [22, 26]. Additionally, Bergman's Comprehensive Encyclopedia of Human Anatomic Variation reports that muscles of the index finger are rarely absent; however, the authors do not indicate the prevalence of absent EI [2]. An early study of 263 upper extremities did not report absent EI [5]. However, in the same study Cauldwell et al. [5] referenced 5 cases of absent EI muscle that were published between 1806 and 1936. It was not indicated whether these were unilateral or bilateral. Hence, the current case of bilateral complete absence of EI is rare.

Furthermore, the current case is unique due to the presence of bilateral additional tendon slips arising from the ED muscle belly to the second digit. A thorough literature review indicated that variations, in the form of additional tendons to the index finger, were observed in two categories. In the first category, the additional tendon did not arise from ED but arose as a separate muscle either from the radius [19, 24] or the ulna [10]. In the second category, the additional tendon to the index finger arose from ED [3]. A dissection-based study of 13 cadavers found 2 (7.69%) cases

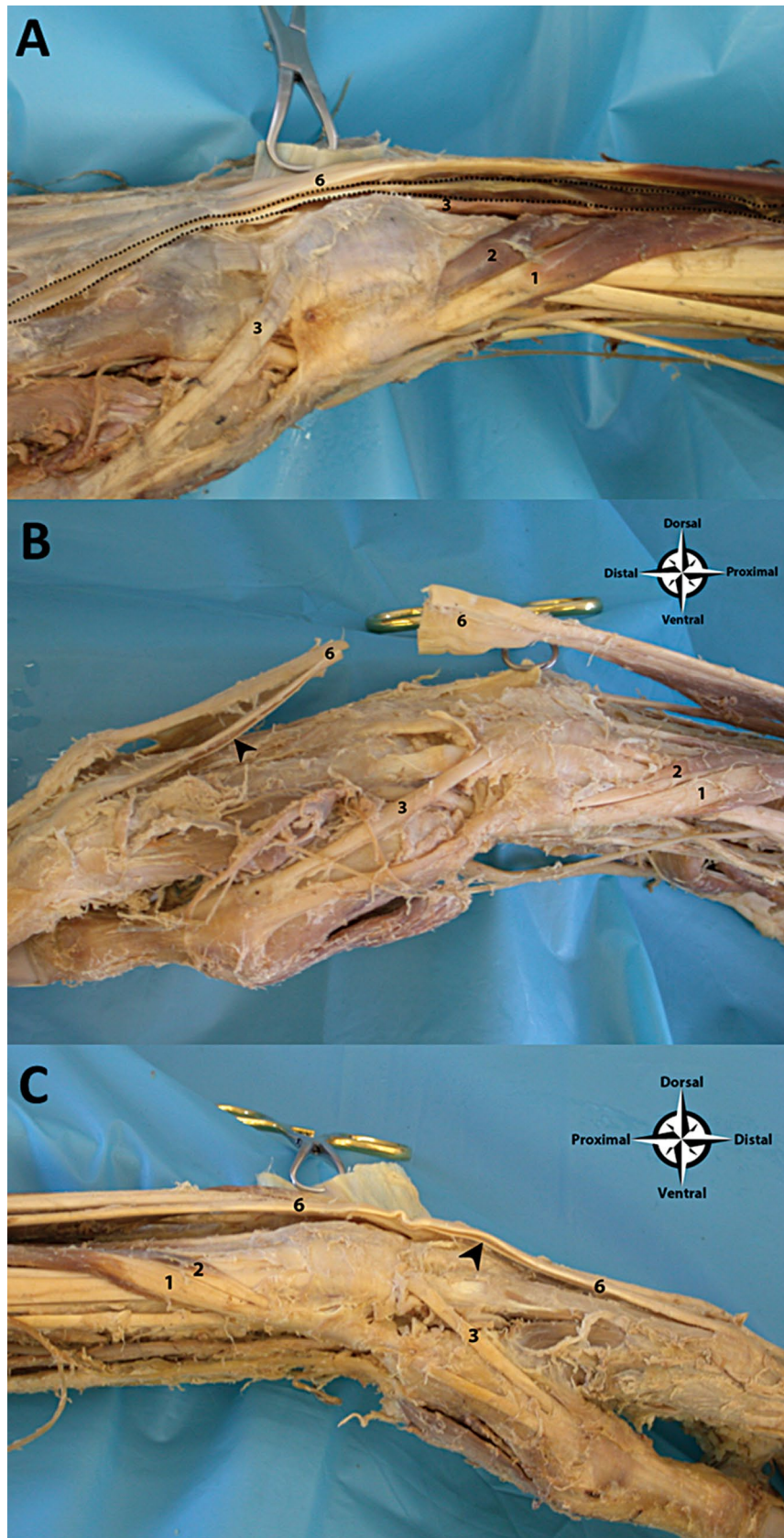


**Figure 1.** A. Normal right hand with extensor indicis present (dotted line); B, C. Right and left hands, respectively, with additional tendinous slip (arrowhead) arising from extensor digitorum; 1 — abductor pollicis longus; 2 — extensor pollicis brevis; 3 — extensor pollicis longus; 6 — extensor digitorum.

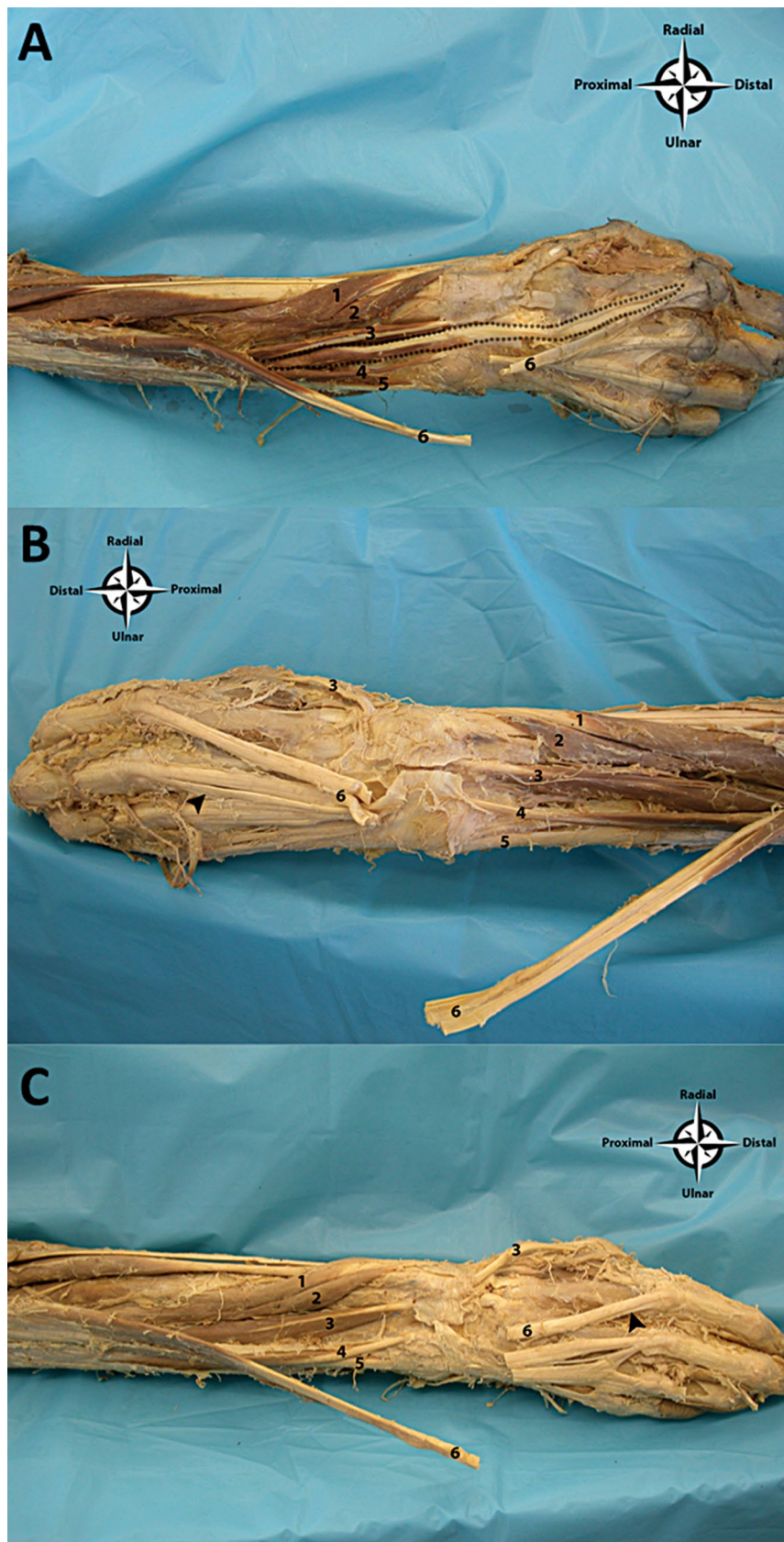


**Figure 2.** A. Normal right hand with extensor indicis present (dotted line); B, C. Left and right hands, respectively, with absent extensor indices. Additional tendinous slip arising from extensor digitorum indicated by arrowhead; 1 — abductor pollicis longus; 2 — extensor pollicis brevis; 3 — extensor pollicis longus; 4 — extensor digiti minimi; 5 — extensor carpi ulnaris; 6 — extensor digitorum (reflected).

in which the ED tendon to the index finger originated as two tendons that fused before reaching the MCP joint and inserted into the extensor expansion of the index finger as a single tendon [1]. The study conducted by Abdel-Hamid et al. [1], on 95 upper limbs, reported 3 (3.2%) cases of double tendons arising from the ED going to the index finger. In the current case, the ED gave two tendons that inserted at the index finger as two tendons. The other three ED tendons, one to each digit 3–5, were typical. Another dissection-based study of 54 upper limbs did not report double tendons that arose from ED to index finger [6].

In summary, the findings of bilateral absence of the EI muscle-tendon [22, 26] and additional slip of ED tendon to index finger have been reported as separate occurrences. The current case is unique in having both variations — bilateral absence of the EI muscle-tendon unit with the presence of bilateral additional tendon slip from ED that inserted onto the index finger.

The functional test for the presence of EI is independent extension of the index finger with the hand fistled. In the complete absence of EI, ED is responsible for extending the index finger. However, the four ED tendons are connected to each other by JT that limit independent extension of the digits. Von Schroeder et al. [23] described three types of JTs: type 1 (thin, fascia-like), type 2 (thicker, fibrous), and type 3 (thickest, tendinous band). Yamine [24] reported the prevalence of JT between the index finger and middle finger as type 1 (95%), type 2 (5%), and type 3 (0%). Furthermore, they showed that type 1 JTs accommodated independent extension of the four medial digits whereas type 2 and 3 JTs were restrictive [24]. In the present case, we observed thin fascia-like JTs similar to that described as type 1. We speculate that the individual, when living, may have had the ability to independently extend the index fingers in the absence of EI.

It is most likely that variations in limb musculoskeletal development resulted in the bilateral absence of the EI muscle-tendon unit and the bilateral presence of additional tendon slips arising from the ED muscle bellies. During embryological development the extensor muscle mass of the forearm differentiates into three sections: radial, superficial and deep [17]. The radial section gives rise to brachioradialis, and extensor carpi radialis longus and brevis. The remaining portion of muscle mass divides into superficial and deep sections. The superficial section differentiates into extensor carpi ulnaris, extensor digitorum, and extensor digiti minimi, and is highly evolutionarily

conserved [23]. The deep section, which has undergone the most significant evolutionary variation, gives rise to the extensor indicis, abductor pollicis longus, and extensor pollicis longus and brevis [10]. These observations are consistent with the variations identified in the present case, although they do not address the bilateral versus unilateral nature of the anomalies.

Clinically, absence of the EI tendon results in significant consequences, as it is the tendon most commonly used for reconstruction of the EPL and abductor pollicis longus (AbPL) tendons [16, 20]. Spontaneous rupture of the EPL tendon, occurring most frequently in patients with rheumatoid arthritis but also secondary to direct trauma and distal radial fracture, results in decreased capacity for extension at the interphalangeal and metacarpophalangeal joints of the thumb [16, 20]. Tendon transfer of the EI is the current gold standard for efficacious EPL reconstruction, although extension deficits of the index finger, as well as loss of pinch strength, have been noted following EI resection [16]. Cases in which only one extensor tendon to the index finger can be located necessitate alternative sources of graft transfer, most commonly palmaris longus. Ultrasound, or other imaging techniques, are used to verify the presence of the EI muscle-tendon unit in preparation for surgical reconstruction [7, 21].

## CONCLUSIONS

This cadaveric case report documents bilateral absence of the EI muscle-tendon unit and bilateral presence of additional tendon slips arising from the ED muscle, running parallel to the ED index tendon, inserting on the second digit. We hypothesize that variations in upper limb musculoskeletal development resulted in the rare bilateral absence of the EI muscle-tendon unit and bilateral presence of an additional tendon slip to the second digit arising from ED muscle belly. To summarise, preservation of hand dynamics through surgical reconstruction requires anticipation of anatomical variations of the hand and verification of the presence of both index tendons in order to avoid potential significant complications.

## Acknowledgements

The authors acknowledge and gratefully thank the individual whose body and tissues were used in this study for the advancement of physician education and patient care.

**Conflict of interest:** None declared

## REFERENCES

1. Abdel-Hamid GA, El-Beshbishy RA, Abdel Aal IH. Anatomical variations of the hand extensors. *Folia Morphol.* 2013; 72(3): 249–257, doi: [10.5603/fm.2013.0040](https://doi.org/10.5603/fm.2013.0040), indexed in Pubmed: [24068687](https://pubmed.ncbi.nlm.nih.gov/24068687/).
2. Akita K, Nimura A. Bergman's Comprehensive Encyclopedia of Human Anatomic Variation. In: Tubbs RS, Shoja MM, Loukas M (eds.). *Forearm muscles*. Wiley Blackwell, New Jersey 2016: 298–314.
3. Arquez HF. An anatomical study of the musculus flexor digitorum brevis. *Int Arch Med.* 2017; 10, doi: [10.3823/2486](https://doi.org/10.3823/2486).
4. Biant LC. Pectoral girdle and Upper limb. In: *Gray's Anatomy: The Anatomical Basis of Clinical Practice*. Elsevier, New York 2016: 837–861.
5. Cauldwell EW, Anson BJ, Wright RR. The extensor indicis proprius muscle - a study of 263 consecutive specimens. *Q Bull Northwest Univ Med Sch.* 1943; 17(4): 267–279.
6. Celik S, Bilge O, Pinar Y, et al. The anatomical variations of the extensor tendons to the dorsum of the hand. *Clin Anat.* 2008; 21(7): 652–659, doi: [10.1002/ca.20710](https://doi.org/10.1002/ca.20710), indexed in Pubmed: [18792963](https://pubmed.ncbi.nlm.nih.gov/18792963/).
7. Dezfuli B, Taljanovic MS, Melville DM, et al. Accuracy of high-resolution ultrasonography in the detection of extensor tendon lacerations. *Ann Plast Surg.* 2016; 76(2): 187–192, doi: [10.1097/SAP.0000000000000524](https://doi.org/10.1097/SAP.0000000000000524), indexed in Pubmed: [26101990](https://pubmed.ncbi.nlm.nih.gov/26101990/).
8. El-Badawi MG, Butt MM, al-Zuhair AG, et al. Extensor tendons of the fingers: arrangement and variations — II. *Clin Anat.* 1995; 8(6): 391–398, doi: [10.1002/ca.980080604](https://doi.org/10.1002/ca.980080604), indexed in Pubmed: [8713158](https://pubmed.ncbi.nlm.nih.gov/8713158/).
9. Garbelotti JS, Yukio FT, Rodrigues PV, et al. Extensor indicis brevis Muscle: an Unusual Muscular Variant. *Int J Morphol.* 2012; 30(3): 1071–1073, doi: [10.4067/s0717-95022012000300050](https://doi.org/10.4067/s0717-95022012000300050).
10. Georgiev GP, Tubbs RS, Iliev A, et al. Extensor indicis proprius muscle and its variants together with the extensor digitorum brevis manus muscle: a common classification. Clinical significance in hand and reconstructive surgery. *Surg Radiol Anat.* 2018; 40(3): 271–280, doi: [10.1007/s00276-018-1981-9](https://doi.org/10.1007/s00276-018-1981-9), indexed in Pubmed: [29383419](https://pubmed.ncbi.nlm.nih.gov/29383419/).
11. Gonzalez M, Weinzwieg N, Kay T, et al. Anatomy of the extensor tendons to the index finger. *J Hand Surg.* 1996; 21(6): 988–991, doi: [10.1016/s0363-5023\(96\)80305-4](https://doi.org/10.1016/s0363-5023(96)80305-4).
12. Gonzalez M, Weinzwieg N, Kay T, et al. Anatomy of the extensor tendons to the index finger. *J Hand Surg.* 1996; 21(6): 988–991, doi: [10.1016/s0363-5023\(96\)80305-4](https://doi.org/10.1016/s0363-5023(96)80305-4).
13. Kitano K, Tada K, Shibata T, et al. Independent index extension after indicis proprius transfer: Excision of juncturae tendinum. *J Hand Surg.* 1996; 21(6): 992–996, doi: [10.1016/s0363-5023\(96\)80306-6](https://doi.org/10.1016/s0363-5023(96)80306-6).
14. Li J, Ren ZF. Bilateral extensor indicis brevis: a rare muscular variant. *Rom J Morphol Embryol.* 2012; 53(1): 185–187, indexed in Pubmed: [22395520](https://pubmed.ncbi.nlm.nih.gov/22395520/).
15. Li J, Ren ZF. Bilateral extensor medii proprius with split tendon of extensor indicis proprius, a rare anatomical variant. *Rom J Morphol Embryol.* 2013; 54(3): 639–641, indexed in Pubmed: [24068417](https://pubmed.ncbi.nlm.nih.gov/24068417/).
16. Matsumae G, Motomiya M, Iwasaki N. Failed reconstruction of the extensor pollicis longus in a patient with a major variation of the extensor indicis proprius tendon: a case report. *J Hand Surg Asian Pac Vol.* 2018; 23(1): 132–136, doi: [10.1142/S2424835518720062](https://doi.org/10.1142/S2424835518720062), indexed in Pubmed: [29409420](https://pubmed.ncbi.nlm.nih.gov/29409420/).
17. Nayak SR, Vadgaonkar R, Krishnamurthy A, et al. An anomalous muscle in the forearm extensor compartment. *Clinics (Sao Paulo).* 2009; 64(3): 262–263, doi: [10.1590/s1807-59322009000300019](https://doi.org/10.1590/s1807-59322009000300019), indexed in Pubmed: [19330255](https://pubmed.ncbi.nlm.nih.gov/19330255/).
18. Ogura T, Inoue H, Tanabe G. Anatomic and clinical studies of the extensor digitorum brevis manus. *J Hand Surg.* 1987; 12(1): 100–107, doi: [10.1016/s0363-5023\(87\)80171-5](https://doi.org/10.1016/s0363-5023(87)80171-5).
19. Ranade AV, Rai R, Prabhu LV, et al. Incidence of extensor digitorum brevis manus muscle. *Hand (N Y).* 2008; 3(4): 320–323, doi: [10.1007/s11552-008-9111-5](https://doi.org/10.1007/s11552-008-9111-5), indexed in Pubmed: [18780016](https://pubmed.ncbi.nlm.nih.gov/18780016/).
20. Schaller P, Baer W, Carl HD. Extensor indicis-transfer compared with palmaris longus transplantation in reconstruction of extensor pollicis longus tendon: a retrospective study. *Scand J Plast Reconstr Surg Hand Surg.* 2007; 41(1): 33–35, doi: [10.1080/02844310601070351](https://doi.org/10.1080/02844310601070351), indexed in Pubmed: [17484183](https://pubmed.ncbi.nlm.nih.gov/17484183/).
21. Taylor J, Casaletto JA. Absence of extensor indicis tendon complicating reconstruction of the extensor pollicis longus. *J Hand Surg Eur Vol.* 2017; 42(5): 528–529, doi: [10.1177/1753193416636609](https://doi.org/10.1177/1753193416636609), indexed in Pubmed: [26936748](https://pubmed.ncbi.nlm.nih.gov/26936748/).
22. Trivedi S, Siddiqui A, Sinha T, et al. Absence of extensor indicis: A rare anatomical variant. *Int J Biomed Res.* 2014; 5(1): 61, doi: [10.7439/ijbr.v5i1.442](https://doi.org/10.7439/ijbr.v5i1.442).
23. von Schroeder HP, Botte M, Gellman H. Anatomy of the juncturae tendinum of the hand. *J Hand Surg Am.* 1990; 15(4): 595–602, doi: [10.1016/s0363-5023\(09\)90021-1](https://doi.org/10.1016/s0363-5023(09)90021-1).
24. Yammine K. The prevalence of the extensor indicis tendon and its variants: a systematic review and meta-analysis. *Surg Radiol Anat.* 2015; 37(3): 247–254, doi: [10.1007/s00276-014-1352-0](https://doi.org/10.1007/s00276-014-1352-0), indexed in Pubmed: [25096501](https://pubmed.ncbi.nlm.nih.gov/25096501/).
25. Yoshida Y. Anatomical studies on the extensor pollicis et indicis accessorius muscle and the extensor indicis radialis muscle in Japanese. *Okajimas Folia Anat Jpn.* 1995; 71(6): 355–363, doi: [10.2535/ofaj1936.71.6\\_355](https://doi.org/10.2535/ofaj1936.71.6_355), indexed in Pubmed: [7739845](https://pubmed.ncbi.nlm.nih.gov/7739845/).
26. Zilber S, Oberlin C. Anatomical variations of the extensor tendons to the fingers over the dorsum of the hand: a study of 50 hands and a review of the literature. *Plast Reconstr Surg.* 2004; 113(1): 214–221, doi: [10.1097/01.PRS.0000091163.86851.9C](https://doi.org/10.1097/01.PRS.0000091163.86851.9C), indexed in Pubmed: [14707639](https://pubmed.ncbi.nlm.nih.gov/14707639/).

# Rare malformations associated with partial anomalous pulmonary venous return: a cadaveric case report

S. Silawal, T. Essing, C. Schaupp, G. Schulze-Tanzil

*Institute of Anatomy and Cell Biology, Paracelsus Medical University, Nuremberg, Germany*

[Received: 13 January 2021; Accepted: 11 February 2021; Early publication date: 1 March 2021]

*A unique partial anomalous pulmonary venous return in combination with other rare malformations such as annular pancreas and a persistent umbilical vein was discovered in a female Caucasian cadaver during an anatomical dissection at the Paracelsus Medical University in Nuremberg, Germany. The pulmonary anomaly comprised the aberrant left superior pulmonary vein connecting the superior lobe of the left lung with the left brachiocephalic vein resulting in a left to right shunt. An annular pancreas without any signs causing duodenal compression was additionally found. To complete the constellation of malformations, a persistent umbilical vein within the round ligament fissure of the liver was also observed, connecting to an inferior branch of the extrahepatic left ramus of the portal vein. This rare constellation of malformations has been illustrated and thoroughly discussed with the currently available literature to develop a hypothesis for the genetic and developmental background. (Folia Morphol 2022; 81, 2: 526–531)*

**Key words:** partial anomalous pulmonary venous return, patent umbilical vein, annular pancreas

## INTRODUCTION

Partial anomalous pulmonary venous return (PAPVR) is a cardiovascular congenital anomaly characterised by a partial alteration in the venous connection of the oxygenated blood of the pulmonary vein to the left atrium resulting in a left to right shunt. The venous drainage point of return of the partial anomalous pulmonary vein can vary in its site; occurring most frequently supracardial (63%), followed by the cardial (20%), mixed (11%) and infracardial (6%) variants [14]. In contrast to the total anomalous pulmonary venous return (TAPVR), which is a deadly anomaly, PAPVR does not necessarily demonstrate clinical symptoms. The actual prevalence could therefore be even higher than the reported 0.4–0.7% of

adults shown in autopsy cases [12]. Although the literature shows that right sided PAPVR is more frequent [1, 7, 21], a study with computed tomography images from 29 adults showed a connection of the superior left pulmonary vein into the left persistent vertical vein in 79% of their studied cases [11].

Partial anomalous pulmonary venous return often exists in combination with other multiple congenital anomalies [21]. An interesting clinical case report about PAPVR with persistent left superior vena cava, ‘bovine arch’ aortic branching, tracheal diverticulum, aberrant lung fissure and an annular pancreas (AP) has been published [17]. We introduce a similar constellation; however, in a cadaveric gross anatomy, where we could find PAPVR combined with other

---

Address for correspondence: Dr. S. Silawal, Institute of Anatomy and Cell Biology, Paracelsus Medical University, Prof.-Ernst Nathan Strasse 1, 90419 Nuremberg, Germany, e-mail: sandeep.silawal@pmu.ac.at

This article is available in open access under Creative Common Attribution-Non-Commercial-No Derivatives 4.0 International (CC BY-NC-ND 4.0) license, allowing to download articles and share them with others as long as they credit the authors and the publisher, but without permission to change them in any way or use them commercially.

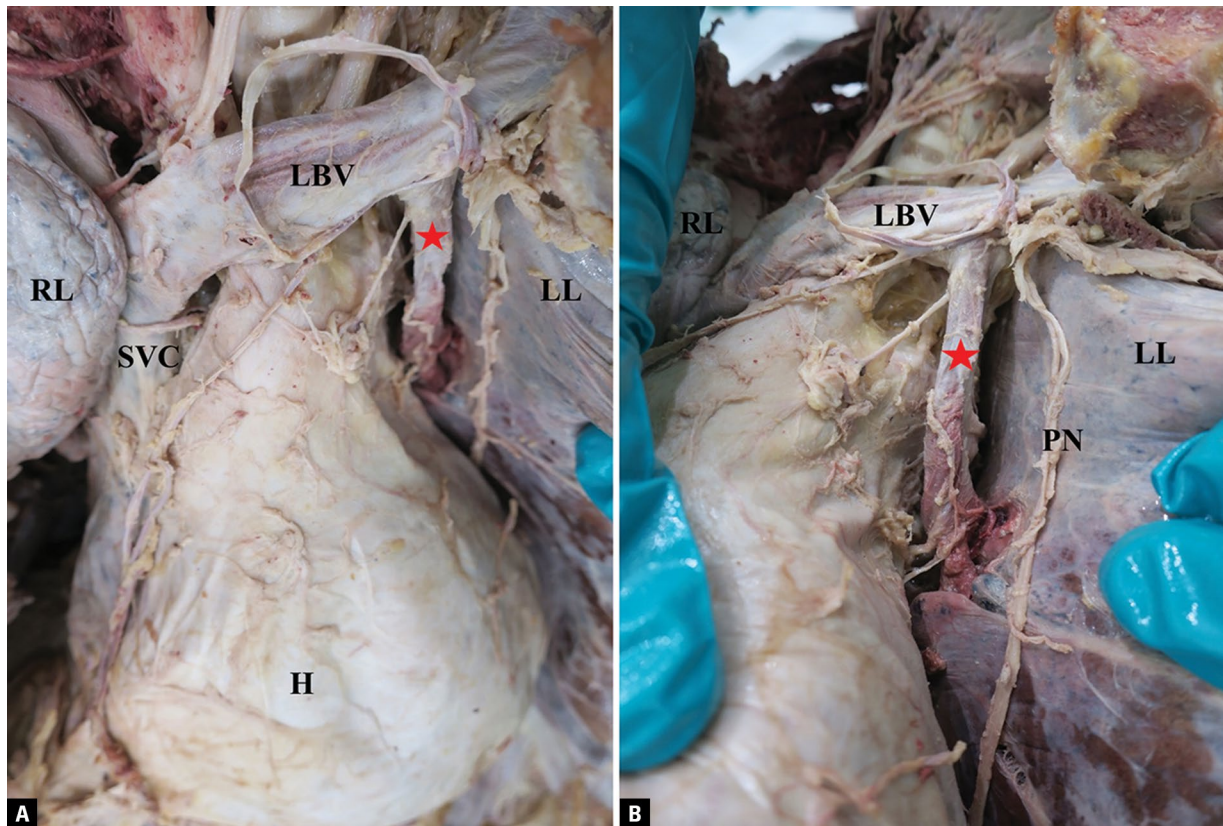


**Figure 1.** **A.** Anterior view on the mediastinum; **B.** Anterolateral view on the mediastinum; RL — right lung; LL — left lung; H — heart (covered by the parietal pericardium); LBV — left brachiocephalic vein; SVC — superior vena cava; PN — phrenic nerve; red star — left superior pulmonary vein with anomalous return.

multiple congenital anomalies (MCA) such as AP and patent umbilical vein (PUV) with connection to the left portal vein of the liver.

Annular pancreas is a congenital anomaly in which the pancreas either completely or partially encircles the descending portion of duodenum. This phenomenon can obstruct the gastrointestinal lumen, occasionally leading to duodenal stenosis [10].

This constellation will be discussed in detail with the available literature of comparable cases for specific genetic mutations being associated with the individual variations observed in the described case and an effort will be made to find a common ground to explain the coexistence of the MCA.

### CASE REPORT

The formalin-fixed cadaver of an 88-year-old female body donor came from the body donor system of the LMU, Munich, Germany. Photos were taken using a Canon Camera (G9 X, Tokyo, Japan) and measurements were taken using a digital calliper (Ovibell GmbH, Mühlheim, Germany). Haematoxylin

and eosin staining was performed in the Institute of Pathology, General Hospital Nuremberg to verify the observation. The histological image was taken using a DM1000 LED light microscope (Leica, Wetzlar, Germany). Literature research related to the anomalies was undertaken using Medline and Google Scholar by searching mesh terms for genetic mutations such as: partial anomalous, persistent right umbilical vein, annular pancreas and persistent umbilical vein.

### Aberrant pulmonary vein

The aberrant/displaced superior left pulmonary vein measuring 63 mm in length and 6.2 mm in diameter drained from the left superior lobe through the pulmonary hilum into the left brachiocephalic vein (Fig. 1A, B). The 37.3 mm long and 12.4 mm thick left brachiocephalic vein joined together with the right brachiocephalic vein to form the superior vena cava, finally draining into the right atrium. However, an additional venal tributary from the lowest portion (segment V) of the left superior lobe drained into the left inferior pulmonary vein from the inferior lobe of the left lung (Fig. 2A, B) entering together

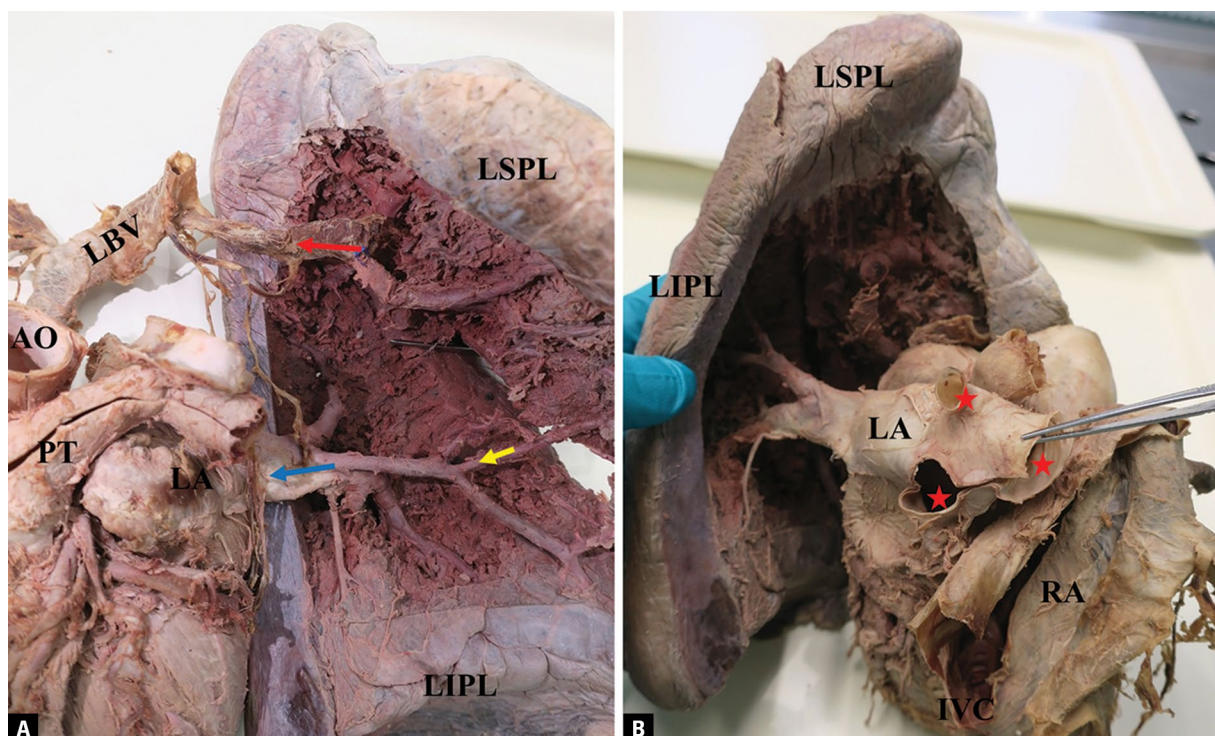


**Figure 2.** **A.** Anterior view after removal of pulmonary arteries, bronchial pathways and partially, of lung parenchyma on the mediastinal side of the left lung; **B.** Posterior view. The atrial wall between entrance of superior and inferior vein has been cut to get the view into the interior of the left atrium. Likewise, the atrial wall between entrance of superior vena cava and inferior vena cava has been cut to get the view into the interior of the right atrium; LIPL — left inferior pulmonary lobe; LSPL — left superior pulmonary lobe; LBV — left brachiocephalic vein; AO — aorta; PT — pulmonary trunk; LA — left atrium; RA — right atrium; IVC — inferior vena cava; red arrow — left superior pulmonary vein (*anomalous*); blue arrow — left inferior pulmonary vein (*regular*); yellow arrow — venal tributary from the lowest portion (segment V) of the left superior lobe draining into the left inferior pulmonary vein; red stars — right pulmonary veins after resection.

as a single left entrance into the left atrium. On the other side there were three separate entries, instead of two, into the left atrium from the three lobes of the right lung (Fig. 2B). The left and right lungs were of normal size and both possessed a regular oblique fissure.

Neither any irregularity in size of the heart chambers nor in any septation of the heart could be observed. The coronary sinus had no connection to the variant vein and was not enlarged.

#### Annular pancreas

The pancreas formed a complete circular ring surrounding the descending part of the duodenum (Fig. 3). The narrowest part of the pancreatic ring measured 8 mm and was located lateral on the right. The anterior part measured 17 mm and the posterior part was 13 mm. The duct system of the pancreas was regular. The common bile duct ended at the descending part of the duodenum just above the AP. It showed no sign of compression, neither of the duodenum nor the common bile duct.

#### Persistent umbilical vein and connection to the portal vein

The persistent umbilical vein had a lumen, which was < 1 mm with a very thick wall of 4 mm (Fig. 4A). Haematoxylin and eosin staining of this vein could verify this observation (Fig. 4B). Interestingly, a connection between this lumen structure and the inferior branch of the extra hepatic left portal vein running in the round ligament fissure of the liver was seen (Fig. 5). Histologically, the thick wall of the persistent umbilical vein consisted of several layers of smooth muscle cells. The inner and outermost layer contained more longitudinally aligned muscle cell bundles and the layer between them had a more oblique orientation. The lumen was lined by flattened cells like an endothelium (Fig. 4B).

#### DISCUSSION

Systematic analyses concerning the frequencies of aberrant pulmonary veins are rare. Among 140 lung resection surgery patients, 23 variations were

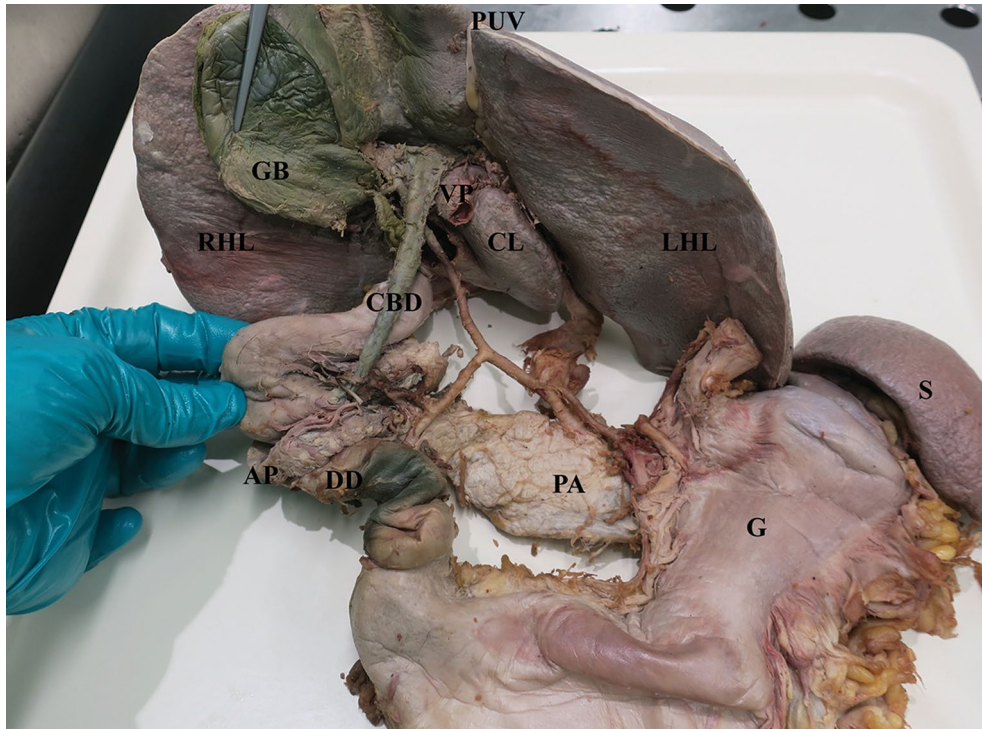


**Figure 3.** Dorsal view of the liver. Duodenum has been turned upside down to view common bile duct (CBD) in full length and its relationship to annular pancreas (AP); LHL — left hepatic lobe; RHL — right hepatic lobe; CL — caudate lobe; PA — pancreas; VP — portal vein; PUV — persistent umbilical vein; GB — gallbladder; DD — duodenum; G — gaster; S — spleen.

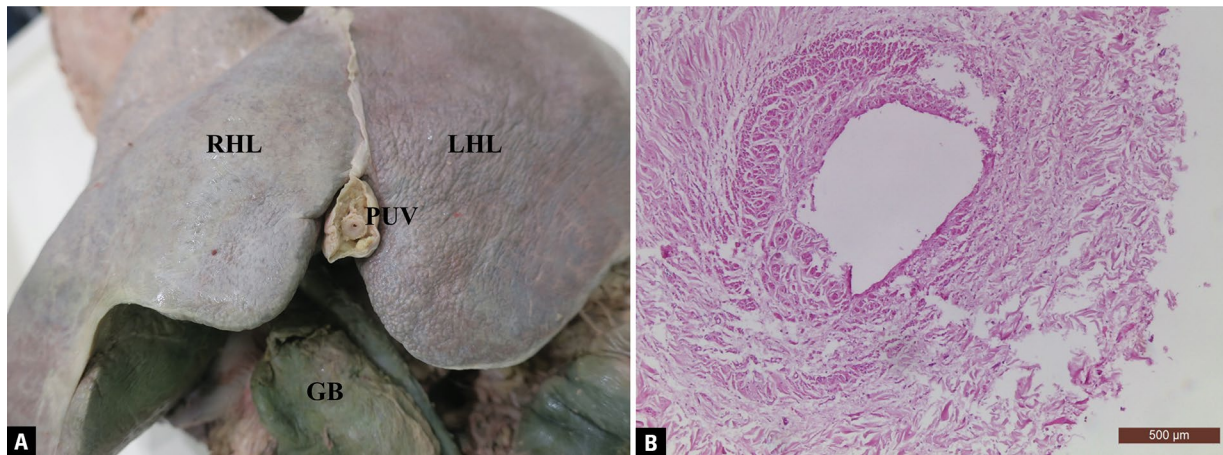


**Figure 4. A.** Inferior view of the liver; LHL — left hepatic lobe; RHL — left hepatic lobe; PUV — persistent umbilical vein; GB — gallbladder; **B.** Haematoxylin and eosin staining of persistent umbilical vein.

found [22], but no case was comparable with the variation presented here. According to the different types of PAPVR mentioned in the introduction section, our case report represents supracardial type where oxygenated blood from the left lung is directly released into the left brachiocephalic vein building a left to right shunt and subsequently collecting the

mixed blood into the superior cava vein. Many of the affected patients do not present evident clinical impairments under normal conditions. However, in circumstances such as thorax surgery this large diameter vein anomaly can present a high risk. Studies have reported that superior pulmonary vein [18] or even the left inferior pulmonary vein [2] joining the

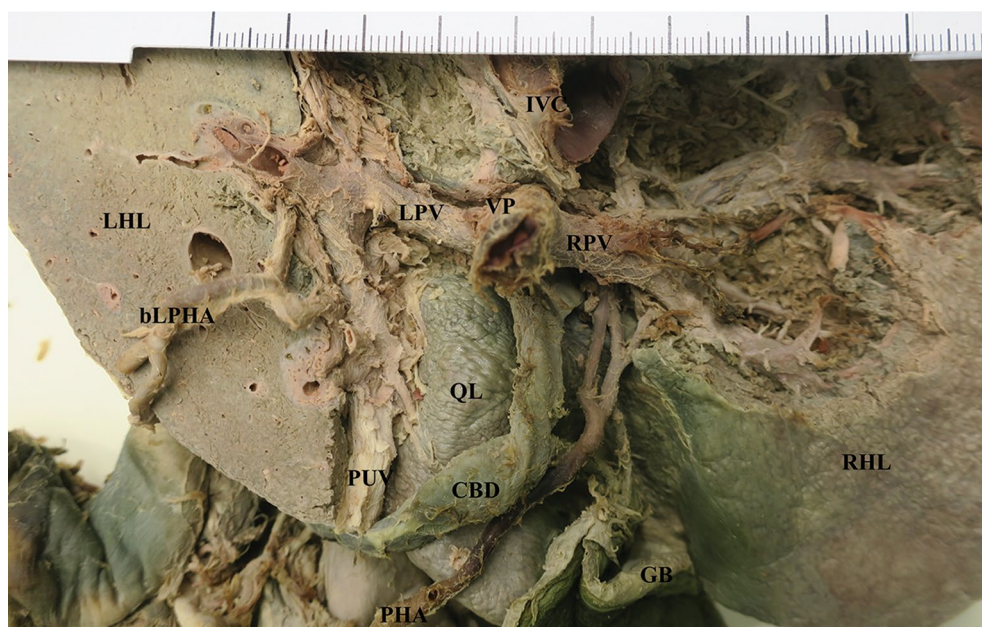


**Figure 5.** Dorsal view of the liver. Caudate lobe has been removed. Partial resection of segment II and III has been performed. Left proper hepatic artery has been cut and flipped aside; LHL — left hepatic lobe; RHL — right hepatic lobe; QL — quadrate lobe; PUV — persistent umbilical vein; GB — gallbladder; PHA — proper hepatic artery; bLPHA — branch of the left proper hepatic artery; RPV — right portal vein; LPV — left portal vein; VP — portal vein; IVC — inferior vena cava; CBD — common bile duct.

left brachiocephalic vein have been detected during clinical examination. Additional clinical relevance of this variation was observed during insertion of central venous catheter [5, 15]. The aforementioned anomalies have been associated with genetic mutations. However, only few candidate genes are known so far. A missense gene mutation of bone morphogenetic protein receptor II could be detected in a case of anomalous unilateral single pulmonary vein [16]. In addition, a phenylalanine-to-leucine substitution that adversely affects Semaphorin 3d has been identified as a putative crucial pulmonary venous patterning cue [6]. A more severe version of this anomaly is the TAPVR, which can be lethal if not corrected at an early stage. A genetic mutation in the centromeric region of chromosome 4, 4p13-q12 has been defined as a candidate for both familial and sporadic cases of TAPVR [4]. A family case of TAPVR has been reported, where a father who underwent surgical correction had 2 children with TAPVR. This supports the hypothesis of a genetic transfer pattern on the development of this anomaly [20].

Interestingly, rare variations including those of pulmonary veins are often combined with other MCA. A combination of AP with malformations of the lung [17] has already been described in a clinical setting. Even

though half of the cases are asymptomatic until the third to fifth decade [10], AP presents the risk of duodenal stenosis [23]. The sonic hedgehog signalling pathway has been implicated in the development of AP [8]. Specific involvement of sonic hedgehog in mouse embryonic lung development, growth and morphogenesis has already been proven [3, 9], but no association with the development of PAPVR has been confirmed yet. Also, chromosome 1p36 deletion syndrome has been implicated in the development of AP [19].

Additionally, a persistent umbilical vein was observed in our case report. The connection of the left umbilical vein into the left portal vein during the embryological development is common. A recent study observed that 56 out of 58 embryos of gestational age 5–7 weeks showed the left sided umbilical vein draining into the left portal vein, which usually closes postnatally [13]. The closing of the umbilical vein can either be due to obliteration or simply due to collapse of the vein. This patent umbilical vein can provide access to the liver for a hepatoportography as a superior approach to diagnosis in liver disease [24]. However, recanalization of the umbilical vein is also associated with cirrhotic or non-cirrhotic portal hypertension. In our case, no macroscopic alteration of the liver could be detected.

## CONCLUSIONS

Even though we could not prove a common genetic mutation for the constellation of the mentioned anomalies, we propose that genomic sequencing in clinical settings with this constellation of anomalies could possibly help to find the genetic common ground and provide an approach in understanding the aetiology. A regular collection of tissue sample before the fixation of the cadavers could make it possible to perform genome sequencing in case of such diagnosis. However, this review should also help to highlight the cadaveric approach to define the anomaly constellation and help surgeons, radiologists and other clinicians to consider the possibility of such a combination of anatomical variations in their setting.

## Acknowledgements

We are very thankful to the body donors for their contribution to the academic teaching and research field of anatomy. We would also like to thank the Institute of Pathology, General Hospital Nuremberg for performing the haematoxylin and eosin staining required for the study. Finally, special thanks to Ms. Laura Seidel for proofreading this article.

**Conflict of interest:** None declared

## REFERENCES

1. Ammash NM, Seward JB, Warnes CA, et al. Partial anomalous pulmonary venous connection: diagnosis by transesophageal echocardiography. *J Am Coll Cardiol.* 1997; 29(6): 1351–1358, doi: [10.1016/s0735-1097\(97\)82758-1](https://doi.org/10.1016/s0735-1097(97)82758-1), indexed in Pubmed: [9137235](https://pubmed.ncbi.nlm.nih.gov/9137235/).
2. Basalus MWZ, Said SAM, Stassen CM, et al. Clinical and diagnostic features of partially anomalous pulmonary venous connection in an adult female patient: a case report and review of the literature. *Neth Heart J.* 2011; 19(5): 256–258, doi: [10.1007/s12471-011-0101-9](https://doi.org/10.1007/s12471-011-0101-9), indexed in Pubmed: [21487753](https://pubmed.ncbi.nlm.nih.gov/21487753/).
3. Bellusci S, Furuta Y, Rush MG, et al. Involvement of Sonic hedgehog (Shh) in mouse embryonic lung growth and morphogenesis. *Development.* 1997; 124(1): 53–63, doi: [10.1242/dev.124.1.53](https://doi.org/10.1242/dev.124.1.53), indexed in Pubmed: [9006067](https://pubmed.ncbi.nlm.nih.gov/9006067/).
4. Bleyl S, Nelson L, Odelberg SJ, et al. A gene for familial total anomalous pulmonary venous return maps to chromosome 4p13-q12. *Am J Hum Genet.* 1995; 56(2): 408–415, indexed in Pubmed: [7847375](https://pubmed.ncbi.nlm.nih.gov/7847375/).
5. Chintu MR, Chinnappa S, Bhandari S. Aberrant positioning of a central venous dialysis catheter to reveal a left-sided partial anomalous pulmonary venous connection. *Vasc Health Risk Manag.* 2008; 4(5): 1141–1143, indexed in Pubmed: [19183765](https://pubmed.ncbi.nlm.nih.gov/19183765/).
6. Degenhardt K, Singh MK, Aghajanian H, et al. Semaphorin 3d signaling defects are associated with anomalous pulmonary venous connections. *Nat Med.* 2013; 19(6): 760–765, doi: [10.1038/nm.3185](https://doi.org/10.1038/nm.3185), indexed in Pubmed: [23685842](https://pubmed.ncbi.nlm.nih.gov/23685842/).
7. ElBardissi AW, Dearani JA, Suri RM, et al. Left-sided partial anomalous pulmonary venous connections. *Ann Thorac Surg.* 2008; 85(3): 1007–1014, doi: [10.1016/j.athoracsur.2007.11.038](https://doi.org/10.1016/j.athoracsur.2007.11.038), indexed in Pubmed: [18291189](https://pubmed.ncbi.nlm.nih.gov/18291189/).
8. Etienne D, John A, Menias CO, et al. Annular pancreas: a review of its molecular embryology, genetic basis and clinical considerations. *Ann Anat.* 2012; 194(5): 422–428, doi: [10.1016/j.aanat.2012.04.006](https://doi.org/10.1016/j.aanat.2012.04.006), indexed in Pubmed: [22694842](https://pubmed.ncbi.nlm.nih.gov/22694842/).
9. Fernandes-Silva H, Correia-Pinto J, Moura RS. Canonical sonic hedgehog signaling in early lung development. *J Dev Biol.* 2017; 5(1), doi: [10.3390/jdb5010003](https://doi.org/10.3390/jdb5010003), indexed in Pubmed: [29615561](https://pubmed.ncbi.nlm.nih.gov/29615561/).
10. Hamm M, Röttger P, Fiedler C. [Pancreas anulare as a rare differential diagnosis of duodenal stenosis in adulthood]. *Langenbecks Arch Chir.* 1997; 382(6): 307–310, doi: [10.1007/s004230050072](https://doi.org/10.1007/s004230050072), indexed in Pubmed: [9498201](https://pubmed.ncbi.nlm.nih.gov/9498201/).
11. Haramati LB, Moche IE, Rivera VT, et al. Computed tomography of partial anomalous pulmonary venous connection in adults. *J Comput Assist Tomogr.* 2003; 27(5): 743–749, doi: [10.1097/00004728-200309000-00011](https://doi.org/10.1097/00004728-200309000-00011), indexed in Pubmed: [14501365](https://pubmed.ncbi.nlm.nih.gov/14501365/).
12. Healey J. An anatomic survey of anomalous pulmonary veins: their clinical significance. *J Thorac Surg.* 1952; 23(5): 433–444, doi: [10.1016/s0096-5588\(20\)31117-x](https://doi.org/10.1016/s0096-5588(20)31117-x).
13. Kim JiH, Jin ZWu, Murakami G, et al. Persistent right umbilical vein: a study using serial sections of human embryos and fetuses. *Anat Cell Biol.* 2018; 51(3): 218–222, doi: [10.5115/acb.2018.51.3.218](https://doi.org/10.5115/acb.2018.51.3.218), indexed in Pubmed: [30310717](https://pubmed.ncbi.nlm.nih.gov/30310717/).
14. Kiseleva IP, Malsagov GU. Differential diagnosis of anomalous pulmonary venous return. A clinical-roentgenological study. *Cor Vasa.* 1984; 26(2): 140–146, indexed in Pubmed: [6734216](https://pubmed.ncbi.nlm.nih.gov/6734216/).
15. Knox S, Madruga M, Carlan SJ. Rare congenital aberrant left superior pulmonary vein discovered with central line placement in a patient with critical cardiorespiratory collapse. *Case Rep Pulmonol.* 2017; 2017: 8728904, doi: [10.1155/2017/8728904](https://doi.org/10.1155/2017/8728904), indexed in Pubmed: [29057135](https://pubmed.ncbi.nlm.nih.gov/29057135/).
16. Koyama K, Sano Go, Hata Y, et al. An anomalous unilateral single pulmonary vein associated with a bone morphogenetic protein receptor II gene mutation. *Intern Med.* 2014; 53(5): 461–466, doi: [10.2169/internalmedicine.53.9245](https://doi.org/10.2169/internalmedicine.53.9245), indexed in Pubmed: [24583436](https://pubmed.ncbi.nlm.nih.gov/24583436/).
17. Lapa T, Vedelago J, Kim H, et al. An unusual constellation of congenital malformations in a single patient including partial anomalous pulmonary venous return, persistent left superior vena cava, aberrant pulmonary fissure, anomalous aortic arch, tracheal diverticulum and annular pancreas. *BMJ Case Rep.* 2014; 2014, doi: [10.1136/bcr-2012-008014](https://doi.org/10.1136/bcr-2012-008014), indexed in Pubmed: [25362184](https://pubmed.ncbi.nlm.nih.gov/25362184/).
18. Low JYL, Nardini M, Zirafa C, et al. A surprise aberrant pulmonary vein. *Interact Cardiovasc Thorac Surg.* 2018; 26(2): 367, doi: [10.1093/icvts/ivx309](https://doi.org/10.1093/icvts/ivx309), indexed in Pubmed: [29049785](https://pubmed.ncbi.nlm.nih.gov/29049785/).
19. Minami K, Boshi H, Minami T, et al. 1p36 deletion syndrome with intestinal malrotation and annular pancreas. *Eur J Pediatr.* 2005; 164(3): 193–194, doi: [10.1007/s00431-004-1581-z](https://doi.org/10.1007/s00431-004-1581-z), indexed in Pubmed: [15717182](https://pubmed.ncbi.nlm.nih.gov/15717182/).
20. Raisher BD, Dowton SB, Grant JW. Father and two children with total anomalous pulmonary venous connection. *Am J Med Genet.* 1991; 40(1): 105–106, doi: [10.1002/ajmg.1320400122](https://doi.org/10.1002/ajmg.1320400122), indexed in Pubmed: [1887837](https://pubmed.ncbi.nlm.nih.gov/1887837/).
21. Snellen HA, van Ingen HC, Hoefsmit EC. Patterns of anomalous pulmonary venous drainage. *Circulation.* 1968; 38(1): 45–63, doi: [10.1161/01.cir.38.1.45](https://doi.org/10.1161/01.cir.38.1.45), indexed in Pubmed: [11712292](https://pubmed.ncbi.nlm.nih.gov/11712292/).
22. Subotich D, Mandarich D, Milisavljevic M, et al. Variations of pulmonary vessels: some practical implications for lung resections. *Clin Anat.* 2009; 22(6): 698–705, doi: [10.1002/ca.20834](https://doi.org/10.1002/ca.20834), indexed in Pubmed: [19637303](https://pubmed.ncbi.nlm.nih.gov/19637303/).
23. Whelan TJ, Hamilton GB. Annular pancreas. *Ann Surg.* 1957; 146(2): 252–262, doi: [10.1097/0000658-195708000-00015](https://doi.org/10.1097/0000658-195708000-00015), indexed in Pubmed: [13459275](https://pubmed.ncbi.nlm.nih.gov/13459275/).
24. White JJ, Skinner GB, MacLean LD. Hepatoportography via the umbilical vein: a superior approach to diagnosis in liver disease. *Can Med Assoc J.* 1966; 95(20): 997–1003, indexed in Pubmed: [5924949](https://pubmed.ncbi.nlm.nih.gov/5924949/).



<b>Structural and functional adaptation of the lingual papillae of the Egyptian fruit bat (<i>Rousettus aegyptiacus</i>): specific adaptive feeding strategies</b> .....	400
R.M. Kandyel, M.M.A. Abumandour, S.F. Mahmoud, M. Shukry, N. Madkour, A. El-Mansi, F.A. Farrag	
<b>Histological analysis of spermatogenesis and the germ cell seasonal development within the testis of domesticated tree shrews (<i>Tupaia belangeri chinensis</i>)</b> .....	412
J. Tang, G. He, Y. Yang, Q. Li, Y. He, C. Yu, L. Luo	
<b>Comparing effects of L-carnitine and sildenafil citrate on histopathologic recovery from sciatic nerve crush injury in female albino rats</b> .....	421
O.I. Zedan, M.A. Bashandy	
<b>The morphologic analysis of a not well-known anatomical structure's calcifications (Bochdalek's flower basket calcifications)</b> .....	435
E. Doğan, C. Elibol	
<b>Inferior oblique muscle of the eye: its foetal development with special reference to understanding of the frequent variants in adults</b> .....	442
Z.W. Jin, S. Umeki, Y. Takeuchi, M. Yamamoto, G. Murakami, S. Abe, J.F. Rodríguez-Vázquez	
<b>Morphological variability of the fibularis tertius tendon in human fetuses</b> .....	451
P. Karauda, F. Paulsen, M. Polgaj, R. Diogo, Ł. Olewnik	
<b>Relationship between maxillary central incisors and incisive canal: a cone-beam computed tomography study</b> .....	458
A.I. Linjawi, H.Y.A. Marghalani	
<b>Relationship between mandibular symphysis dimensions and skeletal pattern in adults</b> .....	464
H.Y.A. Marghalani, G. Guan, P. Hyun, S. Tabbaa, A.I. Linjawi, T. Al-Jewair	
<b>The influence of mandibular divergence on facial soft tissue thickness in class I patients: a cephalometric study</b> .....	472
T.M. Perović, M. Blažej, I. Jovanović	
<b>Assessment of radiographic morphology of mandibular condyles: a radiographic study</b> .....	481
A.H. Shaikh, S. Ahmed, A.R. Ahmed, G. Das, M. Taqi, S. Nisar, O. Khan	
<b>Assessment of morphological changes degree on the articular surfaces of the temporomandibular joints on the historical skeleton material</b> .....	487
A. Stangret, I. Teul	
<b>A gross anatomical study of the styloid proces of the temporal bone in Japanese cadavers</b> .....	493
S. Tanaka, H. Terayama, Y. Miyaki, D. Kiyoshima, N. Qu, K. Umemoto, O. Tanaka, M. Naito, K. Sakabe	
<b>Correlation of morphological and radiological characteristics of degenerative disc disease in lumbar spine: a cadaveric study</b> .....	503
P.A. Pękala, D. Tattera, K. Krupa, M. Paziewski, W. Wojciechowski, T. Konopka, J.A. Walocha, K.A. Tomaszewski	
<b>CASE REPORTS</b>	
<b>Fenestration of the vertebrobasilar junction detected with multidetector computed tomography angiography</b> .....	510
B.R. Omotoso, R. Harrichandparsad, I.G. Moodley, K.S. Satyapal, L. Lazarus	
<b>A novel accessory muscle in the flexor compartment of anterior forearm inserting into the tenosynovium of the flexor pollicis longus</b> .....	515
A. Gurvich, N. Shridhar, A. Felman, M. Shi, A. Pinkas, S.A. Downie, P.L. Mishall	
<b>Pointing in a different direction: a case of bilateral absence of extensor indicis</b> .....	520
A. Ma, J. Kim, C.E. Miller, T.L. Mustapich, J.P. Abraham, S.A. Downie, P.L. Mishall	
<b>Rare malformations associated with partial anomalous pulmonary venous return: a cadaveric case report</b> .....	526
S. Silawal, T. Essing, C. Schaupp, G. Schulze-Tanzil	

## CONTENTS

### ORIGINAL ARTICLES

- Identification of hepatosensitive region and their neural connections in the hippocampus of rats**.....261  
Z. Cheng, R. Wei, N. Cao, Z. Li, M. Li, M. Liu, L. Zhu, C. Xia
- The influence of functional pinealectomy and exogenous melatonin application on healing of a burr hole in adult rat calvaria: a histological and immunohistochemical study** .....271  
H.K. Basaloglu, M. Turgut, C. Şirin, Y. Uyanıkgil, B. Demirci, E.O. Cetin
- N-acetylcysteine protects against cuprizone-induced demyelination: histological and immunohistochemical study**.....280  
S.H. El Sharouny, M.H. Shaaban, R.M. Elsayed, A.W. Tahef, M.K. Abd ElWahed
- Volumetric measurements of the subcortical structures of healthy adult brains in the Turkish population** .....294  
H. Soysal, N. Acer, M. Özdemir, Ö. Eraslan
- Evaluation of olfactory bulb volume and olfactory sulcus depth development with 3 Tesla magnetic resonance imaging in childhood**.....307  
B. Güney, N. Çullu, M.Y. Özdemir
- The evaluation of cerebral venous normal anatomy and variations by phase-contrast cranial magnetic resonance venography** .....314  
E. Doğan, M. Apaydın
- Extracranial guiding structures for navigation to specific topographical sectors of the equine neopallium: an anatomical investigation performing three-dimensional distance measurements in adult warm-blooded horses**.....324  
F. Heun, L. Böing, J. Theunert, H. Gasse
- Arterial hypertension and remodelling of the right ventricle** .....336  
A. Kosiński, G.M. Piwko, R. Kamiński, E. Nowicka, A. Kaczyńska, M. Zajączkowski, K. Czerwicz, M. Gleinert-Rożek, K. Karnecki, T. Gos
- Venous drainage of the heart of the red fox (*Vulpes vulpes*)** .....343  
Y. Akbulut, G. Kirbaş Doğan, İ. Takcı, S. Dalga, E.E. Erkiş, E. Uzlu
- The evaluation of morphology of renal pelvicalyceal system's and infundibulopelvic anatomy of kidney's lower pole in post-mortem series** .....350  
R. Çiçek, G. Dündar, K. Gökçen, G. Gökçe, E.Y. Gültekin
- Anatomical variations of the hepatic artery: a closer view of rare unclassified variants** .....359  
A. Imam, C. Karatas, N. Mecit, A. Durur Karakaya, T. Yildirimoglu, M. Kalayoglu, T. Kanmaz
- Hexafurcated coeliac trunks, trifurcated common hepatic artery, and a new variant of the arc of Bühler** .....365  
B.A. Manta, M.C. Rusu, A.M. Jianu, A.C. Ilie
- Topographic location and branching pattern of the superior mesenteric artery with its clinical relevance: a cadaveric study** .....372  
S. Nigah, A. Patra, S. Chumbar, P. Chaudhary
- Glutamate receptor antagonist suppresses the activation of nesfatin-1 neurons following refeeding or glucose administration** .....379  
S. Serter Kocoglu, C. Oy, Z. Halk, C. Cakır, Z. Minbay, O. Eyigor
- The effect of hyperglycaemia on the macrophages in the cell culture** .....387  
E.R. Megawati, N. Meutia, L.D. Lubis
- Morphological structure of the tongue of the European badger (*Meles meles*)** .....394  
A. Haligur, S. Ozkadif, A. Alan, M. Haligur



INDEXED in: BIOSIS Previews, CAS, CINAHL, CrossRef, Dental Abstracts, EBSCO, Elsevier BIOBASE, EMBIOLOGY, FMJ, Google Scholar, Index Copernicus (160.66), Index Medicus/MEDLINE, Index Scholar, Ministry of Science and Higher Education (70), NCBI/National Center for Biotechnology Information, Polish Medical Bibliography, Scopus, SJR, Thomson Reuters, Thomson Scientific Products — Biological Abstracts, Ulrich's Periodicals Directory, Veterinary Bulletin, WorldCat and Zoological Record.

Cover picture: Type B: two arterial pedicles. Middle colic artery (MCA) and right colic artery (RCA) arising as a common stem (CS). Arrows showing the formation of marginal artery of Drumond by anastomoses among the branches of ileocolic artery, RCA and MCA (specimen no: 15L). For details see: Nigah et al., *Folia Morphol* 2022; 81, 2: 372–378.